João Miguel Sanches
Andrew F. Laine · Jasjit S. Suri *Editors*

Ultrasound Imaging

Advances and Applications

Springer

Ultrasound Imaging

João Miguel Sanches • Andrew F. Laine
Jasjit S. Suri
Editors

Ultrasound Imaging

Advances and Applications

Springer

Editors
João Miguel Sanches
Department of Bioengineering
Institute for Systems and Robotics
Instituto Superior Técnico
Technical University of Lisbon
Lisboa
Portugal
jmrs@ist.utl.pt

Jasjit S. Suri
Biomedical Technologies, Inc.
Denver, CO, USA
and
Idaho State University (Affiliated)
Pocatello, ID, USA
jsuri@comcast.net

Andrew F. Laine
Department of Biomedical Engineering
Columbia University
New York
USA

ISBN 978-1-4614-1179-6 e-ISBN 978-1-4614-1180-2
DOI 10.1007/978-1-4614-1180-2
Springer New York Dordrecht Heidelberg London

Library of Congress Control Number: 2011939302

Preface

Diagnostic and therapeutic Ultrasound has recently taken an explosive growth for better safer, economic, mobile and high quality healthcare. This technology is very appealing for medical applications because it is non-ionizing, non-invasive and is available in most of the medical and clinical facilities. Its low cost, when compared with other medical image modalities, makes it one of the preferred tools for medical monitoring, follow-up and diagnosis. Besides the traditional fields of cardiology and obstetrics, where it is extensively used for long time, it has become also very useful in the diagnosis of diseases of the prostate, liver and coronaries and carotids atherosclerosis.

However, Ultrasound images present poor quality, very low signal to noise ratio and a lot of artifacts. The extraction of useful information from Ultrasound data for diagnosis is a challenge task that makes this medical image modality a very active field of research. The difficulties are being overcome and novel and advanced methods are being proposed for detection, characterization and segmentation of abnormalities in several organs. In fact, Ultrasound application range is vast, covering almost all organs, including the brain where *Transcranial Doppler* (TCD) Ultrasound is very important to assess the brain vasculature.

This book presents some of the recent advances in Ultrasound imaging technology covering several organs and techniques in a *Biomedical Engineering* (BME) perspective. The focus of the book is in the algorithms, methodologies and systems developed by multidisciplinary research teams of engineers and physicians for *Computer-Aided Diagnosis* (CAD) purposes.

Cardiovascular and cancer, the most common life-threatening diseases in western countries, are two of the most important topics focused in the book. However, other advanced issues are also presented such as *Intravascular Ultrasound* (IVUS), 3D and 4D Ultrasound and Ultrasound in *Computer-Aided Surgery* (CAS). Some chapters are direct contributions from medical research groups where Ultrasound has also received great attention in the last decade. By this, new techniques based on Ultrasound were introduced in the clinical practice for diagnosis and therapeutics, mainly in hospital facilities.

Main Feature of the Book

The book contains 14 chapters distributed by 3 sections. It covers a wide range of topics from the physics and statistics associated with the Ultrasound data, in a signal processing point of view, up to high level application tools for CAD based on Ultrasound.

Section 1: Image Formation and Preprocessing

In this section the image formation process is addressed and new statistical models describing the ultrasonic signal are proposed. Reduction of Ultrasound noise, called de-speckling, and textural characterization of tissues are considered.

Section 2: Ultrasound Atherosclerotic Plaque Imaging

Here, the important problem of atherosclerotic plaque characterization is addressed. Methods to assess the severity of the disease are described, such as measuring the *Intima/ Media Thickness* (IMT), as well as new scores to quantify the risk of vascular accident.

Section 3: Advanced Applications

This section covers a wide range of applications involving morphological and textural segmentation of structures from ultrasound images. Detection and characterization of focal lesions in the thyroid, breast and prostate and textural characterization of diffuse diseases of the liver are the main topics.

Contents

Contributors

Al-Nashash, Hasan American University of Sharjah, UAE, hnashash@aus.edu

Angelini, Elsa Associate Professor of Computer Science: Image & Signal Processing, Telecom ParisTech, 46 rue Barrault, 75013 Paris, France, elsa.angelini@telecom-paristech.fr

Balocco, Simone Computer Vision Center, Campus UAB, Edifici O, Bellaterra, Spain

University of Barcelona, Gran Via de Les Cortes Catalanes, 585, 08007 Barcelona, Spain, balocco.simone@gmail.com

Carlier, Stephane G. UZ Brussel, Department of Cardiology, Brussels, Belgium, sgcarlier@hotmail.com

Ciompi, Francesco Computer Vision Center, Campus UAB, Edifici O, Bellaterra, Spain

University of Barcelona, Gran Via de Les Cortes Catalanes, 585, 08007 Barcelona, Spain, fciompi@maia.ub.es

Duan, Qi National Institute of Neurological Disorders and Stroke, National Institutes of Health, 10 Center Drive, Building 10, Room B1D728, MSC 1065, Bethesda, MD 20892-1065, USA, Qi.Duan@nih.gov

Fernandes e Fernandes, José Instituto Cardiovascular de Lisboa and Faculty of Medicine, University of Lisbon, Portugal, jff@me.com

Fernandes e Fernandes, Ruy Instituto Cardiovascular de Lisboa and Faculty of Medicine, University of Lisbon, Portugal, ruyfernandes@mac.com

Ferré, Josepa Mauri Hospital universitari Germans Trias i Pujol, Carretera de Canyet s/n. 08916 Badalona, Spain, jmauri.germanstrias@gencat.cat

Gatta, Carlo Computer Vision Center, Campus UAB, Edifici O, Bellaterra, Spain

University of Barcelona, Gran Via de Les Cortes Catalanes, 585, 08007 Barcelona, Spain, cgatta@cvc.uab.es

Gonçalves, Isabel Department of Clinical Sciences, Experimental Cardiovascular Research Unit, Lund University, Malmo University Hospital, Malmo, Sweden, mgoncalvesadv@mail.telepac.pt

Katouzian, Amin Heffner Biomedical Imaging Lab, Biomedical Engineering Department, Columbia University, 1210 Amsterdam Ave., 373 Eng. Terrace, New York, NY 10027, amin.katouzian@cs.tum.edu

Konofagou, Elisa Associate Professor of Biomedical Engineering and Radiology, 351 Engineering Terrace, 1210 Amsterdam Avenue, 8904 New York, NY 10027, ek2191@columbia.edu

Laine, Andrew F. Vice-Chair, Professor of Biomedical Engineering and Radiology (Physics), 351 Engineering Terrace MC-8904, Biomedical Engineering Department, 1210 Amsterdam Avenue, Columbia University, MC-8904 New York, NY 10027, laine@columbia.edu

Loizou, Christos P. Department of Computer Science, School of Sciences, Intercollege, 92 Ayias Phylaxeos Str., P.O. Box 51604, CY-3507, Limassol, Cyprus, loizou.christos@ucy.ac.cy

Marinho, Rui Tato Liver Unit, Department of Gastroenterology and Hepatology, Hospital de Santa Maria, Medical School of Lisbon, Lisbon, Portugal, rui.marinho@mail.telepac.pt

Meiburger, Kristen M. Biolab, Department of Electronics, Politecnico di Torino, Corso Duca degli Abruzzi, 24, 10129 Torino, Italy, kristen.meiburger@polito.it

Molinari, Filippo Biolab, Department of Electronics, Politecnico di Torino, Corso Duca degli Abruzzi, 24, 10129 Torino, Italy, filippo.molinari@polito.it

Nicolaides, Andrew Vascular Screening and Diagnostic Centre, London, UK

Department of Biological Sciences, University of Cyprus, Nicosia, Cyprus, anicolaides1@gmail.com

Pantziaris, Marios Cyprus Institute of Neurology and Genetics, Nicosia, Cyprus, pantzari@cing.ac.cy

Pareek, Gyan Division of Urology, Section of Minimally Invasive Urologic Surgery, The Warren Alpert Medical School of Brown University, Rhode Island Hospital, 2 Dudley Street, Suite 174, Providence, RI 02905, USA, gyan_pareek@brown.edu

Patel, Sutchin R. Division of Urology, Section of Minimally Invasive Urologic Surgery, The Warren Alpert Medical School of Brown University, Rhode Island Hospital, 2 Dudley Street, Suite 174, Providence, RI 02905, USA, sutchin_patel@yahoo.com

Pattichis, Constantinos S. Department of Computer Science, University of Cyprus, Nicosia, Cyprus, pattichi@ucy.ac.cy

Pedro, Luís Mendes Instituto Cardiovascular de Lisboa and Faculty of Medicine, University of Lisbon, Portugal, lmendespedro@clix.pt

Pujol, Oriol Computer Vision Center, Campus UAB, Edifici O, Bellaterra, Spain

University of Barcelona, Gran Via de Les Cortes Catalanes, 585, 08007 Barcelona, Spain, oriol@maia.ub.es

Qaddoumi, Nasser N. American University of Sharjah, UAE, nqaddoumi@aus.edu

Radeva, Petia Computer Vision Center, Campus UAB, Edifici O, Bellaterra, Spain

University of Barcelona, Gran Via de Les Cortes Catalanes, 585, 08007 Barcelona, Spain, petia@cvc.uab.es

Ribeiro, Ricardo Institute for Systems and Robotics and Instituto Superior Tócnico/Technical University of Lisbon, Lisbon, Portugal

Escola Superior de Tecnologia da Saúde de Lisboa, Lisbon, Portugal, ricardo.ribeiro@estesl.ipl.pt

Sanches, João Miguel Institute for Systems and Robotics, Department of Bioengineering from the Instituto Superior Técnico/Technical University of Lisbon, Portugal, jmrs@ist.utl.pt

Seabra, José Institute for Systems and Robotics, Department of Bioengineering from the Instituto Superior Técnico/Technical University of Lisbon, Portugal, mail2jseabra@gmail.com

Sturm, Bernhard Manager, Signal and Image Processing, Volcano Corporation, 2870 Kilgore Road, Rancho Cordova, bsturm@volcanocorp.com

Suri, Jasjit S. Biomedical Technologies, Inc., Denver, CO, USA

Idaho State University (Affiliated), Pocatello, ID, USA, jsuri@comcast.net

Zeng, Guang MBF Bioscience Inc. Williston, VT, USA, gzeng@clemson.edu

Part I
Image Formation and Preprocessing

RF Ultrasound Estimation from B-Mode Images

José Seabra and João Miguel Sanches

Abstract This chapter describes a method to estimate/recover the ultrasound RF envelope signal from the observed B-mode images by taking into account the main operations usually performed by the ultrasound scanner in the acquisition process.

The proposed method assumes a Rayleigh distribution for the RF signal and a nonlinear logarithmic law, depending on unknown parameters, to model the compression procedure performed by the scanner used to improve the visualization of the data.

The goal of the proposed method is to estimate the parameters of the compression law, depending on the specific brightness and contrast adjustments performed by the operator during the acquisition process, in order to revert the process.

The method provides an accurate observation model which allows to design robust and effective despeckling/reconstruction methods for morphological and textural analysis of Ultrasound data to be used in *Computer Aided Dagnosis* (CAD) applications.

Numerous simulations with synthetic and real data, acquired under different conditions and from different tissues, show the robustness of the method and the validity of the adopted observation model to describe the acquisition process implemented in the conventional ultrasound scanners.

1 Introduction

Ultrasound statistical-based image processing for denoising, segmentation, and tissue characterization is an attractive field of research nowadays [1–3] and may positively influence some diagnostic decisions in the near future.

J. Seabra (✉) • J.M. Sanches
Institute for Systems and Robotics, Department of Bioengineering from the Instituto Superior Técnico/Technical University of Lisbon, Portugal
e-mail: mail2jseabra@gmail.com; jmrs@ist.utl.pt

J.M. Sanches et al. (eds.), *Ultrasound Imaging: Advances and Applications*,
DOI 10.1007/978-1-4614-1180-2_1, © Springer Science+Business Media, LLC 2012

It is widely recognized that speckle in B-mode Ultrasound (BUS) images arises from the coherent interaction of random scatterers within a resolution cell when a certain anatomical region is scanned. The common model for speckle formation assumes a large number of scatterers where the sum of signals may be formulated according to a typical phasors random walk process [4]. This condition, known as fully developed speckle, determines Rayleigh statistics for the *Envelope Radio-Frequency* (ERF) data [5]. In addition, different nonlinear processing operators are used to improve the visualization of the displayed image, here termed B-mode image. In particular, the amplitude of the ERF signal is logarithmically compressed and nonlinearly processed so that a larger dynamic range of weak to strong echoes can be represented in the same image.

The compressed data, typically acquired in a polar grid, is in turn interpolated and down-sampled in order to convert it to a Cartesian grid that is more appropriated for visualization in the rectangular monitors of the scanners. Finally, in a clinical setting, physicians typically adjust other parameters such as brightness and contrast to improve image visualization.

Many research work has been developed for speckle reduction aiming at providing clearer images for visualization [6]. However, very few approaches either focusing on speckle reduction or tissue classification take into account the pre-processing operations used to create the BUS images [7, 8]. Studies based on image processing from BUS images naturally need to follow a rigorous acquisition protocol, otherwise results will be non-reproducible and non-comparable since they will depend on the kind of ultrasound equipment and on each specific operating conditions. To avoid these difficulties some researchers [9–11] use the RF signal extracted directly from the ultrasound machine. However, this kind of data is not usually available at the scanners and is only provided for research purposes. In fact, besides the previously referred transformations of re-sampling, coordinate transformation, and logarithmic compression (cf. Fig. 1), the B-mode observed images are the result of other proprietary nonlinear mappings specific of each scanner that is usually not known and not documented .

In this chapter we show that, despite the lack of knowledge about the complete processing operations performed in the scanner, it is possible to revert the compression operation and compensate for the contrast and brightness adjustments performed by the operator during the exam. The interpolation is also addressed. The estimated *Log-Compression Law* (LCL) is able to provide an image more compatible with the physics of the image formation process than the B-mode one that may be used to design more accurate and effective denoised algorithms.

The remainder of this chapter is organized as follows. In Sect. 2 it is made a review of the most relevant work published about ultrasound image decompression and estimation of operating settings over the last years. Section 3 formulates the *Log-Compression* model and describes the statistics associated with the compressed image. In addition, simulations of the most significant operations affecting the statistical properties of the original data are shown and some observations are drawn about the way the shape of the distributions are affected. Subsequently, Sect. 4 details the method to estimate the parameters of the compression law,

specifically the contrast ($\hat{a}$) and brightness ($\hat{b}$) parameters. Section 5 first tests the effectiveness of estimating the decompression parameters with the proposed method using synthetic ultrasound data. To further investigate how realistic the proposed model is, the decompression method is applied to a real BUS image, from which the raw data is known, and comparison between original and estimated data is made.

The robustness of the decompression method is also evaluated using real images acquired under different operating conditions and a detailed interpretation of the obtained results is performed. Finally, *Goodness of Fit* (GoF) [12] tests are conducted in estimated ERF images to sustain the hypothesis that most envelope RF data can be well modeled by Rayleigh statistics. Section 6 concludes the study about decompression and envelope RF estimation from BUS data.

2 Related Work

A considerable amount of work dedicated to speckle suppression and tissue characterization relies on accurate statistical models for RF data. Such models albeit being ideally and robustly tailored to describe the envelope data in different conditions throughout the image, are not feasible and practical because RF data is usually not available. Thus, there is a need to develop realistic observation models that incorporate the most significant nonlinear processing operations affecting the envelope data, when only BUS images are provided. In order to compute the RF intensity signal it becomes crucial to (1) explain the statistics of the compressed signal and (2) invert the logarithmic compression and other nonlinear signal processing performed by the ultrasound machine. Commercial ultrasound scanners perform a set of operations on the RF signal, e.g., log-compression and interpolation [13], that change the statistical distribution of the complex raw RF signal which is no longer *Circular Symmetric Complex Gaussian* (CSCG) [14] and, therefore, the Rayleigh statistics of the ERF signal are no longer valid.

Seminal work conducted in [7, 15, 16] have addressed the analytic study of log compressed Rayleigh signals in medical ultrasound images. From thereon, several decompression strategies were developed aiming at estimating some of the nonlinear processing parameters [17–19] or providing an estimate of the envelope RF data [8, 20, 21]. In order to compute the ERF intensity signal, the logarithmic compression and other nonlinear operations must be inverted. A common model for the compression law used in the literature is the following

$$I_{\text{BUS}} = a \log(I_{\text{ERF}}) + b, \tag{1}$$

where a and b are unknown parameters. The work developed in [20] demonstrated that such mapping is able to approximately invert the compression algorithms employed by a number of different ultrasound machine manufacturers, given that the parameters are originally known. The additive parameter, b, does not affect the shape

of the statistics used to speckle because it only shifts the distribution function which does not happen with the gain parameter a. The study developed by Crawford et al. [20] proposed a systematic method to compensate for nonlinear amplification based on several measurements based on a calibrated phantom, while the study reported by Kaplan et al. [15] requires accessing the data before processing which is not feasible in most commercial machines.

The work from Prager et al. [8] introduced the fractional moments iterative algorithm for recovering the envelope intensity signal from B-Mode data using speckle patches. In such patches, where fully developed speckle holds, the envelope intensity signal, $\mathbf{Y}_p$, can be estimated by inverting the compression mapping,

$$\mathbf{Y}_p = \exp\left(\frac{\mathbf{Z}_p}{a}\right), \tag{2}$$

where $\mathbf{Z}_p$ is the B-Mode intensity on a given patch, p. According to [5], $\mathbf{Y}_p$ follows approximately an exponential distribution,

$$p(\mathbf{Y}_p) = \frac{1}{2\sigma^2}\exp\left(\frac{-\mathbf{Y}_p}{2\sigma^2}\right), \tag{3}$$

where the nth order moment is given by [22],

$$\langle \mathbf{Y}_p^n \rangle = (2\sigma^2)^n \Gamma(n+1) = \langle \mathbf{Y}_p \rangle^n \Gamma(n+1), \tag{4}$$

where $\Gamma(n)$ is the Gamma function. Therefore, the normalized moments are,

$$\frac{\langle \mathbf{Y}_p^n \rangle}{\langle \mathbf{Y}_p \rangle^n} = \Gamma(n+1). \tag{5}$$

This approach [8] compares the measured normalized moments on known speckle patches, $\mathbf{Y}_p$, with the theoretical expected values for an exponential distribution. The optimal value of the contrast parameter, a, can then be found by minimizing the difference between these two set of values. This algorithm produces similar results to the faster approach proposed in [15] for pure logarithmic compression, but also works in the presence of nonlinear mapping where the Kaplan [15] formula does not apply.

A more recent work presented by Marques et al. [21] and used in a 3D US reconstruction problem enables to model the nonlinear compression considering that the ERF data is Rayleigh distributed. The estimation of the log compression parameters is simultaneously performed with the image reconstruction procedure by optimizing the same objective function (PDF of the unknown parameters). Such parameters are obtained by considering the theoretical expressions for the mean and standard deviation of the Fisher–Tippet distribution [22] early demonstrated to be a feasible model for the compressed data [7].

Although the estimator of b has shown to be biased, this work presented promising results particularly in terms of image reconstruction. It has been shown that the reconstruction algorithm performs better when compensation is considered. The estimated images and profiles obtained by compensating the log compressed images are sharper, presenting a larger dynamic range, and the anatomical details are more clearly visible when compared with those obtained assuming no compression.

3 Log-Compression Model

Figure 1 depicts the processing block diagram of a generic ultrasound imaging system, including the most significant operations performed on the RF signal generated by the ultrasound probe: (1) interpolation and grid geometry conversion, from polar to rectangular to appropriate image display, (2) logarithmic compression, used to reduce the dynamic range of the input echo signal to match the smaller dynamic range of the display device and to accentuate objects with weak backscatter [13], (3) contrast, a, and (4) brightness, b adjustments. Some equipments perform an automatic adjustment of the parameters a and b which can further be tuned by the operator to improve image visualization in each specific exam. The model displayed in Fig. 1, illustrating the *Log-Compressed Law*, allows to simulate the generic processing operations of the ultrasound equipment, and to recover, whenever the original raw data is not available, an estimate of the ERF image.

As shown in Sect. 5 the interpolated data is better described by a Gamma distribution than by a Rayleigh one. However, the results displayed also show only a marginal improvement of the Gamma distribution with respect to the Rayleigh model, mainly at the transitions. Therefore, here, the interpolation is not taken into account in the designing of the ERF estimation algorithm.

The *Log-Compression model* (LCM) described in this section assumes a fully developed speckle noise formation model to describe the ERF image formation process. This condition is valid when images are reasonably homogeneous and

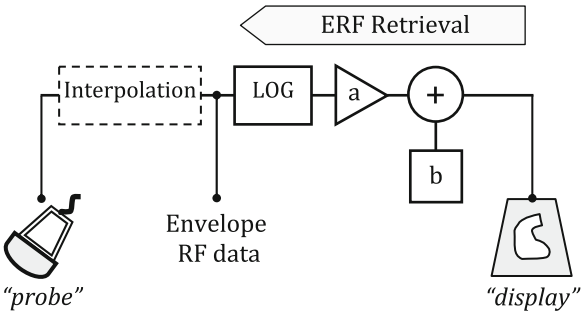

Fig. 1 Block diagram of the generic processing operations of an ultrasound imaging system

do not show high intensity scattering sites. Under these assumptions the ERF signal intensity can be described by a Rayleigh distribution [23], whose parameters, $\Sigma = \{\sigma_{i,j}\}$, associated with each pixel intensity of the ERF image, $y_{i,j}$, are related to the tissue acoustic properties [24] at the corresponding location, $x_{i,j}$.

Let $\mathbf{Z} = \{z_{i,j}\}$ be a $N \times M$ BUS image corrupted by speckle where each pixel is generated according to the following LCL,

$$z_{i,j} = a \log(y_{i,j} + 1) + b, \tag{6}$$

where (a, b) are unknown parameters used to model the contrast and brightness of the observed image, respectively. In the assumption of fully developed speckle the pixels of the ERF image, $Y = \{y_{i,j}\}$, are Rayleigh distributed [25]

$$p(y_{i,j}) = \frac{y_{i,j}}{\sigma_{i,j}^2} \exp\left(-\frac{y_{i,j}^2}{2\sigma_{i,j}^2}\right), \tag{7}$$

where $\sigma_{i,j}$ is the parameter of the distribution to be estimated. Consequently, the distribution of the observed pixels, $z_{i,j}$, given by $p(z) = \left|\frac{\mathrm{dy}}{\mathrm{dz}}\right| p(y)$ [14] corresponds to

$$p(z_{i,j}) = \frac{y_{i,j}(y_{i,j} + 1)}{a\sigma_{i,j}^2} \exp\left(-\frac{y_{i,j}^2}{2\sigma_{i,j}^2}\right). \tag{8}$$

Figure 2a–d simulates the BUS image formation process. The pixel intensities of the noisy image, displayed in Fig. 2b, were generated from Rayleigh distributions with parameters corresponding to the pixel intensities of the phantom displayed in Fig. 2a. To illustrate how the most relevant operations performed by the ultrasound scanner affect the statistical properties of the ERF signal the following simulations are performed. The noisy image is first interpolated and then compressed according to (6) and the final result, displayed in Fig. 2d, represents a typical image obtained with ultrasound equipment.

Figure 2e, f presents the shape of the data distribution throughout the processing operations for different contrast and brightness parameters used in (6). In general, the transformed image is significantly different from the original data from both statistical (histogram) and visual appearance points of view.

Only in the case of the interpolation operation the differences are not very relevant. The histogram of the independent Rayleigh distributed pixels inside the window k_y (see Fig. 2b) is not significantly different from the histogram of pixels inside the window k_y^i (see Fig. 2b). See both histograms displayed in Fig. 2e.

The effect of the interpolation operation is mainly low pass filtering the data leading to a slight reduction on the intensity variance of the transformed image. Variations on the brightness parameter, b, shift the distribution of the transform data along the gray-scale axis, as shown in (Fig. 2e). Moreover, as expected, the dynamic range parameter, a, produces the effect of compressing or stretching the distribution as a decreases or increases, respectively (Fig. 2f).

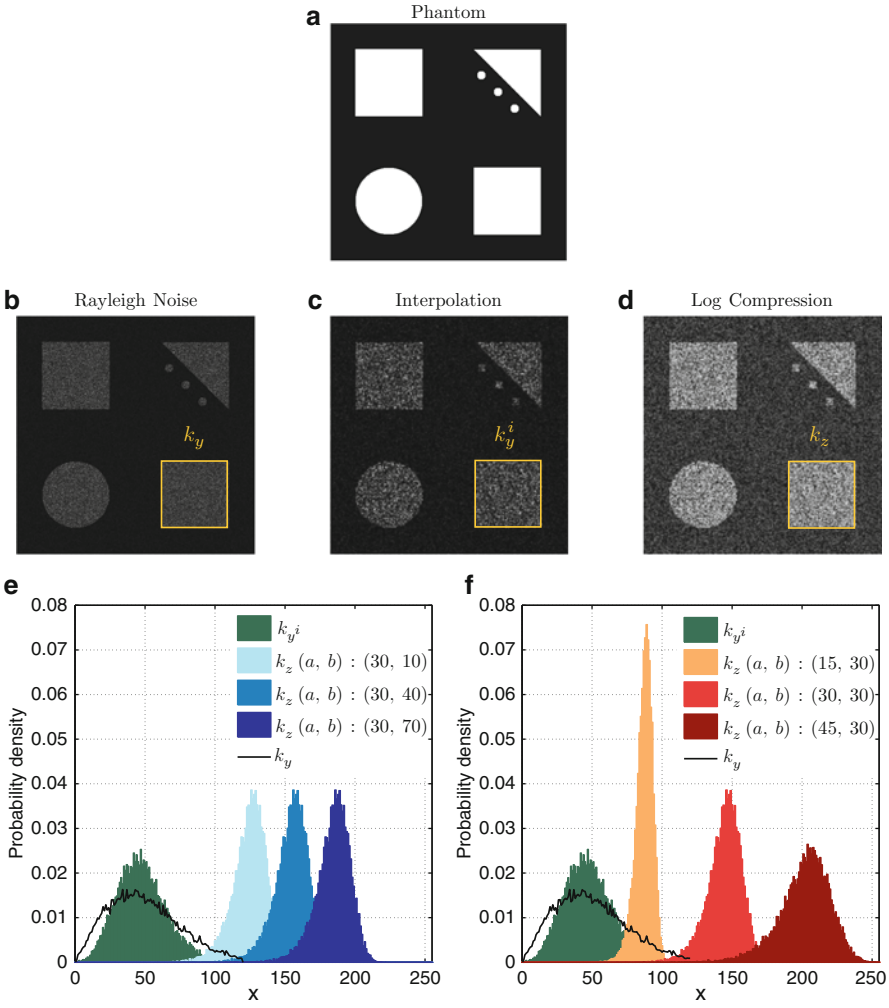

Fig. 2 BUS image formation model, starting from a phantom object (**a**). The method for generating synthetic BUS images includes corruption with Rayleigh noise (**b**), interpolation (**c**), and application of the LCL (**d**). Probability densities in k_y and k_y^i, and k_z when the parameters a (**e**) and b (**f**) are made variable

In the next section the estimation procedure to estimate the parameters a and b form (6) is described in order to decompress the data and estimate the unobserved ERF image, $y_{i,j}$, from the observed ultrasound B-mode one, $z_{i,j}$, by using the transformation

$$y_{i,j} = \exp\left(\frac{z_{i,j} - \hat{b}}{\hat{a}}\right) - 1, \tag{9}$$

where $(\hat{a}, \hat{b})$ are the estimated contrast and brightness parameters.

4 Estimation of Decompression Parameters

This method described here to estimate the *Log-Compression* parameters in (6) is an improved version of the method described in [21].

The estimation of the compression parameters (a,b) would be easier if the Rayleigh parameter, $\sigma_{i,j}$, was known. However, it is not known and varies across the image.

Let us approximate (9) by $y \approx \exp\left(\frac{z-b}{a}\right)$, the distribution (8) can be written as follows

$$p(z) = \frac{2}{a}\exp\left(-\theta - \exp(-\theta)\right), \tag{10}$$

where $\theta = \log(2\sigma^2) - 2\dfrac{z-b}{a}$. Equation (10) defines the *Fisher-Tippet* distribution [22], also known as double exponential. The mean and standard deviation (SD) of this distribution are:

$$\mu_z = \frac{a}{2}\left[\log(2\sigma^2) - \gamma\right] + b, \tag{11}$$

$$\sigma_z = \frac{\pi a}{\sqrt{24}}, \tag{12}$$

where $\gamma = 0.5772...$ is the Euler–Mascheroni constant.

To overcome the difficulty associated with the lack of knowledge of $\sigma_{i,j}$ let us now consider small $n \times m$ windows, $w_{i,j}$, centered at each pixel (i,j). The distribution parameters $\sigma_{k,l}$ within these small windows are assumed constant and equal to the parameter of the corresponding center pixel, $\sigma_{i,j}$, to be estimated.

If $a_{i,j}$ is assumed constant inside the small window $w_{i,j}$ it can be easily derived from (12)

$$\hat{a}_{i,j} = \sqrt{24}\frac{\sigma_{z_{i,j}}}{\pi}, \tag{13}$$

where $\sigma_{z_{i,j}}$ is the standard deviation of the observations inside the small window $w_{i,j}$

The parameter a, which is considered constant across the image, is estimated by averaging the parameters $\hat{a}_{i,j}$:

$$\hat{a} = \frac{1}{NM}\sum_{i,j=1}^{N,M}\hat{a}_{i,j}. \tag{14}$$

The estimation process of b is more challenging than the estimation of a, thus requiring a more elaborated and complex procedure. Let us consider the set of $n \times m = L$ unknown non compressed pixels $\mathbf{y} = \{y_{k,l}\}$ inside the window $w_{i,j}$ as being independent and identically Rayleigh distributed with parameter $\sigma_{i,j}$

$$p(y_{k,l}|\sigma_{i,j}) = \frac{y_{k,l}}{\sigma_{i,j}^2}\exp\left(-\frac{y_{k,l}^2}{2\sigma_{i,j}^2}\right). \tag{15}$$

As shown in [21], the distribution of the minimum of $\mathbf{y}$, $t = \min(\mathbf{y})$, is also Rayleigh distributed with parameter $\sigma_{i,j}^2/L$

$$p(t|\sigma) = \frac{t}{\sigma_{i,j}^2/L} \exp\left(-\frac{t^2}{2\sigma_{i,j}^2/L}\right). \tag{16}$$

The minimum of the observed pixels inside the window $w_{i,j}$, $\mathbf{z} = \{z_{k,l}\}$ where $z_{k,l} = a\log(y_{k,l}+1)+b$, is

$$\begin{aligned} s = \min(\mathbf{z}) &= a\log(\min(\mathbf{y})+1)+b \\ &= a\log(t+1)+b, \end{aligned} \tag{17}$$

which means

$$b = s - a\log(t+1). \tag{18}$$

The distribution of b, computed by $p(b|s,\sigma_{i,j}) = |\mathrm{d}t/\mathrm{d}b|p(t|\sigma_{i,j})$, is therefore given by

$$p(b|s,\sigma_{i,j}) = \frac{L}{a\sigma_{i,j}^2} t(t+1)\exp\left(-\frac{L}{2\sigma_{i,j}^2}t^2\right), \tag{19}$$

where $t = \exp\left(\frac{s-b}{a}\right) - 1$. $\sigma_{i,j}$, the distribution parameter associated with the (i,j) pixel, is not known neither constant across the image. However, if it is considered constant inside the small window $w_{i,j}$ a local estimation of b is possible to derive. Since $\mathbf{y}$ is assumed Rayleigh distributed an appropriated approximation for $\sigma_{i,j}$ is

$$\tilde{\sigma}_{i,j} = \sqrt{\frac{1}{2nm}\sum_{k,l}\tilde{y}_{k,l}^2}, \tag{20}$$

where

$$\tilde{y}_{k,l} = \exp\left(\frac{z_{k,l}-\tilde{b}}{a}\right) - 1, \tag{21}$$

and

$$\tilde{b} = \min(\mathbf{z}). \tag{22}$$

Since b is not known $\tilde{b} \approx b$ is used in (21) instead of b. As it will be shown in the section of experimental results this approximation is valid.

Let $\hat{b}_{i,j}$ be the estimated value of b, computed from the pixels within the small window $w_{i,j}$. Its value is nothing more than the expected value of b with respect to the distribution (19) with the parameter computed in (20),

$$\hat{b}_{i,j} = \int_{-\infty}^{\infty} b_{i,j} p(b_{i,j}|s, \tilde{\sigma}_{i,j}) \mathrm{d}b_{i,j}. \tag{23}$$

The closed form solution of (23) is difficult to compute and a numeric approach is adopted, such that:

$$\hat{b}_{i,j} = \sum_{k=1}^{L} b_{i,j}(k) p(b_{i,j}(k)|s, \tilde{\sigma}_{i,j}), \tag{24}$$

where $b_{i,j}(k) = ks/(L-1), k = 0, 1, ..., L-1$ are L uniformly distributed values in the interval $[0, s]$, since it is assumed that $b \geq 0$ and from (18), $b \leq s$.

The global value of b, once again, is obtained by averaging the estimated $\hat{b}_{i,j}$:

$$\hat{b} = \frac{1}{NM} \sum_{i,j=1}^{N,M} \hat{b}_{i,j}. \tag{25}$$

The estimated parameters $(\hat{a}, \hat{b})$ are then used to revert the Log-compression performed by the ultrasound equipment in order to recover the original RF signal:

$$y_{i,j} = \exp\left(\frac{z_{i,j} - \hat{b}}{\hat{a}}\right) - 1, \tag{26}$$

which is assumed, in the remainder of this chapter, to be Rayleigh distributed.

5 Experimental Results

In this section, different results are presented aiming to assess the performance of the proposed method. First, the accuracy on the decompression parameters (a, b) estimation procedure is computed by using synthetic ultrasound data. The validity of the decompression method is also assessed by using real data. A comparison is made between the original ERF image, obtained from raw data, and the estimated ERF image, obtained from the BUS image.

In addition, the adequacy and robustness of the ERF image retrieval method is investigated in the real case using two sets of experiments, including the application of the decompression method in (1) different BUS images acquired with fixed brightness and contrast parameters and (2) static BUS images acquired with variable operating parameters.

Finally, GoF tests with Rayleigh and Gamma distributions are conducted in estimated ERF images which enables to support the hypothesis that most envelope RF data can be well modeled by these two distributions. The interpretation of the obtained results suggest the use of the simpler Rayleigh distribution to decompress that data.

The decompression method is initially tested in synthetic data by using Monte Carlo tests. Particularly, in this experiment it is intended to assess the estimation accuracy of the decompression parameters, (a,b), for different images and amounts of noise. For each pair of decompression parameters 50 Monte Carlo runs were performed. In each run, two different types of synthetic images are used to revert the compression method and estimate the parameters $(\hat{a},\hat{b})$, uniform and non uniform. Three uniform synthetic images are corrupted with Rayleigh noise with parameters $\sigma^2 = \{10^2, 10^3, 5 \cdot 10^3\}$. The non uniform image is the Shepp–Logan phantom also corrupted by the same three different amounts of noise used with the uniform phantoms. In both cases the noisy images are interpolated and log-compressed according to (6).

Figure 3 presents the average and SD of the 50 estimated decompression parameters, $(\hat{a},\hat{b})$, obtained for each true pair (a,b), by using the first phantom (Fig. 3a) and the non-uniform Shepp–Logan phantom (Fig. 3b).

Similar results are obtained in both cases which suggests that the decompression method has similar behavior for uniform and non-uniform images, and its performance is apparently independent on the severity of speckle noise contamination. The later conclusion is confirmed in Fig. 3a where the observed results do not depend on the value of the Rayleigh parameter σ used to generate the noisy image.

In general, the estimation $\hat{a}$ is non biased and its SD increase mainly with a_0 (see Fig. 3a, b, top left). The variability of $\hat{a}$ tends to be less significant as b increases (see Fig. 3a, b, bottom left). The average values of the uncertainties associated with $\hat{a}$, $SD(\hat{a})/a_0$, are: 0.54%, 0.60%, and 0.60% for the uniform image with $\sigma^2 = 100, 1{,}000$, and 5,000, respectively, and 0.61% for the non-uniform image. As far as the ratio $SD(\hat{a})/a$ is concerned, the uncertainty associated with $\hat{a}$ is almost residual.

The estimation of b, $\hat{b}$, is also non biased (see Fig. 3a, b, top right). In particular, the average values of the uncertainties associated with $\hat{b}$, $SD(\hat{b})/b$, are: 2.4%, 2.4%, and 2.4% for the uniform image with $\sigma^2 = 100, 1{,}000$, and 5,000, respectively, and 2.3% for the non-uniform image. The uncertainty associated with the decompression parameter $\hat{b}$ increases linearly with a. In fact, this behavior is similar to the one obtained for $\hat{a}$, except for very small values of a, where the uncertainty about $\hat{b}$ increases with b (see Fig. 3a, b, bottom right).

The method here proposed is able to invert the compression operations when synthetic images are given. Moreover, it is important to study the feasibility of the method when raw data is provided by the manufacturer. Notice that the challenge of decompression from BUS images is only raised because raw data is generally not available in a clinical setting, thus limiting the application of algorithms which are based on statistical modeling of speckle or RF data.

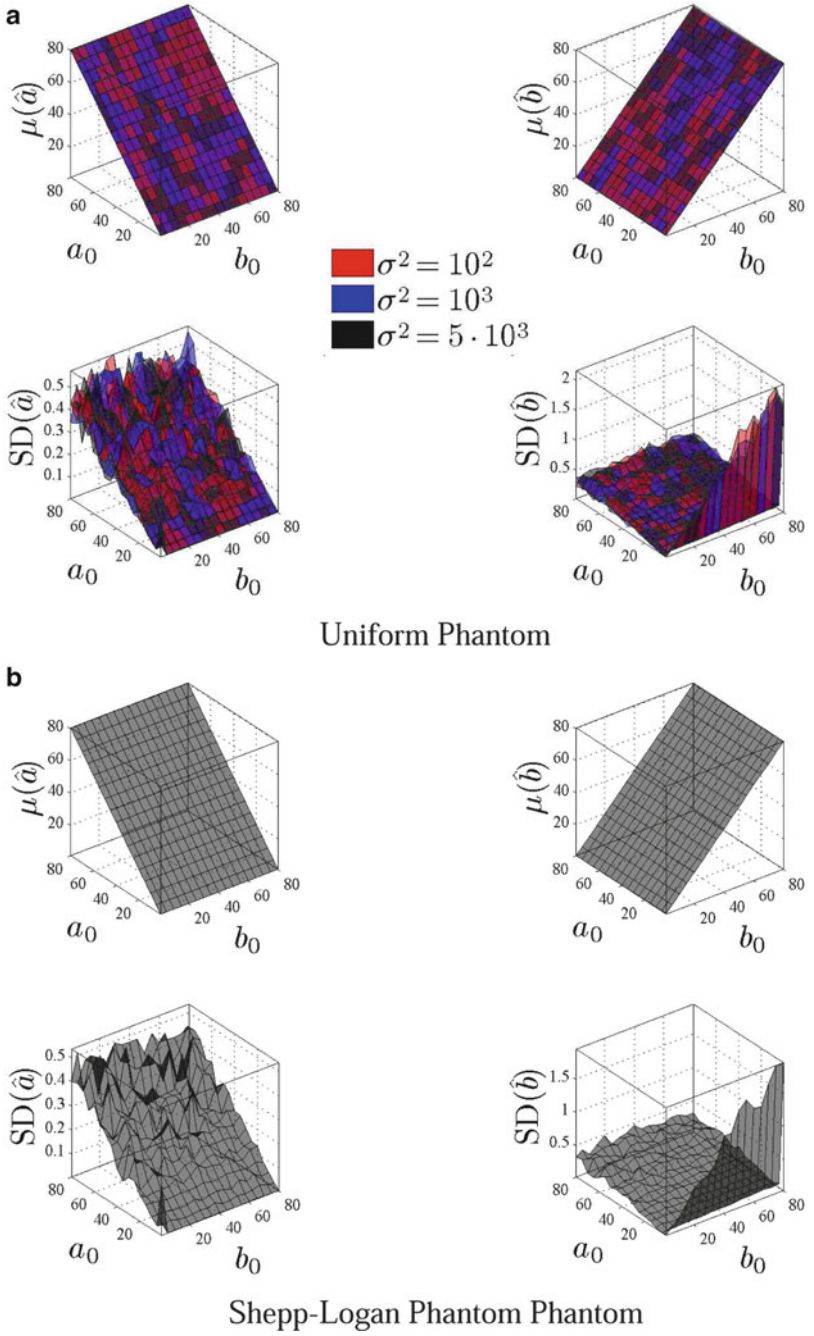

Fig. 3 Estimation of the decompression parameters using Monte Carlo tests. Performance is assessed by computing the mean and SD of ($\hat{a}$,$\hat{b}$) in simulated log compressed images of a noisy uniform image created with Rayleigh parameters (**a**) and noisy Shepp–Logan phantom (**b**)

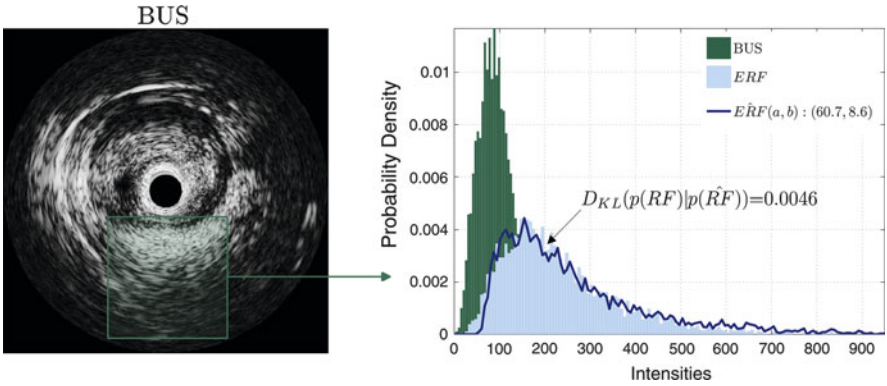

Fig. 4 Application of the RF image retrieval (decompression) method to a BUS image representing a coronary artery. PDFs of the BUS, original ERF, and estimated ERF images, extracted from a given ROI

Hence, in this study it was used an IVUS BUS image corresponding to a cut of the coronary artery (Fig. 4a) together with the RF image obtained from raw RF data, obtained with specialized equipment (Galaxy II IVUS Imaging System, Boston Scientific, Natick, MA, United States). The RF image retrieval(decompression) method is applied to the BUS image, resulting in an estimate of the envelope data, the $E\hat{R}F$ image. As shown in Fig. 4b, the statistical properties of the original and estimated ERF images are closely similar. This observation supports the adequacy of the proposed method to provide an estimate of the envelope RF data which resembles the original one.

So far the decompression method was validated using an IVUS image from which the raw data was known. Moreover, it is also pertinent to investigate the robustness of the method according to different acquisition settings and scenarios. To this purpose, the RF image retrieval method is tested under two different conditions: first, by changing the probe position and keeping the operating parameters constant, and second by maintaining the probe steady and varying the contrast and brightness parameters.

Figure 5a–c presents results of the application of the decompression method proposed in this chapter. In particular, three image sets were acquired for different anatomical structures/tissues by slightly changing the probe position between each image acquisition. For each set of RF estimated images, a homogeneous region was selected and its intensity histogram computed as shown in Fig. 6a–c (left). These results show that the statistical properties of the estimated RF images are comparable, suggesting that the decompression method is robust to small changes in image appearance. The decompression parameters from each image set are depicted in Fig. 6a–c (right). The SDs for $\hat{a}$ and $\hat{b}$ are $(3.83; 2.97)$, $(4.26; 2.01)$, and $(1.96; 1.80)$, respectively for each set of decompressed images, which shows that the uncertainty about the estimated LCL parameters is low in different imaging conditions.

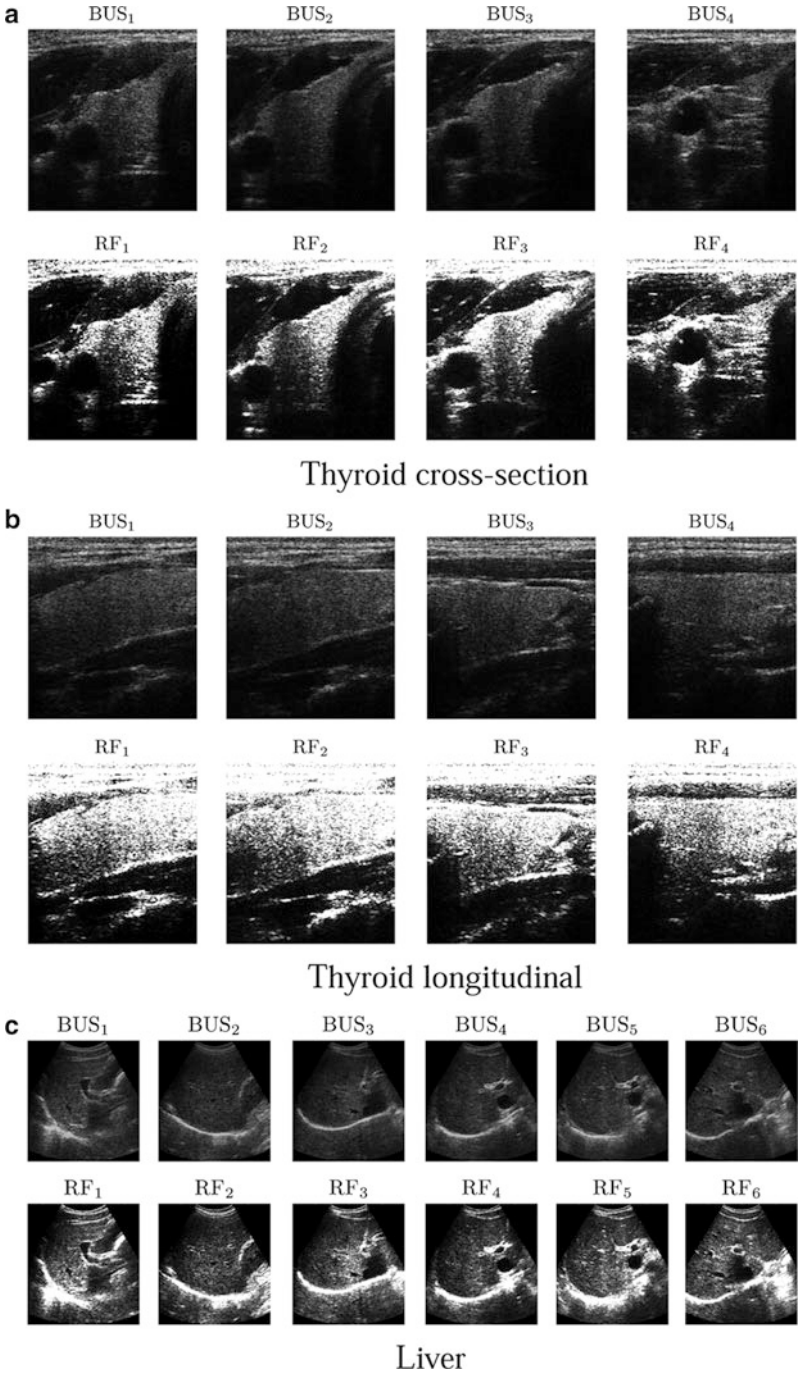

Fig. 5 Application of the decompression method to different sets of images acquired from different tissues using fixed operating conditions

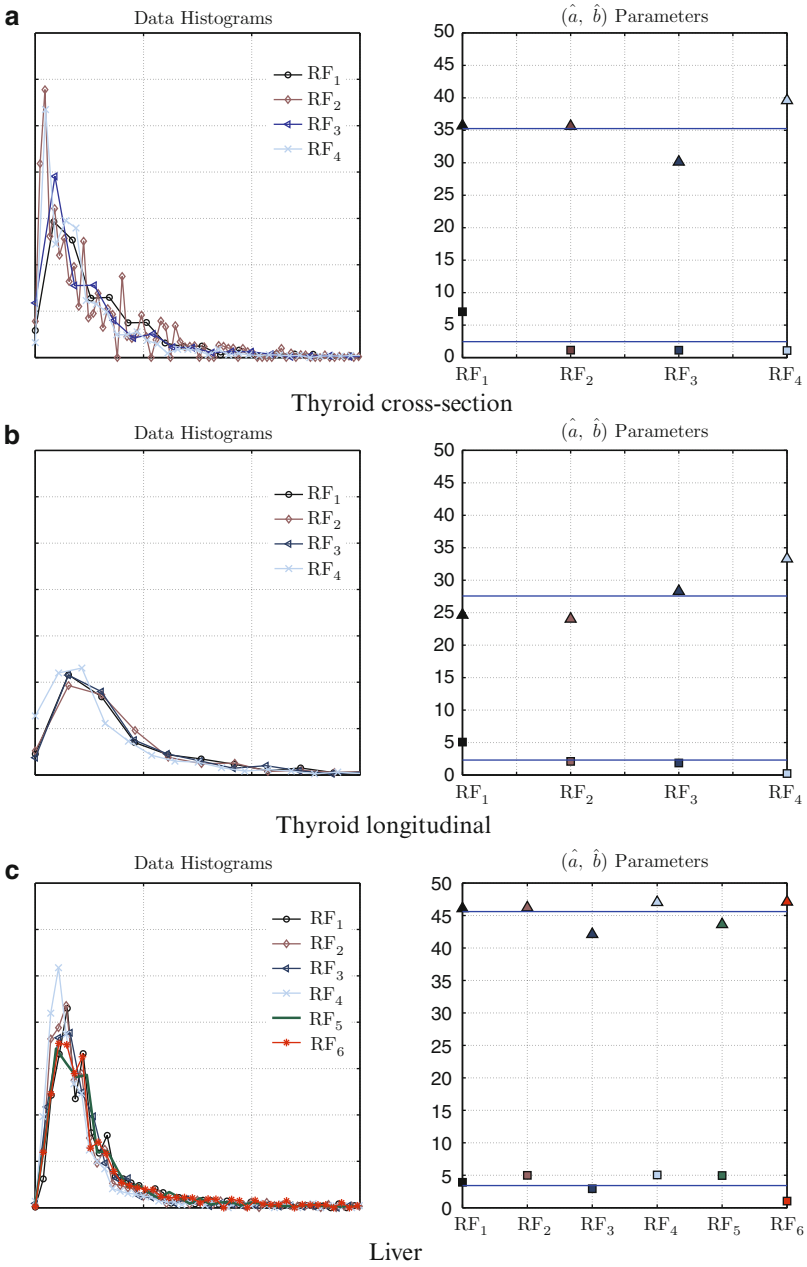

Fig. 6 (*Left side*) Data histograms extracted from regions of interest in the estimated ERF images, shown in Fig. 5. (*Right side*) Decompression parameters

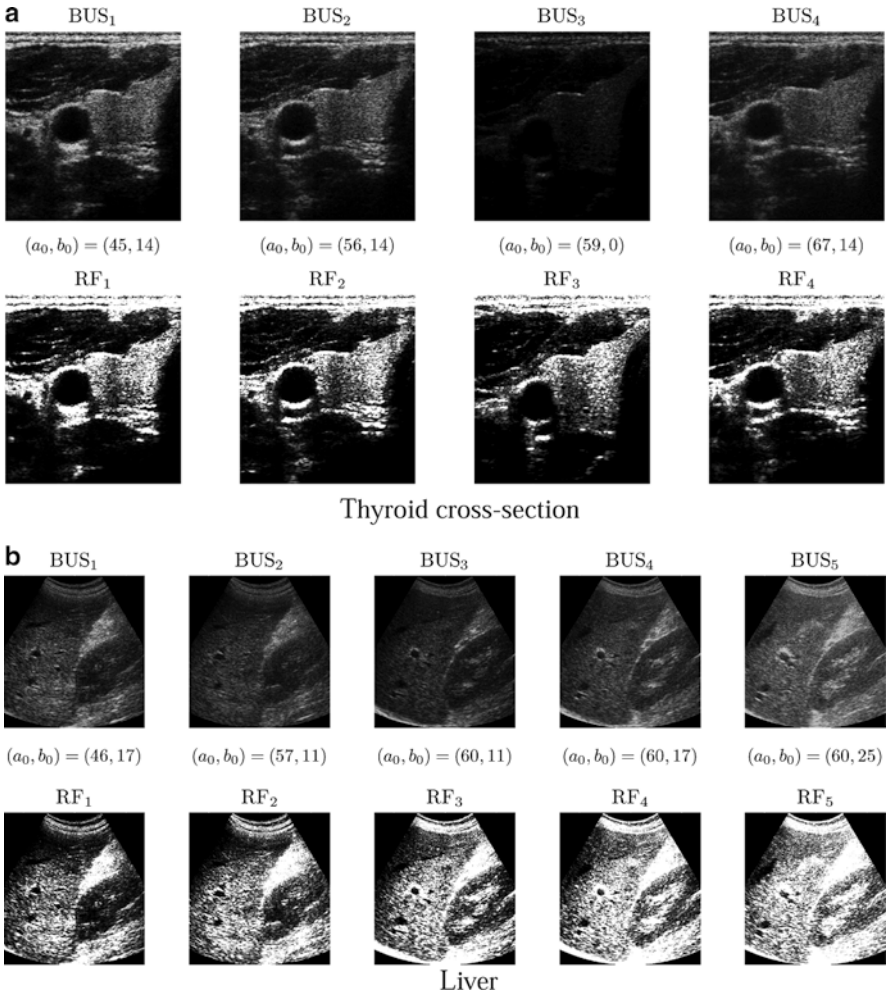

Fig. 7 Application of the decompression method to sets of images acquired from different tissues, acquired with a steady probe and variable operating parameters

As previously mentioned, the second experiment consisted in acquiring a series of BUS images by keeping the probe steady and varying the operating parameters. Results of the application of the decompression method in two different image sets are shown in Fig. 7. In terms of gray-scale image appearance, the obtained ERF images present similar dynamic range and brightness. Histogram analysis of data extracted from homogeneous regions in such images (Fig. 8a, b on the left) suggests similar statistical properties among the estimated ERF images. A comparison between the contrast and brightness parameters given by the US scanner with the estimated decompression parameters is given in Fig. 8a, b on the right. Although a

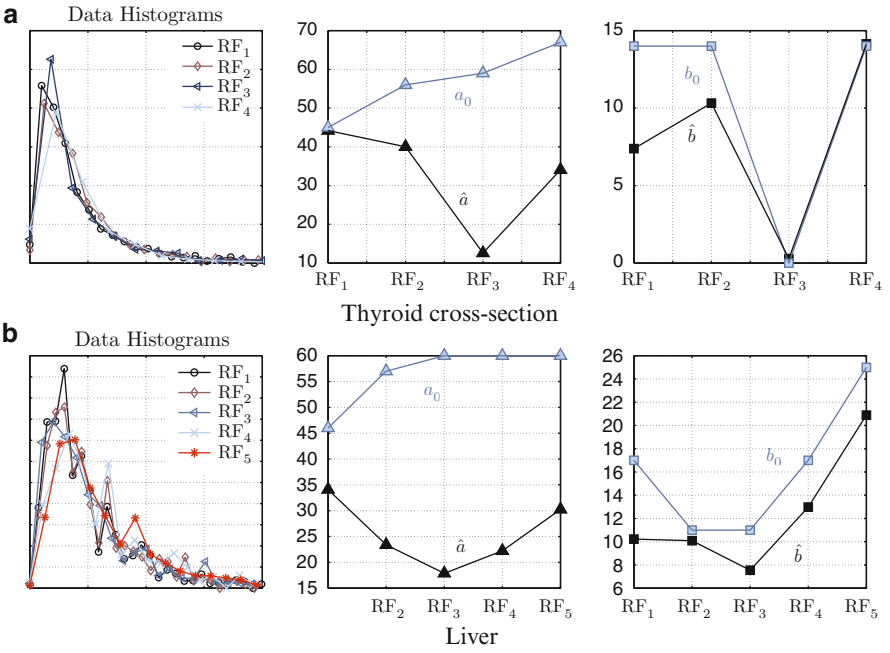

Fig. 8 (*Left side*) Data histograms extracted from regions of interest in the estimated ERF images, shown in Fig. 7. (*Right side*) Decompression parameters estimated with proposed method vs. machine operating settings

numerical comparison is naturally unfeasible because the equipment's settings may not directly correspond to the values assigned to the operating parameters being estimated, it is pertinent to investigate how the estimated parameters change with respect to the original settings of the machine. Considering the estimated parameters $\hat{a}$ these appear to change approximately in inverse proportion with respect to the original dynamic range settings a. Moreover, the estimated parameters $\hat{b}$ vary roughly in direct proportion according to the original linear gain settings b. These results support the ability of the proposed method to estimate the decompression parameters, evoking a similarity association between these values and the settings defined with the ultrasound equipment.

Results aiming at assessing the adequacy and robustness of the proposed decompression method in the aforementioned real cases are detailed in Table 1. Besides the decompression parameters obtained for each image of the data set, it is also shown the Kullback–Leibler distance [26] of each distribution with respect to the first distribution of each set. Observations taken from Table 1 support, from a quantitative point of view, the robustness of the decompression method in estimating precisely the decompression parameters and the ERF images.

It is relevant to investigate whether the assumptions made initially about the adequacy of the Rayleigh distribution to model the pixel intensities in ERF images

Table 1 Decompression parameters $(\hat{a}, \hat{b})$, and Kullback–Leibler distances computed from ERF data histograms, as result of the application of the RF image retrieval under two different conditions (constant and variable operating parameters)

		Thyroid cross-section			Thyroid longitudinal			Liver		
Parameters	ID	$\hat{a}$	$\hat{b}$	$d_{KL}(h_1, h_{ID})$	$\hat{a}$	$\hat{b}$	$d_{KL}(h_1, h_{ID})$	$\hat{a}$	$\hat{b}$	$d_{KL}(h_1, h_{ID})$
Constant	RF_1	35.71	7.05	–	24.65	5.07	–	46.09	3.91	–
	RF_2	35.64	1.14	−1.61	24.04	2.10	0.02	46.22	4.98	−0.01
	RF_3	30.14	1.13	0.26	28.30	1.85	0.01	42.12	2.92	2.62
	RF_4	39.60	1.08	−0.84	33.30	0.22	−0.28	47.04	5.04	0.42
	RF_5							43.64	4.95	1.72
	RF_6							47.10	1.02	0.25
Variable	RF_1	57.17	3.18	–				34.09	10.22	–
	RF_2	44.20	7.38	2.40				23.41	10.09	0.11
	RF_3	40.02	10.32	2.10				36.35	0.02	3.28
	RF_4	12.60	0.28	4.02				17.88	7.55	0.81
	RF_5	34.07	14.15	5.01				22.23	12.90	1.02
	RF_6							30.26	20.89	1.27

are realistic or not. It is known that the assumption of fully developed speckle determines Rayleigh statistics for the amplitude of the envelope RF data, although the Gamma distribution seems to provide a better approximation [27, 28], mainly when interpolation is involved, which is the case.

Hence, the purpose of the study presented in Fig. 10 is to investigate whether the Rayleigh and Gamma distributions are capable of locally describing the estimated ERF images (Fig. 9). Given this, the *Maximum Likelihood* (ML) estimates of the Rayleigh and Gamma distribution were computed locally for each image. This computation is done in 8×8 sliding blocks with 2×2 overlapping borders, throughout the images. For each block the probability density functions (PDFs) are computed according to the ML-based Rayleigh and Gamma estimates. Moreover, a correlation coefficient measure is computed to compare each distribution with the data histogram, given by:

$$\rho_{xy} = \frac{\delta_{xy}}{\sigma_x \sigma_y}, \tag{27}$$

where δ_{xy} is the covariance matrix of the mentioned PDFs and σ_x and σ_y are their standard deviations. When the correlation coefficient, ρ_{xy}, is 1 it means the distribution under investigation (either Rayleigh or Gamma) perfectly models the local data. Figure 10 consists of color-scaled GoF maps, including the local comparison of ERF data vs. ML estimated Rayleigh distribution (Fig. 10a), ERF data vs. ML estimated Gamma distribution (Fig. 10b) and finally, Rayleigh vs. Gamma distribution (Fig. 10c).

In both cases, the Gamma distribution is able to better describe the data when compared to the Rayleigh distribution. An interesting observation is that the

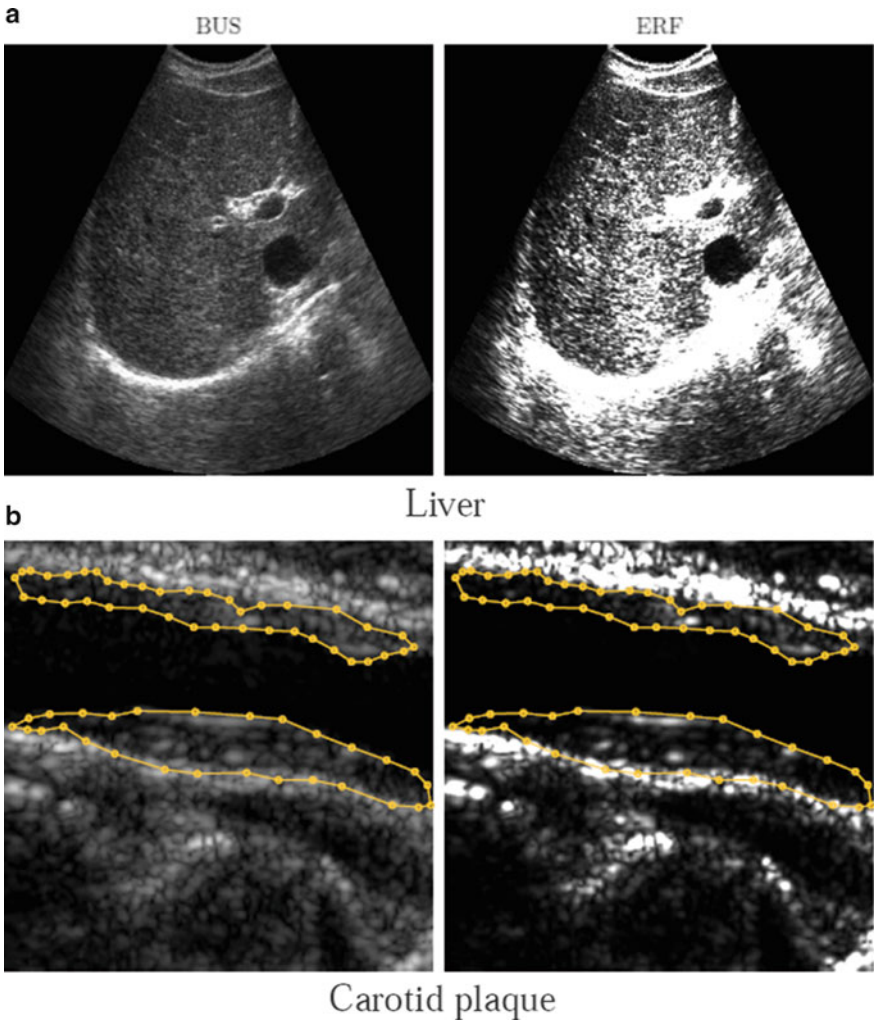

Fig. 9 Application of the decompression method to BUS image of the liver (**a**) and carotid plaque (**b**). The plaque contour is marked for ease of visualization

Rayleigh distribution provides a good description of the data in a very significant part of the images, essentially where strong scattering phenomena do not occur. Moreover, when the local comparison between the Gamma and Rayleigh distributions is carried out, it is observed that in most regions of the studied images, the Rayleigh distribution closely approaches the Gamma distribution. The only exceptions occur in regions of substantial echogenicity, where the Gamma distribution is more suitable to describe the data. These results validate the adopted decision and does not include in the proposed decompression method the interpolation operation. This operation is the source of the Gamma distribution, but as it was confirmed in

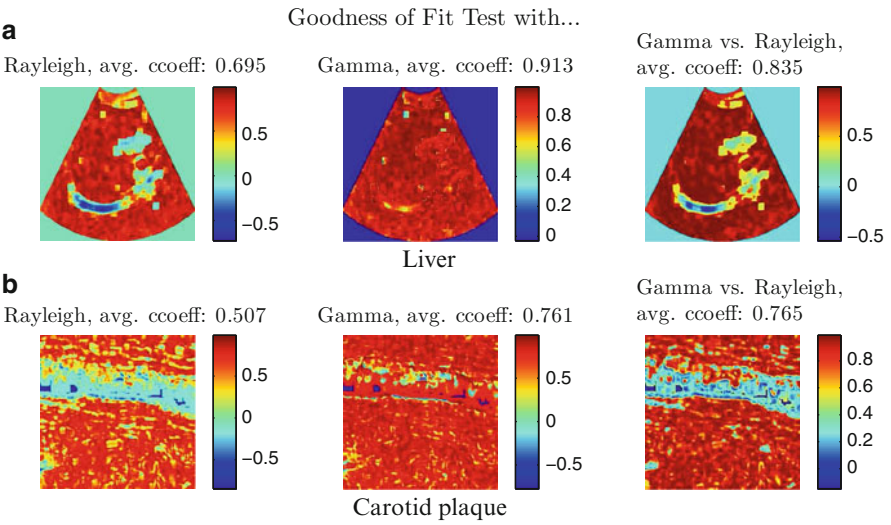

Fig. 10 Color-scaled maps of the GoF test when the data is locally compared with ML Rayleigh distribution (*left*), Gamma distribution (*middle*). GoF map associated with the local comparison between ML Rayleigh and Gamma local distributions (*right*)

this last comparison study, the simpler Rayleigh distribution is able to describe the data in almost all regions of the images but at the transitions.

6 Conclusions

Standard ultrasound equipment performs nonlinear compression of the envelope data thus changing some of its attractive statistical properties.

This chapter proposes a statistical model for log-compressed BUS data which allows to parameterize the most significant operating settings of ultrasound equipments and revert the nonlinear compression, providing an estimate of ERF data. The estimated envelope intensity can be used by a variety of algorithms that rely on the statistics of the ultrasound signal. These include segmentation and speckle tracking algorithms, speckle reduction methods (proposed in the next chapter), tissue classification methods, etc.

The method here presented relies on statistics of the compressed signal, which follows a double-exponential distribution and makes use of a realistic mapping function, designated as LCL, first proposed in [20] which is able to provide an estimate of the ERF image given that parameters related to dynamic range and linear gain are known. The decompression method makes use of this prior knowledge to accurately estimate such parameters and recover the ERF image.

Experiments performed in synthetic and real data show the accuracy of the estimates obtained for the decompression parameters. Moreover, this method is robust because it is able to provide similar outcomes for images acquired with different operating settings. On the other hand, similar decompression parameters were obtained for different images acquired with fixed operating settings.

The Rayleigh distribution has shown to correctly describe the ERF estimated data which has important consequences in the assumptions made for designing the decompression method presented in this chapter.

Finally, a study recently presented in [29] compared the compression parameter estimation of the well-established method proposed in [7, 8] with the approach described in this chapter, observing that the later provides better results in terms of parameter estimation accuracy. As pointed out in [29] this could be explained as the decompression method proposed in this chapter is based on the statistics for the compressed signal, while the approach presented in [7, 8] uses statistics for the uncompressed signal, and attempts to match theoretically calculated normalized moments with those determined directly from the image. The process of fitting the moments calculated in the image with theoretical moments of the exponential distribution (cf. [8]) is extremely sensitive to the order of the moment n, and this could create uncertainty on the decompression parameter to be estimated.

References

1. Shankar PM et al (2003) Classification of breast masses in ultrasonic B scans using Nakagami and K distributions. Phys Med Biol 48(14):2229–2240
2. Aysal T, Barner K (2007) Rayleigh-maximum-likelihood filtering for speckle reduction of ultrasound images. IEEE Trans Med Imag 26(5):712–727
3. Mougiakakou S, Golemati S, Gousias I, Nicolaides AN, Nikita KS (2007) Computer-aided diagnosis of carotid atherosclerosis based on ultrasound image statistics, laws' texture and neural networks. Ultrasound Med Biol 33(1):26–36
4. Goodman JW (2007) Speckle phenomena in optics. Roberts and Company, Atlanta
5. Wagner RF, Smith SW, Sandrik JM, Lopez H (1983) Statistics of speckle in ultrasound B-scans. IEEE Trans Son Ultrason 30(3):156–163
6. Michailovich O, Tannenbaum A (2006) Despeckling of medical ultrasound images. IEEE Trans Ultrason Ferroelectrics Freq Contr 53(1):64–78
7. Dutt V, Greenleaf JF (1996) Adaptive speckle reduction filter for log-compressed b-scan images. IEEE Trans Med Imag 15(6):802–813
8. Prager RW, Gee AH, Treece GM, Berman LH (2003) Decompression and speckle detection for ultrasound images using the homodyned k-distribution. Pattern Recogn Lett 24(4–5):705–713
9. Cramblitt RM, Parker KJ (1999) Generation of non-Rayleigh speckle distributions using marked regularity models. IEEE Trans Ultrason Ferroelectrics Freq Contr 46(4):867–874
10. Kim H, Varghese T (2007) Attenuation estimation using spectral cross-correlation. IEEE Trans Ultrason Ferroelectrics Freq Contr 54(3):510–519
11. Dantas R, Costa E (2007) Ultrasound speckle reduction using modified Gabor filters. IEEE Trans Ultrason Ferroelectrics Freq Contr 54(3):530–538
12. Orfanidis SJ (1996) Optimum signal processing. An introduction. Prentice-Hall, Englewood Cliffs
13. Szabo TL (2004) Diagnostic ultrasound imaging: inside out. Academic, New York

14. Moon TK, Stirling WC (2000) Mathematical methods and algorithms for signal processing. Prentice-Hall, Englewood Cliffs
15. Kaplan D, Ma Q (1994) On the statistical characteristics of the log-compressed rayleigh signals: theoretical formulation and experimental results. J Acoust Soc Am 95:1396–1400
16. Loupas T, McDicken W, Allan P (1989) An adaptive weighted median filter for speckle suppression in medical ultrasonic images. IEEE Trans Circ Syst 36:129–135
17. Gary N, Hendee B (2004) Ultrasonic diagnostic imaging system with automatically controlled contrast and brightness. Acoust Soc Am J 116:2725–2725
18. Lee D, Kim YS, Ra JB (2006) Automatic time gain compensation and dynamic range control in ultrasound imaging systems, vol 6147. SPIE, CA
19. Sathyanarayana S (2008) Systems and methods for automatic time-gain compensation in an ultrasound imaging system. Acoust Soc Am J 123(5):2475
20. Crawford DC, Bell DS, Bamber JC (1993) Compensation for the signal processing characteristics of ultrasound b-mode scanners in adaptive speckle reduction. Ultrasound Med Biol 19(6):469–85
21. Sanches J, Marques J (2003) Compensation of log-compressed images for 3-d ultrasound. Ultrasound Med Biol 29(2):247–261
22. Abramowitz M, Stegun IA (1964) Handbook of mathematical functions with formulas, graphs, and mathematical tables. Dover, New York; Ninth dover printing, Tenth gpo printing edition
23. Eltoft T (2006) Modeling the amplitude statistics of ultrasonic images. IEEE Trans Med Imag 25(2):229–240; Comparative Study.
24. Sehgal C (1993) Quantitative relationship between tissue composition and scattering of ultrasound . Acoust Soc Am J 94:1944–1952
25. Abbot J, Thurstone F (1979) Acoustic speckle: theory and experimental analysis. Ultrasound Imag 1(4):303–324
26. Kullback S, Leibler R (1951) On information and sufficiency. Ann Math Stat 22(1):79–86
27. Tao Z, Tagare H, Beaty J (2006) Evaluation of four probability distribution models for speckle in clinical cardiac ultrasound images. IEEE Trans Med Imag 25(11):1483–1491
28. Aja-Fernandez S, Vegas G, Martinez D, Palencia C (2010) On the influence of interpolation on probabilistic models for ultrasonic images. In: ISBI'10: Proceedings of the 2010 IEEE international conference on Biomedical imaging, Piscataway, NJ, 2010. IEEE Press, New York, pp 292–295
29. Paskas M (2009) Two approaches for log-compression parameter estimation: comparative study. Serbian J Electr Eng 6(3):419–425

A Rayleigh Mixture Model for IVUS Imaging

José Seabra, Francesco Ciompi, Petia Radeva, and João Miguel Sanches

Abstract Carotid and coronary vascular problems, such as heart attack or stroke, are often originated in vulnerable plaques. Hence, the accurate characterization of plaque echogenic contents could help in diagnosing such lesions.

The Rayleigh distribution is widely accepted as an appropriate model to describe plaque morphology although it is known that other more complex distributions depending on multiple parameters are usually needed whenever the tissues show significant heterogeneity.

In this chapter a new model to describe the tissue echo-morphology by using a mixture of Rayleigh distribution is described. This model, called *Rayleigh Mixture Model* (RMM), combines the robustness of a mixture model with the mathematical simplicity and adequacy of the Rayleigh distributions to deal with the *speckle* multiplicative noise that corrupts the ultrasound images.

The method for the automatic estimation of the RMM mixture parameters by using the *Expectation Maximization* (EM) algorithm is described.

The performance of the proposed model is evaluated with a database of in-vitro IVUS samples. We show that the mixture coefficients and Rayleigh parameters explicitly derived from the mixture model are able to accurately describe different plaque types and to significantly improve the characterization performance of an already existing methodology.

J. Seabra (✉) • J.M. Sanches
Institute for Systems and Robotics, Department of Bioengineering from the Instituto Superior Técnico/Technical University of Lisbon, Portugal
e-mail: mail2jseabra@gmail.com; jmrs@ist.utl.pt

F. Ciompi • P. Radeva
Computer Vision Center, Campus UAB, Edifici O, Bellaterra, Spain

University of Barcelona, Gran Via de Les Cortes Catalanes, 585, 08007 Barcelona, Spain
e-mail: fciompi@maia.ub.es; petia@cvc.uab.es

J.M. Sanches et al. (eds.), *Ultrasound Imaging: Advances and Applications*,
DOI 10.1007/978-1-4614-1180-2_2, © Springer Science+Business Media, LLC 2012

1 Introduction

Atherosclerotic plaques may eventually present high risk of rupture, consequently leading to brain stroke or heart attack [1]. Albeit vulnerable plaque is a concept well accepted as a clinical entity with potential harmful consequences, its echo-morphology, and pathological evolution it is not yet well understood. Hence, it is important to objectively characterize the plaque echo-morphology to identify this kind of lesions and develop or refine methods for risk prediction.

Ultrasound images are corrupted by a characteristic granular pattern, called *speckle* [2], that depends on the number of scatterers (reflectors) as well as their size. This speckle signal is usually considered noise and there is a lot of work in the literature proposing methods to its removal [3–6]. However, *speckle* encodes information about tissue acoustic properties [7] that can be used for diagnostic purposes.

As pointed out in [8], features extracted from these noisy images can be considered as tissue histological descriptors. Moreover, IVUS is an imaging technique which enables to clearly assess the arterial wall internal echo-morphology. The technical procedure of acquiring IVUS data consists in introducing a catheter, carrying a rotating ultrasound emitter inside the vessel. During rotation, a piezoelectric transducer transmits US waves and collects the reflected components which are afterward converted into electrical signals (A-lines) and sampled by an Analog to Digital Converter (see Fig. 1b). The IVUS image is obtained by processing the received echoes is a 360-degree tomographic view of the inner arterial walls (Fig. 1a). The proximity of the ultrasound probe from the inner arterial walls makes

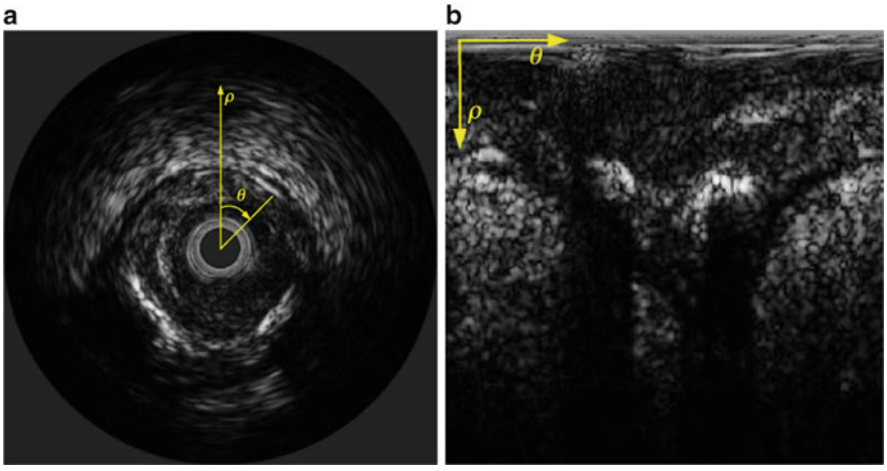

Fig. 1 (**a**) IVUS image represented in cartesian coordinates and (**b**) its corresponding polar representation; ρ represents the depth in the tissue and θ the position (angle) in the rotation of the probe

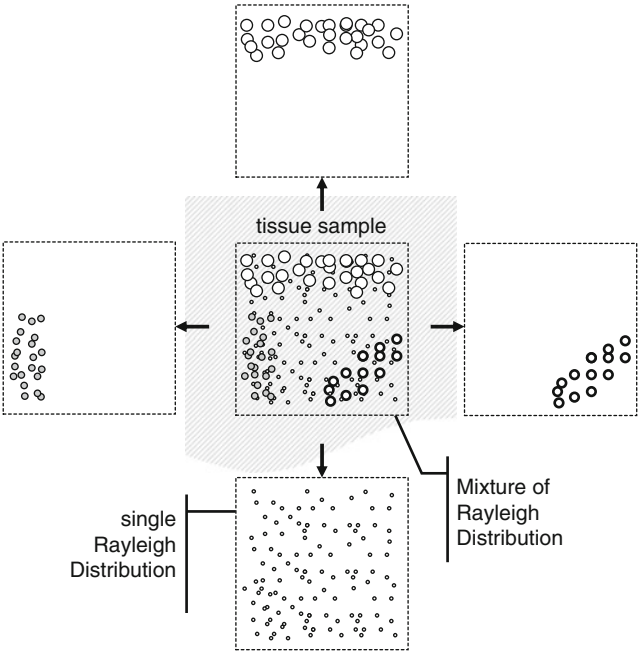

Fig. 2 Hypothetical acoustic tissue model, including different scattering phenomena which points out the need for using a mixture model of distributions

it possible to use high frequency US probes and therefore obtain high quality US images. Consequently, IVUS is commonly considered a suitable technique for accurate *in-vivo* characterization of the coronary plaques composition [9].

Studies which rely on tissue appearance [10, 11] were pursued to qualitatively and subjectively characterize plaque echo-morphology as soft (echolucent), fibrous (intermediate echogenicity), mixed (several acoustical subtypes), and calcified (strongly echogenic). Given the high variability in tissue appearance, the IVUS imaging parameters (such as brightness and contrast) are often tuned to improve visualization. This pre-processing operation modifies the IVUS signal properties, hinders the comparison of tissues on different images and prevents the application of appearance-based methods. Thus, analysis from RF data is needed to obtain discrimination of plaques. Recently, automatic quantitative methods for plaque characterization have been proposed, based either on high-order statistical texture analysis [12–14] and on spectral features extracted from the raw RF signals acquired by the IVUS equipment [15–17].

The work presented in this chapter aims to model the atherosclerotic plaque through the analysis of the envelope backscattered IVUS data. For this purpose, an hypothetical model is considered where a scanned tissue sample suffers from a certain number of scattering phenomena, as depicted in Fig. 2.

The commonest model for speckle formation is known as fully [18] and considers a tissue or region composed by a large number of scatterers, acting as echo reflectors. These scatterers arise from structural inhomogeneities with size approximately equal or smaller than the wavelength of the ultrasound, such as in the parenchyma, where there are changes in acoustic impedance on a microscopic level within the tissue. Under fully developed speckle, pixel intensities in envelope images are well modeled by Rayleigh PDFs [2, 19]. When this condition does not hold, other more complex parametric models, such as K [20], Rician [21], homodyned-K [22], and Nakagami [23] are suitable to describe the data.

The motivation to use the single parameter Rayleigh distribution comes from the fact that the regions defining atherosclerotic tissue are piecewise homogeneous and do not present strong scatterers nor edges, as it happens across the rest of the image, where other speckle conditions are verified and other statistical models are more convenient. These other models, such as Rice, K or Nakagami distributions, depend on a large number of parameters which makes the estimation of tissue echo-morphology a hard task.

Plaque echo-morphology may result from different types of components, spatial organization, and complexity which determine different scattering phenomena where the Rayleigh distribution would be a reasonable approximation but a compound statistical model would be more appropriate. Hence, the description of tissue echo-morphology may be tackled with complex distributions depending on multiple parameters or with a mixture of simple distributions. In this chapter a combination of Rayleigh distributions, called *Rayleigh Mixture Model* (RMM), is proposed to describe the tissue echo-morphology in atherosclerotic plaques from IVUS images. The coefficients of the mixture are estimated with the *Expectation Maximization* (EM) algorithm [24] adapted to this kind of mixture.

The RMM consists of a technique to describe a particular data distribution by linearly combining different Rayleigh PDFs. Up to our knowledge, the RMM was never used for tissue characterization in ultrasound, although these models have been successfully employed in other fields, such as in underwater acoustics and speech processing problems [25, 26].

This chapter is organized as follows. First, in Sect. 2.1 a comprehensive mathematical formulation of the mixture model is provided, using the EM algorithm for estimating the coefficients and Rayleigh parameters of the mixture. Second, the adequacy of the proposed model to describe the envelope ultrasound data is evaluated on validated IVUS data of different plaque types (Sect. 3.3). Moreover, the RMM is applied for modeling plaques as monolithic objects, i.e., by considering all the pixels enclosed in the plaque. The features explicitly obtained from the mixture model (cf. Sect. 2.1) are used to investigate the discriminative power of the model for identifying different tissue types, namely fibrotic, lipidic, and calcified ones. In Sect. 3.4 the ability of the RMM for pixel-wise classification of plaque composition is evaluated when using only the proposed features and when combining them with textural and spectral features recently proposed [27]. Finally, we investigate the significance of the obtained classification improvement when using the RMM features (cf. Sects. 3.5 and 3.6).

2 Methods

In this section a mathematical formulation of the problem is provided and the estimation algorithm for the coefficients of the mixture (weights) and Rayleigh parameters of each component, by using the EM algorithm, is described.

2.1 Rayleigh Mixture Model

Let $Y = \{y_i\}, 1 \leq i \leq N$, be a set of pixel intensities of a given region of interest, particularly a plaque, from an ultrasound image. Pixel intensities are considered random variables which are described by the following mixture of L distributions

$$p(y_i|\Psi) = \sum_{j=1}^{L} \theta_j \phi_j(y_i), \tag{1}$$

where $\Psi = (\theta_1, ..., \theta_L, \sigma_1, ..., \sigma_L)$ is the vector of parameters to estimate. θ_j are the coefficients of the mixture and σ_j are the parameters of each Rayleigh component, $\phi_j(y_i) = p(y_i|\sigma_j)$,

$$p(y_i|\sigma_j) = \frac{y_i}{\sigma_j^2} \exp\left(-\frac{y_i^2}{2\sigma_j^2}\right), \tag{2}$$

The condition $\sum_{j=1}^{L} \theta_j = 1$ must hold to guarantee that $p(y_i|\Psi)$ is a true distribution function.

The parameters σ_j associated with the pixel intensity y_i, characterize the acoustic properties of the tissue at the ith location [28]. The effect of changing σ in the shape of the distribution and thus in the image intensity is illustrated in Fig. 3. The joint distribution of the pixel intensities, considered independent and identically distributed (i.i.d.), is given by,

$$p(\mathbf{Y}|\Psi) = \prod_{i}^{N} p(y_i|\Psi). \tag{3}$$

The goal is to estimate Ψ by maximizing the *likelihood* function,

$$\hat{\Psi}_{\text{ML}} = \arg\max_{\Psi} \mathscr{L}(\mathbf{Y}, \Psi), \tag{4}$$

where

$$\mathscr{L}(Y, \Psi) = \log p(\mathbf{Y}|\Psi) = \sum_{i=1}^{N} \log\left(\sum_{j=1}^{L} \theta_j p_j(y_i|\sigma_j)\right). \tag{5}$$

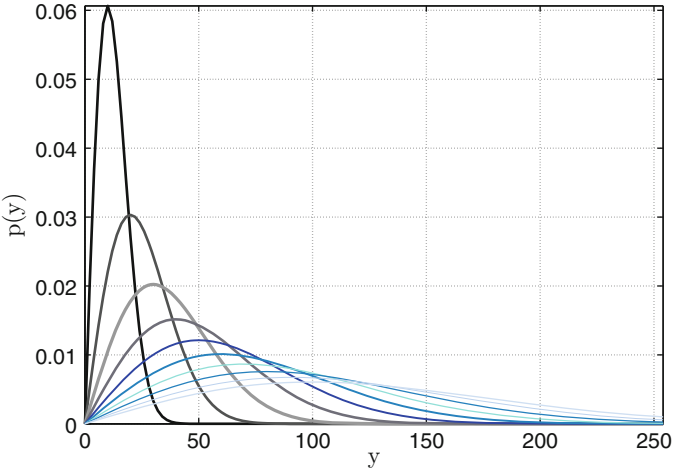

Fig. 3 Rayleigh PDFs generated with parameter $10^2 < \sigma < 10^3$ (from darker to lighter curves)

The maximization of (5) is a difficult task because it consists of a logarithmic function of a sum of terms. To overcome this difficulty the EM [24] method is used where a set of hidden variables are introduced, $K = \{k_i\}$ with $k_i \in \{1, ..., L\}$. The value of $k_i = j$ informs us about the mixture component j that generated the ith pixel intensity, y_i, with probability $p(y_i|\sigma_{k_i})$ defined in (2).

Each nth iteration of the EM method is composed of two steps

- *E step:* Where the *expectation* of the new *likelihood* function, $\mathscr{L}(\mathbf{Y}, \mathbf{K}, \Psi)$, is computed with respect to $\mathbf{K}$,

$$\mathscr{Q}(\mathbf{Y}, \Psi^n, \Psi) = E_{\mathbf{K}}[\mathscr{L}(\mathbf{Y}, \mathbf{K}(\Psi^n), \Psi)] \tag{6}$$

and

- *M step:* Where a new estimate of Ψ, Ψ^{n+1}, is obtained by maximizing the function $\mathscr{Q}$,

$$\Psi^{n+1} = \arg\max_{\Psi} \mathscr{Q}(\mathbf{Y}, \Psi^n, \Psi). \tag{7}$$

These two steps alternate until convergence is achieved, which happens when $|\Psi^{n+1} - \Psi^n| < \xi$, e.g., $\xi = 10^{-3}$.

The *likelihood* function involving all unknowns, visible and hidden, is

$$\begin{aligned} \mathscr{L}(\mathbf{Y}, \mathbf{K}, \Psi) = \log p(\mathbf{Y}, \mathbf{K}|\Psi) &= \sum_{i=1}^{N} \log p(y_i, k_i|\Psi) \\ &= \sum_{i=1}^{N} \log p(y_i|\sigma_{k_i}) + \log \underbrace{p(k_i|\sigma_{k_i})}_{\theta_{k_i}}, \end{aligned} \tag{8}$$

where $p(y_i|\sigma_{k_i})|_{k_i=j}$, defined in (2), is the k_i^{th} component of the RMM and θ_{k_i} is the mixture coefficient associated with the k_i^{th} component. The maximization of (8) is impossible because the hidden variables $\mathbf{K}$ are not known. Therefore, the *expectation* with respect to $\mathbf{K}$ is computed as follows,

$$\begin{aligned}\mathcal{Q}(\Psi,\hat{\Psi}) &= E_{\mathbf{K}}\left[\mathcal{L}(\mathbf{Y},\mathbf{K},\Psi)|\mathbf{Y},\hat{\Psi}\right] \\ &= \sum_{i=1}^{N} E_{k_i}\left[\log p(y_i|\sigma_{k_i}) + \log p(k_i|\sigma_{k_i})\right] \\ &= \sum_{i=1}^{N}\sum_{j=1}^{L} \gamma_{i,j}[\log p(y_i|\sigma_j) + \log\theta_j], \end{aligned} \tag{9}$$

where $\hat{\Psi} = (\hat{\theta}_1,...,\hat{\theta}_L,\hat{\sigma}_1,...,\hat{\sigma}_L)$ is the previous estimation of the parameters and $\gamma_{i,j}(\hat{\Psi})$ is the distribution of the unobserved variables which is defined as follows,

$$\gamma_{i,j} = p(k_i = j|y_i,\hat{\Psi}) = \frac{p(y_i|\hat{\sigma}_j)p(k_i=j)}{p(y_i|\hat{\Psi})}, \tag{10}$$

where

$$\sum_{j=1}^{L}\gamma_{i,j} = 1. \tag{11}$$

In (10), $p(y_i|\hat{\sigma}_j)$ is computed as in (2), $p(k_i = j) = \hat{\theta}_j$ and, by definition,

$$p(y_i|\hat{\Psi}) = \sum_{j=1}^{L}\theta_j p(y_i|\hat{\sigma}_j). \tag{12}$$

The *likelihood* function (9) contains two independent terms, one depending on θ_j and the other on σ_j. Therefore, the function $\mathcal{Q}$ can be minimized independently with respect to each one. The log-*likelihood* function in (9) can be rewritten by separating the terms which depend exclusively on θ_j and σ_j. Taking into account (2) leads to

$$\mathcal{Q}(\Psi,\hat{\Psi}) = \sum_{i=1}^{N}\sum_{j=1}^{L}\gamma_{i,j}\log(\theta_j) + \sum_{i=1}^{N}\sum_{j=1}^{L}\gamma_{i,j}\left[\log\left(\frac{y_i}{\sigma_j^2}\right) - \frac{y_i^2}{2\sigma_j^2}\right]. \tag{13}$$

Hence, the function $\mathcal{Q}$ can now be minimized independently with respect to θ_j and σ_j.

By using the method *Lagrange multipliers* [29] the term of (13) depending on θ can be maximized under the constraint

$$\sum_{j=1}^{L}\theta_j = 1. \tag{14}$$

which also provides a necessary condition for optimality in constrained problems [29]. By introducing a new variable (λ) and solving the partial derivative of the term depending on θ, the following expression is obtained,

$$\frac{\partial}{\partial \theta_r}\left[\sum_{i=1}^{N}\sum_{r=1}^{L}\gamma_{i,r}\log(\theta_r)+\lambda\left(\sum_{r}\theta_r-1\right)\right]=0, \tag{15}$$

which leads to

$$\sum_{i=1}^{N}\gamma_{i,r}=-\lambda\,\theta_r. \tag{16}$$

By summing both sides of (16) over r,

$$\underbrace{\sum_{i=1}^{N}\sum_{r=1}^{L}\gamma_{i,r}}_{(11)}=-\lambda\underbrace{\sum_{r=1}^{L}\theta_r}_{(14)}, \tag{17}$$

we get that $N=-\lambda$, which leads to

$$\hat{\theta}_r=\frac{1}{N}\sum_{i=1}^{N}\gamma_{i,r}. \tag{18}$$

The mixture parameters σ_j are found by differentiating the term in (13), depending exclusively on σ_j, and setting it to zero, as follows,

$$\frac{\partial}{\partial \sigma_r}\left[\sum_{i=1}^{N}\sum_{r=1}^{L}\gamma_{i,r}\left(\log\left(\frac{y_i}{\sigma_r^2}\right)-\frac{y_i^2}{2\sigma_r^2}\right)\right]=0, \tag{19}$$

which is easily solved for σ_r to obtain,

$$\hat{\sigma}_r=\frac{\sum_{i=1}^{N}\gamma_{i,r}\frac{y_i^2}{2}}{\sum_{i=1}^{N}\gamma_{i,r}}=\sqrt{\frac{1}{N}\sum_{i=1}^{N}\gamma_{i,r}\frac{y_i^2}{2}}. \tag{20}$$

The EM algorithm is initialized with L uniformly weighted coefficients $\Theta=\{\theta_j=\frac{1}{L}\}$ while the mixture parameters are assigned with the *Maximum Likelihood* (ML) estimator [30], $\hat{\sigma}_{\mathrm{ML}}=\sqrt{\frac{1}{2N}\sum_{i=1}^{N}y_i^2}$.

The initial choice of components was set arbitrarily to $L=10$. However, when $|\sigma_m-\sigma_n|<\varepsilon=1$ (ad hoc setting), meaning that two distributions are closely similar, with $(m\neq n)=\{1,\ldots,L\}$, then $\sigma_j=\frac{\sigma_m+\sigma_n}{2}$ and $\theta_j=\theta_m+\theta_n$. This constraint assures stability of the RMM, particularly, for modeling plaque echo-morphology. Preliminary observations allowed to verify that $L=10$ is an overestimated guess (excessive number of mixture components) which has also implications in the

computational cost of the RMM algorithm. The study of an effective input value for the number of mixture components to be used in the plaque characterization problem is further investigated in Sects. 3.3 and 3.4.

In the next section of experimental results the RMM will be applied in the scope of atherosclerotic plaque characterization and classification for diagnosis purposes.

3 Experimental Results

In this section we first provide a description of the methods used to acquire and process the IVUS data and we briefly introduce the classification framework adopted for tuning the RMM algorithm and performing plaque characterization. Then, two distinct experiments are conducted. The first studies the adequacy of the RMM for describing different tissue types. This experiment is designated as *monolithic description* since the mixture model is estimated by considering all the pixels enclosed in the plaque. The second experiment refers to plaque characterization made pixel-by-pixel (hence, called *plaque local characterization*), where the RMM is applied not to the entire plaque but to each processing block centered at the pixel to be characterized. In order to apply the RMM technique on a classification problem, in local basis, the RMM must be estimated locally and descriptive features must be extracted. Given the envelope image (cf. Sect. 3.1), local RMM features are computed by means of a $K_s \times K_s$ sliding window, moved by a step of $S = \frac{3}{4}K_s$. For each position, a $2L+1$-feature array is obtained and presented in the following manner: the first L positions correspond to the Rayleigh parameters sorted in ascending order, followed by the L respective coefficients, arranged accordingly. The last position corresponds to the number of effective mixture components, $\tau = \{1,\ldots,L\}$.

The ability of the RMM for local characterization of plaque composition is evaluated when using only the RMM features and when combining them with other texture and spectral features recently proposed in [27].

Finally, we present a statistical analysis that supports the relevance of the obtained classification improvement when using the RMM features.

3.1 In-Vitro Data Processing

The adequacy of the proposed RMM to describe real tissue types is evaluated through an in-vitro study of atherosclerotic plaques from an IVUS database. The IVUS data set has been recently presented in [27] and consists of 8 post-mortem arteries, resulting in 45 frames with 24 fibrotic, 12 lipidic and 31 calcified plaques. This data set, composed of 67 plaques, has been validated by histological analysis.

Real-time Radio-Frequency (RF) data acquisition has been performed with the Galaxy II IVUS Imaging System (Boston Scientific) with a catheter Atlantis SR Pro

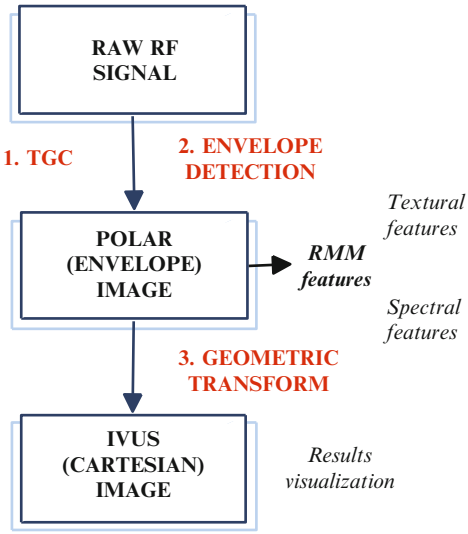

Fig. 4 IVUS data processing (see text for details)

40 MHz (Boston Scientific). To collect and store the RF data the imaging system has been connected to a workstation equipped with a 12-bit Acquiris acquisition card with a sampling rate of 200 MHz. The RF data for each frame is arranged in a data matrix of $N \times M$ samples, where $M = 1{,}024$ is the number of samples per *A-line*, and $N = 256$ is the number of positions assumed by the rotational ultrasound probe.

The information encoded in the visual appearance of tissues naturally represents a relevant feature for their description. However, during acquisition the imaging parameters of the IVUS equipment are typically changed to enhance tissue visualization. Hence, parameters like contrast depth and brightness can change from patient to patient or even from image to image. When the IVUS images are then processed for feature extraction, this fact may generate non-comparable features.

To avoid the aforementioned errors and to produce normalized data, the used data follows a rigorous acquisition protocol where the IVUS images have been directly reconstructed from the raw RF signals rather than using the ones produced by the IVUS equipment. For this purpose, we follow the image reconstruction algorithm [27, 31] outlined in Fig. 4. The reconstruction operations are applied to the RF data, where a preliminary Time Gain Compensation (TGC) function is used,

$$\mathrm{TGC}(r) = 1 - \mathrm{e}^{-\beta r}, \tag{21}$$

where $\beta = \ln 10^{\alpha f/20}$, α is the attenuation coefficient for biological soft tissues ($\alpha \approx 0.8$ dB/MHz.cm for $f = 40$ MHz [32]), f is the central frequency of the transducer in MHz and r is the radial distance from the catheter in cm. After signal compensation, using TGC, and envelope detection, using the Hilbert transform, the signal processing procedure described in [27] is applied to get the polar

representation of the IVUS image, or simply the envelope image, resulting in a non-compressed, 256×256 pixels image (cf. Fig. 1b). We recall that the polar image is used to estimate the RMM and to extract the corresponding features. To improve the visualization the polar image is transformed to Cartesian coordinates and its pixels intensities are re-scaled to normalize the observed IVUS image.

This data is exclusively used to represent the image and not for feature extraction.

3.2 Classification Framework

As stated before, the weights and parameters of the mixture, whose estimation was early described, are used as features to describe different types of plaque. In order to evaluate the correct model to be used in a multi-class classification framework that has been successfully used in plaque characterization [27]. The role of the classification scheme is twofold: (1) it allows to evaluate the discriminative power of RMM features and (2) it is used to support a cross-validation process, adopted to tune the L parameter (number of mixture components) in RMM model and the kernel size (image window size where the RMM is estimated).

The classification framework is based on [27] for discriminating among fibrotic, lipidic, and calcified plaques. The multi-class problem is tackled by combining binary classifiers in the *Error-Correcting Output Codes* (ECOC) framework [33]. In fact, ECOC is a technique to decompose a multi-class problem into several binary problems. Each binary problem is here solved by using the *Adaptive Boosting* (AdaBoost) classifier [34] where the weak classifiers are *decision stumps* [35].

The classifier performance is evaluated by means of the *Leave-One-Patient-Out* (LOPO) [31] cross-validation technique, where the training set is built by taking at each validation fold, all patients' data except one, used for testing. Note that each patient data may consist of different number of images (hence, different number of plaques).

Performance results are given in terms of Sensitivity: $S = \frac{\mathrm{TP}}{\mathrm{TP+FN}}$, Specificity: $K = \frac{\mathrm{TN}}{\mathrm{TN+FP}}$, Precision: $P = \frac{\mathrm{TP}}{\mathrm{TP+FP}}$, and global Accuracy: $A = \frac{\mathrm{TP+TN}}{\mathrm{TP+TN+FP+FN}}$, where TP = True Positive, TN = True Negative, FP = False Positive, and FN = False Negative.

3.3 Plaque Monolithic Description with RMM

The first experiment consists of considering a set of fibrotic, lipidic, and calcified plaques from the entire data set, according to histological analysis. Figure 5a–c shows three examples of IVUS images containing one (or more) distinct tissue types.

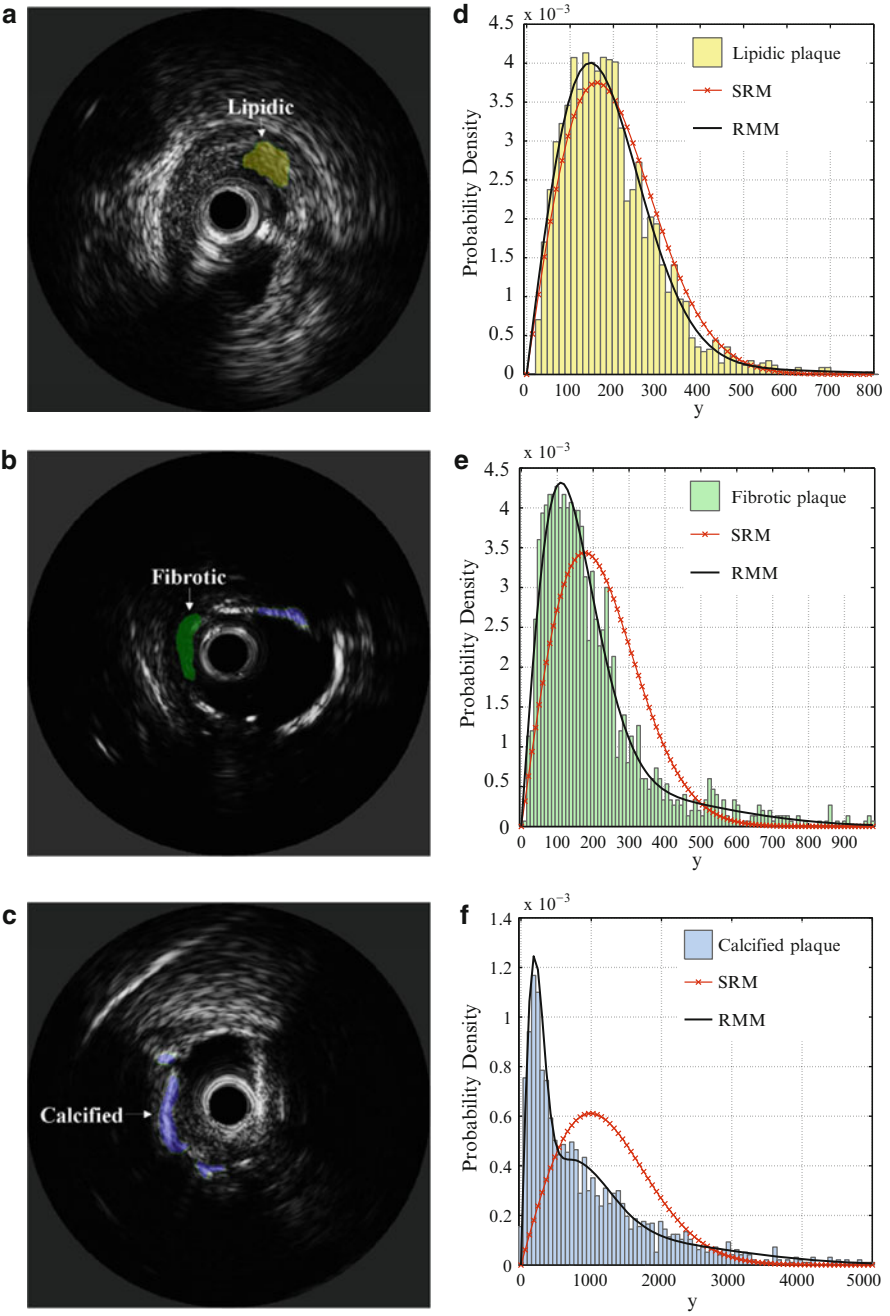

Fig. 5 (**a**)–(**c**) RMM modeling of three tissue types. (**d**)–(**f**) 3-component mixture PDFs estimated for each tissue type, overlapped with single Rayleigh PDFs

Table 1 Accuracy values for tuning the number of mixture components in RMM (Best performance is indicated in bold)

LOPO	No. mixture components			
(%)	1	2	3	4
A	44.16 (36.28)	68.52 (33.29)	**85.56 (18.85)**	69.82 (31.00)

Table 2 Performance of RMM, SRM, and median features for monolithic classification (Performance of RMM presented in bold)

LOPO (%)	S_{fib}	S_{cal}	S_{lip}	A
Median	65.00 (39.09)	81.53 (20.34)	44.00 (37.82)	66.30 (15.92)
SRM	41.67 (46.85)	0.00 (0.00)	90.42 (15.84)	44.16 (36.28)
RMM	**91.67 (13.94)**	**93.75 (15.30)**	**82.00 (24.90)**	**85.56 (18.85)**

The purpose of the current study is to verify the ability of the RMM to describe and distinguish among the three different tissue types. In this particular experiment, the RMM algorithm is applied to the entire set of pixels enclosed in each plaque. Given this, the monolithic plaque area can be characterized by a unique set of RMM features which define a unique plaque type.

Note that this global monolithic approach differs from the other one, described in the next section, where a local analysis make it possible to detect different overlapped types of plaques in the same image. In that approach mixtures are estimated over the pixels of a sliding window the sweeps the whole image.

The classification framework is used to tune the parameters of the RMM method. The most critical parameter to be defined is the number of components to use in the mixture model. In order to determine the optimal L value, we use the LOPO cross-validation method where the classification accuracy is considered as the parameter to maximize.

For each plaque, we apply the RMM algorithm for different number of mixture components from $L = 1$ to $L = 10$. This process results in a set of features having different lengths. For instance, for $L = 3$ we get a 7-length feature vector whereas for $L = 4$ we get a feature vector with 9 elements for each plaque. The training sets composed of RMM features created with $L = (1, \ldots, 10)$ are used in the cross-validation process. Results, reported in Table 1, show that the best accuracy is achieved when 3 Rayleigh PDFs (components) are used in the mixture model. Therefore we will use 3 components for this specific plaque classification application. For the sake of simplicity, since classification performance decreases substantially for $L > 4$, we only show the obtained results with L varying from 1 to 4.

In order to demonstrate the effectiveness of RMM when compared to the single distribution, here termed *Single Rayleigh Model* (SRM), or the median gray intensity, we show on Table 2 a comparison of these three types of features for classifying monolithic plaques. The single parameter estimation of the SRM, obtained with the ML criterion [30], is given by $\hat{\sigma}_{\text{ML}} = \sqrt{\frac{1}{2N}\sum_{i=1}^{N} y_i^2}$, where y_i is

Table 3 Kullback–Leibler divergence tests using RMM and SRM: geometric mean computed over 67 plaques

KL	Calcified	Fibrotic	Lipidic
RMM	**1.77E-4**	**7.68E-4**	**2.20E-3**
SRM	1.62E-3	4.93E-3	6.54E-3

Table 4 Mean values of Rayleigh parameters and Mixture coefficients estimated with RMM applied for the data set of 67 plaques

RMM	Components	Lipidic	Fibrotic	Calcified
Rayleigh parameters	1	188	140	318
	2	410	275	1171
	3	–	555	3390
Mixture coefficients	1	0.82	0.51	0.33
	2	0.18	0.39	0.46
	3	–	0.10	0.21

the intensity of the i^{th} pixel within the plaque. It is clear that the application of RMM outperforms the classification results obtained with the other tested features (note that the SRM completely fails in identifying calcified plaques).

Figure 5d–f shows normalized data histograms of lipidic, fibrotic, and calcified tissues, together with the estimated mixture (RMM) and single (SRM) distributions, respectively. Visually, the mixture model composed of three components (early determined to be the best value) describes significantly better the data when compared to the single distribution. Interestingly, as we move from lipidic to fibrotic and calcified tissue, the difference between the mixture distribution and the single distribution increases. At this point, we quantify the adequacy of the mixture model for describing each type of tissue. For this purpose, the mixture and single distributions were estimated for each plaque and the *Kullback–Leibler* (KL) divergence [36] of such distributions with respect to the data was computed. Hence, the smaller the KL divergence is between a given distribution and the data, the more similar they are. We summarize the results by computing the geometric mean of the KL divergence for RMM and ML distributions for each plaque (Table 3).

Observations made in Fig. 5, supported by the results presented in Table 3 reinforce the idea that a single distribution is not sufficient to describe the data, suggesting that different plaque types can be correctly described with different mixture distribution (and thus different RMM parameters). This fact confirms the usefulness of RMM in a tissue modeling problem.

The RMM estimation algorithm is applied to the entire data set, where for each plaque the RMM takes into account all the pixels enclosed in it. The obtained RMM features are presented in Table 4. Particularly, it is observed that lipidic plaques are well described by 2 mixture components, while calcified and fibrotic plaques are modeled by 3 components, where the main difference lies in the range of estimated Rayleigh parameters (Table 4). It is worth noting that in fibrotic tissue estimation the "peakedness" of the single Rayleigh distribution is lower than the observed histogram. There is, indeed, a considerable amount of pixels with high intensity

which means that the maximum likelihood parameter of the Rayleigh distribution (computed as in Sect. 3.3) has a higher value than the expected. As a consequence, the shape of the single Rayleigh distribution will move slightly toward the right direction, as observed in Fig. 5e. This fact enforces the need for a mixture model to correctly model tissues.

The main conclusions that can be obtained from these results are:

1. Lipidic tissues are predominantly modeled by a single Rayleigh distribution. The KL divergence is of the same order for SRM and RMM (see Table 3) and the optimum order of the mixture is one (see Table 4).
2. Fibrotic tissues are approximately described by a mixture of second order.
3. Calcified tissues are better described by three components.
4. There is no significant overlapping between the range of Rayleigh parameters obtained for the lipidic and fibrotic tissues when compared to calcified tissues.

3.4 Plaque Local Characterization

We have established the usefulness of using a mixture of distributions to model the plaque content in a monolithic experiment. It is worth to note that, in practice, plaques are not individually segmented, thus the RMM estimation considering all the pixels enclosed in the plaques is not generally a feasible method for plaque characterization. Nevertheless, a region of interest which includes the plaque(s) can be at least pointed out by the physician without compromising the time of a diagnostic exam. Thus, a local-wise characterization, made pixel-by-pixel, becomes a natural and more appropriate strategy. This strategy consists in estimating the RMM over successive processing blocks within the plaque region and assigning the RMM features to each center pixel. Subsequently, each pixel is classified into a specific tissue type (lipidic, fibrotic, or calcified) and then confronted with the ground truth.

As previously mentioned, in order to apply the RMM algorithm to a local analysis, we first need to define the dimension of the kernel to be used. The computational cost associated with the local-wise estimation of RMM features using a processing block (kernel) of size k_s is $\mathcal{O}(2k_s)$. The tuning of this critical parameter is performed again by means of the cross-validation process. For this purpose, the RMM-based features are computed inside a kernel of size $k_s = \{2,4,8,16,24,32\}$. Hence, 6 different data sets have been obtained, and for each one of them the cross-validation has been performed, while varying the number of mixture components $L = \{2,3,4\}$. Results in terms of global accuracies are depicted in Fig. 6. Given the obtained results, $k_s = 16$ and $L = 3$ are adopted. Hence, the length of the RMM-based feature set extracted from each kernel is $2L+1 = 7$.

In order to assess the true contribution of the proposed RMM algorithm, the plaque characterization problem is solved under three different conditions, where distinct features were computed from polar RF data (cf. Fig. 4). First, only the RMM

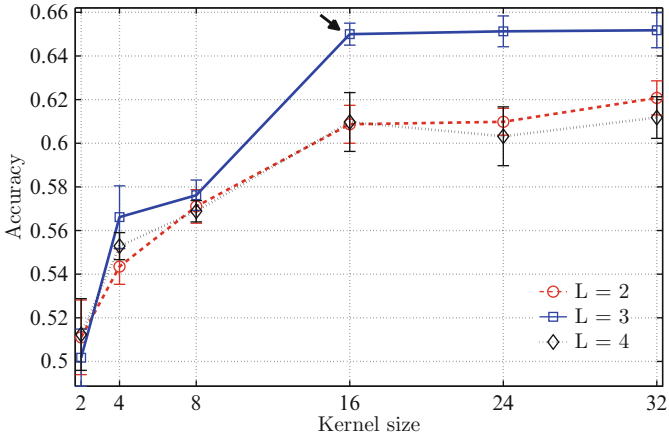

Fig. 6 Classification based on RMM features according to the kernel size and number of mixture components

features are used for tissue discrimination in the classification framework: the obtained classifier is here named $C.1$. Then, a set of 51 textural and spectral features presented in [27] is used to train a second classifier ($C.2$). Finally, RMM features are joined to the textural and spectral features, thus creating a 59-element feature vector, used to train a third classifier ($C.3$).

The three classifiers are used to characterize the plaques of the database according to the LOPO technique. At each fold of both training and validation process, the data set for each kind of plaque has been randomly down-sampled up to the maximum value of the less represented class over all the cases (around 2,000 points per class) in order to obtain a balanced data set among classes.

For each cross-validation fold we compute the aforementioned performance criteria (cf. Sect. 3.2); consequently, for the entire LOPO experiment (eightfolds) we take the average and standard deviation of the results obtained for each fold. Classification results have been obtained by repeating 20 times the cross-validation and finally by averaging the obtained performance parameters.

The comparison of $C.1$, $C.2$, and $C.3$ classifiers gives an important evidence of the effectiveness of the RMM features as well as their discriminative power. Classification results achieved with the proposed classifiers are shown in Fig. 7; a more detailed description is given in Table 5.

The use of features estimated with the RMM ($C.1$) provides good results in terms of calcified and fibrotic sensitivity and overall accuracy. A poor performance in terms of correct detection of lipidic tissue is, however, observed. Nevertheless, this is a meaningful achievement in the context of automatic plaque characterization if we consider that the dimension of the feature set is small and exclusively originated from a data source (envelope image, cf. Fig. 4). The combination of the proposed RMM features ($C.1$) with spectral and textural features [27] ($C.2$) is expected

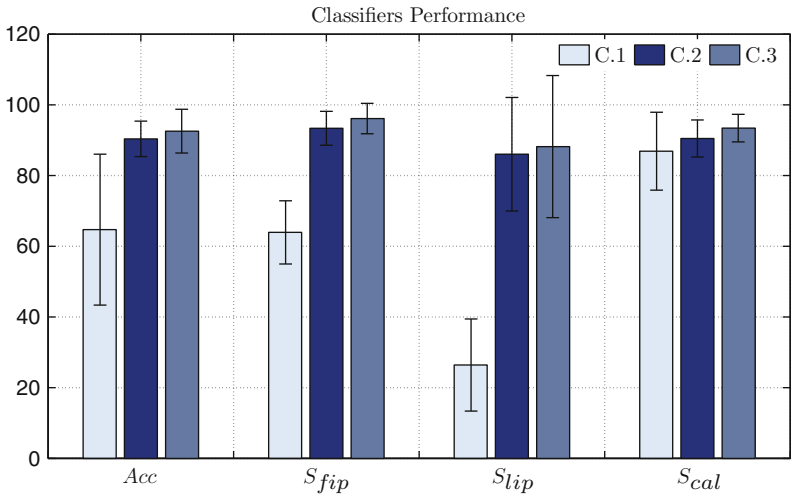

Fig. 7 Bar graph comparing different classifiers (C.1, C.2, C.3) according to performance measures (Acc, $S_{\text{lip}}, S_{\text{fib}}, S_{\text{cal}}$)

Table 5 Performance of plaque characterization: results presented as mean (std)

LOPO (%)	$C.1$	$C.2$	$C.3$
A	64.70 (21.35)	91.37 (5.02)	**92.56 (6.18)**
S_{fib}	63.93 (8.94)	94.38 (4.79)	**96.12 (4.30)**
S_{lip}	26.41 (13.03)	87.03 (16.06)	**88.19 (20.10)**
S_{cal}	86.89 (11.02)	91.48 (5.24)	**93.42 (3.90)**
K_{fib}	74.68 (25.95)	92.49 (6.22)	**94.02 (5.32)**
K_{lip}	80.98 (14.59)	97.18 (2.85)	**97.69 (3.41)**
K_{cal}	94.27 (11.36)	95.22 (5.61)	**95.90 (6.85)**
P_{fib}	88.55 (11.28)	94.34 (6.74)	**95.69 (4.71)**
P_{lip}	86.78 (21.06)	69.26 (28.52)	**69.71 (29.94)**
P_{cal}	94.99 (8.44)	96.89 (3.59)	**96.86 (5.18)**

to produce improvements on the classification performance. Hence, as shown in Fig. 7 and Table 5, the classifier $C.3$ yields the best classification accuracy, around 92.6% and brings the class sensitivity up to 96.1%, 88.2%, and 93.4% for fibrotic, lipidic, and calcified plaques, respectively. This represents an improvement of more than 1% in accuracy, about 2% in fibrotic-class, more than 1% in lipidic-class and around 2% in calcified-class sensitivities, when compared to the classifier which only considers textural and spectral features ($C.2$). These observations support the relevance of the RMM features for plaque characterization.

This result shows that features extracted from RMM are complementary to the rest of the features. Examples of plaque characterization using the $C.3$ classifier are shown in Fig. 8.

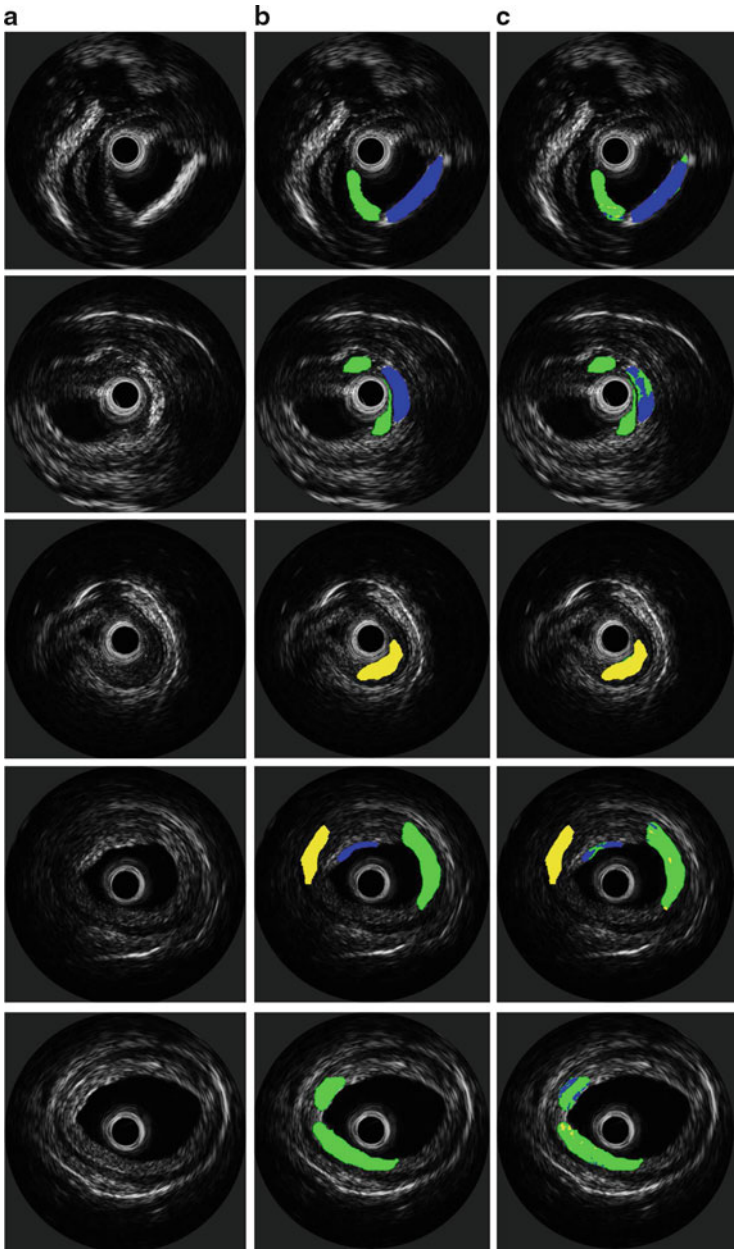

Fig. 8 Examples of plaque classification using the *C*.3 classifier. (**a**) IVUS images, (**b**) ground truth images, segmented according to the histological analysis, and (**c**) classification. In *blue* (*dark*), *green* (*mid-gray*), and *yellow* (*light-gray*) are indicated calcified, fibrotic, and lipidic tissues, respectively

Table 6 Mean rank for the accuracy of each classifier

Classifier	$C.1$	$C.2$	$C.3$
Mean rank	2.8438	1.8938	**1.2625**

3.5 Statistical Analysis

In order to reinforce the usefulness of the RMM approach, we perform a test on the statistical significance of results.

To assess the statistical significance among the classifiers performance, we apply the *Friedman* and *Bonferroni–Dunn* test [37]. First of all, the ranking r_j^i for each separate classification test i and each classifier j is computed. Then, the mean ranking R_j for each one of the jth classifier is computed as $R_j = \frac{1}{\widehat{N}} \sum_{i=1}^{\widehat{N}} r_j^i$, where $\widehat{N} = MN_p$ is the total number of rounds. Obtained results are reported in Table 6. Note that the best rank corresponds to the $C.3$ classifier, i.e., the classifier trained with the whole feature set.

In addition, in order to reject the *null-hypothesis* that the differences on the measured classification performance are due to randomness, the *Friedman* test is performed. For this purpose, the *Friedman statistic value* is computed,

$$\chi_{\mathrm{F}}^2 = \frac{12\widehat{N}}{k(k+1)} \left[\sum_j R_j^2 - \frac{k(k+1)^2}{4} \right], \tag{22}$$

where $k = 3$ is the number of considered classifiers. The obtained value is $\chi_{\mathrm{F}}^2 = 202.74$. As reported in [37], given the conservative property of the Friedman value, the *Iman-Davenport* correction value is preferred,

$$F_{\mathrm{F}} = \frac{(\widehat{N}-1)\chi_{\mathrm{F}}^2}{\widehat{N}(k-1) - \chi_{\mathrm{F}}^2}. \tag{23}$$

The value obtained in this case is $F_{\mathrm{F}} = 274.9$. With three methods and a total of $\widehat{N} = 160$ experiments, F_{F} is distributed according to the F distribution with 2 and 318 degrees of freedom. The critical value of $F(2,\infty)$, for $\alpha = 0.05$ is 2.99. Since the obtained value for F_{F} is higher than the critical value, the null-hypothesis is rejected, i.e., the differences in the obtained results are not due to randomness.

Once the null-hypothesis has been rejected, we check if the classifier $C.3$, resulting in the best discriminative power, is significantly better than the other classifiers. For this purpose, the *Bonferroni–Dunn* test [37] is performed. The performance of two classifiers is significantly different if the corresponding average ranks differ by at least the *critical difference*,

$$CD = q_\alpha \sqrt{\frac{k(k+1)}{6\widehat{N}}}, \tag{24}$$

where q_α is based on the Studentized range statistic divided by $\sqrt{2}$. Since our goal is the comparison of the $C.3$ classifier with respect to the others, the *Bonferroni–Dunn* test is suitable, and a correction factor must be considered in the q_α value (cf. [37] for details). In our case we obtain $CD = 0.2949$ which is smaller than each difference among the mean rank of the classifier $C.3$ and the rank of each other classifier. For this reason, we can infer that the classifier is significantly better than the rest with a confidence of 95%.

3.6 Features Weight Analysis

Finally, we want to evaluate the importance of the included features in the quality of the classifier $C.3$. The AdaBoost algorithm [38] assigns a certain weight to each weak classifier selected at each round, during the training process [34]. Since the decision stump weak classifier is only related to a single feature [35], we can use the weight assigned by AdaBoost to evaluate the importance of each feature during the training process. Note that each feature can be selected more than one time: in that case, the sum of each weight for a specific feature is considered.

Let us define N_P the number of in-vitro cases, N_F the number of features, K the number of binary problems, $f = 1,\ldots,N_\mathrm{F}$ the index of each feature, $k = 1,\ldots,K$ the index of each binary problem, N_R the number of rounds by which the computation has been repeated and $\alpha^f_{k,p,r}$ the weight assigned to the fth feature. The normalized weight assigned by AdaBoost to each feature can be computed as $W_f = \max\{w^1_f,\ldots,w^1_f\}$, where

$$w^k_f = \frac{1}{N_\mathrm{P} N_\mathrm{R}} \sum_{p=1}^{N_\mathrm{P}} \sum_{r=1}^{N_\mathrm{R}} \frac{\alpha^f_{k,p,r}}{\max\left\{\alpha^1_{k,p,r},\ldots,\alpha^{N_\mathrm{F}}_{k,p,r}\right\}} \tag{25}$$

In Fig. 9 the normalized weights of each feature are represented together with their detailed description. It is worth to note the importance given by the classifier to the RMM features, particularly to feature #1 (1st Rayleigh parameter), feature #6 (3rd mixture coefficient), and feature #7 (no. effective mixture components). Given the high discriminative power of the $C.3$ classifier, the expressive weights assigned to the RMM-based features corroborate the importance of the RMM model, as well as its capability for discriminating different tissues. Hence, this experiment illustrates the relevance of the RMM features for the AdaBoost classifier. Naturally, the information provided about the most discriminant features for classification may be used on a feature selection procedure in future work related to tissue characterization.

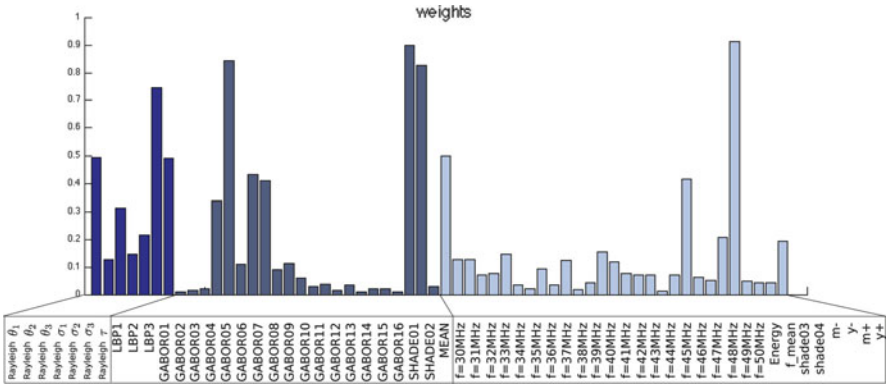

Fig. 9 Analysis of the normalized weight for each feature of the $C.3$ classifier

4 Conclusions

This chapter proposes a method for plaque characterization in IVUS data based on a mixture of Rayleigh distributions. The coefficients and parameters of the mixture model are used as features for describing fibrotic, lipidic, and calcified plaques.

The RMM algorithm was evaluated and tuned using a classification framework based on a multi-class problem applied to a validated IVUS data set and following a cross-validation strategy. Results suggest that the optimal RMM method for plaque characterization consists of $L = 3$ mixture components and should be computed on a kernel of size $k_s = 16$.

First, the true value of RMM features for tissue characterization was evaluated through a plaque monolithic problem using a cross-validation strategy, providing a global accuracy of 86%. This result highlights the relevance of RMM features for discriminating among the three different types of tissue.

Furthermore, the method was evaluated on a local-wise classification problem when using only the RMM tuned features and when combining them with textural and spectral features used in an authors' previous study. The inclusion of RMM features demonstrates to generally improve the classification performance up to a global accuracy of 92.6%. According to the most significant performance parameters, such as accuracy and class sensitivity, fusing RMM features with textural and spectral features represents a general improvement of more than 1% and in some cases about 2%.

Finally, statistical analysis using the *Friedman and Bonferroni–Dunn* shows that the classifier which includes RMM, textural, and spectral features is significantly better than the other studied ones, thus reinforcing the significance of the obtained improvement when using RMM features.

The analysis of features relevance attributed by AdaBoost demonstrates that the RMM features give an important contribution to the plaque characterization problem.

The method is intended to characterize tissues enclosed in a previously segmented plaque. Moreover, automatic segmentation capabilities can be potentially achieved by classifying the whole image and then by post-processing the labeled regions. Without a deep analysis on features similarities between different vessel areas, the classification result on regions different from plaques cannot be stated. Indeed, it can be guessed that, at least for what concerns the textural features, regions enclosing struts (in presence of stent) can be classified as calcified plaque, and the whole adventitia layer as fibrotic plaque. No guessing can be done for the blood region.

Hence, this chapter has demonstrated that the RMM has a high impact on plaque characterization and could significantly contribute to a more accurate study of plaque composition, and consequently to an objective identification of vulnerable plaques.

References

1. Spagnoli LG (2004) Extracranial thrombotically active carotid plaque as a risk factor for ischemic stroke. J Am Med Assoc 292(15):1845–1852
2. Burckhardt C (1978) Speckle in ultrasound B-mode scans. IEEE Trans Son Ultrason SU-25(1):1–6
3. Nicolaides AN, Kakkos SK, Griffin M, Sabetai M, Dhanjil S et al (2005) Severity of asymptomatic carotid stenosis and risk of ipsilateral hemispheric ischaemic events: results from the ACSRS study. Eur J Vasc Endovasc Surg 30(3):275–284
4. Loizou CP, Pattichis CS (2008) Despeckle filtering algorithms and software for ultrasound imaging. Morgan & Claypool, San Rafael
5. Loizou CP, Pattichis CS, Christodoulou CI, Istepanian RSH, Pantziaris M (2005) Comparative evaluation of despeckle filtering in ultrasound imaging of the carotid artery. IEEE Trans Ultrason Ferroelectrics Freq Contr 52(10):1653–1669
6. Sanches JM, Nascimento JC, Marques JS (2008) Medical image noise reduction using the sylvester-lyapunov equation. IEEE Trans Image Process 17(9):1522–1539
7. Szabo TL (2004) Diagnostic ultrasound imaging: inside out. Academic, New York
8. Thijssen J (2003) Ultrasonic speckle formation, analysis and processing applied to tissue characterization. Pattern Recogn Lett 24(4–5):659–675
9. Diethrich E et al (2007) Virtual histology intravascular ultrasound assessment of carotid artery disease: the carotid artery plaque virtual histology evaluation (CAPITAL) study. J Endovasc Therap 14(5):676–686
10. Gussenhoven E, Essed C, Frietman P (1989) Intravascular ultrasonic imaging: histologic and echographic correlation. Eur J Vascu Surg 3:571–576
11. Mintz GS, Nissen SE, Anderson WD (2001) American college of cardiology clinical expert consensus document on standards for acquisition, measurement and reporting of intravascular ultrasound studies (ivus). J Am College Cardiol 37:1478–1492
12. Zhang X, McKay CR, Sonka M (1998) Tissue characterization in intravascular ultrasound images. IEEE Trans Med Imag 17(6):889–899
13. Pujol O, Rosales M, Radeva P, Nofrerias-Fernandez E (2003) Intravascular ultrasound images vessel characterization using adaboost. In: Functional imaging and modelling of the heart: lecture notes in computer science, pp 242–251
14. Granada J et al (2007) In vivo plaque characterization using intravascular ultrasound virtual histology in a porcine model of complex coronary lesions. Arterioscler Thromb Vasc Biol 27(2):387–393

15. Nair A, Kuban B, Tuzcu E, Schoenhagen P, Nissen S, Vince D (2002) Coronary plaque classification with intravascular ultrasound radiofrequency data analysis. Circulation 106:2200–2206
16. DeMaria A, Narula J, Mahamud E, Tsimikas S (2006) Imaging vulnerable plaque by ultrasound. J Am College Cardiol 47(8):32–39
17. Sathyanarayana S, Carlier S, Li W, Thomas L (2009) Characterisation of atherosclerotic plaque by spectral similarity of radiofrequency intravascular ultrasound signals. EuroIntervention 5(1):133–139
18. Lopes A, Touzi R, Nezry E (1990) Adaptive speckle filters and scene heterogeneity. IEEE Trans Geosci Remote Sens 28(6):992–1000
19. Eltoft T (2006) Modeling the amplitude statistics of ultrasonic images. IEEE Trans Med Imag 25(2):229–240; Comparative Study.
20. Prager RW, Gee AH, Treece GM, Berman LH (2003) Decompression and speckle detection for ultrasound images using the homodyned k-distribution. Pattern Recogn Lett 24(4–5):705–713
21. Jakeman E (1984) Speckle statistics with a small number of scatterers. Optic Eng 23:453–461
22. Dutt V, Greenleaf JF (1994) Ultrasound echo envelope analysis using a homodyned k distribution signal model. Ultrason Imag 16(4):265–287
23. Shankar PM (2001) Ultrasonic tissue characterization using a generalized Nakagami model. IEEE Trans Ultrason Ferroelectrics Freq Contr 48(6):1716–1720
24. Dempster AP, Laird NM, Rdin DB (1977) Maximum likelihood from incomplete data via the EM algorithm. J Roy Stat Soc Ser B 39:1–38
25. Gallaudet T, de Moustier C (2003) High-frequency volume and boundary acoustic backscatter fluctuations in shallowwater. J Acoust Soc Am 114(2):707–725
26. Sorensen K, Andersen S (2007) Rayleigh mixture model-based hidden markov modeling and estimation of noise in noisy speech signals. IEEE Trans Audio Speech Lang Process 15(3):901–917
27. Ciompi F, Pujol O, Gatta C, Rodriguez O, Mauri F, Radeva P (2009) Fusing in-vitro and in-vivo intravascular ultrasound data for plaque characterization. Int J Cardiovasc Imag (formerly cardiac imaging) 26(7):763–779. doi:10.1007/s10554-009-9543-1.
28. Sehgal C (1993) Quantitative relationship between tissue composition and scattering of ultrasound. Acoust Soc Am J 94:1944–1952
29. Hadley G (1964) Nonlinear and dynamic programming. Addison-Wesley, Reading
30. Harris JW, Stocker H (1998) Maximum likelihood method In: Handbook of mathematics and computational science. Springer, New York, p 824
31. Caballero KL, Barajas J, Pujol O, Rodriguez O, Radeva P (2007) Using reconstructed ivus images for coronary plaque classification. In: Proceedings of IEEE international conference on engineering in medicine and biology, Cit Internationale, Lyon, France, pp 2167–2170
32. Rosales M, Radeva P (2005) A basic model for IVUS image simulation. In: Handbook of biomedical image analysis, Topics in biomedical engineering international book series. Springer, New York, pp 1–55
33. Dietterich TG, Bakiri G (1995) Solving multiclass learning problems via error-correcting output codes. J Artif Intell Res 2:263–286
34. Schapire RE (1997) Using output codes to boost multiclass learning problems. In Proceedings of 14th international conference on machine learning. Morgan Kaufmann, CA, pp 313–321
35. Rennie J (2003) Boosting with decision stumps and binary features. Technical report, MIT, MA
36. Cover TM, Thomas JA (1991) Elements of information theory. Wiley-Interscience, NY
37. Demšar J (2006) Statistical comparisons of classifiers over multiple data sets. J Mach Learn Res 7:1–30
38. Schapire RE (2001) The boosting approach to machine learning: an overview. In: MSRI workshop on nonlinear estimation and classification. Berkeley, CA, USA

Ultrasound Despeckle Methods

Simone Balocco, Carlo Gatta, Josepa Mauri Ferré, and Petia Radeva

Abstract Speckle, a form of multiplicative noise, affects imaging applications such as medical Ultrasound (US). The effectiveness of a segmentation and registration process can be improved when the noise is removed without affecting important image features. This chapter details the main speckle reducing filtering categories and provides an extended comparison of various state-of-the-art algorithms focusing on the anisotropic filters family. A series of in silico experiments has been designed with the aim to compare the performances of the state-of-the-art approaches on synthetic images corrupted by a controlled amount of speckle noise. Additional in vivo experiments have been designed for illustrating the interest of using an accurate filtering method as pre-processing stage, in order to improve the performance of the segmentation methods.

1 Introduction

Speckle, a form of multiplicative noise, affects imaging applications such as medical Ultrasound (US). Speckle is the primary factor that limits the contrast in diagnostic ultrasound imaging, thereby reducing the effective application of image processing and analysis algorithms (i.e., edge detection, segmentation) and 2-D and 3-D volume rendering [1]. The effectiveness of a segmentation and registration process can be improved when the noise is removed without affecting important image features. The denoising process, however, should not destroy anatomical details relevant

S. Balocco (✉) • C. Gatta • P. Radeva
Computer Vision Center, Campus UAB, Edifici O, Bellaterra, Spain

University of Barcelona, Gran Via de Les Cortes Catalanes, 585, 08007 Barcelona, Spain
e-mail: balocco.simone@gmail.com; cgatta@cvc.uab.es; petia.ivanova@ub.edu

J.M. Ferré
Hospital universitari Germans Trias i Pujol, Carretera de Canyet s/n. 08916 Badalona, Spain
e-mail: jmauri.germanstrias@gencat.cat

J.M. Sanches et al. (eds.), *Ultrasound Imaging: Advances and Applications*,
DOI 10.1007/978-1-4614-1180-2_3,

from a clinical point of view. For instance, the noise corrupting the ultrasound images often contains relevant medical information useful for diagnosis purposes [2–4]. A significant effort has been made in the last decades to develop reliable and fast algorithms to remove noise without distorting or destroying relevant clinical information [5]. Speckle removal filters are often used as a pre-processing step for region-based detection, segmentation, and classification algorithms [6–8]. Their goal is to selectively remove the noise without destroying important image features and enhance object boundaries. Despite the huge advances in the computer technology, the computational efficiency is still a key issue, since the amount of information grows as we extend the analysis from 2D images to 3D and 4D data [9–12].

The most efficient filters obtain the edge-preservation property by embedding noise statistics in the filter framework. For this reason, Sect. 2 of this chapter details the speckle noise statistics and describes the main equations for the synthetic image simulation. Successively the main speckle reducing categories are introduced, providing a short description of the principle behind each filter family. Section 4 provides an extended comparison of various state-of-the-art algorithms focusing on the anisotropic filters family. The final section is devoted to the conclusion.

2 Speckle Noise Analysis

2.1 Speckle Noise Statistics

Speckle is a random, deterministic, interference pattern in an image due to the interactions and reflection of the Ultrasound wave with the sub-resolution scatterers of a medium. In particular, speckle appears in medical images when the characteristic size of the scatterers is small compared to the wavelength. An elementary resolution cell, defined as an arbitrary volume with dimension equals to the wavelength, is a function of the lateral and axial resolution of the transducer. Under the hypothesis of fully developed speckle, valid when an elementary resolution cell contains about ten scatterers [13], biological tissue can be modeled by a network of identical discrete scatterers, randomly distributed in a homogeneous media [14]. The radiofrequence echo signal accounts for each independent scatterer contribution and is described as a complex Gaussian probability function with zero mean [15]. Envelope detection removes the phase component, generating a speckle distribution whose statistic can be described by a Rayleigh probability function:

$$P_{\mathrm{RL}}(f(p),\sigma) = \frac{f(p)}{\sigma^2}\exp\left(\frac{-f(p)^2}{2\sigma^2}\right) \tag{1}$$

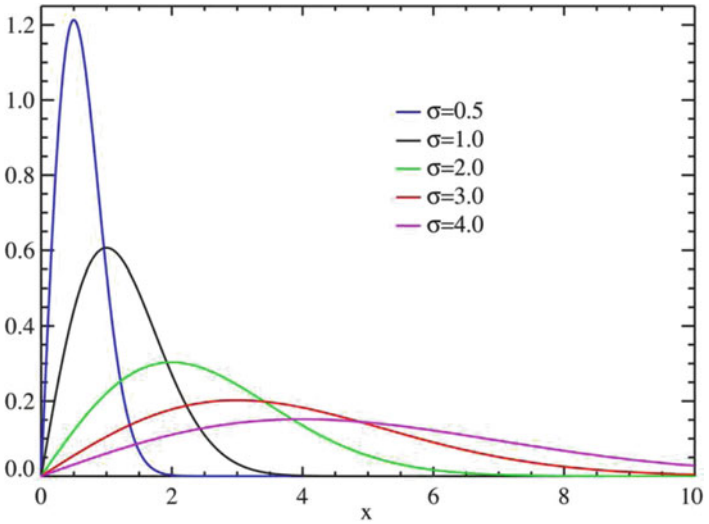

Fig. 1 Probability density function $P_{\mathrm{RL}}(f(p), \sigma)$ for different σ values

where $f(p)$ is a pixel intensity and σ is the shape parameter of P_{RL} related to the mean of the local pixel distribution μ by $\mu = \sigma \sqrt{\frac{\pi}{2}}$.

Speckle is a multiplicative noise, i.e., it is proportional to the local gray level in any area of the image. Figure 1 illustrates the probability density function $P_{\mathrm{RL}}(f(p), \sigma)$ for different σ values.

2.2 Speckle Noise Simulation

Synthetic images corrupted by speckle noise can be simulated either using an Ultrasound simulators, or reproducing the speckle statistical distribution (convolutional approach) [16, 17]. The use of an Ultrasound simulator in general provide a more flexible interface, the choice between a wider number of simulation parameters and a deeper control about the geometry of the simulated tissues and acoustic probes. However the simulation complexity is high, and the generation of a sequence of images (or a volume) may require hours of computation. On the other hand the convolutional approach, which is based on the same acoustic principles and equations of most ultrasound simulators, can provide the simulation of a sequence of images in a few seconds, with a reasonable accuracy. A complete list of the available Ultrasound simulators can be found at (see http://www.ieee-uffc.org/ultrasonics/software.asp) while the main principle of the convolutional simulation are detailed here.

The main assumption of the convolutional simulation is a linear imaging system, which can be described using a space-invariant point spread function (PSF). Let

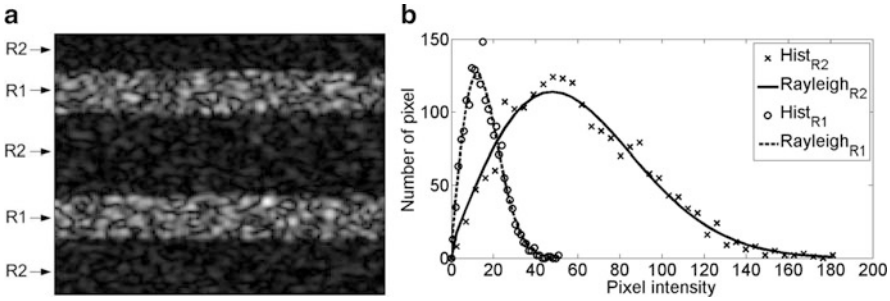

Fig. 2 (**a**) Synthetic Ultrasound envelope-detected images $B(x,y)$ (128×128 pixels size), simulated using a 5 MHz central frequency, and $\sigma_x = 2$ and $\sigma_y = 1.5$ PSF parameters. (**b**) Histogram and Rayleigh curve fitting in B^{R1} and B^{R2}

$I_0(x,y)$ be an echogenicity model (an image with different intensities corresponding to different tissues of the object being imaged) in which the variables x and y are the lateral and axial coordinates, respectively. Firstly, subresolution variations in object impedance should be introduced by multiplying the echogenicity model by a Gaussian white noise with zero mean and unitary variance:

$$T(x,y) = I_0(x,y) \times G(x,y) \tag{2}$$

$T(x,y)$, accounts for acoustic impedance inhomogeneities in the object due to density and acoustic speed perturbation that generates the scattering.

The $V(x,y)$ ultrasonic radiofrequency (RF) echo data can then be obtained by a convolution:

$$V(x,y) = h(x,y) * T(x,y) \tag{3}$$

where $h(x,y)$ is the PSF or impulse response of a hypothetical US imaging system. It is assumed [16, 17] that $h(x,y)$ is separable, i.e., $h(x,y) = h_1(x)\,h_2(y)$ where h_1 is a Gaussian-weighted sinusoidal function determined by:

$$h_1(x,\sigma_x) = \sin(k_0 x)\exp\left(-x^2/2\sigma_x^2\right) \tag{4}$$

where $k_0 = 2\pi f_0/v$, v is the speed of sound in tissue, f_0 is the center frequency, and σ_x represents the pulse-width of transmitting ultrasonic wave. The spatial response for the transmitting and receiving aperture $h_2(x)$ is determined by:

$$h_2(y) = \exp\left(y^2/2\sigma_y^2\right) \tag{5}$$

where σ_y represents the beam-width of transmitting ultrasonic wave.

The image of the envelope-detected amplitude, $B(x,y)$ shown in Fig. 2a, is given by:

$$B(x,y) = \left|V(x,y) + i\hat{V}(x,y)\right| \tag{6}$$

where $\hat{V}(x,y)$ is the Hilbert transform of $V(x,y)$ and i is the imaginary unit.

3 Ultrasound Speckle Reduction Methods

In literature, the problem of speckle reduction has been tackled by means of different techniques. In this section will be presented the main categories of speckle reduction filters along with a brief description of each filter principle.

3.1 Linear Filters

Linear filtering, e.g., Wiener filter [18], was the first adaptative approach used to deal with multiplicative noise [19]. Although linear filtering reduces the amount of noise in the image it over-smooths the transitions and anatomical details that should be preserved [20]. This difficulty arises because images corrupted with this type of noise often present low *signal to noise ratio* (SNR) and the non-linear and multiplicative nature of the corrupting process makes the linear approach not appropriate [21]. This difficulty can be overcome by adopting specific multiplicative models to describe the speckle noise [15, 22–24]. So in the last two decades, non-linear filtering methods have been successfully used to deal with the multiplicative noise using several approaches [25], e.g., median filtering, Bayesian and wavelet based methods and anisotropic Diffusion (AD) [16].

3.2 Median Filters

Median filter has been extensively used to process multiplicative and impulsive noise [24, 26] because it is a very simple technique and the visual results are good with a limited tuning. Several variants of the basic median filter were proposed, e.g., adaptive median filters. An example is the *Weighted Median Filter* (WMF) proposed in [27] for despeckling of ultrasound images. The filter considers a small window centered at each pixel as usual but each element of the input image is considered several times according to the local statistics of the image. More recently [28] proposes a novel stochastically driven filtering method with constant and variable size windows. A simpler version of this filter with constant window, is proposed in [29]. In [28] a novel despeckling method iteratively removes outliers by determining the local mean and standard deviation from an adaptively varying window. By removing outliers (local extrema) at each iteration, this method produces a convergent sequence of images by squeezing the stochastically distributed pixels values to a limiting value. It was experimentally shown by the authors that the proposed filter outperforms all the median filters considered in the experiments. Another technique is proposed in [30] where a new efficient 3D median despeckling algorithm is described and implemented in VHDL. Experimental tests performed by the authors lead to a processing time of 0.03 s to filter a $128 \times 128 \times 128$ 3D volume using a 50 MHz processor.

3.3 Wavelet-Based Filters

Wavelet-based despeckling algorithm has also been extensively used in medical imaging since the seminal works of Donoho on soft-thresholding were published [31]. This method is based on the multi-scale decomposition of the noisy image and in the processing of the image coefficients at coarser scales [25, 32–36]. For example, in [33] the authors compute the multi-scale decomposition of the logarithmic of the ultrasound image and model the coefficients at each scale by the alpha-stable heavy-tailed distribution. A Bayesian-based non-linear operator is then used to remove the speckle noise at each scale. A similar approach is described in [35] using *generalized Gaussian distribution (GGD)*. In [34] the same multi-scale decomposition is used to identify wavelet coefficients at different scales with high correlation. It is assumed that these coefficients describe anatomical details of the image which should be preserved. This allows the elimination of the noise without removing anatomical information. Comprehensive surveys on Wavelets in medical imaging can be found in [37, 38]. The wavelet denoising algorithms for images corrupted with multiplicative noise usually use a logarithmic version of the noisy original image, by assuming that multiplicative noise is converted into additive Gaussian one as suggested in [24] although, this assumption is not true, as discussed in [20].

3.4 Bayesian Filters

A different group of algorithms, called Bayesian methods, formulates the denoising task as an estimation problem, where the likelihood function and a prior distribution are jointly maximized. Let X be a $N \times M$ unknown image to be estimated/reconstructed from a noisy image, Y. The *maximum a posteriori* (MAP) estimate of X is the solution of the following optimization problem

$$\hat{X} = \arg\min_X E(X,Y) \tag{7}$$

where

$$E(X,Y) = \underbrace{E_Y(X,Y)}_{\text{Data fidelity term}} + \underbrace{E_X(X)}_{\text{Prior term}} \tag{8}$$

$E_Y(X,Y) = -\log p(Y|X)$, is called the *data fidelity term* and attracts the solution toward the data while $E_X(X) = -\log p(X)$, is called the *prior* or *internal energy* and regularizes the solution removing the noise.

The computation of X, based on the minimization of the data fidelity term $E_Y(X,Y)$, is the *maximum likelihood* (ML) estimation problem and it is usually an ill-posed problem because the solution is not unique and it may not depend continuously on the data [39–41]. To overcome this difficulty a regularization term

is added, turning the problem into a well-posed problem. The distribution $p(X)$ introduces prior knowledge about the image to be estimated, and it usually favors smooth solutions. The MAP energy function, $E(X,Y)$ has a global minimum, called MAP solution, which is, very often, difficult to find because the MAP optimization function (8) may not be convex.

It is usually assumed that there are no natural priors for medical images. The common assumption about these images is that they are band-limited, changing slowly in space except near the organs boundaries where abrupt transitions are expected. This is a difficult criterion because the location of the transitions are unknown and must be estimated. This can be done by modeling X as *Markov Random Field* (MRF) where neighboring pixels should have similar intensities, except if they are located at a transition. Three issues must be chosen in this framework: (1) the statistical observation model, (2) the prior distribution and (3) the optimization method [41]. A unifying Bayesian framework, based on the Sylvester–Lyapunov equation able to deal with Rayleigh and Poisson noise and with several prior distributions was recently proposed by Sanches [42]. Bayesian methods are often combined with the wavelet decomposition leading to efficient and fast algorithms [43–45].

3.5 Anisotropic Diffusion Filters

AD algorithms were introduced by Perona and Malik [46] in 1990. The general equation is $\frac{\partial I}{\partial \Omega(p)} = div\left(\left(g\left|\nabla I\right|\right)\nabla I\right)$ where ∇ is the gradient operator, $\Omega(p)$ is the spatial neighborhood of the coordinate of a generic pixel p in the noisy image I and *div* is the divergence operator.

This filter removes the noise by computing a local average of the central pixel intensity with the ones of its neighbors. The iterative process achieves a balance between averaging (in homogeneous regions) and the identity filter (where edges exist) according to a coefficient proportional to the directional gradient. This balance depends on the *coefficient of variation* $\left(g\left|\nabla I\right|\right)$ inside the neighborhood Ω. If $\left(g\left|\nabla I\right|\right) \to 0$ the algorithm behaves as an all-pass filter while when $\left(g\left|\nabla I\right|\right) \to 1$ an isotropic diffusion is achieved (Gaussian filtering). The general anisotropic equation was successively improved by several authors [16, 47] by proposing a *coefficient of variation* able to better estimate the edge orientations. In particular the Speckle Reducing Anisotropic Diffusion (SRAD) algorithm [16], was based on a coefficient able to enhance the boundaries. The filler preserves the object shapes by inhibiting diffusion across boundaries and, at the same time, enhance the shape frontiers by promoting the AD on either side of the edge. Successively, Krissian [48] proposed an extension of SRAD called Oriented Speckle Reduction Anisotropic Diffusion (OSRAD), that allows different levels of filtering along the image contours and their principal curvature directions.

In 1998, Tomasi [49] introduced the Bilateral Filter (BF) framework in which the output pixel's value is a Gaussian-weighted average of its neighbors in both space and intensity range. The general BF functional can be expressed as:

$$h(p) = \Gamma^{-1}(p) \int_{\Omega(p)} f(\xi)\, c(\xi, p)\, s(f(\xi), f(p))\, d\xi \tag{9}$$

with the normalization factor:

$$\Gamma(p) = \int_{\Omega(p)} c(\xi, p)\, s(f(\xi), f(p))\, d\xi \tag{10}$$

where f is the input image, h is the output image, $\Omega(p)$ is the spatial neighborhood of a pixel p in the image, ξ is the integration variable representing pixels coordinates in Ω. The classical BF framework [49] defines both c and s functions as unbiased isotropic Gaussian functions.

Comaniciu [50] proposed the mean shift approach based on a statistical local modes analysis of the image distribution in the joint spatial-range domain. The relationship between AD, adaptive smoothing, bilateral filtering and mean shift procedure was finally established by Barash and Comaniciu [51] in 2004 demonstrating that such families of filters, under specific conditions, are formally identical. More recently, adaptive filters based on local noise statistics were proposed by Guo and Thakur [52, 53]. Dantas [54] introduced a filter based on a set of modified Gabor filters (MGFs). However, most filters are developed independently of the image nature and its noise statistical model. In contrast, Aysal [1] embedded in a basic filter framework the Rayleigh noise statistics. Finally Balocco [55] proposed a fully automatic speckle reducing bilateral filter tailored to US Images called SRBF. In [55], the edge-preserving feature for US images is obtained by embedding noise statistics in the filter framework by modifying both c and s functions of the classical BF framework. As a consequence, the filter is able to tackle the noise multiplicative behavior modulating selectively the smoothing strength with respect to local statistics.

4 Filter Comparison

This last category (anisotropic filters, described in Sect. 3) has been proved to obtain the strongest reduction of speckle noise, while maintaining a low computational cost. For this reason the next section will present various experiments, extracted by the article [55], focusing on a comparison of such filter categories. In each subsection several state-of-the-art filters are compared through experiments performed on both in silico and in vivo data. In particular, an experiment has been designed for illustrating the interest of using an accurate filtering method as pre-processing stage, in order to improve the performance of the segmentation stages.

4.1 Anisotropic Filters Comparison

This section presents two experiments comparing the performance of several state-of-the-art anisotropic filters. Specific details about the noise distributions can be found in [55].

The first set of experiments (Sect. 4.1.1) assesses the performance and the robustness of all the denoising filters when applied to in silico images corrupted with Rayleigh noise. Then, a second experiment (Sect. 4.1.2), compares qualitatively and quantitatively the best two algorithm of the first experiment on in vivo Ultrasound images This second study aims at evaluating how each denoising filter improves the performance of a segmentation algorithm.

4.1.1 In Silico Experiments

A set of in silico experiments was designed to compare the performance of the anisotropic filters on images characterized by a controlled amount of noise. The edge-preserving performance in this case has been tested by evaluating the Sum of Square Differences (SSD) criterion between the ground truth and the denoised images which provides local comparison of the filtering results with the ground-truth data.

Experimental Image Set

A set of US synthetic images, consisting of two regions, of low (R2) and high (R1) scatterer intensity respectively, was generated using the convolutional approach [16, 17] detailed in the Sect. 2.2. The echogenicity model amplitude in R1 (I_0^{R1}) is unitary, while in R2 (I_0^{R2}) can be tuned using a parameter $\gamma = I_0^{R1}/I_0^{R2}$ representing the brightness contrast between the two areas. Since the noise is multiplicative, γ indirectly indicates the SNR. The higher is the contrast between the two areas the higher is the SNR. The use of the γ variable does not relate with the amplitude of US equipment contrast.

In the whole set of images, a 5 MHz central frequency probe is simulated, and an anisotropic noise distribution is obtained using a PSF with parameters $\sigma_x = 1 \times k$ and $\sigma_y = 1.5 \times k$, where k will be used as noise scaling factor.

Fig. 1 illustrates a 128×128 pixel image of the set with echogenicity model amplitudes $I_0^{R1} = 1$ and $I_0^{R2} = 0.2$. The histogram computed in two uniform regions of the image exhibits two Rayleigh distributions (Fig. 2b), with $\hat{\sigma}_{R2} = 0.272$ and $\mu_{R2} = 0.154$ (in the central region) and $\hat{\sigma}_{R1} = 1.55$ and $\mu_{R1} = 1.55$ (in the upper bright region) respectively. The ratio between the Rayleigh parameter estimators in the bright (R1) and the dark (R2) areas of the envelope image (Fig. 2a) are equal to the ratio of I_0^{R1} over I_0^{R2} since speckle noise is purely multiplicative.

Performance Comparison

In this section, various state-of-the-art speckle reducing techniques based on the AD framework are compared. Classic Bilateral Filter (CLASSIC BF)[49], AD [47], Rayleigh-Maximum-Likelihood Filter (RMLF) [1], Adaptive filter based on second order statistics filter (AF) [53], MGF [54], Guo filter (GUO) [52], mean-shift (MEAN-SHIFT)[1] [51], Speckle reduction anisotropic diffusion[2] (SRAD) [16], Oriented speckle reduction AD[3] (OSRAD) [48] and SRBF [55] are applied to a set of 50 synthetic images generated with the same contrast and speckle size ($\gamma = 5$ and $k = 1$) in order to qualitatively (Fig. 3) and quantitatively (Table 1) evaluate the respective performances.[4] Particularly Table 1, for each method, lists the parameters, compares the features (number of iterations, computational time), and reports the similarity scores.

As it can be observed in Fig. 3a, b, the SRBF [55] presents a superior edge-preserving behavior, thus outperforming filtering method based on zero mean noise assumptions. RMLF, AF, MGF, and GUO and MEAN-SHIFT methods are unable to fully remove the speckle noise in the uniform area although they exhibit border preservation properties (see Fig. 3c–g). On the other hand, SRAD and OSRAD better smooth the noise close to the lower edge of the image, thanks to their edge-enhancing feature. Even though SRAD and OSRAD use a fixed spatial support, the latter achieves better performances since it emphasizes the smoothing behavior along the tangential direction to the object boundary (Fig. 3h, i).

These results are in agreement with the average SSD similarity score, computed over the 50 synthetic images, reported in Table 1 (last column). In this experiment the reconstruction accuracy of SRBF and OSRAD are similar; however, it is worth noting that SRBF is faster (about 20 times) and fully automatic, as summarized in the feature description listed in Table 1.

Filter Robustness

The previous section illustrated that among the considered anisotropic approaches, the OSRAD and SRBF filters provide the best denoising outcome. In this section we designed a set of experiment to investigate the robustness of such filters when the size of the speckle changes. Both filters are applied to synthetic images generated with different speckle sizes (by varying k while keeping $\gamma = 5.7$) and the results are illustrated in Fig. 4.

---

[1] EDISON: Code for the Edge Detection and Image SegmentatiON system, http://www.caip.rutgers.edu/riul/research/code/EDISON/index.html

[2] http://viva.ee.virginia.edu/research_ultrasounddenoising.html

[3] http://serdis.dis.ulpgc.es/~krissian/HomePage/

[4] Implementation in Matlab software and computed on a Pentium IV dual core Intel processor.

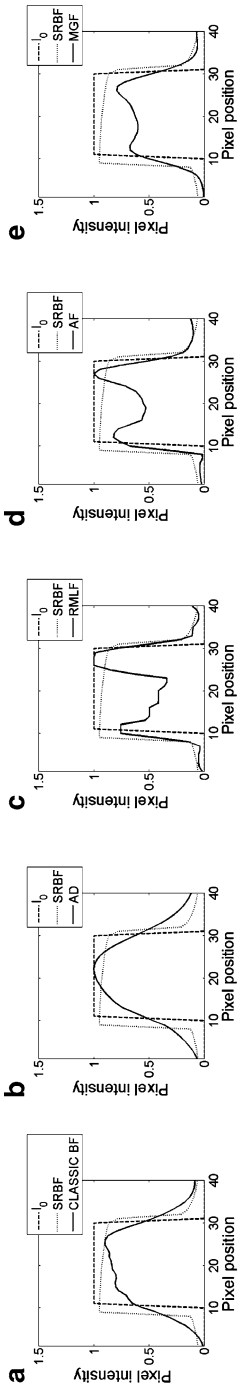

Fig. 3 Normalized Intensity profile of denoised images, superimposed on the ground-truth shape I_0. Pairwise filtering comparison of (**a**) CLASSIC BF, (**b**) AD, (**c**) RMLF, (**d**) AF, (**e**) MGF, (**f**) GUO, (**g**) MEAN-SHIFT, (**h**) SRAD and (**i**) OSRAD versus SRBF algorithm.

Table 1 Features and performance comparison of speckle reducing filters

	Support	User interaction	Experimental parameters	Iterations n.	Computational time (128×128 pixels)	SSD (mean ± std)
Noised image I_0	–	–	–	–	–	7,104 ± 180
CLASSIC BF [49]	User defined N	Fully automatic	8	6	0.364 [s]	2,736 ± 130
AD [47]	Four neighbors	Noise variance size (σ)	σ =1.3	300	1.411 [s]	3,692 ± 139
RMLF [1]	Eight neighbors	2 smoothing coefficients ($k_{1,2}$) 1 coefficient of variation (τ)	$k_1 = 0.5$ $k_2 = 0.05$ $\tau = 0.05$	1	0.028 [s]	3,138 ± 114
MGF [54]	Frequency filter	Probe central frequency k_0, Lateral and axial Gabor Filter orientations $\sigma_{ax}, \sigma_{lat}$	$k_0 = 4$ $\sigma_{ax} = 5$ $\sigma_{ax} = 10$	1	0.055 [s]	2,384 ± 190
AF[53]	Adaptive W	α_0,D,CT,L_{inv},H_{inv},L_{asm} H_{asm},E_t as described in [53]	$W = 2$, $\alpha_0 = 0.04$ $D = 2$, $CT = 3.2$, $E_t = 1$ $L_{\text{inv}} = 0.4$, $L_{\text{asm}} = 0.05$ $H_{\text{inv}} = 0.8$, $H_{\text{asm}} = 0.2$	1	47 [s]	2,810 ± 148
GUO [52]	Twenty four neighbors	Fully automatic	None	1	3.117 [s]	2,622 ± 129
MEAN-SHIFT [51]	User defined N	Noise variance (σ)	$N = 6$, $\sigma = 1$	10	3.312 [s]	2,246 ± 129
SRAD [16]	Four neighbors	Choice of uniform region	Top stripe of I^{R2}	1,000	1.57 [s]	1,913 ± 153
OSRAD [48]	Four neighbors	Choice of uniform region	Top stripe of I^{R2}	1,000	6.305[s]	1,635 ± 168
SRBF [55]	Adaptive	Fully automatic	None	6	0.364 [s]	1,288 ± 127

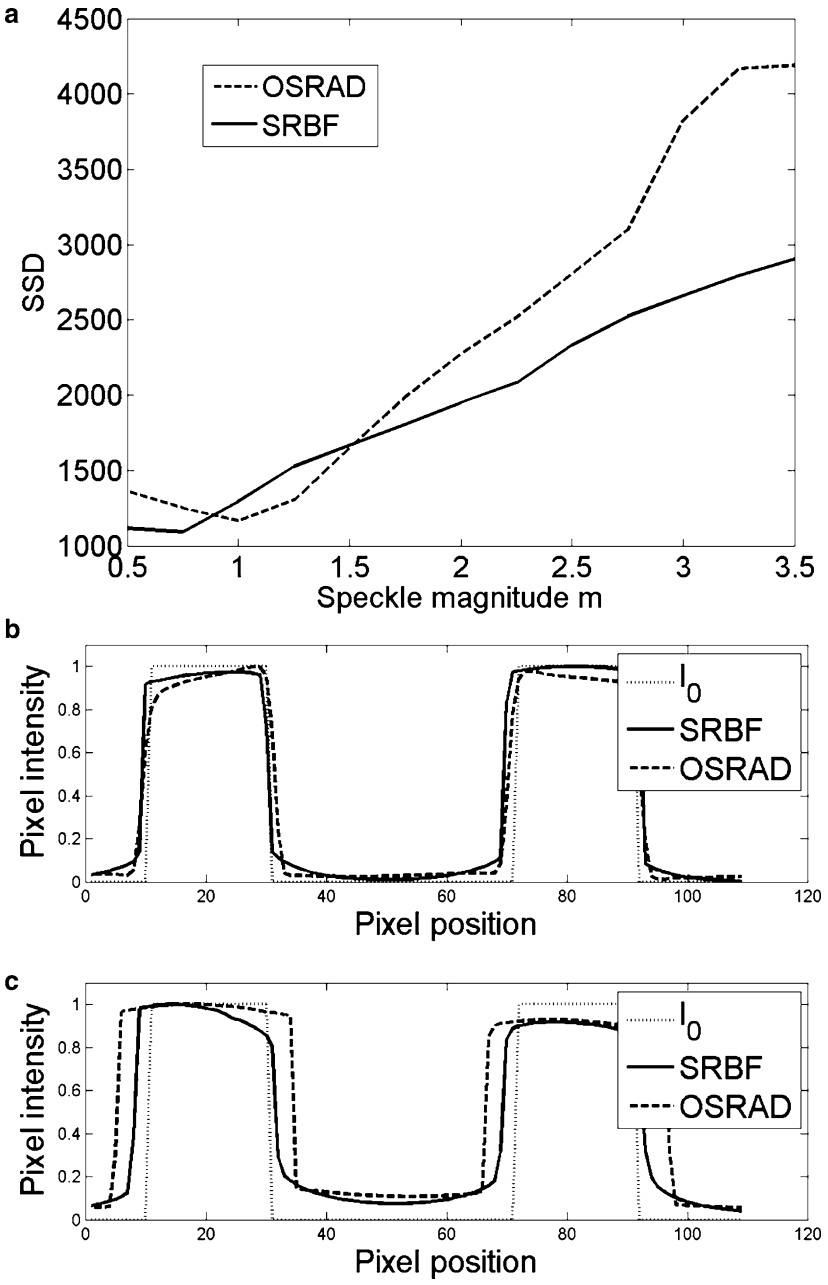

Fig. 4 Average SSD (**a**) between the echogenicity image I_0 and the image filtered using OSRAD and SRBF when the speckle noise scaling factor k ranges from 0.5 to 3.5. Intensity profile of I_0 (**b–c**) superimposed on the OSRAD and SRBF filtering result when the noise scaling is equal to 1 and to 2.5, respectively.

As shown in Fig. 4a, the performance of OSRAD is comparable to SRBF when the noise pattern is small, and progressively decreases in the presence of big speckle patterns. In this last case, as it can be seen in Fig. 4c, OSRAD enlarges the edges. The same behavior can be observed at different contrasts (γ). The performance decrease of OSRAD filter is probably due to its constant size neighbor support, while SRBF automatically adapts its spatial support depending on the speckle pattern. Concluding, SRBF exhibits higher robustness because of its fully automatic settings of relevant parameters, the speckle noise statistics, and the speckle size.

4.1.2 In Vivo Experiments

Despeckle algorithms are generally used as pre-processing step for automatic segmentation of US images. The performance of the sole filter can be hardly validated on in vivo images since reference denoised data is obviously not available. Instead, the accuracy improvement of a segmentation algorithm is quantified when the images are denoised.

For this purpose, the best two algorithm (SRBF and OSRAD) listed in Table 1 are compared on Intravascular Ultrasound (IVUS) images because of their challenging properties: the anisotropy of the speckle patterns, the presence of artifacts, and the variable echogenicity of the tissues.

IVUS In Vivo Images

Fifty slices, chosen to represent different vascular structures (plaque and vessel shape, presence of stent, lumen area, and diameter), were extracted from a data base of 3,000 in vivo coronary images. The acquisition was performed using an IVUS Galaxy II System with a catheter Atlantis SR Pro 40 MHz (Boston Scientific). For each slice the RF signal is available.

From all the 50 slices in polar coordinates different sets of images are computed: the envelope of the RF signal (data-set $\mathscr{A}$), the OSRAD filtered envelope (data-set $\mathscr{B}$), and the SRBF filtered envelope (data-set $\mathscr{C}$). In order to avoid the discontinuity at $0/360^\circ$ of the IVUS image, we mirrored the leftmost (0°) and rightmost (360°) texture before filtering, copying 30° of both on the opposite side, thus obtaining a continuous signal at the boundaries. The catheter ring-down artifact located at the top of the polar image was suppressed by filling the region with a uniform color computed as the mean intensity of the underlying stripe, 0.3 mm thick, adjacent to the catheter area. The same stripe, containing only blood, has been defined as uniform region required by the OSRAD filter. All the images, were log compressed and converted to cartesian coordinates prior to segmentation and visualization.

A classic level-set active contour (snake) algorithm[5] [56], commonly used to segment US medical images [57], is applied to the three data-sets. The initialization shape and the level-set smoothness parameter are fixed and tuned to obtain the best performance on the envelope data-set. The same settings are used when the snake is applied to the data-sets $\mathscr{B}$ and $\mathscr{C}$. The snake propagates from an initial circular contour until stopping at an energy-stable configuration dependent on the image gradients. The snake inner area is obtained from the zero level-set shape at convergence. Ground-truth shapes, indicating the expected segmentation result, were manually delineated in each of the IVUS frames by two independent experts. The operator performing the analysis was blinded to the automatic and to the other manual segmentation results.

Segmentation Comparison

Figure 5 presents the manual delineated border and the results of the automatic segmentation for seven representative frames of the three data-sets $\mathscr{A}$, $\mathscr{B}$, and $\mathscr{C}$. Frame #1 illustrates an accurate automatic segmentation obtained in all the three data-sets. In frame #2, the snake crosses the vessel border between the stent wires (highly echogenic spots) and spreads in the surrounding tissue. On the contrary, the snake propagation stops correctly at the lumen frontier in data-sets $\mathscr{B}$ and $\mathscr{C}$, since both filters enhance the outline of the vessel membrane by smoothing the noise and by preserving the sharp vessel edges. Similarly in frame #3 the denoising methods enhance the borders making the segmentation easier. However in this case (frame #3) the segmentation of data-set $\mathscr{B}$ is slightly less accurate, since the filtering method fuses a small catheter ringing artifact with the vessel border, creating an artificial boundary. The same behavior can be observed in frame #4 where, in data-set $\mathscr{B}$, the noise lying between the catheter artifact and the vessel is not removed but homogenized.

Frame #5 illustrates that the high amount of noise (data-set $\mathscr{A}$) may hamper the snake propagation on the envelope data, while an efficient smoothing promote an accurate and automatic segmentation (data-sets $\mathscr{B}$ and $\mathscr{C}$). However it is worth to note that, in data-set $\mathscr{B}$ (frame #5), the image filtered with OSRAD is locally smoothed, but radial ripples are still present since OSRAD has a fixed support. On the other hand, SRBF better homogenizes uniform areas, since the spatial support controlled by the function c is wider and has been designed to automatically contain consecutive scatter peaks. For this reason probably, in frame #6 the snake applied to $\mathscr{B}$ gets trapped in a local minima and stops propagating after 560 iterations, while in $\mathscr{C}$ the snake keeps spreading inside the whole lumen. Finally in frame #7 the snake spans outside the vessel for data-sets $\mathscr{A}$ and $\mathscr{B}$, but not in $\mathscr{C}$. In this frame, the OSRAD filter enhances the shadow area on the left of the catheter, and creates an undesired gradient attracting the snake in $\mathscr{B}$, while SRBF homogenizes the shadow

[5] http://www.shawnlankton.com/2007/05/active-contours/

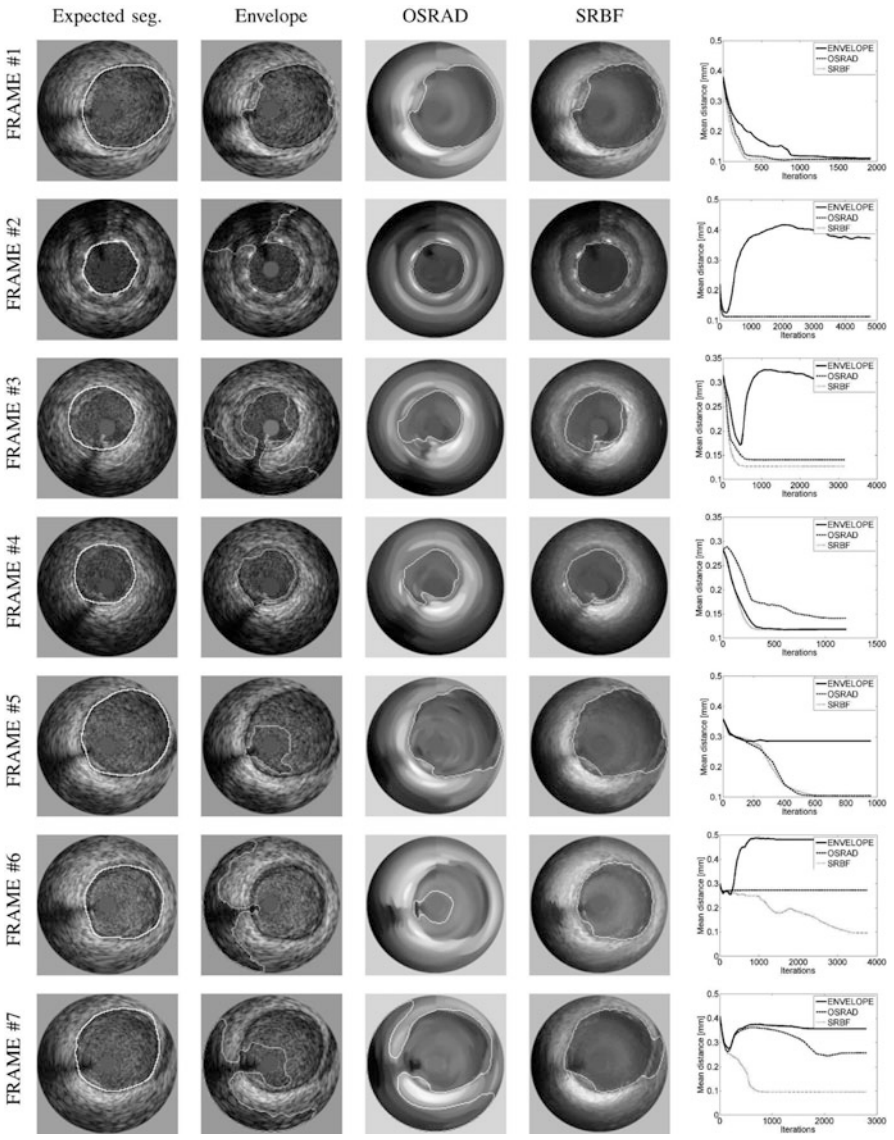

Fig. 5 Snake manual (first column) and automatic (second, third, and forth columns) segmentations of seven representative frames from the three data-sets $\mathscr{A}$, $\mathscr{B}$, and $\mathscr{C}$. The last column illustrates the average distance of each automatic segmentation to the manual segmentations

region with the rest of the lumen in *C*. In fact, compared to OSRAD which is a zero mean filter, the SRBF noise model fits better the speckle distribution at low image intensities and discriminate more accurately between noise and tissues.

The last column of Fig. 5 represents the average distance of the automatic segmentation to the two manual segmentations. In frame #1 the high slope of the curve indicates that the snake converges faster in filtered data-sets ($\mathscr{B}$ and $\mathscr{C}$) since the noise is accurately removed. In frame #4, a similar behavior can be observed, but the segmentation of $\mathscr{B}$ results as the slowest and the less accurate because of the wrinkled lumen region. In frame #2, #3, and #5 the segmentation applied to the non-filtered image diverges, while the two filters show similar convergence speed. These examples illustrate the interest of using an accurate filtering method before the segmentation stage. In frame #6 the snake applied to data-set $\mathscr{B}$ stops expanding earlier than data-set $\mathscr{C}$ leading to an incorrect vessel segmentation and to a lumen area under-estimation. Finally, in frame #7 the SRBF filtered the snake applied to data-set $\mathscr{A}$ and $\mathscr{B}$ diverges, and only the snake applied to the data-set $\mathscr{C}$ converges to the vessel wall. In all the cases, the segmentation on data-set $\mathscr{C}$ is either the fastest or the only one converging to the vessel boundary, showing the superior performances of SRBF.

Figures 6 and 7 show a pairwise error comparison for all the frames of the three data-sets ($\mathscr{A}$, $\mathscr{B}$, and $\mathscr{C}$). In particular, Fig. 6 illustrates the error between the automatic and ground-truth border segmentations, while Fig. 7 shows the error in the lumen area estimations.

In Fig. 6a most of the markers are located below the solid line of unitary slope, indicating that the average distance between the automatic and the manual segmentations is smaller in the filtered data-sets ($\mathscr{B}$, $\mathscr{C}$) that in the non-filtered ($\mathscr{A}$). Figure 6b, shows the superior accuracy obtained by filtering the images with SRBF.

The average distance over all the images of the data-sets $\mathscr{A}$, $\mathscr{B}$, and $\mathscr{C}$ with respect to the manual segmentations are 0.27 ± 0.47 mm, 0.15 ± 0.24 mm, and 0.12 ± 0.14 mm respectively, confirming that the contours obtained from the data-set $\mathscr{C}$ exhibit the lowest segmentation error. The average distance over all the images of the inter-observer variability is 0.021 mm.

In order to quantify the error in estimating the area for the three data-sets the Jaccard coefficient [58] defined as the ratio $R = \frac{|\Phi \cap \Psi|}{|\Phi \cup \Psi|}$ is used, where Φ is the set of pixels of the manual segmentation, and Ψ is the set of pixels resulting from automatic segmentation [59]. The score R is one when the areas matches exactly and rapidly decreases when one of the two areas differs from the other.

The performance of the automatic segmentation on the filtered data-sets $\mathscr{B}$ and $\mathscr{C}$, is superior to the non-filtered images $\mathscr{A}$ (see Fig. 7a), since R is higher than the line with unitary slope for most of the images. Analyzing the scatter plot of Fig. 7b, and comparing directly the performance of the snake on the two denoised data-sets, it can be noticed that the R-score is similar, but some outliers, representing unsuccessful segmentations of data-set $\mathscr{B}$, are present.

In more than 50% of the images, the R-score corresponding to OSRAD filter ranges from 0.12 to 0.33, while for SRBF R varies from 0.06 to 0.24 (Fig. 6b). Analyzing the scatter plot of Fig. 7b in detail, it can be noticed that in about 50% of the images, OSRAD R-score ranges from 0.2 to 0.8, while for SRBF R varies from 0.6 to 0.9. The average R-score over all the images of the data-sets $\mathscr{A}$, $\mathscr{B}$ and

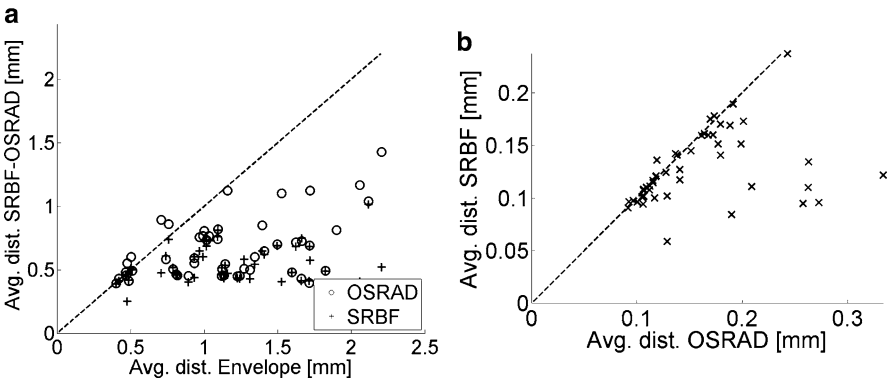

Fig. 6 Average distance of the automatic segmentation to the two manual segmentations. (**a**) comparison of data-sets $\mathscr{B}$ and $\mathscr{C}$ vs $\mathscr{A}$; (**b**) pairwise comparison of data-sets $\mathscr{B}$ vs $\mathscr{C}$

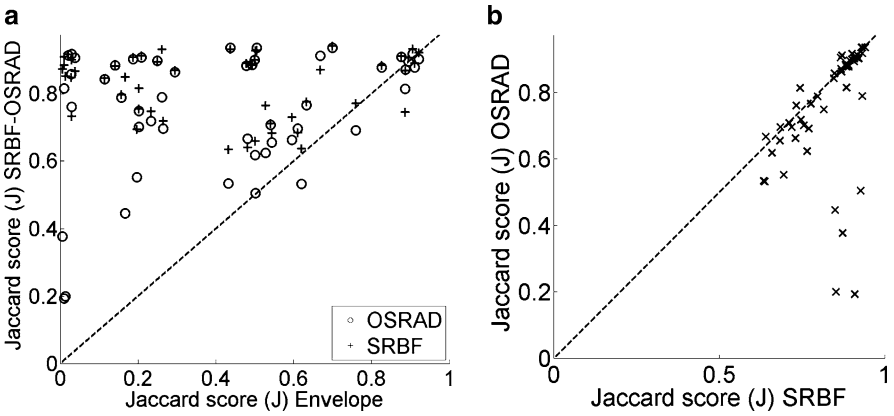

Fig. 7 Area ratio R representing the likeness between the automatically segmented areas. (**a**) comparison of data-sets $\mathscr{B}$ and $\mathscr{C}$ vs $\mathscr{A}$; (**b**) pairwise comparison of data-sets $\mathscr{B}$ and $\mathscr{C}$

$\mathscr{C}$ are 0.41 ± 0.29, 0.76 ± 0.18 and 0.83 ± 0.09 respectively, showing that the areas recovered on the data-set $\mathscr{C}$ are the most similar to the manually segmented regions.

ANOVA and t-test statistical analysis were performed for both segmentation distances and R-scores in data-sets $\mathscr{A}$, $\mathscr{B}$, and $\mathscr{C}$. In all cases the scores of data-sets $\mathscr{B}$ and $\mathscr{C}$ are significantly different (p-values ¡1×10^{-9} for both ANOVA and t-test) from data-set $\mathscr{A}$. Comparing data-sets $\mathscr{B}$ and $\mathscr{C}$, the ANOVA provides p-values of 0.0032 and 0.0153 respectively for the distances and R-scores; and the t-test provides p-values of 5.5×10^{-4} and 0.0039 respectively for the distances and R-scores. These tests confirm the statistical significance of the results. The R-score over all the images of the inter-observer variability is 0.95.

Concluding, SRBF outperforms the filtering methods based on zero mean noise assumptions. Compared to OSRAD, SRBF approach is fully automatic, locally adaptive, and the number of iterations needed to reach the optimal solution is smaller. Additionally, SRBF results in a more robust algorithm suitable for a wide ranges of speckle noise sizes.

5 Conclusion

In this chapter, several speckle denoising filters are proposed and compared. Particularly one family of filters (anisotropic algorithms) are analyzed both qualitatively and quantitatively on ultrasound data. A series of in silico experiments has been designed with the aim to compare the performances of the state-of-the-art approaches on synthetic images corrupted by a controlled amount of speckle noise. Additional in vivo experiments has been designed for illustrating the interest of using an accurate filtering method as pre-processing stage, in order to improve the performance of the registration and segmentation methods.

Finally the computational cost of most of the algorithm is provided in order to evaluate the applicability in unsupervised filtering of large amounts of clinical data.

References

1. Aysal TC, Barner KE (2007) Rayleigh-maximum-likelihood filtering for speckle reduction of ultrasound images. IEEE Trans Med Imaging 26(5):712–727
2. Stoitsis J, Golemati S, Nikita KS, Nicolaides AN (2004) Characterization of carotid atherosclerosis based on motion and texture features and clustering using fuzzy c-means, Engineering in Medicine and Biology Society, 2004. IEMBS '04. 26th Annual International Conference of the IEEE 1(1–5):1407–1410 Sept. doi: 10.1109/IEMBS.2004.1403437
3. Christodoulou CI, Pattichis CS, Pantziaris M, Nicolaides A (2003) Texture-based classification of atherosclerotic carotid plaques. IEEE Trans Med Imaging 22(7):902–912
4. Bleck JS, Ranft U, Gebel M, Hecker H, Westhoff-Beck M, Thiesemann C, Wagner S, Manns M (1996) Random field models in textural analysis of ultrasonic images of the liver. IEEE Trans Med Imaging 15(6):796–801
5. Noble JA, Boukerroui D (2006) Ultrasound image segmentation: a survey. IEEE Trans Med Imaging 25(8):987–1010
6. Munteanu C, Morales FC, Fernandez JG, Rosa A, Deniz LG (2008) Enhancing obstetric and gynecology ultrasound images by adaptation of the speckle reducing anisotropic diffusion filter. Artif Intell Med 43(3):223–242
7. Li B, Acton ST (2007) Active contour external force using vector field convolution for image segmentation. IEEE Trans Image Process 16(8):2096–2106
8. Tsai DY, Watanabe S (1998) A method for optimization of fuzzy reasoning by genetic algorithms and its application to discrimination of myocardial heart disease. Proc IEEE Nucl Sci Symp Med Imag Conf 3:1756–1761
9. Hua Li, Anthony Yezzi (2007) Local or Global Minima: Flexible Dual-Front Active Contours. IEEE Transactions on Pattern Analysis and Machine Intelligence 1–14, January

10. Lee TS, Segars WP, Tsui BMW (2005) Study of parameters characterizing space-time gibbs priors for 4d map-rbi-em in gated myocardial perfusion spect. Nucl Sci Symp Conf Rec 4:2124–2128
11. Deschamps T, Malladi R, Ravve I (2004) Fast evolution of image manifolds and application to filtering and segmentation in 3d medical images. IEEE Trans Vis Comput Graph 10:525–535
12. Delingette H (2000) General object reconstruction based on simplex meshes. Int J Comput Vis 32(2):111–146
13. Jensen A.J (1996) A signal processing approach, Cambridge University Press, New York, ISBN 0-521-46484-6
14. Chivers RC (1977) The scattering of ultrasound by human tissues, some theorical models. Ultrasound Med Biol 3:1–13
15. Wagner RF, Smith SW, Sandrik JM, Lopez H (1983) Statistics of speckle in ultrasound b-scans. IEEE Trans Sonics Ultrasonics 30(3):156–163
16. Yu Y, Acton S (2002) Speckle reducing anisotropic diffusion. IEEE Trans Image Process 11(11):1260–1271
17. Bamber JC, Dickinson RJ (1980) Ultrasonic b-scanning: a computer simulation. Phys Med Biol 25(3):463–479
18. Moon TK, Stirling WC (2000) Mathematical Methods and Algorithms for Signal Processing. Moon (Vol. 204, p. 937). Prentice Hall.
19. Abbot J, Thurstone F (1979) Acoustic speckle: theory and experimental analysis. Ultrasound Imag 1:303–324
20. Michailovich O, Tannenbaum A (2006) Despeckling of medical ultrasound images. IEEE Trans Ultrason Ferroel Freq Contr 53(1):64–78
21. Gravel P, Beaudoin G, De Guise JA (2004) A method for modeling noise in medical images. 23(10):1221–1232
22. Dainty JC (1984) Laser speckle and related phenomena. Laser speckle and related phenomena, XVII, 342 pp. 146 figs. Springer-Verlag, Berlin, Heidelberg, New York. Also topics in applied physics, vol 9
23. Wagner RF, Insana MF, Smith SW (1988) Fundamental correlation lengths of coherent speckle in medical ultrasonic images. IEEE Trans Ultrason Ferroelectr Freq Control 35(1):34–44
24. Jain AK (1989) Fundamentals of digital image processing, Prentice-Hall, Inc. Upper Saddle River, NJ, USA © 1989. ISBN:0-13-336165-9
25. Loizou C, Pattichis C, Christodoulou CI, Istepanian R, Pantziaris M, Nicolaides A (2005) Comparative evaluation of despeckle filtering in ultrasound imaging of the carotid artery. IEEE Trans Ultrason Ferroel Freq Contr 52(10):1653–1669
26. Huang T, Yang G, Tang G (1979) A fast two-dimensional median filtering algorithm. IEEE Trans Acoust Speech, Signal Process 27(1):13–18
27. Loupas T, McDicken W, Allan P (1989) An adaptive weighted median filter for speckle suppression in medical ultrasonic images. IEEE Trans Circuit Syst 36:129–135
28. Tay PC, Acton ST, Hossack JA (2006) A stochastic approach to ultrasound despeckling. Biomedical Imaging: Nano to Macro, 3rd IEEE International Symposium on, 6–9 April, 221–224, doi: 10.1109/ISBI.2006.1624892
29. Tay PC, Acton ST, Hossack JA (2006) Ultrasound Despeckling Using an Adaptive Window Stochastic Approach. Image Processing, 2006 IEEE International Conference on, 8–11 Oct. 2549–2552, doi: 10.1109/ICIP.2006.312979
30. Jiang M, Crookes D (2006) High-performance 3d median filter architecture for medical image despeckling. Electron Lett, 42(24):229–240
31. Donoho D (1994) De-noising by soft-thresholding. 41(3):613–627
32. Zhong S, Cherkassky V (2000) Image denoising using wavelet thresholding and model selection. Int conf Image Process 3:262–265
33. Achim A, Bezerianos A, Tsakalides P (2001) Novel bayesian multiscale method for speckle removal in medical ultrasound images. IEEE Trans Med Imaging 20:772–783
34. Bao P, Zhang L (2003) Noise reduction for magnetic resonance images via adaptative multiscale products thresholding. IEEE Trans Med Imaging 22(9):1089–1099

35. Gupta S, Kaur L, Chauhan RC, Saxena SC (2004) A wavelet based statistical approach for speckle reduction in medical ultrasound images. Med Biol Eng Comput 42:534–537
36. Figueiredo MAT, Nowak RD (2005) A bound optimization approach to waveletbased image deconvolution. Image Processing, 2005. ICIP 2005. IEEE International Conference on, 2:II–782–5, 11–14 Sept. doi: 10.1109/ICIP.2005.1530172
37. Laine AF (2000) Wavelets in temporal and spatial processing of biomedical images. Annual Rev Biomed Eng 2:511–550
38. Y. Jin, E. Angelini, A. Laine (2005) Wavelets in Medical Image Processing: Denoising, Segmentation, and Registration, in Handbook of Biomedical Image Analysis Vol 1- Segmentation Models - Part a, Ed.: D. L. W. Jasjit Suri, Swamy Laximinarayan Kluwer Academic/ Plenum Publishers, 305–358
39. Hadamard J (1902) Sur les problèmes aux dérivées partielles et leur signification physique. Princeton University Bulletin 13:49–52
40. Shepp LA, Vardi Y (1982) Maximum likelihood reconstruction in positron emission tomography. 1(2):113–122
41. Vogel CR (2002) Computational methods for inverse problems, 10:183 SIAM
42. Sanches JM, Nascimento JC, Marques JS (2008) Medical image noise reduction using the sylvester-lyapunov equation. IEEE Trans Image Process 17(9):1522–1539
43. Huang CY, Soltz MA, Kopacz M, Mow VC, Ateshian GA (2003) Experimental verification of the roles of intrinsic matrix viscoelasticity and tension–compression nonlinearity in the biphasic response of cartilage. J Biomech Eng 125:84–93
44. Gleich D, Datcu M (2006) Gauss-markov model for wavelet-based sar image despeckling. IEEE Signal Process Lett 13(6):365–368
45. Xu J, Osher S (2007) Iterative regularization and nonlinear inverse scale space applied to wavelet-based denoising. IEEE Trans Image Process 16(2):534–544
46. Perona P, Malik J (1990) Scale space and edge detection using anisotropic diffusion. IEEE Trans Pattern Anal Machine Intell 12:629–639
47. Black M, Sapiro G, Marimont D, Heeger D (1998) Robust anisotropic diffusion. IEEE Trans Image Process 7(3):421–432
48. Krissian K, Westin CF, Kikinis R, Vosburgh KG (2007) Oriented speckle reducing anisotropic diffusion. IEEE Trans Image Process 16(5):1412–1424
49. Tomasi C, Manduchi R (1998) Bilateral filtering for gray and color images, Computer Vision. Sixth International Conference on , pp.839–846, 4–7 Jan doi: 10.1109/ICCV.1998.710815
50. Comaniciu D, Meer P (2002) Mean shift: a robust approach toward feature space analysis. IEEE Trans PAMI 24(5):603–619
51. Barash D, Comaniciu D (2004) A common framework for nonlinear diffusion, adaptive smoothing, bilateral filtering and mean shift. Image Vis Comput 22(1):73–81
52. Guo Y, Cheng HD, Tian J, Zhang Y (2009) A novel approach to speckle reduction in ultrasound imaging. Ultrasound Med Biol 35(4):628–640
53. Thakur A, Anand RS (2007) Speckle reduction in ultrasound medical images using adaptive filter based on second order statistics. J Med Eng Technol 31(4):263–279
54. Dantas RG, Costa ET (2007) Ultrasound speckle reduction using modified gabor filters. IEEE Trans Ultrason Ferroel Freq Contr 54(3):530–538
55. Balocco S, Gatta C, Pujol O, Mauri J, Radeva P (2010b) Srbf: speckle reducing bilateral filtering. Ultrasound Med Biol 36(8):1353–1363
56. Chan TF, Vese LA (2001) Active contours without edges. IEEE Trans Image Process 10(2):266–277
57. Michailovich O, Tannenbaum A (2007) Segmentation of medical ultrasound images using active contours. Int Conf Image Process 5:513–516
58. Jaccard P (1912) The distribution of the flora in the alpine zone. New Phytologist 11(2):37–50
59. Eran B, Shimon U (2002) Class-specific, top-down segmentation, 109–124, ECCV

Balocco Simone Balocco Simone is a lecturer professor of the Universitat de Barcelona, and works in the Medical Imaging group lead by Petia Radeva. He obtained a PhD degree in Acoustics at the laboratory Creatis, University Lyon1, Lyon (France) and contemporaneous Ph.D. in Electronic and Telecommunication in MSD Lab, University of Florence (Italy). His research interests are: vascular and cardiac tissue modeling, Ultrasound and Magnetic Resonance signal and image processing and inverse problem solution.

Carlo Gatta Carlo Gatta obtained the degree in Electronic Engineering in 2001 from the UniversitÃ degli Studi di Brescia (Italy). In 2006 he received the Ph.D. in Computer Science at the UniversitÃ degli Studi di Milano (Italy) with a thesis on perceptually based color image processing. In September 2007 he joined the Computer Vision Center at Universitat Automona de Barcelona (UAB) as a postdoc researcher working mainly on medical imaging. He is member of the Computer Vision Center and the BCN Perceptual Computing Lab. His main research interests are image processing, medical imaging, computer vision and contextual learning.

Josepa Mauri Ferré Josepa Mauri received the title of MD in 1982 at Universitat Autònoma de Barcelona. In 1992 she received the Laurea summa Cum Laude in Medicine at the Universitat de Barcelona. Since 2000, she is the Director of Cardiac Catherization Laboratory in the Hospital Universitari "Germans Trias I Pujol de Badalona". From 2002 to 2005 she was the President of the Diagnostic Intracoronary Technics/IVUS Working Group of the Spanish Society of Cardiology. From 2006 to 2009 she was the President of the Spanish Working Group in Cardiac Interventions of the Spanish Society of Cardiology. Her clinical research areas have been in coronary angioplasty and Dilated Cardiomyopathy, dilated Cardiomiopathy, coronary angioplasty, stents, endothelial disfunction and IVUS studies. She is currently involved in international educational projects in interventional cardiology.

Petia Radeva Petia Radeva (PhD 1998, Universitat Autònoma de Barcelona, Spain) is a senior researcher at UB. She has more than 150 publications in international journals and proceedings. Her present research interests are development of learning-based approaches (in particular statistical methods) for computer vision and medical imaging. She has led one EU project and several Spanish projects. She has 12 patents in the field of medical imaging. Currently, she is heading projects in the field of cardiac imaging and wireless endoscopy in collaboration with Spanish hospitals and international medical imaging companies.

Ultrasound Speckle/Despeckle Image Decomposition for Tissue Analysis

José Seabra and João Miguel Sanches

Abstract Speckle corrupting Ultrasound images depends on the acoustic characteristics of the observed tissues. De-speckling methods are usually employed to improve visualization and interpretation of anatomical details and the information encoded in speckle pattern is usually discarded. This information, however, may contain useful information for diagnostic purposes.

This chapter proposes a joint method to estimate the despeckled and speckle components from the ultrasound data for morphological and textural analysis of the tissues. The method is based on a two-step approach. In the first step a denoised image is computed and in the second step the speckle field is obtained from the despeckle data obtained on the first step and from the original image.

The despeckle image provides morphological and anatomical information of the region under analysis while the speckle field is suitable to compute textural information mainly related with tissue micro-structure.

The adequacy of the proposed decomposition method is assessed by using both synthetic and real data from distinct tissues. Several different case studies and applications are presented to illustrate the usefulness of the method for tissue characterization purposes.

1 Introduction

Ultrasound imaging has become a standard procedure for medical diagnosis worldwide, particularly in assessing arterial diseases [1, 2]. Although diagnosis by using ultrasound imaging is considered a harmless technique and allows real-time non-invasive scanning of anatomical details, B-mode ultrasound (BUS) images are

J. Seabra (✉) • J.M. Sanches
Institute for Systems and Robotics, Department of Bioengineering from the Instituto Superior Técnico/Technical University of Lisbon, Portugal
e-mail: mail2jseabra@gmail.com; jmrs@ist.utl.pt

J.M. Sanches et al. (eds.), *Ultrasound Imaging: Advances and Applications*,
DOI 10.1007/978-1-4614-1180-2_4,

pervaded by a severe type of multiplicative noise, called *speckle*, that makes its interpretation a difficult process highly depending on the subjective appreciation of the operator.

The presence of speckle noise in such images has been documented since the early 1970s, when researchers such as Burckhardt [3], Wagner [4], and Goodman [5] described the fundamentals and statistical properties of speckle. Speckle is the primary factor which limits the contrast resolution in images, thereby hindering the detection of small, low contrast lesions and turning the interpretation of images into a challenging task. Speckle also limits the effective application of image processing and analysis algorithms for region, edge detection, segmentation, and classification purposes.

There is described in the literature a large number of methods for speckle reduction either for medical ultrasound imaging [6] and other modalities involving coherent radiation such as synthetic aperture radar (SAR) [7] and LASER [8]. Such wide spectrum of techniques suggests that the problem remains a topic of interest for the image processing community and is far from being completely solved.

De-speckling is always a trade-off between noise suppression and loss of information, which is a critical issue specially when medical diagnosis is involved. Most of the work aims at removing noise for image quality improvement [9–13]. However, other works also explore the information contained in the noise pattern for the extraction of echo-morphology and texture features for tissue analysis [14–17].

Ultrasound speckle [3] arises from constructive and destructive interferences between diffuse scatterers within a certain resolution cell. The most popular model to describe speckle formation is the fully speckle condition which considers a large number of scatterers whose reflected signals combine according to a random walk process of component phasors sum. This speckle model implies a Rayleigh statistics for the envelope of the backscattered (amplitude) signal [18]. For what concerns the gray-level image appearance the Rayleigh distribution has shown to be a good approximation for modeling pixel intensities in homogeneous regions despite other distributions, including the K- [19], Nakagami [20], and Rician Inverse Gaussian [18], are more convenient, mainly when the image presents bright edges/transitions or strong isolated scatterers.

Speckle pattern is often referred as being multiplicative since its variance depends on the underlying signal intensity, meaning more noise power in brighter regions than in darker ones. Thus, de-noising methods based on the common *Additive White Gaussian Noise* (AWGN) observation model is not unappropriated to deal with this type of noise. Additionally, other methods have been proposed for de-noising and reconstruction based on median and adaptive filtering [21], wavelets [22], anisotropic diffusion [23], or other approaches [12, 13].

This chapter presents a joint framework for image de-noising and speckle estimation which takes into account the multiplicative nature of the speckle signal. The de-noising procedure, that is usually an *ill-posed* [24] problem, may be tackled by using a Bayesian approach [25] which considers *a priori* information about the unknown noiseless image to be estimated.

The problem is formulated as an optimization task where a two-term energy function is minimized. In particular, the first term pushes the solution toward the observations (noisy pixel intensities) and the second regularizes it. Regularization is performed with a suitable edge-preserving prior, designated as *log-Euclidean*, which is used with a twofold purpose: (1) being edge-preserving, and (2) allowing to formulate the de-speckling task as a convex optimization problem. This method is also referred throughout this chapter as *Rayleigh-Log Total Variation* (RLTV) filter.

The main contribution of this chapter is to introduce a speckle reducing method based on a Bayesian approach [25] which assumes a Rayleigh observation model to describe the ultrasound pixel intensities and uses *a priori* information about the speckle-free image to be estimated. Such prior information, based on TV (*Total Variation*) [26], allows to regularize the solution by removing speckle while preserving the relevant anatomic details.

As previously mentioned, the information encoded in ultrasound speckle is often discarded but it is widely recognized that this phenomenon is dependent of the intrinsic acoustic properties of tissues [27]. The proposed method assumes the relevance of speckle for tissue analysis. Therefore, the method is designed to estimate both the noiseless and speckle components (images) from the ultrasound data. Hence, the de-speckling method, which will be further detailed provides clear images for medical interpretation and speckle fields for echo-morphology and texture characterization.

The remainder of this chapter is organized as follows. Section 2 describes the various steps of the speckle decomposition method, as depicted in Fig. 1. First, the mathematical formulation on the basis of the de-speckling algorithm is detailed, together with the optimization strategy adopted to find the noiseless solution. Subsequently, Sect. 2.1 describes the procedure to extract the speckle component from the estimated noiseless image. Furthermore, Sect. 2.2 presents a feature extraction procedure which enables to extract echogenicity and textural information from the image components previously obtained with the speckle decomposition method.

Section 3 exposes two types of results. The first exemplifies the speckle decomposition method, providing separation of BUS images into noiseless and speckle components. The adequacy of the proposed ultrasound image processing is assessed with both synthetic and real data. Second, insight on the usefulness of features extracted from noiseless and speckle images for tissue analysis is exploited through different case studies.

Finally, Sect. 4 concludes this chapter.

2 Methods

The decomposition method comprises two main steps; (1) speckle removal from the noisy ultrasound image to obtain a cleaned noiseless image with morphological information about the organs and (2) speckle isolation, obtained form the noiseless

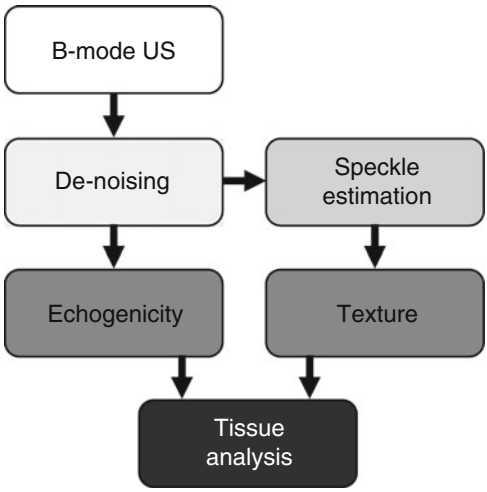

Fig. 1 Ultrasound speckle decomposition framework

and original noisy image, containing the textural information about the tissues. The first procedure, the more complex of both steps, is formulated in a Bayesian framework, where the unknown noiseless image $\Sigma = \{\sigma_{i,j}\}$ is estimated form the noisy one, $Y = \{y_{i,j}\}$. The *Maximum a Posteriori* criterion (MAP) [28] is adopted to deal with the *ill-poseness* [24] nature of the problem. Therefore, the *despecking* problem is formulated as an optimization task where an energy function is minimized,

$$\hat{\Sigma} = \arg\min_{\Sigma} E(\mathbf{Y}, \Sigma), \tag{1}$$

where

$$E(\mathbf{Y}, \Sigma) = E_d(\mathbf{Y}, \Sigma) + E_p(\Sigma). \tag{2}$$

$E_d(\mathbf{Y}, \Sigma)$, called *data fidelity* term, pushes the solution toward the data and $E_p(\Sigma)$, called *prior* term, regularizes the solution by introducing prior knowledge about Σ.

The *data fidelity* term is the *log-likelihood* function $E_d(\mathbf{Y}, \Sigma) = -\log(p(\mathbf{Y}|\Sigma))$ and by assuming statistical independence of the pixels, $p(\mathbf{Y}|\Sigma) = \prod_{i,j=1}^{N,M} p(y_{i,j}|\sigma_{i,j})$ where $p(y_{i,j}|\sigma_{i,j})$ is a Rayleigh distribution,

$$p(y_{i,j}|\sigma_{i,j}) = \frac{y_{i,j}}{\sigma_{i,j}^2} \exp\left(-\frac{y_{i,j}^2}{2\sigma_{i,j}^2}\right). \tag{3}$$

The estimation of Σ by simply using the *ML* criterion, corresponding to the minimization of $E_d(\mathbf{Y}, \Sigma)$, is an *ill-posed* problem in the Hadamard sense because the solution is not unique and it may not depend continuously on the data [24, 29]. A regularization term is added to overcome this difficulty, turning the problem into a well-posed problem. The distribution $p(\Sigma)$ introduces prior knowledge about the image to be estimated, thus regularizing and favoring smooth solutions. Even with a

regularization term the minimization procedure of $E(\mathbf{Y}, \Sigma)$ may be a difficult task, mainly when the energy function (2) is not convex. Therefore, two main issues must be taken into account in the designing of the prior function: (1) the inclusion of realistic constraints and (2) convexity of the whole energy function.

The determination of a suitable prior distribution is difficult to attain, particularly in medical applications where straightforward assumptions about the prior distribution may lead to wrong diagnosis. The common assumption about these images is that they are band-limited, changing slowly in space except near the organs boundaries where abrupt transitions are expected. This prior information is difficult to implement because the location of the transitions are unknown and must be estimated. Nevertheless, Σ can be modeled as a MRF (*Markov random field*) under the assumption that neighboring pixels are likely to have similar intensities, except if they are located at a transition.

From the Hammersley–Clifford theorem [30], the joint probability density function (PDF) of Σ, assuming that it is a MRF, is a Gibbs distribution

$$p(\Sigma) = \frac{1}{Z} \exp\left(\underbrace{-\alpha \sum_{i,j}^{N,M} \rho(c_{i,j})}_{\text{Gibbs energy}} \right), \tag{4}$$

where Z is the partition function [31], $\rho(\,)$ is designated as *potential function* and $c_{i,j}$ is the set of pixels involved in the $(i,j)^{th}$ *clique* of the neighborhood system S defined in Σ, as it is shown in Fig. 2a. The parameter α models the interaction strength between neighbors. As α increases, the prior becomes more significant than the data fidelity term, yielding a smoother solution.

Thus, the prior term is

$$E_p(\Sigma) = -\log(p(\Sigma)) = \alpha \sum_{i,j=1}^{N,M} \rho(c_{i,j}) + K, \tag{5}$$

where K is a constant. Differences between neighboring nodes are penalized by the prior term while the overall energy of the *cliques* is minimized, therefore contributing to speckle suppression.

Typical potential functions are based on the L_1 (*Manhattan*) and L_2 (*Euclidean*) norms [32], corresponding to $\rho(c_{i,j}) = |\sigma_{i,j} - \sigma_{i-1,j}| + |\sigma_{i,j} - \sigma_{i,j-1})|$ and $\rho(c_{i,j}) = (\sigma_{i,j} - \sigma_{i-1,j})^2 + (\sigma_{i,j} - \sigma_{i,j-1})^2$, respectively. Particularly, when the L_2 norm is used, the differences in neighboring pixel intensities are quadratically penalized. This potential function is able to efficiently remove the noise but is also able to attenuate or remove important anatomical details.

The Log-Euclidean prior, proposed in [33], is particular suitable in positive-constrained optimization problems, such as in this de-speckling problem where the Rayleigh parameters to be estimated are $\sigma_{i,j} > 0$. This prior is based on the

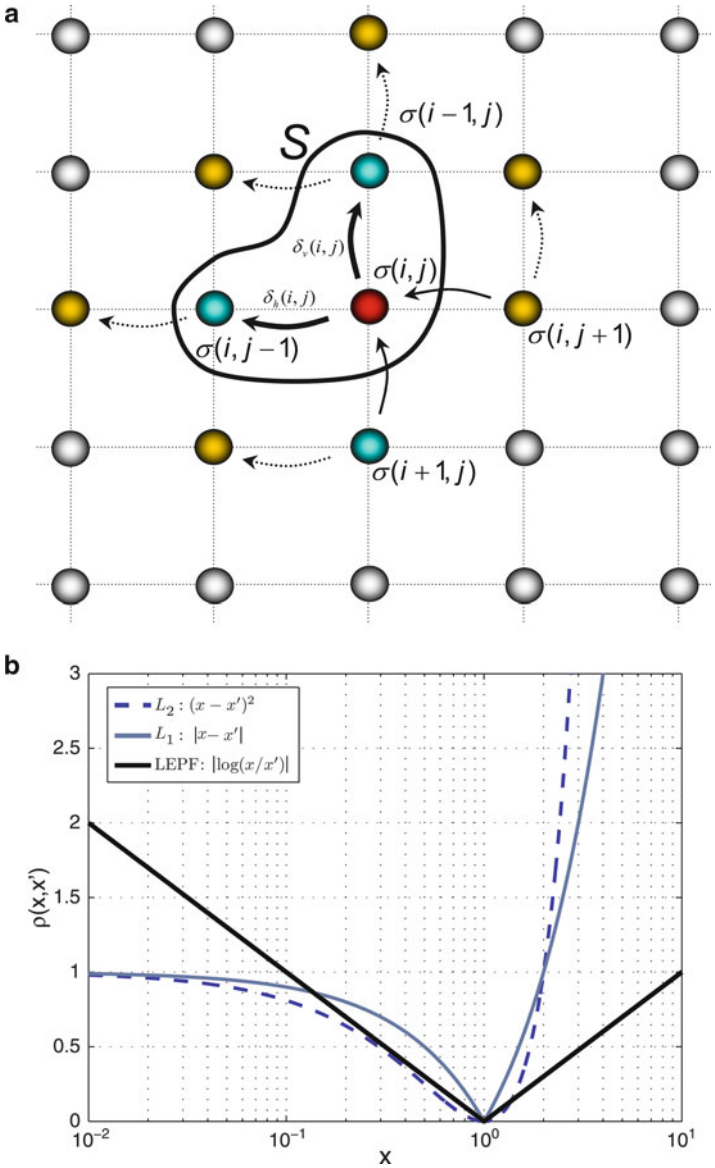

Fig. 2 Log-Euclidean prior. (**a**) 4-pixel neighboring system S and a 3-pixel *clique*. (**b**) Comparison of different potential functions $\rho(x,x')$ for a 2-pixel *clique* with $x' = 1$

distance function $\rho(x,x') = |\log(x/x')|$, where x' is a neighboring pixel of x, which is in fact a metric because the following conditions hold: (1) $\rho(x,x') \geq 0$, (2) $\rho(x,x') = 0$ if and only if $x = x'$, (3) $\rho(x,x') = \rho(x',x)$ and $\rho(x,x'') + \rho(x'',x') \geq \rho(x,x')$. As mentioned before, the Log-Euclidean prior is here employed due to its

edge-preserving properties and also because it turns the optimization problem formulated in (1) into a convex problem [34]. The potential function associated with this prior is

$$\rho(c_{i,j}) = \sqrt{\log^2(\sigma_{i,j}/\sigma_{i-1,j}) + \log^2(\sigma_{i,j}/\sigma_{i,j-1})}, \tag{6}$$

where in each *clique* three nodes are involved, $c_{i,j} = \{\sigma_{i,j}, \sigma_{i-1,j}, \sigma_{i,j-1}\}$. Figure 2b displays the LEPF (*Log-Euclidean potential function*), $|\log(x/x')|$ jointly with the common $L_1 = |x - x'|$ and $L_2 = (x - x')^2$ for a two pixel *clique* where x' is an unit intensity pixel, $x' = 1$. As it is observed the penalization introduced by the Log-Euclidean potential function (LEPF) when x and x' are similar is larger than the L_2 prior and smaller than L_1, meaning better performance than the L_2 prior to remove speckle but poorer than the L_1 norm. However, when the difference between x and x' is large the penalization introduced by the LEPF is much smaller than the one introduced by the other two norms, thus leading to better preservation of the transitions which hypothetically contain relevant anatomical information. Additionally, for a given value of x', when x goes to zero the penalization introduced by the L_1 and L_2 norms goes to a constant value while the penalization introduced by the LEPF continues to grow, which is very convenient in this case where the parameter of the Rayleigh distribution is strictly positive, $\sigma_{i,j} > 0$, but can be arbitrarily small.

The overall energy function, obtained from (2) is the following:

$$E(\mathbf{Y}, \Sigma) = \sum_{i,j} \left[\frac{y_{i,j}^2}{2\sigma_{i,j}^2} + \log(\sigma_{i,j}^2) \right] + \alpha \sum_{i,j} \sqrt{\log^2\left(\frac{\sigma_{i,j}^2}{\sigma_{i-1,j}^2}\right) + \log^2\left(\frac{\sigma_{i,j}^2}{\sigma_{i,j-1}^2}\right)} \tag{7}$$

which is non-convex because, although the data fidelity term is convex, the prior term is concave. Its minimization is a difficult task mainly when gradient-descent methods are used [34]. However the following change of variable can be performed to transform (7) into a convex function, $x = \log(\sigma^2)$. The new convex energy function is,

$$E(\mathbf{Y}, \mathbf{X}) = \sum_{i,j} \left[\frac{y_{i,j}^2}{2} \exp(-x_{i,j}) + x_{i,j} \right] + \alpha \underbrace{\sum_{i,j} \sqrt{(x_{i,j} - x_{i-1,j})^2 + (x_{i,j} - x_{i,j-1})^2 + \varepsilon}}_{TV(\mathbf{X})}. \tag{8}$$

where the prior term, the TV of $\mathbf{X} = \{x_{i,j}\}$, is now convex because all of its terms are convex (second derivative is positive).

The stationary point of (8), $\nabla_{\mathbf{X}} E(\mathbf{Y}, \mathbf{X}^*) = 0$, that minimizes the energy function is iteratively computed by use of a line search [34] algorithm,

$$\tilde{\mathbf{X}}_{k+1} = \tilde{\mathbf{X}}_k + \omega_k \tilde{D}_k, \tag{9}$$

where the descent direction, $\tilde{D}_k$, is found with the Newton method [24]

$$\tilde{D}_k = H^{-1}(\tilde{\mathbf{Y}}, \tilde{\mathbf{X}}) \nabla_{\tilde{\mathbf{X}}} E(\tilde{\mathbf{Y}}_k, \tilde{\mathbf{X}}_k). \tag{10}$$

In (10), $\tilde{\mathbf{X}}$ and $\tilde{\mathbf{Y}}$ are column vectors obtained by lexicographic ordering of $\mathbf{X}$ and $\mathbf{Y}$, respectively. In addition, $\nabla_{\mathbf{X}} E(\tilde{\mathbf{Y}}_k, \tilde{\mathbf{X}}_k)$ is the gradient column vector of $E(\tilde{\mathbf{Y}}_k, \tilde{\mathbf{X}}_k)$ with respect to $\tilde{\mathbf{X}}$ and $H(\tilde{\mathbf{Y}}, \tilde{\mathbf{X}}) = [h_{i,j}]$ is the corresponding Hessian matrix where:

$$h_{i,j} = \frac{\partial^2 E(\tilde{\mathbf{Y}}, \tilde{\mathbf{X}})}{\partial \tilde{x}_i \partial \tilde{x}_j}. \tag{11}$$

The Hessian matrix is a $NM \times NM$ hepta-diagonal sparse matrix where for each pixel (i, j) seven partial derivatives are computed, $(\tilde{x}_{i,j};\tilde{x}_{i,j})$, $(\tilde{x}_{i,j};\tilde{x}_{i,j-1})$, $(\tilde{x}_{i,j};\tilde{x}_{i-1,j})$, $(\tilde{x}_{i,j};\tilde{x}_{i,j+1})$, $(\tilde{x}_{i,j};\tilde{x}_{i+1,j})$, $(\tilde{x}_{i+1,j};\tilde{x}_{i+1,j-1})$, $(\tilde{x}_{i,j+1};\tilde{x}_{i-1,j+1})$.

The iterative numerical technique adopted in (9) chooses, at each iteration k, a search direction by moving along $\tilde{D}_k$ given by (10) while taking an appropriate step size ω_k. One useful way to identify a step size that achieves adequate reductions in $E(\mathbf{Y}, \mathbf{X})$ at minimal cost is by using the *Armijo* rule [35]. Given an initial step size, $s > 0$ and $\beta \in [0, 1]$ choose ω_k to be the largest value in $\{s, s\beta, s\beta^2, ...\}$ such that:

$$E(\tilde{\mathbf{Y}}_k, \tilde{\mathbf{X}}_k + \omega_k \tilde{D}_k) \leq E(\tilde{\mathbf{Y}}_k, \tilde{\mathbf{X}}_k) + c_1 \omega_k \nabla^T_{\tilde{\mathbf{X}}} E(\tilde{\mathbf{Y}}_k, \tilde{\mathbf{X}}_k) \tilde{D}_k. \tag{12}$$

The Armijo rule is used with the following parameters: $s = 1$, $\beta = 0.5$, and $c_1 = 10^{-4}$. Hence, the strategy to choose ω_k ensures a strictly decreasing sequence of energy values $E()$ along the iteration process.

Moreover, a continuous variation strategy, also known as *cooling*, is used where a small decreasing constant ε, updated at each iteration, is added in order to deal with the non-smooth term of (8).

The main steps of the overall de-speckling (RLTV) algorithm are listed in **Algorithm 1**. Finally, the estimated speckle-free image is obtained from $\mathbf{X}$ by making $\Sigma = \exp(\mathbf{X})$.

2.1 Speckle Extraction

The previous section described the algorithm employed to estimate a noiseless image from BUS data. Here, the estimation of speckle is derived from obtaining the denoised and original images.

Speckle corrupting the ultrasonic data is multiplicative in the sense that its variance depends on the underlying signal $\Sigma = \{\sigma_{i,j}\}$. Hence, the image formation model may be formulated as follows

$$y_{i,j} = \sigma_{i,j} \eta_{i,j}, \tag{13}$$

Algorithm 1 convex optimization

Require: $\tilde{Y} \in \Re_0^+$

Initialize: $k = 0$, $\tilde{Y}_0 = \log(\frac{\tilde{Y}^2}{2})$, $\tilde{X}_0 = \log(\tilde{Y}_0)$, $\eta = 10^{-6}$, $s = 0.3$
$\varepsilon_N = 1$ (cooling), $c_1 = 10^{-4}$ and $\beta = 0.5$ (Armijo)
while $\varepsilon_N \geq \eta$ **do**
  compute $E(\tilde{Y}, \tilde{X}_k, \varepsilon_N)$ and $\nabla E(\tilde{Y}, \tilde{X}_k, \varepsilon_N)$
  if $|\nabla_{\tilde{X}} E(\tilde{Y}, \tilde{X}_k, \varepsilon_N)| < \eta$ **then**
    $\varepsilon_N \leftarrow s \times \varepsilon_N$
    compute $E(\tilde{Y}, \tilde{X}_k, \varepsilon_N)$ and $\nabla_{\tilde{X}} E(\tilde{Y}, \tilde{X}, \varepsilon_N)$
  end if
  compute $H(\tilde{Y}, \tilde{X})$ and $\tilde{D}_k$
  $\omega = 1$
  while $E(\tilde{Y}, \tilde{X}_k + \alpha \tilde{D}_k) > E(\tilde{Y}_k, \tilde{X}_k) + c_1 \omega \nabla_{\tilde{X}}^T E(\tilde{Y}, \tilde{X}_k) \tilde{D}_k$ **do**
    $\omega \leftarrow \beta \omega$
  end while
  $X_{k+1} \leftarrow X_k + \omega d_k$
  $k \leftarrow k + 1$
end while

where $\sigma_{i,j}$ is the intensity of pixel (i, j) of the despeckled image, while $y_{i,j}$ and $\eta_{i,j}$ are the observed (noisy) and speckle images, respectively.

In this model the speckle field $N = \{\eta_{i,j}\}$ is independent of the signal as occurs in a common AWGN model where the noisy pixels, $y = \sigma + \eta$, are corrupted by noise, η, which is independent of the underlying signal σ. In the case of multiplicative model the operation is not additive but multiplicative as shown in (13). By assuming a Rayleigh distribution for the ERF image,

$$p(y|\sigma) = \frac{y}{\sigma^2} exp\left(-\frac{y^2}{2\sigma^2}\right) \tag{14}$$

the distribution for η is

$$p(\eta) = \left|\frac{dy}{d\eta}\right| p(y) = \eta \exp\left(-\frac{\eta^2}{2}\right), \quad \eta \geq 0, \tag{15}$$

which shows that the noise image η is an unit parameter Rayleigh distribution independent of σ.

This result suggests that speckle does not carry significant echogenic information when studied locally, providing a more suitable source for describing textural characteristics.

The speckle field, $N = \{\eta_{i,j}\}$, is computed straightforwardly from the original ultrasound image, $\mathbf{Y} = \{y_{i,j}\}$, and the speckle-free version, $\Sigma = \{\sigma_{i,j}\}$, estimated from (13),

$$\eta_{i,j} = \frac{y_{i,j}}{\sigma_{i,j}}. \tag{16}$$

2.2 Features Extraction

The decomposition method described in the previous sections will be used for tissue analysis where different types of features are computed from the estimated noiseless and speckle components. Afterward, we investigate the usefulness of such features for tissue analysis in different case studies.

The following features are considered:

2.2.1 Echogenicity Index

The *echogenicity index*, referring to tissue distinct acoustic properties in a specific region, is represented by the averaged value $\bar{\sigma}_W$ of local echogenicity values $\sigma_{i,j}$ inside the $n \times m$ window $w = \{\sigma_{i,j}\}$ extracted from the de-speckled image $\hat{\Sigma}$.

2.2.2 Local Rayleigh Estimators

In a previous work [36] the authors propose to compute features, to locally characterize the acoustic properties of tissues, directly form the estimated noiseless image, $\Sigma = \{\sigma_{i,j}\}$. This is done by using the analytical expressions for several statistics depending on the parameter of the distribution, estimated during the denoising operation. This means, we will estimate this statistics not directly from the observed noisy data but from the estimated parameters of the distribution that generates that data, in this case, Rayleigh distributions.

The statistics used in this work are the mean, $\sigma_\mu(i,j)$, median, $\sigma_\upsilon(i,j)$, *standard deviation* (SD), $\sigma_\sigma(i,j)$, and percentile 40, $\sigma_{P_{40}}(i,j)$. The percentile 40 refers to the percentage of pixels with echogenicity index lower than 40. This measure is particularly useful to identify low echogenic sites within a region of interest and is often used in the literature for characterizing atherosclerotic plaques [37]. Their analytical expressions for the Rayleigh distribution are

$$\begin{cases} \sigma_\mu(i,j) &= \sqrt{\frac{\hat{\sigma}(i,j)^2\pi}{2}} \\ \sigma_\upsilon(i,j) &= \sqrt{2\log(2)\hat{\sigma}(i,j)^2} \\ \sigma_\sigma(i,j) &= \sqrt{\frac{4-\pi}{2}\hat{\sigma}(i,j)^2} \\ \sigma_{P_{40}}(i,j) &= 1 - \exp\left(\frac{-40^2}{2\hat{\sigma}(i,j)^2}\right). \end{cases} \tag{17}$$

2.2.3 Echogenicity Decay

The intensity decay along depth is a common phenomenon occurring in diffuse liver disease [38] and is also visible in high-reflectivity tissues, like calcified carotid and coronary plaques [39]. The feature referring to *echogenicity decay*, s_d, is obtained

by linear regression over the mean values of each line of the block $k = \{\sigma_{m,n} : m = 1,...,M, n = 1,...,N\}$, $\bar{\sigma}_m^k = \sum_{n=1}^{N} \sigma_{m,n}$. It is obtained by minimizing the following cost function,

$$J = \sum_{m=1}^{M} (s_d\, m + b - \bar{\sigma}_m^k)^2. \tag{18}$$

Figure 7(b.1, b.2) illustrates the distinct intensity profiles from de-speckled images of normal and pathologic livers, overlayed with the estimated *echogenicity decays* for each case.

2.2.4 Speckle-Derived Wavelet Energies

The structure and directionality of speckle is hypothesized as being a relevant feature for tissue discrimination. Thus, suitable texture descriptors could be extracted from the isolated speckle field by considering the first Haar wavelet decomposition energies, particularly the approximation energy E_a, together with horizontal E_{dH} and vertical E_{dV} detail energies. Additionally, to quantify the relative detail in each direction, the ratio of horizontal to vertical detail energies, $r_{HV} = E_{dH}/E_{dV}$ is computed, where $r_{HV} \approx 1$ means that there is no predominant speckle directionality.

3 Experimental Results

The speckle decomposition method produces a despeckled image, carrying information about the local tissue echogenicity, and a speckle field, related to the structure and the characteristic pattern of tissues.

3.1 RLTV Filtering

In this section the performance of the de-speckling method is evaluated by using a phantom image (w) depicted in Fig. 3a. The pixel values of this image are used to generate the log-compressed noisy image z, displayed in Fig. 3b, that simulate the BUS image acquired by the scanner. The denoised image, σ, obtained with the RLTV algorithm is displayed in Fig. 3c.

Pixel intensity diagonal profiles of images w, z, and σ are presented in Fig. 3d. Moreover, in Fig. 3e the Rayleigh distributions obtained with averaged parameters computed in $\sigma(W_1)$, $\sigma(W_2)$, $\sigma(W_3)$ are overlapped with data histograms in $z(W_1)$, $z(W_2)$, and $z(W_3)$. As it is observed in Fig. 3d and e, the algorithm is able to correctly estimate the Rayleigh local parameters used to produce the phantom image.

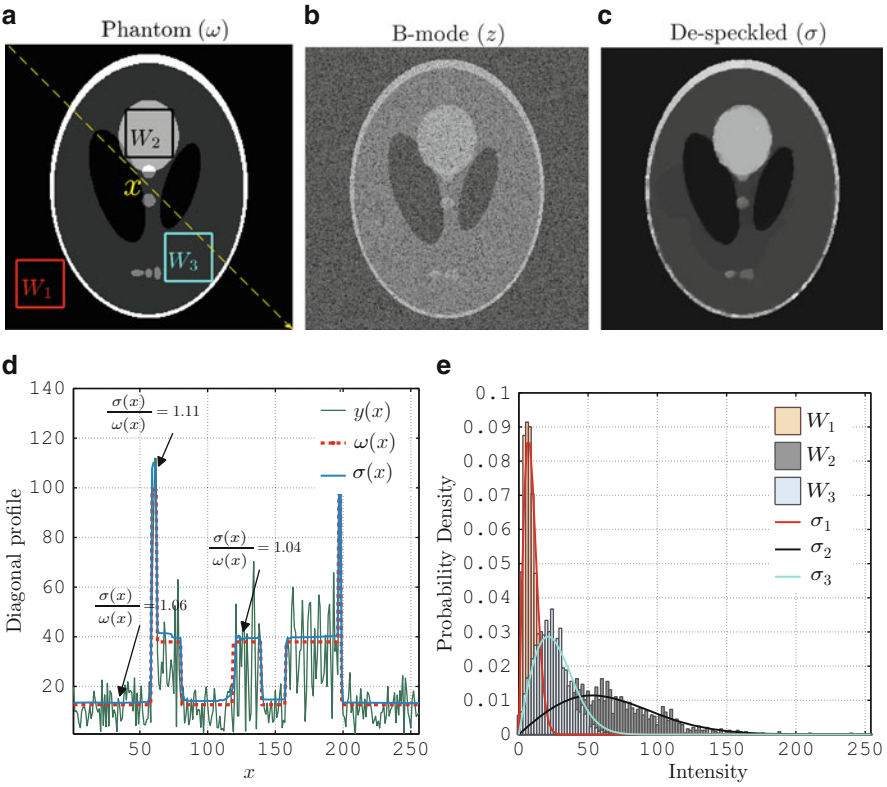

Fig. 3 (**a**–**c**) RLTV filtering in a phantom image. (**d**) Diagonal profiles of (**a**–**c**). (**e**) PDFs and data histograms

3.2 Filters Comparison

Moreover, we compare the speckle reduction results of the proposed de-noising method (RLTV) with other related work. From the view point of filter comparison it is important to study distinct filtering approaches rather than making a biased description of speckle suppression techniques. Hence, we have collected a set of techniques based on distinct concepts and formulations. In particular, we have used linear filters, such as the LSF (*Linear Scaling Filter*) [40], the pixel-wise adaptive Wiener method (WIE) [41] and the LHMAF (*Linear Homogeneous Mask Area Filter*) [42], non-linear filters, namely the MF (*Median filters*) [43] and the MHOPNF (*Maximum Homogeneity Over Pixel Neighborhood Filter*) [44], diffusion filters, including the ADF (*Anisotropic Diffusion Filter*) and the SRADF (*Speckle Reducing Anisotropic Diffusion Filter*) [23], wavelet filtering such as the WAVF (*WAVelet-based Filter*) and other more recent and sophisticated strategies, including the NLMF (*Non-Local Means Filter*) [13], the SBF (*Squeeze Box Filter*) [12], the MGF (*Modified Gabor Filter*) [45], and the WRMLF (*Weighted Rayleigh Maximum Likelihood Filter*) [46].

For medical ultrasound images, quality can be objectively assessed in terms of performance in clinically relevant tasks such as lesion detection, segmentation, and classification [47]. In the synthetic case, where the original images are available, a number of quantitative measures aiming at comparing the outcome of different filters can be studied, however dealing with real images poses some limitations. As a consequence, we assess the quality of each filter result according to three different criteria, including visual inspection, edge maps obtained from the denoised images and quantitative criteria. Image quality in terms of visual inspection refers to contrast enhancement, speckle pattern suppression, and edge-preservation. Moreover, the computation of edge maps foresees the application of segmentation algorithms in the noiseless images. Given this, an edge map which contains most of the anatomical details and very few outliers will theoretically produce the best segmentation results. Finally, we have used some quantitative measures, namely the SSNR (*Speckle Signal to Noise Ratio*) [4], and the MPVR (*Mean Preservation Variance Reduction*). The latter can be assessed by computing the mean and variance in different regions within the image. The closer the computed mean within the noiseless and original image is, and the lower the variance, the better the filtering method is. Moreover, we use a test of reasonableness (naturalness) of each filter outcome. The application of some filters could lead to artificial images, although visually appealing in terms of speckle suppression and edge enhancement. Knowing that the first digit of the gradient magnitude in natural images follows the Benford law [48, 49] we perform the Kolmogorov–Smirnov conformity test using the Benford law as well as the uniform distribution. If the Benford law-based test is close to 0 this means that the filter outcome produces a natural image.

Moreover, the computational efficiency of speckle removal filters, as these methods are supposed to be part of real time medical applications, becomes an unavoidable need. All the filters were implemented in Matlab and computed on an Intel Core 2 CPU @ 1.66GHz.

The effectiveness of the proposed RLTV filter is compared with other state-of-the-art methods, using a real ultrasound image of the thyroid. First, we show the outcomes of each filter in Fig. 4a. From visually inspecting the noiseless images it becomes clear that the best results are obtained with the SRADF, NLMF, and RLTV filter, according to efficient speckle suppression in homogeneous regions and excellent edge-preservation of relevant anatomical details. Some other methods, such as the MGF and the ADF are capable of removing most of the speckle but they tend to blur the image.

Moreover, because de-speckling is often used as a pre-processing step for segmentation purposes, we have computed edge maps from each filter outcome using the Canny detector [50]. These results are depicted in Fig. 4b. As it can be observed, the edge maps obtained from the SRADF and RLTV filter provide the most relevant edges in the image, particularly the ones that allow to outline the thyroid, while removing outlier edges.

Finally, Fig. 4c presents the image intensity profiles of some filters along a path marked in Fig. 4a. This result reinforces the regularization effect produced by the

Table 1 Comparison of filters performance using different FOM

	Figures of Merit (FOM)								
Filter	$\mu_1^{100.52}$	$\mu_2^{18.23}$	$\sigma_1^{19.56}$	$\sigma_2^{9.18}$	$SSNR_1^{5.14}$	$SSNR_2^{1.99}$	p_{Benf}	p_{Unif}	t (s)
LSF	100.32	18.24	10.21	6.91	9.82	2.64	1.11E-016	0.063	0.31
LHMAF	102.64	19.72	19.19	8.91	5.35	2.21	2.22E-016	0.26	333.29
WIE	100.26	18.00	11.40	6.91	8.80	2.60	2.22E-016	0.13	0.082
MF	99.98	17.67	12.32	7.03	8.11	2.51	4.44E-016	0.083	6.22
MHOPNF	100.49	18.24	16.49	8.30	6.10	2.20	2.22E-016	0.074	6.57
ADF	100.32	18.25	10.27	6.92	9.77	2.64	2.22E-016	0.06	8.00
SRADF	78.93	14.82	5.87	5.24	13.44	2.83	3.33E-016	0.42	4.31
WAV	100.53	18.23	16.75	8.28	6.00	2.20	3.33E-016	0.079	1.04
SBF	99.79	18.32	16.11	8.81	6.19	2.08	0	0.12	2.33
NLMF	99.71	18.36	8.44	6.33	11.82	2.90	0.11	0.12	380.90
WRMLF	81.52	14.37	12.71	6.054	6.41	2.37	5.55E-016	0.017	10.98
MGF	88.33	16.26	7.03	5.74	12.56	2.83	3.33E-016	0.16	1.16
RLTV	102.09	17.55	5.05	6.66	21.61	2.63	9.22E-014	0.089	192.07

RLTV filter, which is clearly able to eliminate most of the noise causing intensity variability while keeping abrupt intensity transitions due to transitions.

Filter comparison is also evaluated from a quantitative viewpoint. Table 1 presents some quantitative measures obtained for each filter outcome, using different FOM. Some of these FOM are computed from the marked regions in Fig. 4a. A detailed observation enables to conclude that the RLTV method provides excellent results in terms of mean preservation and SD reduction, while it outperforms other methods in terms of SSNR.

3.3 Speckle Decomposition

In the previous experiment we have demonstrated the excellent speckle suppression and edge-preserving properties of the proposed RLTV filter. Here, we investigate the incorporation of such method into the so-called speckle decomposition method, providing not only the filter outcome but also a speckle field.

Figure 5 presents different examples of the application of the proposed ultrasound speckle decomposition algorithm in different image types. To investigate the robustness of the de-speckling method we have used ultrasound data from different structures and tissues (see Fig. 5), including thyroid (a), carotid artery (b), heart (c), and liver (d). Optimization results were obtained in $67(109.9s)$, $50(82.2s)$, $55(92.5s)$, and $61(101.6s)$ iterations, respectively. These results illustrate the ability of the RLTV algorithm to deal with different types of real images.

To complete this set of experiments related with speckle image decomposition, an example with *intra-vascular ultrasound* (IVUS) image of the coronary artery is provided in Fig.6a. Additionally, the *Speckle Signal-to-Noise Ratio* (SSNR) is computed within a sliding window across the whole speckle image and the SSNR

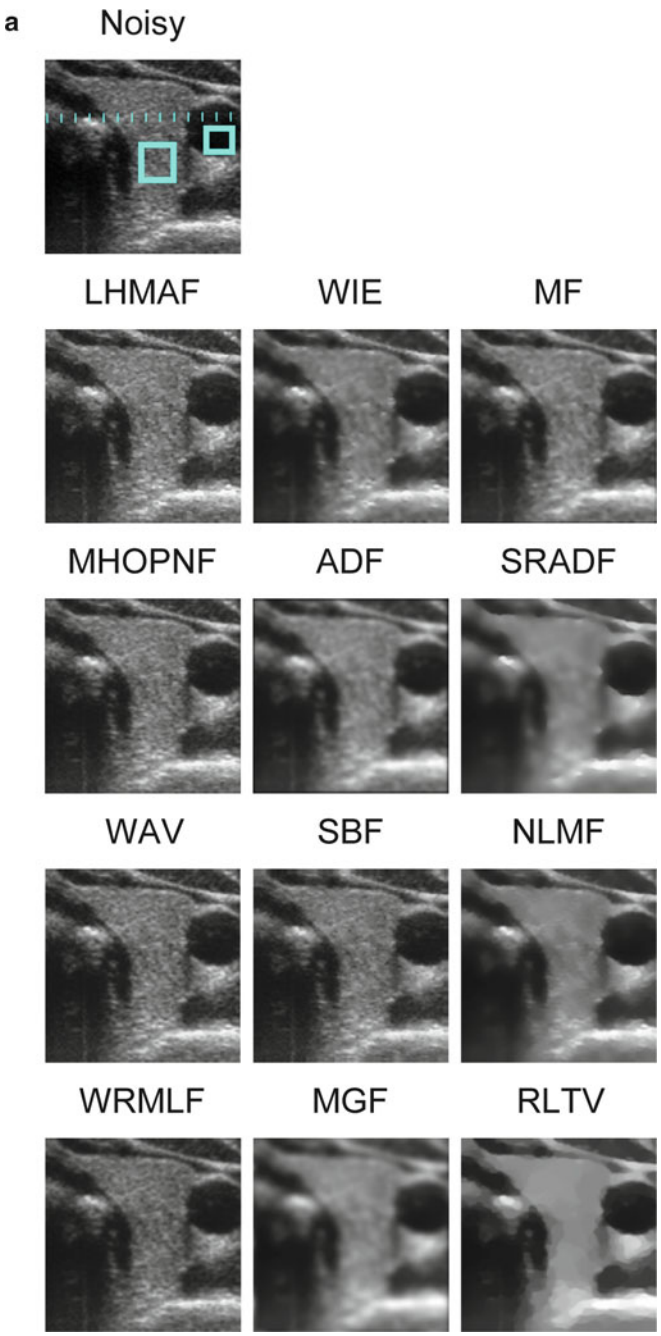

Fig. 4 Comparison of the proposed RLTV filter and other approaches described in the literature, according to de-speckled images (**a**), edge maps (**b**), and image intensity profiles (**c**)

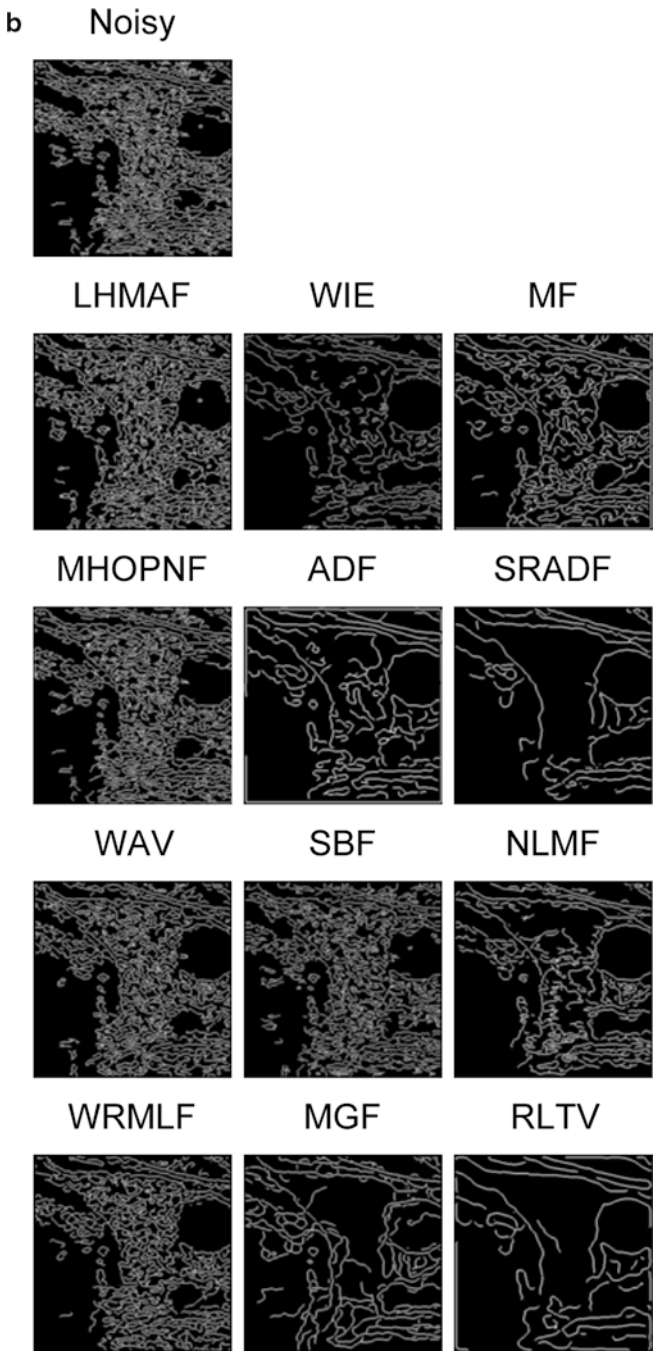

Fig. 4 (continued)

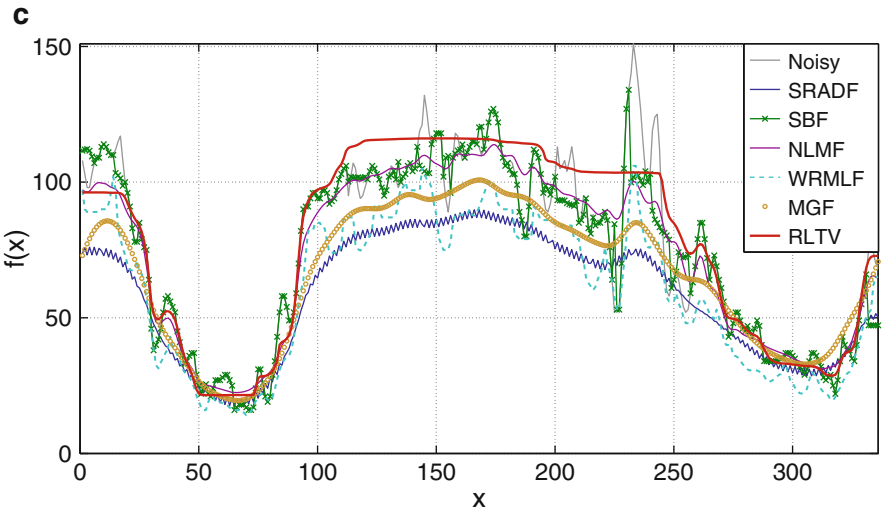

Fig. 4 (continued)

map is shown in Fig. 6b. A precursor study [3] conducted in real ultrasound images, showed experimentally that when fully developed speckle occurs, the SSNR is in the range of 1.5–2.5. Given this, it is observed that the speckle field has statistical properties resembling a Rayleigh distributed signal, which strongly suggests the likelihood of the assumption of the Rayleigh observation model for the RLTV despeckling method.

Results of the speckle decomposition method have just been presented. Hence, it is now important to show that the outcomes of the proposed method are useful image sources of information for tissue analysis. Consequently, we present different case studies using distinct ultrasound data:

3.3.1 Evidence of Tissue-Dependent Textural Features

The speckle field of ultrasound images from different tissue types, in particular of carotid plaque, thyroid, and liver (Fig. 7a) are used to show that the energies associated with the first wavelet decomposition fields with Haar functions, E_a, E_d, and r_{HV}, differ significantly from one anatomical structure to another, as well as from one tissue area to another. In particular, the wavelet energies and energy ratios are (see Fig. 7a): $E_a(w_a) = 99.6$, $E_d(w_a) = 0.4$, $r_{HV}(w_a) = 2.8$; $E_a(w_b) = 95.4$, $E_d(w_b) = 4.6$, $r_{HV}(w_b) = 4.7$; $E_a(w_{c.1}) = 92.3$, $E_d(w_{c.1}) = 7.7$, $r_{HV}(w_{c.1}) = 2.3$; $E_a(w_{c.2}) = 94.3$, $E_d(w_{c.2}) = 5.7$, $r_{HV}(w_{c.2}) = 3.1$; $E_a(w_{c.3}) = 96.3$, $E_d(w_{c.3}) = 3.7$, $r_{HV}(w_{c.3}) = 2.1$.

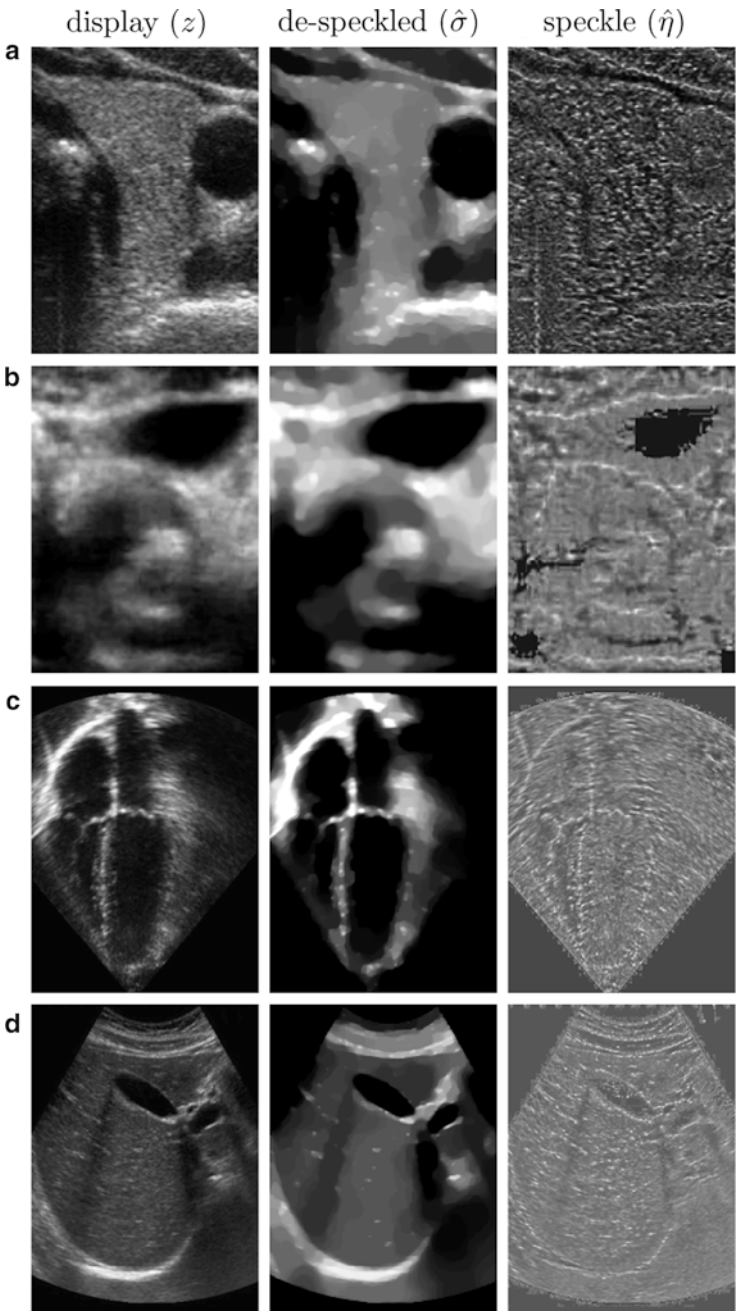

Fig. 5 Ultrasound speckle decomposition method applied to different tissue types

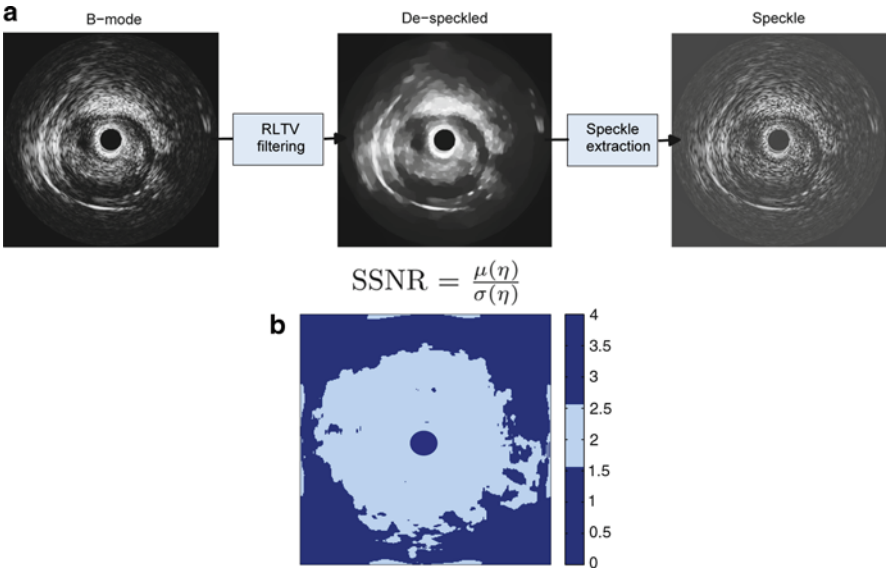

Fig. 6 (**a**) Despeckled and speckle component estimates obtained from BUS IVUS image. (**b**) SSNR map computed over the speckle field $\hat{\eta}$

3.3.2 Liver Steatosis Binary Classification

A Bayes classifier trained with features related to *echogenicity decay* (see Fig. 7b) and wavelet energies is used in a binary classification problem. Features were extracted from a dataset of 20 livers, which were clinically validated as normal or steatotic (with abnormal lipid retention) [51], yielding the following feature set and values: for normal liver, $\bar{s}_d = 0.48\ (0.18)\ \bar{E}_dH = 9.79\ (2.68)\ \bar{E}_dV = 6.78\ (1.63)$; and for fatty liver, $\bar{s}_d = 0.80\ (0.11)\ \bar{E}_dH = 19.97\ (4.54)\ \bar{E}_dV = 4.66\ (1.61)$. Results, given in terms of sensitivity ($S = 1.00$) and specificity ($K = 0.95$), support the usefulness of features extracted both from the noiseless and speckle image sources for a specific tissue classification problem.

3.3.3 Subject Identification Based on Thyroid Ultrasound Data

A subject identification problem based on thyroid tissue ultrasonic data was performed [52], considering a population of 10 subjects (several samples per subject). Again, features were extracted from both the estimated de-speckled image (echogenicity index) and speckle field (wavelet energies) as depicted in Fig. 7c.

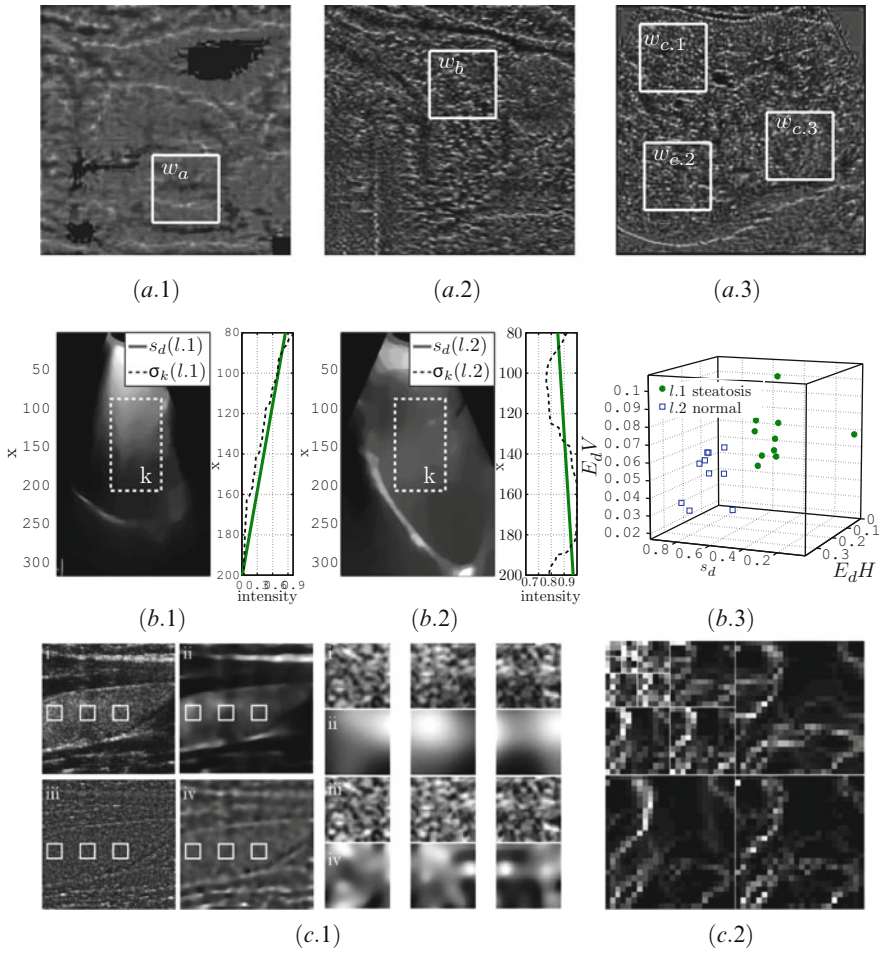

Fig. 7 Feature extraction based on ultrasound speckle decomposition applied to different case studies. (**a**) first Haar wavelet energies based on speckle from plaque (1), thyroid (2), and liver (3). (**b**) feature based on *echogenicity decay* (1–2) and feature space of normal and steatotic livers. (**c**) Sample extraction from noiseless and speckle components, obtained from thyroid images (1); wavelet decomposition from speckle field (2)

Subsequently, the estimated feature set was used for training a bayesian classifier. Sensitivity results obtained for the problem of subject identification were: $S = 0.79$, with echogenicity index features, $S = 0.70$, with wavelet energies and $S = 0.94$ with a combination of both. Again, this example shows that distinct feature values can be obtained from thyroid tissue on the basis of the proposed ultrasound speckle decomposition method.

4 Conclusions

This chapter describes a new strategy for decomposing ultrasound B-mode images into its noiseless and speckle components, as well as, a new state of the art algorithm for de-speckling.

First, a suitable de-noising algorithm is presented which aims at providing clearer yet edge-preserving images for medical interpretation. Subsequently, because speckle has multiplicative nature, an image containing the speckle pattern is estimated after knowing the corresponding noiseless image.

The adequacy of the RLTV filtering method has been compared with other filters, and afterward established through synthetic examples and ultrasound images having different types. Moreover, as theoretically expected, an example using IVUS data, clearly shows that the speckle field has statistical properties resembling a Rayleigh distributed signal.

Furthermore, we have computed different features from noiseless and speckle image sources, arguing that such information is useful for tissue analysis. Hence, we have shown the convenience of working with the estimated echogenicity and textural features for tissue description through distinct real cases.

The first study is conducted to illustrate how features computed from the speckle field differ from a tissue to another and even within the same tissue. Wavelet detail and approximation energies together with the relative directional energy ratio have shown to be relevant tissue descriptors. The second and third examples use features extracted both from noiseless and speckle image sources. In particular, the second study uses a feature computed from the despeckled image (echogenicity decay) which is very convenient in the investigated two-class problem. In the two classification problems presented, the use of information resulting from the proposed speckle decomposition procedure leads to high-classification scores.

Thus, we have shown that the proposed algorithm is able to provide more suitable images for visual diagnosis as well as useful sources of information for tissue analysis in different clinical scenarios.

References

1. Nelson T, Pretorius DH , Downey D, and Fenster A (1999) Three-dimensional ultrasound. Lippincott Williams & Wilkins PA, USA
2. Lamont D et al (2000) Risk of cardiovascular disease measured by carotid intima-media thickness at age 49–51: lifecourse study. Br Med J 320(7230):273–278
3. Burckhardt C (1978) Speckle in ultrasound B-mode scans. IEEE Trans Sonics Ultrason SU-25(1):1–6
4. Wagner RF, Smith SW, Sandrik JM, Lopez H (1983) Statistics of speckle in ultrasound B-scans. IEEE Trans Sonics Ultrason 30(3):156–163
5. Goodman JW (1986) Statistical properties of laser speckle patterns. IEEE Trans Ultrason Ferroelectr Freq Control 33(6):754–758

6. Loizou CP, Pattichis CS, Christodoulou CI, Istepanian RSH, Pantziaris M (2005) Comparative evaluation of despeckle filtering in ultrasound imaging of the carotid artery. IEEE Trans Ultrason Ferroelectr Freq Control 52(10):1653–1669
7. Lu B, Zhang L, Xing F (2010) Sar speckle reduction based on nonlocal means method. In: Proceedings of the 2010 second international conference on computer modeling and simulation - Volume 02, ICCMS '10. IEEE Computer Society, Washington, pp 156–159
8. Martinsen R, Kennedy K, Radl A Speckle in laser imagery: efficient methods of quantification and minimization. In: Lasers and electro-optics society 1999 12th annual meeting. LEOS '99. IEEE, Vol 1, pp 354–355, Vol 1, 1999
9. Michailovich O, Tannenbaum A (2006) Despeckling of medical ultrasound images. IEEE Trans Ultrason Ferroelectr Freq Control 53(1):64–78
10. Nascimento J, Sanches J, Marques JS (2007) An unified framework for Bayesian denoising for several medical and biological imaging modalities. In Proceedings EMBC 2007, IEEE Engineering in Medicine and Biology Society, Lyon, France, pp 6268–6271
11. Gilboa G, Sochen N, Zeevi Y(2006) Variational denoising of partly textured images by spatially varying constraints. IEEE Trans Image Process 15(8):2281–2289
12. Tay PC, Acton ST, Hossack JA (2006) Ultrasound despeckling using an adaptive window stochastic approach. In Proceedings of the international conference on image processing (ICIP 2006), Atlanta, April 2006, pp 2549–2552
13. Buades A, Coll B, Morel JM (2005) A review of image denoising algorithms, with a new one. Multiscale Model Simul 4(2):490–530
14. Christodoulou CI, Pattichis CS, Pantziaris M, Nicolaides A (2003) Texture-based classification of atherosclerotic carotid plaques. IEEE Trans Med Imag 22(7):902–912
15. Mohamed SS, Salama M (2008) Prostate cancer spectral multifeature analysis using TRUS images. IEEE Trans Med Imag 27(4):548–556
16. Thijssen J et al (2008) Computer-aided B-mode ultrasound diagnosis of hepatic steatosis: a feasibility study. IEEE Trans Ultrason Ferroelectr Freq Control 55(6):1343–1354
17. Hope AT, Gregson PH, Linney NC, Schmidt MN, Abdolell M (2008) Selecting and assessing quantitative early ultrasound texture measures for their association with cerebral palsy. IEEE Trans Med Imag 27(2):228–236
18. Eltoft T (2006) Modeling the amplitude statistics of ultrasonic images. IEEE Trans Med Imag 25(2):229–240
19. Prager RW, Gee AH, Treece GM, Berman LH (2003) Decompression and speckle detection for ultrasound images using the homodyned k-distribution. Pattern Recogn Lett 24(4–5):705–713
20. Shankar PM (2001) Ultrasonic tissue characterization using a generalized Nakagami model. IEEE Trans Ultrason Ferroelectr Freq Control 48(6):1716–1720
21. Dutt V, Greenleaf JF (1996) Adaptive speckle reduction filter for log-compressed b-scan images. IEEE Trans Med Imag 15(6):802–813
22. Gupta S, Kaur L, Chauhan RC, Saxena SC (2004) A wavelet based statistical approach for speckle reduction in medical ultrasound images. Med Biol Eng Comput 42(2):189–192
23. Yu Y, Acton ST (2002) Speckle reducing anisotropic diffusion. IEEE Trans Image Process 11(11):1260–1270
24. Vogel CR (2002) Computational methods for inverse problems. Society for industrial and applied mathematics. Philadelphia, PA, USA. ISBN:0898715075
25. Sanches JM, Nascimento JC, Marques JS (2008) Medical image noise reduction using the sylvester-lyapunov equation. IEEE Trans Image Process 17(9):1522–1539
26. Nascimento J, Sanches J (2008) Total variation with automatic hyper-parameter estimation. In Proceedings EMBC 2008, IEEE Engineering in Medicine and Biology Society, Vancouver, Canada, Aug 2008, pp 443–446
27. Sehgal C (1993) Quantitative relationship between tissue composition and scattering of ultrasound . J Acoust Soc Am 94:1944–1952
28. Harris JW, Stocker H (1998) Maximum likelihood method, Handbook of mathematics and computational science. Springer-Verlag, New York, p 824

29. Hadamard J (1902) Sur les problèmes aux dérivés partielles et leur signification physique, Princeton University Bulletin 13:49–52
30. Besag JN (1986) On the statistical analysis of dirty pictures. J R Statist Soc B 48(3):259–302
31. Geman S, Geman D (1987) Stochastic relaxation, gibbs distributions, and the bayesian restoration of images. J Appl Stat 20(5):25–62
32. Moon TK, Stirling WC (2000) Mathematical methods and algorithms for signal processing. Prentice-Hall, NJ, USA
33. Arsigny V, Fillard P, Pennec X, Ayache N (2006) Log-Euclidean metrics for fast and simple calculus on diffusion tensors. Magn Reson Med 56(2):411–421
34. Boyd S, Vandenberghe L (2004) Convex optimization. Cambridge University Press, United Kingdom
35. Shi Z, Shen J (2005) New inexact line search method for unconstrained optimization. J Optim Theory Appl 127(2):425–446
36. Seabra JC, Pedro LM, Fernandes eFernandes J, Sanches JM (2009) A 3D ultrasound-based framework to characterize the echo-morphology of carotid plaques. IEEE Trans Biomed Eng 56(5):1442–1453
37. Pedro LM, Fernandes JF, Pedro MM, Gonalves I, Dias NV (2002) Ultrasonographic risk score of carotid plaques. Eur J Vasc Endovasc Surg 24:492–498
38. Lee CH et al (2006) Usefulness of standard deviation on the histogram of ultrasound as a quantitative value for hepatic parenchymal echo texture; preliminary study. Ultrasound Med Biol 32(12):1817–1826
39. Saijo Y, Tanaka A, Sasaki H, Iwamoto T, Filho E, Yoshizawa M, Yambe T (2004) Basic ultrasonic characteristics of atherosclerosis measured by intravascular ultrasound and acoustic microscopy. Int Congr Ser 1274:116–121
40. Strand TC, Kuan DT, Sawchuk AA, Chavel P (1985) Adaptive noise smoothing filter for images with signal-dependent noise. IEEE Trans Pattern Anal Mach Intell 7(2):165–177
41. Prager RW, Gee AH, Treece GM, Berman L (2002) Speckle detection in ultrasound images using first order statistics. Technical Report CUED/F-INFENG/TR 415, Cambridge University, Cambridge
42. Nagao M, Matsuyama T (1979) Edge preserving smoothing. Comput Graph Image Process 9(5):394–407
43. Loupas T, McDicken W, Allan P (1989) An adaptive weighted median filter for speckle suppression in medical ultrasonic images. IEEE Trans Circuits Syst 36:129–135
44. Ali SM, Burge RE (1988) New automatic techniques for smoothing and segmenting sar images. Signal Process 14(4):335–346
45. Dantas R, Costa E (2007) Ultrasound speckle reduction using modified Gabor filters. IEEE Trans Ultrason Ferroelectr Freq Control 54(3):530–538
46. Aysal T, Barner K (2007) Rayleigh-maximum-likelihood filtering for speckle reduction of ultrasound images. IEEE Trans Med Imag 26(5):712–727
47. Krupinski EA, Berbaum KS (2009) The medical image perception society update on key issues for image perception research. Radiology 253(1):230–233
48. Hill T (1996) The first-digit phenomenon. Amer Sci 86:358–363
49. Jolion JM (2001) Images and benford's law. J Math Imaging Vis 14(1):73–81
50. Canny J (1986) A computational approach to edge detection. IEEE Trans Pattern Anal Mach Intell 8(6):679–698
51. Ribeiro R, Sanches J (2009) Fatty liver characterization and classification by ultrasound. In: IbPRIA '09: proceedings of the 4th Iberian conference on pattern recognition and image analysis, Springer-Verlag, Berlin, Heidelberg, pp 354–361
52. Seabra J, Fred A (2010) Towards the development of a thyroid ultrasound biometric scheme based on tissue echo-morphological features. In: Biomedical engineering systems and technologies, communications in computer and information science. Springer-Verlag, Berlin, pp 286–298

Part II
Ultrasound Plaque Imaging

Media and Intima Thickness and Texture Analysis of the Common Carotid Artery

Christos P. Loizou, Marios Pantzaris, and Constantinos S. Pattichis

Abstract The intima–media thickness (IMT) of the common carotid artery (CCA) is widely used as an early indicator for the development of cardiovascular disease (CVD). It was proposed but not thoroughly investigated that the media layer (ML) thickness (MLT), its composition, and texture may be indicative of cardiovascular risk and for differentiating between patients with high and low risk. In this study, we investigate an automated snakes segmentation method for segmenting the ML and the intima layer (IL) and measurement of the MLT and the intima layer thickness (ILT) in ultrasound images of the CCA. We furthermore investigate the application of texture analysis of the ML of the CCA and how texture is affected by age and gender. The snakes segmentation method was used, and was evaluated on 100 longitudinal ultrasound images acquired from asymptomatic subjects, against manual segmentation performed by a neurovascular expert. The mean $\pm$ standard deviation (sd) for the first and second sets of manual and the automated IMT, MLT, and ILT measurements were $0.71 \pm 0.17\,\text{mm}, 0.72 \pm 0.17\,\text{mm}, 0.67 \pm 0.12\,\text{mm}, 0.25 \pm 0.12\,\text{mm}, 0.27 \pm 0.14$, and $0.25 \pm 0.11\,\text{mm}$; and $0.43 \pm 0.10\,\text{mm}, 0.44 \pm 0.13\,\text{mm}$, and $0.42 \pm 0.10\,\text{mm}$, respectively. There was overall no significant difference between the manual and the automated IMC, ML, and IL segmentation measurements. Therefore, the automated segmentation method proposed in this study may be used successfully in the measurement of the MLT and ILT complementing the manual measurements. MLT was also shown to increase

C.P. Loizou (✉)
Department of Computer Science, School of Sciences, Intercollege,
92 Ayias Phylaxeos Str., P.O. Box 51604, CY-3507, Limassol, Cyprus
e-mail: loizou.christos@ucy.ac.cy; loizou.c@lim.intercollege.ac.cy

M. Pantzaris
Cyprus Institute of Neurology and Genetics, Nicosia, Cyprus
e-mail: pantzari@cing.ac.cy

C.S. Pattichis
Department of Computer Science, University of Cyprus, Nicosia, Cyprus
e-mail: pattichi@ucy.ac.cy

J.M. Sanches et al. (eds.), *Ultrasound Imaging: Advances and Applications*,
DOI 10.1007/978-1-4614-1180-2_5, © Springer Science+Business Media, LLC 2012

with age (for both the manual and the automated measurements). Following the segmentation of the three structures, we also investigated the application of texture analysis of the ML of the CCA and how texture is affected by age and gender. The 100 images were separated into three different age groups, namely below 50, between 50 and 60, and above 60 years old. Furthermore, the images were separated according to gender. A total of 61 different texture features were extracted from the intima layer (IL), the ML, and the intima–media complex (IMC). We have found that male patients tended to have larger media layer thickness (MLT) values as compared to the MLT of female patients of the same age. We have also found significant differences among texture features extracted from the IL, ML, and IMC from different age groups. Furthermore, for some texture features, we found that they follow trends that correlate with a patient's age. For example, the gray-scale median GSM of the ML falls linearly with increasing MLT and with increasing age. Our findings suggest that ultrasound image texture analysis of the media layer has potential as an assessment biomarker for the risk of stroke.

Keywords Snakes • Ultrasound imaging • Media layer • Texture analysis • Common carotid artery

1 Introduction

Cardiovascular disease (CVD – coronary artery disease, cerebrovascular disease, and peripheral artery disease) is the third leading cause of death and adult disability in the industrial world after heart attack and cancer (as reported by the World Health Organization). According to [1], 80 million American adults have one or more types of CVD of whom about half are estimated to be of age 65 or older. Of all the deaths caused by CVD among adults aged 20 and older, an estimated 13 millions are attributed to coronary heart disease and to stroke, with atherosclerosis as the underlying cause. A recent study by the World Health Organization estimates that by 2015, 20 million people will die from cerebrovascular disease (mainly from heart attack and stroke).

Atherosclerosis causes thickening of the artery walls and the intima–media thickness (IMT) (see Fig. 1a) is used as a validated measure for the assessment of atherosclerosis [2]. Specifically, an increased IMT is correlated with an augmented risk of brain infarction or cardiac attack [3]. Moreover, the presence of carotid plaques has been correlated not only to CVD but also to degenerative pathologies such as vascular dementia and Alzheimer's disease [4]. Hence the assessment of carotid wall status is also essential for early identification of risk conditions in asymptomatic patients. Traditionally, the IMT is measured by manual delineation of the intima and the adventitia layers [2] (see Fig. 1a, interface I5 and I7). Manual tracing of the lumen diameter (see Fig. 1a, band Z4) and the IMT by human experts requires substantial experience; it is time consuming, and varies according to the training, experience, and the subjective judgment of the experts. The manual measurements suffer, therefore, from considerable inter- and intra-observer variability [2–10]. It should be noted that parts of this work were also published in [11, 12].

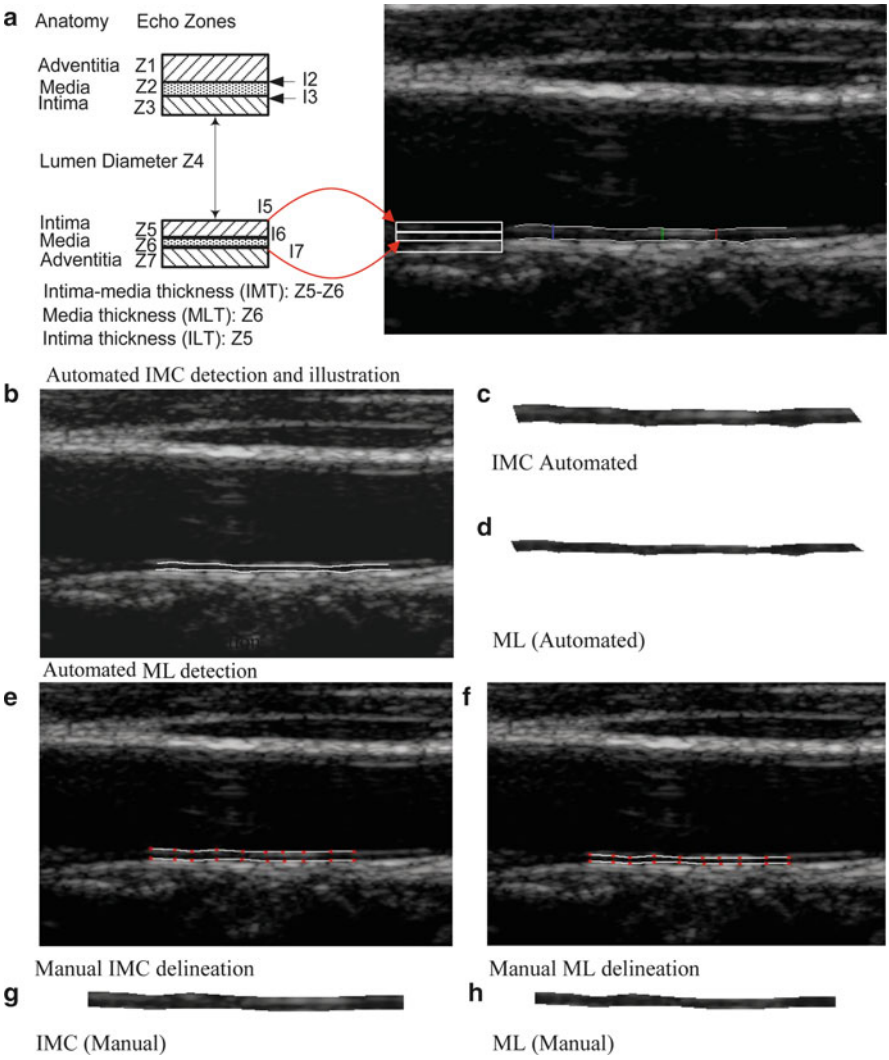

Fig. 1 (**a**) Illustration of the intima–media complex (IMC, bands Z5 and Z6) of the far wall of the common carotid artery and the automatic IMC segmentation [10]. The media layer thickness (MLT) is defined as the distance between the intima–media and the media–adventitia interface (band Z6), (**b**) automated ML detection, (**c**) automated extracted IMC band, (**d**) automated extracted ML, (**e**) manual IMC delineation, (**f**) manual ML delineation, (**g**) manual extracted IMC, and (**h**) manual extracted ML. Source [12], © IEEE 2009

In the last 20 years, several automated techniques for the segmentation and measurement of the IMT from longitudinal ultrasound images of the common carotid artery (CCA) have been developed [9–14]. However, there are no studies published in the literature reporting both the manual and the automated segmentation and

measurement of the media layer (ML) and the intima layer (IL) of the CCA in ultrasound imaging. There are only three studies in the literature where manual measurements of the MLT were reported [8, 15, 16]. Earlier research showed that the media layer thickness (MLT) in peripheral arteries does not change significantly with age and that it ranges from 125 to 350 μm [8]. In [15], manual measurements of the thickness of the CCA IMT and MLT were carried out by an expert on 100 subjects aged 70 years old. In this study [15], it was shown that subjects with CVD (coronary heart disease, myocardial infarction, or stroke) had a significantly thinner ML and a thicker IL than healthy subjects. Furthermore, in [16], the IMT, MLT, and ILT of 90 healthy subjects (aged between 10 and 90 years) were manually measured at their radial and anterior tibial arteries. It was shown that age was strongly related with IMT, MLT, and ILT for both peripheral arteries.

The objective of this study was to develop and evaluate a snakes segmentation system enabling the automated segmentation and measurement of the ML and IL in ultrasound images of the CCA and investigate their variability with age groups. We also propose to study changes in textural characteristics that can be associated with disease progression for different age groups. Here, we note that for fully developed plaques in the CCA, texture features derived from statistical, model based, and Fourier based methods have been used to characterize and classify carotid atheromatous plaques from B-mode ultrasound images [11, 30]. We, furthermore, investigated whether textural characteristics extracted from the IL, the ML, and the IMC of the CCA, segmented manually by an expert and automatically by a snakes segmentation system [10, 12], can be associated with the increase in age gender or MLT. Ultimately, texture feature characteristics that vary with age, gender, or MLT might be used to asses the risk of stroke.

The ML (see Fig. 1a, band Z6) is ultrasonographically characterized by an echolucent region, predominantly composed of smooth muscle cells of the media band of the arterial wall and probably by the extracellular matrix of the intima band, which cannot be distinguished from the smooth muscle cell with ultrasound [17]. Due to the acoustic impedance mismatches, the arterial wall bands (intima–media–adventitia) can produce typical bright–dark–bright patterns on ultrasound images [2]. It is, furthermore, proposed but not thoroughly investigated, that not only the IMT but rather the ML (its composition and thickness) may be used for evaluating the risk of a patient to develop a stroke and accounts in general for the risk of the CVD by differentiating between patients with high and low risk.

The IL is a thin layer, the thickness of which increases with age, from a single cell layer at birth to 250 μm at the age of 40 for nondiseased individuals [5]. Further, adaptive physiological thickening of the IL occurs at places where the wall tension is increased, such as arterial bifurcations and on the ML of the artery and may be either eccentric or diffuse [5]. Furthermore, the intima–media complex (IMC) (see also Fig. 1a) becomes more difficult to detect as the age of patients increases, due to the presence of acoustic holes (echo-dropouts), in the IL [6]. The intimal band (see band Z5 in Fig. 1a) may appear as a thin low-contrast structure and, therefore, it is difficult to reliably draw boundaries because smoothing can move the structure edges or make them disappear [2, 7].

Earlier research [8] showed that the media layer thickness (MLT) does not change significantly with age ($125\,\mu m < MLT < 350\,\mu m$). In a recent study by our group, the median (IQR) of intima layer thickness (ILT), MLT, and IMT were computed from 100 ultrasound images of 42 female and 58 male asymptomatic subjects aged between 26 and 95 years old, with a mean age of 54 years to be as follows: 0.43 mm (0.12), 0.23 mm (0.18), and 0.66 mm (0.18), respectively [12].

In [33], a method has been presented for quantifying the reflectivity of the ML of the distal CCA. It was shown that the GSM of the IM layer is the earliest change representing atherosclerotic disease in the arterial wall that can currently be imaged in vivo. This may be the first marker of atherosclerosis and may precede the development of a significant increase in IMT. This would enable earlier identification of high-risk individuals based on the analysis of the CCA artery wall textural characteristics. In [34], the early structural changes of the CCA in familial hypercholesterolemia were investigated. It was shown that textural characteristics extracted from the IMC were significantly different between patients with and without hypercholesterolemia. In [35], the authors reported on the properties of the GSM of the IMC from a random sample of 1,016 subjects aged exactly 70. They found that the GSM of the IMC of the CCA is closely related to the echogenecity in overt carotid plaques.

While there are several earlier studies suggesting that the instability of the carotid atheromatous plaques can be characterized from B-mode ultrasound images [6, 30], we have not found any other studies reported in the literature where the ML textural characteristics have been shown to be associated with the risk of stroke. While in [6, 30], the echogenecity in atherosclerotic carotid plaques was evaluated through the gray-scale median (GSM), there are very few attempts made to characterize the IL, the ML, and the intima–media complex (IMC) with a similar gray-scale image intensity analysis. It is evident from the visual inspections of the IMC in the CCA that a great variation in echogenecity does exist. However, the usefulness of this information has not yet been studied.

In [30], the morphology of atherosclerotic carotid plaque was investigated based on the textural characteristic extracted from 230 ultrasound images of carotid plaque, where it was shown that it is possible to identify a group of patients, symptomatic or asymptomatic, at risk of stroke based on these texture features. It was further documented in [36], that carotid endarterectomy in asymptomatic individuals with stenosis greater than 70% reduces the risk of stroke from 2% per year to 1% per year. In another study [37], the relationship of the IMT in the CCA and atherosclerosis was investigated on 182 symptomatic patients (mean age 67 years). It was shown that the IMT was correlated to age, male gender, ischemic heart disease, and presence of plaque or stenosis in any of the carotid bifurcations. In a recent study [38], where the alterations of the CCA with age in ultrasound images were investigated, it was shown that the diastolic and systolic lumen diameters are increasing with age. This reduces wall stress as the elasticity of the wall decreases with age.

2 Materials and Methods

2.1 Recording of Ultrasound Images

A total of 100 B-mode longitudinal ultrasound images of the CCA used for the IMC, ML, and IL segmentations were recorded using the ATL HDI-3000 ultrasound scanner (Advanced Technology Laboratories, Seattle, USA), with a linear probe (L74), with a recording frequency of 7 MHz, a velocity of 1,550 m/s and 1 cycle per pulse, which resulted to a wavelength (spatial pulse length) of 0.22 mm and an axial system resolution of 0.11 mm. The technical characteristics of the ultrasound scanner (multielement ultrasound scan head, operating frequency, acoustic aperture, and transmission focal range) have already been published in [10]. Digital images were resized using the bicubic method to a standard pixel density of 16.66 pixels per mm with a resolution of 0.06 mm. This was carried out due to the small variations in the number of pixels per mm of image depth (i.e., for deeply situated carotid arteries, image depth was increased and, therefore, digital image spatial resolution would have decreased) and in order to maintain uniformity in the digital image spatial resolution [19]. The images were logarithmically compressed and were recorded digitally on a magneto-optical drive at size of 768 $\times$ 576 pixels with 256 gray levels. The images were recorded at the Cyprus Institute of Neurology and Genetics, Nicosia, Cyprus, from 42 female and 58 male asymptomatic subjects aged between 26 and 95 years old, with a mean age of 54 years. The images were separated into three different age groups depending on age, namely, below 50, between 50 and 60, and above 60 years old, with 27, 36, and 37 subjects in each group, respectively, and also separated into 58 male and 42 female subjects. These subjects had not developed clinical symptoms, such as a stroke or a transient ischemic attack (TIA).

2.2 Image Normalization

Brightness adjustments of ultrasound images were carried out in this study based on the method introduced in [20] and also used in [10]. It was shown that this method improves image compatibility by reducing the variability introduced by different gain settings, different operators, different equipment, and facilitates ultrasound tissue comparability. Algebraic (linear) scaling of the image was performed by linearly adjusting the image so that the median gray level value of the blood was 0–5, and the median gray level of the adventitia (artery wall) was 180–190 [20]. The scale of the gray level of the images ranged from 0 to 255. Thus the brightness of all pixels in the image was readjusted according to the linear scale defined by selecting the two reference regions. It is noted that a key point to maintaining a high reproducibility was to ensure that the ultrasound beam was at right angles to the adventitia, adventitia was visible adjacent to the plaque, and that for image normalization a standard sample consisting of the half of the width of the brightest area of adventitia was obtained.

2.3 Manual Measurements

A neurovascular expert delineated manually (using the mouse) the IMC [10], the ML, and the IL on 100 longitudinal ultrasound images of the CCA after image normalization. The IMC was measured by selecting 20–40 consecutive points for the intima (see Fig. 1a, interface I5) and the adventitia (see Fig. 1a, interface I7) layers, and the ML (see Fig. 1a, band Z6) by selecting 10–20 consecutive points for the media (see Fig. 1, interface I6) and the adventitia layers at the far wall of the CCA. The IL (see Fig. 1a, band Z5) was then derived by subtracting the ML from the IMC. The manual delineations were performed using a system implemented in MATLAB® from our group. The measurements were performed between 1 cm and 2 cm proximal to the bifurcation of the CCA on the far wall [10] over a distance of 1.5 cm starting at a point 0.5 cm and ending at a point 2.0 cm proximal to the carotid bifurcation. The bifurcation of the CCA was used as a guide and all measurements were made from that region. The IMT, the MLT, and the ILT were then calculated as the average of all the measurements. The measuring points and delineations were saved for comparison with the snakes segmentation method. Two sets of measurements were carried out by the neurovascular expert with a 6-month interval. All sets of manual segmentation measurements were performed by the expert in a blinded manner, both with respect to identifying the subject and to the image delineation.

2.4 IMC, ML, and IL Snakes Segmentation

A total of 100 ultrasound images of the CCA were segmented using the automated segmentation system presented in [12], to identify IMC, ML, and IL. Segmentation was carried out after image normalization using the automated snakes segmentation system proposed and evaluated on ultrasound images of the CCA in [10], which is based on the Williams and Shah [21]. Initially the IMC was segmented by a snake segmentation system as proposed in [21], where the boundaries I5 (lumen–intima interface) and I7 (media–adventitia interface) were extracted. Details about the implementation of the algorithm can be found in [10].

The upper side of the ML (see Fig. 1, Z6) was estimated by deforming the lumen–intima interface (boundary I5) by 0.36 mm (6 pixels) downwards and then deformed by the snakes segmentation algorithm proposed in [10] in order to fit to the media boundary (see Fig. 1a, interface I6). This displacement of 0.36 mm is based on the observation that the manual mean IMT (IMT_{mean}) is 0.71 mm (12 pixels), and lies between 0.54 mm (minimum or 9 pixels) and 0.88 mm (maximum or 15 pixels) [10]. Therefore, the displacement of the contour, in order to estimate the media should be in average 0.36 mm (6 pixels times 0.06 mm) downwards, which is half of the size of the IMT (the distance between I5 and I7, where I7 is the media–adventitia interface).

In order to achieve standardization in extracting the thickness of IMC, ML, and IL, segments with similar dimensions were divided based on the following procedure. A region of interest of 9.6 mm (160 pixels) in length, located 1–2 cm proximal to the bifurcation of the CCA on the far wall, was extracted. This was done by estimating the center of the IMC area and then selecting 4.8 mm (80 pixels) left and 4.8 mm (80 pixels) right of the center of the segmented IMC. The selection of the same ML area in length from each image is important in order to be able to make comparable measurements between images and patient groups.

The novelty of the proposed methodology lies in the algorithmic integrated approach that facilitates the automated segmentation and measurements of IL and ML.

2.5 Texture Analysis

In order to estimate textural characteristics extracted from the IL, ML, and the IMC, a total of 61 different texture features were extracted both from the manual and the automated segmented regions of interest where only the most significant are presented. The following texture feature set algorithms were used: (i) statistical features [11,12]: (a) mean, (b) variance, (c) median value, (d) skewness, (e) kurtosis, (f) energy, and (g) entropy. (ii) Spatial gray level dependence matrices (SGLDM) as proposed by Haralick et al. [39]: (a) angular second moment, (b) contrast, (c) correlation, (d) sum of squares variance, (e) inverse difference moment, (f) sum average, (g) sum variance, (h) sum entropy, (i) entropy, (j) difference variance, (k) difference entropy, and (l) information measures of correlation. For a chosen distance d (in this work $d = 1$ was used) and for angles $\theta = 00, 450, 900$, and 1,350, we computed four values for each of the above texture measures. (iii) Gray level difference statistics (GLDS) [40]: (a) homogeneity, (b) contrast, (c) energy, (d) entropy, and (e) mean. The above features were calculated for displacements $\delta = (0,1),(1,1),(1,0),(1,-1)$, where $\delta \equiv (\Delta x, \Delta y)$, and their mean values were taken. (iv) Neighborhood gray tone difference matrix (NGTDM) [41]: (a) coarseness, (b) contrast, (c) busyness, (d) complexity, and (e) strength. (v) Statistical feature matrix (SFM) [42]: (a) coarseness, (b) contrast, (c) periodicity, and (d) roughness. (vi) Laws texture energy measures (LTEM) [42]: LL-texture energy from LL-kernel, EE-texture energy from EE-kernel, SS-texture energy from SS-kernel, LE-average texture energy from LE- and EL-kernels, ES-average texture energy from ES- and SE-kernels, and LS-average texture energy from LS- and SL-kernels. (vii) Fractal dimension texture analysis (FDTA) [42]: The Hurst coefficients for dimensions four, three, and two were computed. (viii) Fourier power spectrum (FPS) [42]: (a) radial sum and (b) angular sum.

2.6 Statistical Analysis

We computed the mean and median values for the IMT (IMT_{mean}, IMT_{median}), the MLT (MLT_{mean}, MLT_{median}), and the ILT (ILT_{mean}, ILT_{median}), the inter-observer error for the IMT, MLT, and the ILT ($se = \sigma\sqrt{2}$) [9] as well as the IMT ratio [15] ($IMT_{ratio} = MLT/ILT$). We also calculated the coefficient of variation, CV%, for the IMT, MLT, and ILT, respectively, which describes the difference as a percentage of the pooled mean values, where for the media $CV\%_{media} = (se_{media} \times 100)/MLT_{media}$ [9]. The above measurements were also computed for the three different age groups, namely, below 50, between 50 and 60, and above 60 years old and for the male and female subjects. Additionally, in order to assess the intra-observer variability for the neurovascular expert, the manual MLT measurements were repeated 6 months after the first set of measurements.

The Wilcoxon rank sum test, which calculates the difference between the sum of the ranks of two dependent samples, was also used in order to identify if a significant difference (S) or not (NS) exists at $p < 0.05$, between the manual and the snakes segmentation measurements, of IMC, ML, IL, and for the IMT_{ratio} for all 100 image, and between the manual and the automated segmentation measurements IMC, ML, and IL for the three different age groups (below 50, between 50 and 60, and above 60 years old). Furthermore, the Mann–Whitney rank sum test was also applied in order to identify differences between male and female subjects. Also the correlation coefficient, ρ, between the manual and the automated IMT, MLT, and ILT measurements, was investigated, which reflects the extent of a linear relationship between two data sets [22].

In order to investigate how the automated media snakes segmentation method differs from the manual delineation results, we have investigated the regression lines for the mean values of the MLT vs. age. Regression analysis was also used in order to demonstrate the relationship between the IMT, MLT, and ILT mean manual measurements and age of the subjects. Bland–Altman plots [23], with 95% confidence intervals, were also used to further evaluate the agreement between the manual and the automated media segmentation measurements. The results of this analysis are, however, not presented in this study as are the expansion of the studies are published in [10–12]. Furthermore, box plots for the manual and the automated IMT, MLT, and ILT mean measurements were plotted, as well as for the manual IMT, MLT, and ILT measurements for the three different age groups (below 50, between 50 and 60, and above 60 years old).

3 Results

Figure 1 illustrates an original normalized ultrasound image of the carotid artery with the automated segmentation of the IMC and ML in (a) and (b), the extracted automated IMC and ML bands in (c) and (d), the manual delineations of the IMC and ML in (e) and (f), and the extracted manual IMC and ML bands in (g) and (h),

respectively. It should be noted that the size of the IMC and ML areas presented in Fig. 1c, d, g, h is larger than its original size (enlarged to 300×20 pixels in order to be better visualized) and does not represent the original truth size (see also Sect. 2.4).

The manual (first and second set of measurements) and the automated mean and median measurements for all 100 images, and for the three different age groups, of the IMC, ML, and IL, are presented in Table 1, as well as the inter-observer error, se, the coefficient of variation, CV%, and the IMT_{ratio}. Table 1 shows that the mean $\pm$ sd for the manual first set and the automated IMT measurements at time zero were 0.71 ± 0.17 mm and 0.67 ± 0.12 mm, for the manual first set and the automated MLT measurements were 0.25 ± 0.12 mm and 0.25 ± 0.11 mm, and for the manual first set and the automated ILT measurements were 0.43 ± 0.10 mm and 0.42 ± 0.13 mm, respectively. The inter-observer errors, se, for the manual first set and the automated IMT segmentation measurements were 0.11 and 0.08, whereas for the MLT and ILT measurements were 0.09 and 0.08, and 0.07 and 0.07, respectively. The coefficients of variation, CV%, for the manual first set and the automated IMT measurements were 17.3% and 12.6%, whereas for the manual first set and the automated MLT and ILT segmentation measurements, were 34% and 12.3%, and 16.7% and 11.7%, respectively. The IMT_{ratio}, for the first set of manual measurements for all 100 images and for the three different age groups (below 50, between 50 and 60, and above 60 years old) were 0.5834 ± 0.323 mm, 0.4314 ± 0.242 mm, 0.634 ± 0.273 mm, 0.6867 ± 0.273 mm, respectively. Similar values, but slightly higher, were observed for the second set of manual measurements carried out at month 6, for the IMT, MLT, and ILT (see Table 1). For the IMT_{ratio} using the Wilcoxon rank sum test, there was no significance difference between the automated and the second set of manual measurements ($p = 0.698$); however, there was a significance difference between the automated and the first set of manual measurements ($p = 0.031$) and between the first and the second set of manual measurements ($p = 0.011$).

Table 2 presents the results of the Mann–Whitney rank sum test performed between the male and the female subjects for all three segmentation measurements (IMT, MLT, and ILT) and the IMT_{ratio}. There was no significant difference for the MLT between the male and the female subjects for the first set and automated measurements. Significant differences between the male and the female subjects were only found for the second set of manual measurements for the IMT ($p = 0.01$) and ILT ($p = 0.013$). There was also no significant difference for the IMT_{ratio} between the male and the female subjects.

The Wilcoxon rank sum test between the manual and the automated IMT, MLT, ILT, and IMT_{ratio} measurements was also performed between the three different age groups and it is shown in Table 3. The Wilcoxon rank sum test and the correlation coefficient (with 95% confidence) results performed between the manual and the automated measurements for the IMT, MLT, ILT, and IMT_{ratio} showed that there were no significant differences between these sets of measurements.

The automated MLT values (MLT_A) vs. age using regression analysis gave an equation of $MLT\_A = 0.029 + 0.0041 \times AGE$, where the standard error for intercept and slope were 0.0661 and 0.001, respectively. The mean square error due to regression was 0.1509, the residual mean square was 0.013 resulting in an

Table 1 Manual and automated IMC, ML, and IL segmentation measurements in mm for all subjects and for the age groups below 50, between 50 and 60, and above 60 years old

Set of measurements	Thickness (mm)	Mean ± SD (mm)	Median (IQR)	se	CV (%)	IMT_{ratio}
First set of manual measurements at time 0 months	IMT	0.71 ± 0.17	0.66 (0.18)	0.11	17.3	0.583 ± 0.323
	IMT_50	0.59 ± 0.13	0.57 (0.13)	0.09	14.9	0.431 ± 0.242
	IMT_60	0.74 ± 0.18	0.73 (0.23)	0.12	16.8	0.634 ± 0.273
	IMT_g60	0.82 ± 0.15	0.81 (0.2)	0.10	12.6	0.687 ± 0.273
	MLT	0.25 ± 0.12	0.23 (0.17)	0.09	34	
	MLT_50	0.17 ± 0.09	0.13 (0.15)	0.07	38	
	MLT_60	0.26 ± 0.08	0.26 (0.08)	0.06	23.8	
	MLT_g60	0.31 ± 0.12	0.33 (0.15)	0.1	12.6	
	ILT	0.43 ± 0.10	0.43(0.10)	0.07	16.7	
	ILT_50	0.41 ± 0.05	0.39 (0.09)	0.04	10.0	
	ILT_60	0.43 ± 0.12	0.42 (0.10)	0.08	19.2	
	ILT_g60	0.46 ± 0.08	0.44 (0.06)	0.05	11.4	
Second set of manual measurements at time 6 months	IMT	0.72 ± 0.17	0.68 (0.19)	0.12	17.5	0.613 ± 0.307
	IMT_50	0.7 ± 0.2	0.67 (0.26)	0.14	20.2	0.551 ± 0.297
	IMT_60	0.66 ± 0.13	0.63 (0.15)	0.09	14.2	0.652 ± 0.312
	IMT_g60	0.78 ± 0.15	0.73 (0.17)	0.11	14.0	0.632 ± 0.225
	MLT	0.27 ± 0.14	0.25 (0.09)	0.07	9.8	
	MLT_50	0.24 ± 0.12	0.26 (0.21)	0.08	33.5	
	MLT_60	0.25 ± 0.08	0.23 (0.11)	0.11	23.2	
	MLT_g60	0.29 ± 0.12	0.26 (0.13)	0.07	22.4	
	ILT	0.44 ± 0.13	0.44 (0.10)	0.10	21.3	
	ILT_50	0.45 ± 0.14	0.44 (0.10)	0.09	21.1	
	ILT_60	0.41 ± 0.11	0.40 (0.11)	0.10	18.4	
	ILT_g60	0.48 ± 0.11	0.46 (0.08)	0.08	16.1	

(continued)

Table 1 (continued)

Set of measurements	Thickness (mm)	Mean ± SD (mm)	Median (IQR)	se	CV (%)	IMT_{ratio}
Automated segmentation measurements	IMT	0.67 ± 0.12	0.66 (0.12)	0.08	12.6	0.597 ± 0.286
	IMT_50	0.61 ± 0.11	0.59 (0.09)	0.08	12.6	0.461 ± 0.261
	IMT_60	0.68 ± 0.10	0.69 (0.12)	0.07	10.3	0.618 ± 0.236
	IMT_g60	0.74 ± 0.13	0.73 (0.11)	0.1	12.9	0.760 ± 0.320
	MLT	0.25 ± 0.11	0.25 (0.10)	0.08	12.3	
	MLT_50	0.19 ± 0.11	0.17 (0.09)	0.08	14.0	
	MLT_60	0.26 ± 0.10	0.26 (0.12)	0.12	27.1	
	MLT_g60	0.32 ± 0.13	0.11 (0.11)	0.10	29.7	
	ILT	0.42 ± 0.10	0.42(0.90)	0.07	11.7	
	ILT_50	0.25 ± 0.12	0.42(0.90)	0.07	11.7	
	ILT_60	0.25 ± 0.12	0.42(0.90)	0.07	11.7	
	ILT_g60	0.25 ± 0.12	0.42(0.90)	0.07	11.7	

IMC intima–media complex, *IMT* intima–media thickness for all 100 measurements; IMT_50, IMT_60, and IMT_g60: IMT values for the age groups below 50, between 50 and 60, and above 60, respectively; MLT: media layer thickness for all 100 measurements; MLT_50, MLT_60, and MLT_g60: MLT values for the age groups below 50, between 50 and 60, and above 60, respectively; ILT: intima layer thickness for all 100 measurements; ILT_50, ILT_60, and ILT_g60: ILT values for the age groups below 50, between 50 and 60, and above 60, respectively; sd: standard deviation; IQR: inter-quartile range; se: inter-observer error; CV%: coefficient of variation; IMT_{ratio} = MLT/ILT. Source [12], © IEEE 2009

Table 2 Comparison between sex groups (male = M and female = F) for the IMC, IM, IL, and IMT_{ratio} using the Mann–Whitney rank sum test

	First set manual of measurements				Second set of manual measurements				Automated measurements			
	IMT	MLT	ILT	IMT_{ratio}	IMT	MLT	ILT	IMT_{ratio}	IMT	MLT	ILT	IMT_{ratio}
Sex	NS	NS	NS	NS	S	NS	S	NS	NS	NS	NS	NS
(M/F)	(0.8)	(0.193)	(0.971)	(0.137)	(0.01)	(0.128)	(0.013)	(0.964)	(0.362)	(0.332)	(0.96)	(0.362)

IMT intima–media thickness, *MLT* media layer thickness, *ILT* intima layer thickness, IMT_{ratio}: IMT ratio = MLT/ILT. The p value is also shown in parentheses (S = significant difference at $p < 0.05$, NS = nonsignificant difference at $p > 0.05$) Source [12], © IEEE 2009

Table 3 Comparison between the IMC, ML, IL, and IMT_{ratio} for the manual and the automated segmentation measurements based on the Wilcoxon rank sum test for the three different age groups, below 50 (< 50), between 50 and 60 (50–60), and above 60 (> 60) years old

			Second set of manual measurements												Automated Measurements											
			IMT			MLT			ILT			IMT_{ratio}			IMT			MLT			ILT			IMT_{ratio}		
			<50	50–60	>60	<50	50–60	>60	<50	50–60	>60	<50	50–60	>60	<50	50–60	>60	<50	50–60	>60	<50	50–60	>60	<50	50–60	>60
First set of manual measurements	IMT	<50	S	NS	S										S	S	S									
		50–60	NS	S	S										S	S	S									
		>60	S	S	NS										S	S	S									
	MLT	<50				S	S	S										NS	NS	S						
		50–60				NS	NS	NS										S	NS	S						
		>60				NS	S	NS										S	NS	NS						
	ILT	<50							S	NS	S										NS	NS	NS			
		50–60							NS	NS	S										NS	NS	NS			
		>60							NS	S	NS										S	S	S			
	IMT_{ratio}	<50										S	S	S										NS	S	S
		50–60										NS	NS	NS										S	NS	S
		>60										S	NS	NS										S	NS	NS

Second set of manual measurements	IMT	<50	S	NS	NS												
		50–60	NS	NS	S												
		>60	S	S	NS												
	MLT	<50				S	NS	NS									
		50–60				NS	NS	S									
		>60				S	NS	NS									
	ILT	<50							NS	NS	NS						
		50–60							NS	NS	NS						
		>60							S	S	S						
	IMT_{ratio}	<50										NS	NS	S			
		50–60										S	NS	S			
		>60										S	NS	NS			

IMT intima–media thickness, *MLT* media layer thickness, *ILT* intima layer thickness, IMT_{ratio} = MLT/ILT; S = significant difference at $p < 0.05$; NS = nonsignificant difference at $p > 0.05$. Source [12], © IEEE 2009

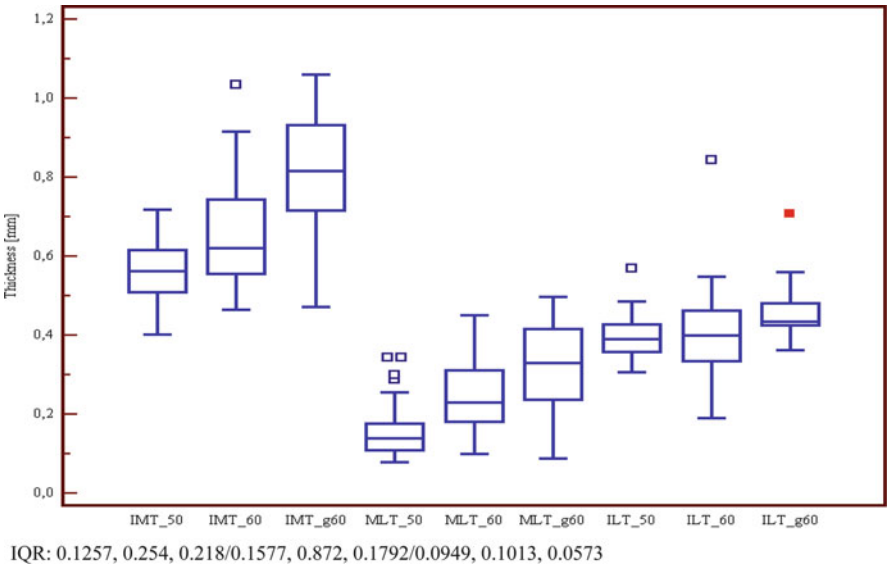

Fig. 2 Box plots for the manual measurements of the IMT, MLT, and ILT for the age groups below 50 (50), between 50 and 60 (60), and above 60 years (g60) old (i.e., IMT_50, ILT_60, and MLT_g60 represent the values below the age of 50 for IMC, ML, and IL, respectively). Source [12], © IEEE 2009

F-ratio of 11.6 with a corresponding significance level of $p = 0.001$. This supports the assumption of a linear relationship between age and MLT. The correlation coefficient was $\rho = 0.33$. It was shown that the MLT at the age of 55 is 0.25 mm and that the 95% confidence interval limits for the MLT are both ± 0.24 mm.

The Bland–Altman plot between the first set manual measurements and the snakes segmentation MLT measurements showed that the difference between the manual and the snakes segmentation measurements was -0.01 mm with limits of agreement lying between 0.16 mm and -0.18 mm (note that the pixel resolution was 0.08 mm). The Bland–Altman plot between the second set manual measurements and the snakes segmentation MLT measurements showed that the difference between the manual and the snakes segmentation measurements was 0.01 mm with limits of agreement lying between 0.24 mm and -0.23 mm. The Bland–Altman plot between the first and second set of manual measurements showed that the difference between the first and the second set of the manual measurements was -0.02 mm with limits of agreement lying between 0.16 mm and -0.19 mm. There was also a negative bias, as estimated by the mean difference, which showed that on an average the snakes segmentation algorithm underestimates the area relative to normal delineation.

Figure 2 presents box plots of the IMT, MLT, and ILT, for the three different age groups, extracted from the manual IMC, ML, and IL segmentations for all 100 images of the CCA for the three different age groups (below 50, between 50 and 60, and above 60 years).

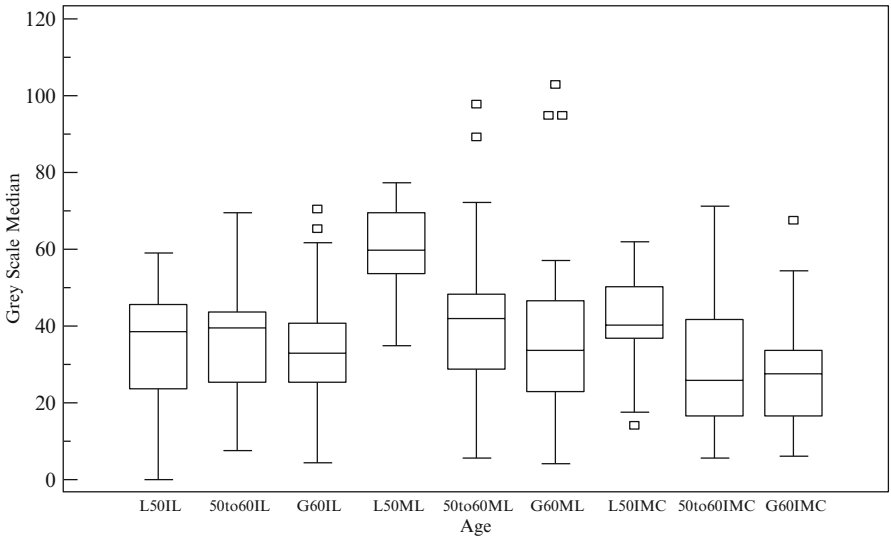

Fig. 3 Box plots of the gray-scale median (GSM) texture feature extracted from IL, ML, and IMC. Here we are using automated segmentations. In our description we let IQR denote the inter-quartile distance. From left to right, for the first three plots we have: L50IL for the IL for patients younger than 50 (IQR = 22), 50 to 60 IL for the IL for patients from 50 to 60 years old (IQR = 18.4), and G60IL for the IL for patients who are older than 60 years old (IQR = 15.4). For the next three plots (middle), we have the same age groups for the ML and IQR values of 16, 19.5, and 23.7, respectively. The last three plots (leftmost) show the GSM values for the IMC with IQR values 13.6, 25.2, and 16.9, respectively. In each plot we display the median, lower, and upper quartiles and confidence interval around the median of the GSM. Straight lines connect the nearest observations with 1.5 of the inter-quartile range (IQR) of the lower and upper quartiles. Unfilled rectangles indicate possible outliers with values beyond the ends of the $1.5 \times$ IQR. Source [12], © IEEE 2009

Figure 3 presents box plots of the GSM texture features for the three different age groups. These measurements were extracted using the automated IL/ML/IMC segmentations.

Table 4 presents the median and inter-quartile range (IQR) of selected texture features extracted from the automated IL, ML, and IMC segmentations of the 100 ultrasound images investigated. From Table 4, we can see that most of the texture features extracted from the ML exhibit lower median and IQR values when compared with those extracted from the IL and IMC (e.g.: mean, GSM, STD, contrast, ASM, and coarseness).

In Table 5, we use the Wilcoxon rank sum test to compare selected texture features extracted from automated and manual segmentations. We can see similar results for both manual and automated segmentations. However, we note that there are differences. To avoid issues associated with segmentation differences, we are only interested in textural features that give significant differences for both manual

Table 4 Texture features (median (IQR)) for the IL, ML, and IMC using automated segmentations

	IL	ML	IMC
Mean	35 (19.3)	21 (25)	33 (22)
GSM	35 (18.5)	28 (18)	30 (21.3)
STD	16 (6.6)	14 (7)	16 (5.7)
Contrast	52 (75)	28 (32)	61 (57)
DV	16 (27.8)	81 (56)	32 (32)
Complexity	1,704 (3,175)	6,041 (6,762)	4,166 (5,888)
ASM	0.09 (0.04)	0.002 (0.003)	0.003 (0.002)
Coarseness	20 (14.5)	13 (11)	24 (11.3)
SS-TEL	38 (33)	78 (53)	56 (38)
Entropy	5.7 (1.15)	6 (1.2)	6.6 (0.7)
Roughness	2.46(0.187)	2.2 (0.100)	2.238 (0.079)
Periodicity	0.8 (0.07)	0.9 (0.06)	0.8 (0.2)

IQR inter-quartile range, *GSM* gray-scale median, *STD* standard deviation, *DV* difference variance, *ASM* angular second moment, *SS-TEL* SS-texture energy laws. Source [11], © CMIG 2009

Table 5 Wilcoxon rank sum comparison tests performed on texture features (first column) extracted from the IL, ML, and IMC using manual (M) and automated (A) segmentations. In boldface, we have the texture features identified by the automated segmentation method that also exhibits significant differences for manual segmentation

	Manual (M)			Automated (A)		
	IL–ML	IL–IMC	ML–IMC	IL–ML	IL–IMC	ML–IMC
Mean	S (0.01)	NS (0.5)	S (0.001)	**S (0.02)**	NS (0.81)	**S (0.004)**
GSM	NS (0.39)	NS (0.62)	S (0.001)	NS (0.3)	NS (0.45)	**S (0.04)**
Stand. Dev.	S (0.01)	S (0.001)	S (0.001)	**S (0.001)**	NS (0.1)	**S (0.001)**
Contrast	S (0.001)	S (0.001)	S (0.001)	**S (0.001)**	NS (0.23)	**S (0.001)**
Diff. Var.	S (0.001)	S (0.001)	S (0.01)	**S (0.001)**	**S (0.007)**	NS (0.09)
Complexity	S (0.001)	S (0.001)	S (0.04)	**S (0.001)**	**S (0.001)**	NS (0.09)
ASM	NS (0.3)	S (0.001)	NS (0.13)	**S (0.004)**	**S (0.001)**	**S (0.001)**
Coarseness	S (0.001)	S (0.021)	S (0.001)	**S (0.001)**	**S (0.005)**	**S (0.001)**
SS-TEL	S (0.009)	S (0.009)	NS (0.13)	**S (0.001)**	**S (0.02)**	NS (0.18)
Entropy	S (0.017)	S (0.001)	NS (0.85)	**S (0.001)**	**S (0.001)**	**S (0.008)**
Periodicity	S (0.001)	NS (0.92)	S (0.001)	**S (0.001)**	NS (0.07)	**S (0.02)**

IL intima layer, *ML* media layer, *IMC* intima–media complex. The p value is shown in parentheses (S = significantly different at $p < 0.05$, NS = nonsignificantly different at $p \geq 0.05$). Source [11], © CMIG 2009

and automated segmentations. For better visualization, we put these features in bold face (see Table 5). Between the IL and the ML, we have significant differences in 10 out of 11 features. Between the IL and the IMC, we have six texture features with significant differences. Similarly, we have eight texture features that exhibit significant differences between the IL and the ML in Table 5. We refer to Table 6 for a summary of the texture feature values.

Table 6 Texture characteristics of IL vs. ML based on the texture feature values given in Table 1

Corresponding features from Table 1	IL	ML
Mean, GSM	Brighter	Darker
Contrast, ASM	Higher contrast	Less contrast
Complexity, entropy	Low complexity	High complexity
Coarseness	More coarse, i.e., large areas with small gray tone variations	Less coarse, i.e., less local uniformity in intensity
Roughness	Slightly rougher	Smoother
Periodicity	Less periodical, more heterogeneous	More periodical, more homogeneous

Source [11], © CMIG 2009

Table 7 presents the Mann–Whitney rank sum test performed on selected texture features extracted from the automated IL, ML, and IMC segmentations for the three different age groups. It is shown that some of the texture features (GSM, STD, DV, complexity, coarseness, and SS-TEL) exhibit significantly different values between different age groups.

4 Discussion

In this study, both manual and automated IMT, MLT, and ILT measurements are reported for 100 longitudinal ultrasound images of the CCA and their variation with age and sex. The importance of the CCA ML for the evaluation of the risk of CVD was outlined in [2] and shown in [15], that the MLT was thinner for this group of subjects. Also it was shown in [16] that the MLT was strongly related with age for the radial and anterior tibial arteries. It was also found (see Table 6) that the ML is less dark, has less contrast, is more periodic, and is less coarse compared to IL. We have found a decrease of ML GSM with increasing age, as well as decrease with thickness (MLT), that can be attributed to the fact that, at the initial stages of atherosclerosis disease, there is an increased concentration of lipids and hyperplasia of muscle fibers in the ML, which produces hypoechoic (echolucent) structures. It was also shown that the GSM of male patients is brighter than that of the female patients.

Table 1 showed that the manual IMT measurements are larger and have a larger range of values, whereas the first set of manual and the automated MLT measurements are almost the same, while the second set of manual measurements were higher. Similar IMT findings were also reported in [9, 10, 14]. The manual $\text{IMT}_{\text{mean}} \pm \text{SD}$ measurements reported in this study (0.71 ± 0.17 mm and 0.72 ± 0.17 mm for manual first and second sets, respectively) were larger than the snakes segmented measurements (0.67 ± 0.12 mm), and this finding was also reported in other studies. More specifically, the manual vs. the snakes segmented IMT measurements reported

Table 7 Statistical comparisons between texture features extracted from the IL, ML, and IMC for different age groups. Here we use automated (first row) and manual (second row) segmentations. Statistical comparisons were based on the Mann–Whitney rank sum test for the three different age groups. Automated and manual IL, ML, and IMC segmentation measurements in mm (last row)

			IL			ML			IMC		
			<50	50–60	>60	<50	50–60	>60	<50	50–60	>60
Automated and manual segmentation measurements	GSM	<50		NS (0.3)	NS (0.3)		**S (0.01)**	**S (0.003)**		NS (0.08)	**S (0.03)**
				NS (0.23)	NS (0.23)		**S (0.02)**	**S (0.03)**		NS (0.43)	**S (0.03)**
		50–60			NS (0.22)			NS (0.25)			NS (0.22)
					NS (0.11)			**S (0.01)**			NS (0.26)
	STD	< 50		NS (0.36)	**S (0.01)**		NS (0.55)	**S (0.04)**		NS (0.65)	**S (0.03)**
				NS (0.33)	**S (0.03)**		NS (0.09)	**S (0.004)**		NS (0.23)	**S (0.04)**
		50–60			NS (0.11)			NS (0.08)			NS (0.06)
					NS (0.3)			NS (0.07)			NS (0.3)
	Contrast	<50		NS (0.92)	**S (0.001)**		NS (0.7)	NS (0.8)		NS (0.3)	NS (0.25)
				NS (0.56)	**NS (0.01)**		NS (0.26)	NS (0.76)		**S (0.04)**	NS (0.06)
		50–60			NS (0.55)			NS (0.55)			S (0.22)
					NS (0.3)			NS (0.22)			S (0.5)
	DV	<50		NS (0.33)	NS (0.87)		NS (0.18)	**S (0.01)**		NS (0.55)	**S (0.04)**
				NS (0.45)	NS (0.73)		NS (0.19)	NS (0.63)		**S (0.03)**	**S(0.02)**
		50–60			NS (0.8)			NS (0.44)			NS (0.17)
					NS (0.67)			NS (0.44)			NS (0.7)
	Complexity	<50		NS (0.97)	**S (0.0001)**		NS (0.56)	**S (0.005)**		NS (0.55)	NS (0.33)
				NS (0.78)	NS (0.13)		NS (0.7)	NS (0.09)		NS (0.1)	NS (0.1)
		50–60			NS (0.05)			NS (0.35)			NS (0.42)
					NS (0.07)			NS (0.87)			NS (0.65)

	Coarseness	<50		NS (0.19)	NS (0.08)		NS (0.56)	**S (0.004)**	NS (0.4)	NS (0.3)
				NS (0.37)	NS (0.3)		NS (0.5)	**S (0.01)**	NS (0.5)	NS (0.4)
		50–60			NS (0.7)			**S (0.003)**		NS (0.2)
					NS (0.6)			**S (0.01)**		NS (0.08)
	SS-TEL	<50		NS (0.07)	NS (0.14)		**S (0.008)**	**S (0.0001)**	NS (0.83)	NS (0.71)
				NS (0.24)	NS (0.22)		**S (0.02)**	**S (0.04)**	NS (0.78)	NS (0.25)
		50–60			NS (0.06)			NS (0.09)		NS (0.27)
					NS (0.2)			NS (0.11)		NS (0.09)
	Entropy	<50		NS (0.65)	NS (0.9)		NS (0.34)	NS (0.08)	NS (0.83)	**S (0.02)**
				NS (0.59)	NS (0.7)		NS (0.9)	NS (0.3)	S (0.81)	**S (0.04)**
		50–60			NS (0.88)			NS (0.36)		NS (0.27)
					NS (0.5)			NS (0.7)		NS (0.4)
Thickness (mm)			0.42 ± 0.10	0.42 ± 0.10	0.42 ± 0.10	0.19 ± 0.11	0.26 ± 0.10	0.32 ± 0.13	0.61 ± 0.11	0.68 ± 0.10	0.74 ± 0.13
			0.41 ± 0.05	0.43 ± 0.12	0.46 ± 0.08	0.17 ± 0.09	0.26 ± 0.08	0.31 ± 0.12	0.59 ± 0.13	0.74 ± 0.18	0.82 ± 0.15

IL intima layer, *ML* media layer, *IMC* intima–media complex. The p value is shown in parentheses (S = significant difference at $p < 0.05$, NS = nonsignificant difference at $p \geq 0.05$). Source [11], © CMIG 2009

in other studies were (0.93 mm vs.0.88 mm) [9], (0.72 mm vs. 0.63 mm) [13], (0.8 mm vs. 0.7 mm) [14], and (0.92 mm vs. 0.88 mm) [29]. There is a large variation in the IMT measurements between the different studies because different material and different measuring methodologies were used.

The manual first set MLT, ILT measurements, and IMT_{ratio} in our study were 0.25 ± 0.12 mm, 0.43 ± 0.10 mm, and 0.5834 ± 0.323 mm, respectively (similar values were obtained for the second set of manual measurements and the automated measurements). In [15], the manual IMT, MLT, and ILT measurements carried out for the CCA by an expert using high-resolution ultrasound with a broadband probe and a 25 MHz center frequency, between subjects with and without CVD, were $0.75, \pm 0.17$ mm vs. 0.72 ± 0.20 mm ($p = 0.4$), 0.45 ± 0.14 mm vs. 0.38 ± 0.16 mm($p < 0.05$), and 0.17 ± 0.006 mm vs. 0.22 ± 0.06 mm ($p < 0.0001$), respectively. It was shown in [15] that subjects with CVD (coronary heart disease, myocardial infarction, or stroke) had a significantly thicker IL and a thinner ML than healthy subjects. The IMT_{ratio} also differed significantly between subjects with and without a diagnosis of CVD (0.43 ± 0.20 vs. 0.75 ± 0.48, $p = 0.0002$). The MLT and ILT were manually measured from the radial and tibial arteries in 90 subjects (10 to 90 years old), using a 55 MHz two-dimensional ultrasound transducer [16]. The values reported for the MLT ranged from 0.159 ± 0.039 mm to 0.227 ± 0.038 mm, whereas for the ILT the values ranged from 0.49 ± 0.08 mm to 0.81 ± 0.019 mm, respectively. Finally, in [8], it was found that the median MLT of muscular arteries was 0.6 mm in the absence of a lesion, decreasing to 0.1 mm in the area of maximal atherosclerosis. The in vivo study was performed in 29 patients undergoing coronary or peripheral vascular procedures using intravascular ultrasound with a 30 MHz frequency ultrasound probe.

It is shown from Table 1 that for the MLT measurements, the standard deviation, sd, for both the manual (0.12 and 0.14 for the first and second set of manual measurements, respectively) and the automated (0.11) and the coefficient of variation, CV% (34% and 9.8% for the first and second set of manual measurements, and 12.3% for the automated measurements), are large. This is explained due to the fact that the ML is very small with complex texture and, therefore, very difficult to be estimated correctly either manually or automatically.

Table 1 also shows that the inter-observer errors, se, for the IMT and the MLT, are larger for the manual segmentation measurements (for both the first set and the second set of manual measurements). Also, the results from Table 1 showed that high intra-observer variabilities occur when manual measurements are made. Smaller values for se were obtained for the automated segmentation measurements, indicating a better performance of the automated vs. the manual measurements as documented in [10, 22].

Table 2 showed that no significant differences were found between men and women for the IMT, MLT, ILT, and the IMT_{ratio}, as also shown in [15] and that the IMT_{ratio} did not differ significantly between male and female groups.

The nonsignificant (NS) differences between the manual and the automated segmentation method, estimated by the Wilcoxon rank sum test show that the manual measurements may be replaced by the snakes segmentation measurements

with confidence. It was also shown that the manual measurements of the expert at time 0 vs. time 6 months were NS. The correlation coefficient, ρ, showed that the strongest relationship existed between the MLT manual first set and the automated segmentation measurements (with $\rho = 0.72$), where higher values were reported. The Wilcoxon rank sum test performed in Table 3 showed that the first set of manual and automated IMT measurements between all the age groups are mostly significantly different (S), whereas the manual and automated measurements of the MLT and ILT are mostly nonsignificantly different (NS). Furthermore, the Wilcoxon rank sum test for the IMT_{ratio} showed that there are no clear statistical significance between the different age groups; therefore, this measure may not be used as an indicative value for atherosclerotic disease with increasing age.

Based on the Bland–Altman test a small discrepancy, of around 0.01 mm, was found between the manual and the automated MLT measurements. On this basis the two methods (manual and snakes segmentation) can be considered interchangeable. There are no other studies reported in the literature, where Bland–Altman plots were used for comparing the manual and automated MLT measurements. The Bland–Altman plot was used in [29], where 24 carotid ultrasound images were analyzed by two experts for validating the results of IMT measurements using a newly developed system by comparing them with those obtained using previous methods and showed no evidence of bias between the two methods.

This study shows that there might be a linear relationship between MLT automated measurements and age, where all measurements showed an increase with age. Similar findings were also reported for the IMT in [10]. It was also shown that in this study the values of the mean IMT in a carotid artery vary between 0.54 mm and 0.88 mm, depending on age, and this is also consistent with other studies [2, 6, 14, 28], whereas the values of the MLT vary between 0.13 mm and 0.37 mm. Furthermore, in [16], the IMT, MLT, and ILT of 90 healthy subjects (aged between 10 and 90 years), were manually measured at their radial and anterior tibial artery. It was shown that age was strongly related with IMT, MLT, and ILT of both peripheral arteries.

Similar to [37], we have also found that the IMT is generally larger in men than in women. Furthermore, in agreement with [28, 36], we have also found that the IMT increases linearly with age.

In [43], increased IMT has been found in young adults with childhood-onset chronic kidney disease (CKD). The disease stage at which these patients first develop abnormalities of arterial texture is unknown. It was also shown that in 55 children with stages 2 to 4 CKD, thickening of IMT occurs early in the course of the disease and is most prominently marked in dialyzed patients. Furthermore, morphologic alterations were found in both muscular and elastic type arteries as early as in the second decade of life. The degree of thickening depends on the degree of renal dysfunction. The authors also found that 61% of children with stages 2 to 4 CKD had IMT equal to or exceeding the 95th percentile for age.

It was shown in [33] that the GSM of the IM layer is the earliest change representing atherosclerotic disease in the arterial wall that can currently be imaged in vivo. This may be the first marker of atherosclerosis and may precede the

development of significant increase in IMT. This would enable earlier identification of high-risk individuals based on the analysis of the CCA artery wall textural characteristics.

In [34], the texture features of 12 subjects (28 ± 2 years) with familial hypercholesterolemia (FCH) and without CVD, before and 3 months after treatment with atorvastatin were investigated, where the entropy and the ASM were extracted from the IMC band. Before treatment of atorvastatin significantly higher entropy (normal: 0.082 ± 0.02 vs. FCH : 0.57 ± 0.12) and lower ASM (normal: 0.01 ± 0.0011 vs. FCH : 0.004 ± 0.0001) values were found when compared to the normal tissue.

The normalization method used in this study was documented to be helpful in the manual contour extraction [25] as well as the snakes segmentation of the IMC [10] and the atherosclerotic carotid plaque segmentation [26] and texture analysis [11]. Moreover, this method increased the classification accuracy of different plaque types as assessed by the experts [27]. Ultrasound image normalization was carried out, prior to segmentation of the IMT in [24], where histogram equalization was performed on carotid artery ultrasound images for increasing the image contrast.

4.1 Study Limitations

It has been demonstrated in [2, 31] that the blood–endothelium (intima) interface and the media–adventitia interface correspond to their anatomical/histological counterparts. This is not the case with the intima–media interface because the width of the white band closer to the lumen is gain dependent and, therefore, variable. Thus the measurement of the MLT represents only an ultrasonic measurement (as also discussed above). It should be noted, however, that part of the ML, shown in ultrasound image as an echolucent band (Fig. 1a, band Z6), contains the hypo echoic muscular arterial tunica media and perhaps hypo echoic part of the arterial tunica intima. It is well known that atherosclerosis causes an increase of the arterial tunica intima thickness. As has been also reported earlier in the literature [13], the histological boundaries between the arterial tunica intima and media (internal elastic lamina) in ultrasound images cannot be accurately delineated. Therefore, we hypothesize that the increase of the MLT with age as reported in our study (see also [10]) may be a misleading finding, since part of the ML, as shown in ultrasound images, may belong to the arterial tunica intima. We recommend that the above hypothesis should be taken into account in future studies aiming in studying the ML texture and morphology. It should be furthermore noted that there are no other studies reported in the literature where ML segmentation and measurements were performed on longitudinal ultrasound images of the CCA.

While IMT is an established measure of the vascular wall disease [2], GSM is less commonly used while other features have not been used before. GSM analysis has previously mainly been performed on plaques and then found to be related to histological features of the plaque, such as the elastin and calcium content, as well as to the size of the lipid-rich necrotic core [44]. However, the histological correlate

to variation in the ML texture features has to be evaluated and the prognosis impact of these new variables has to be investigated. It has also been observed that there is an increase in the granularity in association with atherosclerotic disease [31]. A granular IMC indicates more advanced atherosclerosis, which may precede the development of significant IMT thickening.

A limitation of the proposed method is that the manual and automated ML and IL segmentation measurements were performed in linear segments of the CCA because in the clinical praxis, the experts are delineating the IMC and the ML only in those parts of the vessel where there are no significant artifacts, signal drop outs, and structure irregularities [2, 9, 10, 20, 27, 35].

Another limitation of the proposed method is the presence of acoustic shadowing together with strong speckle noise, which hinders the visual and automatic analysis in ultrasound images [9, 10]. Such images as well as images with extensive echolucency and calcification, where the ML was not well visually recognized, were excluded from the study. Backscattered ultrasound is also angle dependent. During the recording of the images, a standard recording technique was used to adjust the position of the probe so that the ultrasound beam was at right angles to the arterial wall. This improved the IMC visualization. Moreover, the new spatial compound imaging technique might optimize further carotid ultrasound imaging [25, 27]. Due to the small size of the ML and the estimation and positioning of the initial snake contour may sometimes result to segmentation errors. This should be placed as close as possible to the area of interest, otherwise it may be trapped into local minima or false edges and converge to a wrong location.

As it has already been mentioned in Sect. 2.1, the axial resolution of the system used was 0.11 mm, which indicates that structures greater than 0.11 mm can be correctly visualized and measured (see also [32]). In addition, it is noted that the pixel resolution was 0.06 mm. For structures thinner than 0.11 mm, the two echo interfaces (i.e., of ML) cannot be separated and measurements of these structures are not possible. For the dataset investigated in this study, 6% of the measurements were below 0.11 mm; therefore, these measurements may be considered as unreliable. It should be noted, however, that with new ultrasound equipment and new probes, that are available having a recording frequency in the range of 15 MHz, this problem will be highly limited. In another study where the variability of the IMT between experts and between the manual and the automated IMT measurements was investigated [32], it was shown that the reproducibility of the IMT measurements may be further improved if the IMT mean value is computed from multiple ultrasound images (frames) of the carotid, instead of the mean value obtained from only one frame [32]. These can be also investigated in a future study for the case of the MLT and the ILT measurements.

In the present study, in less than 8% of the cases, the positioning of the initial snake contour was not calculated correctly. Furthermore, there were also another 6% of the cases where the ML structure was very small and the two snake contours were trapped together. For these cases the user of the proposed system may run the snakes initialization procedure again in order to estimate the correct initial snake contour, and during the snakes deformation the user may interact and manually correct the contour.

5 Concluding Remarks and Future Work

It was clearly illustrated in this study that both manual and automated IMT, MLT, and ILT measurements could be carried out successfully. Also, it was shown that there was overall no significant difference between the manual and the automated measurements, between the male and the female subjects, as well as that these increase with age.

The segmented IMC, ML, and IL bands may be used for extracting texture features [30], which might be able to differentiate between subjects with high and low risk of stroke. Furthermore, the change of these textural characteristics with age may give additional information for characterizing subjects in different risk groups. In a recent study [35], it was shown that the gray-scale median of the IMC of the CCA is closely related to the echogenecity in overt carotid plaques. This finding suggests that the gray-scale median and other texture features extracted from the IMC or the ML bands could have prognostic impact for the assessment of cardiovascular risk. However, the IMT_{ratio} was not found to be statistically of significant difference with increasing age.

Our texture analysis showed that: (a) there are significant differences between some texture features extracted from the IL, ML, and IMC (mean, gray-scale median (GSM), standard deviation, contrast, difference variance, and periodicity), (b) some of the texture features can be associated with the increase (difference variance, entropy) or decrease (GSM) of patient's age, (c) the GSM of the ML falls linearly with increasing ML thickness (MLT) and with increasing age, (d) the GSM of male subjects is larger than that of female subjects (se, Fig. 5.4), and (e) male and female subjects may be better distinguished using texture features extracted from the IMC.

Risk factors like smoking, blood pressure, inflammation markers, and cholesterol correlate to the traditional carotid IMT [1, 3, 4, 16]. It would have been valuable to relate these risk factors to AM–FM analysis and not only the age as done in this study. Ongoing studies from our group will give more data on this topic.

Future work will investigate whether it is possible to identify a group of patients at risk of atherosclerosis based on their texture features extracted from the IL, the ML, and the IMC of high-resolution ultrasound images of the CCA. It may also be possible to identify and differentiate those individuals into high- and low-risk groups according to their cardiovascular risk before the development of plaques. The proposed methodology may also be applied to a group of people, which already developed plaques in order to study the contribution of the ML texture features to cardiovascular risk. Both groups of patients may benefit by prognosing and managing future cardiovascular events. Another possible future application of the proposed methodology is that it can be used to investigate possible effects of statins or other drugs in texture feature changes of the ML of the CCA.

The methodology presented in this study will be further evaluated on ultrasound images of the CCA collected on a large-scale epidemiological study by our group as well as for the segmentation and measurement of curved segments of the bifurcation bulb of the CCA.

References

1. American Heart Association (2007) Heart disease and stroke statistics-2008, update, Dallas. http://www.americanheart.org/presenter.jhtml.
2. Pignoli P, Tremoli E, Poli A, Oreste P, Paoleti R (1986) Intima plus media thickness of the arterial wall: a direct measurement with ultrasound imaging. Atherosclerosis 74(6):1399–1406
3. Touboul P-J, Labreuche J, Vicaut E, Amarenco P (2005) Carotid intima–media thickness, plaques, and Framingham risk score as independent determinants of stroke risk. Stroke 36(8):1741–1745
4. Watanabe T, Koba S, Kawamura M, Itokawa M, Idei T, Nakagawa Y, Iguchi T, Katagiri T (2004) Small dense low-density lipoprotein and carotid atherosclerosis in relation to vascular dementia. Metabolism 53(4):476–482
5. Mario CD, Gorge G, Peters R, Pinto F, Hausmann D, von Birgelen C, Colombo A, Murda H, Roelandt J, Erbel R (1998) Clinical application and image interpretation in coronary ultrasound. Study group of intra-coronary imaging of the working group of coronary circulation and of the subgroup of intravascular ultrasound of the working group of echocardiography of the European Society of Cardiology. Eur Heart J 19(2):201–229
6. Grønhold ML, Nordestgaard BG, Schroeder TV, Vorstrup S, Sillensen H (2001) Ultrasonic echolucent carotid plaques predict future strokes Circulation 104(1):68–73
7. Wilhjelm JE, Grønholdt MLM, Wiebe B, Jespersen SK, Hansen LK, Sillensen H (1998) Quantitative analysis of ultrasound B-mode images of carotid atherosclerotic plaque: correlation with visual classification and histological examination. IEEE Trans Med Imaging 17(6):910–922
8. Gussenhoven EJ, Frietman PA, van Suylen SHRJ, van Egmond FC, Lancee CT, van Urk H, Roelandt JR, Stijnen T, Bom N (1991) Assessment of medial thinning in atherosclerosis by intravascular ultrasound Am J Cardiol 68:1625–1632
9. Wendelhag I, Liang Q, Gustavsson T, Wikstrand J (1997) A new automated computerized analysing system simplifies reading and reduces the variability in ultrasound measurement of intima media thickness. Stroke 28:2195–2200
10. Loizou CP, Pattichis CS, Pantziaris MS, Tyllis T, Nicolaides AN (2007) Snakes based segmentation of the common carotid artery intima media. Med Biol Eng Comput 45:35–49
11. Loizou CP, Pantziaris M, Pattichis MS, Kyriakou E, Pattichis CS (2009) Ultrasound image texture analysis of the intima and media layers of the common carotid artery and its correlation with age and gender. Comput Med Imaging Graph 33(4):317–324
12. Loizou CP, Pattichis CS, Nicolaides A, Pantziaris M (2009) Manual and automated media and intima thickness measurements of the common carotid artery. IEEE Trans Ultrason Ferroelectr Freq Control 56(5):983–994
13. Gutierrez M, Pilon P, Lage S, Kopel L, Carvalho R, Furuie S (2002) Automatic measurement of carotid diameter and wall thickness in ultrasound images. Comput Cardiol 29:359–362
14. Delsanto S, Molinari F, Giustetto P, Liboni W, Badalamenti S, Suri JS (2007) Characterization of a completely user independent algorithm for carotid artery segmentation in 2-D ultrasound images. IEEE Trans Instrum Meas 56(4):1265–1274

15. Rodriguez-Maciasa KA, Lindbc L, Naessena T (2006) Thicker carotid intima layer and thinner media layer in subjects with cardiovascular diseases: an investigation using noninvasive high-frequency ultrasound. Atherosclerosis 189(2):393–400
16. Osika W, Dangardt F, Grönros J, Lundstam U, Myredal A, Johansson M, Volkmann R, Gustavsson T, Gan LM, Friberg P (2007) Increasing peripheral artery intima thickness from childhood to seniority. Arterioscler Thromb Vasc Biol 27:671–676
17. Mintz GS, Nissen SE, Anderson W, Bailey SR, Erbel R et al (2001) American college of cardiology clinical expert consensus document on standards for acquisition, measurements and reporting intravascular ultrasound studies (IVUS). J Am Coll Cardiol 37:1478–1492
18. Loizou CP, Pattichis CS, Pantziaris M, Nicolaides A, Georgiou N, KyriakouE (2007) Media thickness measurement of the common carotid artery. Proceedings of the 29th annual international conference of the IEEE engineering in medicine and biology society, Cite Int., Lyon, FrP1B6.5, 23–26 Aug 2007
19. Kyriakou E, Pattichis MS, Christodoulou CH, Pattichis CS, Kakkos S, Griffin M, Nicolaides AN (2005) Ultrasound imaging in the analysis of carotid plaque morphology for the assessment of stroke. In: Suri JS, Yuan C, Wilson DL, Laxminarayan S (eds) Plaque imaging: pixel to molecular level, IOS, pp 241–275
20. Tegos TJ, Sabetai MM, Nicolaides AN, Elatrozy TS, Dhanjil S, Stevens JM (2001) Patterns of brain computed tomography infraction and carotid plaque echogenicity. J Vasc Surg 33:334–339
21. Williams DJ, Shah M (1992) A fast algorithm for active contour and curvature estimation. Comput Vis Image Underst 55(1):4–26
22. Chalana V, Kim Y(1997) A methodology for evaluation of boundary detection algorithms on medical images. IEEE Trans Med Imaging 16(5):642–652
23. Bland JM, Altman DG (1986) Statistical methods for assessing agreement between two methods of clinical measurement. Lancet 1(8476):307–310
24. Mojsilovic A, Popovic M, Amodaj N, Babic R, Ostojic M (1997) Automatic segmentation of intravascular ultrasound images: a texture based approach. Ann Biomed Eng 25:1059–1071
25. Loizou CP, Pattichis CS, Pantziaris MS, Tyllis T, Nicolaides AN (2006) Quantitative quality evaluation of ultrasound imaging in the carotid artery. Med Biol Eng Comput 44(5):414–426
26. Loizou CP, Pattichis CS, Pantziaris MS, Nicolaides AN (2007) An integrated system for the segmentation of atherosclerotic carotid plaque. IEEE Trans Inf Technol Biomed 11(5):661–667
27. Nicolaides AN, Kakkos SK, Griffin M, Sabetai M, Dhanjil S, Thomas D et al (2005) Effect of image normalization on carotid plaque classification and the risk of ipsilateral hemispheric events: results from the asymptomatic carotid stenosis and risk of stroke study. Vascular 1(4):211–221
28. Graf S, Gariery J, Massonneau M, Armentano R, Mansour S, Barra J, Simon A, Levenson J (1999) Experimental and clinical validation of arterial diameter waveform and intimal media thickness obtained from B-mode ultrasound image processing Ultrasound Med Biol 25(9):1353–1363
29. Mancini GBJ, Abbott D, Kamimura C, Yeoh E (2004) Validation of a new ultrasound method for the measurement of carotid artery intima medial thickness and plaque dimensions. Can J Cardiol 20(13)1355–1359
30. Christodoulou CI, Pattichis CS, Pantziaris MS, Nicolaides AN (2003) Texture-based classification of atherosclerotic carotid plaques. IEEE Trans Med Imaging 22(7):902–912
31. Belcaro G, Nicolaides AN, Laurora G, Cesarone MR, De Sanctis M, Incandela L, Barsotti A (1996) Ultrasound morphology classification of the arterial wall and cardiovascular events in a 6-year follow-up study. Arterioscl Thromb Vasc Biol 16:851–856
32. Schmidt C, Wendelhag I (1999) How can the variability in ultrasound measurements of intima–media thickness be reduced? Studies of interobserver variability in carotid and femoral arteries. Clinic Physiol 19(1):45–55
33. Ellis SM, Sidhu PS (2000) Granularity of the carotid artery intima–medial layer: reproducibility of quantification by a computer-based program. Br J Radiol 37:595–600

34. Bartolomucci F, Paterni M, Morizzo C, Kozakova M et al (2001) Early structural changes of carotid artery in familial hypercholesterolemia. J Clin Hypertens 14:125A–126A
35. Lind L, Andersson J, Roenn M, Gustavsson T (2007) The echogenecity of the intima–media complex in the common carotid artery is closely related to the echogenecity in plaques. Atherosclerosis 195:411–414
36. (2004) Prevention of disampling and fatal strokes by successful carotid endarterectomy in patients without recent neurological symptoms: randomized control trial, Lancet 363(9420):1491–1502
37. Rosfors S, Hallerstam S, Jensen-Urstad K, Zetterling M, Carlstroem C (1998) Relationship between intima–media thickness in the common carotid artery and atherosclerosis in the carotid bifurcation. Stroke 29:1378–1382
38. Balasundaram JK, Wahida Banu RSD (2006) A non-invasive study of alterations of the carotid artery with age using ultrasound images. Med Biol Eng Comput 44:67–72
39. Haralick RM, Shanmugam K, Dinstein I (1973) Texture features for image classification. IEEE Trans Syst Man Cybern SMC 3:610–621
40. Weszka JS, Dyer CR, Rosenfield A (1976) A comparative study of texture measures for terrain classification. IEEE Trans Syst Man Cybern SMC 6:269–285
41. Amadasun M, King R (1989) Textural features corresponding to textural properties. IEEE Trans Syst Man Cybern 19(5):1264–1274
42. Wu CM, Chen YC, Hsieh K-S (1992) Texture features for classification of ultrasonic images. IEEE Trans Med Imaging 11:141–152
43. Litwin M, Wuehl E, Jourdan C, Trelewicz J, Niemirska A, Fahr K, Jobs K, Grena R, Wawer ZT, Rajszys P, Troeger J, Mehls O, Shaefer F (2005) Altered morphological properties of large arteries in children with chronic renal failure and after and after renal transplantation. J Am Soc Nephrol 16:1494–1500
44. Goncalves I,Lindholm MW, Pedro LM et al (2004) Elastin and calcium rather than collagen or lipid content are associated with echogenecity of human carotid plaques. Stroke 35:795–800

Christos P. Loizou was born in Cyprus in October 1962 and received his BSc degree in Electrical Engineering, the Dipl.-Ing. (MSc) degree in Computer Science and Telecommunications from the University of Kaisserslautern, Kaisserslautern, Germany, and the PhD degree from the Department of Computer Science, Kingston University, London, UK, on ultrasound image analysis of the carotid artery in 1990 and 2005, respectively. He is currently an Assistant Professor with the Department of Computer Science at Intercollege in Cyprus. His research interests include medical imaging, in investigating the risk of stroke and the multiple sclerosis disease.

Marios Pantziaris received the M.D. degree in neurology from the Aristotelion University, Thessaloniki, Greece, in 1995. Currently, he is working with Cyprus Institute of Neurology and Genetics, Nicosia, Cyprus, as a Senior Neurologist in the Neurological Department and is the Head of the Neurovascular Department. He has been trained in Carotid Duplex–Doppler ultrasonography at St. Mary's Hospital, London, in 1995. In 1999, he was a visiting doctor in acute stroke treatment at Massachusetts General Hospital, Harvard University, Boston. He has considerable experience in carotids–transcranial ultrasound, has participated in many research projects, and has several publications to his name. He is also the Head of the Multiple Sclerosis (MS) Clinic where he is running research projects towards the aetiology and therapy of MS.

Constantinos S. Pattichis was born in Cyprus on January 30, 1959, and received his diploma as a technician engineer from the Higher Technical Institute in Cyprus in 1979, BSc in Electrical Engineering from the University of New Brunswick, Canada, in 1983, MSc in Biomedical Engineering from the University of Texas at Austin, USA, in 1984, MSc in Neurology from the University of Newcastle Upon Tyne, UK, in 1991, and PhD in Electronic Engineering from the University of London, UK, in 1992. He is currently Professor with the Department of Computer Science of the University of Cyprus. His research interests include ehealth, medical imaging, biosignal analysis, and intelligent systems.

CAUDLES-EF: Carotid Automated Ultrasound Double Line Extraction System Using Edge Flow

Filippo Molinari, Kristen M. Meiburger, Guang Zeng, Andrew Nicolaides, and Jasjit S. Suri

Abstract The evaluation of the carotid artery wall is essential for the diagnosis of cardiovascular pathologies or for the assessment of a patient's cardiovascular risk.

This chapter presents a complete user-independent algorithm, which automatically extracts the far double line (lumen–intima and media–adventitia) in the carotid artery using an Edge Flow technique based on the directional probability maps using the attributes of intensity and texture. Specifically, the algorithm traces the boundaries between the lumen and intima layer (line one) and between the media and adventitia layer (line two). The Carotid Automated Double Line Extraction System based on Edge Flow (CAUDLES-EF) is characterized and validated by comparing the output of the algorithm with the manual tracing boundaries carried out by three experts. We also benchmark our new technique with the two other completely automatic techniques (CALEXia and CULEXsa) that we had previously published.

Our multi-institutional database consisted of 300 longitudinal B-mode carotid images with normal and pathologic arteries. We compared our current new method

F. Molinari (✉) • K.M. Meiburger
Biolab, Department of Electronics, Politecnico di Torino, Corso Duca degli Abruzzi, 24, 10129 Torino, Italy
e-mail: filippo.molinari@polito.it; kristen.meiburger@polito.it

G. Zeng
MBF Bioscience Inc. Williston, VT, USA
e-mail: gzeng@clemson.edu

A. Nicolaides
Vascular Screening and Diagnostic Centre, London, UK

Department of Biological Sciences, University of Cyprus, Nicosia, Cyprus
e-mail: anicolaides1@gmail.com

J.S. Suri
Biomedical Technologies, Inc., Denver, CO, USA

Idaho State University (Affiliated), Pocatello, ID, USA
e-mail: jsuri@comcast.net

J.M. Sanches et al. (eds.), *Ultrasound Imaging: Advances and Applications*,
DOI 10.1007/978-1-4614-1180-2_6,

with previous methods, and showed the mean and standard deviation for the three methods: CALEXia, CULEXsa, and CAUDLES-EF as: 0.134 ± 0.088mm, 0.74 ± 0.092 mm and 0.043 ± 0.097 mm, respectively. Our IMT was slightly underestimated with respect to the ground truth of the IMT, but showed a uniform behavior over the entire database. As in view of regards the Figure of Merit (FoM) for CALEXia and CULEXsa showed the values of 84.7%, and 91.5%, respectively, while our new approach, CAUDLES-EF performed the best at 94.8%, showing a good improvement compared to previous methods.

Keywords Carotid artery • Ultrasound • Multi-resolution • Edge Flow • Localization • Intima–media thickness • Hausdorff distance • Polyline distance

1 Background

Numerous studies from around the world have demonstrated that there is a strong correlation between the risk of cerebrovascular diseases and the characteristics of the carotid artery wall [1–3]. Ultrasound examination is a widely used diagnostic tool for assessing and monitoring the plaque build up via the carotid window. Ultrasounds offer several advantages in clinical practice:

1. They only propagate mechanical (i.e., non-ionizing) radiation.
2. No short-term or long-term adverse biological effects have been demonstrated in the power and intensity range commonly used in clinical scans.
3. The examination is quick and safe.
4. The ultrasound equipment is one among the more inexpensive equipment when compared to other imaging devices.

However, ultrasound examinations are operator-dependent and the ultrasound images can tend to be quite noisy and require training for correct interpretation.

The intima–media thickness (IMT) is the most used and validated marker of progression of carotid artery diseases [4, 5] and can be measured using image processing strategies and ad-hoc computer techniques. The goal is to first segment the carotid artery distal wall, so as to then find the lumen–intima (LI) and media–adventitia (MA) boundaries. The distance calculated between these two interfaces is taken as an estimate of the IMT.

The segmentation process can conceptually consist of two cascading stages:

- Stage I: recognition of the carotid artery (CA) and delineation of the far adventitia layer (AD_F) in the two-dimensional B-mode ultrasound image.
- Stage II: tracing of the LI/MA wall boundaries in the ROI of the recognized CA.

In Stage I, the carotid artery must be correctly located within the ultrasound image frame. This stage is generally performed better by human experts, who can mark the position of the CA by either tracing rectangular regions-of-interest (ROI) or by placing the markers. In Stage II, the guidance zone is created in which the LI and MA border are estimated. The IMT can be subsequently measured once the LI and MA borders are determined during the segmentation process. These two stages

cannot be independent from each other. In fact, Stage I is of fundamental importance since the AD_F profile is found and used as a starting point for Stage II, which is also automated. The performance of Stage I will directly affect the initialization of Stage II, and also affect the final results. This fact emphasizes the importance of the need of an accurate yet versatile technique to perform Stage I.

In order to achieve complete automation, both of these stages must be designed to be independent of the user. To do so, first of all appropriate detection strategies are required to automatically locate the carotid artery in the image. These strategies must be robust with respect to noise and must be able to process carotids with different geometrical appearance.

The majority of the algorithms proposed in the literature for the automated segmentation of the CA in ultrasound images require a certain degree of user-interaction, which precludes real complete automation. Any user-interaction that slows down the analysis process would introduce a dependence on the operator if gain settings are not optimal, bringing subjectivity into the process. Complete automation, instead, can be an asset for multi-center large studies since it enables the processing of large image databases.

This chapter presents a complete user-independent Carotid Automated Double Line Extraction System using Edge Flow (CAUDLES-EF) algorithm, which performs both Stages I and II. Starting from the ultrasound image, the algorithm first segments the distal border of the CA and then performs the automatic detection of the LI and MA interfaces. Neither of these processes requires any user-interaction. The first part of our new algorithm is based on scale-space multi-resolution analysis while the second part is based on flow field propagation. CAUDLES-EF was specifically designed for the IMT measurement of the far (distal) wall of the common carotid artery. We also show the characterization of this algorithm in terms of automatic versus human traced segmentation, and we also benchmarked the results with two other completely automatic techniques that we had previously developed [6–10]. Our image database consisted of 300 images coming from two different institutions consisting of both normal and pathological arteries. Two different technicians acquired the images, using two different ultrasound scanners. We used the Hausdorff distance as a performance metric for Stage I and we measured the distance between the computed far adventitial wall and the LI/MA profiles that were manually traced by experts, the so-called ground truth. For assessing the performance of Stage II, we used the Polyline distance and calculated the error between the IMT estimated using our algorithm and ground truth IMT.

2 Materials and Methods

2.1 Image Database and Preprocessing Steps

We tested an image database consisting of 300 images coming from two different Institutions. Two hundred images were acquired using an ATL HDI 5000 ultrasound

scanner equipped by a 10–12 MHz probe at the Neurology Division of Gradenigo Hospital (Torino, Italy), from one hundred and fifty asymptomatic patients who referred to the Neurology Division for carotid assessment (age: 69 ± 16 years old; range: 50–83 years old). Ninety-three subjects were male. Of these subjects, 80 had hypertension history, 40 had hypercholesterolemia, and 30 had both. Ten patients were diabetic. Resampling was set to 16 pixels/mm, leading to an axial resolution equal to 62.5 μm/pixel. The remaining one hundred images were acquired at The Cyprus Institute of Neurology and Genetics (Nicosia, Cyprus) from asymptomatic individuals (age: 54 ± 24; range: 25–95 years) using a Philips ATL HDI 3000 ultrasound scanner equipped with a linear 7–10 MHz probe. These images were resampled at a density of 16.67 pixels/mm, therefore obtaining an axial spatial resolution equal to 60 μm/pixel. Both of the Institutions made sure to obtain written informed consent from the patients prior to enrolling them in the study and also got approval by the respective IRBs. Both the experimental protocol and the data acquisition procedure were approved by the respective local Ethical Committees. Three different expert sonographers (a cardiologist, a vascular surgeon, and a neurologist – all with more than 20 years of experience in their field) independently manually segmented the images by tracing the boundaries of the lumen–intima (LI) and media–adventitia (MA) interfaces, and the average tracings were considered as ground truth (GT).

In order to discard the surrounding black frame containing device headers and image/patient test data, the raw ultrasound image is automatically cropped in one of two ways. The first method is for DICOM images with fully formatted DICOM tags: we used the data contained in the specific field named `SequenceOfUltrasoundRegions`, which contains four subfields that mark the location of the image which contains the ultrasound representation. These fields are named `RegionLocation` (with their specific labels being: $x_{\min}$, $x_{\max}$, $y_{\min}$, and $y_{\max}$) and they mark the horizontal and vertical extensions of the image. The raw B-Mode DICOM image is then cropped in order to extract only the portion which contains the carotid morphology. If, however, the image was not in a DICOM format or if the DICOM tags were not fully formatted, the second method was applied: adopting a gradient-based procedure, we computed the horizontal and vertical Sobel gradients of the image. When computed outside of the region of the image containing the ultrasound data, gradients are equal to zero. Hence, the beginning of the image region containing the ultrasound data can be found as the first row/column with a gradient different from zero. Similarly, the last non-zero row/column of the gradient marks the end of the ultrasound region.

2.2 Architecture of CAUDLES-EF

2.2.1 Stage I: Far Adventitia Estimation

Since the CAUDLES-EF algorithm was developed to help in reducing the human operator dependence and therefore be totally user-independent, the first stage of

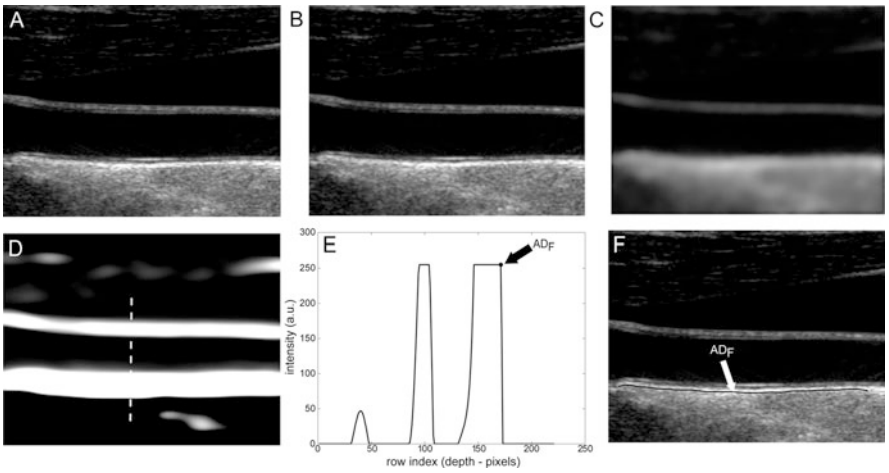

Fig. 1 CAUDLES-EF procedure for AD_F tracing. **(A)** Original cropped image. **(B)** Downsampled image. **(C)** Despeckled image. **(D)** Image after convolution with first-order Gaussian derivative ($\sigma = 8$). **(E)** Intensity profile of the column indicated by the vertical dashed line in panel D. (AD_F indicates the position of the far adventitia wall). **(F)** Cropped image with far adventitia profile overlaid

the algorithm is the completely automatic recognition of the CA. This is done through a novel and low-complexity procedure, which detects the far adventitia border using a method based on scale-space multi-resolution analysis. Starting from the automatically cropped image (Fig. 1a), the automated Stage I is divided into different steps which is described in detail here:

- *Step 1*: *Fine to Coarse Down-sampling*. The image is first down-sampled by a factor of two (i.e., the number of rows and columns of the image is halved) (Fig. 1b) and implementing the down-sampling method as discussed by Ye et al. [11] by adopting a bi-cubic interpolation. This method was tested on ultrasound images and showed a good accuracy and a low computational cost [11].
- *Step 2*: *Speckle reduction*. Speckle noise is attenuated using a first-order local statistics filter (called *lsmv* by the authors [12, 13]), which has given the best performance in the specific case of carotid imaging. This filter is defined by the following equation:

$$J_{x,y} = \bar{I} + k_{x,y}\left(I_{x,y} - \bar{I}\right) \tag{1}$$

where $I_{x,y}$ is the intensity of the noisy pixel, $\bar{I}$ is the mean intensity of a $N \times M$ pixel neighborhood, and $k_{x,y}$ is a local statistic measure. The noise-free central pixel in the moving window is indicated by $J_{x,y}$. Louizou et al. [12, 13] mathematically $k_{x,y} = \frac{\sigma_I^2}{\bar{I}^2\sigma_I^2 + \sigma_n^2}$, where σ_I^2 represents the variance of the pixels in the neighborhood, and σ_n^2 the variance of the noise in the cropped image. An optimal neighborhood size was demonstrated to be 7×7. Figure 1c shows the despeckled image.

- *Step 3*: *Higher order Gaussian derivative filter.* The despeckled image is then filtered using a 35×35 pixels first-order derivative of a Gaussian kernel. The scale parameter of the Gaussian derivative kernel is taken equal to 8 pixels. This value is chosen because it is equal to half the expected dimension of the IMT value in an original fine resolution image, since an average IMT value equal to 1 mm corresponds roughly to about 16 pixels in the original image scale and therefore 8 pixels in the down-sampled image. The white horizontal stripes in Fig. 1d show the proximal (near) and distal (far) adventitia layers.
- *Step 4*: *Automated Far Adventitia (AD_F) tracing.* Figure 1e shows the intensity profile of one column (from the upper edge of the image to the lower edge of the image) of the Gaussian filtered image. The proximal (near) and distal (far) walls are clearly identifiable as intensity maxima saturated to the maximum value of 255. A heuristic search is then applied to the intensity profile of each column to automatically trace the profile of the distal (far) wall. The image convention uses (0, 0) as the top left-hand corner of the image, and so this search is done starting from the bottom of the image (i.e., from the pixel with the highest row index) and searching for the first white region consisting of at least 6 pixels (computed empirically). The deepest point of this region (i.e., the pixel with the highest row index) marks the position of the far adventitia AD_F layer on that column. The overall automated AD_F tracing is found as the sequence of points resulting from the heuristic search for all of the image columns.
- *Step 5*: *Up-sampling of the far adventitia (AD_F) boundary locator.* The AD_F profile that is found is then subsequently up-sampled to the original fine scale and superimposed over the original cropped image (Fig. 1f) for both visualization and performance evaluation.

This Stage I consists essentially of an architecture based on fine-to-coarse sampling for vessel wall scale reduction, speckle noise removal, higher-order Gaussian convolution, and automated recognition of the far adventitia border. This multi-resolution method prepares the vessel wall's edge boundary so that the thickness of the vessel wall is roughly equivalent to the scale of the Gaussian kernels. This allows an optimal detection of the CA walls since when the kernel is located close to a near gray level change, it enhances the transition. Consequently, the most echoic image interfaces are enhanced to white in the filtered image. This fact is clearly shown in Fig. 1d, e, is what allows this procedure to detect the far adventitia layer.

2.2.2 Stage II: Double Line (LI/MA) Border Estimation

The whole idea of double line extraction for IMT measurement in stage II is to first extract the strong LI/MA edges which lie between lumen region and AD_F border. There are two kind of strong edges: LI strong edges and MA strong edges. The search for the double line (LI/MA borders) strong edges is performed in the grayscale guidance zone. This grayscale guidance zone is computed empirically from the knowledge database. The strong edge estimation in this guidance zone

is implemented using our Edge Flow algorithm. Since the intensity of the strong edge is not uniform, hence some edges are weak along the carotid arterial wall. The weak edges in the guidance zone are estimated using a labeling process, which then joins the strong edges. The strong and the weak edges are then combined to form the raw LI/MA borders or double lines. These extracted double lines are finally smoothed using spike reduction method leading to smooth LI/MA borders. Thus the layout of this section is as follows. The guidance zone estimation is presented under the section "Guidance Zone Mask Estimation." Edge Flow algorithm is presented under the section "Stage II (A): Edge Flow Magnitude and Edge Flow Direction." Sub-section 2.2.3 presents the weak MA border estimation while sub-section 2.2.4 presents the weak LI border estimation.

Guidance Zone Mask Estimation

Stage II consists of automatic extraction of a Guidance Zone Mask, which is estimated from AD_F profile by extending it towards the upper edge of the image by Δ_{ROI}. We set the Δ_{ROI} value equal to 50 pixels. The choice of this mask height was obtained after empirically computing the distances from AD_F profile w.r.t. ground truth LI/MA borders. The original image is then cropped with the smallest rectangle possible that includes the entire Guidance Zone Mask. Consequently, the Edge Flow algorithm is run on the cropped grayscale guidance mask image to obtain the initial edges.

Stage II (A): Edge Flow Magnitude and Edge Flow Direction

The Edge Flow algorithm, originally proposed by Ma and Manjunath [14], facilitates the integration of different image attributes into a single framework for boundary detection and is based on the construction of an Edge Flow vector $F(s,\theta)$ defined as:

$$F(s,\theta) = F\left[E(s,\theta), P(s,\theta), P(s,\theta+\pi)\right], \tag{2}$$

where:

- $E(s,\theta)$ is the edge energy at location s along the orientation θ.
- $P(s,\theta)$ represents the probability of finding the image edge boundary if the corresponding Edge Flow "flows" in the direction θ.
- $P(s,\theta+\pi)$ represents the probability of finding the image edge boundary if the Edge Flow "flows" backwards, i.e., in the direction $\theta+\pi$.

The final single Edge Flow vector can be thought of as the combination of Edge Flows obtained from different types of image attributes. Since ultrasound image near the walls have higher intensities and texture like distribution, the image attributes we choose were: intensity and texture. In order to calculate the edge energy $E(s,\theta)$ and the probabilities of forward and backward Edge Flow direction, a few definitions must first be clarified, specifically the first derivative of Gaussian (GD) and the

Table 1 List of the parameters used in the Edge Flow algorithm and refinement functions

Parameter	Value	Description
Δ_{ROI}	50 pixels	Vertical size of the Guidance Zone Mask (page 8)
σ	5 pixels	Sigma value of the Gaussian kernels used by Edge Flow (3)
ϕ	0.1	Area ratio in MA border detection (18)
φ	7 pixels	Threshold for detecting connectable edge objects (20)
IM_{ratio}	0.4	Threshold value used for LI segmentation (23)
λ	5 pixels	Threshold value for determining if an edge object can be classified as belonging to the LI segment (24). This is the average distance of and edge object from the MA boundary

difference of offset Gaussian (DOOG). Considering the Gaussian kernel $G_\sigma(x,y)$, where σ represents the standard deviation, the first derivative of the Gaussian along the x-axis is given by:

$$GD_\sigma(x,y) = -\left(\frac{x}{\sigma^2}\right) G_\sigma(x,y) \tag{3}$$

and the difference of offset Gaussian (DOOG) along the x-axis is defined as:

$$DOOG_\sigma(x,y) = G_\sigma(x,y) - G_\sigma(x+d,y), \tag{4}$$

where d is the offset between centers of two Gaussian kernels and is chosen proportional to σ. This parameter is significant in the calculation of the probabilities of forward and backward Edge Flow, as it is used to estimate the probability of finding the nearest boundary edge in each of these directions. This is the only parameter that is required for running the Edge Flow algorithm. As suggested in previous studies from [14], we selected a σ equal to 2 pixels. Higher values would cause the deletion of any image boundary smaller than σ itself, therefore precluding the recognition of thin boundaries. We found that 2 pixels is an optimal value for the detection of LI/MA borders in ultrasound carotid images. Table 1 reports the list of parameters we used in this algorithm.

By rotating these two functions, we can generate a family of previous functions along different orientations θ and they can be denoted as $G_{\sigma,\theta}(x,y)$ and $DOOG_{\sigma,\theta}(x,y)$, respectively:

$$GD_{\sigma,\theta}(x,y) = GD_\sigma(x',y'), \tag{5}$$

$$DOOG_{\sigma,\theta}(x,y) = DOOG_\sigma(x',y'), \tag{6}$$

where: $x' = x\cos\theta + y\sin\theta$, and $y' = -x\sin\theta + y\cos\theta$.

Intensity Edge Flow

Considering the original image $I(x,y)$ at a certain scale σ, $I_\sigma(x,y)$ is obtained by smoothing the original image with a Gaussian kernel $G_\sigma(x,y)$. The Edge Flow

energy $E(s,\theta)$ at scale σ, defined to be the magnitude of the gradient of the smoothed image $I_\sigma(x,y)$ along the orientation θ, can be computed as:

$$E(s,\theta) = |I_\sigma(x,y) \times \mathrm{GD}_{\sigma,\theta}(x,y)|, \tag{7}$$

where s is the location. This energy indicates the strength of the intensity changes. The scale parameter is very important in that as it controls both the edge energy computation and the local flow direction estimation so that only edges larger than the specified scale are detected.

To compute $P(s,\theta)$, two possible flow directions (θ and $\theta+\pi$) are considered for each of the edge energies along the orientation θ at location s. The prediction error towards the surrounding neighbors in these two directions can be computed as:

$$\mathrm{Error}(s,\theta) = |I_\sigma(x+d\cos\theta, y+d\sin\theta) - I_\sigma(x,y)| = |I(x,y) \times \mathrm{DOOG}_{\sigma,\theta}(x,y)|, \tag{8}$$

where d is the distance of the prediction and it should be proportional to the scale at which the image is being analyzed. The probabilities of Edge Flow direction are then assigned in proportion to their corresponding prediction errors, due to the fact that a large prediction error in a certain direction implies a higher probability of locating a boundary edge in that direction:

$$P(s,\theta) = \frac{\mathrm{Error}(s,\theta)}{\mathrm{Error}(s,\theta) + \mathrm{Error}(s,\theta+\pi)}. \tag{9}$$

Texture Edge Flow

Texture features are extracted from the image based on Gabor decomposition. This is done basically by decomposing the image into multiple oriented spatial frequency channels, and then the channel envelopes (amplitude and phase) are used to form the feature maps.

Given the scale σ, two center frequencies of the Gabor filters (the lowest and the highest) are defined. The range of these center frequencies generates an appropriate number of Gabor filters $g_i(x,y)$. The complex Gabor filtered images are defined as:

$$O_i(x,y) = I \times g_i(x,y) = m_i(x,y)\exp[\Phi_i(x,y)], \tag{10}$$

where $1 \le i \le N$, N is the total number of filters and i is the sub band, $m_i(x,y)$ is the magnitude, and $\Phi_i(x,y)$ is the phase. A texture feature vector $\Psi(x,y)$ can then be formed by taking the amplitude of the filtered output across different filters at the same location (x,y):

$$\Psi(x,y) = [m_1(x,y), m_2(x,y), \ldots, m_N(x,y)]. \tag{11}$$

The change in local texture information can be found using the texture features, thus defining the texture edge energy:

$$E(s,\theta) = \sum_{1 \le i \le N} |m_i(x,y) \times GD_{\sigma,\theta}(x,y)| \cdot w_i, \tag{12}$$

where $w_i = \frac{1}{||\alpha_i||}$ and $||\alpha_i||$ is the total energy of the sub band i.

The direction of the texture Edge Flow can be estimated similarly to the intensity Edge Flow, using the prediction error:

$$\text{Error}(s,\theta) = \sum_{1 \le i \le N} \left| m_i(x,y) \times \text{DOOG}_{\sigma,\theta}(x,y) \right| \cdot w_i \tag{13}$$

and the probabilities $P(s,\theta)$ of the flow direction can be estimated using the same method as was used for the intensity Edge Flow.

Texture and Intensity Edge Flow Integration

For general-purpose boundary detection, the Edge Flows obtained from the two different types of image attributes can be combined:

$$E(s,\theta) = \sum_{a \in A} E_a(s,\theta) \cdot w(a), \quad \sum_{a \in A} w(a) = 1, \tag{14}$$

$$P(s,\theta) = \sum_{a \in A} P_a(s,\theta) \cdot w(a), \tag{15}$$

where $E_a(s,\theta)$ and $P_a(s,\theta)$ represent the energy and the probability of the Edge Flow computed from the image attributes a (in our case, *intensity* and *texture*). $w(a)$ is the weighting coefficient among various types of image attributes. For searching the nearest boundary, we identify the best direction. We therefore consider the Edge Flows $\{F(s,\theta)|_{0 \le \theta \le \pi}\}$ and identify a continuous range of flow directions that maximizes the sum of probabilities in that half plane:

$$\Theta(s) = \arg\max_{\theta} \left\{ \sum_{\theta \le \theta' \le \theta + \pi} P\left(s,\theta'\right) \right\}. \tag{16}$$

The vector sum of the Edge Flows with their directions in the identified range is what defines the final resulting Edge Flow and is given by:

$$\overrightarrow{F}(s) = \sum_{\Theta(s) \le \theta \le \Theta(s) + \pi} E(s,\theta) \cdot \exp(j\theta), \tag{17}$$

where $\overrightarrow{F}(s)$ is a complex number whose magnitude represents the resulting edge energy and whose angle represents the flow direction.

Flow Propagation and Boundary Detection

Once the Edge Flow $\overrightarrow{F}(s)$ of an image is computed, boundary detection can be performed by iteratively propagating the Edge Flow and identifying the locations where two opposite direction of flows encounter each other. The local Edge Flow is then transmitted to its neighbor in the direction of flow if the neighbor also has a similar flow direction. The steps which describe this iterative process are as follows:

STEP 1:	***Set*** $n = 0$ ***and*** $\overrightarrow{F}_0(s) = \overrightarrow{F}(s)$
STEP 2:	***Set the initial Edge Flow*** $\overrightarrow{F}_{n+1}(s)$ ***at time*** $n+1$ ***to zero***
STEP 3:	***At each image location*** $s = (x, y)$, ***identify the neighbor*** $s' = (x', y')$ ***which isin the direction of Edge Flow*** $\overrightarrow{F}_n(s)$
STEP 4:	***Propagate the Edge Flow if*** $\overrightarrow{F}_n(s') \cdot \overrightarrow{F}(s) > 0$ $\overrightarrow{F}_{n+1}(s') = \overrightarrow{F}_{n+1}(s') + \overrightarrow{F}_n(s)$ ***Otherwise***, $\overrightarrow{F}_{n+1}(s) = \overrightarrow{F}_{n+1}(s) + \overrightarrow{F}_n(s)$
STEP 5:	***If nothing has been changed, stop the iteration***. ***Otherwise***, ***set*** $n = n+1$ ***and go to Step*** 2.

The image boundaries can then be detected once the Edge Flow propagation reaches a stable set by identifying the locations which have a nonzero Edge Flow coming from two opposite directions. For all of the images, we consider eight different orientations, starting from 0° and going to 315° with equal degree of intervals in between. Figure 2a shows the total energy of the Edge Flow $E(s, \theta)$ obtained for the various orientations, while Fig. 2b shows the total probabilities of the Edge Flow $P(s, \theta)$.

Once the image boundaries are detected, the final image is generated by performing region closing (i.e., morphological closing operation). This operation helps in limiting the number of disjoint boundaries. The basic idea is to search for the nearest boundary element within the specified search neighborhood at the unconnected ends of the contour. If a boundary element is found, a smooth boundary segment is generated to connect the open contour to another boundary element. The neighborhood search size is taken to be proportional to the length of the contour itself.

This approach of edge detection has the following characteristic features: (a) the usage of a predictive coding model for identifying and integrating the different types of image boundaries; (b) the use of flow field propagation for boundary detection; and (c) the need for a single parameter controlling the whole segmentation process.

Figure 3a shows an example of an output image from the Edge Flow algorithm while Fig. 3b shows this output binary image overlaid on the original image in white, once it is converted back to the original image size.

As Fig. 3b clearly shows, the Edge Flow algorithm over-segments in many different points, due partly, to the fact that the image was cropped to contain

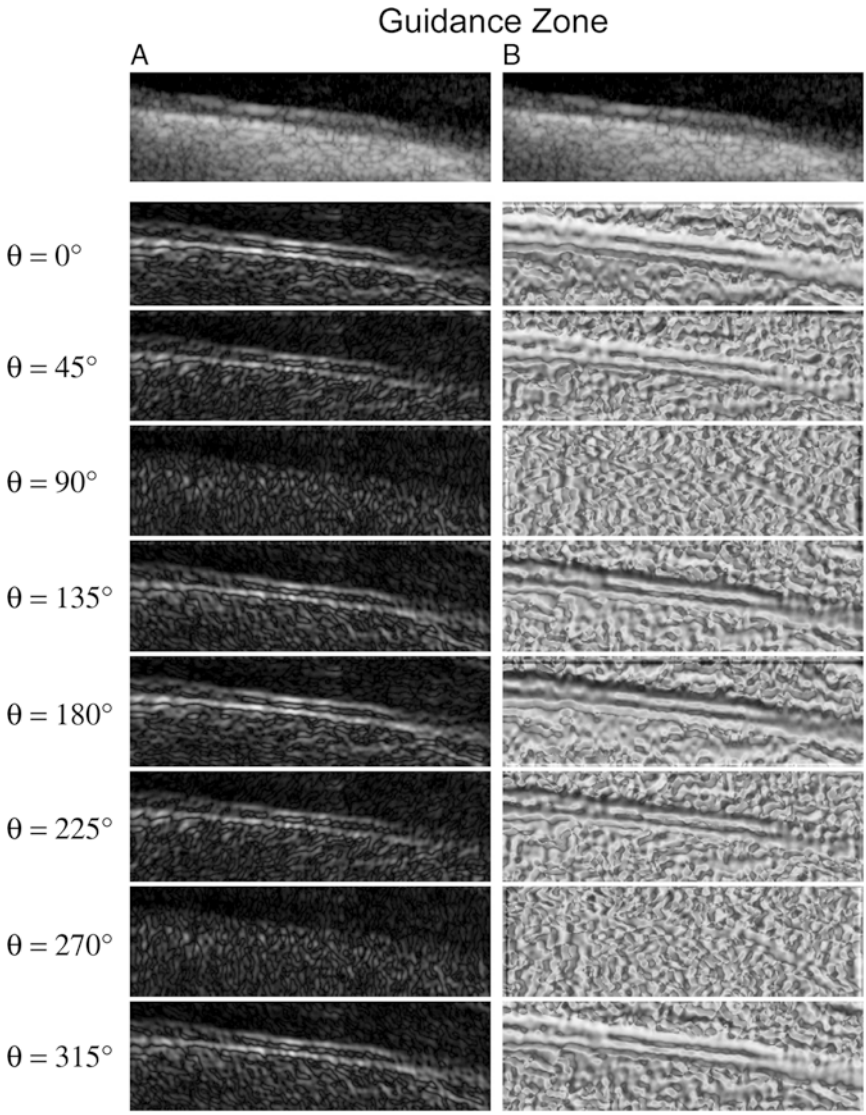

Fig. 2 Example of the total Edge Flow computed in eight orientations. **(A)** Total Edge Flow energy. (**B**) Total Edge Flow probability. On top of the columns, the grayscale Guidance Zone is showed

the entire Guidance Zone Mask and therefore may contain sections of the image that are found below the AD_F profile. This problem could be even more serious in the presence of a curved or inclined artery, because more tissue structures below the AD_F would be enclosed into theGuidance Zone. Figure 3b also shows

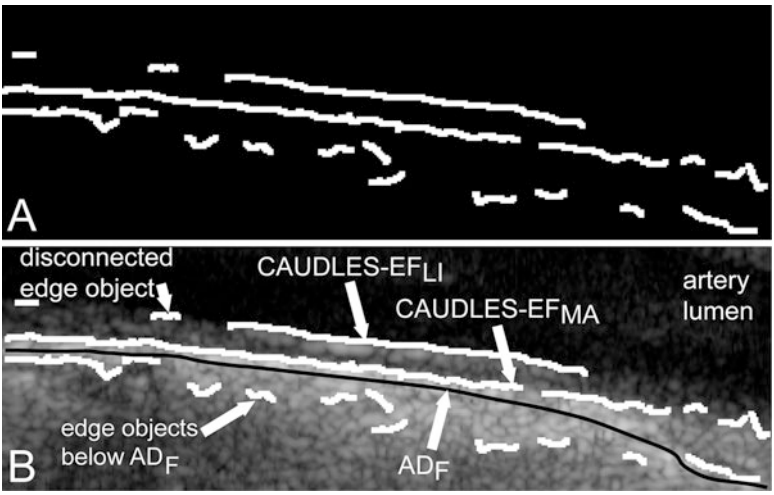

Fig. 3 (**a**) Binary edge output from the Edge Flow algorithm. **(b)** Superposition of the binary edges on the corresponding grayscale carotid region of interest image

a disconnected edge object. Also, while part of the MA and LI edge estimation may be done using the Edge Flow algorithm, yet the segmentation cannot be considered complete as there are still some missing weak MA and weak LI edges and the edges found must be classified as either belonging to the MA profile or the LI profile. This refinement and classification process is done using a strong dependency on the edges found by the Edge Flow algorithm and via labeling and connectivity, which will be explained further in detail in the next two sections.

2.2.3 Stage II (b): Weak MA or Missing MA Edge Estimation Using Strong MA Edge Dependency via Labeling/Connectivity and Complete MA Estimation

Before we discuss the challenges, we first define the concept of an edge object. It is defined as a connected component in the binary image.

As said in the previous sub-section, Edge Flow causes discontinuities in the edge objects. Three types of problem are connected to discontinuity edges: the first is the presence of edge objects that are not overlaid on the correct interface (i.e., edge objects located below the far carotid wall and, thence, the AD_F profile), the second is the presence of many small segments, and the third is the breaking of the LI/MA profile into disconnected edge objects. For the sake of clarity, we will call as *incorrect edge objects* the edge objects that were traced below the AD_F profile; *small edge objects* those who are very short when compared to the length of the image, and *disconnected edge objects* those which are possibly be a part of the correct MA

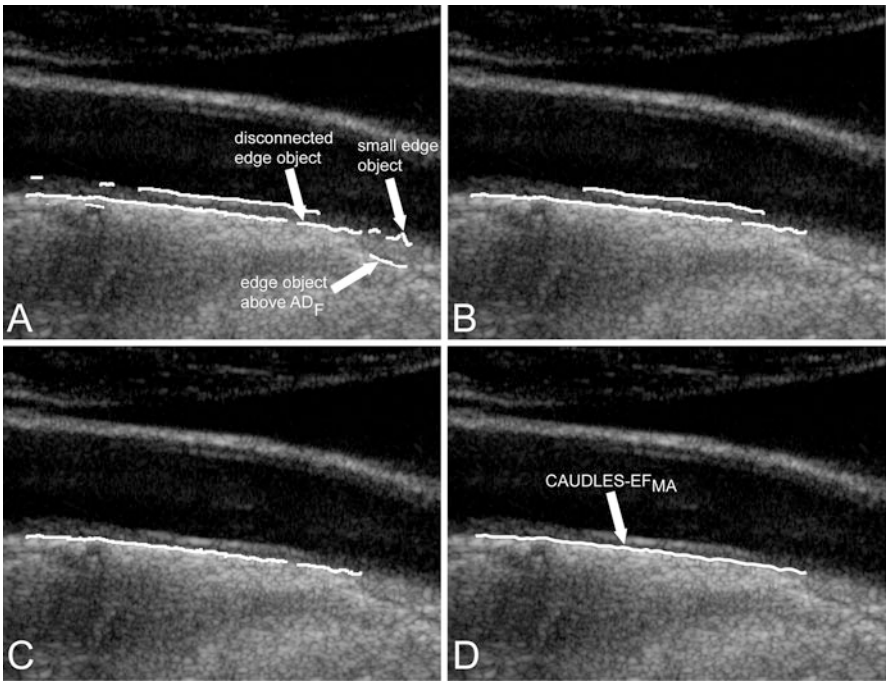

Fig. 4 Steps showing the refinement of weak MA or missing MA edges: **(a)** Results of the Edge Flow segmentation showing edge objects located below the AD_F, isolated small edge object, and disconnected edge objects. **(b)** Removal of edge objects that are below the AD_F and isolated edge object. **(c)** Edge objects that are classified as being part of the MA segment overlaid on the original grayscale image. **(d)** Final MA profile on the original image

profile, but which are disconnected from it. Therefore, overall our system handles these three main challenges:

(a) removing the incorrect edge objects outside the region of interest
(b) removing the small edge objects in the region of interest
(c) connecting disconnected edge objects

The solution to challenge (a) is simply the deletion of all the edge objects in the output image that are not included in the Guidance Zone. Figure 4a shows the effect of the deletion of the incorrect edge objects from the initial segmentation as shown in Fig. 3b.

The solution to challenge (b) requires the definition of a small edge object. Small edge objects around the ROI are defined as those that have an area ratio below a limit ϕ when compared to the totality of the edge objects of the image. The area ratio is defined by the following equation:

$$\text{Area Ratio} = \frac{\text{Area}_{\text{Edge Object}}}{\text{Area}_{\text{All Edge Object}}} \leq \phi \Rightarrow \text{Small Edge Object.} \tag{18}$$

Our experimental data showed that $\phi = 0.1$ is an optimal value to guarantee the rejection of the small edge objects. Such small edge objects are discarded and therefore removed from the image; an example is shown in Fig. 4b.

The solution to challenge (c) is based on the identification of those disconnected edge objects, which can be linked to form the final MA edge object. The MA segment is first initialized as being the edge object with the highest pixel row index (i.e., the lowest edge object in the image) and its right top (RT) and left top (LT) end points are called as $\mathrm{RT_{MA}}$ and $\mathrm{LT_{MA}}$, respectively. These end points are characterized by the two coordinates, so that, for example, $\mathrm{RT_{MA}}(x)$ refers to the column index of the edge point $\mathrm{RT_{MA}}$ and $\mathrm{RT_{MA}}(y)$ to its row index. The remaining (disconnected) edge objects are then sorted by their mean pixel row index value so as to examine the edge objects starting from those, which are lowest in the image and working upwards. The edge objects are then classified by following these steps:

1. Find the unconnected end points of the i-th edge object as the right top and left top pixels of the examined edge object (RT_i and LT_i, respectively).
2. Determine the correct unconnected end point pair (either $\mathrm{LT_{MA}}$ and RT_i or LT_i and $\mathrm{RT_{MA}}$) as the pair which yields a lesser column difference in absolute value. Hence, we check the following condition:

$$|\mathrm{LT}_i(x) - \mathrm{RT_{MA}}(x)| < |\mathrm{LT_{MA}}(x) - \mathrm{RT}_i(x)| \tag{19}$$

   and if it is true, then the edge points to be connected are LT_i and $\mathrm{RT_{MA}}$ (i.e., the edge object is located on the right of the MA edge object), otherwise the connectable edge points are $\mathrm{LT_{MA}}$ and RT_i (i.e., the edge object is located to the left of the MA edge object). From now on, let's call the unconnected edge points as LT and RT.
3. Calculate the respective row distance in absolute value ($|\mathrm{LT}(y) - \mathrm{RT}(y)|$) and column distance ($\mathrm{LT}(x) - \mathrm{RT}(x)$) between the correct unconnected end points. The examined (disconnected) edge object can be classified as being a part of the MA segment if:

$$|\mathrm{LT}(y) - \mathrm{RT}(y)| \leq \varphi, \tag{20}$$

$$\mathrm{LT}(x) - \mathrm{RT}(x) > 0, \tag{21}$$

   where φ is the maximum acceptable row distance. The condition (21) on the column distance is needed to ensure that the edge object considered does not overlap the already existing MA segment, while the condition (20) on the row distance is necessary so as to avoid including edges that are too far above the existing MA edge object.

   Pilot studies were performed on our image dataset and it showed that $\varphi = 7$ is a suitable threshold for detecting connectability between MA and disconnected edge objects. In fact, 7 pixels are approximately corresponding to 0.45 mm, which is half of the value of the IMT. With this φ value we can link disconnected

edge objects even if they are not perfectly aligned with the MA edge object, and this ensures the possibility of correctly linking disconnected edge objects in presence of curved vessels or of arteries that are not horizontally placed in the image. Lower values of φ would cause the deletion of a large amount of disconnected edge objects, resulting in a reduced and incomplete MA edge object, whereas higher values would allow the linking of disconnected edge objects too far from MA and, therefore, possibly incorrect.

4. Repeat steps 1–3 until all edge objects have been examined. Figure 4c shows the edge objects that were classified as being part of the MA segment overlaid in white on the original image. Once all of the weak edge objects have been examined, those which are classified as being part of the MA segment are then connected together and B-spline is fitted to produce the final MA profile (Fig. 4d).

This post-processing and refinement algorithm has the advantage of linking disconnected edge objects and removing small edge objects on the basis of thresholds that are relative (i.e., like ϕ in (18)) or linked to the calibration factor of the image (i.e., like φ in (20)). The threshold value of φ should therefore be adjusted if the calibration factor is very different from the value of 0.06–0.0625 mm/pixel as we have in our images. Table 1 summarizes the parameters we used in our procedure, whereas we clarify the rationale for their selection in the discussion section.

2.2.4 Stage II (c): Weak LI and LI Missing Edge Estimation Using Strong LI Edge and MA Borders

The post-processing of the LI edge is more complicated with respect to that of MA. Beside the problem of discontinuous edges (i.e., of the LI profile broken into disconnected edge objects), there is the problem of false edge objects located in the vessel lumen (i.e., above LI) and in the media layer (i.e., in between MA and LI).

We developed a technique for the LI missing edge estimation that is completely dependent on the MA profile (determined in Stage II (b)). In fact, the guidance zone is created starting from the MA profile and extending it upwards 50 pixels (Fig. 5a). This is used so as to find solely the edge objects above the MA profile and that have at least some common support with it (Fig. 5b). The common support between two profiles was defined as the range of column coordinates that was common to both the profiles. The remaining i edge objects are processed by this sequence of following steps:

1. Find the common support between the MA profile and the i-th edge object and cut the MA profile to the common support (call it – MAcut_i).
2. Create a mask starting from [MAcut_i and extending it upwards 10 pixels and calculate the mean (call it Image Mask mean – $\mathrm{IM}_{\mathrm{mean}}$) and standard deviation (call it Image Mask standard deviation – $\mathrm{IM}_{\mathrm{std}}$) of the pixel values found in the mask (Fig. 5c). We chose a value of 10 pixels in order to include, in this mask,

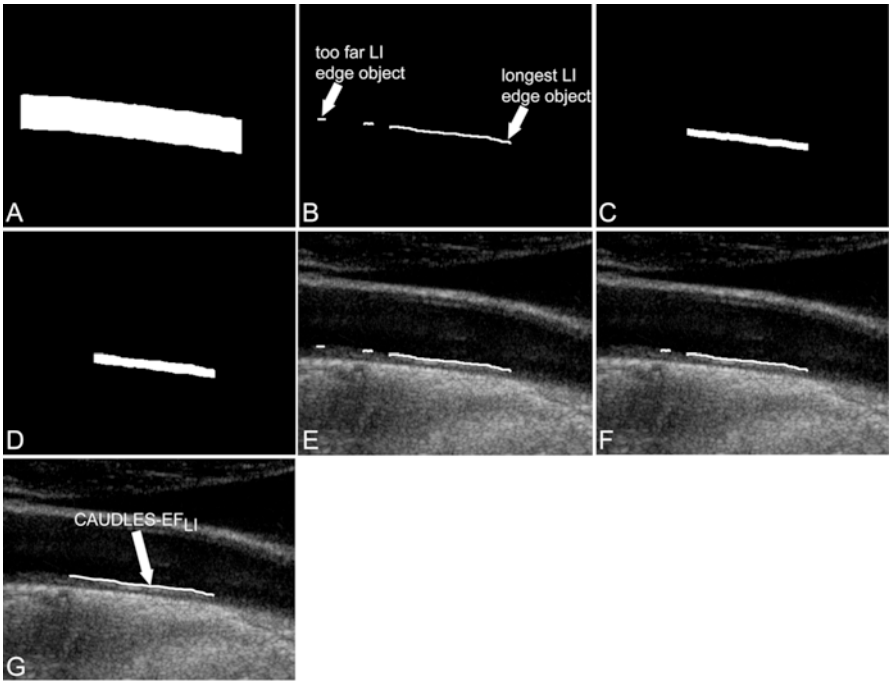

Fig. 5 Process of weak LI edge or missing LI edge estimation: **(a)** Guidance zone obtained using the MA profile and extending it upwards. **(b)** Objects which are above the MA profile and have a common support with it. **(c)** Example of a mask obtained for one edge object starting from the cut MA profile and extending it upwards 10 pixels. **(d)** Example of a mask obtained for one edge object starting from the cut MA profile and extending it up to the examined edge object. **(e)** Edge objects that were classified as being part of the LI segment overlaid on the original grayscale image (all three edge objects are part of the LI profile). **(f)** Edge objects that are part of the longest LI segment found overlaid on the original grayscale image (the far edge object has been removed). **(g)** Final LI profile on the original grayscale image, where the two edge objects belonging to LI have been linked and the third one have been removed because too far

only pixels belonging to the media layer. Thus, we expect relatively low $\mathrm{IM}_{\mathrm{mean}}$ and $\mathrm{IM}_{\mathrm{std}}$ values (in our sample dataset, the average $\mathrm{IM}_{\mathrm{mean}} \pm \mathrm{IM}_{\mathrm{std}}$ value was equal to about 63 ± 19 in a scale range of 0–255).

3. Create a second mask starting from MAcut_i and extending it up to the i-th edge object (Fig. 5d). For each pixel found in this mask, determine if it can be defined as an acceptable pixel based on the following relation:

$$|\text{Pixel Value} - \mathrm{IM}_{\mathrm{mean}}| < \mathrm{IM}_{\mathrm{std}} \Rightarrow \text{Acceptable Pixel}. \tag{22}$$

This check rejects too bright and too dark pixels, thus avoiding incorrect edge objects located into the vessel lumen and in the media layer. Also, we determined an $\mathrm{IM}_{\mathrm{ratio}}$ as the ratio between the number of acceptable pixels found and the total number of pixels considered.

4. Calculate the row distance between the left unconnected end point of the *i*-th edge object and the first point of $\text{MAcut}_i(\text{LT}_i(y) - \text{LT}_{\text{MA}}(y))$ and the row distance between the right unconnected end point of the *i*-th edge object and the last point of $\text{MAcut}_i(\text{RT}_i(y) - \text{RT}_{\text{MA}}(y))$.
5. Determine that the edge object can be classified as being part of the LI segment if the following two conditions are met:

$$\text{IM}_{\text{ratio}_i} > 0.4, \tag{23}$$

$$\text{mean}(\text{LT}_i(y) - \text{LT}_{\text{MA}}(y), \text{RT}_i(y) - \text{RT}_{\text{MA}}(y)) > \lambda. \tag{24}$$

   The first condition is important in that it avoids classifying an edge object which is found in the lumen since the pixel values in the lumen are considerably lower than $\text{IM}_{\text{mean}_{\text{GT}}}$ and those pixels would therefore not be classified as an acceptable pixel, lowering by a good deal the calculated IM_{ratio}. The second condition is necessary so as to not include discontinuous edge objects, which are located too close to the MA profile (i.e., in between the MA and LI profiles.). We selected a value $\lambda = 5$ (further discussion is reported in Table 1).
6. Repeat Steps 1–5 until all edge objects are examined.
   Figure 5e shows the edge objects that were classified as being part of the LI segment overlaid in white on the original image.

Once all of the edge objects are examined, those found to be part of the LI segment (good edge objects) must be tested to see if the distance between two adjacent edge objects is too high. This is to avoid connecting the two edge objects which are too far from each other, which could have a negative effect on the outcome of the final LI profile. To do this, the good edge objects are considered by adjacent pairs. Once all good edge objects are examined, the final LI segment is determined by those that are part of the longest LI segment found (Fig. 5f).

The edge objects that are part of the final LI segment are then connected together and B-spline is fitted to produce the final LI profile (Fig. 5g).

2.3 Design of the Performance Metric

Our algorithm was tested on a multi-institutional database consisting of 300 longitudinal B-mode ultrasound images of the common CA. We then had three expert operators independently and manually to trace the LI and MA profiles in all the images. The operators manually segmented the images by using a MATLAB interface that we had previously developed. The manual profiles were interpolated by a B-spline and averaged. The averaged profile was considered as ground truth (GT).

Our performance evaluation method consisted of two different strategies:

1. To assess the performance of the automated tracing of the far adventitial border.
2. Overall system distance of the LI/MA traced profiles from GT and of the IMT measurement bias.

Concerning (1), we calculated the Hausdorff distance (HD) between the AD_F profile and the LI_{GT} profile and then between the AD_F profile and the MA_{GT} profile for each image, to find the LI and MA distances between AD_F and GT ($\varepsilon^{LI}_{AD_F-GT}$ and $\varepsilon^{MA}_{AD_F-GT}$, respectively). The HD between two boundaries is a measure of the farthest distance that must be covered moving from a given point on one boundary and travelling to the other boundary. So first of all, given two boundaries B_1 and B_2, the Euclidean distances of each vertex of B_1 from the vertices of B_2 must be calculated. For every vertex of B_1, the minimum Euclidean distance is kept. Then once all B_1 vertices have been examined, the maximum distance between all of these minimum distances is kept and we can indicate it with d_{12}. Likewise, we can calculate the Euclidean distances of each vertex of B_2 from the vertices of B_1 and find d_{21}. The HD can then be mathematically defined as:

$$\mathrm{HD} = \max\{d_{12}, d_{21}\}. \tag{25}$$

This assessment helps to give a general idea of how far the AD_F tracing is from the actual distal wall LI and MA borders. Since this distance measure is sensitive to the longest distance from the points of one boundary to the points of the other, we cut the computed profiles to the same support of GT, rendering the HD unbiased by points that could perhaps be located out of the GT support.

Regarding the second point (2), to assess the performance of the automatic tracings of the LI and MA profiles, we calculated the polyline distance (PD) as proposed by Suri et al. in 2000 [15].

Considering the two boundaries B_1 and B_2, we can define the distance $d(v,s)$ between a vertex v and a segment s. Let's consider the vertex $v = (x_0, y_0)$ on the boundary B_1 and the segment s formed by the endpoints $v_1 = (x_1, y_1)$ and $v_2 = (x_2, y_2)$ of B_2. The PD $d(v,s)$ can then be defined as:

$$d(v,s) = \begin{cases} d_\perp & 0 \le \lambda \le 1 \\ \min\{d_1, d_2\} & \lambda < 0, \lambda > 1 \end{cases} \tag{26}$$

where

$$d_1 = \sqrt{(x_0 - x_1)^2 + (y_0 - y_1)^2}, \tag{27}$$

$$d_2 = \sqrt{(x_0 - x_2)^2 + (y_0 - y_2)^2}, \tag{28}$$

$$\lambda = \frac{(y_2 - y_1)(y_0 - y_1) + (x_2 - x_1)(x_0 - x_1)}{(x_2 - x_1)^2 + (y_2 - y_1)^2}, \tag{29}$$

$$d_\perp = \frac{(y_2 - y_1)(x_1 - x_0) + (x_2 - x_1)(y_0 - y_1)}{\sqrt{(x_2 - x_1)^2 + (y_2 - y_1)^2}}, \tag{30}$$

d_1 and d_2 being the Euclidean distances between the vertex v and the endpoints of segment s, λ the distance along the vector of the segment s, and $d_\perp$ the perpendicular distance between v and s. The polyline distance from vertex v to the boundary B_2 can be defined as $d(v,B_2) = \min_{s\in B_2}\{d(v,s)\}$. The distance between the vertices of B_1 to the segments of B_2 is defined as the sum of the distances from the vertices of B_1 to the closest segment of B_2:

$$d(B_1,B_2) = \sum_{v\in B_1} d(v,B_2). \tag{31}$$

Similarly, the distance between the vertices of B_2 to the closest segment of $B_1(d(B_2,B_1))$ can be calculated by simply swapping the two boundaries. Finally, the polyline distance between two boundaries is defined as:

$$\mathrm{PD} = \frac{d(B_1,B_2)+d(B_2,B_1)}{(\#\mathrm{vertices}_{B_1}+\#\mathrm{vertices}_{B_2})}. \tag{32}$$

Using the polyline distance metric, one can then compute the IMT using Edge Flow method and compare that with the IMT using the GT LIMA borders:

$$\mathrm{IMT}_{\mathrm{CAUDLES-EF}} = \mathrm{PD}(\mathrm{LI}_{\mathrm{CAUDLES-EF}}, \mathrm{MA}_{\mathrm{CAUDLES-EF}}). \tag{33}$$

$$\mathrm{IMT}_{\mathrm{GT}} = \mathrm{PD}(\mathrm{LI}_{\mathrm{GT}}, \mathrm{MA}_{\mathrm{GT}}). \tag{34}$$

$$\varepsilon^{\mathrm{IMT}}_{\mathrm{CAUDLES-EF}} = \mathrm{MT}_{\mathrm{CAUDLES-EF}} - \mathrm{IMT}_{\mathrm{GT}}. \tag{35}$$

The PD measures the distance between each vertex of a boundary and the segments of the other boundary.

This assessment helps to evaluate the performance of the IMT using CAUDLES and the error is purposefully calculated without an absolute value so as to see how much the algorithm under-estimates and/or over-estimates the IMT measure. The units of the calculated HD and PD are initially in pixels, but for our performance evaluation we converted the calculated pixel distances into millimeters, using a calibration factor, which is equal to the axial spatial resolution of the images. In our database, the 200 images acquired at the Neurology Division of Torino had a calibration factor equal to 0.0625 mm/pixel while the 100 images acquired at the Cyprus Institute of Neurology had a calibration factor equal to 0.0600 mm/pixel.

Third, for an overall assessment of the algorithm performance, we calculated Figure of Merit (FoM) which is defined by the following formula:

$$\mathrm{FoM} = \left(1 - \frac{|\mathrm{IMT}_{\mathrm{GT}} - \mathrm{IMT}_{\mathrm{CAUDLES-EF}}|}{\mathrm{IMT}_{\mathrm{CAUDLES-EF}}}\right) \times 100. \tag{36}$$

3 Results: Performance Evaluation and Benchmarking

3.1 Segmentation Results on Healthy and Diseased Carotids

Figure 6 demonstrates the performance of CAUDLES-EF on two different kinds of images. The first column represents the original B-mode images; the middle column shows the tracings of the far adventitial wall with the ultrasound image in the background; the last column depicts the tracings of the LI and MA borders with the ultrasound image in the background. Figure 6a shows a normal CA that is not horizontally oriented in the frame and in which the central portion of the image is corrupted by high blood backscattering. Figure 6b shows the capability of CAUDLES-EF to follow the curved vessel while avoiding the noise due to backscattering, and Fig. 6c finally shows how the LI and MA borders were properly segmented, in spite of these potential challenges. Figure 6d depicts an image in which the jugular vein is clearly present and whose artery wall is thicker due to deposition. Figure 6e shows how CAUDLES-EF was able to correctly identify the CA, and Fig. 6f finally shows how the algorithm can effectively segment the image avoiding problems due to the presence of a thicker artery wall and jugular vein.

Figure 7 shows the comparison between CAUDLES-EF and GT tracings of the LI and MA profiles in the same two cases as depicted in Fig. 6. The GT tracings were obtained as the average of the three experts' tracings. The continuous solid lines represent the CAUDLES-EF tracings, while the dotted lines represent the GT tracings.

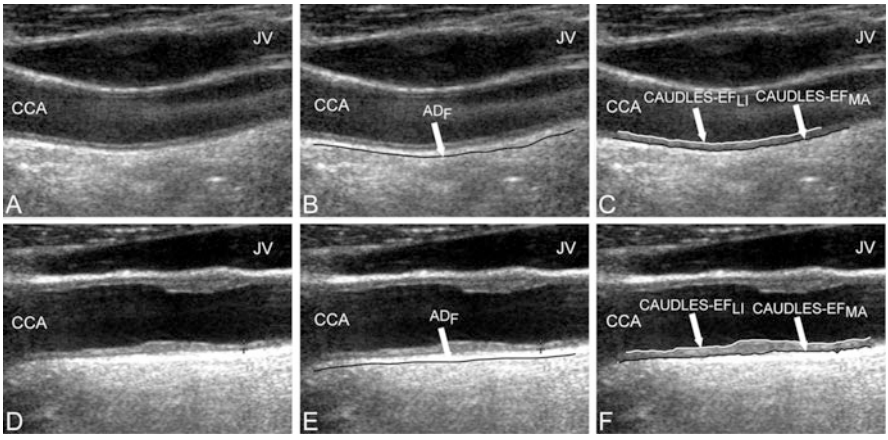

Fig. 6 Examples of CAUDLES-EF performance on normal but non-horizontal carotid artery and carotid artery in the presence of jugular vein. *First column*: the original cropped images; *Middle column*: AD_F profile (Stage-I output) overlaid on the original cropped grayscale images; *Last column*: LI and MA borders estimated using CAUDLES-EF algorithm overlaid on the original grayscale images. *Top row*: Normal CA that is not horizontal and that is corrupted by blood backscattering. *Bottom row*: Vessel with a thicker artery wall and presence of the jugular vein in the image. (CCA – common carotid artery; JV – jugular vein)

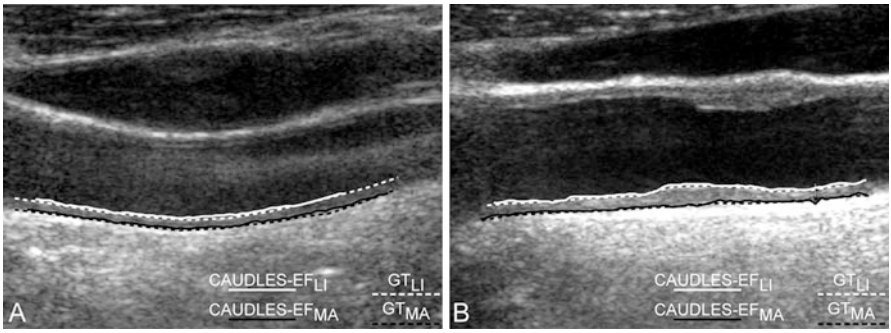

Fig. 7 Comparison between CAUDLES-EF and expert tracings (GT) of the LI and MA borders. The CAUDLES-EF tracings are depicted by continuous solid lines, whereas dotted lines indicate the GT tracings. *Left image*: non-horizontal geometry; *Right image*: carotid artery in the presence of jugular vein

3.2 Performance Evaluation of CAUDLES-EF

CAUDLES-EF correctly identified the carotid artery by tracing of the AD_F profile in all the 300 images (100% success rate). The first row in Fig. 8 shows the CAUDLES-EF distribution of $\varepsilon^{LI}_{AD_F-GT}$ and $\varepsilon^{MA}_{AD_F-GT}$ (i.e., the LI and MA errors between AD_F and GT, respectively) on the 300 tested images. This error data was interpreted using the cumulative distribution plots. The horizontal axis of the histogram represents the class center values, while the vertical axis represents the cumulative frequency. Figure 8a is relative to the LI border, Fig. 8b is relative to the MA border. The black lines represent the cumulative functions of the error distributions. We consider the maximum height of a guidance zone one can support efficiently to compute accurate LI and MA borders to be equal to 60 pixels ($\Delta_{lim_{pixels}}$). To convert this to millimeters, we considered the worst cases of a calibration factor equal to 0.06 mm/pixel, that yielded a maximum height of a guidance zone equal to 3.6 mm ($\Delta_{lim_{mm}}$). The histogram in Fig 8a shows that 94% of the errors between AD_F and LI_{GT} are below $\Delta_{lim_{mm}}$. However, as the histogram clearly shows, some of the remaining 6% of the MA errors can reach some very high values, in one case almost 4 times more than $\Delta_{lim_{mm}}$. This distribution is an evidence that CAUDLES-EF tracings are overall accurate and can be used for the definition of a guidance zone for IMT computation, even though in a few cases the error can reach higher values.

Analogous results can be observed in Fig. 8b, which shows the MA errors between AD_F and GT_{MA}: 95% of the MA errors are below $\Delta_{lim_{mm}}$, while remaining 5% still can reach slightly higher values.

Considering all the images, the AD_F profiles using CAUDLES-EF has a mean error between AD_F and GT_{LI} equal to 2.327 mm with a standard deviation equal to 1.394 mm; the MA error has a mean of 1.632 mm with a standard deviation equal to 1.584 mm. Table 2 summarizes these results.

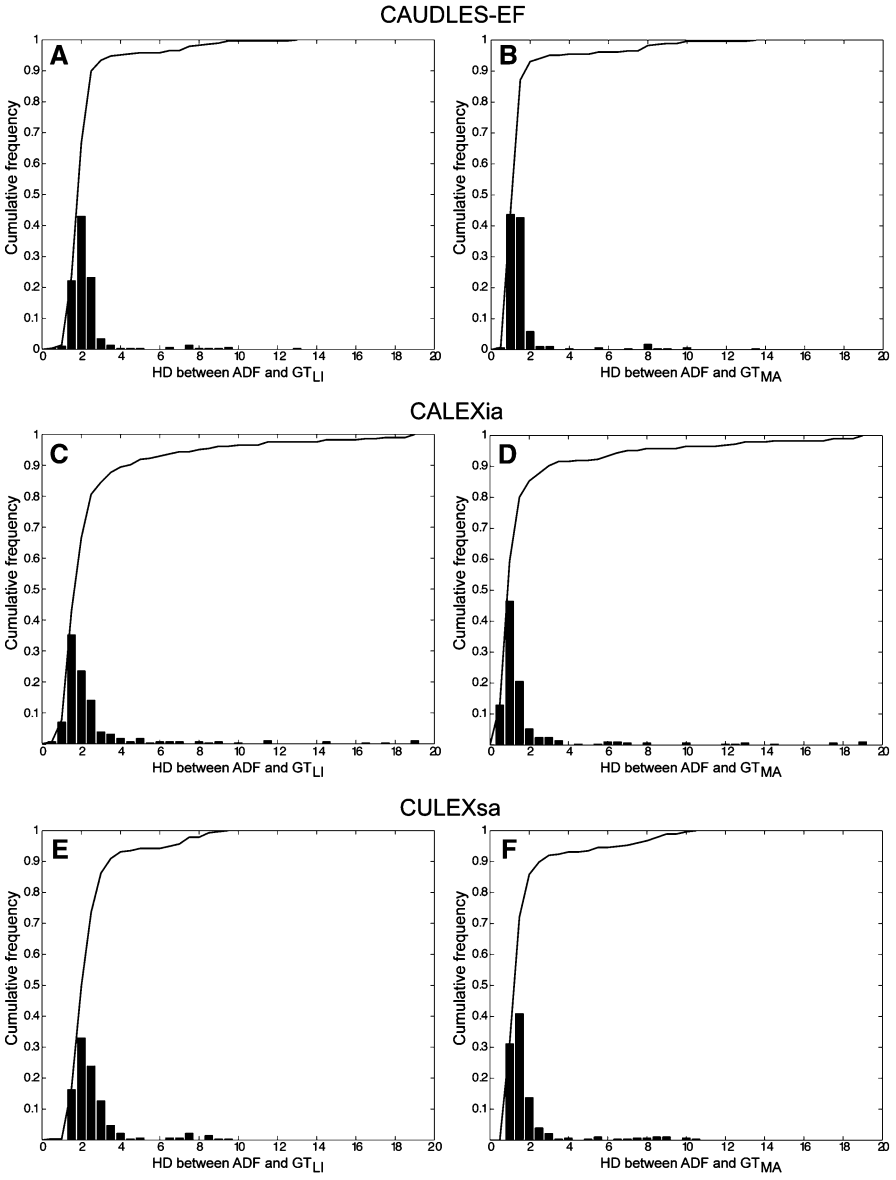

Fig. 8 Distribution of $\varepsilon^{\mathrm{LI}}_{\mathrm{ADF-GT}}$ and $\varepsilon^{\mathrm{MA}}_{\mathrm{ADF-GT}}$ for CAUDLES-EF, CALEXia, and CULEXsa. **(a)** and **(b):** LI and MA distances for CAUDLES-EF, respectively. **(c)** and **(d):** LI and MA distances for CALEXia, respectively. **(e)** and **(f):** LI and MA distances for CULEXsa, respectively. The horizontal axis represents the distance classes in millimeters and the vertical axis represents the cumulative frequency. The *black lines* represent the cumulative function of the distance distributions

Table 2 Performance Evaluation of CAUDLES-EF, CALEXia, and CULEXsa

	ADF w.r.t. GT–LI	ADF w.r.t. GT–MA	Automated LI w.r.t GT–LI	Automated MA w.r.t GT–MA
CAUDLES-EF	2.327 ± 1.394 mm	1.632 ± 1.584 mm	0.475 ± 1.660 mm	0.176 ± 0.202 mm
CALEXia	2.733 ± 2.895 mm	2.036 ± 3.024 mm	0.406 ± 0.835 mm	0.313 ± 0.850 mm
CULEXsa	2.651 ± 1.436 mm	1.965 ± 1.733 mm	0.124 ± 0.142 mm	0.118 ± 0.126 mm

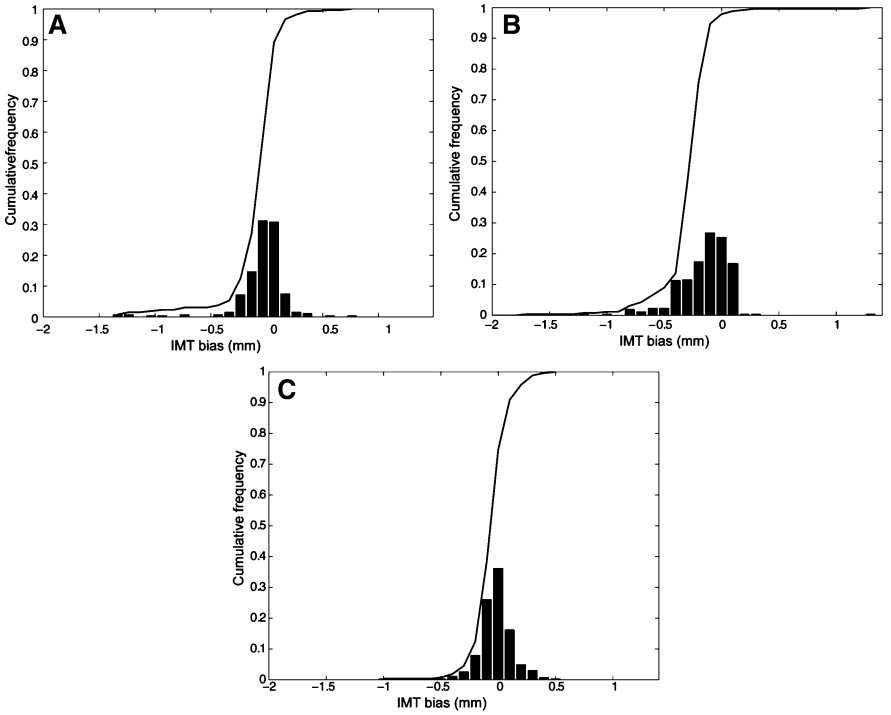

Fig. 9 Distribution of $\varepsilon^{\mathrm{IMT}}$ for CAUDLES-EF, CALEXia, and CULEXsa once removing the images with an unacceptable AD_F profile. (**a**) Distribution for CAUDLES-EF. (**b**) Distribution for CALEXia. (**c**) Distribution for CULEXsa. The horizontal axis represents the error classes in millimeters and the vertical axis represents the cumulative frequency. The *black lines* represent the cumulative function of the error distributions

Figure 9a shows the CAUDLES-EF distribution of $\varepsilon^{\mathrm{IMT}}_{\mathrm{CAUDLES-EF}}$ without five images that were found problematic (a detailed description of the possible CAUDLES-EF error sources is reported in the discussion section). We then calculated the PD in millimeters between the two computed boundaries and binned the error values in intervals having an extension of 0.1 mm. The horizontal axis of the histogram represents the class center values, while the vertical axis represents

Table 3 Overall automated IMT measurement performances of the CAUDLES-EF, CALEXia, and CULEXsa algorithms compared to Ground Truth

	Computer estimated IMT	GT IMT	IMT bias	FoM (%)
CAUDLES-EF	0.861 ± 0.276 mm	0.818 ± 0.246 mm	-0.043 ± 0.222 mm	94.8
CALEXia	0.746 ± 0.156 mm	0.880 ± 0.164 mm	0.134 ± 0.152 mm	84.7
CULEXsa	0.805 ± 0.248 mm	0.879 ± 0.237 mm	0.074 ± 0.233 mm	91.5

the cumulative frequency. The black lines represent the cumulative functions of the error distributions. The histogram in Fig. 9a reveals that 97.3% of the images processed have an absolute value of $\varepsilon^{\text{IMT}}_{\text{CAUDLES-EF}}$ that is equal to or less than 0.5 mm. The mean $\varepsilon^{\text{IMT}}_{\text{CAUDLES-EF}}$ is equal to 0.043 mm while the standard deviation is equal to 0.097 mm. Table 3 summarizes the results about the IMT measurement. In Table 3, the Ground Truth IMT average value shows a slight difference for the three techniques. This is due to the exclusion of images on which the technique did not satisfactorily perform. This distribution suggests that the CAUDLES-EF LI and MA tracings can be clinically used for IMT computation. The overall FoM was found to be equal to 94.8%, and we found that CAUDLES-EF under-estimates and over-estimates the true IMT value in a similar manner, with a slight tendency towards under-estimation, which is observable in Fig. 9a.

3.3 Benchmarking CAUDLES-EF with Existing Automated Techniques

For better evaluating the performance of our new algorithm, we benchmarked the results with two other completely automatic techniques for IMT measurement that was previously developed by our research group, CALEXia (Carotid Artery Layer EXtraction using an integrated approach) and CULEXsa (Completely User-independent Layer EXtraction based on signal analysis). Complete and more detailed explanations of these two algorithms can be found in our previous papers [6–10]. This comparison can be quite meaningful because the three main characteristics of the techniques are the same: i.e., (1) there is no need for human interaction, (2) they are designed to work in normal as well as for pathologic images, and (3) they trace all three profiles of interest: the far adventitial layer, the LI border, and the MA interface. All three of these algorithms were tested on the same database.

Figure 8c, d shows the LI and MA errors, respectively, between $P\text{AD}_{\text{F}}$ and GT for CALEXia while Fig. 8e, f shows these errors for CULEXsa. Figure 9b, c show the distribution of $\varepsilon^{\text{IMT}}_{\text{CALEXia}}$ and $\varepsilon^{\text{IMT}}_{\text{CULEXsa}}$, respectively. Tables 2 and 3 reports the segmentation errors and the IMT measurement bias for the three techniques. The overall FoM for CALEXia was found to be equal to 84.7%, while for CULEXsa it was equal to 91.5%. We found that CALEXia under-estimates the IMT, while CULEXsa tends to under-estimate the IMT value in a manner more similar to CAUDLES-EF (even though with slightly more marked tendency towards under-estimation).

4 Discussion

We have developed a novel technique for automatic computer-based measure of IMT in longitudinal B-mode ultrasound images. This new technique consists of two stages: (1) an automatic tracing of the AD_F profile based on scale-space multi-resolution analysis and (2) an automatic tracing of the LI and MA profiles based on a flow field propagation and the subsequent IMT measure which is obtained by calculating the Polyline distance between the computed LI and MA boundaries. We tested our method on a database of 300 images coming from two different institutions acquired from two different ultrasound scanners and compared it with expert human tracings. We validated our new method by benchmarking the results with two other completely automatic techniques that we had previously developed.

4.1 Rationale for Using the Hausdorff and Polyline Distances

The Hausdorff Distance measure how far is the two different subsets are from each other. In a nutshell, these two sets can be considered to be close based on the HD measure if every point of either set is close to at least one other point in the other set. The far adventitia boundary that is automatically detected is a guiding boundary, which represents the region of coarse identification of the carotid artery. It is quite likely that this boundary is not a smooth boundary, with the possibility of having sharp curvature changes. As a result, we are interested in finding the farthest possible distance between the computed AD_F and the GT borders. HD is an ideal choice for evaluating the performance of the AD_F boundary since this measure reveals the worst limit of the boundary.

The Polyline Distance, on the other hand, seems to be a more robust and reliable indicator of the distance between two given boundaries, and is very robust since it does not depend on the number of points in either boundary. This last property is very crucial when calculating the error between an IMT measure that is obtained with boundaries that have one point for every column (i.e., our automatically computed LI and MA profiles) and an IMT measure that is obtained with a much more limited number of points (i.e., the GT_{LI} and GT_{MA} profiles).

4.2 Overall Performance of CAUDLES-EF and Its Interpretation

The first row of Table 2 summarizes the overall performance of the CAUDLES-EF method. Comparing the CAUDLES-EF performance with the other two automatic techniques that we examined, we can see that our new algorithm presents very promising results.

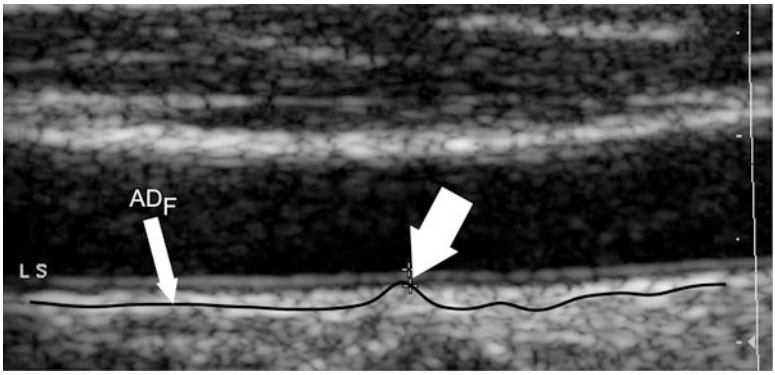

Fig. 10 Sample of inaccurate AD_F tracing due to the presence of image markers. The *continuous black line* represents the AD_F profile. The *thick white arrow* indicates the inaccurate adventitia tracing showing the bump

First, CAUDLES-EF outperformed both CALEXia and CULEXsa in the automatic Stage I (Table 2), by providing AD_F tracings closer to the ground truth for LI/MA boundaries of the far wall.

Second, it also outperformed CALEXia in the automatic Stage II and showed an average comparable performance with CULEXsa (the performance was, however, not statistically different from that of CULEXsa when tested by a 'Student's *t*-test', resulting in a *p*-value higher than 0.3), with a slightly higher standard deviation.

The major advantage of this new technique is versatility of the Edge Flow, which always reached convergence. The convergence of CAUDLES-EF was superior to that of CULEXsa. Being based on snakes, CULEXsa showed convergence issues when in presence of small plaques or of deformed vessels. In fact, it is very difficult to fine-tune the snake tension and elasticity parameters in order to cope with possible different carotid wall morphologies. As a result, CULEXsa could not process 14 images out of 300.

The computational time was comparable. Using MATLAB on a dual 2.5 GHz PC equipped with 8 MB of RAM, CAUDLES-EF took 6 s compared to 50 s for CULEX. CALEXia was fastest and its MATLAB implementation took 3 s.

4.3 Possible Error Sources

Presence of hyperechoic structures: the automated technique for the AD_F profile that we presented still could not reach a 100% satisfactory performance. We observed inaccurate AD_F tracings in four images. Figure 10 reports a sample of inaccurate AD_F tracing. The white arrow indicates a section of the profile, which overlaps the MA profile. This is an error condition, since the AD_F profile should always be below the MA boundary so as to be able to correctly define a guidance zone. This problem is given by image markers that are present in the image, which

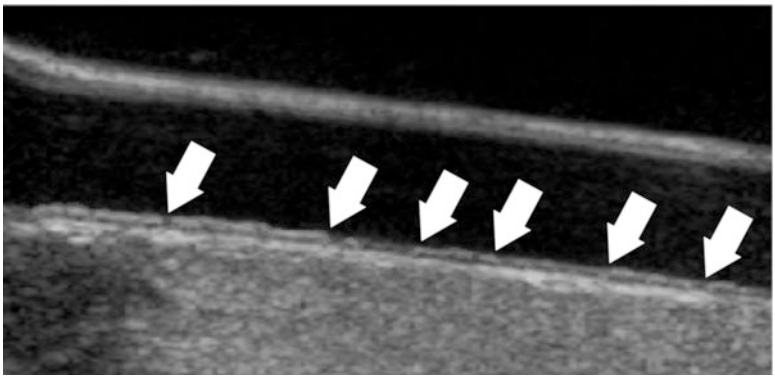

Fig. 11 Sample of Edge Flow inaccurate segmentation. The LI and MA boundaries are merged together in a single profile. The *white arrows* indicate some points where the edge object bumps between LI and MA (or vice versa). This is an error condition, which showed in only two images out of 300

attract the AD_F profile. We never experienced such error if markers were not present on the image. We adopted a spike-rejection algorithm to correct such possible problem. This algorithm identifies spikes by detecting the zero crossings of the AD_F derivative. Spikes are removed by interpolation between previous and following AD_F values. This technique enabled us to correct three images out of four.

Edge Flow algorithm and Refinement Process: there are two error conditions originated by the Edge Flow operator. The first one is depicted in Fig. 11: the Edge Flow algorithm outputs one single profile, which is partly overlaid to the LI border and partly to the MA. The white arrows marked in Fig. 11 show the transitions of the edge object between the LI and the MA border. In such condition, no refinement is possible. Two images gave this error.

The second error condition caused by Edge Flow is represented in Fig. 12: the MA profile is inaccurate, it is traced to be too close to the AD_F and not to the actual MA interface, and it is broken into many small edge objects. The arrow marked 1 in Fig. 12a indicates small edge objects, whereas the arrow marked 2 the MA edge objects that are below the AD_F (black line). In such condition, all the edge objects below AD_F profile and the small edge objects are removed by the refinement procedure (Fig. 12b). The subsequent step of deletion of the small edge objects removes the remaining MA edge objects (Fig. 12c). As consequence, the MA boundary can be totally erased. Two images gave this error.

4.4 Sensitivity of the Parameters

Table 1 summarizes the parameters of the CAUDLES system. In the second column of Table 1 we reported the parameter values that we used in our work. Such values were selected after a careful testing and tuning of our system.

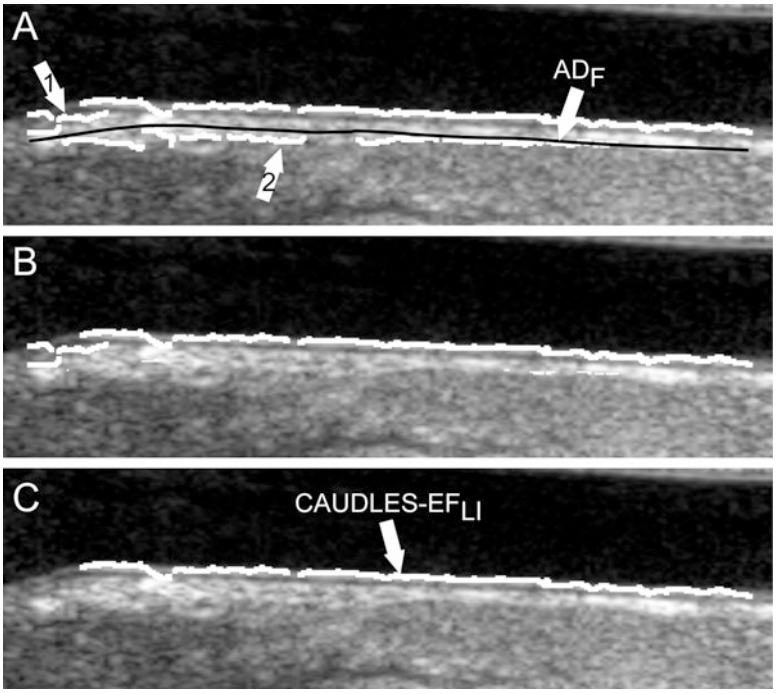

Fig. 12 Sample of inaccurate segmentation of the LI and MA border. The initial MA edge estimation is weak and therefore leads to an incorrect classification of the MA border. **(a)** Output image from the Edge Flow algorithm overlaid on the original image. The *white arrow* indicates edge objects located below the black line indicates the AD_F. The *arrow marked 1* indicates the discontinuity of the edge objects of Edge Flow producing many small edge objects. The *arrow marked 2* indicates the edge objects of the MA profile that are incorrectly traced below AD_F. (**b**) Binary image containing only the edge objects above the AD_F profile overlaid in white on the original image. Binary image obtained after removing the small edge objects. The MA border has been removed

The first parameter we introduced was Δ_{ROI}, which is the size of the Guidance Zone Mask. This value is used as vertical size: the AD_F profile is repeated Δ_{ROI} pixels above. We set Δ_{ROI} to be 50 pixels (approximately corresponding to 3 mm), which is three times the maximum value of IMT. This value ensures that we have comprised the entire distal wall in every condition into the Guidance Zone: straight and curved artery. Also, this value ensured a correct segmentation of small atherosclerotic plaques (see Fig. 6f). Lower values of Δ_{ROI} caused the LI border to partially fall out of the Guidance Zone, whereas higher values increase computational time.

The parameter σ is value of the derivative Gaussian kernels used by Edge Flow for DOOG computation. We took σ equal to 5 pixels. The size of the Gaussian derivative kernel must be comparable to the size of the interfaces that one wants to detect in the image. We found that higher values of σ caused the deletion of the LI/MA borders.

The parameter ϕ represents the area ratio used for detecting small edge objects in MA border refinement. Higher values caused the deletion of edge objects of significant length, thus shortening the final MA profile length to few pixels.

The parameter φ, which we took equal to 7 pixels, is the threshold for detecting connectable edge objects. This value was established on the basis of the calibration factor of the images: 7 pixels correspond to about 0.45 mm, which is half the expected value of the IMT. Therefore, such limit avoids connecting edge objects belonging to different boundaries (i.e., LI edge objects cannot be connected with MA, and vice versa).

By IM_{ratio} we indicated the threshold value for determining if an edge object can be classified as belonging to the LI segment. Lower values of this parameter caused the incorrect assignment of edge objects located into the vessel lumen (and detected by Edge Flow because of blood rouleaux) to the LI segment.

Finally, λ is the threshold value for determining if an edge object can be classified as belonging to the LI segment. This is the average distance of the edge object from the MA boundary. This value avoids the assignment to the LI segment of edge objects too close to the MA profile. Lower values would be too selective and not suited to be curved or not horizontal vessels. Higher values would have caused the deletion of too many edge objects.

Overall, we found that the selection of these parameters is not very specific and strict. Our database was multi-ethnic, multi-institutional, multi-scanner, and multi-operator, and, overall, the parameters values were suitable for all the images.

4.5 Relationship Among the Three Paradigms

There are still many challenges in developing fully automated techniques for the carotid wall IMT measurement. These can be grouped in Stage-I and Stage-II. The major challenges in Stage-I are: (1) the presence of the jugular vein (JV), (2) the presence of hyperechoic structures located in-between the LI and MA profiles, and (3) resolution and gain setting challenges. The major challenges in Stage-II are: (1) the presence of noise backscattering in the vessel lumen, (2) the hypoechoic representation of the LI layer, (3) the presence of a plaque on the distal wall, and (4) the presence of image artifacts (such as, shadow cones originated by calcium deposits and reverberations of the ultrasound waves). These factors increase the dataset variability (especially when the dataset is multi-institutional) and, consequently, limit the performance of the fully automated techniques. CULEXsa, being based on parametric models, needed an accurate tuning in order to reach optimal performance. When the image characteristics changed, the snake model needed re-tuning. Moreover, the presence of blood backscattering in the vessel lumen was a potential limit to lumen detection that was based on statistical classification. This

was the bottleneck in Stage-I of CULEXsa [7]. CALEXia showed an improved accuracy in the segmentation of the MA border, but a lower accuracy in the LI. Also, the robustness of CALEXia in Stage-I was higher than that of CULEXsa [10]. Though fully automated, the overall performance in terms of IMT measurement did not completely reach the best reproducibility standards. CAUDLES is a step ahead in both Stage-I and Stage-II architectures. The scale-space multi-resolution edge-based Stage-I brought 100% carotid identification. Stage-II, which was intensity and texture-based the edge flow method offered satisfactory LI/MA segmentation performance and proved effective in following any vessel morphology. The major advantage of CAUDLES with respect to CULEXsa was the possibility of tracing LI/MA profiles in any morphological condition without changing the system parameters. When compared with CALEXia, the Stage-II of CAUDLES is more robust with respect to image noise. Therefore, even though the three methodologies can be seen as technically very different, they have a common aim of developing a versatile and an effective technique coupling 100% identification accuracy in Stage-I and noise robustness, and optimal LI/MA segmentation in Stage-II.

5 Conclusions

The CAUDLES-EF algorithm we developed can be proficiently used for the segmentation of B-mode longitudinal ultrasound images of the common CA wall. It is completely user-independent: the raw US image can be completely processed without any interaction with the operator. It is based on a scale-space multi-resolution analysis to determine initial location of the CA in the image and is then based on a flow field propagation based on intensity and texture to determine edges, which are then classified and refined to provide the final contours of the LI and MA interfaces.

We tested this algorithm on a set of 300 images from two different institutes, which were acquired by two different operators using two different scanners. The image database contained images of both normal and diseased arteries. The performances of our new technique were validated against human tracings and benchmarked with two other completely user-independent algorithms. The average segmentation errors were found to be comparable or better than the other techniques and provided acceptable results, both in cases of normal CAs and those with plaques. We find that the results are very encouraging and we are porting the system for clinical usage.

From a clinical point of view, the algorithm traces the boundaries of both the intima and media layers, which can be used for measurements and also in algorithms of image co-registration and image fusion and for the accurate analysis of the carotid wall texture.

References

1. Amato M et al (2007) Carotid intima–media thickness by B-mode ultrasound as surrogate of coronary atherosclerosis: correlation with quantitative coronary angiography and coronary intravascular ultrasound findings. Euro Heart J 28(17):2094–2101
2. Rosvall M et al (2005) Incidence of stroke is related to carotid IMT even in the absence of plaque. Atherosclerosis 179(2):325–331
3. Saba L, Mallarini G (2009) A comparison between NASCET and ECST methods in the study of carotids Evaluation using Multi-Detector-Row CT angiography. Eur J Radiol
4. Touboul PJ et al (2007) Mannheim carotid intima–media thickness consensus (2004–2006). An update on behalf of the Advisory Board of the 3rd and 4th Watching the Risk Symposium, 13th and 15th European Stroke Conferences, Mannheim, Germany, 2004, and Brussels, Belgium, 2006. Cerebrovasc Dis 23(1):75–80
5. Touboul PJ et al (2004) Mannheim intima–media thickness consensus. Cerebrovasc Dis 18(4):346–349
6. Delsanto S et al (2005) CULEX-completely user-independent layers extraction: ultrasonic carotid artery images segmentation. Conf Proc IEEE Eng Med Biol Soc **6**:6468–6471
7. Delsanto S et al (2007) Characterization of a Completely User-Independent Algorithm for Carotid Artery Segmentation in 2-D Ultrasound Images. Instrum Meas IEEE Trans 56(4):1265–1274
8. Molinari F et al (2009) Automatic computer-based tracings (ACT) in longitudinal 2-D ultrasound images using different scanners. J Mech Med Biol 9(4):481–505
9. Molinari F Zeng G, Suri JS (2010) An integrated approach to computer- based automated tracing and its validation for 200 common carotid arterial wall ultrasound images: A new technique. J Ultras Med 29:399–418
10. Molinari F Zeng G, Suri JS (2010) Intima–media thickness: setting a standard for completely automated method for ultrasound. IEEE Trans Ultrason Ferroelect Freq Control 57(5):1112–1124
11. Zhen Y et al. (2005) Four image interpolation techniques for ultrasound breast phantom data acquired using Fischer's full field digital mammography and ultrasound system (FFDMUS): a comparative approach. In: Image Processing, 2005. ICIP 2005. IEEE International Conference
12. Loizou CP et al. (2005) Comparative evaluation of despeckle filtering in ultrasound imaging of the carotid artery. Ultrason Ferroelect Freq Contr IEEE Trans 52(10):1653–1669
13. Loizou CP et al. (2006) Quality evaluation of ultrasound imaging in the carotid artery based on normalization and speckle reduction filtering. Med Biol Eng Comput 44(5):414–426
14. Ma WY Manjunath BS (1997) Edge Flow: A Framework of Boundary Detection and Image Segmentation. In: Computer Society Conference on Computer Vision and Pattern Recognition. San Juan
15. Suri JS Haralick RM Sheehan FH (2000) Greedy algorithm for error correction in automatically produced boundaries from low contrast ventriculograms. Pattern Anal Appl 3(1):39–60

Filippo Molinari, PhD is an Assistant Professor in Biomedical Engineering at the Department of Electronics of the Politecnico di Torino (Torino, Italy). His main research interests include biomedical signal processing and medical imaging. He is an expert in automated techniques for aiding the diagnostic process in ultrasound imaging. Vascular sonography, atherosclerosis, and tumor detection are his main research topics.

He has published more than 70 peer reviewed contributions and authored three collaborative books. Dr. Molinari is a member of the IEEE EMBS, of the European Society for Molecular Imaging (ESMI), and of the American Institute of Ultrasounds in Medicine (AIUM). He is the Regional Associate Editor for Europe of the Journal of Medical Imaging and Health Informatics and he is on the Editorial Board of other five international journals.

Kristen M. Meiburger, MSc, received the Italian Laurea in Biomedical Engineering from Politecnico di Torino in 2010. She joined the Biolab of the Department of Electronics of the Politecnico di Torino as research assistant in the same year. Her research interest covers the ultrasound technologies and the medical imaging applied to the neurovascular field. Dr. Meiburger is graduate student member of the IEEE EMBS.

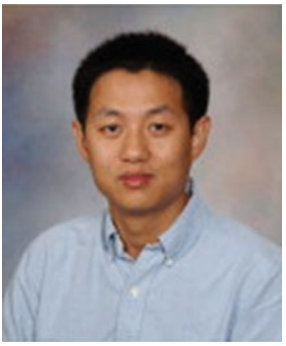

Guang Zeng, PhD received the B.S. degree from Xiangtan University, China in 1998. He received the M.S. degree in 2005 and the Ph.D. degree in 2008 from Clemson University, SC, USA, both in Electrical Engineering. He is currently working in the Aging and Dementia Imaging Research Laboratory, Mayo Clinic, Rochester, MN. His research interests include biomedical image processing, pattern recognition, and computer vision.

Andrew Nicolaides, MS, FRCS, PhD (Hon) graduated from Guy's Hospital Medical School, London University, London, UK, in 1962. He received the M.S. degree from the Royal College of Surgeons of England, London, UK, and the F.R.C.S., and F.R.C.S.E. degrees from the Royal College of Surgeons of England, London, and the Royal College of Surgeons of Edinburgh, Midlothian, UK, in 1967. He is currently the Professor Emeritus at Imperial College, London and an Examiner for M.S. and Ph.D. degrees for London University, London. He is also a "Special Scientist" at the University of Cyprus, Nicosia, Cyprus, and the Medical Director of the Vascular Screening and Diagnostic

Centre, London. His current research interests include the genetic risk factors for cardiovascular disease, identification of individuals at risk and the development of effective methods of prevention, especially stroke. He is Editor-in-Chief of International Angiology and is on the Editorial Board of many vascular journals. He is the coauthor of more than 500 original papers and editor of 14 books.

Jasjit S. Suri, PhD, MBA, Fellow AIMBE, is an innovator, visionary, scientist, and an internationally known world leader, has spent over **25** years in the field of biomedical engineering/sciences and its management. During his career in biomedical industry/imaging, he has had an upstream growth and responsibilities from scientific Engineer, Scientist, Manager, Director R&D, Sr. Director, Vice President to Chief Technology Officer (CTO) level positions in industries like *Siemens Medical Systems, Philips Medical Systems, Fisher Imaging Corporation, Eigen Inc., and Biomedical Technologies*, respectively and managed upto100 people. Dr. Suri has written over **300** publications covering US/European patents, peer reviewed journals, proceedings and book chapters. His major contributions are in the area of diagnosis and therapeutic devices covering heart, brain, spine, thyroid, eye, vasculature, breast, and prostate. He has championed the field of image segmentation and registration for image guided surgical applications. During his leadership, he has released over six different products along with the FDA approvals such as: Voyager, SenoScan, and Artermis.

Hereceived his Masters from University of Illinois, Chicago, Doctorate from University of Washington, Seattle, and Executive Management from Weatherhead School of Management, Case Western Reserve University (CWRU), Cleveland. Dr. Suri has been board member of several international journals and conference committees. Dr. Suri was crowned with President's Gold medal in 1980 and the *Fellow of American Institute of Medical and Biological Engineering* (AIMBE), awarded by National Academy of Sciences, Washington DC in 2004. Dr. Suri has been the chairman of IEEE Denver section and has won over 50 awards during his career.

Activity Index: A Tool to Identify Active Carotid Plaques

Luís Mendes Pedro, Isabel Gonçalves, Ruy Fernandes e Fernandes, José Seabra, João Miguel Sanches, and José Fernandes e Fernandes

Abstract Carotid bifurcation disease is a major cause of stroke in the western population. Atherosclerotic plaques located at the carotid bifurcation are a source of atheroembolization into the brain and may also cause flow restriction. Severity of stenosis is related with the risk of stroke as shown in multicenter studies. Nevertheless, in asymptomatic disease, the risk is lower and the number of operations needed to prevent one stroke is substantial. This led to the investigation of other factors beyond stenosis and related to the structure of the carotid lesion aiming to identify those lesions associated to increased risk (active plaques). High definition ultrasonography with computer-assisted analysis allows the objective investigation of plaque echogenicity and structure. The authors present an ultrasonographic index (Activity Index) which was shown to be accurate in the identification of symptomatic (active) carotid plaques and provided to be useful for clinical decisions.

L.M. Pedro (✉) • R.F. e Fernandes • J.F. e Fernandes
Instituto Cardiovascular de Lisboa and Faculty of Medicine, University of Lisbon, Portugal
e-mail: lmendespedro@clix.pt; ruyfernandes@mac.com; jff@me.com

I. Gonçalves
Department of Clinical Sciences, Experimental Cardiovascular Research Unit, Lund University, Malmo University Hospital, Malmo, Sweden
e-mail: mgoncalvesadv@mail.telepac.pt

J. Seabra • J.M. Sanches
Institute for Systems and Robotics, Department of Bioengineering from the Instituto Superior Técnico/Technical University of Lisbon, Portugal
e-mail: mail2jseabra@gmail.com; jmrs@ist.utl.pt

J.M. Sanches et al. (eds.), *Ultrasound Imaging: Advances and Applications*,
DOI 10.1007/978-1-4614-1180-2_7,

1 Introduction

Carotid bifurcation disease is a major cause of stroke in the western population. Atherosclerotic plaques located at the carotid bifurcation are a source of atheroembolization into the brain and may also cause flow restriction. Severity of stenosis is related with the risk of stroke as shown in well designed multicenter studies [1–4] and luminal restriction >70% has been identified as a determinant for clinical decisions in both symptomatic and asymptomatic patients.

Analysis of surgical specimens removed during endarterectomy demonstrated different morphological characteristics of the atherosclerotic plaques, and presence of erosion on the fibrous cap, ulceration, and intra-plaque haemorrhage were more frequent in symptomatic lesions [5]. Observations from acute coronary syndromes [6] also suggested that acute ischemic events were frequently associated with moderate stenosis complicated by acute thrombosis drawing attention to the characteristics and contents of the atherosclerotic lesions and their importance for the pathogenesis of clinical complications, leading to the concept of *unstable* or *active* plaques. Plaque surface irregularities on angiographic examinations was an independent predictor of stroke risk in the medical arm of the ECST [7] data subsequently confirmed from the NASCET trial [8] and the ACSCEPT study [9].

Active lesions were associated with increased clinical and neurological risk. Its morphological characterization before open surgery or endovascular stenting became a relevant topic for clinical research, aiming to a better selection of patients requiring invasive treatment to effectively prevent carotid-related strokes.

Different diagnostic tools have been developed from sophisticated ultrasound B-mode examinations to MRI and angio CT studies [10,11] aiming to identify markers of unstable disease within the carotid plaques. Functional bio-imaging methods using ultrasound contrast angiography to detect increased neovascularization in the plaques, isotope-labelled molecules to identify metabolic increased activity [12] have been suggested, in order to identify physiologic and pathogenic mechanisms inside the plaque such as inflammation, macrophage proliferation, and cholesterol uptake, thrombus formation and/or presence of neovascularisation. These technologies are presently under investigation and are not yet quite adequately used for routine use within the framework of a busy clinical practice as their cost is relatively high.

High definition ultrasonography (HDU) with computerized assistance [13–28] allows visualization of superficial arteries like the carotid bifurcation and provides a detailed information about arterial wall modifications and plaque structure and its precise outline. Operator dependency and need for consistent imaging standardization in order to minimize quality of the equipment, and image acquisition are the limitations associated with the technique.

Digital image processing methods represented a significant improvement for an accurate standardization of ultrasound images allowing for comparison between different observers and equipments and also improved intra- and inter-observer as

well as intra- and inter-center reproducibility [13–23]. Its advantages are wide availability, low cost, and possibility of repeated examinations without any deleterious side effects.

Carotid plaque characterization may play a relevant role for clinical decision in two cohorts of patients: (1) Identification of subgroups of asymptomatic patients with a high stroke risk thus reducing the number of unnecessary invasive treatments such as endarterectomy or stenting;

(2) Diagnosis of unstable lesions prone to increased stroke rate during carotid stenting [24], and (3) Patients with 50–70% stenosis at a higher stroke risk.

The aim of the present investigation [25–28] was to develop High-Definition Ultrasound (HDU) with computer-assisted plaque analysis to identify new morphological markers of plaque activity in patients with carotid bifurcation disease.

2 Method

All patients were studied with HDU using colour-flow duplex-scan equipment (ATL – Advanced Technology Laboratories – model HDI 3000) with 7–10 MHz probe, 60 dB dynamic range and post-processing linear curves. All the HDU examinations were blindly performed by the same observer (LMP) without knowledge of the clinical and CT-scan evaluation.

Carotid bifurcation was imaged in longitudinal and transverse sections and the best longitudinal section was chosen and recorded in black and white for further analysis.

The computer-assisted evaluation used the software Adobe Photoshop® 3.0 for standardization and echogenicity analysis. Standardization was achieved by attributing a normalized pre-set value of 190 for the adventitia and 0 for the blood, thus producing a modification of the characteristics of the entire image equal for all examinations [14, 15].

In this standardized image the plaque was outlined (segmentation) and a histogram of the gray-scale distribution of pixels of the entire area of the lesion was obtained. The following parameters were determined from the histogram: (1) the gray-scale median (GSM); (2) the percentile 40 (P40), which represents the percentage of "black" pixels ("echolucent" pixels). These two parameters were considered as a measure of the whole echogenicity of the plaque and were analysed in all plaques.

Carotid plaques were divided into homogenous and heterogenous according to its echo-structure and ultrasonographic equivalents of the pathologic findings in symptomatic lesions that were identified and are shown in Fig. 1.

For each lesion the degree of stenosis was also quantified using end-systolic and end-diastolic velocity criteria combined with cross-section area reduction was measured in transverse images of the lesion.

For statistical analysis software STATA 4.0 was used with categorial variables analyszd by Chi-square and Fisher's exact test and continuous variables were analyzed by variance analysis and Student's test.

HISTOLOGIC PARAMETER	ULTRASONOGRAPHIC	
	HOMOGENOUS	HETEROGENOUS
Wide lipid/necrotic	Echolucenc	Echolucenc % echolucent
Juxtaluminal lipid/necrotic	-	Juxtaluminal echolucent area
Intra-plaque	Echolucenc	Echolucenc
Thin fibrous	Thin or invisible echogenic % echogenic	Thin or invisible echogenic
Disruption of plaque	Disruption of surface,	Disruption of surface,

Fig. 1 Ultrasonographic equivalents of morphologic and histologic markers of active plaques

The investigation proceeded into three steps:

Step 1 – Univariate analysis (Chi-square and Fisher exact test for categorial variables and variance analysis and Student's *T* test for continuous variables) were used to determine the variables that were significant for the identification of symptomatic plaques.
Step 2 – Determination of the probability of occurrence of symptomatic plaque (odds value) for each significant variable:

Odds=number of symptomatic plaques with each significant variable/total number with each significant variable.

Then, we proceed to a resizing of the odds value to a 0–100 numerical scale to determine a score for each variable or subgroup inside the variable, in order to calculate that a plaque with all significant variables present would have a total score of 100. The Activity Index is the sum of the scores for each variable.
Step 3 – Multivariate logistic regression analysis was used to determine the true statistical significance of different odds for each subgroup or variable when compared with the respective reference group (lower probability group).

3 Study 1: Relationship Between Global Plaque Echogenicity and Neurological Symptoms and Cerebral Infarction

3.1 Population

The study included 106 carotid bifurcation plaques from 74 patients: 58 males and 16 females. The mean age was 67 years (38–80) and all the patients had a

neurologic evaluation. The carotid lesion was considered symptomatic when associated with amaurosis fugax or appropriate neurologic events (transitory, reversible or established) on the ipsilateral carotid territory. A CT-Scan was obtained for all the patients and was considered positive when cerebral infarcts were present in the area of anterior and middle cerebral arteries.

3.2 Results

Thirty nine (37%) plaques were symptomatic and 66 (63%) were asymptomatic. The mean degree of stenosis was 68% with the following distribution:

More than 70% stenosis – 54 lesions (51%)
Stenosis between 51% and 69% – 21 lesions (20%)
Stenosis between 30% and 50% – 30 lesions (29%)

Sixty seven plaques (63%) were classified as homogenous and 38 lesions (37%) were considered as heterogenous.

By univariate analysis, the significant factors associated with symptomatic lesions were provided the following (See Table 1):

(a) Homogenous lesions: the GSM and P40 of symptomatic plaques were significantly lower than of asymptomatic plaques (respectively 36 versus 46 $p = 0.03$ and 63 versus 46 $p = 0.01$). This finding was observed in homogenous and heterogeneous lesions and the best cut-off to discriminate between symptomatic and asymptomatic lesions was 32 for the GSM and 43 for the P40. Plaque surface disruption was also more common in symptomatic plaques (53% versus 12% $p < 0.01$).
(b) Heterogenous lesions: the GSM and P40 of symptomatic plaques were significantly lower than of asymptomatic plaques (respectively 31 versus 44 $p = 0.02$ and 61 versus 49 $p = 0.02$). Evidence of plaque surface disruption was diagnosed in 72% of the symptomatic plaques but only in 29% of asymptomatic ($p < 0.01$). In heterogenous symptomatic plaques there was evidence of a juxta-luminal location of the echolucent region in 72% against 28% in asymptomatic plaques ($p < 0.01$).

The results of the assessment are relatively important for each significant parameter to calculate the probability values that are presented in Tables 2 and 3. Resizing these odds value for a 0–100 scale allowed the obtention of a numerical score indicated in Table 4. The Activity Index (AI) of each plaque is obtained by the sum of the scores (Fig. 2). A plaque with heterogenous structure, with the echolucent region juxta-luminal, >90% degree of stenosis, GSM < 32 and P40 > 42 is associated with maximal AI of 100.

Table 1 Results of the univariate analysis of symptomatic and asymptomatic plaques

	Symptomatic	Asymptomatic	*p*
Homogenous plaque			
• GSM	36	46	0.03
• P40	63	46	0.01
• Echogenic cap	28%	41%	NS
• Plaque surface disruption	53%	12%	<0.01
• Echogenic cap thickness/plaque thickness	12	12	NS
Heterogenous plaque			
• GSM	31	44	0.02
• P40	61	49	0.02
• Plaque surface disruption	72%	29%	<0.01
• Juxta-luminal location of the echolucent region without echogenic cap	72%	28%	<0.01
• Echogenic cap thickness/plaque thickness	20	16	NS
• % of echolucent region	59%	57%	NS
• Index echogenicity-area	0.5	0.5	NS

Table 2 Calculation of the odds values, odds-ratios and confidence intervals for symptomatic plaque in the group of *HOMOGENOUS PLAQUES* (reference groups: no plaque disruption; stenosis <50%; GSM > 40; P40 < 42)

	Odds	Odds ratio	C.I. 95%	*p*
Homogenous plaque	0.22			
Plaque surface disruption				
No	0.13	–	–	
Yes	0.57	8.9	(2.3–32.9)	<0.001
Degree of stenosis				
<50	0.11	–	–	
50–69	0.14	1.25	(0.1–15.8)	0.863
70–79	0.15	1.67	(0.2–1.4)	0.631
80–89	0.40	6.67	(1.9–25.8)	0.032
>90	0.50	10.0	(1.6–33.1)	0.014
GSM				
<20	0.80	37.3	(3.1–63.0)	<0.001
20–32	0.38	11.2	(2.2–56.1)	<0.001
33–40	0.18	5.6	(1.2–26.7)	0.031
>40	0.09	–	–	–
*P*40				
<42	0.07	–	–	–
42–55	0.18	4.9	(2–35)	0.036
56–63	0.27	6.5	(1.2–32.4)	0.021
>63	0.47	11.4	(2.0–36.1)	<0.001

Table 3 Calculation of the odds values, odds-ratios and confidence intervals for symptomatic plaque in the group of *HETEROGENOUS PLAQUES* (reference groups: homogenous plaque; central echolucent region; no plaque disruption; stenosis < 50%; GSM > 40; P40 < 42)

	Odds	Odds ratio	C.I. 95%	*p*
Heterogenous plaque	0.64	6.19	(2.6–14.8)	<0.001
Location of the echolucent region				
Central	0.14	–	–	–
Juxta-luminal	0.72	6.8	(1.8–21.2)	0.021
Plaque surface disruption				
No	0.41	–	–	–
Yes	0.82	6.4	(1.5–27.4)	<0.001
Degree of stenosis				
<50	0.00	–	–	–
50–69	0.14	–	–	–
70–79	0.43	5.9	(2.4–10.7)	0.034
80–89	0.57	6.6	(3.7–12.5)	0.020
<90	1.00	22.1	(4.5–121.7)	<0.001
GSM				
<20	1.00	7.2	(1.7–29.6)	0.011
20–32	0.57	3.2	(0.9–10.7)	0.061
33–40	0.42	2.5	(0.7–10.1)	0.121
<40	0.12	–	–	–
*P*40				
<42	0.23	–	–	–
42–55	0.44	2.7	(0.7–10.9)	0.288
56–63	0.53	3.3	(0.8–12.6)	0.092
<63	1.00	9.7	(1.8–26.6)	<0.001

4 Study 2: Evaluation of the Diagnostic Accuracy of the AI

4.1 Population and Method

We studied 109 plaques from 67 patients with a mean age of 69 years (47–88); 27 (25%) were symptomatic, while 82 (75%) were asymptomatic.

The diagnostic accuracy of the AI was assessed and the same factors of plaque echogenicity and echostructure, mentioned before, have been calculated, leading to the determination of the AI for each plaque.

Then, the diagnostic parameters (sensitivity, specificity, positive predictive value, negative predictive value, and overall accuracy) for the identification of the symptomatic plaque have been calculated using the ROC curve analysis methodology.

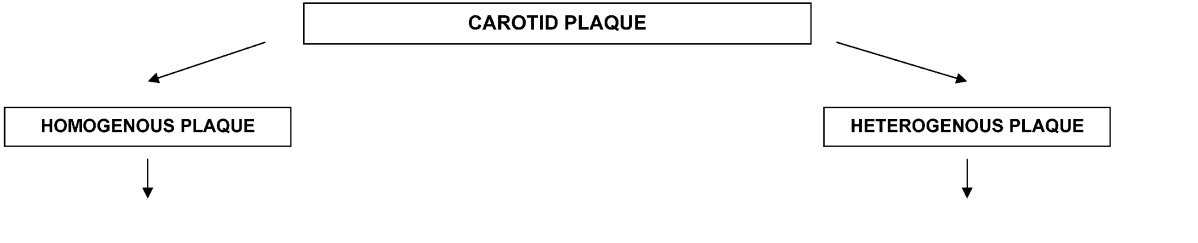

	"SCORE"
Homogenous plaque	9
Plaque surface disruption	
▪ No	5
▪ Yes	22
Degree of stenosis	
▪ < 50	4
▪ 50-69	5
▪ 70-79	6
▪ 80-89	16
▪ > 90	20
GSM	
▪ < 20	31
▪ 20-32	15
▪ 33-40	7
▪ > 40	4
P 40	
▪ < 43	3
▪ 43-55	7
▪ 56-63	11
▪ > 63	18

	"SCORE"
Heterogenous plaque	12
Location of the echolucent region	
▪ Central with echogenic cap	3
▪ Juxta-luminal without echogenic cap	14
Plaque surface disruption	
▪ No	8
▪ Yes	16
Degree of stenosis	
▪ < 50	0
▪ 50-69	3
▪ 70-79	8
▪ 80-89	11
▪ > 90	19
GSM	
▪ < 20	19
▪ 20-32	11
▪ 33-40	8
▪ > 40	2
P 40	
▪ < 43	4
▪ 43-55	9
▪ 56-63	10
▪ > 63	19

Table 4 "Scores" for calculation of the ACTIVITY INDEX (symptomatic plaque)

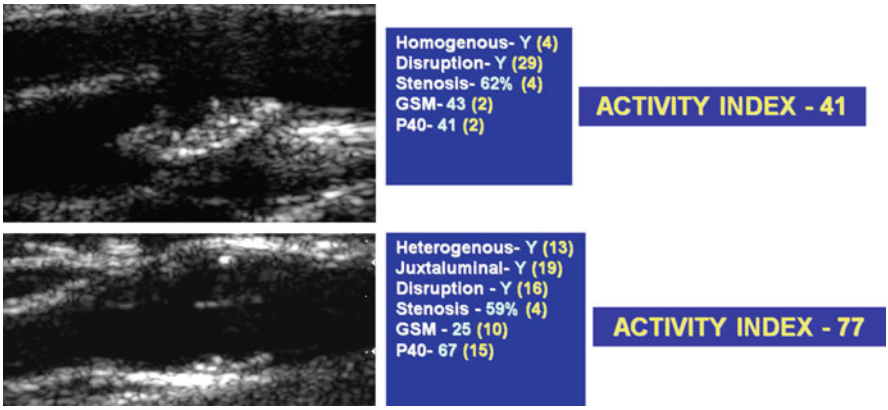

Fig. 2 Example of the calculation of the Activity Index in two separate plaques

4.2 Results

The mean degree of stenosis was 73% (31–99). Seventy one plaques (65%) were classified as homogenous and 38 lesions (35%) were considered as heterogenous.

In symptomatic plaques the mean AI was 75 (41–100) and in asymptomatic plaques the mean AI was 43 (22–100). We observed that 93% of symptomatic plaques have an AI superior to 50 and 78% superior to 60. Eighty-two percent of asymptomatic plaques have an AI lower than 60 and 70% lower than 50. The cut-off point between the two groups, allowing the greater difference between them, is the value of 52.

The calculation of diagnostic parameters using ROC curve analysis shows that the best cut-off level for the AI in homogenous plaques is the value 53–60, associated with sensitivity of 56%, specificity of 92%, positive predictive value of 50%, negative predictive value of 93%, and accuracy of 87%. For heterogenous plaques the best cut-off levels were the values 52–53, associated with sensitivity of 89%, specificity of 43–48%, positive predictive value of 59%, and negative predictive value of 83–100%, and accuracy of 75–76%.

5 Discussion

The characterization of subgroups of carotid lesions associated with increased neurological risk involves the detection of symptomatic plaques and asymptomatic lesions prone to become symptomatic.

Since the publication of the major multicenter trials for both symptomatic [1, 2] and asymptomatic [3, 4] carotid disease, the degree of stenosis became the most important determinant of the therapeutical decision. Nevertheless, information

about plaque characteristics is obtained from endarterectomy specimens and from coronary and carotid histologic studies it is confirmed that features such as intra-plaque hemorrhage [29, 30] and ulceration [31], wide- [32, 33] and juxta-luminal lipid/necrotic center [34], thin or ruptured fibrous cap [31] and an increased infiltration by inflammatory cells were more frequently present in symptomatic lesions. These parameters may be considered as markers of plaque instability and increased neurological risk. Also a higher lipid [35] and blood content may increase the plaque susceptibility to hemodynamic stress.

The concept of unstable carotid disease should therefore include two subgroups: plaques with ruptured cap and vulnerable lesions which are prone to rupture, leading to local thrombosis and appropriate clinical events, by embolization or ischemia due to artery occlusion. Reported observations from carotid occlusions [36, 37] suggested an association of moderate degrees of stenosis with markers of vulnerability or with ruptured fibrous cap, thus reproducing a similar situation already recognized in acute coronary occlusions.

The importance of morphological characteristics of carotid lesions such as the presence of plaque surface irregularity on angiography was recognized in the medical arm of the Europen Carotid Stenosis Trial (ECST) [7] where its presence increased the risk of neurological events at 2 years irrespective of the severity of carotid stenosis, thus suggesting that alterations in plaque structure are independent determinants of clinical risk.

B-mode ultrasonography and duplex scan provide analysis of the structure of the atheromatous plaque beyond what can be unveiled by angiography, but its reproducibility and diagnostic efficacy will be clearly improved by standardization of images and objective and quantitative evaluation.

Newer generation of colour-flow duplex scan equipments, with improved quality and high definition ultrasonographic image and computer-assisted plaque analysis through digital image processing, and standardization provides objective study of plaque structure thus in reducing variability and operator dependency [10].

Low plaque echogenicity demonstrated by the gray-scale median (GSM) [13,26] obtained from pixel distribution within the plaque standardized image and the amount of “echolucent” pixels (P40) [26–28] were associated with symptomatic lesions and with the presence of brain infarcts in the carotid territory. Echolucency has been related to increased content of blood and lipids, which are known components of increased plaque vulnerability [38–40].

Our study expands in the evaluation of regional components of the plaque and its distribution beyond single global echolucency measurements including features recognized in pathological specimens as markers of plaque instability. Its distribution within the lesion can be evaluated by measurement of Heterogeneity Index [41], use of multiple cross-sectional views [42], and detailed plaque texture analysis (DPTA) [43] but our method provides a unique objective analysis of all the markers of instability that can be assessed by HDU. In heterogenous lesions, we have introduced a new parameter – the juxta-luminal location of the echolucent area – that may correspond to a lipid-necrotic core close to the vessel lumen either with or without a fibrous (echogenic) cap overlying it as suggested in previous pathological observations [26,27].

The concept of an Activity Index encompassing the sum of the individual scores for each significant parameter related with symptomatic (active) plaques including echogenicity and other components of plaque structure, like surface disruption and juxta-luminal location of the echolucent region in heterogenous plaques [27] may provide a more objective evaluation of plaque activity that correlates with the presence of appropriate neurologic symptoms in the carotid territory.

The Activity Index measurement may also contribute for the identification of a subset of "dangerous" plaques particularly in asymptomatic patients with higher neurological risk, thus contributing for a better selection for carotid endarterectomy and thus reducing the number of unnecessary operations.

References

1. North American Symptomatic Carotid Endarterectomy Trial Collaborators. (1991) Beneficial effect of carotid endarterectomy in symptomatic patients with high grade carotid stenosis. N Engl J Med 325:445–463
2. European Carotid Surgery Trialists' Collaborative Group. (1991) MRC European Carotid Surgery Trial. Interim results for symptomatic patients with severe (70–99%) and with mild (0–29%) stenosis. Lancet 337:1235–1243
3. Executive Committee for the Asymptomatic Carotid Atherosclerosis Study. (1995) Endarterectomy for asymptomatic carotid artery stenosis. JAMA 273:1421–1428
4. Halliday A, Mansfield A, Marro J, Peto C, Peto R, Potter J, Thomas D (2004) MRC Asymptomatic Carotid Surgery Trial (ACST) Collaborative Group. Prevention of disabling and fatal strokes by successful carotid endarterectomy in patients without recent neurological symptoms: randomised controlled trial. Lancet 363:1491–1502
5. Merrit C, Bluth E (1992) Ultrasound identification of plaque composition. *In:* Labs K (ed): Diagnostic Vascular Ultrasound. Edward Arnold, London
6. Langsfeld M, Gray-Weale AC, Lusby RJ (1989) The role of plaque morphology and diameter reduction in the development of new symptoms in asymptomatic carotid arteries. J Vasc Surg 9:548–557
7. Rothwell PM, Gibson R, Warlow CP (2000) Interrelation between plaque surface morphology and degree of stenosis on carotid angiograms and the risk of ischemic stroke in patients with symptomatic carotid stenosis. On behalf of the European Carotid Surgery Trialists' Collaborative Group. Stroke 31:615–621
8. Eliasziw M, Streifler JY, Fox AJ, Hachinski VC, Ferguson GG, Barnett HJ (1994) Significance of plaque ulceration in symptomatic patients with high-grade carotid stenosis. North American Symptomatic Carotid Endarterectomy Trial. Stroke 25:304–308
9. Troyer A, Saloner D, Pan XM, Velez P, Rapp JH (2002) Major carotid plaque surface irregularities correlate with neurologic symptoms. J Vasc Surg 35:741–747
10. Zhao X, Underhill HR, Zhao Q, Cai J, Li F, Oikawa M, Dong L, Ota H, Hatsukami TS, Chu B, Yuan C (2011) Discriminating carotid atherosclerotic lesion severity by luminal stenosis and plaque burden: a comparison utilizing high-resolution magnetic resonance imaging at 3.0 Tesla. Stroke 42(2):347–353
11. Feuchtner GM, Cury RC, Jodocy D, Friedrich GJ, Blumenthal RS, Budoff MJ, Nasir K (2011) Differences in coronary plaque composition by noninvasive computed tomography angiography in individuals with and without obstructive coronary artery disease. Atherosclerosis 215(1):90–95
12. Hoogi A, Adam D, Hoffman A, Kerner H, Reisner S, Gaitini D (2011) Carotid plaque vulnerability: quantification of neovascularization on contrast-enhanced ultrasound with histopathologic correlation. AJR Am J Roentgenol 196(2):431–436

13. Elatrozy T, Nicolaides A, Tegos T, Zarka AZ, Griffin M, Sabetai M (1998) The effect of B-mode ultrasonic image standardisation on the echodensity of symptomatic and asymptomatic carotid bifurcation plaques. Int Angiol 17:179–186
14. Elatrozy T, Nicolaides A, Tegos T, Griffin M (1998) The objective characterisation of ultrasonic carotid plaque features. Eur J Vasc Endovasc Surg 16:223–230
15. Sabetai MM, Tegos TJ, Nicolaides AN, Dhanjil S, Pare GJ, Stevens JM (2000) Reproducibility of computer-quantified carotid plaque echogenicity: can we overcome the subjectivity? Stroke 31:2189–2196
16. Tegos TJ, Kalomiris KJ, Sabetai MM, Kalodiki E, Nicolaides AN (2001) Significance of sonographic tissue and surface characteristics of carotid plaques. AJNR Am J Neuroradiol 22:1605–1612
17. Tegos TJ, Stavropoulos P, Sabetai MM, Khodabakhsh P, Sassano A, Nicolaides AN (2001) Determinants of carotid plaque instability: echoicity versus heterogeneity. Eur J Vasc Endovasc Surg 22:22–30
18. Sabetai MM, Tegos TJ, Clifford C, Dhanjil S, Belcaro G, Kakkos S, Kalodiki E, Stevens JM (2001) Nicolaides AN. Carotid plaque echogenicity and types of silent CT-brain infarcts. Is there an association in patients with asymptomatic carotid stenosis. Int Angiol 20:51–57
19. Tegos TJ, Sabetai MM, Nicolaides AN, Elatrozy TS, Dhanjil S, Stevens JM (2001) Patterns of brain computed tomography infarction and carotid plaque echogenicity. J Vasc Surg 33:334–339
20. Tegos TJ, Sabetai MM, Nicolaides AN, Robless P, Kalodiki E, Elatrozy TS, Ramaswami G, Dhanjil S (2001) Correlates of embolic events detected by means of transcranial Doppler in patients with carotid atheroma. J Vasc Surg 33:131–138
21. Tegos TJ, Sohail M, Sabetai MM, Robless P, Akbar N, Pare G, Stansby G, Nicolaides AN (2000) Echomorphologic and histopathologic characteristics of unstable carotid plaques. AJNR Am J Neuroradiol 21:1937–1944
22. Sabetai MM, Tegos TJ, Nicolaides AN, El Atrozy TS, Dhanjil S, Griffin M, Belcaro G (2000) Geroulakos G. Hemispheric symptoms and carotid plaque echomorphology. J Vasc Surg 31:39–49
23. Tegos TJ, Kalodiki E, Nicolaides AN, Sabetai MM, Stevens JM, Thomas DJ. Brain CT (2001) infarction in patients with carotid atheroma. Does it predict a future event. Int Angiol 20:110–117
24. Biasi GM, Froio A, Diethrich EB, Deleo G, Galimberti S, Mingazzini P, Nicolaides AN, Griffin M, Raithel D, Reid DB, Valsecchi MG (2004) Carotid plaque echolucency increases the risk of stroke in carotid stenting: the Imaging in Carotid Angioplasty and Risk of Stroke (ICAROS) study. Circulation 110:756–762
25. Pedro LM, Pedro MM, Goncalves I, Carneiro TF, Balsinha C, Fernandes e Fernandes R, Fernandes e Fernandes J (1999) Placa de ateroma da bifurcação carotídea. Como identificar a lesão activa. Rev Port Cardiol 18:699–708
26. Pedro LM, Pedro MM, Goncalves I, Carneiro TF, Balsinha C, Fernandes e Fernandes R, Fernandes e Fernandes J (2000) Computer-assisted carotid plaque analysis: characteristics of plaques associated with cerebrovascular symptoms and cerebral infarction. Eur J Vasc Endovasc Surg 19:118–123
27. Pedro LM, Fernandes e Fernandes J, Pedro MM, Gonçalves I, Dias NV, Fernandes e Fernandes R, Carneiro TF, Balsinha C (2002) Ultrasonographic risk score of carotid plaques. Eur J Vasc Endovasc Surg 24:492–498
28. Pedro LMA (2003) Window to atherosclerosis: high definition ultrasonography in the study of the arterial wall. University of Lisbon, Lisbon, Portugal
29. Lusby RJ, Ferrell LD, Ehrenfeld WK et al (1982) Carotid plaque hemorrhage: its role in production of cerebral ischemia. Arch Surg 117:1479
30. Imparato AM, Riles TS, Mintzer R et al (1983) The importance of hemorrhage in the relationship between gross morphologic characteristics and cerebral symptoms in 376 carotid artery plaques. Ann Surg 197:195

31. Carr S, Farb A, Pearce WH, et al (1996) Atherosclerotic plaque rupture in symptomatic carotid artery stenosis. J Vasc Surg 23:755
32. Gertz SD, Roberts WC (1990) Hemodynamic shear force in rupture of coronary arterial atherosclerotic plaques. Am J Cardiol 66:1368–1372
33. Davies MJ, Richardson PW, Woolf N et al (1993) Risk of thrombosis in human atherosclerotic plaques: role of extracellular lipid, macrophage and smooth muscle cell content. Br Heart J 69:377–381
34. Bassiouny HS, Sakaguchi Y, Mikucki SA, et al (1997) Juxtalumenal location of plaque necrosis and neoformation in symptomatic carotid stenosis. J Vasc Surg 26:585
35. Gronholdt ML, Nordestgaard BG, Wiebe BM (1998) Echolucency of computerized ultrasound images of carotid atherosclerotic plaques are associated with increased levels of triglyceride-rich lipoproteins as well as increased plaque lipid content. Circulation 97:34–40
36. Lammie GA, Path MR, Sandercock PA, Dennis MS (1999) Recently occluded intracranial and extracranial carotid arteries. Relevance of the unstable atherosclerotic plaque. Stroke 30:1319–1325
37. Torvik A, Svindland A, Lindboe CF (1989) Pathogenesis of carotid thrombosis. Stroke 20:1477–1483
38. Gonçalves I, Moses J, Dias N, Pedro LM, Fernandes e Fernandes J, Nilsson J, Ares MP (2003) Changes related to age and cerebrovascular symptoms in the extracellular matrix of human carotid plaques. Stroke 34:616–622
39. Gonçalves I, Moses J, Pedro LM, Dias N, Fernandes e Fernandes J, Nilsson J, Ares MP (2003) Echolucency of carotid plaques correlates with plaque cellularity. Eur J Vasc Endovasc Surg 26:32–38
40. Gonçalves I, Lindholm MW, Pedro LM, Dias N, Fernandes e Fernandes J, Fredrikson GN, Nilsson J, Moses J, Ares MP (2004) Elastin and calcium rather than collagen or lipid content determine the echogenicity of human carotid plaques. Stroke 35:2795–2800
41. El-Barghouty GG, Nicolaides AN et al (1995) Computer-assisted carotid plaque characterization. Eur J Vasc Endovasc Surg 9:389
42. Russell DA, Wijeyaratne SM, Gough MJ (2007) Changes in carotid plaque echomorphology with time since a neurologic event. J Vasc Surg 45(2):367–372
43. Madycki G, Staszkiewicz W (2006) Detailed plaque texture analysis as the alternate method of ultrasound image analysis in predicting the risk of intraoperative microembolism and perioperative complications. Vasa 35(2):78–85

Coronary Atherosclerotic Plaque Characterization By Intravascular Ultrasound

Francesco Ciompi, Oriol Pujol, Josepa Mauri Ferré, and Petia Radeva

Abstract The accurate characterization of in vivo atherosclerotic plaques represents an important task during percutaneous intervention. Intravascular Ultrasound (IVUS) is a catheter-based imaging technique that provides a detailed cross-sectional representation of the internal morphology of the vessel, thus allowing to assess plaque amount and composition. In this chapter the state of the art methods for automatic plaque characterization in IVUS are analyzed. The main classification techniques as well as the most discriminative features are illustrated. Furthermore, a recently presented technique for the fusion of in vivo and in vitro IVUS data is illustrated.

1 Introduction

Coronary heart disease represents the 21% of mortality cause and accounts for 2 millions of lives in Europe. Atherosclerotic plaque formation results from the thickening of the *intimal-medial* segments and an overall thickening of the vessel wall. The term *vulnerable plaque* is commonly attributed to an atherosclerotic plaque that is likely to rupture or fissure, leading to thrombosis, and then to acute coronary syndrome: myocardial infarction, unstable angina pectoris, or sudden cardiac death [1–6]. An accurate analysis of in vivo plaque composition is then an important task in diagnosis and detection of vulnerable atheroma before plaque rupture.

F. Ciompi (✉) • O. Pujol • P. Radeva
Computer Vision Center, Campus UAB, Edifici O, Bellaterra, Spain

University of Barcelona, Gran Via de Les Cortes Catalanes, 585, 08007 Barcelona, Spain
e-mail: fciompi@maia.ub.es; oriol@maia.ub.es; petia@cvc.uab.es

J.M. Ferré
University Hospital Germans Trias i Pujol, Carretera de Canyet s/n. 08916 Badalona, Spain
e-mail: mauritri@gmail.com

J.M. Sanches et al. (eds.), *Ultrasound Imaging: Advances and Applications*,
DOI 10.1007/978-1-4614-1180-2_8,

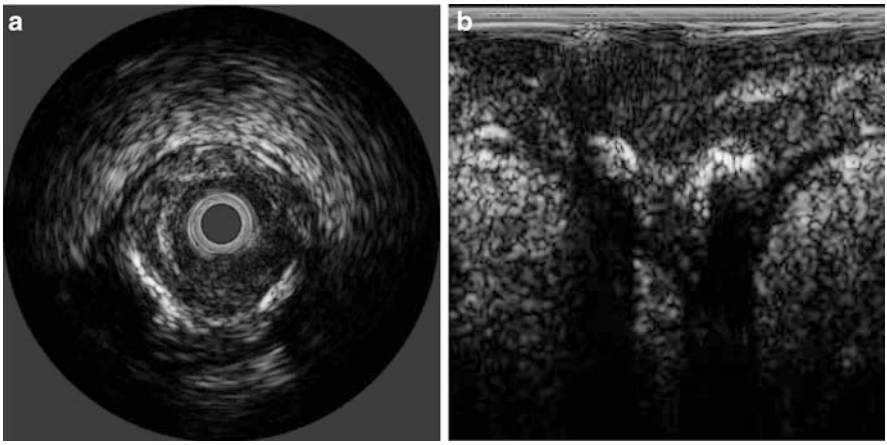

Fig. 1 (**a**) In vivo IVUS image in cartesian coordinates, representing the *cross-sectional* IVUS image and (**b**) in polar coordinates

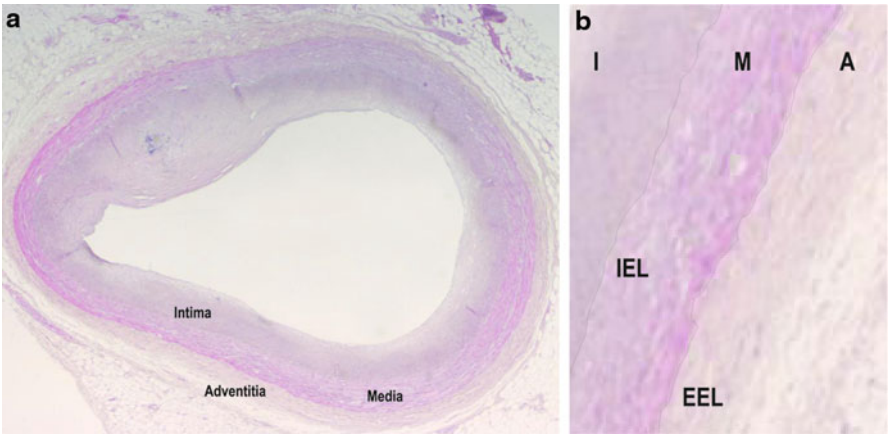

Fig. 2 Histological image (at the microscope) of ex vivo coronary section (**a**). The three layers are marked and (**b**) the detail of the interfaces (internal and external elastic lamina) is shown

Intravascular Ultrasound (IVUS) is a catheter-based imaging modality that provides an accurate luminal and transmural image of vascular structures [7]. It allows the visualization of the full circumference of the vessel wall, thus showing the tissue morphology and composition [8, 9] (see Fig. 1).

The use of IVUS facilitates direct measurements of lumen size, including minimum and maximum diameter and cross-sectional area as well as the characterization of atheroma size, plaque distribution, and lesion composition [10]. Three main regions, surrounding the luminal area of the vessel, can be distinguished in an IVUS image: the *intima*, the *media*, and the *adventitia* (see Fig. 2).

The *intima* is normally a thin layer of endothelial cells: this layer substantially and often unevenly thickens into atherosclerosis. The *media* consists of multiple layers of smooth muscle cells arranged helically and circumferentially around the lumen of the artery. Finally, the *adventitia* is the external layer, essentially composed by fibrous tissue, i.e., collagen and elastin [11]. Estimation of the vessel area is based on the measurements of the media-adventitia border, and plaque area is derived by subtracting lumen area from vessel area.

Several IVUS-based approaches for the automatic assessment of plaque composition have been proposed in the last ten years, mainly based on image texture analysis [12–14] as well as on raw Radio Frequency (RF) signals processing [15–20]. Some approaches use Autoregressive Models (ARM) [15–17] or the Fourier Transform [18, 20] to obtain a description of the tissue in the frequency domain, from which spectral features are extracted. Approaches using the *Integrated Backscatter* parameter [21–23] or the *Wavelet coefficients* [24] have been also proposed.

Most of the proposed methods for the automatic plaque characterization are based on a model that learns the plaque properties by labeled IVUS examples. In order to correctly train a model, reliable labeled IVUS data are necessary. The reliable correspondence between an atherosclerotic plaque and the corresponding IVUS data can only be obtained by histological analysis of *post-mortem* coronary arteries. Histology is in fact the only procedure that allows to know the real plaque nature in a certain position of the vessel. Unfortunately this methodology suffers from the complicated procedure of obtaining in vitro data: scarce arteries availability, frequent tissue spoiling during analysis and the difficulty in finding the right correspondence between IVUS and histological image.

In addition, in almost all the known plaque characterization methods, the discriminative power is assessed on in vitro plaques, then implicitly extending the discriminative property to in vivo data as well. This erroneous assumption is implicitly based on the hypothesis that differences between in vivo and in vitro IVUS data are negligible.

In this chapter some of the most important state-of-the-art techniques for automatic plaque characterization in Intravascular Ultrasound are presented. Furthermore, recent advances in the research topic of fusing in vivo and in vitro IVUS data for plaque characterization are described, and some results are provided.

2 In Vitro Data Validation Procedure

A possible procedure for the acquisition and validation of *post-mortem* IVUS data is now described. The coronary artery (separated from the heart) is first put on a mid-soft plane and filled (using a catheter) with physiological saline solution at constant pressure (around 100 mmHg), simulating blood pressure (see Fig. 3). In the panel the distal and proximal position, together with left and right hand are marked to be used as a reference during histology. The probe is then introduced and RF data are

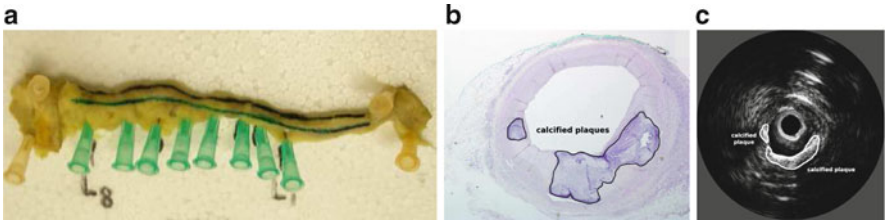

Fig. 3 Set up for IVUS acquisition from post-mortem artery. (**a**) Coronary artery on the plane with marked positions clearly shown; (**b**) plaque segmentation on histological image and (**c**) segmentation on corresponding IVUS image

acquired in correspondence of plaques. These positions can be clearly marked on the external part of the artery. The artery is then cut in correspondence of previously marked positions and plaque composition is determined by histological analysis.

As an alternative, a specially designed box containing the artery can be used, allowing the automatic cut of the vessel at a fixed number of positions by superimposing a dedicated set of knives [18]. With this procedure, a set of equally-spaced artery cuts of the artery are obtained.

For each cut, an image of the tissue at the microscope is obtained. Given the reference points in the panel and in the IVUS image orientation it is possible to put in correspondence the plaques detected by histology with their respective areas in the IVUS image. The different conditions and modalities in which the two images are acquired are profoundly different. The mechanical consistence given to the artery while acquiring IVUS data is lost when cutting the vessel. Phenomena of tissue spoiling and a certain error in finding the exact correspondence between the IVUS and histological image make hard to get a good registration and, consequently, a reliable automatic labeling. Hence, the labeling process can be performed manually by joint cooperation of experts and pathologist or by using a dedicated software able to register the two images obtained by different modalities and different approaches [16,17]. The plaques in IVUS data are thus validated and a ground truth is obtained.

3 Plaque Characterization by Intravascular Ultrasounds

Different tissue types exhibit different acoustic properties and, consequently, different intensity and shape of the reflected ultrasonic wave; furthermore, the contribution of the scattered component is also different for each tissue. As a result, in the IVUS image, areas corresponding to different tissues exhibit different grey-level intensity and textures.

Most of the proposed plaque characterization methods are formulated as *pattern recognition* problems. For this reason, two main steps can be identified in each method: (1) the definition and extraction of discriminative features, describing the properties of different tissues; (2) the training of a classifier, used to characterize

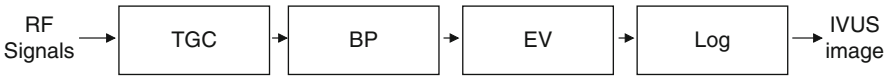

Fig. 4 Schematic example of IVUS image formation from RF signals

each position of the IVUS frame as belonging to one of the known plaque types. In this section the features used in the state-of-the-art methods are first presented, then the most common classification techniques used in the plaque characterization field are described.

3.1 Features Extraction

In the state-of-the-art plaque characterization methods, two main groups can be recognized: the methods based on *image analysis* and the methods based on *radio frequency analysis*. In this section, the features used in the two approaches are presented.

3.1.1 Image-Based Features

The first plaque characterization method based on the analysis of the texture in the IVUS image has been presented in [12]. The features used in this approach are: (1) *radial profile*, (2) *long-run emphasis*, and (3) *fractal dimension*. Despite of the high accuracy achieved, the main problem of using the IVUS images obtained with the IVUS equipment is the lack of normalization in data they provide. In order to improve the tissue visualization, physicians are used to change the imaging parameters of the IVUS equipment, thus making the set of images and, consequently, image-based features, not comparable. In order to avoid this problem, the raw radio frequency signals captured by the IVUS equipment can be used to reproduce the image formation process [14]. A common approach to IVUS image formation from RF data foresees, at least, the following steps (see Fig. 4):

- *Time Gain Compensation (TGC):* as the US propagating in the tissue is affected by an attenuation due to depth, it is necessary to compensate it by a TGC function. One possible TGC function could be: $T(r) = 1 - \mathrm{e}^{-\beta r}$, where $\beta = \ln 10^{\alpha f/20}$, α is the attenuation factor of the tissue measured in $dB/MHz \cdot cm$, f is the frequency of the transducer in MHz, and r is the radial distance from the catheter in cm.
- *Band Pass filtering:* data can be then filtered by a band-pass filter in order to reduce the noise effect and spurious harmonic components outside the band of interest. For this purpose, a Butterworth filter is suitable, given that its frequency response is as flat as mathematically possible in the passband.

- *Envelope:* after filtering, the envelope of the signal has to be recovered, in order to change from bipolar to unipolar signal and to achieve the final conversion between 0 and 255. This can be done for example by taking the absolute value of the Hilbert transform of the signal.
- *Logarithmic compression:* This transformation maps a narrow range of low gray-level values in the input image into a wider range of output levels; the following formula can be used [25]: $\mathrm{RF}_{\log} = \frac{\log(1+(e^t-1)\mathrm{RF}_{\mathrm{env}})}{t}$, where $\mathrm{RF}_{\mathrm{env}}$ represents the RF data after the envelope computation, and $\mathrm{RF}_{\log}$ the output of the logarithmic compression.

In [14] the reconstruction process is used to create a set of IVUS images of in vivo cases. Textural features are then extracted by using: (1) *co-occurrence matrix*, (2) *local binary patterns*, and (3) *gabor filters*.

3.1.2 Radio Frequency-Based Features

RF data from the unprocessed backscattered ultrasound signal provide an alternative to greyscale image analysis. Theoretically, the analysis of the IVUS-RF data provides a more accurate and reproducible technique for measuring tissue properties because it is not subject to machine-dependent processing, subsampling, interpolation, quantization, and even operator-dependent settings [26].

The most important approaches based on RF data processing are now analyzed by focusing on the analysis of the used features. Most of the methods process the RF data frame, formed by N A-lines and M samples.

Acoustic Impedance (Z)

It is known that the US wave propagates with different velocity in different tissues; this comes from the equation of the wave propagating through a tissue with density ρ and with acoustic impedance ζ. Then, the information on the relative acoustic impedance can be used as a parameter to classify plaque types, since they are considered as different tissues. The method presented in [19] is based on this phenomenon. It assumes that ultrasound pulse is well approximated by using the Plane Wave Born Approximation (PWBA) deconvolved inverse scattering technique [27].

Integrated Backscatter (IB)

The first method based on IB was proposed in 1989 and was oriented to the detection of acute myocardial infarction and re-perfusion via M-mode echocardiography [28].

Table 1 Integrated backscatter values obtained by histological analysis of post-mortem tissues. The values are provided as mean value ± 1 dB. Data extracted from [22]

Histology	IB [dB]
Calcified tissue	$-30 < \text{IB} \leq -23$
Mixed lesion	$-55 < \text{IB} \leq -30$
Fibrotic tissue	$-63 < \text{IB} \leq -55$
Lipidic core	$-73 < \text{IB} \leq -63$
Thrombus	$-88 < \text{IB} \leq -80$

The IB is an intrinsic parameter of the electrical US signal and can be computed as [21]:

$$\text{IB} = 20 \log \left(\frac{\frac{1}{T} \sum_0^T V^2}{\frac{1}{T} \sum_0^T V_0^2} \right), \tag{1}$$

where V is the signal voltage from a selected Region of Interest (ROI) in the RF data frame, V_0 is the smallest signal voltage that the system can detect, and T is the integration interval.

It has been shown that the IB parameter combined with two-dimensional echo can differentiate the tissue characteristics in both in vivo and ex vivo studies [21,22]. In Table 1 the computed value of the IB parameter when characterizing tissues in in vitro cases are presented when discriminating calcifications, mixed lesions, fibrous tissue, lipidic core, and thrombus. Since no overlaps in the obtained values are encountered, the discriminative power of this parameter is confirmed (see Table 1).

A plaque characterization system based only on IB parameter is now distributed only in Japan (YD Co. Ltd, Tokyo).

Power Spectrum

Based on the hypothesis that different tissues behave differently in the frequency domain, several approaches based on the analysis of power spectrum have been proposed. Mainly, given the RF representation of an IVUS frame, for each ROI of N_r samples and M_r contiguous A-lines, a power spectrum is associated to each point by averaging the power spectra computed in the lines belonging to the ROI. The power spectrum can be computed by means of the Fast Fourier Transform (FFT) [15, 18, 20] or by using the AutoRegressive Model (ARM) [14, 16, 17, 29].

Given the power spectrum, a set of spectral features can be extracted. Some features have been successfully used in plaque characterization techniques, as the mean power (dB), maximum power (dB), spectral slope (dB/MHz) (a least-squares linear regression over the given bandwidth), y-axis intercept of spectral slope (dB) (intercept of the straight line with the y-axis at 0 Hz) [15]. In addition, the value of the frequencies corresponding to maximum and minimum power can be used [16, 17]. In [16, 17] these features are extracted in a frequency range of

17–42 MHz, corresponding to the −20 dB bandwidth of the system. This set of features, commonly known in literature as the *seven-features* approach, together with the Integrated Backscatter (IB) represent the basis of a commercial product called *Virtual Histology* (VH), implemented in the Volcano (Rancho Cordova, CA) IVUS clinical scanners that offer near-realtime tissue characterization in vivo [30].

Alternatively to the presented spectral features, a *full-spectrum* approach can be considered, where the Fourier Transform is used [18, 20]. The use of a full-spectrum analysis demonstrated to produce more accurate results, compared with the seven-features approach, classifying fibrolipidic, lipidic, fibrotic, and calcified tissue: when using a 40 MHz catheter in fact, a lot of variations can be found in the main bandwidth of the signal (20–60 MHz), thus justifying a full-spectrum analysis [18]. In the full-spectrum approach the power spectrum, with frequency range from 0 to 100 MHz, is discretized using a certain number of bins and then used as feature vector for each point (the center of a ROI) of the IVUS frame. This approach is implemented in the iMap Plaque Characterization software provided with the iLab IVUS equipment (Boston Scientific).

Wavelet-Based Approach

The wavelet analysis of RF signals has been also studied in recent years [24, 31]. A wavelet is mainly a waveform of limited duration and zero average amplitude [32]. The wavelet analysis, applied to IVUS-RF signal, consists in the computation of wavelet coefficients, localized by the amplitude and the position of wavelets.

The hypothesis in this kind of approach is that the IVUS-RF signal belonging to different tissues exhibits different behavior when analyzed by wavelet, and that the wavelet coefficients, computed at different scales, could be the discriminative measures to be used in the tissue characterization [26].

This approach has been proved to be appropriate in discriminating the fibrous from the fatty areas within atherosclerotic plaques [24].

Joining Textural and Spectral Features

Recently [29], an approach that proposes to combine both textural and spectral features provided interesting results in the field of plaque characterization. The used feature vector is constructed by concatenating image textural and spectral features with the aim of blending the appearance of the tissues with information obtained from their spectral content. The main idea is that image-based and RF signal analysis provide complementary data for the accurate description of tissue composition and leads to a rich set of features to be selected and weighted by the classifier. The approach leads to an overall accuracy $A = 89.93\%$ in classifying fibrotic, lipidic, and calcified plaques in vitro [29].

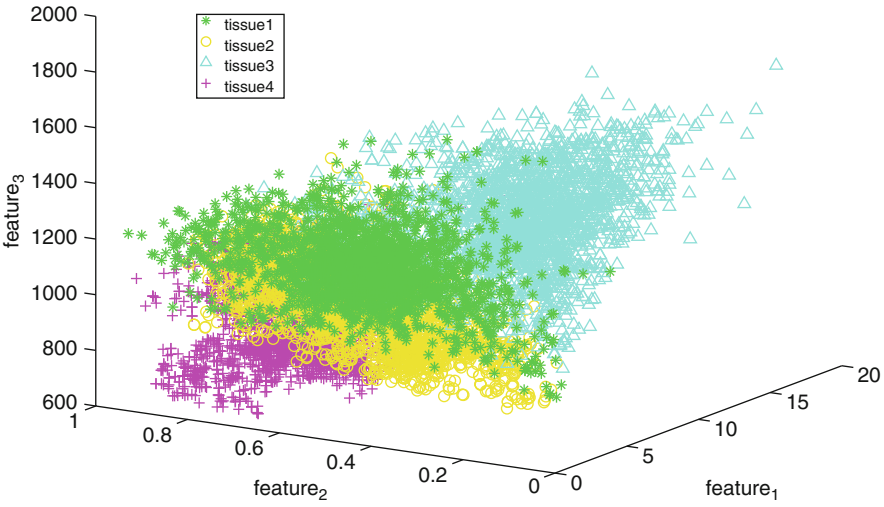

Fig. 5 Feature space. A set of point acquired from four different tissue types are represented in the space of three discriminant features

3.2 Tissue Classification

A classifier is a probabilistic model (discriminative or generative) with a set of parameters determined (learned) during the training process. The model is in fact able to learn the features of the input data, and to tune its parameters according to data. When the training process is over, the set of learned parameter is finally saved and the classifier is ready to be used to characterize unknown examples.

The atherosclerotic plaque characterization problem implies the definition of a multi-class classifier. Except for some approaches that discriminate for example fibrotic from fatty (lipidic) plaques, the main scenario implies in fact the discrimination among fibrotic, lipidic, and calcified plaques. Furthermore, the necrotic core, fibrolipidic, and lipidic with calcifications tissues are also considered in some approaches. The characterization problem consists in separating, in the feature space, clouds of points belonging to multiple classes (Fig. 5).

Several approaches have been presented to solve the multi-class tissue characterization problem: we will refer to them with the word "architecture," since they often consist in combining a set of simple classifiers into a more complex framework.

3.2.1 Decision Tree

One simple architecture for the discrimination of different tissues is the *decision tree* [16,17]. Starting from the main node (root), during the training process, at each node the input data are split into sub-groups according to the most discriminative feature in that node.

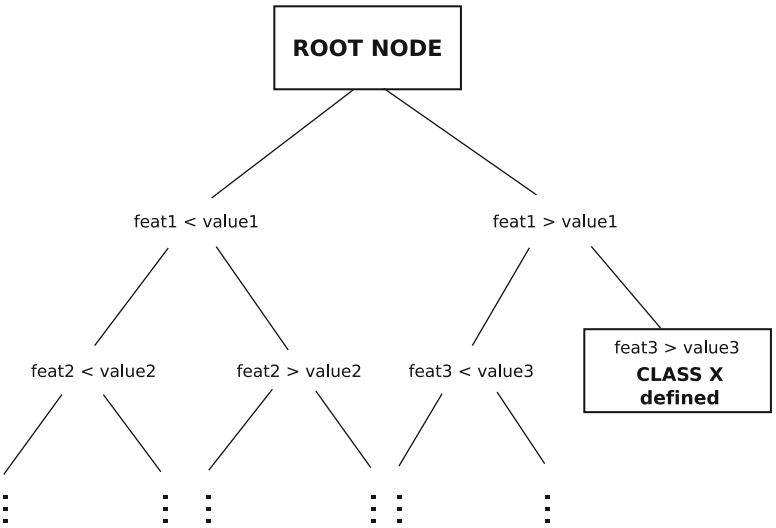

Fig. 6 Decision tree. Starting from the ROOT NODE, at each node the most discriminant feature is computed, thus defining the "path" to the recognition of each class

When a new unknown example is classified, its features are then compared with the value learned at each node, thus assigning it a label. Several measures can be used to assign the most discriminant feature to a node and to define its value. The most important ones are based on the *Entropy*, the *Information Gain*, the *Gini Index* and the *Partition Distance*. In Fig. 6 an example of Decision Tree is depicted. In each node, the generic feature $feat_i$ is considered to partition the data into two subgroups. A test data sample that exhibits $feat_1 > value_1$ and $feat_3 > value_3$ is then classified as belonging to the class X.

3.2.2 Error-Correcting Output Code

Another effective approach for the solution of multi-class plaque characterization problem is the use of Error-Correcting Output Code (ECOC) [14, 29, 33, 34].

ECOC [35] is a technique that combines N binary classifiers to solve a K-classes classification problem. A binary classifier is a model trained to discriminate two set of data. Given an unknown example as input, the binary classifier is able to label it as belonging to the class 1 or to the class 2, thus producing a $+1$ or -1 output value, respectively. For each class a *codeword* $c_k = \{1,-1\}^{1\times N}$ is obtained ($k = 1,...,K$). Based on a chosen coding strategy, a matrix $\mathbf{M} = \{1,0,-1\}^{K\times N}$ is designed (Fig. 7), in which each column represents a binary classifier H_j (*dichotomy*) and each row represents a class. A value 1 in position $\mathbf{M}(k,j)$ means that the j^{th} dichotomy classifies an unknown example as belonging

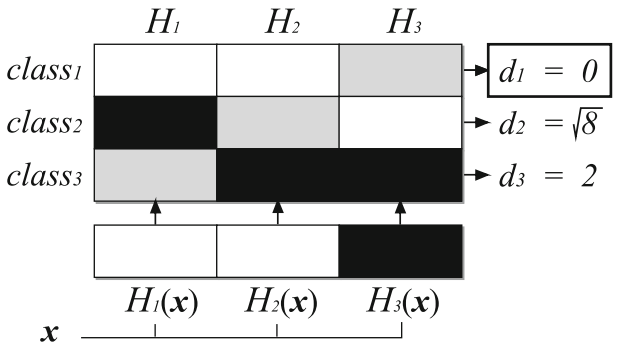

Fig. 7 ECOC matrix for a 3-class problem, One-vs-One coding technique and attenuated Euclidean distance (AED) technique; the distance values are showed for each row of the matrix. *White*, *black* and *gray rectangles* represent the values (1, −1, and 0), respectively

to the class k, a value -1 means that it belongs to the class $q \neq k$ and a 0 value means that we do not care about that result, regarding class k. Therefore, to classify an unknown example, the distance between the obtained codeword and each row m_k of the matrix $\mathbf{M}$ is computed: the output class corresponds to the value k reporting the minimum distance. Different *coding* technique can be used. The most popular one is the *one-vs-one*, in which each pair of classes is considered and the respective classifiers are trained. Alternatively, a *one-vs-all coding* can be used, where each class is discriminated against the other classes. With respect to the *decoding* technique, different distance measures can be used. The most common ones are the *Euclidean* and *Hamming* distance. The benefits in using an ECOC framework are mainly (1) the possibility of combining several binary classifiers into a multi-class framework, (2) the automatic error-correction property of ECOC of correcting some errors in the prediction, and finally (3) the flexibility of a multi-class architecture in which several variations, like the sub-class classification [33] can be easily adopted.

In Fig. 7 an example of multi-class classification using ECOC is depicted. The number of classes is three and the coding technique is the *One-vs-One*; hence, three dichotomy are required: $H_i(\mathbf{x})$, for $i = 1, 2, 3$. The test example $\mathbf{x}$ is then classified by each binary classifier H_i and a binary code $\mu = [110]$ is obtained. The Euclidean distance between μ and each row of the ECOC matrix is then computed, resulting in the three values $d_1 = 0$, $d_2 = \sqrt{8}$ and $d_3 = 2$. According to the decoding criterium, the most probable class for $\mathbf{x}$ is the first one.

3.2.3 Ensemble Architecture

The last multi-class architecture that is presented is the Ensemble framework [20]. Usually, during a standard training process, a classifier is trained, in order to learn parameters according to input data. We can call it an “expert” for that particular

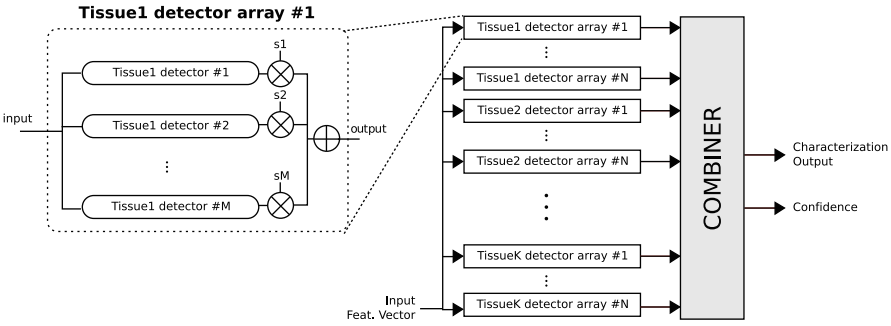

Fig. 8 Bagging/ensemble architecture. Given the number of K classes, an array of M binary classifiers is constructed. Their prediction is combined taking into account the classification reliability s_i of each one. The output is then repeated N times for each one of the K classes and then combined to produce the output. Optionally, a classification confidence measure can be obtained

data characterization problem. The main idea of an ensemble architecture consists in using several experts, instead of one, i.e., several classifiers, trained to solve the same problem.

According to the combination policy of these experts different ensemble architectures can be built. Two of the most popular ones are *boosting* and *bagging*. The *boosting* procedure combines experts in an incremental way. Given a set of experts, at each step of the boosting process a new expert is added to the ensemble so that it focusses on data that was previously misclassified. This selected set is usually combined by means of a weighted additive model.

Another important family of ensembles comes from the *bagging* process. This process specializes each expert on a different sampling of the data set. Then, by means of voting procedure these experts are combined. This process results in very robust classifiers. For example, in the problem of discriminating the fibrotic from the rest of tissues, N binary classifiers are trained: each classifier is trained with a set of data randomly selected, with reinsertion, from the original training dataset. Hence, M classifiers are obtained for each binary problem, and each one of them shows a certain classification accuracy, depending on how the randomly selected dataset is representative of the global training dataset: this accuracy is taken into account by weighting the result of each single prediction with the weight s_i. Then, in order to discriminate a tissue, a combination of the predictions of the M classifiers is considered; this combination can be seen as a monolithic macro-block (array) for the detection of this particular tissue (Fig. 8). In the multi-class classification problem, following the bagging architecture, these blocks are repeated N times for each considered tissue, thus generating the final predicition on an unknown example by further combining the predictions of each macro-block.

Similar to that exhibited by the ECOC framework, this approach embeds a kind of error-correction capability, given by the contribution of several “experts” and by

the combination of their "opinions." Furthermore, the architecture foresees the use of a large number of macro-blocks ($M \times N \times K$) and though this fact decreases the probability of error, it increases the computational time.

3.3 Validation of the Methodology

Validated IVUS data are obtained from a set of ex vivo cases. Even though they consist in post-mortem cases, the intra-patients variability in data properties is still applicable. For this reason, the procedure of validating the discriminative power of the plaque characterization method must carefully assign data of different patients to the training and the test data set. The training set represents in fact the data used to train the classifier, while the test data set is used to assess the discriminative power of the trained classifier. It is clear that when the classifier is used to characterize examples of the training set, the classification error tends to zero, since the discriminative bounds in the feature space have been actually modeled on that data. For this reason, it is extremely important that no examples of the test data set are included into the training data set. Furthermore, in order to obtain completely reliable numerical values, the testing procedure must be repeated a certain set of times (rounds) and then statistical results must be extracted.

3.3.1 N-Fold Cross-Validation

The most common cross-validation technique is called *N-fold cross-validation*. It consists in considering the whole available data set and partitioning it into N parts (blocks) containing the same number of data examples. A classifier is then trained by using $N-1$ blocks and its discriminative power is assessed by testing the remaining block. This process is repeated N times and the final classification performance is given as mean value and standard deviation of the obtained results.

The performance parameters typically considered in a plaque characterization problem are:

- Accuracy (A) $= \frac{\mathrm{TP}+\mathrm{TN}}{\mathrm{TP}+\mathrm{TN}+\mathrm{FP}+\mathrm{FN}}$
- Sensitivity (S) $= \frac{\mathrm{TP}}{\mathrm{TP}+\mathrm{FN}}$
- Specificity (K) $= \frac{\mathrm{TN}}{\mathrm{TN}+\mathrm{FP}}$
- Precision (P) $= \frac{\mathrm{TP}}{\mathrm{TP}+\mathrm{FP}}$

where TP = true positive, TN = true negative, FP = false positive, and FN = false negative.

Among the N-fold cross-validation techniques, the ten-fold and the five-fold [36] are largely used.

3.3.2 Leave One Patient Out

Even though the N-fold technique is largely used, it may produce overconfident results, due to the fact that a random sampling does not ensure *i.i.d.* data splits. In particular, data from the same patient may be erroneously considered in both training and testing process. This may bias the results of the method because each example on the dataset is not independent with respect to the rest of the examples of the same patient.

An effective technique for assessing the reliable quality of a classifier, in the context of plaque characterization is the *Leave-One-Patient-Out* (LOPO). It can be considered as a special case of the N-fold cross-validation, where N now consists in the number of patients and each block actually consists in the set of all examples of each individual subjects. In this way, the complete separation between the training and the validation set is assured, and the intra-patients variability is taken into account. For these reasons, the results provided by the LOPO technique can be considered as indicative of the behavior of the designed model in presence of a new unknown clinical case. During the cross-validation method in fact, the validation subject is a completely unknown patient.

4 Fusing In Vivo and In Vitro Data for Plaque Characterization

It is known that the presence of *blood* in vivo may modify the ultrasound echo with respect to in vitro cases. Furthermore, even when the protocol of in vitro data acquisition aims to reproduce the in vivo conditions as much as possible (for example by filling the post-mortem artery with blood [18, 20]), it is impossible to exactly reproduce the morphological and mechanical properties of an in vivo artery. Hence, data from these two acquisition modalities cannot be considered as perfectly comparable.

Nevertheless, the two data types could share areas in the feature space, and the inclusion of in vivo data, after a proper selection process, could enhance the in vitro data set generalizing the separation among classes.

In [29] a data fusion process, based on a reformulated version of the *Sequential Floating Forward Selection* (SFFS) algorithm [37] is presented. The main idea consists in keeping the in vitro data set as a seed in the feature space and enhance its distribution by feeding it with a selected set of in vivo data. The goal is to create an *enhanced* data set used to train a classifier that can fulfill the following requirements: (1) to exhibit the same (compared with the classifier trained with the initial in vitro data set) or even better discriminative power on the in vitro validation set and (2) to provide more accurate plaque classification on in vivo cases as well. The process is regulated by a classification performance function J, in the context of plaque characterization (named *pSFFS*), and results are evaluated by *Leave-One-Patient-Out* (LOPO) [34] cross-validation technique. The method aims at discriminating among *fibrotic*, *lipidic* and *calcified* tissues, and the multi-class

classification problem is solved by adopting the *Error-Correcting Output Code* (ECOC) technique [35, 38] using AdaBoost [39] with Decision Stumps as weak classifier. The main parts of the methodology are now described.

4.1 Sequential Floating Forward Selection

SFFS has been proposed in [37] as a features selection algorithm, based on inclusion and conditional exclusion of data. In the pSFFS approach, an IVUS *frame* is considered as containing different plaques which are considered as a monolithic block of information, i.e., all the plaques in a frame can be included or removed from the data set but partial inclusion/exclusion of a specific class example (e.g., removing the *calcified* and keeping the *fibrotic* plaque) is not allowed. This approach is justified by the idea that the inter-patient differences in appearance of plaques will be preserved if the information of a single frame is treated as monolithic; furthermore, the over-fitting phenomenon of the classifier on a specific set of examples is potentially avoided.

Algorithm 1 Function $\widehat{CP} = CP(X^p, \bar{Y}, f_{cv})$

Require: X^p {The *in-vitro training* set}
Require: $\bar{Y}$ {The *in-vivo* data set}
Require: f_{cv} {The cross-validation function}
Ensure: $\widehat{CP}$ {A classification performance parameter}
1: define N {number of folds required by the cross-validation technique}
2: initialize $CP[N] = 0$ {N-elements empty vector}
3: **for** i = 1:N **do**
4: define $x_i \subset X^p$ {*test* set}
5: define $TRAIN_i = \{X^p \setminus x_i\} \cup \bar{Y}$
6: define $TEST_i = x_i$
7: $classifier = training(TRAIN_i)$
8: $CP[i] = test(classifier, TEST_i)$
9: **end for**
10: $\widehat{CP} = mean(CP) \pm std(CP)$

As shown in Fig. 9, the inclusion criterion actually consists in evaluating a classification performance parameter while including data. For this purpose, a proper definition of the *training/testing* process represents a key part of the algorithm. Let us define as $p = 1, \ldots, N_P$ the index of in vitro cases. In order to define the data sets to use in the data fusion algorithm, the in vitro data set is split into three parts (Fig. 10): the first part, called X^p, is obtained by removing the p^{th} necro case from the whole data set and it is used in the selection process, thus representing the *training* data set, while the second part, called X^p_{val} is not used during the selection process and represents the *validation* data set. The third part is related to the data inclusion process and is defined below.

The parameter that controls the data selection process in the *pSFFS* is called J and it is a value that depends on the result of a classification step. In this approach,

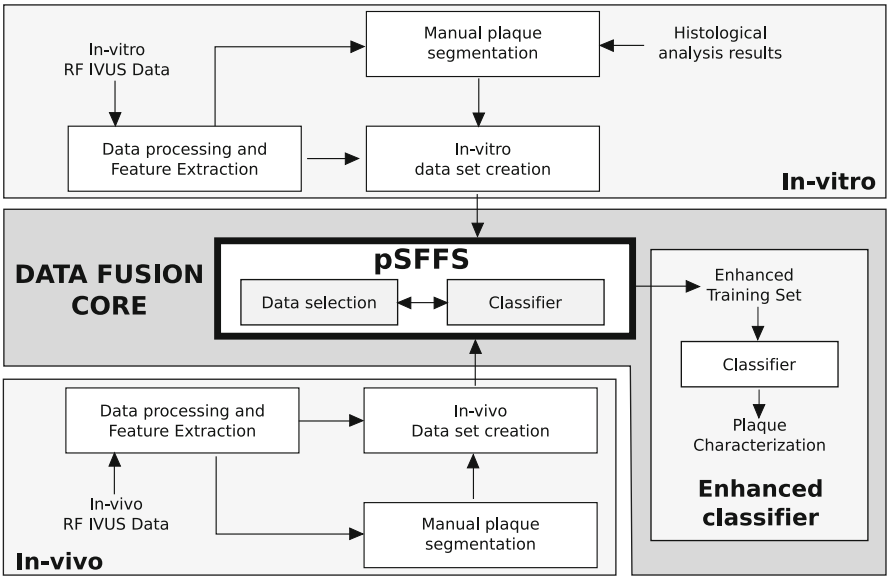

Fig. 9 Schema of the plaque characterization framework. The in vitro and in vivo blocks represent the IVUS data acquisition and processing task. The *pSFFS* block represents the data fusion algorithm, including a task for in vivo data selection and a classifier that evaluates the classification performance at each step, regulating the inclusion process

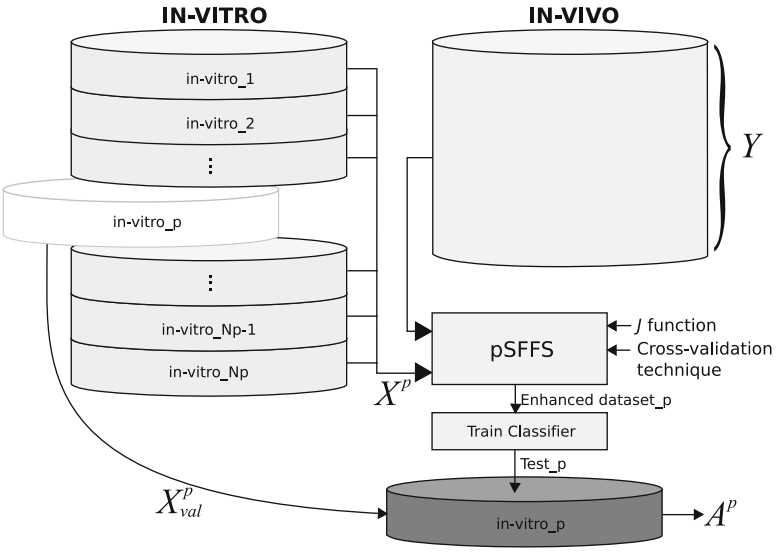

Fig. 10 Detailed description of the data fusion core (see Fig. 9). According to the Leave-One-Patient-Out technique, the in vitro data set is used in both the data fusion process and in validating the discriminative power of the enhanced classifier, while the in vivo data is solely involved into the data fusion process

the classification is performed on in vitro data, being the only reliable data set to use while looking for an improvement in tissue discrimination. In order to produce stable and reliable classification results, a cross-validation technique must be used. The J parameter is then a function of the classification performance, computed according to the defined cross-validation process.

Once the cross-validation technique is defined, the third part of the data set is then obtained as a subset of the X^p *in vitro training* data set and represents the *test* data: it is used during the in vivo data selection process, to assess the classification performance at each iteration k of the process.

4.2 Cross-Validation Scheme

Before illustrating the *pSFFS* algorithm, the cross-validation procedure used to obtain the classification performance parameters necessary to compute the value of J is defined. Let us call f_{cv} the chosen cross-validation function (for example *Leave One Patient Out* or *N-fold cross validation*), $\bar{Y}$ a generic set (or subset) of in vivo data, and $\widehat{CP}$ a generic classification parameter (for example $\widehat{CP}$ = *overall accuracy*). The classification performance is then obtained as depicted[1] in Algorithm 1. Finally, the J value is computed as $J(\widehat{CP})$. The formulation and properties of J will be explained in Sect. 4.4. As suggested in [36], the *five-fold* cross-validation is used as appropriate during the data selection process.

4.3 Data Selection Process

The data selection process of the *pSFFS* algorithm for the creation of the enhanced data set is now formulated.

Let us call X the initial *training* set composed of frames from in vitro (actually X_p) and Y the set of frames of in vivo cases. The *pSFFS* requires the definition of a function of the classifier performance J, that controls the inclusion–exclusion process, and also a cross-validation technique to use while computing J. When both initial data and the required functions are defined, the *pSFFS* method can be formulated (see Algorithm 2). The algorithm alternates two phases: an *inclusion* loop (lines 12–18) and a *conditional exclusion* of one frame (lines 23–28). The condition to include one frame is that the training/test process by cross-validation on the data set X_{k+1} produces a score J that is greater than before (lines 12–13); with the same rule, the exclusion step can remove one of the frames already included in the set if this increases J (lines 24–25). If during the conditional exclusion none of the candidate frames increases J, the algorithm checks the number of times the

[1]The function is described in pseudo-Matlab code.

Algorithm 2 pSFFS

Require: X {The set of *in-vitro* frames}
Require: Y {The set of *in-vivo* frames}
Require: $J()$ {The J function definition}
Require: f_{cv} {The cross-validation function}
Ensure: X_{EN} {The enhanced (fused) data set}
1: Note: to simplify the formulation, $J(CP(X,Y_T,f_{cv})) = J(X)$
2: $k = 0$
3: $d = 0$
4: set d_M
5: $X_0 = X$
6: $Y_T = \emptyset$
7: $X_{EN} = X$
8: STOP = *false*
9: INCLUDE = *true*
10: **while** !STOP **do**
11: **if** INCLUDE **then**
12: $y^+ = \arg\max_{y \in Y \setminus X_k} J(X_k \cup y)$
13: **if** $J(X_k \cup y^+) > J(X_k)$ **then**
14: $Y_T = Y_T \cup y^+$
15: $X_k = X_0 \cup Y_T$
16: $X_{EN} = X_0 \cup Y_T$
17: $Y = Y \setminus y^+$
18: $k = k + 1$
19: **else**
20: INCLUDE = *false*
21: **end if**
22: **else**
23: $y^- = \arg\max_{y \in X_k} J(X_k \setminus y)$
24: **if** $J(X_k \setminus y^-) > J(X_k)$ **then**
25: $Y_T = Y_T \setminus y^+$
26: $X_k = X_0 \cup Y_T$
27: $X_{EN} = X_0 \cup Y_T$
28: $k = k + 1$
29: INCLUDE = *true*
30: **else**
31: $d = d + 1$ {Increase the number of time J decreased}
32: **if** $d > d_M$ **then**
33: STOP = *true*
34: **else**
35: $y^+ = \arg\max_{y \in Y \setminus X_k} J(X_k \cup y)$
36: $Y_T = Y_T \cup y^+$
37: $X_k = X_0 \cup Y_T$
38: $Y = Y \setminus y^+$
39: $k = k + 1$
40: **end if**
41: **end if**
42: **end if**
43: **end while**

J value decreased (line 32). In the case J decreased too many time, actually more than d_{M} times, the algorithm stops, otherwise the algorithm admits an *unconditional inclusion* and updates d value. This stop procrastination procedure is necessary to avoid stopping the algorithm at the first maximum value since it can be suboptimal. In each case, the optimal set is stored (lines 16,27), in order to obtain the best achievable classification performance. Hence, at the end of the selection process, the enhanced data set consists in the combination of in vitro/in vivo data obtained in correspondence of $J_{\max} = J(X_{\mathrm{EN}})$.

4.4 Design of J Function

The whole *pSFFS* is regulated by the function J, thus its definition is critical for the algorithm performance. In this section the analytical formulation of the parameter J as a function of classification performance parameter is defined.

Given a generic classification results, the *sensitivity* (S) parameter can be defined as

$$S = \frac{\mathrm{TP}}{\mathrm{TP} + \mathrm{FN}},$$

where TP = *true positives* and FN = *false negatives*. In the plaque characterization problem, it is clear that a high sensitivity in classifying the test set assures that validated plaques are classified as such. Hence, the mean sensitivity, together with the overall accuracy

$$A = \frac{\mathrm{TP} + \mathrm{TN}}{\mathrm{TP} + \mathrm{TN} + \mathrm{FP} + \mathrm{FN}},$$

where TN = *true negatives* and FP = *false positives*, are the parameters to maximize. For this reason, J is defined as a weighted linear combination of the *weighted averaged sensitivity* over all the classes and the *overall accuracy* as

$$J_k = \alpha \underbrace{\sum_{l=1}^{N_c} w_k^l S_k^l}_{J^S} + (1-\alpha) A_k, \tag{2}$$

where S_k^l and w_k^l are the *sensitivity* and the *weighting* for the class l at algorithm iteration k, respectively, N_c is the number of classes, A_k is the overall accuracy and $\alpha \in [0,1]$ is a coefficient that regulates the importance of each term. To avoid the algorithm to increase the sensitivity of a class at the cost of an excessive reduction of other classes sensitivity, w_k^l is dynamically defined to be inversely proportional to the class *sensitivity* itself:

$$w_k^l = \frac{\log\left(\frac{1}{S_k^l}\right)}{\sum_{l=1}^{N_c} \log\left(\frac{1}{S_k^l}\right)} \tag{3}$$

During iteration k, if one of the classes has a *sensitivity* close to one, the corresponding weight tends to zero. For this reason, this class will poorly influence the inclusion/exclusion process letting the *pSFFS* algorithm to search for frames that improve other classes sensitivity. The sensitivity-based term of J equation is denoted as J^S. Finally, the term proportional to the accuracy guarantees an inclusion process in which not only the sensitivities are balanced, but also the global classification performance is improved. The importance of both the sensitivity and accuracy terms is regulated by the α coefficient, experimentally set to 0.4 by cross validation.

Table 2 Performance as MEAN (STD) of IvtD and pSFFS methods when classifying in-vitro data. The *overall accuracy* (*A*), the *sensitivity* (*S*), *specificity* (*K*) and *precision* (*P*) are computed when discriminating *fibrotic* (*fib*), *lipidic* (*lip*) and *calcified* (*cal*) plaque

	IvtD	*pSFFS*
A	89.93 (0.29)	91.59 (0.47)
S_{fib}	90.46 (0.60)	92.58 (0.95)
S_{lip}	80.49 (0.80)	85.21 (0.59)
S_{cal}	92.20 (0.46)	92.29 (0.75)
K_{fib}	92.16 (0.41)	93.85 (0.34)
K_{lip}	95.50 (0.17)	96.47 (0.37)
K_{cal}	96.15 (0.48)	96.21 (0.38)
P_{fib}	93.34 (0.33)	94.72 (0.30)
P_{lip}	69.48 (0.86)	74.78 (2.09)
P_{cal}	92.48 (0.86)	93.23 (0.62)

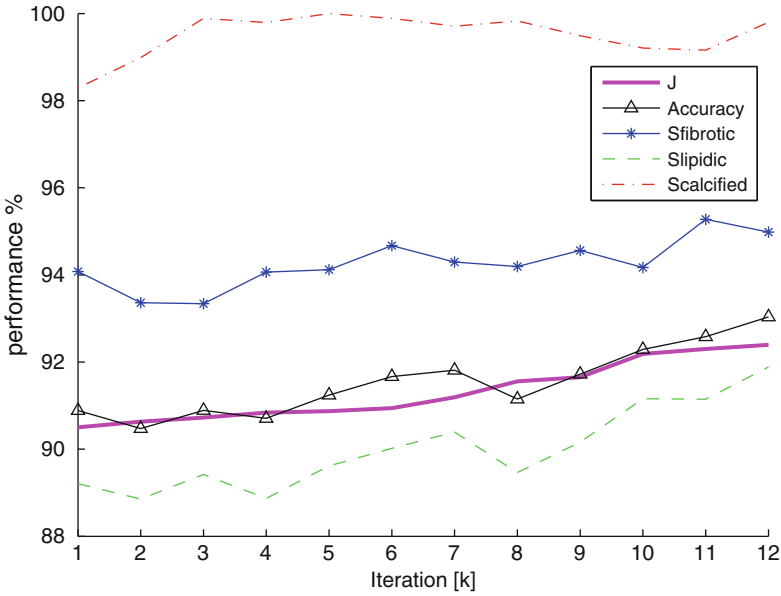

Fig. 11 Example of the *pSFFS* algorithm performance up to 12th iteration. This case is specific for a generic *p*th necro case. *J* is the value achieved at each iteration during the data selection process, while the *overall accuracy* and *sensitivity* (*S*) for each tissue type are computed by characterizing the X^p_{val} data at each iteration

4.5 Test In Vitro

Table 2 shows the classification parameters for the *pSFFS* methods when characterizing in vitro data, compared with the initial plaque characterization performance using exclusively in vitro data (*IvtD*) as training set. In *pSFFS*, the classifier has been trained by using the enhanced data set obtained by applying the data fusion method. Note that the algorithm provides a mean improvement in performance parameters

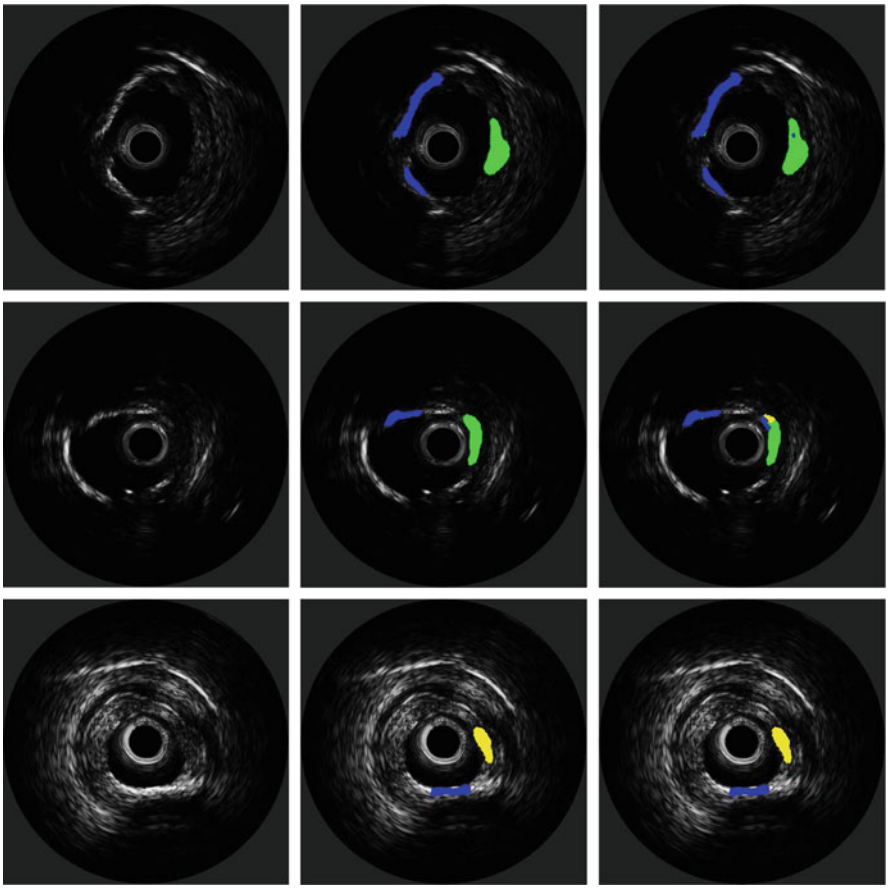

Fig. 12 Plaque characterization on IVUS data. First column: original IVUS images; second column: histologically validated ground-truth plaque segmentation; third column: classification result in the regions defined by histology. *Yellow*, *green* and *blue* (corresponding to *light*, *medium* and *dark grey*) colors indicate *lipidic*, *fibrotic* and *calcified* tissue, respectively

of 1.9% with respect to the *IvtD* case. Figure 11 shows an example of the changes of performance parameters during the *pSFFS* algorithm for a generic patient. Figure 12 shows some examples of plaque characterization in IVUS images where tissues are labeled using the enhanced classifier.

4.6 Test In Vivo

The results on Table 2 prove that the enhanced classifier outperforms a classifier trained and validated only on in vitro cases. Note that the last approach has been

Table 3 Performance as MEAN (STD) of *Ivt* vs *pSFFS* methods in classifying in-vivo data. The overall accuracy *(A)*, the *sensitivity (S), specificity (K)* and *precision (P)* are computed when discriminating *fibrotic (fib), lipidic (lip)* and *calcified (cal)* plaque

	IvtD	*pSFFS*
A	74.05 (1.34)	87.09 (0.33)
S_{fib}	88.49 (3.36)	90.66 (0.43)
S_{lip}	27.87 (3.50)	58.46 (1.61)
S_{cal}	99.62 (0.11)	99.37 (0.22)
K_{fib}	67.54 (1.53)	85.86 (0.55)
K_{lip}	97.53 (1.49)	98.56 (0.09)
K_{cal}	96.67 (0.26)	96.32 (0.24)
P_{fib}	55.90 (1.27)	73.85 (0.72)
P_{lip}	83.93 (7.95)	92.59 (0.33)
P_{cal}	94.74 (0.38)	95.82 (0.26)

followed by almost all the plaque characterization methods presented in the last ten years, on the hypothesis that the differences between in vitro and in vivo data are negligible.

In the data fusion approach, the training data set is designed by fusing in vivo and in vitro IVUS data. It is then reasonable to assume that the enhanced classifier could exhibit better performance in discriminating in vivo data with respect to a classifier trained only with in vitro data. Note that this assumption does not imply any hypothesis on the similarity between in vivo and in vitro data; it is in fact naturally deduced since the enhanced data set includes examples of in vivo data, thus providing to the classifier a knowledge about the spatial distribution of in vivo points. In order to prove the last hypothesis, the classification results of both the *IvtD* and the *pSFFS* classifiers when discriminating plaques in in vivo cases are compared: Table 3 shows the obtained classification performance in both cases.

Given the impossibility of obtaining the absolute knowledge on in vivo tissue composition by histological analysis, it is clear that the obtained results cannot be considered as a reliable, though *qualitative* results. Notwithstanding that, the increment of about 13% in overall accuracy when the *pSFFS* classifier is used indicates the benefits achieved in using an enhanced data set instead of a pure in vitro training set.

References

1. Shah PK (2003) Mechanism of plaque vulnerability and rupture. JACC 41(1):15–22
2. Burke AP, Farb A, Malcom GT, Liang Y, Smialek J, Virmani R (1997) Coronary risk factors and plaque morphology in men with coronary disease who died suddenly. New Engl J Med 336:1276–1281
3. Fuster V, Moreno PR, Fayad ZA, Corti R, Badimon JJ (2005) Atherothrombosis and high-risk plaque. JACC 46(6):937–54
4. Ehara S, Kobayashi Y, Yoshiyama M, Shimada K, Shimada Y, Fukuda D, Nakamura Y, Yamashita H, Yamagishi H, Takeuchi K, Naruko T, Haze K, Becker AE, Yoshikawa J, Ueda M (2004) Spotty calcification typifies the culprit plaque in patients with acute myocardial infarction: An intravascular ultrasound study. Circulation 110:3424–3429

5. Willerson JT, Wellens HJJ, Cohn JN, Holmes DR (2007) Atherosclerotic vulnerable plaques: Pathophysiology, detection, and treatment. Cardiovasc Med 10:621–639
6. Davies MJ, Thomas AC (1985) Plaque fissuring – the cause of acute myocardial infarction, sudden ischaemic death, and crescendo angina. Br Heart J 53(4):363–73
7. Schaberle W (2004) Ultrasonography in vascular diagnosis. Springer, Berlin
8. Gorge G, Ge J, Baumgart D, von Birgelen C, Erbel R (1998) In vivo tomographic assessment of the heart and blood vessels with intravascular ultrasound. Basic Res Cardiol 93(4):219–240
9. Nissen SE, Yock P (2001) Intravascular ultrasound: Novel pathophysiological insights and current clinical applications. Circulation 103:604–616
10. Ellis SG, Holmes DR Jr (eds) (2006) Strategic approaches in coronary intervention, 3rd edn. Lippincott Williams & Wilkins, PA
11. Siegel RJ (ed) (1998) Intravascular ultrasound imaging in coronary artery disease Informa Healthcare; 1st edition (January 15, 1998)
12. Zhang X, McKay CR, Sonka M (1998) Tissue characterization in intravascular ultrasound images. TMI 17(6):889–899
13. Caballero KL, Barajas J, Pujol O, Salvatella N, Radeva P (2006) In-vivo ivus tissue classification: A comparison between rf signal analysis and reconstructed image. Progr Pattern Recognit Image Anal Appl 4225/2006:137–146
14. Caballero KL, Barajas J, Pujol O, Rodriguez O, Radeva P (2007) Using reconstructed ivus images for coronary plaque classification. EMBS, pp. 2167–2170
15. Moore M et al (1998) Characterisation of coronary atherosclerotic morphology by spectral analysis of radiofrequency signal: In vitro intravascular ultrasound study with histological and radiological validation. Heart 79(5):459–467
16. Nair A, Kuban BD, Tuzcu EM, Schoenhagen P, Nissen SE, Vince DG (2002) Coronary plaque classification with intravascular ultrasound radiofrequency data analysis. Circulation 106:2200–2206
17. Nair A, Kuban BD, Obuchowski N, Vince GD (2001) Assessing spectral algorithms to predict atherosclerotic plaque composition with normalized and raw intravascular ultrasound data. UMB 27(10):1319–1331
18. Katouzian A, Sathyanarayana S, Baseri B, Konofagou EE, Carlier SG (2008) Challenges in atherosclerotic plaque characterization with intravascular ultrasound (ivus): From data collection to classification. TITB 12(3):315–327
19. Bedekar D (2003) Atherosclerotic plaque characterization by acoustic impedance analysis of intravascular ultrasound data. IEEE Ultrason Symp, pp. 1524–1527
20. Sathyaranayana S, Carlier S, Wenguang L, Thomas L (2009) Characterization of atherosclerotic plaque by spectral similarity of radiofrequency intravascular ultrasound signals. EuroIntervention 5:133–139
21. Kawasaki M, Takatsu H, Noda T, Ito Y, Kunishima A, Arai M, Nishigaki K, Takemura G, Morita N, Minatoguchi S, Fujiwara H (2001) Noninvasive quantitative tissue characterization and two-dimensional color-coded map of human atherosclerotic lesions using ultrasound integrated backscatter. JACC 38(2):486–492
22. Kawasaki M, Takatsu H, Noda T, Sano K, Ito Y, Hayakawa K, Tsuchiya K, Arai M, Nishigaki K, Takemura G, Minatoguchi S, Fujiwara T, Fujiwara H (2002) Invivo quantitative tissue characterization of human coronary arterial plaques by use of integrated backscatter intravascular ultrasound and comparison with angioscopic findings. Circulation 105:2487–2492
23. Kawasaki M, Sano K, Okubo M, Yokoyama H, Ito Y, Murata I, Tsuchiya K, Minatoguchi S, Zhou X, Fujita H, Fujiwara H (2005) Volumetric quantitative analysis of tissue characteristics of coronary plaques after statin therapy using three-dimensional integrated backscatter intravascular ultrasounds. JACC 45(12):1946–1953
24. Murashige A, Hiro T, Fujii T, Imoto K, Murata T, Fukumoto Y, Matsuzaki M (2005) Detection of lipid-laden atherosclerotic plaque by wavelet analysis of radiofrequency intravascular ultrasound signals: In vitro validation and preliminary in vivo application. JACC 45(12):1954–1960

25. Gonzalez RC, Woods RE (2001) Digital image processing, 2nd edn. Prentice Hall, NJ
26. Mehta SK, McCrary JR, Frutkin AD, Dolla WJS, Marso SP (2007) Intravascular ultrasound radiofrequency analysis of coronary atherosclerosis: An emerging technology fot the assessment of vulnerable plaque. Eur Heart J 28:1283–1288
27. Tobocman W, Santosh K, Carter JR, Haacke EM (1994) Tissue characterization of arteries with 4MHZ ultrasound. Ultrasonics 33:331–339
28. Milunski MR, Mohr GA, Perez JE, Vered Z, Wear KA, Gessler CJ, Sobel BE, Miller JG, Wickline SA (1989) Ultrasonic tissue characterization with integrated backscatter. acute myocardial ischemia, reperfusion, and stunned myocardium in patients. Circulation 80:491–503
29. Ciompi F, Pujol O, Gatta C, Rodriguez-Leor O, Mauri-Ferre J, Radeva P (2010) Fusing in-vitro and in-vivo intravascular ultrasound data for plaque characterization. IJCI 26:763–779
30. Carlier SG, Tanaka K, Katouzian A (2007) Atherosclerotic plaque characterization from radio frequency ultrasound signal processing. US Cardiovascular Disease, pp 54–56
31. Katouzian A, Baseri B, Konofagou EE, Laine AF (2008) Automatic detection of blood versus non-blood regions on intravascular ultrasound (ivus) images using wavelet packet signatures. Proc SPIE 6920, pp 1–8
32. Addison PS (2002) The illustrated wavelet transform handbook. Publishing, Institute of Physics
33. Escalera S, Pujol O, Mauri J, Radeva P (2008) Ivus tissue characterization with sub-class error-correcting output codes. J Signal Process Syst 55:35–47
34. Ciompi F (2008) Ecoc-based plaque classification using in-vivo and ex-vivo intravascular ultrasound data. Master thesis
35. Dietterich TG, Bakiri G (1995) Solving multiclass learning problems via error-correcting output codes. JAIR 2:263–286
36. Rifkin R, Klautau A (2004) In defense of one-vs-all classification. JMLR 5:101–141
37. Pudil P, Ferri FJ, Novovicova J, Kittler J (1994) Floating search methods for feature selection with nonmonotonic criterion functions. ICPR 2:279–283
38. Allwein EL, Schapire RE, Singer Y (2000) Reducing multiclass to binary: A unifying approach for margin classifiers. Proceedings of the Seventeenth International Conference on Machine Learning, pp 9–16
39. Schapire R (2002) The boosting approach to machine learning: an overview. MSRI Workshop on Nonlinear Estimation and Classification, pp 1–23

Francesco Ciompi F. Ciompi received the MS degree in Electronic Engineering from the Università di Pisa in 2006 and the MS in Computer Vision and Artificial Intelligence from the Universitat Autónoma de Barcelona in 2008. He is currently a PhD student at the dept. of Applied Mathematics and Analysis at the Universitat de Barcelona. His research interests include the use of machine learning techniques for the classification and segmentation of Intravascular Ultrasound data.

Oriol Pujol Oriol Pujol is associate professor at dept. of Applied Mathematics and Analysis of University of Barcelona since 2008, and senior researcher at Computer Vision Center. He has been since 2004 an active member in the organization of several activities related to image analysis, computer vision, machine learning and artificial intelligence. In applied research he is working in medical image analysis, object recognition, wearable computing and augmented reality.

Josepa Mauri Ferré Josepa Mauri received the title of MD in 1982 at Universitat Autònoma de Barcelona. In 1992 she received the Laurea summa Cum Laude in Medicine at the Universitat de Barcelona. Since 2000, she is the Director of Cardiac Catherization Laboratory in the Hospital Universitari "Germans Trias I Pujol de Badalona". From 2002 to 2005 she was the President of the Diagnostic Intracoronary Technics/IVUS Working Group of the Spanish Society of Cardiology. From 2006 to 2009 she was the President of the Spanish Working Group in Cardiac Interventions of the Spanish Society of Cardiology. Her clinical research areas have been in coronary angioplasty and Dilated Cardiomyopathy, dilated Cardiomiopathy, coronary angioplasty, stents, endothelial disfunction and IVUS studies. She is currently involved in international educational projects in interventional cardiology.

Petia Radeva Petia Radeva (PhD 1998, Universitat Autònoma de Barcelona, Spain) is a senior researcher at UB. She has more than 150 publications in international journals and proceedings. Her present research interests are development of learning-based approaches (in particular statistical methods) for computer vision and medical imaging. She has led one EU project and several Spanish projects. She has 12 patents in the field of medical imaging. Currently, she is heading projects in the field of cardiac imaging and wireless endoscopy in collaboration with Spanish hospitals and international medical imaging companies.

Three-Dimensional Ultrasound Plaque Characterization

José Seabra, Jasjit S. Suri, and João Miguel Sanches

Abstract The chapter proposes a framework for extending the analysis of the atherosclerotic disease to a three-dimensional perspective. Different data acquisition systems, either based on a robotic arm setup or free-hand are proposed, in order to collect image sequences that completely describe the plaque anatomy. A 3D reconstruction method is proposed, comprising a Rayleigh based de-speckling approach and interpolation. As a consequence, 3D maps accounting for plaque echogenicity and texture, according to appropriate local Rayleigh estimators are obtained. Furthermore, the application of a segmentation approach which makes use of the Graph-cuts method, provides an efficient way to segment and locally identify unstable regions throughout the plaque. This information, complemented with a more accurate inspection of plaque morphology, may have an important clinical impact in disease diagnosis.

1 Introduction

Atherosclerosis is a disease which generally affects large and medium-sized arteries and its most important feature is plaque formation due to progressive sub-endothelial accumulation of lipid, protein, and cholesterol esters in the blood vessel wall.

Several studies recognize that the degree of stenosis, obstruction to the blood flow, is an important physiological landmark of stroke but that other parame-

J. Seabra (✉) • J.M. Sanches
Institute for Systems and Robotics, Department of Bioengineering from the Instituto Superior Técnico/Technical University of Lisbon, Portugal
e-mail: mail2jseabra@gmail.com; jmrs@ist.utl.pt

J.S. Suri
Biomedical Technologies, Inc., Denver, CO, USA

Idaho State University (Affiliated), Pocatello, ID, USA
e-mail: jsuri@comcast.net

J.M. Sanches et al. (eds.), *Ultrasound Imaging: Advances and Applications*,
DOI 10.1007/978-1-4614-1180-2_9, © Springer Science+Business Media, LLC 2012

ters, such as plaque echo-morphology and texture should also be considered for designing a plaque risk profile. Additionally, it has been observed that vulnerable plaques are usually associated with fibrous cap thinning and infiltration of inflammatory cells consequently leading to rupture. Other studies reported a positive correlation between the presence of fatty contents and hemorrhage with neurological symptoms, thus suggesting that inflammatory activity potentially determines plaque instability. In Pedro et al. [1, 2], the location and extension of these regions are identified as sensitive and relevant markers of stroke risk.

Numerous research groups conducted studies aiming at characterizing and identifying the main features of the symptomatic lesion [1, 3–8]. Among these, the gray-scale median and P_{40} can be used to characterize the plaque from an echogenic viewpoint. However, the interpretation of these parameters values will fail to reveal possible unstable foci within the plaque, specially when plaques are heterogeneous or present significant hypoechogenic areas.

The risk assessment of plaque rupture through conventional 2D techniques is limited to a subjective selection of a representative image of plaque structure and it is hardly reproducible. An accurate diagnostic procedure based on 3D is known to be valuable but has not yet been adopted in clinical practice, mainly because such technology is not usually available in most medical facilities. Recently, less operator-dependent methods based on 3D US have been proposed from better assessment of plaque vulnerability [9, 10]. These studies aim at quantifying the plaque volume, degree of stenosis [11], and the extension of surface ulceration [12].

The focus of this chapter is to assess the atherosclerotic disease on a 3D perspective providing better visualization of the lesion and characterization of potential risk. The carotid disease study in 3D is rooted on the reconstruction of 3D maps starting with 2D information extracted from noisy BUS images. To achieve the proposed objectives, different 3D image acquisition methods are explored and powerful methods for identifying vulnerable foci within the plaque volume are used.

2 Development of DAQ Systems for 3D Ultrasound

Medical US has benefited from major advances in technology and is considered an indispensable imaging modality due to its flexibility and non-invasive character.

Currently, there are accurate methods to assess the disease severity based on CT [13] or MRI [14]. However their application is expensive, time consuming, and requires equipment which is not yet available and accessible in most clinical facilities. On the other hand, 2D ultrasound is widely available and provides real time data acquisition and visualization, so it has been so far the preferred technique in the diagnosis and monitoring of the disease.

Although all anatomy is 3D in form, the vast majority of US imaging is 2D. Most of the times, this technique provides sufficient information for diagnosis but there are clearly identifiable limitations, such as, non-ability to perform quantitative

volume measurements or to obtain optimal 2D scan views of the anatomical ROI (*Region of Interest*). Consequently, 3D US is a logical solution to allow better, more complete and objective diagnostic results. In this imaging modality, the 2D US images are combined by a computer to form an objective 3D image of the anatomy and pathology. This data can be manipulated and measured in 3D both in real time or later off-line. Moreover, unlike CT and MR imaging, in which 2D images are usually acquired at a slow rate as a stack of parallel slices, in a fixed orientation, US provides images at a high rate (15–60 s^{-1}) and in arbitrary orientations.

Most 3D US systems make use of a conventional transducer to obtain a sequence of images by sweeping the probe along the anatomical ROI, and differ only in acquisition and position sensing [9]. In this way, images can be acquired mechanically, free-handed with or without an optical or electromagnetic spatial locator and using 2D arrays. Some of these systems were validated in various clinical applications, such as obstetrics, cardiology, and vascular imaging in order to increase the diagnosis confidence [15].

2.1 Robotic Arm Prototype

Depending on the organ or tissue to be scanned, it is necessary to apply different scanning strategies or protocols which comprise linear, rotatory, and free-hand scanning, just to name the most common ones. Most imaging systems are not optimally adapted for such a wide range of applications. Hence, a 3D US prototype robotic system which can control, standardize, and accurately perform the acquisition process is presented. This system may assist the operator in defining suitable scanning paths for each patient according to the ROI to be scanned. Different acquisition properties can be assigned in each examination, such as the duration and rate of image acquisition. Moreover, each image is assigned with its spatial information allowing to further perform follow-up studies or to reconstruct and segment the tissues or organs scanned with higher degree of confidence.

Robotic systems can be regarded as an important diagnosis tool because they can simultaneously control and standardize the image acquisition process. Thus, they can be very suitable for quantifying and accurately monitor the development of cardiovascular diseases, namely, the progression of atheromatous plaques by scanning the carotid or coronary arteries [16]. In addition, the ability to remotely position the US probe with the robotic arm could also be used in telemedicine [17].

Given this, a prototype medical robot is described which can easily be integrated with common ultrasound scanning equipment and provides clinicians with their regular scanning operations. The prototype robotic arm is schematically shown in Fig. 1a and comprises four main components. The first unit is the robotic arm (Scorbot-ER VII, Intelitek, USA) with six degrees of freedom which is operated from the robot controller. The second element is an US portable scanner (Echo Blaster 128, Telemed, LT), equipped with a linear array probe. This probe is attached to the tip of the robotic arm, together with an electromagnetic position sensing

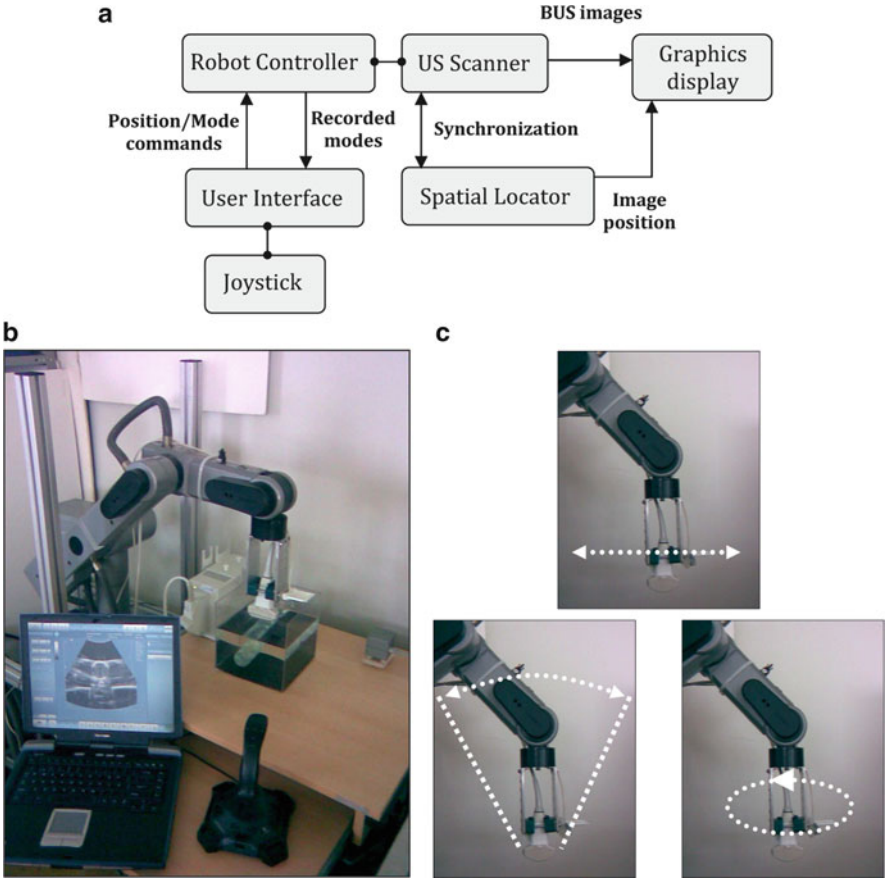

Fig. 1 Robotic Arm Prototype. (**a**) Block diagram of the system components. (**b**) Experimental setup. The robotic arm carries the probe and the position sensing receptor from the US scanner and the spatial locator, respectively. The workstation personal computer controls the movements of the robotic arm with the aid of a joystick. Images are tagged with their spatial location and showed on the screen. (**c**) Acquisition modes: linear (**a**), fan-like (**b**), and rotatory (**c**) scans

device (Fastrak, Polhemus, VT). The last component of the system is the computer workstation, which holds a joystick and the interface to control the medical robot and the US scanner.

A user-friendly graphical interface provides access and setting of the robotic arm controls and movements as well as visualization and tuning of acquisition results. The robotic arm is manipulated using a joystick which allows to move the US probe toward the ROI to be scanned. Moreover, the system features a *learning* mode which enables to store in memory a suitable scan path, and a *replay* mode to reproduce the manually taught path. This attribute of the robotic system is suitable to guarantee reproducible and personalized results since a scan path can be assigned for each patient with controlled speed and accurate position information provided by the spatial locator.

The robot integrates several acquisition modes (see Fig. 1c), providing free-hand, linear, fan-like, and rotatory scans. This should be flexible enough to allow image acquisition from different organs and tissues, where different scanning operations are needed. The system allows to capture BUS images at uniform spacing and user-defined sampling rate. These images are synchronized with the spatial locator and sent with their corresponding probe positions to the workstation for storage and further 3D reconstruction.

Figure 1b shows the experimental robot setup for US image acquisition. A cross-section of a cylindrical latex-made phantom, which resembles a human vessel, was acquired and the result is shown on the computer screen.

This system provides accurate and standardize but at the same time flexible scanning of several organs and tissues. In particular, this can be a reasonable alternative to other 3D US imaging systems for accurately quantifying the progression of cardiovascular diseases.

2.2 Free-Hand Ultrasound

A free-hand system can be also used to acquire BUS images for 3D Ultrasound. This strategy is more flexible than the robotic system presented above since it allows image acquisition with unconstrained movement. In general, a free-hand US image acquisition system consists of a sensor (attached to a probe) that is tracked by a device that calculates the sensor's position and orientation at any point in time. This information is used to compute the 3D coordinates of each pixel of the BUS images. In this context, there are four common technologies to track medical instruments, including mechanical, acoustical, electromagnetic, and optical.

The developed free-hand system is composed of an US duplex scanner (HDI 5000, Philips Medical Systems division, Bothell, WA, USA), depicted in Fig. 2a with a L12-5 scan probe (5–12 MHz broadband linear-array transducer), where a sensor from a tracking device was coupled as illustrated in Fig. 2b. The designed system uses an electromagnetic sensing device (Fastrak, Polhemus, VT, USA) providing storage of six degrees of freedom. The idea behind the electromagnetic system is to have a receiver placed on a probe that measures the induced electrical currents when moved within a magnetic field generated by a transmitter.

Generally, the tracking devices used for free-hand systems have the same operating mode. The device tracks the position and orientation of the sensor on the probe, not the BUS image plane itself. Hence, it is necessary to compute the transformation (rotation, translation, and scaling) between the origin of the sensor mounted on the probe and the image plane itself. This problem can be tackled with the application of an adequate calibration method. Here, calibration was attained with a suitable software (Stradwin, Medical Imaging group at the Department of Engineering, University of Cambridge, UK) where all the experimental apparatus required is a flat plane immersed in a water tank. The flat plane could be as simple as the bottom of the water tank [18, 19].

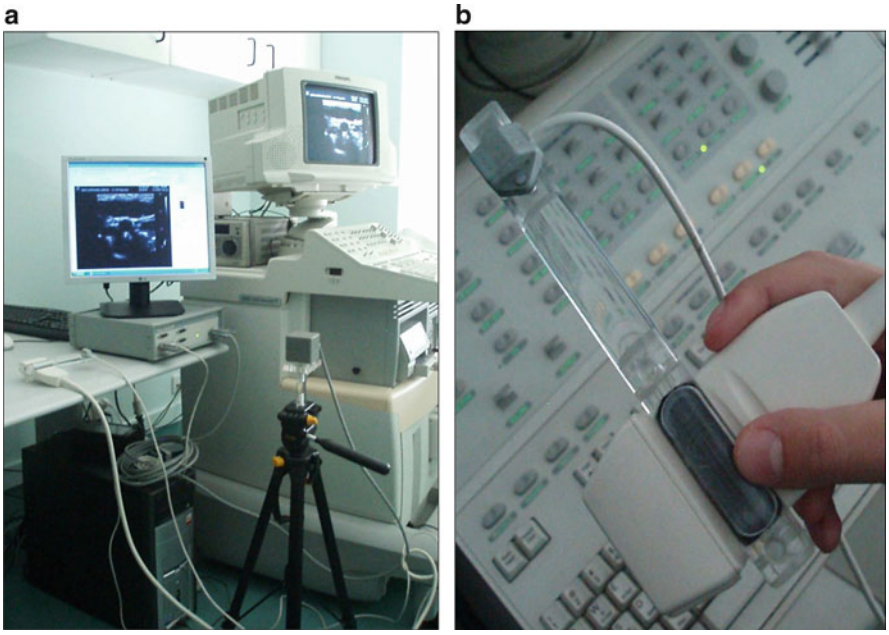

Fig. 2 Free-hand 3D US. (**a**) Experimental setup, comprising a scanner, a spatial locator (**b**) and a computer interface for image visualization and acquisition

After calibration, every pixel in each 2D image is mapped in the 3D coordinate system of the tracking device to reconstruct a geometrically correct volume.

3 Methods

This section addresses the methods developed to study the atherosclerotic lesion from a 3D perspective. Hence, a description of the reconstruction procedure from sequences of BUS images acquired with the free-hand US system is described next. Moreover, a methodology for the local characterization (labeling) of hypoechogenic regions within the plaque volume is presented. The labeling procedure is based on Graph-cuts and it is expected to improve the characterization of plaques, by providing a more appropriate identification of unstable foci inside it.

3.1 Reconstruction

Two approaches are generally considered in organ and tissue reconstruction: surface and volume rendering. Surface rendering [12, 20] can be used to extract the

bifurcation walls of carotid arteries and quantify the degree of stenosis and plaque volume. A volume rendering approach [21] is often used to reconstruct a particular volume of interest from which echo-morphological or textural analysis can be performed. Here, a combination of the two approaches is used. First, volume renderings are obtained from sets of 2D BUS images of the carotid artery. The regions corresponding to atherosclerotic plaques are visually detected in several cross-sections taken from the obtained volume and then segmented using semi-automatic segmentation methods, e.g., active contours [22] guided by experienced physicians. Surface rendering employs the interpolation of these contours providing a three-dimensional representation of the plaque. This procedure has been extensively described in [23].

It is recognized that BUS images are characterized by a speckle pattern which makes data visualization and interpretation a challenging task. The method used here to compute the morphology of the VOI (*Volume of Interest*) containing the carotid plaque is composed of two main steps: (1) de-noising and (2) reconstruction.

The method used to accomplish de-noising is based on the approach described in [24] and can be summarized as follows. Let $Y = \{y_{i,j}\}$ be the original ultrasound image and $\Sigma = \{\sigma_{i,j}\}$ the de-speckled image to estimate. A Bayesian framework with the *Maximum a Posteriori* criterion (MAP) is adopted to deal with the ill posedness nature of this particular de-speckling problem. Hence, the de-speckled image is obtained by minimizing an energy function:

$$\hat{\Sigma} = \arg\min_{\Sigma} E(Y, \Sigma), \tag{1}$$

where $E(Y,\Sigma) = E_d(Y,\Sigma) + E_p(\Sigma)$. $E_d(Y,\Sigma)$, called *data fidelity* term, pushes the solution toward the data and $E_p(\Sigma)$, called *prior* term, regularizes the solution by introducing prior knowledge about Σ. The *data fidelity* term is the *log-likelihood* function, $E_d(Y,\Sigma) = -\log(p(Y|\Sigma))$ where $p(Y|\Sigma) = \prod_{i,j=1}^{N,M} p(y_{i,j}|\sigma_{i,j})$ and $p(y_{i,j}|\sigma_{i,j})$ is the Rayleigh probability density function [25]. The overall energy function obtained after considering the variable change $x = \log(\sigma^2)$ is:

$$E(Y,X) = \sum_{i,j} \left[\frac{y_{i,j}^2}{2} e^{-x_{i,j}} + x_{i,j} \right] + \alpha TV(\mathbf{X}) \tag{2}$$

where the prior term,

$$TV(X) = \sum_{i,j} \sqrt{(x_{i,j} - x_{i-1,j})^2 + (x_{i,j} - x_{i,j-1})^2}, \tag{3}$$

is the so-called *Total Variation* (TV) of $\mathbf{X} = \{x_{i,j}\}$. An example to illustrate the application of the de-speckling algorithm is displayed in Fig. 3.

In the second step, these de-noised images are interpolated to estimate a 3D VOI containing the plaque. The 3D reconstruction of a VOI which completely contains the plaque aims at estimating a 3D field, $F = \{f_p\}$, from the de-noised images

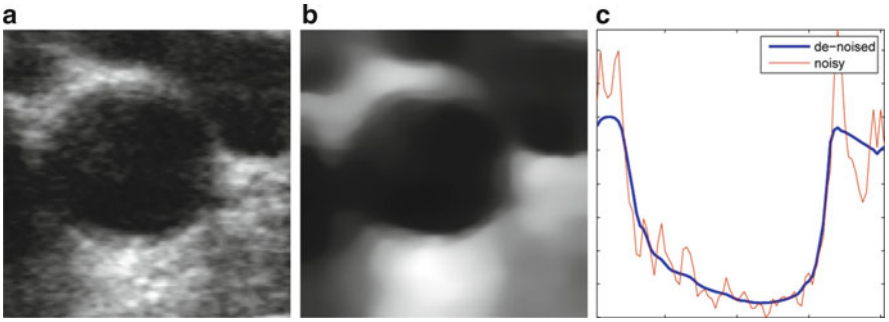

Fig. 3 De-speckling example (**b**) of an original ultrasound image (**a**). The algorithm clearly shows its edge-preserving nature (**c**)

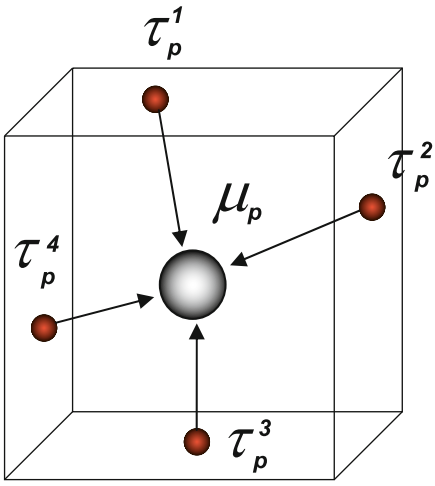

Fig. 4 Voxel representation associated with the node f_p (gray), located at μ_p, and several image pixels, at locations τ_p^r in its neighborhood (red)

computed in the de-speckling step, $\Sigma^t = \{\sigma_{i,j}^t\}$, where t denotes the t^{th} image of the sequence of BUS images acquired with the presented 3D free-hand US system, and $p = (i, j, k)$ represents a node index in the 3D matrix, F. Two problems are naturally raised: (1) the node locations of F, f_p, and the locations of the pixels of Σ^t, $\sigma_{i,j}^t$, do not match, and (2) some nodes may not be observed (missing data). These problems are tackled with an interpolation procedure described as follows.

Let us consider each voxel, f_p, as a cubic region centered at the location of the node μ_p, with dimensions $(\Theta_1, \Theta_2, \Theta_3)$ and the locations of the de-noised pixels $\sigma_{i,j}^t$ as $\tau_{i,j}^t$. Moreover, let $\Upsilon_p = \{\sigma_{r,l}^t : \tau_{r,l}^t \in S_{\Theta_1,\Theta_2,\Theta_3}(\mu_p)\}$ be the set of all pixels inside the neighborhood (voxel), $S_{\Theta_1,\Theta_2,\Theta_3}(\mu_p)$ of the node f_p displayed in Fig. 4.

In a first step, a 3D volume, $Z = \{z_p\}$ with the same dimensions of Σ is computed where each element, $z_p = \langle \Upsilon_p \rangle$, is the weighted mean of the set Υ_p where the weights are the normalized distances of the pixel locations to the center of the voxel,

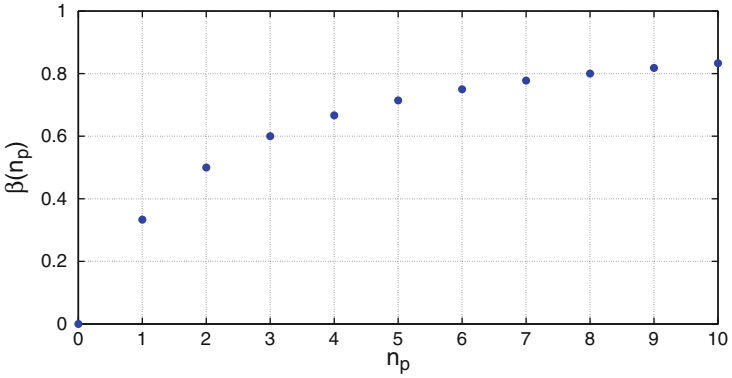

Fig. 5 Regularization parameter function depending on the number of observed pixels

such that $z_p = (\sum_r \|\tau_r - \mu_r)\|\sigma_r)/(\sum_r \|\tau_r - \mu_p\|)$ where τ_r denotes the location of the r^{th} pixel within the set Υ_p. Therefore, each element of Z contains the average intensity of the pixels within the voxel. However, some elements of Z may be undefined when there are no observations (pixels) inside the voxel. In this case an interpolation is needed. This missing data problem may be solved by minimizing the following energy function:

$$E(F,Z) = \sum_p [n_p(f_p - z_p)^2 + g_p^2], \tag{4}$$

where $g_p = \sqrt{(f_{i,j,k} - f_{i-1,j,k})^2 + (f_{i,j,k} - fi, j-1, k)^2 + (f_{i,j,k} - f_{i,j,k-1})^2}$ is the gradient magnitude of F at the voxel p and n_p is the number of observations (pixels) associated with the voxel p. The minimization of (4) can be iteratively solved by optimizing with respect to one unknown at a time, which leads to the following recursion:

$$f_p^t = \beta(n_p) z_p + (1 - \beta(n_p))\overline{f_p^{t-1}}, \tag{5}$$

where $()^t$ denotes the iteration t, $\overline{f_p^{t-1}}$ corresponds to the mean value of the neighbors of f_p computed in the iteration $t-1$, n_p is the number of pixels inside the voxel and

$$\beta(n_p)) = \frac{n_p}{n_p + N_v} \tag{6}$$

is a regularization parameter function with $N_v = 6$, whose behavior is illustrated in Fig. 5. The equation expressed in (5) reveals the underlying interpolation mechanism performed during the minimization of the energy function (4). Each new estimate of F, F^t, is dependent of the previous estimate, F^{t-1}, and of the field of the mean pixel intensities, Z, computed in the previous step. As large is

the number of pixels, n_p, associated with a particular voxel, the closer to the unity is the parameter β, meaning that, in the limit, $f_p^t \approx z_p$. Conversely, a small number of observed pixels leads to small values of β, $\overline{f_p^{t-1}}$, meaning that new estimates of f_p^t are computed part from z_p and part from the neighbors, $\overline{f_p^{t-1}}$, estimated in the previous iteration. In the limit, when no observations are available, $\beta = 0$, and the new estimate is $f_p^t = \overline{f_p^{t-1}}$, that is, it corresponds to the mean intensity of its neighbors. To summarize this method is based on the following concept: when a large number of pixels are available for a given voxel its value is mainly computed from Z, whereas when the number of observations is small or even zero the estimate is obtained from the voxel neighborhood values.

The volume field F, originated from the set of de-speckled images, describes the value of the Rayleigh parameter across the VOI enclosing the carotid plaque and it may be used to compute local intensity and textural indicators which characterize the different components and tissues of the plaque. Volume reconstruction of the plaque interior provides an overall characterization of its composition which is in most cases mentally built up by the clinician.

Traditionally, plaque characterization is based on statistics computed from the observed noisy pixels. Here, instead of computing these indicators from the noisy data, the characterization is based on theoretical statistical estimators depending on F, and consequently on the plaque acoustical properties encoded in the Rayleigh distribution.

Given this, with the purpose of assessing the local echo-morphology of the 3D reconstructed plaque, the median and the P_{40} are computed, since these indicators already demonstrated to be useful for tissue characterization. These statistics, derived from the Rayleigh distribution [26], are given by:

$$\begin{cases} f_v(p) = f_p \sqrt{\log(4)} \\ f_{P_{40}}(p) = 1 - \exp\left(-\frac{40^2}{2f_p^2}\right). \end{cases} \tag{7}$$

Consequently, two different maps, F_v and F_{P40} are computed containing the values of the mentioned estimators at each location $p = (i, j, k)$. By averaging the elements of these 3D matrices, a rough (global) characterization of the plaque echo-morphology can be performed.

3.2 Local Hypoechogenic Region Labeling with Graph-Cuts

As mentioned before, the global characterization of carotid plaques, despite its unquestionable usefulness, may not be accurate for an objective assessment of plaque vulnerability, especially in cases where the plaque is significantly heterogeneous or is plagued by artifacts.

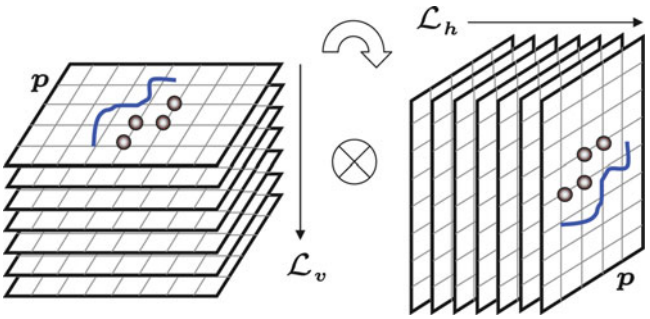

Fig. 6 Labeling procedure performed on a plane by plane basis, providing $\mathscr{L}_v$ and $\mathscr{L}_v$

In this section a local-based labeling approach was developed. The goal is to use statistical estimators (7) to assess the risk of plaque rupture on a localwise basis. This method is expected to identify regions of the plaque whose hypoechogenicity information point toward potential foci of vulnerability. Plaque classification at each location $p = (i, j, k)$ can be made by comparing the statistics derived in (7) with a threshold, defined by the clinician. Considering the median and $P40$, conventional reference values are 32 and 43, respectively [1, 27]. This is done for every voxel, resulting in 3D maps of labels ascribed for each one of the clinical indicators. This thresholding algorithm is simple and fast but it does not take into account spatial correlation between neighboring nodes because the process is performed on a voxel-by-voxel basis.

Here, a more sophisticated and accurate method is used where the labeling procedure considers the intensity value of the statistical function at location p and also the values of its neighboring nodes. The goal is to introduce spatial correlation to reduce the misclassification rate by assuming that the plaque is piecewise homogeneous, that is, composed of homogeneous regions separated by abrupt transitions. This assumption is acceptable from an anatomical perspective and is usually adopted for de-noising and de-blurring in medical imaging.

Let f_p be the estimated value of F at the p^{th} node. The labeled maps, $\mathscr{L}_\tau$ with $\tau = \{v, P_{40}\}$, are performed on a plane-by-plane basis, i.e., each plane is labeled independently of the others. The segmentation is binary, which means $\mathscr{L}(p) \in \{0, 1\}$ where $\mathscr{L}(p)$ is the p^{th} node of the labeled volume. The labeling procedure of the whole volume is performed in three steps, as depicted in Fig. 6: (1) all stacked planes along the vertical direction are independently labeled, (2) all stacked planes along the horizontal direction are independently labeled, and (3) both volumes obtained in the previous steps, $\mathscr{L}_v(p)$ and $\mathscr{L}_h(p)$, are fused by making $\mathscr{L}(p) = \mathscr{L}_v(p) \otimes \mathscr{L}_h(p)$ where $\otimes$ denotes the boolean product.

The labeling process of each plane is performed by solving the following optimization problem:

$$\mathscr{L}_\tau = \arg\min_{\mathscr{L}} E(F_\tau, \mathscr{L}), \tag{8}$$

where the energy function is given by:

$$E_\tau(F_\tau,\mathscr{L}) = \sum_p (\lambda_\tau - f_p)(2\mathscr{L}(p)-1) - 1 + \theta \sum_p \left(\frac{V(\mathscr{L}(p),\mathscr{L}(p_v)) + V(\mathscr{L}(p),\mathscr{L}(p_h))}{\tilde{g_p}} \right), \quad (9)$$

where λ_τ is the threshold associated with the indicator τ, θ is a parameter to tune the strength of smoothness, $\tilde{g_p}$ is the normalized gradient at location p, and p_v and p_h are the locations of the causal vertical and horizontal neighbors of the p^{th} node. In addition, $V(l_1,l_2)$ is a penalization function defined as follows:

$$V(l_1,l_2) = \begin{cases} 0 & l_1 = l_2 \\ 1 & l_1 \neq l_2. \end{cases} \quad (10)$$

The energy function (9) is composed of two terms: the first called *data term* and the second designated as *regularization term*. The first forces the classification to be $\mathscr{L}(p) = 1$ when $f_p \geq \lambda_\tau$ because this leads to a decrease in the term $(\lambda_\tau - f_p)(2\mathscr{L}(p)-1)$ when compared to the alternative classification, $\mathscr{L}(k) = 0$. The opposite occurs if $f_p < \lambda_\tau$. The second term forces the uniformity of the solution because the cost associated with uniform labels is smaller than with non-uniform ones (10). In order to preserve the transitions the terms are divided by the normalized gradient magnitude of f_p, $\tilde{g}_p$. Therefore, when the gradient magnitude increases the regularization strength is reduced at that particular location.

The minimization of (9) formulated in (8) is a huge optimization task performed in the Ω^{NM} high-dimensional space where $\Omega = \{0,1\}$ is the set of labels and N and M are the dimensions of the image. In [28] it is shown that several energy minimization problems in high-dimensional discrete spaces can be efficiently solved by use of *Graph-cuts* [29]. Opportunely, the energy function given in (9) belongs to this class of problems, for which the authors have designed a very fast and efficient algorithm to compute the global minimum. For example, a 200×300 pixel image is processed in 0.2 seconds in an Intel Core2 CPU at 1.83GHz with 2GB RAM, which shows the efficiency and the short processing time of the method.

4 Experimental Results

The first result aims at investigating the adequacy of the labeling procedure to detect piecewise smooth regions in synthetic ultrasound data. For this purpose, it is used a synthetic BUS image (Fig. 7a) created from a plaque phantom presenting two hypoechogenic regions ($f_p = 20$), one low echogenic region ($f_p = 35$) and the echogenic foreground ($f_p = 50$). The background is assumed to be hypoechogenic ($f_p = 20$). The synthetic image is corrupted with Rayleigh noise using MatLab

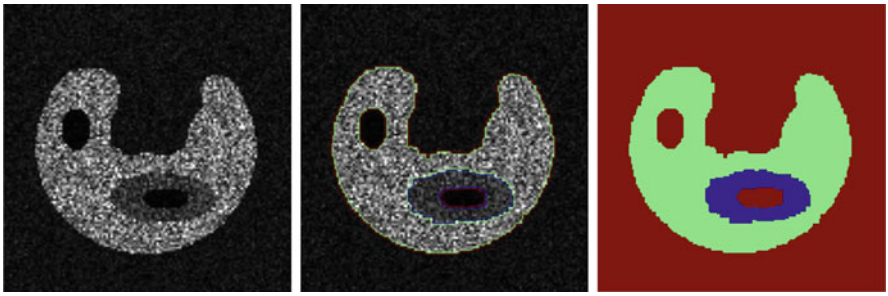

Fig. 7 Illustration of labeling based on Graph-cuts using a synthetic plaque corrupted with Rayleigh noise. Different classes (regions) are correctly labeled

software. Here, the number of classes (regions with homogeneous echogenicity) to detect is set to 3 and the *data term* is simply the image intensities. This simple example provides an illustration of how the Graph-cuts algorithm is able to correctly label the different portions of the synthetic BUS image (Fig. 7b, c).

Furthermore, the performance of 3D reconstruction and labeling was evaluated with a set of 100 synthetic images created as in the aforementioned example. This image set defines a 3D VOI, as illustrated in Fig. 8a. Each image is corrupted with noise and interpolated, thus creating the noisy VOI shown in Fig. 8b. After de-speckling each image and performing 3D reconstruction, the obtained result is shown in Fig. 8c. Clearly, speckle has been significantly suppressed, providing a clearer VOI where the plaque can be easily identified. Moreover, the application of de-speckling followed by 3D reconstruction eases the task of 3D labeling, whose results are shown in Fig. 8d. In fact, the hypoechogenic regions, hypothetically considered as defining *foci* of plaque instability, are correctly identified by use of the labeling procedure based on Graph-cuts, where $f_\lambda = 20$ in (9).

The effectiveness of the labeling procedure based on Graph-cuts for local identification of unstable sites inside the plaque is evaluated in real ultrasound data. Three carotid plaques were reconstructed following the previously proposed method and then locally characterized using the median and $P40$ estimators derived from each reconstructed VOI, f_p, that is, $f_v(p)$ and $f_{P40}(p)$. As mentioned, the analysis of plaque echo-morphology, in particular the GSM (median) and $P40$ determines whether (or not) a plaque is stable by using consensual thresholds given in the literature [1, 2, 30], which in this context corresponds to $f_v(p) < 32$ and $f_{P40}(p) > 43$. This binary classification, based on a thresholding procedure, is very simple and can lead to nonrealistic clinical results as physicians would expect to identify clusters (regions) of vulnerability across the carotid plaques, where isolated or dispersed pixels (outliers) are not expected to occur. Hence, the application of a strategy such as that based on Graph-cuts can be suitable for this particular labeling problem since it favors clustering. The labeling procedure based on Graph-cuts is applied by considering the 3D maps of the median and P_{40}, $f_v(p)$ and $f_{P_{40}}(p)$, and the corresponding reference "cut-offs", $f_\lambda = 32$ and $f_\lambda = 43$, in (9).

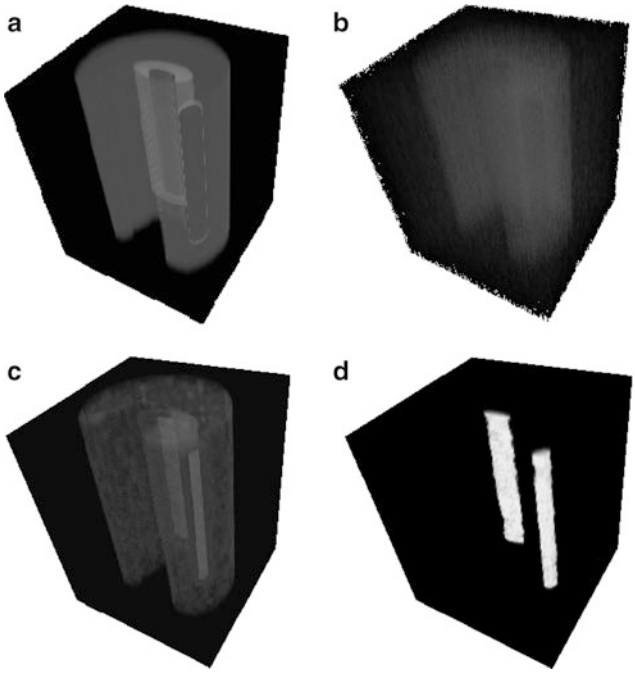

Fig. 8 3D reconstruction and labeling using Graph-cuts from a synthetic image set

Figure 9 displays the labeling of potentially dangerous sites inside the plaque using two labeling strategies, where the first is based on thresholding and the second on Graph-cuts. It is observed that the use of Graph-cuts allows to better discriminate the hypoechogenic sites across the carotid plaques. Volumes labeled with Graph-cuts appear less noisier than when the threshold method is used. This suggests that the use of Graph-cuts may improve the characterization of carotid plaques, namely by providing a more appropriate identification and definition of unstable regions across the plaque. This result can be clinically meaningful since as reported in [1] the degree of extension of these unstable regions and their location throughout the plaque should be considered and used as markers of risk of plaque rupture and thus of stroke risk.

Figure 10 depicts a potential application of the reconstruction and labeling algorithms in the scope of 3D plaque analysis with ultrasound. First, regions of hypoechogenicity are identified by use of the local median estimator, $f_v(p)$), and the Graph-cuts labeling strategy (Fig. 10a). Figure 10b illustrates a potential application of the characterization algorithm based on the inspection of a region which was identified by the algorithm as being more vulnerable. This region can be extracted, its location inside the plaque can be tracked, and its volume can be computed to assess the ratio of its occupation related to the whole plaque.

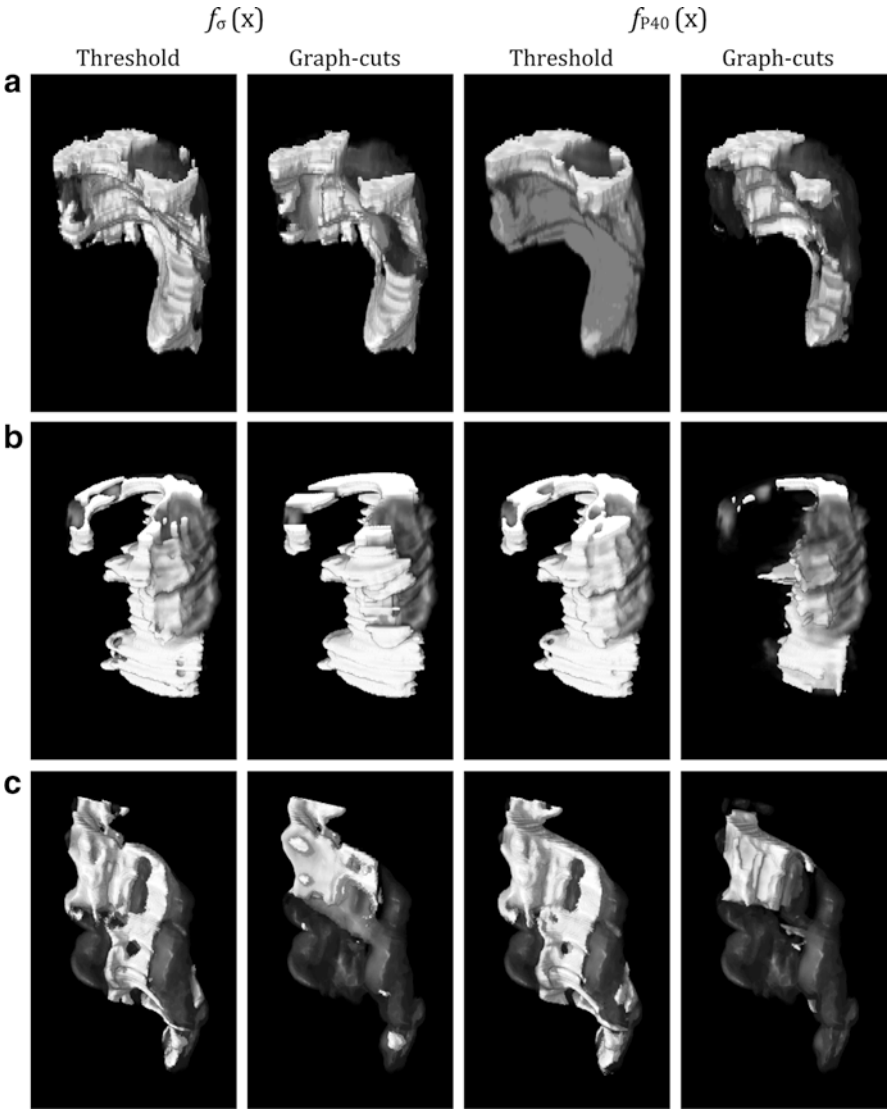

Fig. 9 Comparison of labeling strategies based on simple threshold and Graph-cuts computed from the median and *P*40 3D maps of three reconstructed plaques

Moreover, Fig. 10c shows results of plaque texture, based on the standard deviation estimator which is computed as $f_\sigma(p) = \frac{4-\pi}{2} f_p^2$ [30], providing a gray-scaled indicator of plaque heterogeneity. Regions resulting from the combination of the previous results are thought to be the most important foci of plaque rupture.

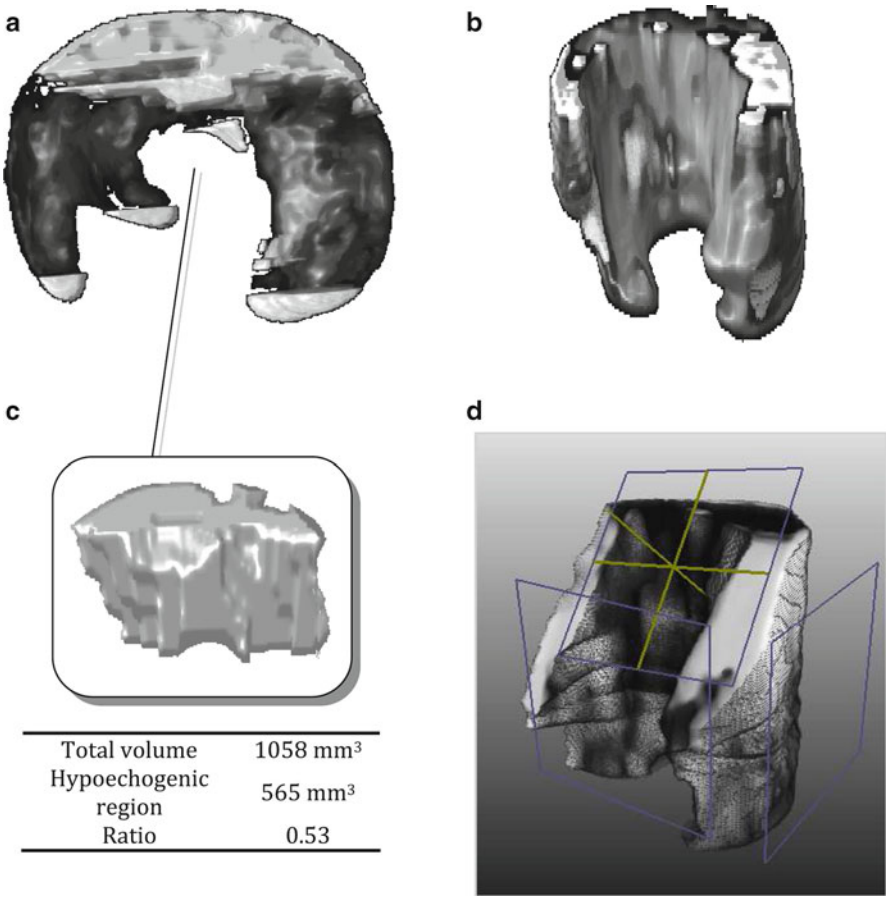

Fig. 10 Potential application of the algorithm: (**a**) Identification of hypoechogenic sites, using the local median parameter; (**b**) Inspection and quantification of a representative vulnerable region detected inside the plaque; (**c**) Gray-scale mapping of plaque texture, using the local standard deviation parameter; (**d**) New cross, section of the plaque from the reconstructed volume

The 3D approach provides the visualization of an unlimited number of cross-sectional cuts of the plaque which naturally eases the analysis of its echo-morphology contents and surface regularity (Fig. 10d).

5 Conclusions

The assessment of plaque morphology, echogenicity, and texture is considered to be critical for an accurate diagnosis of atherosclerotic disease. 2D ultrasound has so far been the preferred imaging technique because it is non-invasive, inexpensive, and

portable. This chapter proposes an extension to the traditional characterization of plaques using a 3D approach. This strategy provides a more complete and objective description of lesion severity because it considers all the information enclosed in the plaque anatomical volume without depending on a subjective selection of a particular image for diagnosis.

Two distinct data acquisition systems developed for 3D ultrasound, either robotic arm and free-hand based, are proposed to obtain a set of cutting planes of the carotid plaque acquired at a high sampling rate and in virtually any arbitrary orientation.

Moreover, the VOI containing the plaque is obtained in two steps, where the first uses the proposed de-speckling algorithm applied to each image of the acquired data sequence and the second considers a reconstruction step. The application of such procedure provides a description of plaque echogenicity and texture in terms of 3D maps of local estimators obtained from the Rayleigh distribution. Consequently, plaque analysis can be performed on a global sense, where the average values of Rayleigh descriptors are computed, or on a local basis.

The latter approach is crucial from a clinical perspective because it potentially allows the identification of sources of plaque rupture. To tackle this problem, a labeling method is introduced using an efficient method based on Graph-cuts. Such labeling procedure improves the segmentation of potential foci of instability across the plaque because it is robust to the presence of noise and favors clustering. Results of local labeling using synthetic and real data show that this strategy outperforms the method based on simple thresholding.

Hence, an entire 3D ultrasound-based framework was introduced, from data acquisition, reconstruction to its analysis, providing a more complete and objective characterization of carotid plaques. This study presents encouraging and meaningful results in terms of plaque inspection, quantification, and local characterization of plaque echo-morphology.

References

1. Pedro LM, Fernandes JF, Pedro MM, Gonalves I, Dias NV (2002) Ultrasonographic risk score of carotid plaques. Eur J Vasc Endovasc Surg 24:492–498
2. Pedro LM (2003) Uma janela para a aterosclerose. A ultrassonografia de alta definição no estudo da parede arterial. PhD thesis, Faculdade de Medicina de Lisboa
3. Christodoulou CI, Pattichis CS, Pantziaris M, Nicolaides A (2003) Texture-based classification of atherosclerotic carotid plaques. IEEE Trans Med Imaging 22(7):902–912
4. Mougiakakou S, Golemati S, Gousias I, Nicolaides AN, Nikita KS (2007) Computer-aided diagnosis of carotid atherosclerosis based on ultrasound image statistics, laws' texture and neural networks. Ultrasound Med Biol 33(1):26–36
5. Kyriacou E et al. (2009) Classification of atherosclerotic carotid plaques using morphological analysis on ultrasound images. Appl Intell 30(1):3–23
6. Elatrozy T, Nicolaides A, Tegos T, Griffin M (1998) The objective characterization of ultrasonic carotid plaque features. Eur J Vasc Endovasc Surg 16:223–230
7. Pedro LM, Pedro MM, Goncalves I, Carneiro TF, Balsinha C (2000) Computer-assisted carotid plaque analysis: characteristics of plaques associated with cerebrovascular symptoms and cerebral infarction. Eur J Vasc Endovasc Surg 19(2):118–123

8. Nicolaides AN, Kakkos SK, Griffin M, Sabetai M, Dhanjil S, et al. (2005) Severity of asymptomatic carotid stenosis and risk of ipsilateral hemispheric ischaemic events: results from the ACSRS study. Eur J Vasc Endovasc Surg 30(3):275–284
9. Fenster A, Downey DB, Cardinal HN (2001) Three-dimensional ultrasound imaging. Phys Med Biol 46(5):67–99
10. Landry A, Spence JD, Fenster A (2004) Measurement of carotid plaque volume by 3-dimensional ultrasound. Stroke 35(4):864–869
11. Ainsworth CD, Blake CC, Tamayo A, Beletsky V, Fenster A (2005) 3D ultrasound measurement of change in carotid plaque volume: a tool for rapid evaluation of new therapies. Stroke 36(9):1904–1909
12. Schminke U, Motsch L, Hilker L, Kessler C (2000) Three-dimensional ultrasound observation of carotid artery plaque ulceration. Stroke 31(7):1651–1655
13. Wintermark M, Jawadi SS, Rapp JH, Tihan T, Tong E, Glidden DV, Abedin S, Schaeffer S, Acevedo-Bolton G, Boudignon B, OrwollB, Pan X, Saloner D (2008) High-resolution CT imaging of carotid artery atherosclerotic plaques. AJNR Am J Neuroradiol 29(5):875–882
14. Saam T, Yuan C, Chu B, Takaya N, Underhill H, Cai J, Tran N, Polissar NL, Neradilek B, Jarvik GP, Isaac C, Garden GA, Maravilla KR, Hashimoto B, Hatsukami TS (2007) Predictors of carotid atherosclerotic plaque progression as measured by noninvasive magnetic resonance imaging. Atherosclerosis 194(2):e34–e42
15. Nelson TR (2000) Three-dimensional imaging. Ultrasound Med Biol 26 Suppl 1:35–38
16. Pierrot F et al. (1999) Hippocrate: a safe robot arm for medical applications with force feedback. Med Image Anal 3(3):285–300
17. Sublett J, Dempsey B, Weaver A (1995) Design and implementation of a digital teleultrasound system for real-time remote diagnosis. In: Symposium on computer-based medical systems, pp 292–298
18. Prager RW, Rohling RN, Gee AH, Berman L (1998) Rapid calibration for 3-D freehand ultrasound. Ultrasound Med Biol 24(6):855–869
19. Hsu P, Prager RW, Gee AH, Treece GM (2006) Rapid, easy and reliable calibration for freehand 3d ultrasound. Ultrasound Med Biol 32(6):823–835
20. Meairs S, Hennerici M (1999) Four-dimensional ultrasonographic characterization of plaque surface motion in patients with symptomatic and asymptomatic carotid artery stenosis. Stroke 30(9):1807–1813
21. Bullitt E, Aylward SR (2002) Volume rendering of segmented image objects. IEEE Trans Med Imaging 21(8):998–1002
22. Xu C, Prince JL (1998) Snakes, shapes, and gradient vector flow. IEEE Trans Image Process 7(3):359–369
23. Seabra JC, Pedro LM, Fernandes e Fernandes J, Sanches JM (2009) A 3D Ultrasound-based framework to characterize the echo-morphology of carotid plaques. IEEE Trans Biomed Eng 56(5):1442–1453
24. Seabra J, Xavier J, Sanches J (2008) Convex ultrasound image reconstruction with log-euclidean priors. In: Proceedings of IEEE international conference on engineering in medicine and biology, IEEE Engineering in Medicine and Biology Society, Vancouver, Canada, Aug 2008, pp 435–438
25. Eltoft T (2006) Modeling the amplitude statistics of ultrasonic images. IEEE Trans Med Imaging 25(2):229–240
26. Abramowitz M, Stegun IA (1964) Handbook of mathematical functions with formulas, graphs, and athematical tables, ninth dover printing, tenth gpo printing edition. Dover, New York
27. El-Barghouty NM, Levine T, Ladva S, Flanagan A, Nicolaides A (1996) Histological verification of computerised carotid plaque characterisation. Eur J Vasc Endovasc Surg 11(4):414–416

28. Kolmogorov V, Zabih R (2004) What energy functions can be minimizedvia graph cuts? IEEE Trans Pattern Anal Mach Intell 26(2):147–159
29. Boykov Y, Veksler O, Zabih R (2001) Fast approximate energy minimization via graph cuts. IEEE Trans Pattern Anal Mach Intell 23(11):1222–1239
30. Baroncini LV, Filho AP, Junior L, Martins AR, Ramos SG (2006) Ultrasonic tissue characterization of vulnerable carotid plaque: correlation between videodensitometric method and histological examination. Cardiovasc Ultrasound 4:32

Part III
Ultrasound Advanced Applications

Real-Time 4D Cardiac Segmentation by Active Geometric Functions

Qi Duan, Andrew F. Laine, and Jasjit S. Suri

Abstract Recent advances in 4D imaging and real-time imaging provide image data with clinically important dynamic information at high spatial or temporal resolution. The enormous amount of information contained in these data, on the other hand, has also raised a challenge for traditional image analysis algorithms in terms of efficiency. In this chapter, a novel deformable model framework, active geometric functions (AGFs), is introduced for the real-time segmentation problem. As an implicit deformable framework in parallel with level-set, AGF has mathematical advantages in efficiency and computational complexity as well as several flexible features similar to level-set framework. The performance of AGF is demonstrated in two cardiac applications: endocardial segmentation in 4D ultrasound and myocardial segmentation in MRI with super high temporal resolution. In both applications, AGF can perform accurate real-time segmentation in several milliseconds per frame, which was less than the acquisition time per frame. Segmentation results are compared to manual tracing with comparable performance with inter-observer variability. The ability of such real-time segmentation will not only facilitate the traditional diagnoses and workflow but also open the paths for novel applications such as interventional guidance and interactive image acquisition with online segmentation.

Q. Duan (✉)
National Institute of Neurological Disorders and Stroke, National Institutes of Health, 10 Center Drive, Building 10, Room B1D728, MSC 1065, Bethesda, MD 20892-1065, USA
e-mail: Qi.Duan@nih.gov

A.F. Laine
Vice-Chair, Professor of Biomedical Engineering and Radiology (Physics), 351 Engineering Terrace MC-8904, Biomedical Engineering Department, 1210 Amsterdam Avenue, Columbia University, MC-8904 New York, NY 10027
e-mail: laine@columbia.edu

J.S. Suri
Biomedical Technologies, Inc., Denver, CO, USA

Idaho State University (Affiliated), Pocatello, ID, USA
e-mail: jsuri@comcast.net

J.M. Sanches et al. (eds.), *Ultrasound Imaging: Advances and Applications*,
DOI 10.1007/978-1-4614-1180-2_10, © Springer Science+Business Media, LLC 2012

1 Introduction

Image segmentation is a critical step for quantitative image analysis. In medical imaging, image segmentation is the prerequisite for quantitative evaluation of organ pathologies and morphologies, and for quantitative diagnosis. For example, in cardiac imaging, delineating borders of chambers of the heart and valves are of great clinical importance. Segmentation of the left ventricular endocardium is required for quantitative evaluation of the LV function, such as ejection fraction or 3D fractional shortening [1]. With recent advances in 3D and 4D imaging techniques towards real-time imaging, the amount of data is becoming prohibitively overwhelming. Manual tracing of these large datasets is tedious and impractical in clinical setting.

In this context, automated or semi-automated segmentation methods have been proposed and applied to medical image analysis to leverage the human efforts involved in the segmentation task. Based on the mathematical foundation of each method, segmentation approaches can be roughly divided into several classes: classification (e.g., thresholding, *k*-means), region growing (such as fuzzy connectedness [2]), deformable models (e.g., snake [3], level-set [4–7]), active shape [8] and active appearance models [9], and probabilistic methods (Markov random field [10], graph cut [11]). Hybrid methods [12] combining different existing methods were also proposed. Among segmentation methods, deformable models are still widely used in medical image analysis, especially for cardiac imaging.

The first deformable model parametric formulation was proposed by Kass et al. in 1987 [3]. The idea was to digitize the object boundary into a set of points with predefined connectivity among the nodes; the contour w deforms under the combination of internal forces (such as elasticity and inertia) and external forces (such as image gradient force) to align with the desired object's boundaries. Parametric deformable models, also called snakes in 2D, have been widely applied in various segmentation tasks [13]. In 1998, Xu and Prince [14] proposed the gradient vector flow, or GVF, as a novel driving force for the snakes. This newly designed force overcame several drawbacks in the original snake framework and increased the performance of the active contour. However, there were still some limitations related to the parametric formulation of active contours, such as difficulties to adapt to the contour to topological changes, especially in 3D.

In the late 1990s, Sethian [15] proposed a new framework called level-set to overcome these limitations. The basic idea was to embed the contour evolution into isovalue curves of a function with higher dimensionality. Such functions were called level-set functions. Topological changes could be naturally handled without additional efforts. Moreover, highly convoluted surfaces, which were very hard to handle for parametric deformable models, could also be easily represented under level-set framework. For this reason, level-set formulations have become a really hot topic in image segmentation in recent years. In 2001, Chan and Vese [16] proposed their famous "active contour without edges." In their framework, no image gradient information was needed as with traditional deformable models. Instead, driving forces were derived via energy minimization of the Mumford–Shah segmentation

functional [17]. Their method could easily deal with noisy images. And as a result, this framework has been widely used in ultrasound segmentation [18], brain segmentation [19], and many other applications. However, the introduction of level-set functions implicitly increased the number of parameters of the surface model, which increases the demand for computational power. Although many optimization modifications such as narrowbanding or fast marching schemes were proposed, generally speaking, level-set framework is still a relatively "slow" approach, especially for 3D or 4D data, in comparison with other deformable model frameworks.

As imaging technology evolves, demands for real-time feedback also increases, mostly for interventional imaging and minimally invasive surgery. The latest 3D and 4D imaging techniques and real-time imaging techniques not only provide better appreciation of the anatomy and function of the body but also raise a great challenge for image segmentation in terms of efficiency. In this context, a new framework called active geometric functions (AGFs) is proposed by the authors to push the limits of real-time segmentation. AGF extends implicit representation in the opposite direction as the level-set framework does. Instead of adding one additional dimension to achieve flexibility in topological changes, AGF is achieving benefit in computational efficiency by reducing the dimensionality of the segmentation problem and utilizing efficient function basis. In the following sections, the general AGF framework is proposed and compared to existing deformable model framework. To illustrate some basic concepts of AGF framework, some straightforward examples on synthetic images are presented. Then, the performance of AGF framework is demonstrated in three cardiac image analysis examples, with an extension to multi-phase segmentation in the second one and multi-phase multi-channel in the last one.

2 General Active Geometric Functions Framework

In image analysis, segmentation refers to the process of partitioning a digital image into multiple segments. Image segmentation is typically used to locate objects and interfaces of these objects (lines, curves, etc.) in images. Thus naturally, a segmentation framework should accomplish two important tasks: representing the interfaces (i.e., boundaries) of different objects and driving the surface representation from its default initialization to the actual locations of object boundaries. Especially for deformable model frameworks, which are composed of two critical parts: the "model" or the surface representation, which represents the interface, and the "deformation scheme" driven by applied forces, which fits the model to the image for desired segmentation, result.

2.1 Interface Representation

In all deformable model methods, interface representation is fundamental since the interface or boundary is the target object that needs to be fitted to the image

information to find the desired boundaries. Mathematically, there are two ways to represent the interface:

1. Explicit representation: that is representing the surface by explicitly listing the coordinates of the boundary points (i.e., a parametric representation). This is the representation that original snakes [20] used. The coordinate system can use either natural basis or other basis as well, depending on applications.
2. Implicit representation: that is representing the surface by embedding the boundary as the isovalue curves of some function f called the *representation function*. Level-set functions [4–7] are a good example by embedding the interface as the zero level-set of a distance function.

2.2 Geometric Function

Most of the recent efforts in segmentation based on implicit interface representation have focused on the level-set framework, given its advantages for topological changes and feasibility to represent convoluted surfaces. As mentioned above, level-set functions add one extra dimension beyond the dimensionality of the image data. For example, to represent a surface in 3D space, the level-set function corresponding to the surface will be a trivariate function. For comparison, original parametric deformable models only required a list of point coordinates in 3D. For level-set, this extra dimension brings various benefits as well as additional computation load, which may degrade computational efficiency.

By looking the *opposite* way of level-set frameworks, it is very natural to think of dimensionality reduction in surface representation to reduce the computational complexity. Using the terminology of interface representation, we are looking for a representation function which has fewer dimensions than the image data, i.e., using a 2D function to represent a 3D surface in space. We call such function a *geometric function* or *surface function*.

Mathematically, in N-dimensional space, we can define a geometric function $g : \mathrm{R}^{N-1} \rightarrow \mathrm{R}$ as a special set of functions representing one of the coordinates constrained by the others. Without losing generality, we can assume that this special coordinate is x_0 and the other coordinates are x_1 to x_{N-1}. That is:

$$x_0 = g(x_1, \ldots x_{N-1}). \tag{1}$$

The corresponding representation function f is defined as:

$$f = x_0 - g(x_1, \ldots x_{N-1}). \tag{2}$$

So that the corresponding boundary is the zero-value curve of the function f, i.e., $f = 0$.

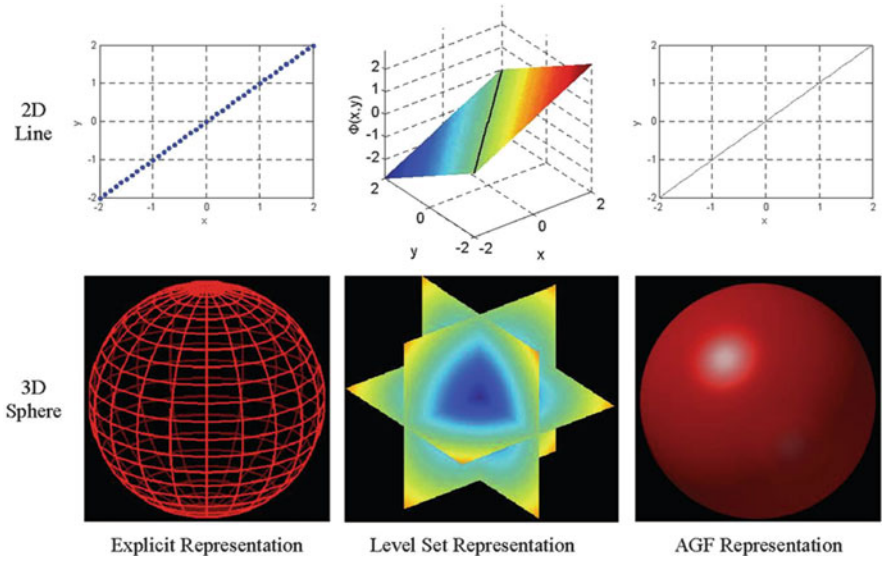

Fig. 1 2D (line interface) and 3D (spherical interface) examples of interface representation using explicit representation, level-set representation, and AGF representation for the same interface

To better shows the differences of explicit representation, level-set representation, and AGF representation, both 2D and 3D examples are shown in Fig. 1.

In 2D, to represent a straight line with slope $= 1$ and passing through the origin $(0, 0)$, there can be three different representations:

1. Explicit representation: such as $\{\ldots(-1, -1), (0, 0), (1, 1), \ldots\}$
2. Level-set: such as the zero level-set of $\Phi(x, y, t) = (x - y)/\sqrt{2}$, note ϕ is a signed distance function, and it is defined on whole x–y plane instead of just on boundary
3. Surface function: such as $y = x$

Similarly in 3D, a unit spherical interface can be represented by an explicit mesh, with corresponding level-set function (Fig. 1b) as a signed distance function is $\Phi(x, y, z) = \frac{1}{\sqrt{3}}(\sqrt{x^2 + y^2 + z^2} - 1)$, and the corresponding geometric function representation (Fig. 1c) is $f(r, \theta, \varphi) = r - 1 = 0$.

Note since these three ways of surface representation are representing the same surface, there are some similarities between the corresponding representation functions for each scheme. It is obvious that both level-set functions and the geometric functions have the same roots, with the fact that the coordinates used in the explicit representation are digitized version of these roots. And geometrically, these roots form the surface we are trying to represent. In other words, explicit representations, level-set distance functions, and surface functions are just three different equivalent forms of the actual interface function f for the targeting surface. The 3D example also illustrates that non-Cartesian coordinate systems can be used in geometric function representation to efficiently represent the desired surfaces.

In this example, however, besides similarity and equivalence, it is more interesting to notice their differences. For example in 2D, the explicit representation is a set of coordinates defined on the 2D x–y plain; the level-set function is an $\mathbb{R}^2 \to \mathbb{R}$ distance function defined on the whole 2D x–y plane; the surface function is an $\mathbb{R} \to \mathbb{R}$ function defined only on a 1D x-axis. As a 1D function, surface function representation has the advantage in efficiency compared with the other two common representations. From the example, we can see that interface representation based on surface function is more accurate than the explicit representation, and has less dimensionality than both other methods. In this way, a surface can be efficiently and accurately represented, which simplifies the downstream mathematical computation such as energy minimizations during image segmentation. A more detailed analysis of the AGF efficiency will come in a later section.

2.3 Driving Force

In general, as a deformable model framework, AGF can utilize any driving forces used in other deformable model framework. In our particular example, we adopt a variational framework in deriving the driving forces given its generic formulization and flexibility in extension for additional energy term that is not covered in our example. For example, we can use the Mumford–Shah segmentation energy functional:

$$E(F, \overrightarrow{C}) = \beta \int_{\Omega \setminus \overrightarrow{C}} (F - G)^2 \mathrm{d}V + \alpha \int_{\Omega \setminus \overrightarrow{C}} |\nabla F|^2 \mathrm{d}V + \gamma \oint_{\overrightarrow{C}} \mathrm{d}s, \tag{3}$$

in which $\overrightarrow{C}$ denotes the smoothed and closed segmented interface, G represents the observed image data, F is a piecewise smoothed approximation of G with discontinuities only along $\overrightarrow{C}$, and Ω denotes the image domain. Given the flexibility of variational frameworks, other segmentation energy functionals may also be easily adopted.

For the segmentation of an N-dimensional image dataset, the active geometric functions framework will solve an $(N-1)$-dimensional variational problem, explicit representation will solve an N-dimensional problem, and the level-set framework will solve an $(N+1)$-dimensional variational problem. It is obvious that AGF framework has advantages in dimensionality reduction when compared with the other two deformable model formulations, at the cost of some flexibility, given the assumption of 1 versus $(N-1)$ coordinate mapping. However, such surface mapping can be further modified via the combination with finite element models. In addition, for typical medical applications, biological surfaces are relatively smooth and well represented with relatively simple geometric functions.

2.4 *Efficiency of AGF*

The efficiency benefit of AGFs comes from three aspects: a dimension-reduced surface representation, use of efficient function basis, and dimension reduction of optimization problem. The first two aspects can greatly reduce the number of parameters used in the optimization procedure.

When comparing the efficiency of different deformable model frameworks, one important factor has to be paid attention to: the number of parameters needed to present the same interface is different for the three methods. Level-set uses every grid point (within the narrowband); explicit parametric models use point lists on the interface, assuming linear connectivity, which usually is less dense than grid points; AGF uses function basis to represent the interface, which extremely reduces the number of parameters. For example, in AGF, only one parameter is needed to represent a circle in any size, whereas the number of parameters needed for level-set and parametric models increases exponentially with the radii of the circle.

For example in 2D, to represent a 100-pixel diameter circle, SFA uses one parameter by using a Fourier basis, a parametric model could use 63-node points $(\pi \times d/5)$ assuming five-pixel spacing (with $63 \times 2 = 126$ parameter), and level-set could use 942 $(3 \times \pi \times d)$ grid points assuming a minimal narrowband used, i.e., three-pixel narrowband (with $942 \times 2 = 1{,}884$ parameters). Here, computational complexity for level-set with narrowband is linear with the parametric model since the dimensionality $N = 2$ and $a^{(N-1)} = a$.

For 3D, it is totally a different story. To present a 100-voxel diameter sphere, SFA uses one parameter by using a Fourier basis, a parametric model could use 1,257 nodes $(\pi \times d^2/(5 \times 5))$ assuming five-pixel spacing (with $1{,}257 \times 3 = 3{,}771$ parameters), and level-set could use 282,743 $(3 \times 3 \times \pi \times d^2)$ grid points assuming a three-pixel wide narrowband (with $282{,}743 \times 3 = 848{,}229$ parameters). Now the computational cost of a level-set formulation is not linear with parametric model. It is a quadratic relationship!

In the general case, for N-D segmentation, let us assume that the number of parameters used in parametric models is L, and AGF can gain some parameter reduction factor of r in each dimension by using surface functions and spacing of parametric nodal points of d-pixels in 1D, and narrowband width of level-sets is b $(b \geq 3)$ in each dimension, then the total number of parameters used in each model is: $(r)^{-(N-1)}L$ for AGF, L for parametric model as the reference, and $d^{(N-1)}b^{(N-1)}L$ for level-sets. In other words, if we use parametric models as the reference method, and represent the computational complexity in terms of the "Big-Oh" representation, then for N-D segmentation, AGF is a $O(-(N-1))$ method in comparison with parametric models and level-sets with narrow-banding which is $O(N-1)$ method. The three models are only comparable when $N = 2$, in which case $N - 1 = 1$ and level-set with narrowband and parametric model are different by a linear factor. However, AGF is still two orders of magnitude faster.

With this analysis, it is clearer of the advantage of AGF in comparison with existing methods, especially for images with higher dimensionality. Nowadays, 3D

and 4D image data are becoming routine in medical image analysis and we think that the advantages for AGF in computational efficiency are critical and nonsubstitutable by existing frameworks.

In general, deformable models usually utilize iterative methods to find the optimal solution for the associated energy minimization framework via curve evolution, which requires an additional variable as an artificial time step added into the functions. In this case, curve evolution with explicit representation with $K-$node points becomes an $N \times K$ variable minimization problem since the evolving curve is represented by

$$\begin{bmatrix} \overrightarrow{X}^0(t) \\ \overrightarrow{X}^1(t) \\ \vdots \\ \overrightarrow{X}^{K-1}(t) \end{bmatrix} = \begin{bmatrix} x_0^0(t) & x_1^0(t) & \cdots & x_{N-1}^0(t) \\ x_0^1(t) & x_1^1(t) & \cdots & x_{N-1}^1(t) \\ \vdots & \vdots & \vdots & \vdots \\ x_0^{K-1}(t) & x_1^{K-1}(t) & \cdots & x_{N-1}^{K-1}(t) \end{bmatrix}, \tag{4}$$

with $N \times$ K evolving variables.

Curve evolution with level-set becomes an $(N+1)$-variate functional minimization problem since the evolving curve is represented by

$$\phi(\overrightarrow{X}, t) = \phi(x_0, x_1, \ldots x_{N-1}, t), \tag{5}$$

which has to be solved for every point on the entire image domain or within the narrowband.

Curve evolution with AGF becomes an N-variate functional minimization problem since the evolving curve can be represented by

$$x_0(t) = f(x_1, x_2, \ldots x_{N-1}, t). \tag{6}$$

The advantage in dimensionality reduction for surface function actives over level-set framework is evident.

The advantage of AGF over explicit expression is in two aspects. First, in explicit representation, for each node point, there are N evolving variables, whereas in surface function representation, there is only one variable for each corresponding points. This will become more evident if we digitize (6) and reformulate in a similar form as in (4) (Note in this case, AGF is operated at degenerated mode with reduced efficiency compared with using basis functions):

$$\begin{bmatrix} \overrightarrow{X}^0(t) \\ \overrightarrow{X}^1(t) \\ \vdots \\ \overrightarrow{X}^{K-1}(t) \end{bmatrix} = \begin{bmatrix} x_0^0(t) & x_1^0 & \cdots & x_{N-1}^0 \\ x_0^1(t) & x_1^1 & \cdots & x_{N-1}^1 \\ \vdots & \vdots & \vdots & \vdots \\ x_0^{K-1}(t) & x_1^{K-1} & \cdots & x_{N-1}^{K-1} \end{bmatrix}. \tag{7}$$

Although the memory usage of (7) is the same as (4), the curve evolution of (7) has $N-1$ less dimensionality than (4), which usually leads to faster and more stable convergence. Generally speaking, the more parameters to be optimized, the larger possibility that local minimums and saddle points exist, especially with the presence of noise. Of course it is not necessarily true for every case that 1D optimization is more stable than N-D; they could be equivalent. But even for that, the searching space for 1D case is much smaller than the N-D one, which leads to faster convergence.

Another aspect is that (6) can be represented via function basis, such as cubic Hermite functions, in which case only a few weighting parameters rather than a lot of digitized node points have to be stored and iterated on. This can further improve the accuracy, efficiency, and numerical stability.

2.5 Beyond Efficiency Benefit

Beside the advantage brought by dimensionality reduction, AGF framework is also benefited from its intrinsic function representation. By utilizing the idea of surface function, rather than an explicit list or an implicit higher order function, AGF can immediately utilizing some basic ideas in the algebra to further improve the performance.

Basis representation is a very basic idea in function representation. By utilizing surface function basis other than the nature Cartesian coordinates, AGF can not only easily deal with enclosed shape as heart, liver, and various tumors but also easily incorporate shape prior information. By utilizing function basis other than natural basis, AGF can not only efficiently represent convoluted surfaces but also naturally enforce prior knowledge on surface smoothness.

By using the concept of piecewise function, AGF can be extended with a combination of finite element patches to capture much more complex shape, like left ventricle. By incorporating repositioning and reorientation, the capture range of AGF can be largely increased, giving less dependence on initialization.

2.6 Comparison with Other Deformable Models

Although as mentioned above, the interface functions for the three deformable models are equivalent in terms of surface representation, different ways to approach interface formulation provide different benefits and limitations.

Parametric active contours with explicit representations provide relative simple representations through interface point coordinates and do not add additional dimensionality to the optimization problem. However, it cannot easily handle topological changes, and usually requires some prior knowledge about the target topology for proper initialization. It is also not trivial to determine whether an

arbitrary pixel is inside or outside the segmented objects. Moreover, in order to compare to other segmentation results such as manual tracing, it is usually not very easy to directly compute quantitative metrics such as surface distances since it requires pairing of closest points.

The level-set framework based on implicit representations via distance functions can automatically deal with topological changes and allows easy determination of whether a point is inside the object or not by simply looking at the sign of the level-set function at the point location. However, the level-set formulation implicitly introduces a new dimension, i.e., the value of the level-set function, for each voxel in the whole image data space, whereas the other two models only focus on the interface itself. This type of formulation implicitly increases the dimensionality of the variational problem and thus increases the computational cost of the optimization process. Even though a narrowband approach can improve the efficiency by focusing only around the interface, it still requires more voxel information than the other two formulations. In terms of segmentation comparison, if the level-set function is the signed distance function, it is very easy to compute the distance between surfaces, although in most of implementations, level-set functions after few iterations do not necessarily remain as signed distance functions, especially for those using narrowband approaches.

Active geometric function is a kind of marriage of the previously discussed models: it focuses only on the interface as the explicit representation, while being formulated as an implicit representation like the level-set framework. It has advantage on dimensionality reduction in surface representation compared with level-set. It can utilize function basis to avoid memory-inefficient boundary point digitizing. Even if a degenerated digitized form has to be used and the surface representation is similar to explicit expression, AGF still has been compared with parametric deformable model. This dimensionality reduction gives AGF advantages in efficiency in both aspects of the deformable model (i.e., surface modeling and deformation scheme). Furthermore, with an implicit representation, it is straightforward to determine whether a point is inside the contour by simply comparing the value of the surface function for that point with the value of the surface function on the boundary. In addition, surface functions enable immediate quantitative evaluation of the segmentation results via surface comparisons and differences in surface function values. However, similar to parametric active contours, it is not trivial to deal with topological changes, with its flexibility in topological changes limited by the function basis used in the model.

3 Illustration on Synthetic Image

To illustrate the performance and some advantages of the active geometric functions, several segmentation examples are presented in this section on a synthetic image. This section specifically focuses on two implicit representation methods: the AGF method and the level-set representation. Both segmentation frameworks use

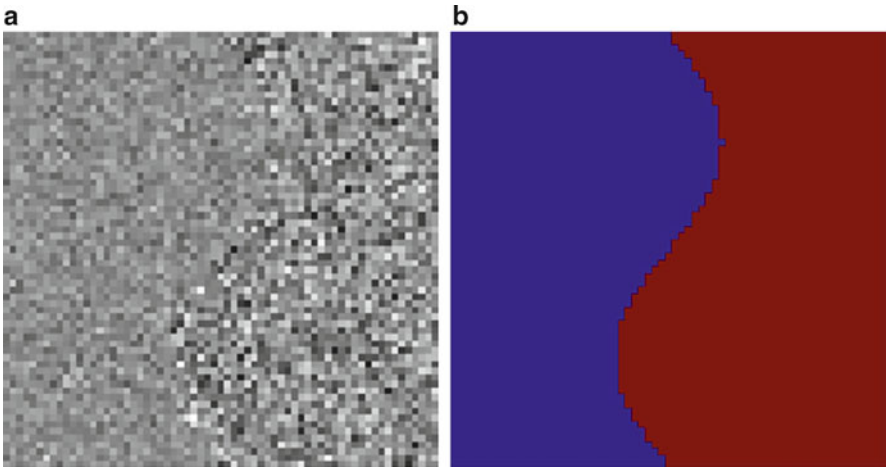

Fig. 2 (**a**) Synthetic image composed of two regions with normal distributions with the same mean values but different standard deviations; (**b**) corresponding binary images indicating the ground truth segmentation. The *blue* region has a standard deviation of 5 and the *red* one has a value of 10 in the original image. The interface is a sine function

variational formulae and interface functions. A fair head-to-head comparison is possible by setting identical segmentation energy functional and numerical schemes for both methods.

3.1 Synthetic Image

To illustrate the flexibility of the proposed AGF framework, instead of using an example on common piecewise smooth images, in this section, both AGF and level-set approach were challenged with textured regions segmentation.

The synthetic image, as shown in Fig. 2a, was composed of two parts. Pixel intensities for each part were randomly sampled from normal distributions with identical mean values and different standard deviations. The corresponding ground-true binary image is shown in Fig. 2b. The blue region had a standard deviation of 5 and the red region had a value of 10. The interface between the regions was a sine function. The dimension of the image was 65 by 65 pixels.

3.2 AGF Using Numerical Solution

Usually in image segmentation, especially for the level-set framework, it is not easy to find a closed form interface function. Instead, a numerical solution or

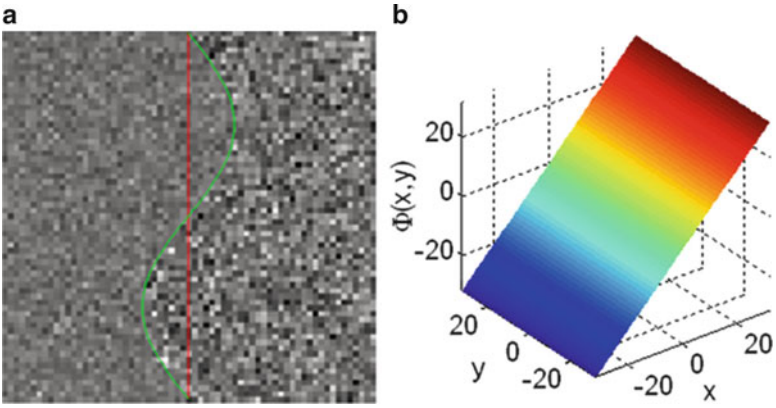

Fig. 3 (**a**) Initialization of the deformable model as in *red* and the ground truth interface in *green*; (**b**) corresponding signed distance function for the level-set initialization

approximation of the interface function is computed via iterative numerical energy minimization. With the level-set functions, this requires computation values of the level-set function at each pixel (or on a narrowband near the interface). With AGF, we only need to compute the surface function values at each pixel on the interface.

Given the texture-based segmentation problem presented in Fig. 2, the following energy functional was selected:

$$E = \int_{\Omega} (\sigma(x, y) - \delta_1)^2 H(x, y) \mathrm{d}x\mathrm{d}y + \int_{\Omega} (\sigma(x, y) - \delta_2)^2 (1 - H(x, y)) \mathrm{d}x\mathrm{d}y, \quad (8)$$

where Ω the image domain, $\sigma(x, y)$ is a standard deviation estimator for pixel (x, y) within a small neighborhood, and H is the Heaviside function, which equals 1 inside the current interface and 0 outside. The parameters δ_1 and δ_2 are computed as the average standard deviations inside and outside the current interface, respectively. The optimal segmentation will partition the image into two regions, with relative homogeneous distributions of the standard deviations within each region. This approach is equivalent to segmenting a representation of local standard deviation $\sigma(x, y)$ values of the image, knowing that for normal distributions $N(\mu, \sigma)$, average standard deviations, converge to the scale parameter σ. The Chan–Vese level-set numerical schemes described in [6] were used for the level-set implementation. For simplification, no curvature constraints were used.

Both methods were initialized as a straight line at the center of the image, as shown in Fig. 3a. The ground truth boundary is shown in green in the same figure. Corresponding surface functions for AGF was just a $1 - D$ constant function as $y(x) = 0, -32 \leq x \leq 32$, whereas the corresponding level-set function was a plane with slope 1 as shown in Fig. 3b.

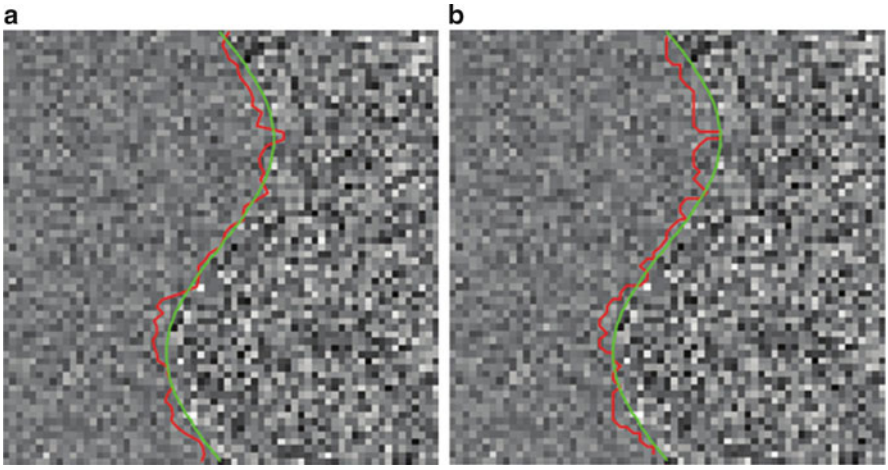

Fig. 4 Final segmentation (*red line*) compared to the ground truth (*green line*) for (**a**) active geometric functions and (**b**) Chan–Vese level-set with identical segmentation energy functionals and numerical schemes

Both methods were implemented in Matlab©. All computations were executed on a 2.4 GHz 64-bit AMD server, running Red Hat Linux Enterprise AS. For each pixel, a 7×7 neighborhood was used to compute the local standard deviations. An artificial time step was set to five for both methods. The stability of the surface was considered as the convergence criterion.

In order to quantitatively evaluate the segmentation result for each method, true positive (TP) fraction ratio and false positive (FP) fraction ratio were computed. In addition, root-mean squared error in distances from the interfaces to the ground truth was estimated.

It took eight iterations (0.38 s) for the AGF to converge, each iteration taking about 47.5 ms. The final segmentation result is shown in Fig. 4a, with red line indicating the automatic segmentation and green line indicating the ground truth. The TP fraction ration was 99.7%, whereas the FP ration was 3.8%. RMS error of the distance to the ground truth was 1.56 pixels.

For comparison, it took 36 iterations (3.43 s) for the level-set approach to converge, each iteration taking about 95.3 ms. Final segmentation result is shown in Fig. 4b, with the red line indicating the automatic segmentation and green line indicating the ground truth. The TP fraction ration was 99.6%, whereas the false positive fraction ration was 4.0%. The RMS error of the distance to the ground truth was 2.15 pixels.

From this experiment, the AGF framework clearly demonstrates advantages in computational efficiency when compared to the level-set framework, with not only a shorter time per iteration but also fewer iterations. This is mainly due to the fact that the level-set function has to be updated over theentire image domain whereas the

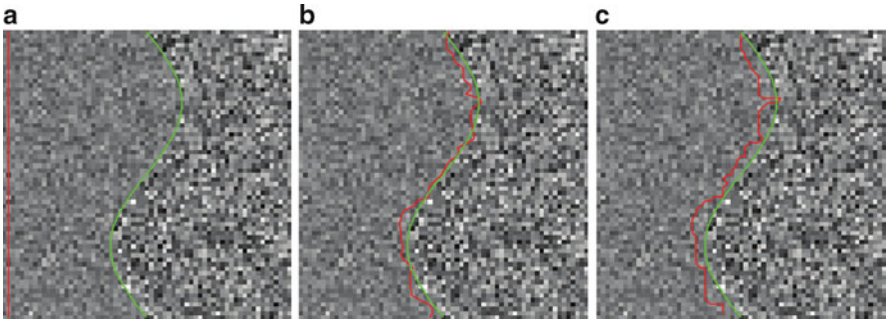

Fig. 5 (**a**) Initialization of the deformable model, in *red*, at left-most of the image with the ground true interface in *green*; corresponding final segmentation (*red line*) compared to the ground truth (*green line*) for (**b**) active geometric functions, and (**c**) Chan–Vese level-set under identical segmentation energy functional and numerical schemes

AGF is only updated at the interface. Quantitative segmentation comparison yielded comparable segmentation performance for both methods, AGF having slightly better performance.

To test the ability of the proposed SFA framework under different and more challenging initialization setups, another initialization on the left-most boundary was tested as well for both methods. The initialization and final results from both methods are shown in Fig. 5.

Both methods spent much more time to reach the final results. It took 25 iterations for the AGF and 75 iterations for the level-set method to converge. Segmentation by AGF yielded a TP of 99.81% and a FP of 4.03%. Segmentation by the level-set framework generated a TP of 99.91% and a FP of 6.58%. RMS errors were 1.61 pixels for AGF and 2.80 pixels for the level-set. Both methods had slightly poorer performance compared with the results using closer initialization. However, the AGF framework still exhibited advantages in efficiency and slightly better performance.

It has to be noted that in numerical solution, AGF was operating in a "deenerated" form which is similar to the parametric deformable model. But it still has the advantage in efficiency over parametric deformable model since only one variable per node is evolving, rather than N variables per node for the explicit representation.

3.3 AGF Using Analytical Solution or Function Basis

Another advantage of the AGF framework is to provide closed-form solution or approximation for the interface, which, as indicated in the method section, can bring additional gain in efficiency. Since the surface function is a $(N-1)-\mathrm{D}$ function for $N-\mathrm{D}$ image data, we can choose arbitrary bases (natural bases or other bases) in the function space to express the surface function. Especially when some

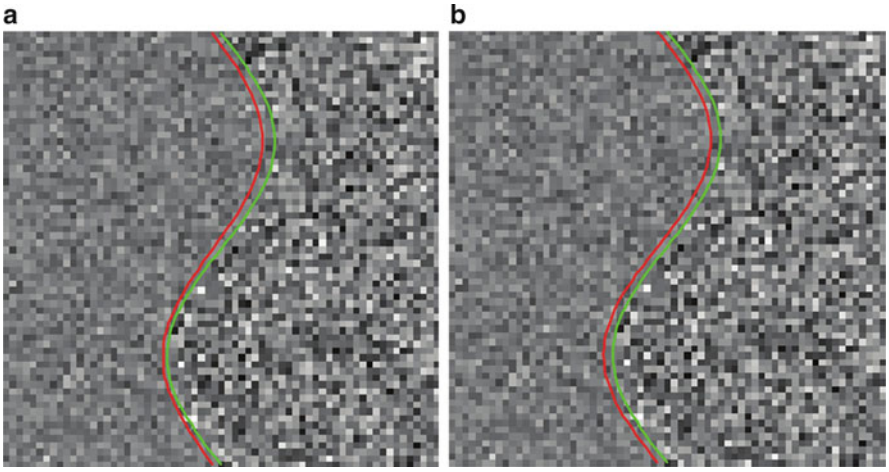

Fig. 6 Final segmentation (*red line*) compared to the ground truth (*green line*) for AGF under (**a**) close initialization and (**b**) far-away initialization

prior knowledge about the interface properties is known, proper choice of basis functions can not only seamlessly incorporate such prior knowledge but also further increase the efficiency of the AGF framework. Moreover, having an analytical form of the interface can provide additional benefits like analytical differentiation in a downstream analysis.

To illustrate this point, assuming that by looking at the original image data, we decided to use the following sine function to describe the interface.

$$y(x) = a\sin(x) + b, \tag{9}$$

the problem was then converted to the identification of the optimal parameters (a, b) that minimize the segmentation functional. Since there were only two parameters to be optimized, only a few pixels were needed during each iteration. In this example, we worked with 9 pixels on the boundary to ensure the overcompleteness of the estimation, compared to all pixels on the boundary as in the numerical solution scenario. This formulation reduces computational cost by utilizing prior knowledge on the shape of the interface. Close and far-away initializations were tested. Final segmentation results are shown in Fig. 6.

It took the AGF 10 iterations to converge under close initialization. Each iteration took 21 ms. The TP ratio was 100%; the FP ratio was 3.79%. The RMS error was 1.26 pixels. Under far-away initialization, it took the AGF 25 iterations to converge. Each iteration took 17 ms. The TP ratio was 100%; the FP ratio was 4.50%. The RMS error was 1.40 pixels.

The presented results showed that by utilizing prior knowledge, both efficiency and accuracy could be improved under the same initialization setups and numerical schemes. Besides, the use of a closed form function provides a continuous expression of the interface which may be of great benefit for downstream analysis.

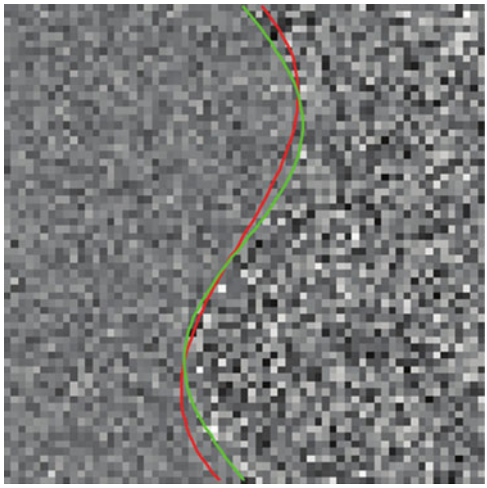

Fig. 7 Final segmentation (*red line*) compared to the ground truth (*green line*) for the AGF using cubic polynomials as the surface approximation

In real applications, it can be difficult to identify an accurate surface function. In this context, an approximation function or approximation basis functions can be used. In the same example, when we used cubic polynomials to approximate the interface, it took longer time, 3.59 s, to converge, with corresponding RMS errors of 1.66 pixels. The final segmentation result is shown in Fig. 7.

4 Endocardial Segmentation in 4D Ultrasound

4.1 Geometric Function Setup

AGF is a generic framework. The actual geometric function is not necessarily defined on Cartesian bases. Any spatial basis can be chosen for the purpose of efficiency in surface representation. In cardiac applications, given the ellipsoidal shape of the left ventricle, usually spherical coordinate system [21] or prolate spheroidal coordinates system [22] can be used to exploit the shape prior knowledge. Generally in 3D space, a geometric function can be described through an equation $v_0 = g(v_1, v_2)$ with coordinates (v_0, v_1, v_2). (v_0, v_1, v_2) can be (r, θ, z) in cylindrical coordinate systems, (r, θ, ϕ) in spherical coordinate systems, and (λ, θ, μ) in prolate spheroidal coordinate systems. In this chapter, although prolate spheroidal coordinate systems proposed by Hunter [23] are used, all formulations are expressed in generic form and free of change in coordinate system.

Another benefit of AGF is that it does not require using a single function to represent the entire surface. Piecewise smooth functions building on conceptual patches can be adopted for accuracy and flexibility. Specifically, in this chapter,

geometric functions described by a conceptual finite element model utilizing cubic Hermite polynomials as geometric function basis were used to efficiently represent the convoluted endocardial surface. The entire endocardial surface was represented by geometric functions built on a "mesh" composed by 8×8 conceptual patches. Given the dimensionality reduction of the geometric function representation, on each conceptual patch, a 2D cubic geometric function was defined, using cubic Hermite polynomials as basis functions. On each node of a four-node patch, there were four Hermite coefficients H^i, $i = 1, 2, 3$, and 4, controlling the weights of each basis function. Given their efficiency in surface representation, Hermite polynomials are widely used in cardiac biomechanics studies for surface representation [1, 24, 25]. A simple 8×8 finite element model (FEM) with intrinsic C^1 continuity can sufficiently represent the geometry of the endocardium [1, 25]. In our implementation, this 8×8 convention was followed.

4.2 Energy Minimization

Following the same rationale used in the Chan and Vese level-set [15] framework, the energy in (3) can be minimized via a Newton downhill method:

$$H^{i,t+dt} = H^{i,t} - dt \frac{\partial E}{\partial H^i}, \tag{10}$$

with dt representing the artificial time-step in numerical iterations. It has been shown in [22] that for binary segmentation problem, into two partitions $\{\Omega^i\}_{i=1,2}$ of the image domain Ω, $\frac{\partial E}{\partial H^i}$ has the surface integral form of

$$\frac{\partial E}{\partial H^i} = \int_{v_1, v_2} \left(2f^i \left(u - \frac{c_1 + c_2}{2} \right) (c_2 - c_1) V + \upsilon \frac{\partial A}{\partial H^i} \right) \mathrm{d}v_1 \mathrm{d}v_2, \tag{11}$$

with f^i representing the surface coefficient with respect to the basis function values at current surface location, c_1 and c_2 representing the average intensity values in the two partitions, V representing the scaling factor due to coordinate transformation and A representing the surface area. Details on the computation of this term can be found in [22]. The second part in the integration is a curvature term, which is composed by two nonlinear terms involving H^i and scaling factors. Due to the intrinsic continuity in the Hermite representation, contribution from this term was usually very small. For this reason, and for cost-effectiveness, this terms can be either suppressed as proposed in [22] or replaced by an equivalent linear term [21] derived from minimizing the curvature instead of the surface area as in the original Chan and Vese framework.

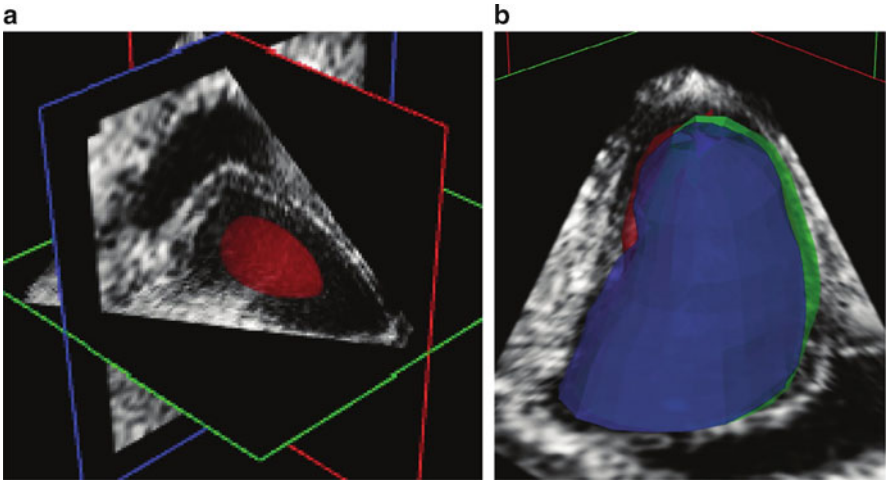

Fig. 8 Illustration of the 4D ultrasound cardiac segmentation of the endocardial surface. (**a**) Automatic initialization of the LV surface with an ellipsoid positioned at the center of the volume overlaid with 4D data at end-diastole. (**b**) Overlaid final segmentation results from AGF (*red*), one expert (*green*), and the other expert (*blue*) over 4D data at end-diastole

4.3 Results

The proposed method was tested on 35 RT3D (3D + time) datasets containing 425 volumetric frames, acquired by a Philips© iE33 ultrasound machine and a X3–1 3D transducer (3 MHz, 25 fps) during five separate canine experiments, with various degrees of induced ischemia as well as controlled stages. Each dataset contained 10 to 15 volumetric frames, depending on the heart rate. Each volume was about $200 \times 200 \times 200$ in matrix size with pixel size of 0.8 mm in each dimension. For quantitative comparison purpose, endocardial borders for all datasets were manually traced by an experienced expert with a computer-aided interface. Eleven datasets were also traced by two other experts to estimate the inter-observer variability. Average distances between two surfaces served as the quantitative metrics to describe surface discrepancy. As illustrated in Fig. 8a, all 425 segmentation experiments were initialized with a small ellipsoid (defined as an isosurface in prolate spheroidal coordinates) at the center of the image volume and aligned with the vertical direction of the image data, without using any prior knowledge on the alignment of the ventricular long-axis. The segmentation was fully automated without any manual modification. A sample frame overlaying RT3D ultrasound data with segmentation from the AGF formulation (red) and manual tracings from two experts (green and blue) are shown in Fig. 8b. All three surfaces were very close to each other. This observation was confirmed by quantitative validation. Over all the set of 425 frames, the mean surface distance between the AGF segmentation and the manually traced surfaces was 4.0 mm (about three

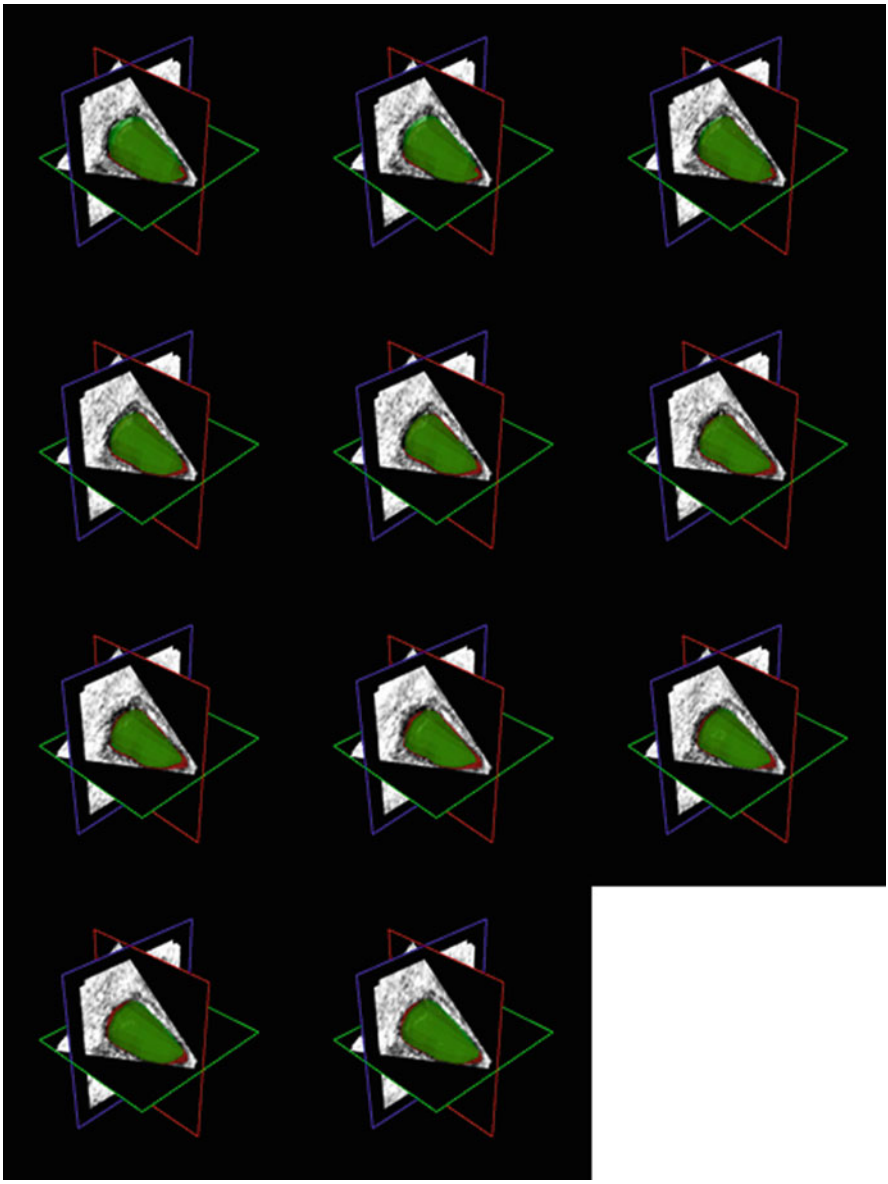

Fig. 9 Segmentation illustration of the endocardial surface on a normal heart over one cardiac cycle: AGF surface (*red*) and manually traced surface from one expert (*green*)

times the pixel diagonal dimension) with a standard deviation of 3.2 mm; the mean distance between two manual tracings was 4.2 mm with a standard deviation of 3.3 mm. Illustrations of dynamic AGF segmentation over entire cardiac cycles on normal and ischemic hearts are presented in Figs. 9 and 10, respectively. On both

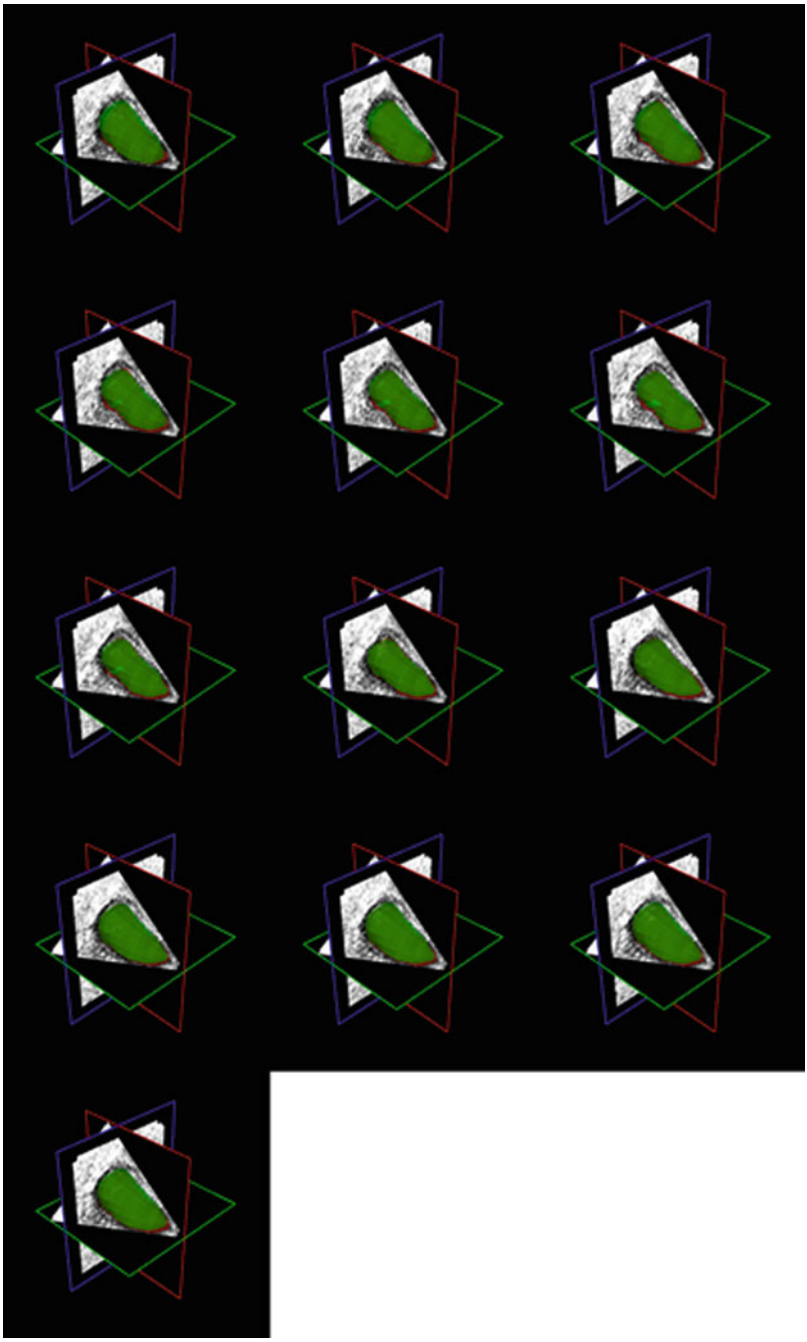

Fig. 10 Segmentation illustration of the endocardial surface on an ischemic heart over one cardiac cycle: AGF surface (*red*) and manually traced surface from one expert (*green*)

types of data, the AGF segmentation yielded endocardial surfaces very close to the manually traced ones, suggesting that our method is not affected by the presence of local abnormal motion patterns.

On average, it took the AGF segmentation framework, implemented in C++, 32.9 ms to converge on a single 3D frame, on a regular Pentium 2.0 GHz PC running Redhat Linux, enabling a potentially 33 frames per second segmentation rate. Note that this rate is faster than the actual imaging acquisition rate (up to 25 Hz), suggesting that the AGF segmentation framework could enable online segmentation.

5 Myocardial Segmentation on High Speed MRI

5.1 Coupled Active Geometric Functions

Each AGF model could divide an image into two partitions, i.e., the object (or the foreground) and the background. In order to simultaneously segment multiple objects, similar to level-set framework [19, 26, 27], more than one deformable model could be introduced at the same time. In order to realize simultaneous multi-object segmentation, these deformable models will be coupled together via some mechanism, such as distance [27] or multi-phase fashion [19, 26].

One benefit of implicit surface representation is that the function value of the representation function could be assigned with some physical meanings that may be convenient during segmentation iterations. In level-set framework, usually signed distance functions [4, 5] are usually chosen as the level-set function, which not only offer an immediate measure or approximation of the distance to the current interface for any given point but also have some nice features, such as unitary slope, that would simplify the energy minimization equations. As another implicit surface representation approach, values of geometric functions also have physical meanings, i.e., the coordinate values along the direction of one spatial basis functions. These values generally do not correspond to the Euclidean distances for given points to the current surface. However, recalling the definition of coordinate values, it is obvious that this value is a distance measure along the corresponding basis direction. If this basis is linear, the function value is thus a signed distance function, with some scaling factor, along the basis direction. Moreover, such distance measures usually are an upper bound to the true point-to-surface distance. And sometime it also has clinical importance and diagnostic values. For example, in cardiac diagnosis, radial displacement and radial thickening are important metrics for cardiac dynamics. By choosing a coordinate system with radial directions, such as polar coordinates, geometric function values can be immediate measures of radial distance.

This nice feature can also be used in coupling active geometric functions models. Specifically for myocardial segmentation in 2D + time cine series, two

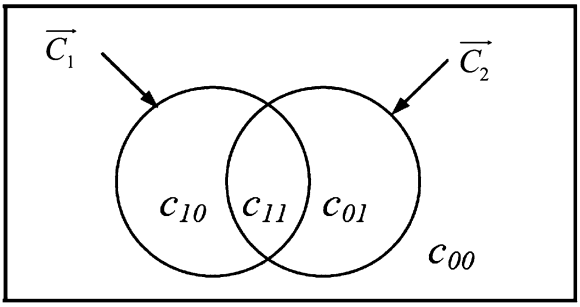

Fig. 11 Partitioning of the image into four phases using two level-set functions. Average intensity values are designed as c_{00}, c_{10}, c_{01}, and c_{11}

geometric functions can be introduced to simultaneous segments, the endocardial and epicardial surfaces. Running this segmentation protocol, both models were driven by forces computed via energy minimization. The total energy was defined by combination of Mumford–Shah energy functionals and a penalty term computed from the signed radial distance between the two surfaces. Specifically, assuming $\overrightarrow{C_1}$ and $\overrightarrow{C_2}$ are the two coupled surfaces with corresponding geometric functions g_1 and g_2, then in polar coordinates system, we had $r = g_1(\theta)$ and $r = g_2(\theta)$. We shall assume $\overrightarrow{C_1}$ targets the endocardial surface and $\overrightarrow{C_2}$ targets epicardial surface. Generally, these two models can divide an image into four different partitions [19, 26], with the average intensity values within each partition defined as c_{00}, c_{10}, c_{01}, and c_{11}, as shown in Fig. 11.

Let a function d be a membership penalty function defining a penalty associated with its function variable. In our implementation, a linear penalty function similar to wavelet soft-thresholding [28] function was used. However, more sophisticated membership function such as fuzzy membership function [29] can be used. The membership function was defined as:

$$d(x) = \begin{cases} x - d_{\max}, x \geq d_{\max} \\ 0, d_{\min} \leq x \leq d_{\max}, \\ x - d_{\min}, x \leq d_{\min} \end{cases} \tag{12}$$

with $d_{\min}$ and $d_{\max}$ defining acceptable range of membership. The shape of the membership penalty function is given in Fig. 12. The idea is to penalize large and small values beyond an admissible range of values for the thickness of the myocardium being segmented.

Lastly, a smoothness constraint was superimposed to each AGF model to ensure that the papillary muscles were excluded in the endocardial segmentation. In our experiments, since the doctors preferred much smoothed segmentation with papillary muscles excluded, strong smoothness constraints were imposed on both surface functions, resulting in circle-like segmentations.

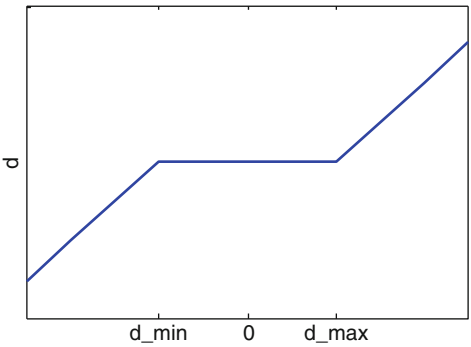

Fig. 12 Shape of membership penalty function

Thus, the final energy functional was defined as:

$$E\left(F,\overrightarrow{C_1},\overrightarrow{C_2}\right)=\lambda_{11}\int\limits_{\substack{\text{inside } C_1\\ \text{inside } C_2}}(u-c_{11})^2+\lambda_{10}\int\limits_{\substack{\text{inside } C_1\\ \text{outside } C_2}}(u-c_{10})^2$$
$$+\lambda_{01}\int\limits_{\substack{\text{outside } C_1\\ \text{inside } C_2}}(u-c_{01})^2+\lambda_{00}\int\limits_{\substack{\text{outside } C_1\\ \text{outside } C_2}}(u-c_{00})^2$$
$$+\gamma_1\oint_{\overrightarrow{C_1}}ds+\gamma_2\oint_{\overrightarrow{C_2}}ds+\upsilon\oint|d(g_2-g_1)|^2 \tag{13}$$

with $\lambda_{ij}, i=0,1;\ j=0,1$ as the parameters balancing the homogeneity measures, γ_1, γ_2 as the weighting factor for the smoothness constraint for each AGF model, and υ as the parameter controlling the weight for membership penalty.

5.2 Results

The proposed algorithm was applied to 414 frames of clinical phase train imaging (PTI) [30] cardiac data with average temporal resolution of 2 ms. Each image frame had a dimension of 160×192 pixels. Manual tracing of the endocardial and the epicardial surfaces was also performed by an experienced expert serving as a gold standard to evaluate the performance of the proposed multi-phase AGF method. The multi-phase version of the AGF algorithm was implemented in Matlab© (The Mathworks, Natick, MA).

The coupled AGF surfaces were automatically initialized in 2D as two small circles with different radii at the center of the image on the first frame of whole MRI series as shown in Fig. 13, based on the fact that for cardiac MRI cine data, the center of the images is set at the center of LV. The segmentation process was run on the first frame and iteratively propagated to the following frames, utilizing

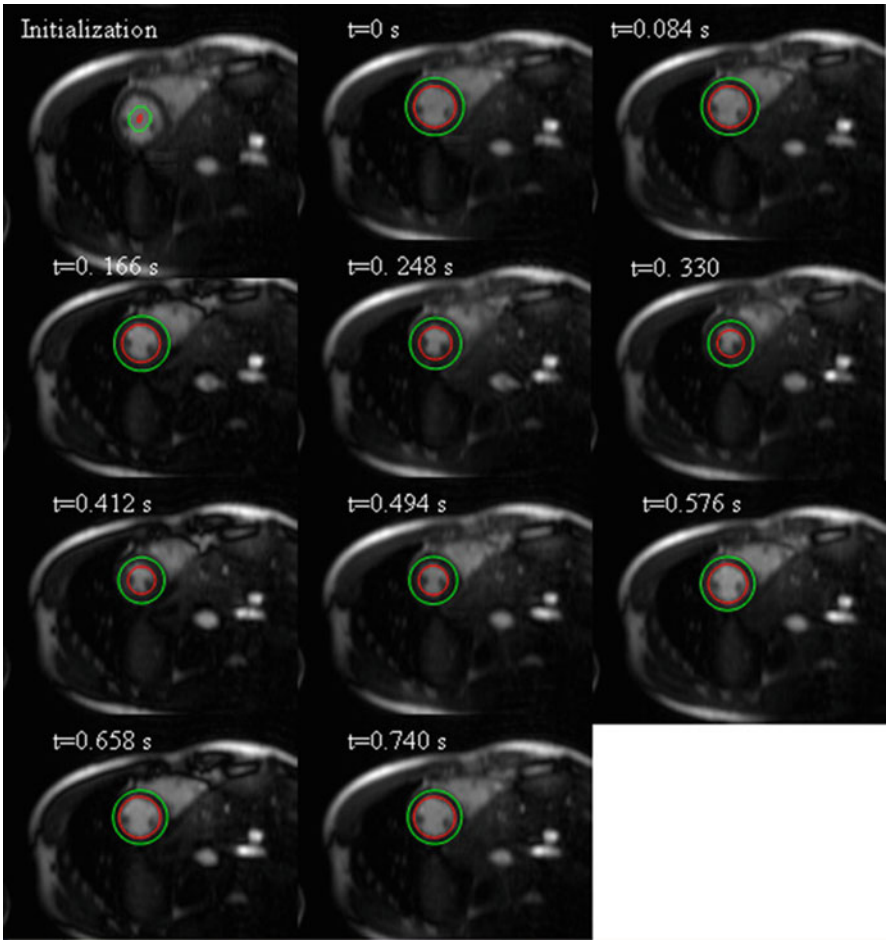

Fig. 13 Illustration of initialization at the first frame and segmentation of endocardium and epicardium on 10 frames out of 414 frames. The *red curves* indicate the automated endocardium segmentation; the *green* ones are automated epicardium segmentation

the high temporal resolution that the PTI data offer, followed by curve evolution until convergence and propagation to the next frame. Figure 13 shows 10 sample frames of the segmentation results taken at different phases of the cardiac cycle. Both endocardial and epicardial surfaces were accurately segmented on all frames with papillary muscle successfully excluded.

The proposed AGF segmentation process took 500 ms to segment all 414 frames. On average, it took six iterations to reach a stable endocardial and epicardial surface segmentation, each iteration using 0.194 ms with a Matlab© implementation. All computations were executed on a 2.4 GHz 64-bit AMD server, running Red Hat Linux Enterprise AS. Quantitative evaluations were performed both on endocardial

and epicardial segmented surfaces, in terms of area difference, true positive volume fraction, and false positive volume fraction. For the endocardial surface, the average surface distance (mean $\pm$ standard deviation) was $8.7 \pm 5.9\%$, the true positive volume fraction was $93.3 \pm 7.0\%$, and the false positive volume fraction was $7.0 \pm 4.6\%$. For the epicardial surface, the average surface distance was $6.8 \pm 5.3\%$, the true positive volume fraction was $95.5 \pm 3.6\%$, and the false positive volume fraction was $7.8 \pm 5.2\%$. Average distance between automated segmented surfaces and manually traced surfaces was 3.0 ± 2.4 pixels. Comparison metrics from a recent systematic study on cardiac MRI segmentation [31] were used as a reference, which suggested that our results were comparable to level-set based methods as well as inter-observer variability. Note that the PTI MRI images had slightly coarser resolution as well as a slightly blurrier appearance than regular cardiac cine MRI due to undersampling in the phase-encoding direction, which may increase inter-observer variability as reported in [31].

6 Segmentation of Cardiac MR Perfusion Images

In this section, we illustrate the feasibility of AGF in multi-phase vector image segmentation on an application for dynamic cardiac MR perfusion image segmentation. In order to segment the myocardial surfaces from cardiac perfusion time series, we used the extension of AGF segmentation framework to vector-valued image space, by treating the time course of each pixel intensity as a vector.

A TurboFLASH pulse sequence was employed on a whole-body 3T scanner (Siemens© TIM Trio) equipped with a 12-element coil array. The relevant imaging parameters included: FOV $= 320 \times 320$ mm, image matrix $= 128 \times 128$, slice thickness $= 8$ mm, flip angle $= 10^{\circ}$, TE/TR $= 1.3/2.5$ ms, BW $= 1{,}000$ Hz per pixel, saturation recovery time delay (TD) $= 10$ ms, and repetition time $= 40$ ms. The AGF model was initialized in 2D as two small circles inside the endocardium on the frame corresponding to peak blood enhancement. Manual tracing of the endocardial and epicardial surfaces was also performed by an experienced expert serving as a gold standard to evaluate the performance of the proposed multi-phase multi-channel AGF segmentation framework. The algorithm was implemented in Matlab© (Natick, MA).

It took the AGF segmentation framework 16 iterations to reach a stable endocardial and epicardial segmentation under a Matlab© implementation. The total processing time was 31 ms. All computations were executed on a 2.3 GHz Intel Xeon workstation, running Windows XP. Quantitative evaluations were performed both on endocardial and epicardial segmented surfaces, in terms of area difference, true positive volume fraction, and false positive volume fraction. For the endocardial surface, the average surface distance was 6.8%, the true positive volume fraction was 91.4%, and the false positive volume fraction was 1.9%. For the epicardial surface, the average surface distance was 1.5%, the true positive volume fraction was 97.8%, and the false positive volume fraction was 3.7%. These results are

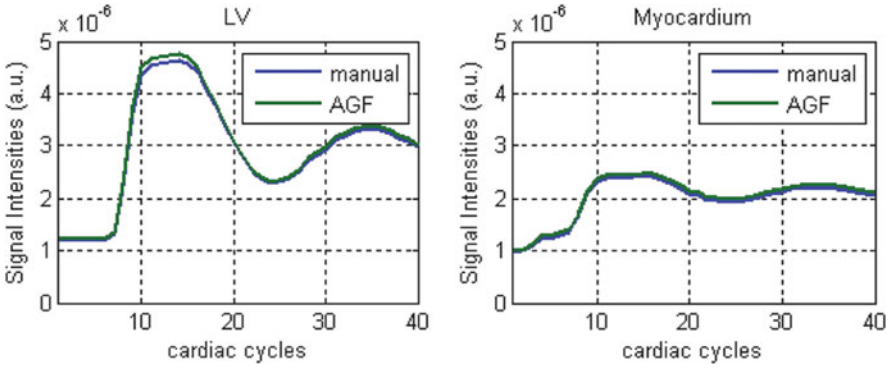

Fig. 14 Multi-phase and multi-channel AGF segmentation on cardiac perfusion MR images. Signal intensity (SI) curves from manual and the AGF segmentation inside the LV blood pool (*left*) and inside the myocardium (*right*)

comparable to a recent systematic study on cardiac MRI segmentation. Temporal curves of the average signal intensity (SI) inside the left ventricular (LV) blood pool and inside the myocardium were derived for both the AGF segmentation and the manual tracing, as illustrated in Fig. 14. Average errors in the SI curves (mean $\pm$ standard deviation) were $1.8 \pm 0.7\%$ for the LV blood pool and $2.8 \pm 0.7\%$ for the myocardium. The proposed AGF segmentation framework only required 31 ms to segment the myocardium on the multi-phase MRI dataset. Besides offline data analysis, the proposed method could be applied to other cardiac applications where real-time feedback is preferred, as in MR guided interventions, or online processing when combined to image acquisition and reconstruction.

7 Conclusion

The active geometric functions (AGFs) framework was presented as a new surface representation framework for image segmentation with deformable models. Unlike existing frameworks including level-set and parametric deformable models, the AGF framework uses an $(n-1)-$D surface representation for an n-D object, based on a close representation of the deforming shape with a shape function defined in a curvilinear coordinate system. The underlying numerical model of the geometric functions and the reformulation of the energy functional in terms of surface integrals bring tremendous benefits in terms of computational efficiency and reduction in complexity for both surface deformation and energy minimization.

Similarly to the level-set framework, the AGF framework can be seamlessly extended to multi-phase (i.e., multi-objects) and multi-channel (or multi-modal) image segmentation, as well as incorporate image or shape prior information, thanks to the straightforward determination of the inside and outside of the curves being deformed. By using the concept of interpolating shape functions, the AGF

framework can be used, when combined with finite element patches, to capture complex shapes with controlled smoothness. By incorporating repositioning and reorientation, the capture range of the AGF framework can be largely increased, and made less dependent on the initialization than with level-sets. In addition, similar to the "signed-distance function" concept in the level-set framework, geometric function values also have physical meanings, which can be directly used in clinical measurements or as a coupling feature in multi-phase segmentation. In summary, the similarities with the level-set formulation provide the AGF framework with the flexibility to virtually import all the new concepts or energy functionals derived for level-set formulation into an AGF framework. The only key difference between these two frameworks is that the level-set formulation, which uses higher order distance-type of functions as surface representation, can allow topological changes, which is not the case with the AGF framework.

The performance and feasibility of the AGF segmentation framework were quantitatively validated and demonstrated on three cardiac applications with large datasets. In an extensive set of synthetic and clinical experiments, presented in this chapter, the AGF segmentation framework was able to achieve real-time segmentation performance, requiring only fractions of a second to reach a stable position, and therefore exhibiting segmentation capabilities faster than actual image acquisition rates. The AGF segmentation framework was not only faster than alternative deformable models implementations but also opens the door to online and real-time segmentation is combined with image acquisition, which would greatly benefit existing and potential clinical applications such as interventional approaches. Therefore, besides being an extremely fast segmentation method for offline image processing, the AGF framework also opens the door to online segmentation, which could fully unleash the power of 4D medical imaging.

References

1. Herz S, Ingrassia C, Homma S, Costa K, Holmes J (2005) Parameterization of left ventricular wall motion for detection of regional ischemia. Ann Biomed Eng 33(7):912–919
2. Udupa JK, Wei L, Samarasekera S, Miki Y, van Buchem MA, Grossman RI (1997) Multiple sclerosis lesion quantification using fuzzy connectedness principles. IEEE Trans Med Imaging 16:598–609
3. Kass M, Witkin A, Terzopoulos D (1987) Snakes: active contour models. Int J Comput Vis 1:321–331
4. Sethian J (1999) Level set methods and fast marching methods vol 3. In: Cambridge monographs on applied and computational mathematics, 2 edn. Cambridge University Press, Cambridge
5. Osher S, Fedkiw R (2003) Level set methods and dynamic implicit surfaces In: Applied mathematical sciences, vol 153. Springer, New York
6. Chan TF, Vese LA (2001) Active contours without edges. IEEE Trans Image Process 10 (2):266–277
7. Angelini E, Homma S, Pearson G, Holmes J, Laine A (2005) Segmentation of real-time three-dimensional ultrasound for quantification of ventricular function: a clinical study on right and left ventricles. Ultrasound Med Biol 31(9):1143–1158

8. Cootes TF, Taylor CJ, Cooper DH, Graham J (1995) Active shape models-their training and application. Comput Vis Image Underst 61(1):38–59
9. Cootes TF, Edwards GJ, Taylor CJ (1998) Active appearance models. In: Lecture notes in computer science, vol 1407. Springer Berlin, pp 484–498
10. Held K, Kops ER, Krause BJ, Wells WM, Kikinis R, Muller-Gartner H-W (1997) Markov random field segmentation of brain MR images. IEEE Trans Med Imaging 16(6):878–886
11. Boykov YY, Jolly M-P (2001) Interactive graph cuts for optimal boundary & region segmentation of objects in N–D images. In: Eighth international conference on computer vision (ICCV'01) 2001, pp 105–112
12. Jin Y, Imielinska C, Laine A, Udupa J, Shen W, Heymsfield S Segmentation and evaluation of adipose tissue from whole body MRI scans. In: Proceedings of the sixth international conference on medical image computing and computer assisted interventions (MICCAI 2003), Montreal, Nov 2003 pp 635–642
13. Mikic I, Krucinski S, Thomas JD (1998) Segmentation and tracking in echocardiographic sequences: active contours guided by optical flow estimates. IEEE Trans Med Imaging 17 (2):274–284
14. Xu C, Prince JL (1998) Snakes, shapes and gradient vector flow. IEEE Trans Image Process 7 (3):359–369
15. Sethian JA (1999) Level set methods and fast marching methods: evolving interfaces in computational geometry, fluid mechanics, computer vision, and materials science. In: Cambridge monographs on applied and computational mathematics Cambridge University Press, Cambridge
16. Chan TF, Vese LA (2001) Active contours without edges. IEEE Trans Image Process 10 (2):266–277
17. Mumford D, Shah J (1985) Boundary detection by minimizing functional. In: International conference on computer vision and pattern recognition, San Francisco, pp 22–26
18. Angelini E, Laine A, Takuma S, Holmes J, Homma S (2001) LV volume quantification via spatio-temporal analysis of real-time 3D echocardiography. IEEE Trans Med Imaging 20 (6):457–469
19. Song T, Angelini ED, Mensh BD, Laine A Comparison study of clinical 3D MRI brain segmentation evaluation. In: Annual international conference IEEE engineering in medicine and biology society (EMBS), San Francisco, 1–5 Sept 2004 pp 1671–1674
20. Kass M, Witkin A, Terzopoulos D (1987) Snakes: active contour models. In: Proceedings of 1st international conferences on computer vision pp 259–268
21. Duan Q, Shechter G, Gutierrez LF, Stanton D, Zagorchev L, Laine AF, Daniel Elgort (2007) Augmenting CT cardiac roadmaps with segmented streaming ultrasound. San Diego, CA. p 65090V65091-65011
22. Vallet B, Angelini E, Laine A (2006) Variational segmentation framework in prolate spheroidal coordinates for 3D real-time echocardiography. 11–16 Feb.; San Diego, CA, USA. p 61444A.61441-61411
23. Hunter PJ, Smaill BH (1988) The analysis of cardiac function: a continuum approach. Progress in Biophysics and Molecular Biology 52:101–164
24. Christie GR, Bullivant DP, Blackett SA, Hunter PJ (2004) Modelling and visualising the heart. Computing and Visualization in Science 4(4):227–235
25. Nielsen PM, LeGrice IJ, Smaill BH, Hunter PJ (1991) Mathematical model of geometry and fibrous structure of the heart. American Journal of Physiology - Heart and Circulation Physiology 260:H1365–H1378
26. Angelini ED, Song T, Mensh BD, Laine AF. Brain MRI segmentation with multiphase minimal partitioning: A comparative study. International Journal of Biomedical Imaging 2006;2007(Article ID 10526):1–15
27. Zeng X, Staib LH, Schultz RT, Duncan JS (1999) Segmentation and measurement of the cortex from 3-D MR images using coupled-surfaces propagation. IEEE Transactions on Medical Imaging 18(10):927–937

28. Jin Y, Angelini E, Laine A (2004) Wavelets in medical image processing: Denoising, segmentation, and registration. In: Suri J, Wilson DL, Laximinarayan S(eds) Handbook of medical image analysis: Advanced segmentation and registration models. New York NY: Kluwer Academic Publishers
29. Udupa JK, Samarasekera S (1996) Fuzzy connectedness and object definition: Theory, algorithms, and applications in image segmentation. Graphical Models and Image Processing 58(3):246–261
30. Pai V, Axel L, Kellman P (2005) Phase Train Approach for very high temporal resolution cardiac imaging. J Cardiovasc Magn Reson 7(1):98–99
31. Duan Q, Moses D, Srichai MB, Pai VM, Laine AF (2006) Semi-automatic ventricular border segmentation package based on multi-phase levelset segmentation. Seattle, WA, USA

Qi Duan received the BS and MS degress in Biomedical Engineering from Tsinghua University, Beijing, China, in 2000 and 2002, respectively. He obtained the PhD degree in Biomedical Engineering (bioimaging) from the Columbia University, New York, USA, in 2007. Between 2008 and 2010, he was a research scientist in the Center for Biomedical Imaging, Department of Radiology, NYU School of Medicine, New York, USA. Since July 2010, he is a staff scientist at NINDS, NIH, USA. His current interests are medical image analysis, MR RF engineering, MR reconstruction methods, cardiac 4D ultrasound segmentation, and strain imaging.

Classification and Staging of Chronic Liver Disease Based on Ultrasound, Laboratorial, and Clinical Data

Ricardo Ribeiro, Rui Tato Marinho, Jasjit S. Suri, and João Miguel Sanches

Abstract Chronic liver disease is a progressive disease, most of the time asymptomatic, and potentially fatal. In this chapter, an automatic procedure to stage the disease is proposed based on ultrasound (US) liver images, clinical and laboratorial data.

A new hierarchical classification and feature selection (FS) approach, inspired in the current diagnosis procedure used in the clinical practice, here called *Clinical-Based Classifier* (CBC), is described. The classification procedure follows the well-established strategy of liver disease *differential diagnosis*. The decisions are taken with different classifiers by using different features optimized to the particular task for which they were designed. It is shown that the *CBC* method outperforms the traditional *one against all* (OAA) method because it take into account the natural evolution of the hepatic disease. Different specific features are used to detect and classify different stages of the liver disease as it happens in the classical diagnosis performed by the medical doctors.

R. Ribeiro (✉)
Institute for Systems and Robotics and Instituto Superior Técnico/Technical University of Lisbon, Lisbon, Portugal

Escola Superior de Tecnologia da Saúde de Lisboa, Lisbon, Portugal
e-mail: ricardo.ribeiro@estesl.ipl.pt

R.T. Marinho
Liver Unit, Department of Gastroenterology and Hepatology, Hospital de Santa Maria, Medical School of Lisbon, Lisbon, Portugal
e-mail: rui.marinho@mail.telepac.pt

J.S. Suri
Biomedical Technologies, Inc., Denver, CO, USA

Idaho State University (Affiliated), Pocatello, ID, USA
e-mail: jsuri@comcast.net

J.M. Sanches
Institute for Systems and Robotics, Department of Bioengineering from the Instituto Superior Técnico/Technical University of Lisbon, Portugal
e-mail: jmrs@ist.utl.pt

J.M. Sanches et al. (eds.), *Ultrasound Imaging: Advances and Applications*,
DOI 10.1007/978-1-4614-1180-2_11, © Springer Science+Business Media, LLC 2012

The proposed method uses multi-modal features, extracted from US images, laboratorial and clinical data, that are known to be more appropriated according to the disease stage we want to detect. Therefore, a battery of classifiers and features are optimized and used in a hierarchical approach in order to increase the accuracy of the classifier.

For the normal class we achieved 100% accuracy, for the chronic hepatitis 69.2%, for compensated cirrhosis 81.48%, and for decompensated cirrhosis 91.7%.

1 Introduction

Chronic liver disease (CLD) is a significant cause of morbidity and mortality in developed countries and commonly is caused by viral hepatitis and alcohol abuse [1].

The initial stages of CLD are usually asymptomatic such as *steatosis* or *hepatitis*. *Hepatitis* is the inflammation of the liver, resulting in liver cell damage and destruction [1]. It is caused by hepatitis viruses, which can have several types, or by other factors, e.g., alcohol. Moreover the natural evolution of the disease may lead to *cirrhosis* or even *hepatocellular carcinoma*, which are more severe pathological conditions, with high morbidity and mortality. *Cirrhosis* is a chronic disease that is characterized anatomically by widespread nodules in the liver combined with fibrosis [2]. It is possible to distinguish two phases in cirrhosis, a stable form, called *compensated cirrhosis*, and a more dangerous from that could lead to widespread failure of the liver, called *decompensated cirrhosis* [3].

Liver biopsy has been the preferred tool in the evaluation and staging of the CLD. However, its invasive nature and the development of other more accurate non-invasive alternatives have lead to a decrease on its usage for assessing the CLD. Among these alternatives, CLD staging based on ultrasound (US) data has proven to be a promising and safer alternative to biopsy.

In the review study presented in [1] it is shown that echogenicity, texture characterization, and surface morphology of the liver parenchyma are effective features to diagnose the CLD. However, the evaluation of these features is normally affected by the subjective assessment of the human operator. This factor may lead to significant errors in the diagnosis and staging of CLD, since US liver images can show great variability, as shown in Fig. 1. Therefore, new objective feature extraction and classification methodologies in a *Computer Assisted Diagnosis* framework are needed.

Several studies presented in the literature use objective features, extracted from US images, and propose classification procedures to assess CLD [4]. Some of the most common features are based on the first-order statistics, co-occurrence matrix, wavelet transform, attenuation and backscattering parameters and coefficients. A brief description of some of these studies is given next.

In [5], an experimental study was performed aiming at to discriminate the liver fibrosis from US images. They computed fractal features, entropy measures, and

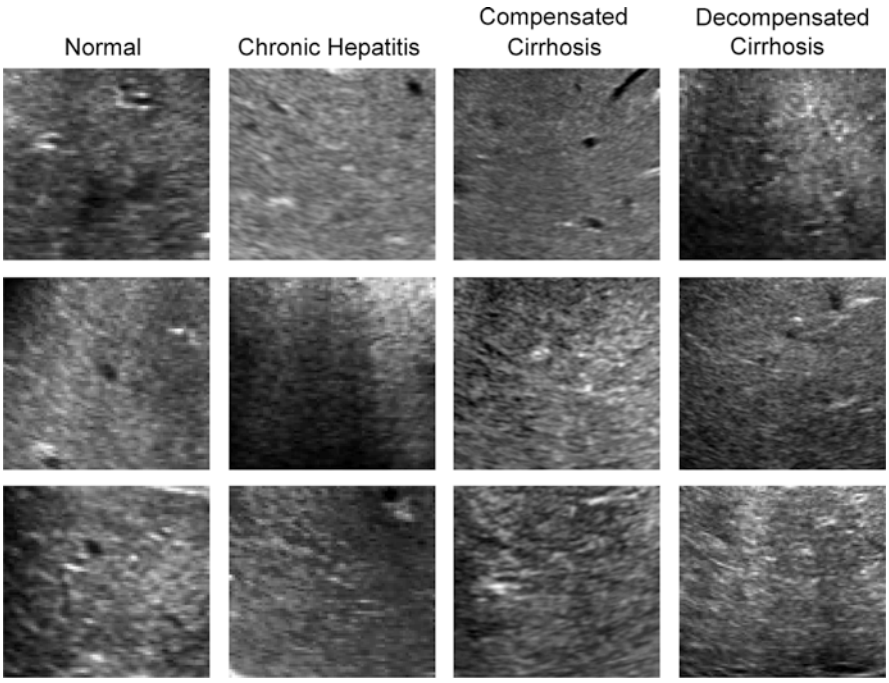

Fig. 1 Ultrasound images variability in the different stages of chronic liver disease

co-occurrence information from US images to characterize the liver parenchyma from a textural point of view and the classification results showed an overall accuracy (OA) of 85.2% using a Fisher linear classifier. Other important work described in [6] shows the ability of the Wavelet coefficients, also computed from US images, to characterize the diffuse disease of the liver. Their goal was to discriminate normal, steatotic, and cirrhotic conditions. An OA of 90% is obtained and comparison results by using other classes of features, such as co-occurrence information, Fourier descriptors and fractal measures, showing that the wavelet-based classifier outperforms the classifiers based on the other features, 87%, 82%, and 69%, respectively.

Lee et al. [7] categorized patient in normal (72), fatty liver (66), and CLD (64), in order to evaluate the usefulness of standard deviation to measure the homogeneity of hepatic parenchyma based on US images. They observe significant differences ($p < 0.0001$) between the CLD group and the normal and fatty liver groups. They also concluded that higher average standard deviation values are related to wide distribution of intensity values within the ROI, as reported for CLD group, which explains the characteristic appearance of heterogeneous echo texture in CLD groups, such as chronic hepatitis and liver cirrhosis. Depict the good results obtained, the authors suggest to be careful in the use of this feature, since it is highly dependent on the ROI location.

Two main contributions for the CLD assessment are presented in this work; (1) multi-modal features, extracted from US images, laboratorial and clinical data and (2) a new classification procedure inspired in the clinical practice, here called *Clinical-Based Classifier* (CBC).

The discriminative power of the automatic classifier can be greatly increased if the natural evolution and staging of the disease is taken into account.

The remainder of this chapter is organized as follows: Section 2 introduces the pre-processing algorithm used, explaining the feature extraction and selection procedures, as well as the classifiers and the dataset used in this work. In Sect. 3 the results are presented showing the feature selection (FS) results and the classification results for each of the used classifier. The discussion of the results is presented in Sect. 4 and conclusions are presented in Sect. 5.

2 Methods

The CBC aims at discriminating normal and three main pathologies in the CLD scope; (1) *Chronic Hepatitis*, (2) *Compensated Cirrhosis*, and (3) *Decompensated Cirrhosis*.

The diagnosis of these pathologies is performed in the today clinical practice based on several sources of medical data such as US liver parenchyma images, laboratorial exams, and clinical indicators recommended in well established and accepted medical guidelines [3]. The diagnosis, however, is obtained by integrating all information based mainly on subjective criteria of the medical doctor.

The CBC is a quantitative and highly automatic procedure that gives the medical doctor objective and accurate information to help in the liver diagnosis process.

The CBC approach is composed by three main components; (1) Features computation from multi-modal sources, (2) design and training of a specific suitable classification strategy that takes into account the CLD specificities, and (3) diagnosis and validation of the method.

The main novelty of the method proposed in this chapter is a hierarchical classifier that mimics the structural approach of *differential diagnosis* followed in the clinical practice to identify the different stages of the CLD [8]. Instead of trying to classify a given liver in one stage of the disease from a set of possible stages by using a *multi-class* classifier, e.g., *k-Nearest Neighbor* (kNN) or *Support Vector Machine* (SVM), the hierarchical approach, represented in Fig. 2, is used. In this strategy several partial binary decisions are taken according to the natural evolution of the disease. In each step, a decision is taken by different binary classifiers trained, tunned, and optimized specifically for that task.

The first classification step (CS) discriminates *normal* versus *pathology* liver. If the liver is classified as pathologic in this first step, discrimination of *chronic hepatitis without cirrhosis* versu *cirrhosis* is attempted. In the last step *compensated cirrhosis* versu *decompensated cirrhosis* are discriminated. The decompensated cirrhosis is assumed as the end-stage of every CLD before *hepatocellular carcinoma*.

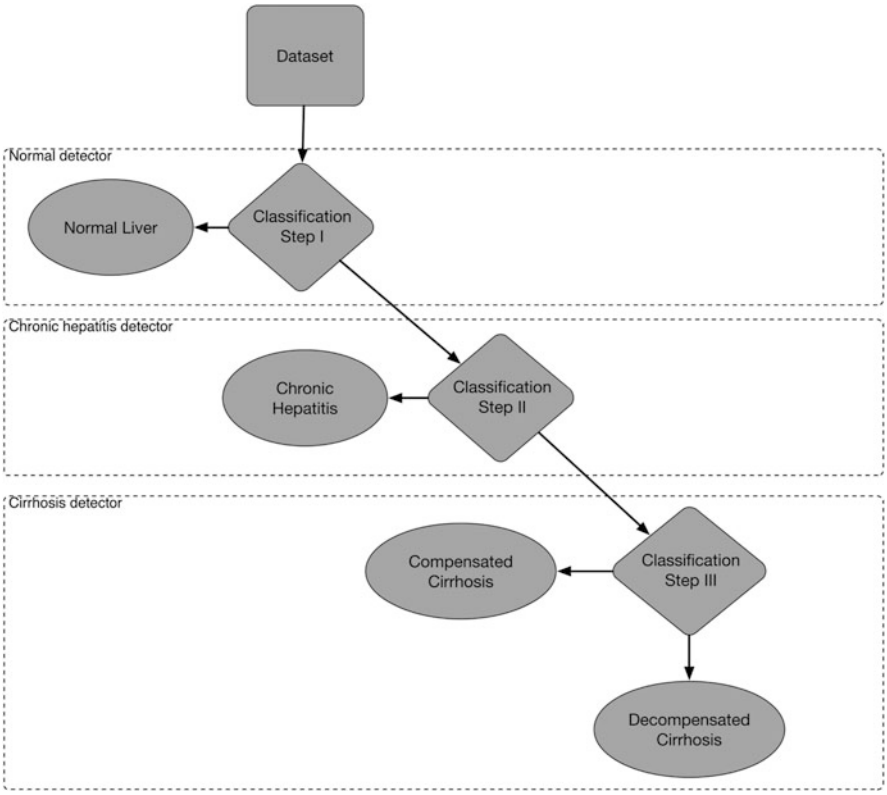

Fig. 2 Design of the CBC decomposition strategy for CLD classification

The CBC (see Fig. 2) design and optimization is performed at two levels: (1) features and (2) classifier type and parametrization selection used specifically in each CS. This means that at each CS of our hierarchical approach the classifier type and features can be different.

The FS procedure is formulated as an optimization task with the sensitivity maximization criterion [9, 10]. The set of features at each CS is tunned for the specificities of the corresponding CLD stage prior to the classifier type selection. This is done by the *sequential forward floating selection* (SFFS) [11] method with the linear discriminant analysis (LDA) criterion. The leave-one-out cross-validation technique is used for error estimation purposes.

The classifier selection at each CS is done with ROC analysis where the selected classifier, kNN or SVM [12], is the one that jointly maximizes the *true positive rate* (TPR) and the *true negative rate* (TNR).

The non-parametric kNN classifier is tested in this study. It classifies a test sample to a class according to the majority of the training neighbors in the feature space by using the minimum Euclidean distance criterion [13,14]. The algorithm for

the *nearest neighbor rule* is summarized as follows [12]; Given an unknown feature vector x and a distance measure, then:

- Out of the N training vectors, identify the k nearest neighbors, regardless of class label.
- Out of these k samples, identify the number of vectors, k_i, that belong to class ω_i, i = 1, 2, ..., M.
- Assign x to the class ω_i with the maximum number k_i of samples.

The other classifier tested in is the SVM classifier. Its aim is to find a decision plane that has a maximum distance (margin) from the nearest training pattern [14, 15]. Given the training data $\{(x_i, \omega_i) | \omega_i = 1 \; or \; -1, \; i = 1, ..., N\}$ for a two-class classification (where x_i is the input feature; ω_i is the class label; and N is the number of training sample), the SVM maps the features to a higher-dimensional space [14]. Then, SVM finds a hyperplane to separate the two classes with the decision boundary set by the support vectors [15].

The general form of the decision function $g(x)$ for the SVM is [15]:

$$g(x) = \sum_{i=1}^{N} \alpha_i y_i z_i^T z + b \tag{1}$$

where the α_i and b are selected during the training process, constrained by $\sum \alpha_i y_i = 0$ and $0 \leq \alpha_i \leq c$, where c is a user-defined penalty term, regulating the general performance of the SVM. Under certain conditions, the computationally intensive mapping process can be reduced with an appropriate kernel function K such that the decision function g(x) becomes,

$$g(x) = \sum_{i=1}^{N} \alpha_i y_i K(x_i, x) + b \tag{2}$$

In this paper, the kernels adopted are the polynomial,

$$K(x_i, x) = \left(x_i^T x + 1\right)^d \tag{3}$$

and the Gaussian radial-basis function,

$$K(x_i, x) = e^{-r|x_i - x|^2}, \tag{4}$$

where d is the degree of the polynomial kernel and r is the radius coefficient of the Gaussian radial-basis function kernel [15].

The performance of the CBC is assessed by comparing the corresponding classification results with the common multi-class decomposition strategy – *OAA*. The *OAA* strategy consists on building one classification procedure per class, trained to distinguish the samples in a single class from the samples in all remaining classes.

The features extracted from US data are some of the most important and discriminative ones to the diagnosis. Therefore, in the next section a detailed description of them and the way they are computed is described.

2.1 Ultrasound Image Pre-processing and Features Extraction

The US images are corrupted by a type of multiplicative noise, called *speckle*, that is usually considered undesirable to interpret the morphological information about the anatomy of the organs under analysis. However, the *speckle* pattern contains useful information about the tissues that can be used in the medical diagnosis [16].

Here, the method described in [16] is used. The B-mode US images, acquired by the commonest US scanner available at most of the medical facilities, are pre-processed and decomposed into two fields: (1) *De-speckle* and (2) *Speckle*.

The pre-processing stage is used to estimate the RF US image that is not usually available in the US scanners but that is needed for the decomposition procedure. The decomposition is performed in two steps; (1) Denoising, where the estimated RF US image, $y_{i,j}$, is filtered to obtain the *De-speckle* field $x_{i,j}$ and (2) *Speckle* extraction, $\eta_{i,j}$, obtained from the RF US noisy image, $y_{i,j}$, and from the *De-speckle* field, $x_{i,j}$, obtained in the previous step, under the adoption of the *Multiplicative White Rayleigh Model* [16],

$$\eta_{i,j} = \frac{y_{i,j}}{x_{i,j}}. \tag{5}$$

The *Denoising* algorithm is formulated in a Bayesian framework were the pixels of the noisy RF US estimated image are assumed to be Rayleigh distributed [16]. Here, the *De-speckle* field is used to extract morphological features, such as liver contour regularity and attenuation coefficient with dept, and the *Speckle* one, containing the noise pattern, is used to extract textural features from the parenchyma of the liver. Figure 3 illustrates an example of the decomposition methodology.

Next a small description of each class of features is provided.

2.1.1 Acoustic Attenuation Coefficient

Acoustic attenuation along depth has been extensively used in the literature and in clinical practice as an indicator of the CLD. However, the true correlation between this indicator and the hepatic disease is still controversial as referred in [17], namely with respect to *cirrhosis* where some authors report strong correlation between attenuation with depth while others do not find any significant relation. Other studies suggested that fibrosis can also produce large attenuation values but it was also reported fibrotic cases with normal attenuation.

In [18] the attenuation/backscatter is computed from the observed B-Mode US image instead of the more common RF US image. This is for the sake of simplicity and availability, since in most of the scanners the RF signal is not available. In their method a ROI corresponding to the biopsy site is selected and a polygonal line, describing the biopsy needle trajectory along the depth direction, is registered. The average gray-level values for each point along a polygonal line is computed

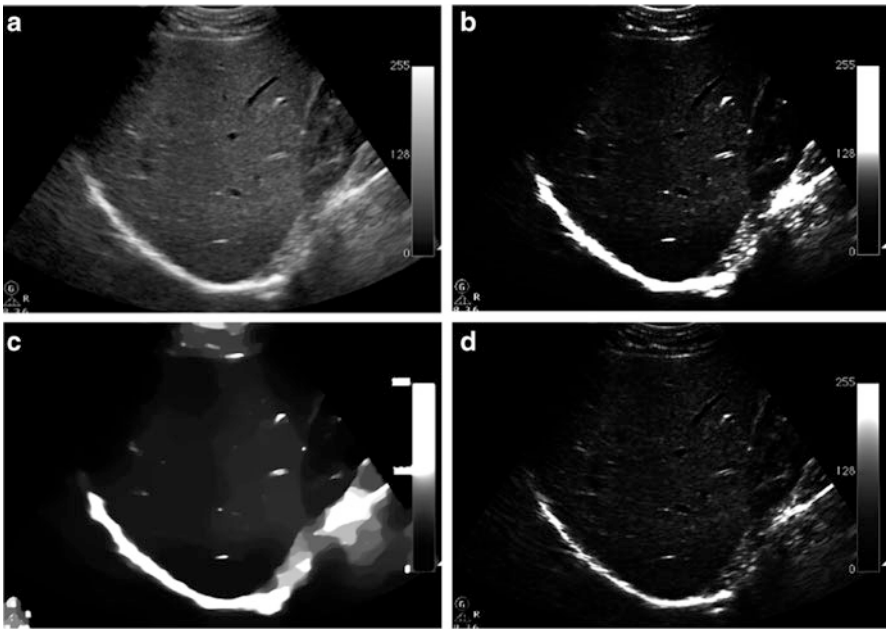

Fig. 3 Decomposition procedure of US liver parenchyma. (**a**) Observed *B-mode* US image. Estimated (**b**) envelope RF image, (**c**) *de-despeckle* and (**d**) *speckle* image fields

by averaging seven horizontal pixels and the attenuation coefficient is obtained by linear regression. They show that the attenuation clearly discriminates pure-fatty from normal livers where the area under the curve (AUC) is equal to 1.00 [18]. Another interesting result indicates that the presence of inflammation or fibrosis, even in cases of severe steatosis, leads to a significant decreasing on the discriminative power of the attenuation slope to distinguish healthy from steatotic livers.

Therefore, the attenuation coefficient, alone, does not have discriminative power for CLD diagnosis. However, together with other features in a more general classification framework, as the one presented here, it can provide valuable information for the performance of the classifier.

The attenuation coefficient, in $dBMHz^{-1}cm^{-1}$, can be obtained as follows [17],

$$\alpha(f) = \frac{1}{2l_{\text{liver}}} 10 \log_{10} \left(\frac{|S_p(f)|}{|S_{p|f}(f)|} \right) \tag{6}$$

where f is the frequency in MHz, l_{liver} is the thickness of the sample, $|S_p(f)|$ is the power spectrum without specimen, and $|S_{p|f}(f)|$ is the power spectrum with specimen. This generates an approximately linear attenuation curve inside the frequency band whose slope, obtained linear regression, is function of frequency. The global value is computed by integrating in frequency.

In this work the attenuation coefficient α is estimated by using the method proposed in [18] that is basically the following linear regression problem

$$\hat{m} = \arg\min_{m} \mathscr{J}(X) \tag{7}$$

where X is the $N \times M$ *De-speckle* field. The objective function is

$$\mathscr{J} = \sum_{l=0}^{N} (\alpha l + b - f(l))^2 \tag{8}$$

where $f(l) = \frac{1}{M}\sum_{c=1}^{M} x_{l,c}$ is the average value intensity of each *De-speckle* image line, in the assumption, that depth increases along each column.

2.1.2 First-Order Statistics

First-order statistics, computed from the histogram, $h(i)$, of the estimated gray-scale RF US image, Y, where pixel spatial correlation is not taken into account, are some of the most important features for the echo texture analysis of the liver parenchyma [7, 13]. The first-order characteristics used in this work are the mean and standard deviation.

$$\mu = \frac{1}{NM}\sum_{i}^{256} h(i), \tag{9}$$

$$\sigma = \sqrt{\left(\frac{1}{NM-1}\sum_{i=1}^{256}(h(i)-\mu)^2\right)}, \tag{10}$$

2.1.3 Co-occurrence

The elements of the *Co-occurrence* tensor, $Co = \{c_{i,j}(\Delta_l, \Delta_c)\}$, describe the gray-level spatial inter-relationship in the image [13]. More precisely, element $c_{i,j}(\Delta_l, \Delta_c)$ represents the joint probability of the pixel intensities i and j in relative spatial position of (Δ_l, Δ_c) [15] and can be computed as follows

$$c_{i,j}(\Delta_l, \Delta_c) = \sum_{l=1}^{N}\sum_{c=1}^{M} \begin{cases} 1 \; if \; (\eta_{l,c} = i) \wedge (\eta_{l+\Delta l, c+\Delta c} = j) \\ 0 \text{ otherwise} \end{cases} \tag{11}$$

In [15] it is reported an OA of 90% using features extracted from the *Co-occurrence* tensor in the detection of the *cirrhosis* condition. They show, in a high-frequency (25 MHz) US study described in [19], that the values of the features obtained from the *Co-occurrence* tensor are able to discriminate cirrhotic,

steatotic, and healthy livers. However, the classification accuracy decreased when discrimination between different grades of steatosis and fibrosis are attempted.

The following statistical features, computed from the *Co-occurrence* tensor for $(\Delta_l, \Delta_c) \in \{(6,0)\}$, as suggested by [6], are used in this work:

- *Contrast*: measure the local variations in the co-occurrence matrix,

$$\sum_{i,j} |i-j|^2 c(i,j) \tag{12}$$

- *Correlation*: measure the joint probability occurrence of the specified pixel pairs,

$$\sum_{i,j} \frac{(i-\mu_i)(j-\mu_j) c(i,j)}{\sigma_i \sigma_j} \tag{13}$$

- *Energy*: also known as the angular second moment [13],

$$\sum_{i,j} c(i,j)^2 \tag{14}$$

- *Homogeneity*: measures the closeness of the distribution of elements in the matrix to the matrix diagonal,

$$\sum_{i,j} \frac{c(i,j)}{(1+|i-j|)} \tag{15}$$

2.1.4 The Wavelet Transform

The *Wavelet Transform* is used here to perform a multi-scale analysis of the *Speckle* field, containing the noise pattern of the estimated RF US image, for liver parenchyma textural characterization purpose. The decomposition is performed according to the Fig. 4 where a sequence of low-pass, (G), and high-pass, (H), filtering operations followed by down-sampling the results, $\downarrow 2$, generates a pyramidal representation of the original image with decreasing resolution comprising a lower resolution low-pass component (approximation component), (LL), and three high-pass components (detailed components) along the horizontal, (HL), vertical, (LH), and diagonal directions, (HH), according to Fig. 5. An example of a multi-scale wavelet transform analysis using the *Speckle* field of an US liver image is provided in Fig. 6.

The high-pass components, (H) contain the detailed information of the image at different resolution scales along three directions while the low-pass versions (L) contain the approximation component.

Tissue characterization based on wavelet multi-resolution analysis has been performed in several works [6, 15, 19, 21]. This approach is effective in the morphological characterization of the image from the approximation fields and

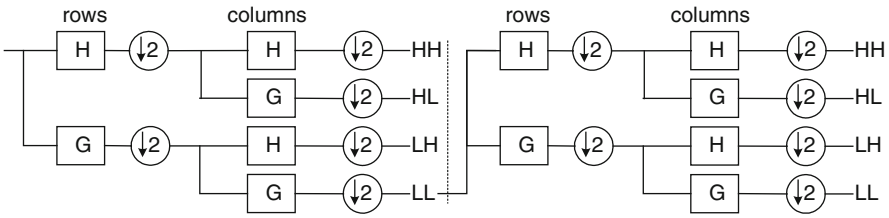

Fig. 4 Discrete image wavelet decomposition scheme (from [20])

Fig. 5 Wavelet pyramidal decomposition of images

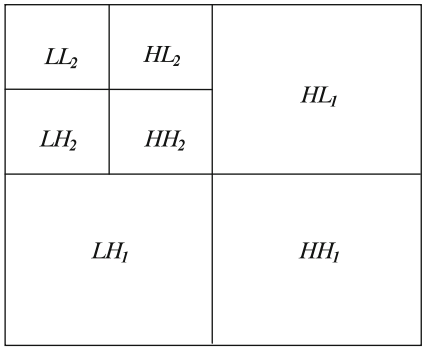

at the same time in a textural characterization at several resolution scales from the detailed fields. For instance, in [6], the application of non-separable wavelet transform features for liver tissue characterization is investigated. The estimation of a texture quality is performed with the four-level *quincunx* decomposition which makes it possible to obtain feature vectors with maximal length of five elements [6] and an overall classification accuracy of 90% and a specificity of 92%. Sensitivity in the detection of cirrhosis and steatosis is 92% and 97%, respectively. Similar results are also reported in [15, 19].

2.1.5 Autoregressive Model

The autoregressive (AR) model approach has been used since long time with success in several applications of engineering where identification and characterization of systems and processes are needed [22]. In the canonical definition of a 1D p-order AR model each sample is modeled as a linear combination of the previous p samples with unknown coefficients, a_k [23]

$$x(n) = \sum_{i=1}^{p} a_i x(n-i) + r(n) \tag{16}$$

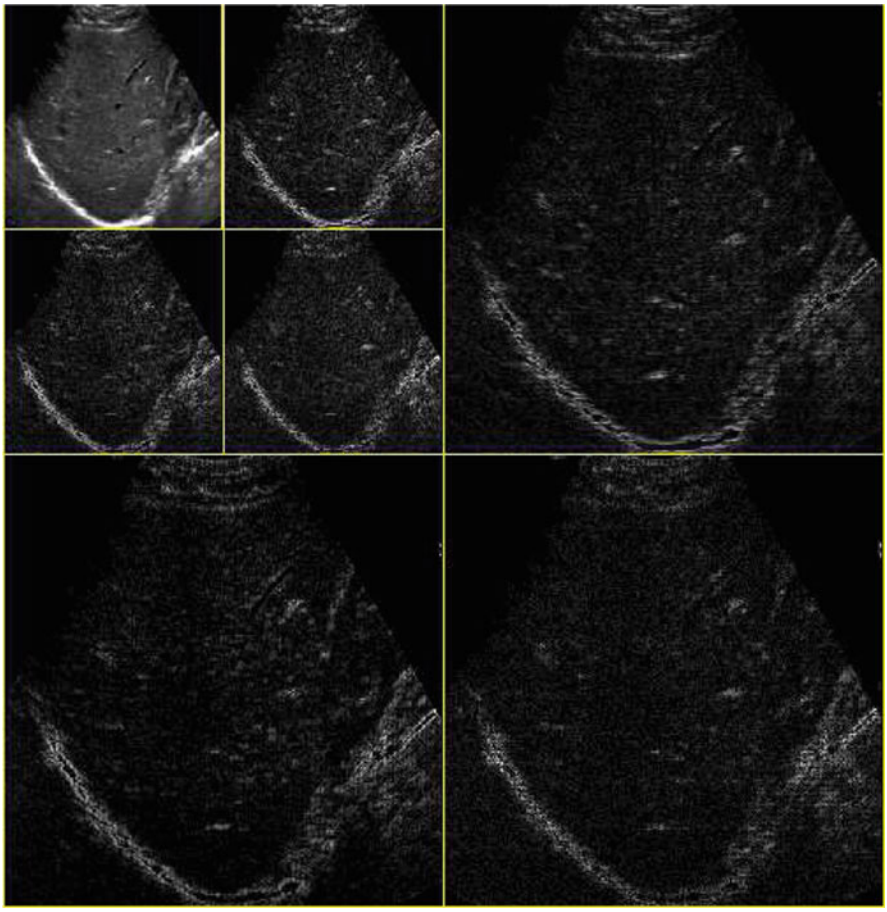

Fig. 6 Wavelet pyramidal decomposition example with the *Speckle* field of an US liver image

where the residue signal, $r(n)$, is assumed to be white and zero mean normal distributed. For image applications the following 2D formulation of the (p,q)-order AR model is used [24]

$$x(n,m) = \sum_{i=0}^{p} \sum_{j=0}^{q} a_{ij} x(m-i, n-j) + r(n,m) \tag{17}$$

where $x(n,m)$ is the ^{n,m}th pixel of the image and $a_{0,0} = 0$.

There are many algorithms to compute AR parameters; Levinson Burg, least-squares, gradient based, lattice filter, and Kalman filter [25]. In this work, we will use the most popular, the least-squares algorithm [25]

The order of the model, (p,q), controls the error associated with the AR signal approximation [26]. Small orders ignore the main and long-term statistical properties of the original signal while larger ones may lead to over-fitting effects [26, 27]. Therefore, choosing the order of the model becomes a key problem and there are several methods to do it [23–27]. Here the first-order model was adopted because it was confirmed by [28] that in this scope it leads to the minimum error probability.

2.1.6 Liver Surface Contour

Beside the textural features used to discriminate the pathologies of the liver, as referred before, US images may also be used to compute morphological features correlated with some of these pathologies. The importance of the US image in the assessment of liver surface nodularity, portal vein mean flow velocity, and the enlargement of the caudate lobe is stressed in [29]. Particularly, liver surface nodularity has been documented as a reliable sign in the detection of liver cirrhosis [3, 30, 31].

An accuracy of more than 70% has been reported by [3] and in [30] the authors showed that the observed liver contour irregularities directly correlated with the gross appearance of the cirrhotic liver as seen at laparoscopy. Liver surface nodularity in US can be well appreciated when ascites (presence of free fluid within the abdominal cavity) is present or when a high-frequency transducer (7.5–12 MHz) is used [32]. In [3], where a low-frequency transducer (3.5–5 MHz) was used, also refer that liver surface is an important parameter associated with the histopathological diagnosis of liver cirrhosis.

Despite the consensual correlation of the liver surface morphology with cirrhosis, the effectiveness of the different diagnosis methods used in the clinical practice is very limited because the analysis is most of the time subjective, non-reproducible, and operator-dependent [33].

Here, a semi-automatic objective method for the liver surface characterization is proposed. The liver surface contour is segmented from the *De-speckle* component of the US image by using a snake technique proposed by [34], as shown in Fig. 7.

The irregularity of the contour is measured by means of the root mean square of the different angles, produced by the points that characterize the contour and the variation of the points of the contour in the y axis. In this approach the contour first point is assumed as the reference point. The first-order statistics (mean and variance) of the referred variables are also extracted.

2.2 Biochemical and Clinical Features

Besides image-based features, several other clinical data and biochemical tests are useful for evaluating and managing patients with hepatic dysfunction.

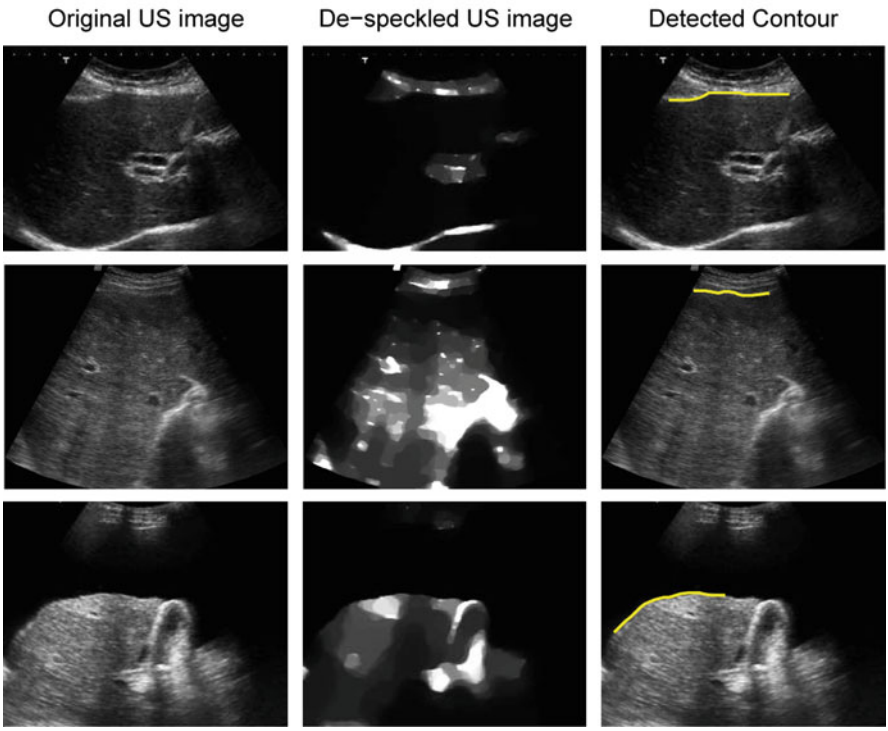

Fig. 7 Method used to detect the liver surface contour. First row corresponds to a normal liver; second row to a compensated cirrhotic liver and the last row to a decompensated cirrhotic liver

These features are selected according to their purported clinical and pathophysiological role in CLD [8]. The clinical and pathophysiological characteristics of CLD can be grouped in terms of hepatic insufficiency, portal hypertension, hyperdynamic circulation, liver inflammation, necrosis and fibrosis, as well as etiologic factors [8, 29, 31]. Hepatic insufficiency is suggested by the Child-Pugh score, albumin, total bilirubin, encephalopathy, and prothrombin time [8]. Portal Hypertension is usually accessed by the presence of ascites, varices, and gastrointestinal bleeding, among others. Creatinine and sodium are variables used for the study of hyperdynamic circulation [8]. Liver inflammation, necrosis, fibrosis, and histology can be evaluated, according to [8], based on aspartate transaminase (AST), gamma glutamyl transpeptidase (gGT), lactate dehydrogenase (LDH), and alanine transaminase (ALT). Also the etiologic factors are taking into account, namely the alcohol abstinence, alcoholic ethiology, hepatitis B and C and other cause for the CLD [29].

The features extracted from the US images, the laboratorial and clinical information that were considered for the FS procedure are listed in Table 1.

Table 1 Features extracted from the US images, Laboratorial and Clinical information

Source	Feature
Liver echogenicity (de-speckle field)	Acoustic attenuation coefficient (F_1), measured by the slope coefficient of the linear regression of intensities along the depth/lines [18]
	First-order statistics, including to the mean (F_2) and standard deviation (F_3) of the pixel intensities.
Liver surface contour (de-speckle field)	Root mean square of the angles produced by the points that characterize the contour (F_4), where the first point was assumed as the reference point.
	Root mean square of the coordinates of the contour points in the y axis (F_5)
	Mean (F_6) and variance (F_7) of the angles
	Variance of the y axis coordinates at each point (F_8).
	Correlation coefficient of the y axis coordinates (F_9).
Liver Texture (speckle field)	Co-occurrence matrix, which enables to derive [35]: the contrast (F_{10}) , correlation (F_{11}) that measures the joint probability occurrence of specific pixel pairs, energy (F_{12}) of the image (obtained by summing of squared elements of the image) and homogeneity (F_{13}) which quantifies the closeness of the distribution of matrix elements to its diagonal.
	Wavelet energies, measured by the vertical (F_{14}) and horizontal (F_{15}) detail energies of the first Haar wavelet decomposition.
	Autoregressive (AR) coefficients of a first-order 2D model, $\{a_{0,0}(F_{16}), a_{1,0}(F_{17}), a_{0,1}(F_{18})\}$.
Laboratorial Information [29]	Total bilirubin (F_{19}) , prothrombin time (F_{20}) , albumin (F_{21}) , creatinine (F_{22}), AST (F_{23}), ALT (F_{24}), gGT (F_{25}) , glycemia (F_{26}), sodium (F_{27}), urea (F_{28}), and lactate dehydrogenase(F_{29}).
Clinical Information [29]	Cause of disease (F_{30}), which include none (0), alcohol (1), hepatitis B (2), hepatitis C (3), alcoholic hepatitis B (4) and C (5) and All (6), and the following binary indicators: tumor (F_{31}), ascites (F_{32}), encephalopathy (F_{33}), Gastro-Intestinal bleeding (F_{34}) infection (F_{35}), alcoholic habits (F_{36}), and Child-Pugh score (F_{37}).

2.3 Data Set

Patients with an established diagnosis of CLD, in the various stages of the disease, were included for this study. A total of 115 US liver images from 115 patients, including 26 normal livers (*Normal*), 26 chronic hepatitis without cirrhosis (*Chronic Hepatitis*), 27 compensated cirrhosis (*Compensated Cirrhosis*), and 36 decompensated cirrhosis (*Decompensated Cirrhosis*), were involved in the experiments.

The patients were selected from the Gastroenterology Department of the Santa Maria Hospital, in Lisbon, with known diagnosis based on liver biopsy results. Their clinical histories, laboratory tests, and US images were obtained in the same day. The study protocol was approved by the Ethics Committee of the referred Hospital, it was explained to the patients and informed consent was obtained in each case, according to the principles of the Declaration of Helsinki.

All patients underwent hepatic US exam, performed by an expertize using a Philips ©CX50 scanner with a broadband curved array transducer with a frequency

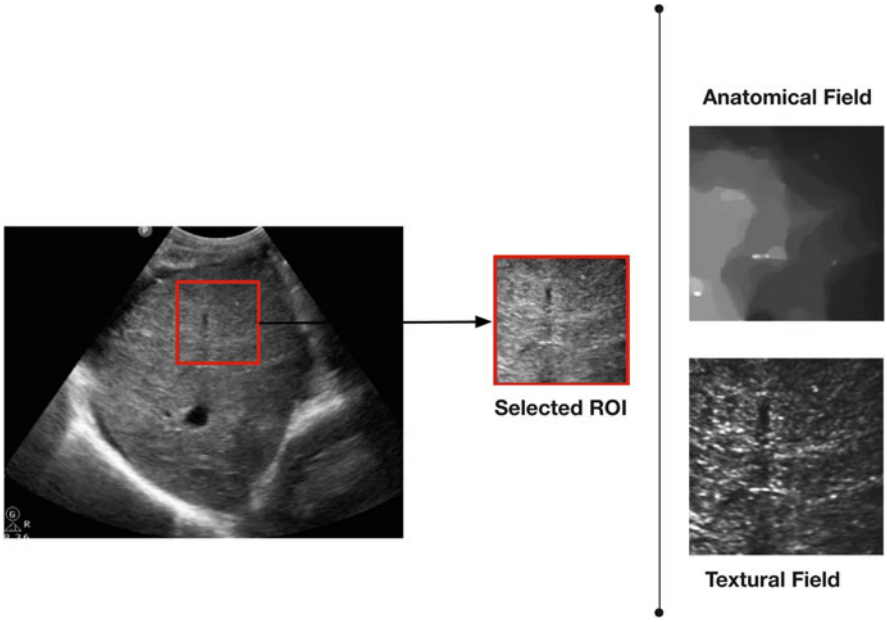

Fig. 8 Generic design for the selection of a ROI from the Ultrasound images and posterior pre-processing result

range of 2.0–5.0 MHz. All US images were stored in DICOM format. A ROI of 128×128 pixels along the medial axis was extracted from each image and pre-processed by using the algorithm described in Sect. 2.1, as shown in Fig. 8.

3 Results

In this section the results with data from real patients, obtained with the Matlab toolbox for Pattern Recognition, PRTools 4.1 [36], are presented to validate the proposed CBC method.

3.1 Feature Extraction and Selection

The features extracted from the different medical modalities computed in this work are all used along the classification pathway of the CBC. However, at each step, only a fraction of the entire set is used, so a FS procedure is needed. Consequently, an optimum sub-set of features from the whole set is selected by maximizing the accuracy result of the LDA classifier. This optimization procedure is used for both classification strategies, OAA and CBC. Notice that at this stage we are interested in

Table 2 Sensitivity and overall performance, in parenthesis, percentage results for the OAA strategy with the US-based feature set (US), with laboratorial and clinical feature set (LabClin) and All features (All) without the feature selection procedure (No FS); and the results using the feature selection (FS) procedure for the OAA strategy with laboratorial and clinical feature set ($OAA_{LabClin}$), with the complete feature set (OAA) and Clinical-Based Classifier (CBC)

	Feature set	Normal	Chronic hepatitis	Compensated cirrhosis	Decompensated cirrhosis
No FS	US	3.9 (67.8)	23.1 (75.7)	25.9 (75.7)	44.4 (67.8)
	LabClin	92.3 (91.3)	11.5 (72.1)	40.7 (74.8)	75.0 (86.0)
	All	88.5 (90.4)	30.8 (70.4)	37.0 (69.6)	72.2 (86.2)
FS	$OAA_{LabClin}$	100.0 (98.0)	62.0 (78.3)	48.0 (77.0)	81 (89.6)
	OAA	**100.0 (100.0)**	**68.0 (80.4)**	56.0 (78.0)	86 (92.0)
	CBC	**100.0 (100.0)**	65.4 (75.3)	**80.5 (82.5)**	**90.7 (82.5)**

choosing the best features and not the best classifiers, that is the reason why only the LDA classifiers is used [9]. For comparison and performance analysis, classification results at each CS without FS are also computed and the results are shown in Table 2.

Table 2 shows the results obtained with only US image, only clinical-based features and with the complete feature set without and with FS procedure. It is observed that by using only US-based features without FS, unacceptable results for clinical practice are obtained with sensitivities of 3.9%, 23.1%, 25.9%, and 44.4% for the *Normal*, *Chronic Hepatitis*, *Compensated Cirrhosis*, and *Decompensated Cirrhosis* class, respectively. Classification only with clinical-based features, and again without FS, which is the usual approach in the daily clinical practice (LabClin), leads also to unsatisfactory results, in particular, for *Chronic Hepatitis* and *Compensated Cirrhosis* with sensitivities of 11.5% and 40.7%, respectively. The combination of both sets of features leads to marginal improvement for the *Chronic Hepatitis* class but a decreasing for all other classes.

Feature selection seems to be a key operation to a good performance of the classification process as it can be observed from Table 2. In the second part of the table the classification results are presented with FS for three different classification strategies; (1) *One-Against-All* (OAA) only with laboratorial and clinical-based features ($OAA_{LabClin}$), (2) OAA, and (3) CBC.

The classifier inspired on *differential diagnosis* (CBC) with both US and LabClin features, selected with the proposed FS scheme, outperforms the other configurations with exception of the *Chronic Hepatitis* where the OAA strategy with FS is the better (68.0(80.4)%), as observed in Table 2.

The specific features for each CS on the CBC and OAA are listed in Table 3.

The optimum features for the *Normal* detector in both strategies are the same, belonging entirely to the LabClin set; clinical $[F_{30}, F_{37}, F_{36}]$ and laboratorial $[F_{24}]$, which means that the traditional approach in clinical practice to detect illness based on clinical and laboratorial indicators seems to be appropriated.

For the *Chronic Hepatitis*, the OAA strategy selects eight features, mainly from the laboratorial, $[F_{19}, F_{24}, F_{25}, F_{26}, F_{28}]$ and clinical, $[F_{33}]$, sets. However, it also selects features from the US images; liver texture $[F_{16}]$ and liver echogenicity $[F_2]$. In

Table 3 Set of features selected for the OAA strategy (OAA) and clinical-based classifier (CBC). N *Normal*, CHC *chronic hepatitis*, CC *compensated cirrhosis*, DC *decompensated cirrhosis*

	OAA			CBC		
	US	Lab	Clinical	US	Lab	Clinical
N	–	–	24, 30, 36, 37	–	–	24, 30, 36, 37
CH	2, 16	19, 24, 25, 26, 28	33	16, 17	19, 24, 26, 28	37
CC	5, 10, 11, 15, 17	19, 20, 29	–	10, 11, 14, 16, 17	–	–
DC	15	21	30, 32, 34	10, 11, 14, 16, 17	–	–

the case of the CBC strategy for the *Chronic Hepatitis* detector, different optimum features are selected; four from the laboratorial set, $[F_{19}, F_{24}, F_{26}, F_{28}]$, two from the US set, texture $[F_{17}, F_{16}]$, and one from the clinical set, $[F_{37}]$.

The optimum set of features in the case of *Compensated Cirrhosis*, with the OAA strategy, are based on US images; texture, $[F_{15}, F_{10}, F_{17}, F_{11}]$, and surface contour, $[F_5]$, and on laboratorial information, $[F_{29}, F_{20}, F_{19}]$. For the *Decompensated Cirrhosis* this same strategy makes use of five features preponderantly from clinical data.

The discrimination of *Compensated* and *Decompensated Cirrhosis* is obtained in the CBC strategy by using only five US-based textural features, $[F_{16}, F_{17}, F_{14}, F_{10}, F_{11}]$.

These are the optimum features used in each CS. Next, the results of a similar procedure by using both strategies, OAA and CBC, for classifier selection are presented.

3.2 Classifier Selection

For each CS one out of two classifiers, kNN or SVM, is selected according to the classification accuracy optimality criterion for that step. Different parameterizations of each classifier are tested and the optimum configuration and classifier are selected for each CS.

3.2.1 kNN Classifier

Nine different neighborhood configurations, corresponding to $k = 1..9$, were tested in each CS with both optimal sets of features obtained in the previous section.

Table 4 illustrates the results obtained for the OAA strategy with the kNN classifier. These results show a sensitivity to discriminate the *Normal* class of 100% for all configurations. The best sensitivities for *Chronic Hepatitis*, *Compensated*

Table 4 TNR, TPR, and OA percentage results of the kNN classifier for the evaluation set of the OAA strategy for each class. N *Normal*, CHC *chronic hepatitis*, CC *compensated cirrhosis*, DC *decompensated cirrhosis*

	N detector			CHC detector			CC detector			DC detector		
	TNR	TPR (N)	OA	TNR	TPR (CHC)	OA	TNR	TPR (CC)	OA	TNR	TPR (DC)	OA
$k = 1$	**100**	**100**	**100**	87.64	42.31	77.39	87.5	29.63	73.91	92.41	88.89	91.3
$k = 2$	100	100	100	93.26	15.38	75.65	95.45	22.22	78.26	96.2	75	89.57
$k = 3$	100	100	100	87.64	46.15	78.26	90.91	44.44	80	**94.94**	**86.11**	**92.17**
$k = 4$	100	100	100	91.01	38.46	79.13	95.45	33.33	80.87	96.2	83.33	92.17
$k = 5$	100	100	100	88.76	46.15	79.13	**93.18**	**37.04**	**80**	92.41	86.11	90.43
$k = 6$	100	100	100	93.26	30.77	79.13	94.32	25.93	78.26	93.67	83.33	90.43
$k = 7$	97.75	100	98.26	**91.0**	**50**	**81.74**	92.05	37.04	79.13	91.14	83.33	88.7
$k = 8$	97.75	100	98.26	94.38	34.62	80.87	95.45	14.81	76.52	93.67	83.33	90.43
$k = 9$	97.75	100	98.26	88.76	50	80	94.32	25.93	78.26	92.41	83.33	89.579

Table 5 TPR, TNR, and OA percentage results of the kNN classifier for the evaluation set of the CBC strategy. N *Normal*, CHC *chronic hepatitis*, CC *compensated cirrhosis*, DC *decompensated cirrhosis*

	CS_1 (Normal detector)			CS_2 (CHC detector)			CS_3 (Cirrhosis detector)		
	TPR (N)	TNR	OA	TPR (CHC)	TNR	OA	TPR (CC)	TNR (DC)	OA
$k = 1$	**100**	**100**	**100**	42.30	87.30	74.16	0	100	77.78
$k = 2$	100	100	100	73.08	68.25	69.66	22.22	100	74.60
$k = 3$	100	100	100	61.54	82.54	76.40	70.37	94.44	84.13
$k = 4$	100	100	100	69.23	71.43	70.78	81.48	88.89	84.13
$k = 5$	100	100	100	57.69	80.95	74.16	**80.78**	**91.67**	**85.71**
$k = 6$	100	100	100	69.23	74.60	73.03	77.78	91.67	84.13
$k = 7$	100	97.75	98.26	65.38	77.78	74.16	74.07	94.44	84.13
$k = 8$	100	97.75	98.26	**73.08**	**74.60**	**74.16**	74.07	94.44	84.13
$k = 9$	100	97.75	98.26	53.85	77.78	70.79	74.07	94.44	82.54

Cirrhosis, and *Decompensated Cirrhosis* are 50.0% (k = 7), 44.44% (k = 2), and 86.11% (k = 2,5), respectively.

The equivalent results obtained by the CBC strategy are shown in Table 5. As in the previous strategy, the performance of the normal detector is optimum, which means, maxima TPR, TNR, and OA, for $k = 1,2,3,4,5,6$.

In the case of the chronic hepatitis detector the best OA (74.16%) is for k = 8, corresponding to a TPR of 73.08% and FPR of 74.6% (cirrhosis detection). In the last CS, the cirrhosis detector, the results reveal an OA of 85.71% for k = 5. The TPR is 80.78% (*Compensated Cirrhosis*) and the TNR is 91.67% (*Decompensated Cirrhosis*).

3.2.2 SVM Classifier with Polynomial Kernel

The same analysis performed previously for the kNN classifier will be now presented for the SVM one.

Several parameterizations of the polynomial kernel were tested. The parameters are the cost, $c = 1,10,100,500$, and the degree, $d = 1,2,3,4,5$. Here, only the best results obtained for $c = 1$ are presented.

The results obtained with the polynomial kernel by using the OAA strategy are listed in Table 6. An ideal classification result is obtained in the normal detector for $d = 4$. For chronic hepatitis and cirrhosis detectors the best result, for $d = 2$, are: sensitivity 73.08% and 59.26% for *Chronic Hepatitis* and *Compensated Cirrhosis*, respectively. The optimum configuration in the *Decompensated Cirrhosis* case is with $d = 4$, corresponding to a sensitivity of 91.67%.

Table 7 shows the results obtained by using the proposed CBC approach. The normal detector for $d = 4$ is ideal under all figures of merit (OA, TPR, TNR = 100%). For the remaining CS the optimal kernel degrees are $d = 1$. In the chronic hepatitis detector the best OA is 79.76%, with a sensitivity of 69.23%. For the

Table 6 TNR, TPR, and OA percentage results of the SVM classifier with polynomial kernel for the evaluation set of the OAA strategy. N *Normal*, CHC *chronic hepatitis*, CC *compensated cirrhosis*, DC *decompensated cirrhosis*

	N detector			CHC detector			CC detector			DC detector		
Degree	TNR	TPR (N)	OA	TNR	TPR (CHC)	OA	TNR	TPR (CC)	OA	TNR	TPR (DC)	OA
1	96.63	100	97.39	89.89	23.08	74.78	81.82	59.26	76.52	91.14	72.22	85.22
2	98.88	100	99.13	**87.64**	**73.08**	**84.35**	**85.23**	**59.26**	**79.13**	93.67	91.67	93.04
3	98.88	100	99.13	85.39	61.54	80	79.55	55.56	73.91	92.41	88.89	91.3
4	**100**	**100**	**100**	89.89	50	80.87	80.68	55.56	74.78	**94.94**	**91.67**	**93.91**
5	98.88	100	99.13	88.76	46.15	79.13	80.68	51.85	73.91	89.87	91.67	90.43

Table 7 TPR, TNR, and OA percentage results of the SVM classifier with polynomial kernel for the evaluation of the CBC strategy. N *Normal*, CHC *chronic hepatitis*, CC *compensated cirrhosis*, DC *decompensated cirrhosis*

	CS_1 (Normal detector)			CS_2 (CHC detector)			CS_3 (Cirrhosis detector)		
Degree	TPR (N)	TNR	OA	TPR (CHC)	TNR	OA	TPR (CC)	TNR (DC)	OA
1	96.63	100	97.39	**69.23**	**84.13**	**79.76**	**77.78**	**91.67**	**85.71**
2	98.87	100	99.13	65.38	79.37	75.28	70.37	86.11	79.36
3	98.87	100	99.13	69.23	82.54	78.65	66.67	80.56	74.60
4	**100**	**100**	**100**	61.54	84.13	77.53	62.96	83.33	74.60
5	98.87	100	99.13	65.38	82.54	77.53	66.67	83.33	76.19

Compensated Cirrhosis the sensitivity is 77.78% while for the *Decompensated Cirrhosis* is 91.67%.

3.2.3 SVM Classifier with Gaussian Radial-Basis Kernel

To optimize the SVM with Gaussian radial-basis kernel, for the different classification tasks, the radius parameter (r) was ranged from 0.1 to 5 with steps of 0.5. The c parameter was also tested in different values, $c = 1, 10, 100, 500$, for each radius value. The best results are obtained for $c = 10$.

The SVM classification results with Gaussian radial-basis kernels for the OAA strategy are summarized in Table 8. For this strategy, this classifier exhibits the worst results for all detectors when compared with the other tested classifiers . The sensitivity is 100% for *Normal* class, with the first three radius values, a sensitivity of 26.92% for *Chronic Hepatitis* class, with $r = 1.6$, 44.44% for *Compensated Cirrhosis*, with a $r = 2.1$, and 86.11% for *Decompensated Cirrhosis* class, with $r = 2.6$.

With the CBC strategy the results are better than using the OAA one as shown in Table 9.As in the previous case, the normal detector presents OA, TPR, and TNR of 100% with $r = 0.1, 0.6, 1.1$. The wort result is for the *Chronic Hepatitis* where the sensitivity is 38.46% and the OA is 78.65% ($r = 1.1$). For the last

Table 8 TNR, TPR, and OA percentage results of the SVM classifier with radial-basis kernel for the evaluation set of the OAA strategy. N *Normal*, CHC *chronic hepatitis*, CC *compensated cirrhosis*, DC *decompensated cirrhosis*

	N detector			CHC detector			CC detector			DC detector		
Radius	TNR	TPR (N)	OA	TNR	TPR (CHC)	OA	TNR	TPR (CC)	OA	TNR	TPR (DC)	OA
0.1	**100**	**100**	**100**	100	0	77.39	100	0	76.52	98.73	22.2	74.78
0.6	100	100	100	95.51	3.85	74.78	100	0	76.52	96.2	75	89.57
1.1	100	100	100	93.26	15.38	75.65	97.73	14.81	78.26	94.94	83.33	91.3
1.6	96.63	100	97.39	**93.26**	**26.92**	**78.26**	96.59	29.63	80.87	91.14	83.33	88.7
2.1	95.51	100	96.52	92.13	23.08	76.52	**96.59**	**44.44**	**84.35**	91.14	83.33	88.7
2.6	96.63	100	97.39	92.13	11.54	73.91	95.45	29.63	80	**91.14**	**86.11**	**89.57**
3.1	95.51	100	96.52	96.63	3.85	75.65	94.32	11.11	74.78	91.14	86.11	89.57
3.6	95.51	100	96.52	98.88	3.85	77.39	93.18	3.7	72.17	91.14	86.11	89.57
4.1	95.51	100	96.52	98.88	3.85	77.39	96.59	0	73.91	91.14	86.11	89.57
4.6	95.51	100	96.52	98.88	3.85	77.39	97.73	0	74.78	91.14	75	86.09

Table 9 TPR, TNR, and OA percentage results of the SVM classifier with radial-basis kernel for the evaluation set of the CBC strategy. N *Normal*, CHC *chronic hepatitis*, CC *compensated cirrhosis*, DC *decompensated cirrhosis*

	CS_1 (Normal detector)			CS_2 (CHC detector)			CS_3 (Cirrhosis detector)		
Radius	TPR (N)	TNR	OA	TPR (CHC)	TNR	OA	TPR (CC)	TNR (DC)	OA
0.1	**100**	**100**	**100**	0	100	70.79	0	100	57.14
0.6	100	100	100	23.08	96.83	75.28	22.22	100	66.67
1.1	100	100	100	**38.46**	**95.24**	**78.65**	70.37	94.44	84.12
1.6	96.63	100	97.39	34.62	95.24	77.53	81.48	88.89	85.71
2.1	95.50	100	96.52	34.62	93.65	76.40	**81.48**	**91.67**	**87.30**
2.6	96.63	100	97.39	23.08	93.65	73.03	77.78	91.67	85.71
3.1	95.50	100	96.52	19.23	95.24	73.03	74.07	94.44	85.71
3.6	95.50	100	96.52	11.54	96.83	71.91	74.07	94.44	85.71
4.1	95.50	100	96.52	11.54	100	74.16	74.07	94.44	85.71
4.6	95.50	100	96.52	11.54	100	74.16	74.07	91.67	84.13

CS of the CBC approach, the optimal radius is $r = 2.1$ resulting in an OA of 87.3%. The individual performances showed a sensitivity of 81.48% and 91.67% for *Compensated Cirrhosis* and *Decompensated Cirrhosis*, respectively.

4 Discussion

The proposed CBC algorithm for diagnosis and staging of the CLD has been applied to an experimental database of 115 patients, with well-established diagnosis, according to the guidelines accepted in the gastroenterology medical community.

The multi-modal feature set proved to be an appropriate approach for this classification problem. An algorithm was designed and implemented to select the optimal set of features for each CS. The performance of the FS algorithm was evaluated and the results compared with the ones obtained without FS procedure. This procedure, based on the SFFS with LDA criterion, leads to a clear improvement of the classification accuracy and sensitivity in all classes/detectors.

The results reveal an important issue: each modality feature set has, at each CS, different discriminative power. In the first CS, laboratorial and clinical features are more discriminative than the US-based features. As already stated before, this fact confirms the appropriateness of the traditional diagnosis method used in clinical practice. For more severe stages of CLD, the FS procedure automatically attributes more and more importance to the US image-based features. US textural features, obtained from the first-order AR model coefficients and the wavelet coefficients obtained from the first Haar wavelet decomposition, are particularly relevant.

This fact corroborates the difficulty reported in the literature [3] in discriminating advanced stages of the CLD only from laboratorial and clinical information. This is particularly visible in the last CS, where only US-based features are automatically selected.

The US textural features selected here are in accordance with the results of several other studies [6, 15, 21, 27]. In these studies, wavelet transform [6, 15, 21] and AR coefficients [27] based features, from US images, are presented as having high discriminative power in the assessment of CLD stages.

Liver contour US-based features were extracted from a semi-automatic post-processing algorithm. Apparently, this set of features is not very important because they are only selected in one of the strategies, the OAA one. In the proposed CBC they are not selected at all. This class of features was included in this study because several works in the literature [3, 30, 31] refer its potential usefulness for CLD diagnosis. However, our results also reinforce the conclusions on [33], where it is stated that the liver surface morphology analysis performed based on US data is subjective and non-reliable.

Another important conclusion is that US echogenicity is not suitable for discrimination in CLD. This confirms previous results in the literature [17, 18] where it was shown the low discriminative power of the features $[F_1, F_2, F_3]$.

The main novelty of this work is the proposal of a new classification and staging strategy for CLD where the natural evolution of the disease is taken into account. The well-established protocol of *differential diagnosis*, used in the medical community, also inspired the design of the CBC. This approach outperforms the OAA strategy.

For the *Normal* class the results showed a perfect accuracy in discriminating the normal from the diseased patients, for all classifiers in both decompositions. It is possible to refer that we improved the reported results described in the literature [6, 13, 15]. This is due to the proposed multi-modal feature and FS approach, since the system only selected clinical and laboratorial data. The disease clinical knowledge proved to be crucial for this CS.

Liver fibrosis is related, in part, with *Chronic Hepatitis* patients without cirrhosis. In the study preformed by [15] it is referred the difficulty in the classification of liver fibrosis based on US images. Their study revealed an OA of 72%, with a sensitivity of 60% for patients with fibrosis grade of 3 (*Chronic Hepatitis* class) and 88.6% for patients with fibrosis grade of 4 (*Cirrhosis* class). In the present study, we were able to improve the detection of the *Chronic hepatitis* class by using the SVM with a polynomial kernel of degree $d = 1$, when compared with the results presented in [15]. Our results are an OA of 79.8% with a sensitivity of 69.2% and 84.1% for *Chronic Hepatitis* and *Cirrhosis* class, respectively.

Concerning the cirrhosis detector, with the CBC strategy, [3] reported that the accuracy in detecting signs of compensated cirrhosis has not been well investigated.

Concerning the cirrhosis detection, our results show how important the US-based features are in CBC. The best results were obtained with the Gaussian radial-basis SVM classifier ($r = 2.1$), where an OA of 87.3% with a sensitivity of 81.48% for the *Compensated cirrhosis* class and 91.7% for the *Decompensated cirrhosis* class were achieved. In [3] a sensitivity of 82.2% for the *Compensated cirrhosis* class was reported.

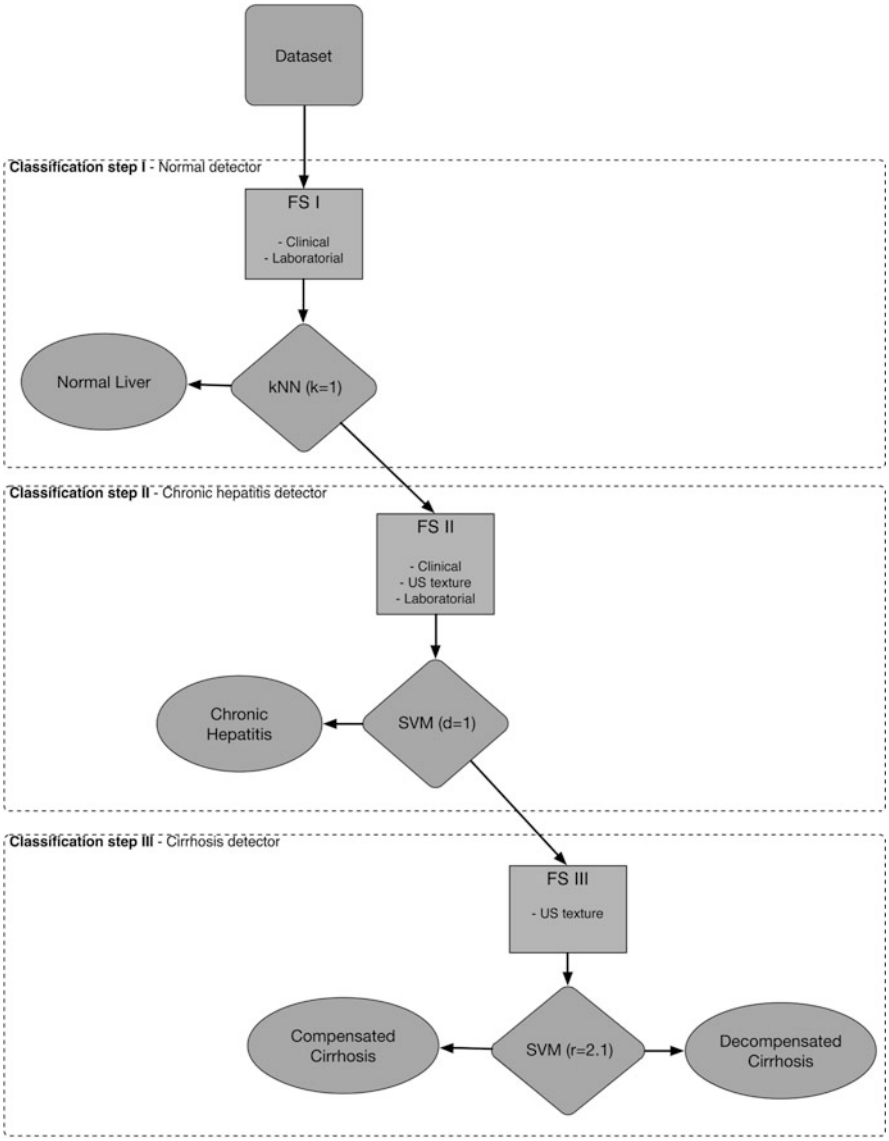

Fig. 9 Proposed algorithm for the classification of Chronic Liver Disease based on US images, clinical and laboratorial features

The final optimized configuration adopted for the CBC classifier, according to the all tests of features and classifiers selection performed in this work, is the following (see Fig. 9): CS_1, Normal detector, is a kNN with ($k = 1$); CS_2, Chronic hepatitis detector, is a polynomial kernel SVM with ($d = 1$); and CS_3, Cirrhosis detector, is a Gaussian radial-basis kernel SVM with ($r = 2.1$).

5 Conclusions and Future Work

Many scientific and medical problems require different concepts or classes to be distinguished. The goal is to extract sufficient discriminatory information to assign an object reliably, which in the medical field is of major importance. In this sense, this study was developed with the premise that the multi-class classification problem should address the normal behavior of CLD. To solve this investigation question, we develop the *CBC* strategy. The proposed multi-feature and multi-classifier system, based on a pre-processing US image decomposition proved to be a useful approach to the CLD classification problem.

The results presented in this study showed that it is possible to identify the different stages of CLD based on US liver images, particularly textural features, as well as laboratorial and clinical features. This is achievable by decomposing the data based on the different stages of the disease: The group with the most severe stage, *Decompensated cirrhosis*, is well discriminate, while patients in lower stages, *Chronic Hepatitis* and *Compensated cirrhosis*, need further analysis, in order to improve even more the classification results.

In future work, the proposed multi-feature approach will be expanded to incorporate more textural and morphological features. Moreover future work will also investigate classifier combination techniques as well as other features selection algorithms.

References

1. Allan R, Thoirs K, Phillips M (2010) Accuracy of ultrasound to identify chronic liver disease. World J Gastroenterol 28(16):3510–3520
2. Bucak İÖ, Baki S (2010) Diagnosis of liver disease by using cmac neural network approach. Expert Syst Appl 37:6157–6164
3. Gaiani S, Gramantieri L, Venturoli N, Piscaglia F, Siringo S, D'Errico A, Zironi G, Grigioni W, Bolondi L (1997) What is the criterion for differentiating chronic hepatitis from compensated cirrhosis? A prospective study comparing ultrasonography and percutaneous liver biopsy. J Hepatol 27(6):979–985
4. Zhou SR, Wan J (2009) A survey of algorithms for the analysis of diffused liver disease from b-mode ultrasound images. In: Proceedings of the 9th international conference on Electronic measurement instruments, 2009. ICEMI '09, pp 2576 –2582, Aug 2009
5. Cao G, Shi P, Hu B (2005) Liver fibrosis identification based on ultrasound images captured under varied imaging protocols. J Zhejiang Univ Sci B 6(11):1107–1114
6. Mojsilovic A, Markovic S, Popovic M (1997) Characterization of visually similar diffuse diseases from b-scan liver images with the nonseparable wavelet transform. Int Conf Image Process 3:547
7. Lee CH, Choi JW, Kim KA, Seo TS, Lee JM, Park CM (2006) Usefulness of standard deviation on the histogram of ultrasound as a quantitative value for hepatic parenchymal echo texture; preliminary study. Ultrasound Med Biol 32(12):1817–1826
8. D'Amico G, Garcia-Tsao G, Pagliaro L (2006) Natural history and prognostic indicators of survival in cirrhosis: a systematic review of 118 studies. J Hepatol 44(1):217–231

9. Jain A, Zongker D (1997) Feature selection: evaluation, application, and small sample performance. IEEE Trans Pattern Anal Mach Intell 19:153–158
10. Sima C, Attoor S, BragNeto U, Lowey J, Suh E, Dougherty ER (2005) Impact of error estimation on feature selection. Pattern Recognit 38(12):2472–2482
11. Pudil P, Novovicov J, Kittler J (1994) Floating search methods in feature selection. Pattern Recognit Lett 15(11):1119–1125
12. Theodoridis S, Koutroumbas K (2008) Pattern recognition, 4th edn. Academic Press. London, UK
13. Kadah Y, Farag A, Zurada JM, Badawi AM, Youssef AM (1996) Classification algorithms for quantitative tissue characterization of diffuse liver disease from ultrasound images. IEEE Trans Med Imaging 15:466–478
14. Duda RO, Hart PE, Stork DG (2000) Pattern Classification, 2nd edn. Wiley-Interscience. New York, USA
15. Yeh W, Jeng Y, Li C, Lee P, Li P (2003) Liver fibrosis grade classification with b-mode ultrasound. Ultrasound Med Biol 29:1229–1235
16. Seabra JC, Sanches JM (2010) On estimating de-speckled and speckle components from b-mode ultrasound images. In: Proceedings of the 2010 IEEE international conference on biomedical imaging: from nano to macro, ISBI'10, pp 284–287. IEEE Press. Rotterdam, The Netherlands
17. Meziri M, Pereira W, Abdelwahab A, Degott C, Laugier P (2005) In vitro chronic hepatic disease characterization with a multiparametric ultrasonic approach. Ultrasonics 43(5): 305–313
18. Gaitini D, Baruch Y, Ghersin E, Veitsman E, Kerner H, Shalem B, Yaniv G, Sarfaty C, Azhari H (2004) Feasibility study of ultrasonic fatty liver biopsy: texture vs. attenuation and backscatter. Ultrasound Med Biol 30(10):1321–1327
19. Yeh W, Jeng Y, Li C, Lee P, Li P (2005) Liver steatosis classification using high-frequency ultrasound. Ultrasound Med Biol 31(5):599–605
20. Li S, Shawe-Taylor J (2005) Comparison and fusion of multiresolution features for texture classification. Pattern Recognit Lett 26(5):633–638
21. Wan J, Zhou SR (2010) Features extraction based on wavelet packet transform for b-mode ultrasound liver images. In: 3rd international congress on image and signal processing (CISP), vol 2, pp 949 –955, Oct 2010
22. Takalo R, Hytti H, Ihalainen H (2005) Tutorial on univariate autoregressive spectral analysis. J Clin Monitor Comput 19(6):401–410
23. Wear K, Wagner R, Garra B (1995) A comparison of autoregressive spectral estimation algorithms andorder determination methods in ultrasonic tissue characterization. IEEE Trans Ultrason Ferroelectr Freq Control 42(4):709–716
24. Stathaki P, Constantinides A (1993) Robust autoregressive modelling through higher order spectralestimation techniques with applications to mammography. In: Conference record of the twenty-seventh asilomar conference on signals, systems and computers 1:189–193, Nov 1993
25. Girault J, Ossant F, Ouahabi A, Kouame D, Patat F (1998) Time-varying autoregressive spectral estimation for ultrasoundattenuation in tissue characterization. IEEE Trans Ultrason Ferroelectr Freq Control 45(3):650–659
26. Farnoud N, Kolios M, Krishnan S (2003) Ultrasound backscatter signal characterization and classification using autoregressive modeling and machine learning algorithms. In: Engineering in medicine and biology society, 2003. Proceedings of the 25th annual international conference of the IEEE, vol 3, pp 2861–2864 Vol 3, Sept 2003
27. Wang T, Saniie J, Jin X (1991) Analysis of low-order autoregressive models for ultrasonic grainsignal characterization. IEEE Trans Ultrason Ferroelectr Freq Control 38(2):116–124
28. Bleck JS, Ranft U, Gebel M, Hecker H, Westhoff-Bleck M, Thiesemann C, Wagner S, Manns M (1996) Random field models in the textural analysis of ultrasonic images of the liver. IEEE Trans Med Imaging 15(6):796–801

29. Sherlock S, Dooley J (2002) Diseases of the liver and biliary system, 11th edn. Blackwell Science Ltd. Milan, Italy
30. Simonovsky V (1999) The diagnosis of cirrhosis by high resolution ultrasound of the liver surface. Br J Radiol 72(853):29–34
31. Berzigotti A, Abraldes JG, Tandon P, Erice E, Gilabert R, Garca-Pagan JC, Bosch J (2010) Ultrasonographic evaluation of liver surface and transient elastography in clinically doubtful cirrhosis. J Hepatol 52(6):846–853
32. Droga V, Rubens D (2004) Ultrasound Secrets. Hanley and Belfus. Philadelphia, USA
33. Ladenheim JA, Luba DG, Yao F, Gregory PB, Jeffrey RB, Garcia G (1992) Limitations of liver surface US in the diagnosis of cirrhosis. Radiology 185(1):21–23
34. Bregler C, Slaney M (1995) SNAKES, Interval Research Corporation
35. Maeda K, Utsu M, Kihaile PE (1998) Quantification of sonographic echogenicity with grey-level histogram width: a clinical tissue characterization. Ultrasound Med Biol 24(2):225–234
36. Duin RPW, Juszczak P, Paclik P, Pkalska E, de Ridder D, Tax DMJ, Verzakov S (2007) PR-Tools4.1, a matlab toolbox for pattern recognition, http://prtools.org. Delft, The Netherlands

Assessment of Bone Healing Using Ultrasound

Hasan Al-Nashash and Nasser N. Qaddoumi

1 Introduction

Human bone has the remarkable capacity of remodeling and self repair through a complex regenerative healing process resulting in the gradual restoration of its mechanical properties and load bearing capacity [1]. Fracture healing goes through three distinct stages: reactive phase which includes inflammatory phase and granulation tissue formation, reparation phase which includes callus formation and lamellar bone deposition, and remodeling phase in which woven bone is replaced by mature bone. Although surgical intervention and fracture immobilization facilitate healing, fracture healing is known to be a physiological process. The connective tissue membrane covering the bone determines the healing process of a fractured bone. This connective tissue is the primary source of bone cells responsible for generating new bone during growth and repair. The length of the healing process depends on the extent of the fracture. It takes up to three weeks for the majority of upper bodily fractures and it takes up to four weeks for lower body fractures.

In clinical settings, monitoring of the fracture healing process is routinely done using manual assessment of the fracture site and evaluation of radiographic images in an attempt to determine the form and intensity of callus calcification. Both methods are subjective and largely dependent on the physician's expertise and clinical judgment which may lead to discrepancy in clinical assessment, premature or late fixation removal, and/or untimely surgical and physical therapy intervention [2, 3]. Manual manipulation is a subjective test of stiffness which is often inconclusive and is clearly limited by the amount of stress safely applied [2]. X-ray radiation exposure is hazardous and considered unsafe especially for repetitive tests. It cannot be used for pregnant women or patients who have had any barium contrast media, or medication containing bismuth. Moreover, while fractures

H. Al-Nashash (✉) • N.N. Qaddoumi
American University of Sharjah, UAE
e-mail: hnashash@aus.edu; nqaddoumi@aus.edu

J.M. Sanches et al. (eds.), *Ultrasound Imaging: Advances and Applications*,
DOI 10.1007/978-1-4614-1180-2_12,

are typically visible on primary radiographs, the first stages of bone healing and soft tissue deposition are difficult to visualize prior to calcification resulting in a phase lag between radiological X-ray assessment and the physiological healing process [3, 4].

The above-mentioned shortcomings of the subjective fracture healing assessment techniques currently used in clinical practice clearly pose many challenges to the treating physicians. These range from the potential inaccurate assessment of delayed unions and nonunions to the incorrect timing of the removal of an internal/external fixation device, and sometimes to the delayed or premature surgical and/or physical therapy intervention. These are serious problems in light of the high rate of remodeling that bone undergoes, since it is a highly active tissue well known to alter its properties and configuration in response to changes in mechanical demand. This implies that any time delays may lead to bone atrophy (or hypertrophy at attachment sites) and diminished mechanical properties affecting the overall healing process [1].

The inherent limitations of the current assessment of fracture healing in clinical practice have prompted researchers to find alternative solutions. Several methods have been proposed for the noninvasive monitoring of fracture healing over the last decade. These include quantitative computed tomography (QCT), dual energy X-ray absorptiometry (DEXA), and single photon absorbiometry (SPA). The main idea behind these techniques is to measure the bone mineral density (BMD) of the regenerated callus during the bone healing process and relate it to the strength and stiffness of the healing bone [5, 6]. While those techniques shed some light on the structural integrity of the healing bone, they were found to be influenced by extrinsic bone properties and type of fracture and could not provide accurate measurements of the callus [7]. Furthermore, these techniques also suffer from X-ray exposure and high cost.

Vibratory devices were also used to study the mechanical behavior of fracture healing of bone [8–12]. These devices consist of mechanical sine wave vibrators that are applied to the fracture site such that a miniature accelerometer captures the response of bone. If the bone is free of fracture, it behaves linearly and an excitation frequency is detected. Fractures result in a nonlinear system behavior and harmonics will be detected by the accelerometer. Unfortunately, vibratory devices suffer from limitations related to increased signal damping and inaccuracies locating the resonance frequency especially with obese [4, 8]

Low-intensity ultrasound is a form of mechanical energy that is transmitted through and into biological tissues as an acoustic pressure wave. It has been widely used in medicine as a diagnostic and therapeutic tool. Literature shows that LIUS has been used for the last 60 years as a biophysical therapeutic form of intervention in the bone healing process, which through several mechanisms accelerates healing of fresh fractures and enhances callus formation in delayed unions and nonunions [13].

Despite the vast body of literature that investigates the therapeutic fracture-enhancement capabilities of ultrasound [14–16], fewer studies examined the potential use of ultrasound as a diagnostic quantitative monitoring tool in bone fracture

healing [4, 17–19]. Malizos et al. summarizes the work done by the various research groups where the majority has used axial-transmission technique. The major shortcomings of the ultrasound systems reviewed are the limited application to peripheral skeletal sites, such as the tibia and radius, and the measurement inaccuracies due to soft tissues interference.

Hijazi et al. [4] proposed a mathematical simulation model to simulate the interaction of continuous ultrasound waves with the human body. Their results show that ultrasound techniques could be used to quantitatively monitor the various stages of the healing process. Bin Sediq et al. [19] also used a mathematical simulation model to investigate the effect of frequency on callus thickness and hardness.

An extensive review of literature shows that while ultrasound provides a promising noninvasive means of monitoring and quantifying the bone healing process, there are no practical ultrasound systems in the market available for clinical applications. Clinicians continue to use conventional subjective means of fracture healing assessment, namely, manual manipulation and radiographic assessment, thereby relying heavily on clinical expertise and judgment and risking errors in detecting complications, assessing end point of healing, or removal of fixation. The main challenges cited as reasons for ultrasound error measurements that hinder its practical use stem from three different sources: (1) surrounding soft tissue, (2) variations in bone shape and size, and (3) inaccurate measurement due to probe separation.

This chapter is organized in four main sections. In Sect. 2, we describe an experimental method for the measurement of acoustic impedance of healing bone using pulsed ultrasound. Results from standard materials and biological materials are presented. In Sect. 3, a mathematical model which describes the interactions of continuous ultrasound waves with a multilayered biological structure is described. The model is developed to compute the reflection coefficient at the transducer side. This coefficient is then used to quantify the bone healing process. Finally, in Sect. 4, another mathematical model which describes the interaction of pulsed mode ultrasound waves with a multilayered biological structure is described. The model is applied to estimate the bone callus thickness and degree of hardness. Different frequencies are utilized to obtain highest measurement sensitivity and accuracy of callus thickness and degree of hardness.

2 Measurement of Acoustic Impedance of Healing Bone

Knowledge of acoustic impedance of healing bone and other tissues is of paramount importance for the quantification of bone healing stage. In this section, we describe an experimental method for the measurement of acoustic impedance using pulsed ultrasound. The acoustic impedance (Z) is the product of the acoustic velocity of the wave and the density of the material. It describes the ability of a material to allow sound waves to propagate through it.

When an ultrasound wave propagates from a medium to another, part of it is transmitted to the second medium and the rest is reflected back. The ratio of the reflected to the incident waves is called the reflection coefficient (Γ). It depends on the physical properties of the two mediums, mainly on their acoustic impedances. The reflection coefficient at the boundary is, therefore, defined as:

$$\Gamma = \frac{Z_2 - Z_1}{Z_2 + Z_1}. \tag{1}$$

In bone healing assessment, it is hypothesized that the reflection coefficient associated with the callus layer of the healing bone is associated with the degree or level of healing process. The rationale behind this hypothesis is based on the fact that the callus layer changes the density and dimensions during the healing process, thus altering the acoustic impedance and reflection coefficient. An accurate measure of the reflection coefficient of pulsed ultrasound will, therefore, make assessment of the level of healing process tractable.

To describe the interaction of pulsed mode ultrasound with the multilayer biological system which includes skin, fat, and callus, a mathematical model is developed. In this model, a single element transducer is used to send an ultrasound pulse to a multilayer structure. Next, we will describe a mathematical model to estimate the acoustic impedance of a flat sheet of a material.

Figure 1 shows a structure composed of three layers including two layers of water and a sheet of material with unknown acoustic impedance. Let Z_1 and Z_2 be the acoustic impedances of water and material, respectively. The incident ultrasound pulse amplitude impinging upon the material is V_i and the reflected portion is V_r1 and therefore:

$$\begin{aligned} V_\mathrm{r1} &= \Gamma V_i \\ V_\mathrm{t1} &= V_i(1+\Gamma). \end{aligned} \tag{2}$$

The transmitted signal V_t1 will be attenuated through layer 2 and reach the front surface of layer 3 as V_i2. At the interface between layers 2 and 3, part of the wave will be reflected and travel through medium 2 to be attenuated to V_i3. Part of V_i3 will be transmitted to layer 1 as V_t3 [20]:

$$V_\mathrm{t3} = -\Gamma\left(1-\Gamma^2\right)\mathrm{e}^{-2\alpha d}V_i, \tag{3}$$

where

α: attenuation factor ($\mathrm{dB\,cm^{-1}\,MHz^{-1}}$)
d: layer 2 thickness (cm)

The transducer will detect the first reflected signal V_r1 followed by the second reflection V_t3 as described by (3). Similarly, the third reflected signal V_t5 can be obtained as:

$$V_\mathrm{t5} = -\Gamma^3\left(1-\Gamma^2\right)\mathrm{e}^{-4\alpha d}V_i. \tag{4}$$

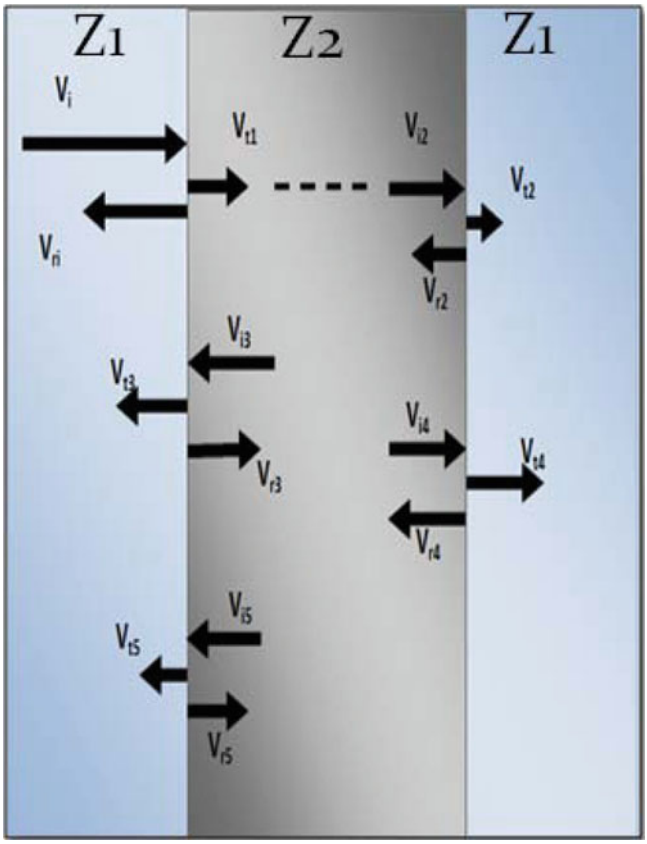

Fig. 1 Multi-reflections of a three-layer system

To obtain the reflection coefficient Γ at the interface between water and the material under investigation, V_{r1}, V_{t3}, and V_{t5} are used [20]:

$$\Gamma = \sqrt{\frac{1}{1 - \frac{K_2}{K_1}}}, \tag{5}$$

where

$$K_1 = \frac{V_{r1}}{V_{t3}} = \frac{1}{-(1 - \Gamma^2)\,e^{-2\alpha d}} \tag{6}$$

and

$$K_2 = \frac{V_{t3}}{V_{t5}} = \frac{1}{\Gamma^2 e^{-2\alpha d}} \tag{7}$$

Table 1 Acoustic impedance results of different materials

Material	Aluminum	Tendon	Cartilage	Bone
Published acoustic impedance (MRayl)	17.0	1.4	1.85	6.43
Obtained value (MRayl)	16.74	1.37	1.88	6.38
%Error	1.52%	2.00%	1.62%	0.80%

As indicated by (5), the reflection coefficient is independent of the thickness and attenuation factor of all layers. It only depends on the ratio of the reflected signals which are easily obtained through measurement. Consequently, if Z_1 is assumed to be known (water in this case), then the unknown Z_2 can be determined using (1) and (5).

This technique was tested on samples of aluminum and some biological materials such as bone, tendon, and cartilage. Since aluminum has a standard and well documented acoustic impedance, it can be used for calibration purposes. A pulsed mode A-scan ultrasound system was used to measure Γ and consequently determine Z.

Table 1 shows the obtained results of the acoustic impedance for the different materials. The results are compared with the published acoustic impedance values of the materials under investigation [21].

3 Continuous Mode Testing of Healing Bone

Ultrasound testing of healing bone can be performed using continuous or pulsed mode techniques. In continuous mode, the ultrasound frequency is a very crucial factor in the image display or resolution. In addition, the propagation speed of the wave is also an important factor. The speed varies depending on the frequency of operation and the acoustic impedance of the medium. Ultrasound imagers transmit sound waves in the megahertz range to the system under investigation using a piezoelectric transducer. Ultrasound waves interact with different materials such as skin, tissue, and bone. Each material has its own distinct acoustic impedance; therefore, some of the sound waves energy will be reflected back to the transducer while the rest propagates through the medium. The reflected waves will be picked up by the same or a second transducer depending on the experimental setup. Thus, ultrasound testing techniques are applied in a monostatic or a bistatic fashion. A general block diagram of a single transducer based continuous mode ultrasound system for the assessment of bone healing process is depicted in Fig. 2. The oscillator, power amplifier, and transducer form the transmitter. The transducer, buffer amplifier, and mixer make the receiver part of the system.

In addition, ultrasound measurements may be conducted from only one side (echo/reflection measurements) or from both sides of the system under inspection (transmission). Generally, the resolution of the measurement is dictated by the footprint of the ultrasound sensor which is usually small in the order of millimeters.

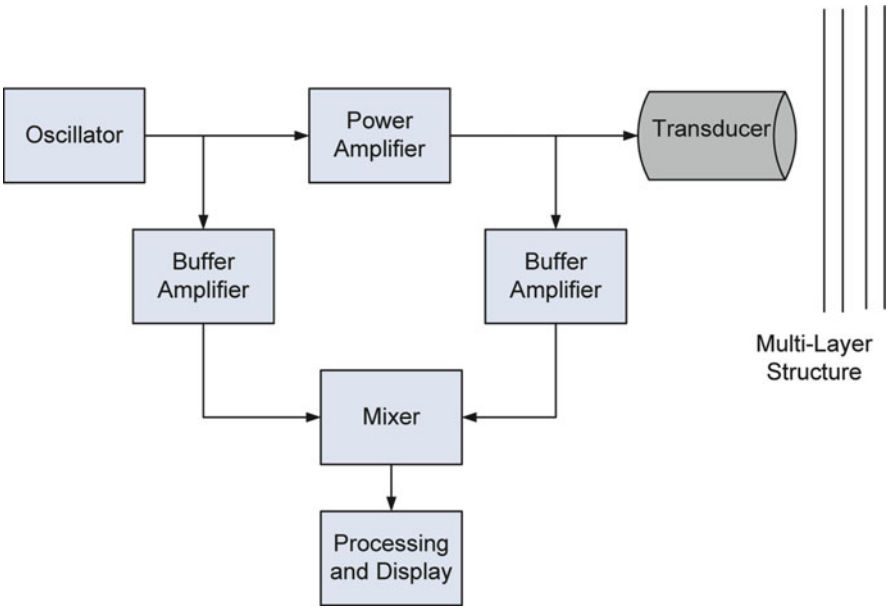

Fig. 2 General block diagram of a single transducer based continuous mode ultrasound system

Fig. 3 Human tibia model at ultrasound frequencies

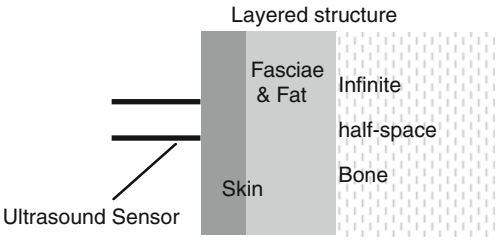

To model the interaction of continuous ultrasound waves and a multi-layered system, a mathematical model is presented next. The model is based on transmission line theory. In an ultrasound regime, the biological structure is modeled as a three layer medium: skin, fasciae, and bone. Each of these layers is characterized by its acoustic impedance. These impedances influence the incident, transmitted, and reflected ultrasound pressure waves. The presence of a fracture or a crack can be modeled as an additional callus layer on top of the bone. When an acoustic wave is incident on a structure, similar to the human body, part of it will be reflected at the boundary between any two layers and the rest will travel through. Waves reflect whenever they travel from one medium (layer) to another medium.

Transmission line technique is used to model the interaction of a pressure wave with a multilayered structure backed by an infinite half-space of bone as shown in Fig. 3.

The position reference ($x = 0$) is assumed to be at the boundary of the first layer and water. The pressure P and velocity u in any layer, n, can be written as [22]:

$$P_n = P_{ni}e^{-j\gamma_n x} + P_{nr}e^{j\gamma_n x} \tag{8}$$

$$u_n = u_{ni}e^{-j\gamma_n x} - u_{nr}e^{j\gamma_n x} = \frac{1}{Z_n}\left(P_{ni}e^{-j\gamma_n x} - P_{nr}e^{j\gamma_n x}\right) \tag{9}$$

where subscript i denotes incident and r denotes reflected. Also, γ_n is the transmission coefficient and Z_n is the acoustic impedance of layer n. To find the effective reflection coefficient, we should find P_{1r} in terms of P_{1i}. The effective reflection coefficient for a structure made of any number of layers may be obtained by starting at the last layer (an infinite half-space of a material). In this last layer, no reflection is present and the waves may be expressed as traveling waves only. By applying the boundary conditions at the interface between the last two layers, an expression of the reflection coefficient at that last interface may be obtained. The process is propagated back till an expression of the reflection coefficient at the first interface is obtained. For example, the reflection coefficient for a three layer structure may be written as:

$$\Gamma = \frac{\frac{Z_1}{Z_0}D - 1}{\frac{Z_1}{Z_0}D + 1}, \tag{10}$$

where

$$D = \frac{1 + Ce^{-2j\gamma_1 d_1}}{1 - Ce^{-2j\gamma_1 d_1}},$$

$$C = \frac{\frac{Z_2}{Z_1}B - 1}{\frac{Z_2}{Z_1}B + 1},$$

$$B = \frac{1 + Ae^{-2j\gamma_2 d_2}}{1 - Ae^{-2j\gamma_2 d_2}},$$

$$A = \frac{\frac{Z_3}{Z_2} - 1}{\frac{Z_3}{Z_2} + 1}.$$

The equations show an obvious pattern that can be seen in the resultant reflection coefficient. There is a reflection at the boundary of each layer followed by a transmission through the layer. The above formulation can be expanded for any number of layers by cascading these reflection, X_k and transmission, Y_k formulae shown below.

$$X_k = \frac{\frac{Z_k}{Z_{k-1}}Y_k - 1}{\frac{Z_k}{Z_{k-1}}Y_k + 1} \quad \text{and} \quad Y_{k-1} = \frac{1 + X_k e^{-2j\gamma_{k-1}d_{k-1}}}{1 - X_k e^{-2j\gamma_{k-1}d_{k-1}}}, \tag{11}$$

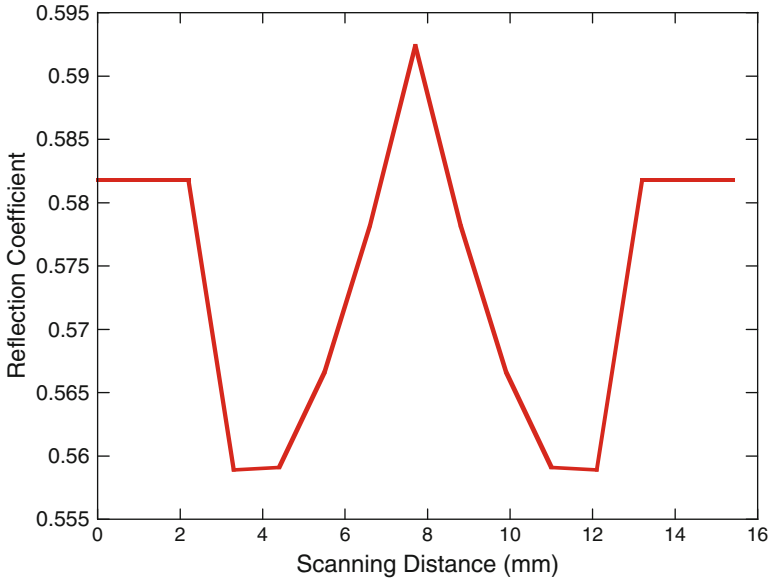

Fig. 4 Reflection coefficient vs. scanning relative position over a structure containing callus [22]

where, k is the layer number. Calculation starts from the last layer, where $Y_n = 1$ for the first iteration if the last layer is an infinite half-space ($n =$ number of layers). By solving for all X_k and Y_k, X_1 will be the effective reflection coefficient.

The developed model was applied to a stratified structure consisting of three planner layers backed by an infinite half-space (layer four) as described below.

Layer 1: skin, $Z = 1.69 \times 10^6\,\mathrm{kg\,m^{-2}\,s^{-1}}$, thickness: 2.5 mm.

Layer 2: fasciae and fat, $Z = 1.38 \times 10^6\,\mathrm{kg\,m^{-2}\,s^{-1}}$, thickness: 1.0 mm.

Layer 3: this layer is a fat layer with a thickness of 0.2 mm except for a small circular area (1 $\mathrm{cm^2}$), where the fat is replaced by callus (with properties like bone). The callus thickness is estimated to be 0.2 mm at the beginning and decays to 0.0 mm when the healing is complete. The thickness of the callus depends on the healing stage. Consequently, monitoring this callus layer reveals information about the healing stage.

Layer 4: bone, $Z = 7.8 \times 10^6\,\mathrm{kg\,m^{-2}\,s^{-1}}$, thickness: infinite half-space.

A frequency of 10 MHz was used throughout the simulation. The reflection coefficient was calculated at the sensor due to the interaction of the ultrasound signal with the layers described above. Figure 4 shows the reflection coefficient calculated as a function of scanning position over a structure containing callus of thickness 0.01 mm. The callus center is located at a scanning distance of 8 mm. The change in the reflection coefficient begins to occur as the transducer (footprint = 1 $\mathrm{cm^2}$) partially begins to overlap with the callus region. The variation ends as the callus is totally out of the footprint of the sensor. The intensity of the ultrasound wave is assumed to be uniform within the footprint.

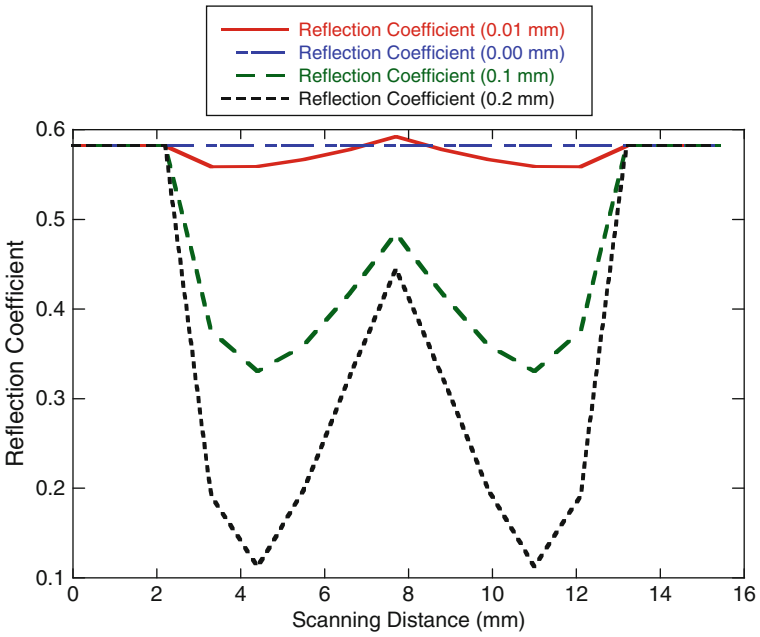

Fig. 5 Reflection coefficient vs. scanning position over a structure with varying callus thickness

To consider the effect of foot print of the sensor, a mixing model based on the portion of the area seen from fat and callus is used to calculate the effective acoustic impedance of the mixture. Consequently, the acoustic impedance of the layer containing callus varies between that of fat to that of callus depending on what is seen by the sensor. Figure 5 shows similar scans to the one shown in Fig. 4 for varying thicknesses of the callus layer. In the situation when callus is decaying from a certain height to zero, simulation results show that the value of the reflection coefficient varies. This is most apparent at the center of the callus region. Additionally, variation of the reflection coefficient for a certain callus thickness indicates that callus dynamics and healing stages may be captured.

4 Pulsed Mode Testing of Healing Bone

In pulsed mode testing, it is assumed that a pulsed ultrasound transducer is radiating into an N-layer structure, terminated by an infinite half-space. The main difference between continuous and pulsed modes of testing is that in continuous mode one reflection at the transducer side may be obtained. This reflection is influenced by all the parameters of the system, i.e., one cannot see the boundaries. On the other hand, in pulsed mode testing, all boundaries are seen and clear reflections at all interfaces may be observed.

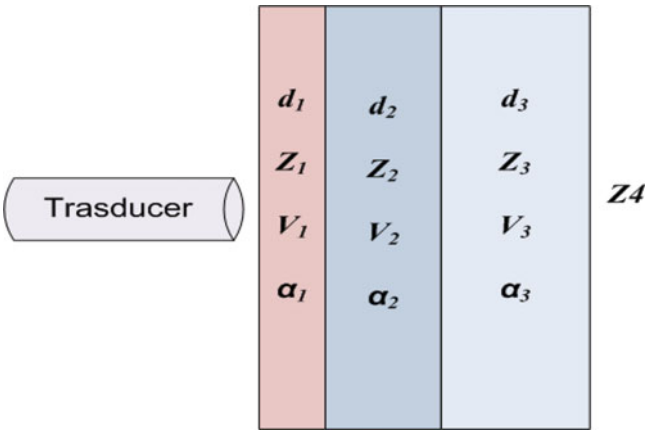

Fig. 6 A three-layer structure terminated by an infinite half-space of a material. Each layer i has thickness d_i, acoustic impedance Z_i, propagation velocity V_i, and attenuation factor α_i

To explain the use of pulsed mode ultrasound in bone healing testing, a similar structure to that used in the previous section is considered. Figure 6 depicts a three-layer structure terminated by an infinite half-space of any material with acoustic impedance Z_4. Each layer is characterized by four parameters:

- Thickness of the ith layer in (m), d_i
- Acoustic impedance of the ith layer in ($\mathrm{kg\,m^{-2}\,s^{-1}}$), Z_i
- Velocity of the wave in the ith layer in ($\mathrm{ms^{-1}}$), V_i
- Attenuation factor of the ith layer in ($\mathrm{dB\,m^{-1}}$), α_i

The ratio of the reflected pressure wave to that of the incident wave is the reflection coefficient (Γ_i) and it is expressed as in (1):

$$\Gamma_i = \frac{Z_{i+1} - Z_i}{Z_{i+1} + Z_i}, \tag{12}$$

where Γ_i is the reflection coefficient from the interface between the i^{th} layer and the $(i+1)$th layer.

For pulsed mode ultrasound, it is assumed that the incident wave is a unit amplitude delta function at a time $t = 0$. In addition to the main first reflections at each interface, there exist additional multiple reflections within each layer. The magnitudes and times of arrival for each reflection can be determined. Although multiple reflections will continue to take place, usually the first two sets of multiple reflections are of significant amplitude relative to the first reflection. Therefore, in this chapter, the first two sets of multiple reflections will be considered. In practice, a dying oscillatory input pulse with finite duration should be considered. Hence, the output is obtained by convolving the impulse response with the oscillatory input pulse $f(t)$.

It can be shown that the main and multiple reflections resulting from the structure described earlier show a recursive pattern [23]. For an N-layer structure, the main reflection in each layer $P_1(i,t)$ and the multiple reflections $P_2(i,t)$ are:

$$P_1(i,t) = \left[\Gamma_i \prod_{k=1}^{k=i-1}\left(1-\Gamma_k^2\right)C_{1i}\right]\left[\delta\left(t-\sum_{j=1}^{i}\frac{2d_j}{V_j}\right)\otimes f(t)\right], \quad i=1\ldots N \tag{13}$$

$$P_2(i,t) = \sum_{m=2}^{\infty}\left[\Gamma_i^m\left(-\Gamma_{i-1}\right)^{m-1}C_{2im}\prod_{k=1}^{k=i-1}\left(1-\Gamma_k^2\right)\right] \times\left[\delta\left(t-\sum_{j=1}^{i}\frac{2d_j}{V_j}-\frac{2md_i}{V_i}\right)\otimes f(t)\right], \quad i=2\ldots N \tag{14}$$

where the attenuation coefficients are:

$$C_{1i} = 10^{-\sum_{j=1}^{j=i}2d_j\alpha_j/20} \quad \text{and} \quad C_{2im} = 10^{-\left(\sum_{j=1}^{j=i}2d_j\alpha_j+2md_i\alpha_i\right)/20}.$$

The model described above was used to simulate the ultrasound interaction with biological structure composed of skin, fat, callus, and infinite half-space of bone as shown in Fig. 6. The structure parameters are as follows:

- Layer 1: delay line of water, $Z = 1.5\times10^6\,\mathrm{kg\,m^{-2}\,s^{-1}}$, thickness $(d_1) = 6\,\mathrm{mm}$, velocity $(V_1) = 1483\,\mathrm{ms^{-1}}$, and attenuation factor $(\alpha_1) = 0.002\,\mathrm{dB\,cm^{-1}\,MHz^{-1}}$.
- Layer 2: skin, $Z = 1.69\times10^6\,\mathrm{kg\,m^{-2}\,s^{-1}}$, $d_2 = 2.5\,\mathrm{mm}$, $V_2 = 1537\,\mathrm{ms^{-1}}$, and $\alpha_2 = 3.5\,\mathrm{dB\,cm^{-1}\,MHz^{-1}}$.
- Layer 3: this layer is a fat layer with a thickness (d_3) of 10 mm except for a small circular area $(1\,\mathrm{cm^2})$ where the fat is replaced by callus. The fat layer has $Z = 1.38\times10^6\,\mathrm{kg\,m^{-2}\,s^{-1}}$, velocity $= 1450\,\mathrm{ms^{-1}}$, and attenuation $= 1.8\,\mathrm{dB\,cm^{-1}\,MHz^{-1}}$. The callus layer has a thickness of 10 mm with properties similar to fat at the early stages of callus formation. The callus acoustic properties change from those of soft callus (similar to fat) to hard callus (similar to bone). In other words, its acoustic impedance, velocity of the wave, and attenuation will increase with time (healing). After the callus hardens, it will begin to decay from 10 mm to 0 mm indicating complete healing. Both the callus thickness and its properties depend on the healing stage. Consequently, monitoring these quantities will reveal information about the healing stage.
- Layer 4: bone, $Z = 7.8\times10^6\,\mathrm{kg\,m^{-2}\,s^{-1}}$, d_4 is an infinite half-space (usually 3 mm thick), $V_4 = 3500\,\mathrm{ms^{-1}}$, and $\alpha_4 = 13\,\mathrm{dB\,cm^{-1}\,MHz^{-1}}$.

Figure 7 shows the reflection coefficient as a function of callus acoustic impedance variation for different callus thicknesses at 3 MHz [23]. The simulation results show the variations in the magnitude of the reflection coefficient as a function of acoustic impedance for different healing stages. The curves show a complete picture of the healing process of the bone starting with soft callus ending with hard callus and the

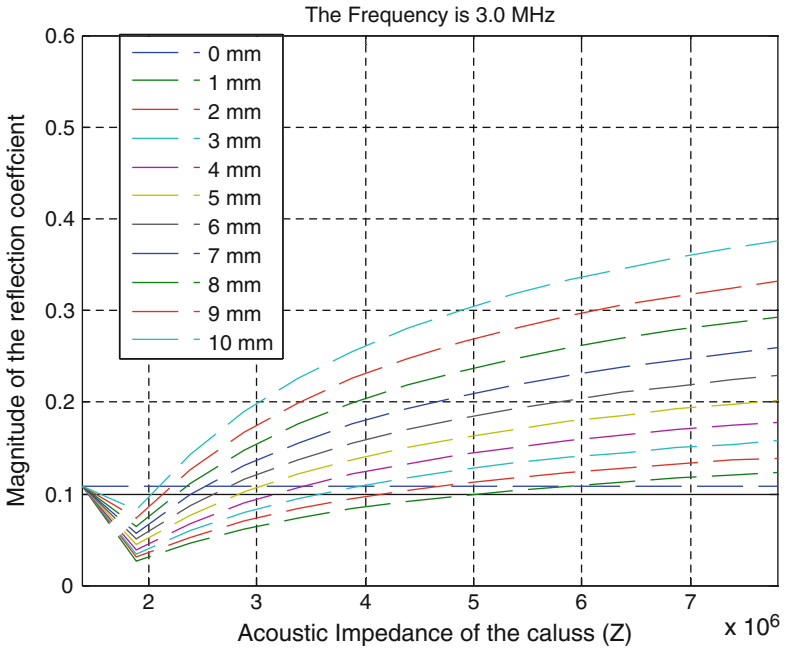

Fig. 7 Magnitude of the reflection coefficient as a function of the acoustic impedance of the callus layer at 3 MHz [23]

decay of callus thickness. The criterion to compare the performance of the different transducers is the difference in the magnitude of the reflection coefficient, which reflects the sensitivity of the transducer to different stages of bone healing.

5 Conclusion

The use of ultrasound inspection of healing bone provides a noninvasive means of quantifying the level of bone healing after fracture. This can be achieved by the assessment or measurement of acoustic impedance of the multilayer biological system composed primarily of skin, fasciae, callus, and bone during the various stages of bone healing.

In this chapter, an experimental method for the measurement of acoustic impedance of healing bone using pulsed ultrasound was described. The method enables the user to obtain the acoustic impedance of an unknown material from the first three reflections without the need for a priori information of attenuation coefficients or thickness.

Two mathematical models which describe the interactions of ultrasound waves with a multilayered biological structure were presented. The first model describes

the utilization of continuous mode ultrasound waves in the measurement of the reflection coefficient which leads to quantification of bone healing stage. In the second model, pulsed mode ultrasound waves are utilized to estimate the acoustic impedance and thickness of the callus layer. Consequently, pulsed mode ultrasound may also be used for the assessment of bone healing level.

Acknowledgments This project was supported by Emirates Foundation Grant Reference Number #2009/028 entitled Quantitative Assessment of Bone Fracture Healing Using Pulsed Mode Ultrasound.

References

1. Nordin M, Frankel VN (2001) Basic biomechanics of the musculoskeletal System. Lippincott Williams & Wilkins, Baltimore
2. Webb J, Herling G, Gardner T, Kenwright J, Simpson AH (1996) Manual assessment of fracture stiffness. Injury 27(5):319–320
3. Blokhuis T, De Bruine J, Bramer J, Den Boer F, Bakker F, Patka P, Haarman H, Manoliu R (2001) The reliability of pain radiography in experimental fracture healing. Skeletal Radiol 30:151–156
4. Hijazy A, Al-Smoudi H, Swedan M, Al-Nashash H, Qaddoumi N, Ramesh KG (2006) Quantitative monitoring of bone healing process using ultrasound. J Franklin Inst 343:495–500
5. Augat P, Merk J, Genant H, Claes L (1997) Quantitative assessment of experimental fracture repair by peripheral computed tomography. Calcif Tissue Int 60:194–199
6. Den Boer F, Bramer J, ka P, Bakker F, Barentsen R, Felizer AJ, De Lange E, Haarman H (1998) Quantification of fracture healing with three-dimensional computed tomography. Arch Orthop Trauma Surg 117:345–350
7. Protopappas V, Baga D, Fotiadis D, Likas A, Papachristos A, Malizos K (2005) An ultrasound wearable system for the monitoring and acceleration of fracture healing in long bones. IEEE Trans Biomed Eng 52(9):1597–1608
8. Webb A (2003) Introduction to biomedical imaging. IEEE and Wiley
9. Collier R, Donarski R (1987) On-invasive method of measuring the resonant frequency of a human tibia in vivo. J Biomed Eng 9:321–331
10. Collier R, Donarski R, Worley A, Lay A (1993) The use of externally applied mechanical vibrations to assess both fractures and hip prosthesis. In: Turner Smith AR (ed) Micromovement in orthopaedics. Oxford University Press, Oxford, pp 151–163
11. Cunningham J, Kenwright J, Kershaw CJ (1990) Biomechanical measurement of fracture healing. J Med Eng Technol 14(3):75–79
12. Lowet G, Dayuan X, Van Der Perre G (1996) Study of the vibrational behavior of a healing tibia using finite element modeling. J Biomech 29(8):1003–1010
13. Malizos K, Protopappas V, Fotiadis D (2006) Guided ultrasound wave propagation in intact and healing long bones. Ultrasound Med Biol 32(5):693–708
14. Heckman J, Ryaby J, McCabe J, Frey JJ, Kilcoyne R (1994) Acceleration of tibial fracture healing by non-invasive, low intensity pulsed ultrasound. J Bone Joint Surg 79(7):26–34
15. Kristiansen T, Ryaby J, McCabe J, Frey JJ, Roe L (1997) Accelerated healing of distal fractures with the use of specific low intensity ultrasound. A multicenter, prospective, randomized, double blind, placebo-controlled study. J Bone Joint Surg 79(7):961–973
16. Hantes M, Mavrodontidis A, Zalavras C, Karantanas A, Karachalios t, Malizos K (2004) Low intensity transosseous ultrasound accelerates osteotomy in a sheep fracture model. J Bone Joint Surg 86(10):2275–2282

17. Lowet G, Van der Perre G (1996) Ultrasound velocity measurement in long bone: measurement method and simulation of ultrasound wave propagation. J Biomech 29(10):1255–1262
18. Njeh C, Kearton J, Hans D, Boivin C (1998) The use of quantitative ultrasound to monitor fracture healing: a feasibility study using phantoms. Med Eng Phys 20:781–786
19. Bin Sediq A, Al-Nashash H, Qaddoumi N (2006) Monitoring of bone fracture healing using pulsed mode ultrasound. Transactions of the Cairo international biomedical engineering conference, pp 1–5, Cairo
20. El-Imam F, Kittaneh S, Shinawy A, Al-Nashash H, Qaddoumi N (2011) Novel measurement technique of acoustic impedance of healing bone using pulsed ultrasound. In: Proceedings of the International Conference on Advances in Biomedical Engineering, Lebanon
21. Wells PNT (1977) Biomedical ultrasonics. Academic, New York
22. Shull PJ (2002) Non-destructive evaluation theory, techniques, and application, 1st edn. Marcel Dekker, New York
23. Qaddoumi N, Al-Nashash H, Bin Sediq A, Al-Shamsi H, Al-Mehrizi M, Khalaf K (2011) Towards an assessment of bone fracture healing using pulsed mode ultrasound. Technology and Health Care 19:261–269

Image-Guided Cryoablation of the Prostate

Sutchin R. Patel, Gyan Pareek, and Jasjit S. Suri

Abstract Minimally invasive treatments continue to evolve as an alternative means for the treatment of prostatic tumors. Of the mainstream ablative procedures reported in the literature, the cryotherapy data appear to be the most durable. The technological innovations in the use of urethral warming devices and real-time transrectal ultrasound sonography have lead to effective tumor ablation with a reduction in the morbidity of the procedure. Although limited long-term survival data utilizing cryotherapy are available, recent series have provided compelling results, promoting interest in prostatic cryoablation. This chapter assesses the importance of imaging technology in the current status of cryotherapy for prostate tumors.

1 Introduction

During the last decade, there has been a resurgence of cryotherapy in the field of urology as a treatment modality for prostate cancer. Much of the interest has been promoted by the advancement of radiographic technology and surgical instrumentation, along with the movement toward providing minimally invasive therapeutic options for patients.

Cryotherapy destroys cells by consecutive rapid freeze and thaw cycles, leading to progressive cell death at nadir temperatures of -19.4°C or less [1]. A sharp

S.R. Patel • G. Pareek (✉)
Division of Urology, Section of Minimally Invasive Urologic Surgery, The Warren Alpert Medical School of Brown University, Rhode Island Hospital, 2 Dudley Street, Suite 174, Providence, RI 02905, USA
e-mail: sutchin_patel@yahoo.com; gyan_pareek@brown.edu

J.S. Suri
Biomedical Technologies, Inc., Denver, CO, USA

Idaho State University (Affiliated), Pocatello, ID, USA
e-mail: jsuri@comcast.net

J.M. Sanches et al. (eds.), *Ultrasound Imaging: Advances and Applications*,
DOI 10.1007/978-1-4614-1180-2_13, © Springer Science+Business Media, LLC 2012

decrease in viability is clear as the majority of cells die as temperatures approach −30°C. Though cell death occurs between −20°C and −30°C, complete cell destruction is incomplete [2, 3]. A double freeze–thaw cycle to −40°C has been shown to be fully lethal [2, 4]. Standard cryosurgical technique used today requires that the tissue be frozen rapidly, thawed slowly and then exposed to a second freeze–thaw cycle. Each phase of the freeze–thaw cycle, including the cooling rate, nadir temperature, and duration of freezing and thawing rate, leads to cell injury and contributes to cellular destruction. The rapid freezing leads to intracellular ice crystal formation which leads to cell membrane disruption via mechanical damage as well as metabolic disturbances related to cellular solutes. The vascular stasis soon after thawing also contributes to cellular injury as the loss of blood supply to the tissue decreases the probability of cell survival. The histologic characteristics of the central portion of the ablated tissue are consistent with coagulative necrosis surrounded by a thin margin at the periphery of the lesion where temperatures were 0°C to −20°C where cell destruction may be incomplete. A well-demarcated transition between frozen and unfrozen tissue has been noted, which correlates well with the ultrasonography findings at the time of ablation [2].

The therapeutic use of cryoablation dates back to mid-nineteenth century England and James Arnott, who used crushed ice and salt solutions to attain temperatures of −20°C [5]. The practical ability to clinically apply deeply cryogenic temperatures was realized when liquefied air gases became available just before 1900. Early approaches were limited to superficial application of the cryogen, usually liquid nitrogen, by either spraying or pouring it over the lesion. These techniques limited the clinical applications of cryotherapy [6]. In 1961, Cooper and Lee successfully built the first apparatus for cryotherapy. Their liquid nitrogen cryogenic probe would pave the way for modern cryoablation [7]. Cryoablation of the prostate was initially introduced in the 1960s by Gonder and associates as a definitive treatment of prostate cancer [8]. They used a single, blunt end, transurethral cryoprobe and monitored the freezing process by digital palpation from the rectum. Flocks et al. in a small series of 11 patients with prostatic extracapsular extension used an open perineal surgical approach and directly applied a flat cryoprobe onto the visible prostate gland in order to preserve the sphincter and reduce the morbidity [9]. Megalli et al. in 1974 were the first to report a transperineal percutaneous approach using a single 18Fr sharp-tipped liquid nitrogen cryoprobe [10]. Their cryoprobe was introduced through skin incisions on either side of the midline in the perineum and was guided by digital palpation. Various modifications of both the open and the percutaneous transperineal techniques were used during this time with guidance either under direct visual or tactile control. Reuter also described the use of the rigid cystoscope as an adjunct to the digital palpation of the prostate gland to directly monitor the bladder and ureteral orifices [11]. However, despite advances in the development of cryoprobes and the ability to effectively ablate tumor tissue, the technical difficulty in precisely placing the cryoprobes and in monitoring the freezing process leads to the abandonment of the procedure until the 1980s.

2 Imaging: Ultrasonography

The resurgence of prostatic cryotherapy in the 1980s was mainly due to the use of real-time transrectal ultrasonography (TRUS) for monitoring and the innovation of urethral warming devices. Initial cryotherapy results prior to this time period were discouraging, with complications including ureteral obstruction and rectourethral fistulas [12–15]. Currently, third-generation machines are being evaluated with the hope of avoiding the devastating complications of first and second-generation machines. Strategies employed by third-generation machines include the use of argon gas for cooling and helium for thawing temperature probes both inside and outside of the prostate and a standardized urethral warming catheter, thereby improving on the limitations of first and second-generation machines [16, 17].

The use of real-time ultrasound for placement of the cryoprobes and continuous monitoring of the freezing process was a significant advance in cryotherapy. The prostate could now be aggressively frozen to encompass the entire gland while protecting the rectum from injury. Since the 1980s, ultrasonography has advanced but despite significant improvements in imaging quality and the introduction of duplex Doppler color it still has limitations.

Ice has an acoustic impedance much different from any tissue, reflecting up to 99% of the incident acoustic signal and thereby creating a very well seen surface. Unfortunately, the strong reflective surface serves as an impenetrable acoustic wall so that everything behind the leading edge of the ice ball is acoustically invisible [18]. This is significant in that it can become particularly difficult to visually monitor the long segment of the rectal wall at risk near the end of the procedure.

Although curvilinear TRUS probes have become popular for TRUS-guided prostate biopsy, they do not permit adequate visualization during the freezing process. The use of a biplane ultrasound probe is valuable with the two crystals providing a cross-sectional and longitudinal image of the prostate interchangeably during the procedure. This further allows adequate monitoring of both cryoprobe placement and the approach of the ice toward the rectum [19]. Color Doppler may also be helpful to monitor tissue vascularity and thus viability as freezing approaches the rectum. It is important to realize that despite advances in ultrasonography, the imaging we use provides us with no information about the temperature distribution of the ice nor does it illustrate the extent of freezing along the borders of the prostate. Because reliable destruction of cancer cells by freezing is dependent on the tissue reaching critical temperatures, the development and use of thermocouples were critical for adequate cryoablation and also to avoid damage to the rectum, external sphincter, and neurovascular bundles. Thermocouple probes should be placed equidistant between cryoprobes at the warmest location so as to not give misleading results. Another maneuver that can also be employed to limit damage to the rectum is the injection of saline into Denonvillier's fascia to increase the space between the rectum and the prostate. Onik et al. have used the saline injection

technique in more than 400 patients and have shown a decrease in the risk of rectal freezing and the complication of urethrorectal fistula without any increase in morbidity [20].

3 Imaging: Advances

Given the limitations of ultrasonography and the continuing advances in technology, a number of different imaging modalities and adjunctive tools are being tested to improve the monitoring and accuracy of cryoablative procedures. Building on the success of two-dimensional real-time ultrasonography, three-dimensional ultrasonography has been used to allow the surgeon to better track the passage of needles as well as monitor the freezing process. Chalasani et al. described a three-dimensional ultrasonography software (Robarts Research Institute) loaded onto a computer that can be connected to a biplanar transrectal probe to aid in placement of cryoprobes [21]. The three-dimensional view may be especially helpful in the tracking of oblique trajectories for cryoprobes. Currently, the Artemis system (Eigen LLC, Grass Valley, CA) has been used to provide a full three-dimensional image of the prostate during real-time ultrasonography with an end-firing probe to aid in the planning, calculation of accurate prostatic volumes, and ultimately increase the precision of prostate biopsies [22]. Transperineal three-dimensional mapping prostate biopsies have been shown to provide better staging information compared to standard two-dimensional TRUS biopsy [23]. Thus, further development of such technologies to allow three-dimensional visualization of the prostate may improve the precision by which we can perform cryoablation of prostate cancer.

Measurement of variations in the modulus of elasticity may provide important information during cryoablation. Because TRUS cannot give us information with regard to tissue temperature, we use thermocouples to help monitor the freezing process. Recent breakthroughs in imaging have lead to the development of novel techniques in “elasticity imaging” known as vibro-acoutsography. Vibro-acoustography produces a map of the mechanical response of an object to a dynamic force applied to the object. The technique uses a radiation force of ultrasound onto the object and the vibration of the object produces a sound field in the medium which is received by an audio hydrophone placed near the object. Mitri et al. were able to show that vibro-acoutsography could be used to produce clear images of a frozen prostate at different temperature stages [24]. Though this imaging modality has been used to delineate breast cancer lesions, evaluation of vibro-acoustography for prostate cryotherapy in vivo still needs to be examined.

Magnetic resonance imaging has been shown to be a valuable imaging modality in the visualization of prostate anatomy and in focal lesions [25]. Though the feasibility of MRI-guided percutaneous renal cryoablation has been evaluated in the canine model, MRI is generally not a real-time modality and currently the magnetic environment increases the complexity of interventional procedures

[26]. However, the development of fusion imaging modalities, where previous magnetic resonance imaging or MR spectroscopy (which can provide the spatial distribution of metabolites specific for prostate cancer) can be fused to real-time ultrasonography, may exploit the advantages of each imaging modality [27].

4 Indications

Primary cryoablation of the prostate is a minimally invasive option for men who either do not want or are not good candidates for radical prostatectomy due to comorbidities. Patients who may not be good candidates for external beam radiation therapy due to previous pelvic radiation, rectal surgery, or inflammatory bowel disease may be considered for prostate cryoablation [28]. Salvage cryotherapy can be a viable treatment option for patients in whom radiation therapy (external beam or interstitial seed implantation) has failed [29, 30]. Patients with biopsy proven persistent organ confined prostate cancer, a PSA less than 10 mg/ml, and a negative metastatic evaluation may be the most appropriate candidates for salvage cryotherapy [28, 31]. Contraindications include advanced local disease, incontinence, and inflammatory bowel disease. The latter is believed to contribute to a higher incidence of anorectal fistula formation [12–15]. Patients with a prior history of transurethral resection of the prostate may not be good candidates for cryotherapy given that they are at increased risk for urethral necrosis due to failure of the urethral warming device to coapt to the mucosa [28]. Cryoablation of the prostate is best performed in glands less than 40 g. Investigators have reported protocols assigning patients to neoadjuvant androgen deprivation to achieve smaller gland sizes prior to instituting treatment [17,32]. Prostate specific antigen (PSA) has also been utilized as a parameter to determine cryotherapy eligibility [17]. Zisman et al. recommended that PSA values greater than 15 ng/ml undergo pelvic lymph node dissection before undergoing cryotherapy [17]. It should also be noted that there is no “dose threshold” for cryoablation of the prostate, so additional freeze–thaw cycles within a single procedure or a repeat treatment at a later session in the event of local recurrence are possible.

5 Technique

Technological advances have led to the development of cryoprobes of various diameters and lengths in order to produce the desired cryolesion based on pre-treatment planning. The cryoprobes used today use an argon gas-based system predicated on the Joule–Thompson effect (accuprobe, Endocare, Irvine, CA, USA) (Fig. 1). The Joule–Thompson effect characterizes gas at high pressures and predicts that gas changes temperature as it expands through a narrow port into a lower pressure zone. These systems allow faster freezing rates which improve the reliability of cancer

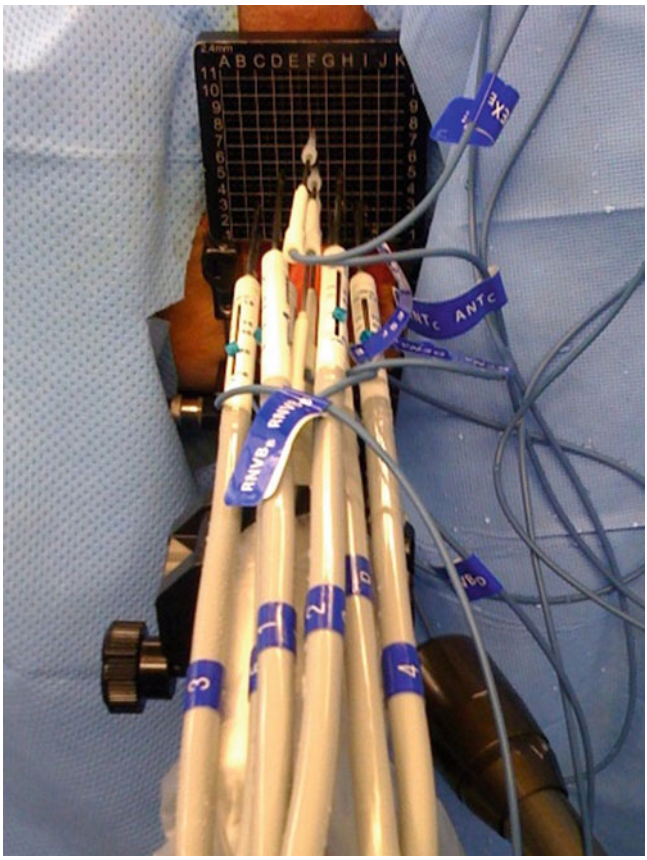

Fig. 1 Set-up of cryoprobes for cryoablation of the prostate

destruction. Argon gas as it expands results in rapid cooling via the Joule–Thompson effect. Some gases such as helium warm up rather than cool when expanded. Thus, argon gas is used for the rapid freezing in cryoprobes and helium gas can be used to help thaw the cryoprobes. The argon gas-based systems have replaced the first and second-generation liquid nitrogen systems because: they reach temperatures equivalent to liquid nitrogen, argon is easily stored without evaporation and is ready for immediate use, the cooling rate for argon gas is much quicker than liquid nitrogen, and the freezing process can be rapidly started and stopped [19, 33]. Cryoprobes are available in various diameters (2.4, 3.0, and 5.0 mm). The number and size of probes used in a case vary depending on the size and site of the tumor. An increase in the total number of cryoprobes to eight has resulted in more uniform freezing temperatures throughout the gland.

Spinal or general anesthesia may be used and the patient is positioned in the dorsal lithotomy position. TRUS is used to delineate prostatic anatomy and the margins of treatment (Fig. 2a). The TRUS transducer is held in place within the

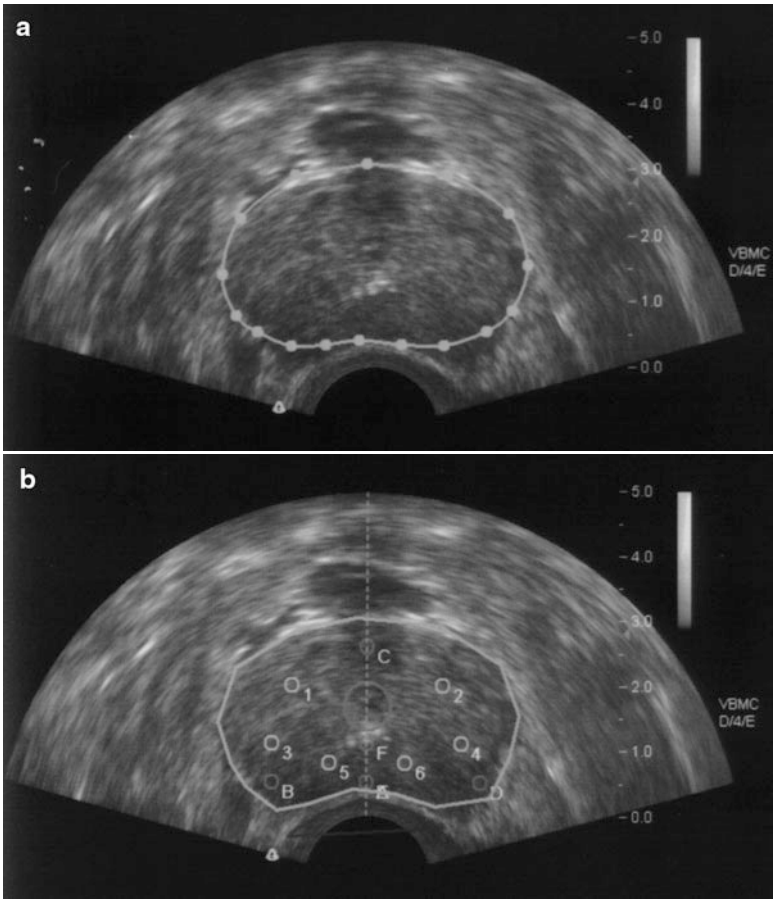

Fig. 2 (**a**) Transverse US image of prostate to aid in cryoprobe placement. (Six cryoprobes placed plus temperature probes placed for left and right seminal vesicles, Denonvillier's fascia.) (**b**) Mapping for probe placement

rectum by a probe holder similar to the gantries used for brachytherapy. Cyroprobes are placed percutaneously using an interstitial radiation therapy template aligned with the perineum. The number of probes placed depends on the prostatic anatomy and treatment zone defined by TRUS (Fig. 2b). The biplane TRUS probe allows the surgeon to switch back and forth between the longitudinal and axial views in order to guide placement of the cryoprobes (Fig. 3). After confirmation of urethral integrity as well as the bladder wall by cystoscopy, a urethral warming catheter is placed for continuous flow of warm fluid. Treatment is carried out by dual freeze–thaw cycle method described above with temperatures reaching −40°C. Treatment is monitored via real-time ultrasonography by viewing the generated ice ball (Fig. 4). Multiple temperature probes both inside and outside the prostate monitor temperature.

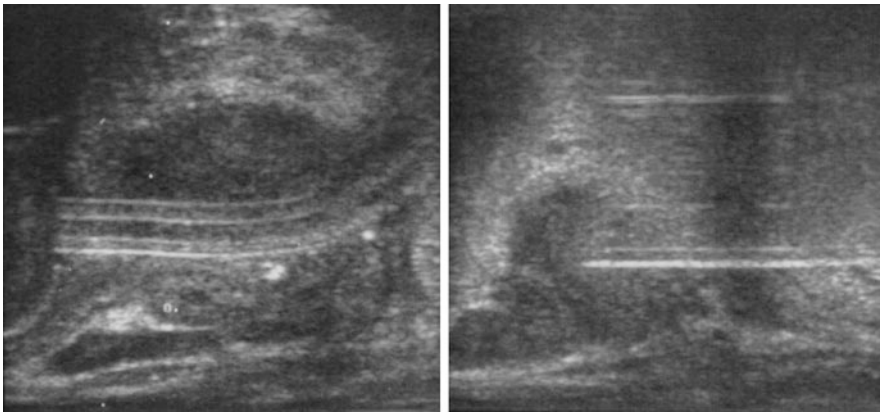

Fig. 3 Sagittal US image to assess depth of cryoprobe placement

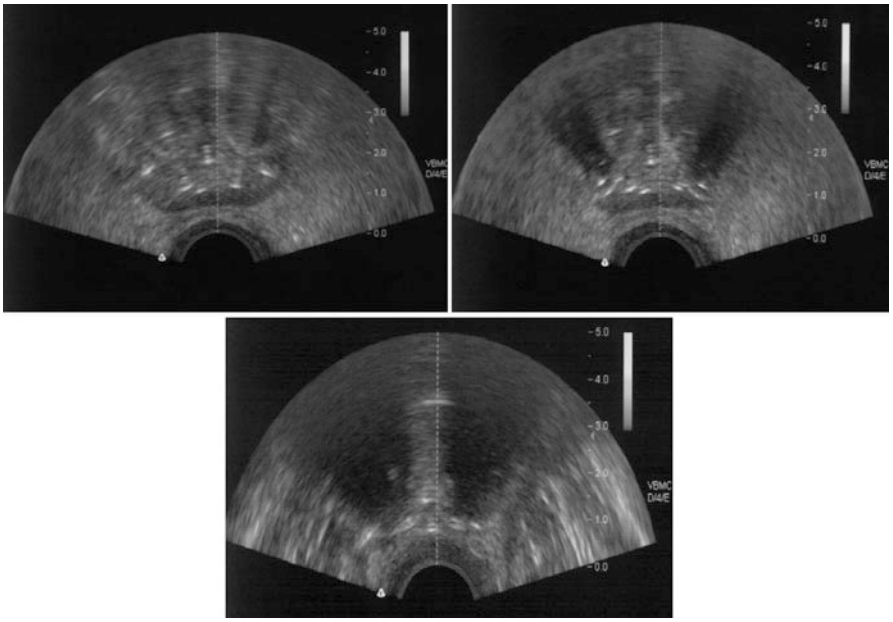

Fig. 4 Visualization of progression of ice ball formation with prominent hypoechoic crescents during cryoablation

6 Follow-Up

The initial post-operative follow-up is performed within the first 2 weeks for foley catheter removal, which is dependent on how much of the gland was treated. Biochemical-free survival as monitored by the measurement of serial PSAs

represents an effective means of following patients following prostatic cryotherapy. However, it should be noted that no universally accepted definition of biochemical failure exists for cryosurgery [33]. Because the urethra is preserved during cryoablation of the prostate, there is potential that PSA-producing tissue may still be present. Thus a completely undetectable PSA level is usually not seen in the long-term. Appropriate salvage therapies, including repeat cryotherapy, radiation, or hormonal therapy and salvage prostatectomy may be offered to patients with biochemical failure.

7 Results

A small number of series have reported 5–10-year follow-up data following primary cryotherapy of the prostate. Many of the original series used second-generation machines (Table 1). Aus et al. treated 54 patients with localized prostate cancer and reported a failure rate of 61% with a median follow-up of 58.5 months [34]. They defined failure as a positive biopsy or a PSA rise >1ng/ml. Another series reported by Donnelly et al. reported on 76 patients with a median follow-up of 50 months [35]. The patient population in their study was selective as they excluded patients with $PSA > 30\,\mathrm{ng/ml}$ and those who had received prior radiation therapy. The PSA recurrence free survival was 59% and 79% at 5 years with PSA recurrence cutoffs of $<0.3\,\mathrm{ng/ml}$ and $<1.0\,\mathrm{ng/ml}$, respectively. As observed in an elegant review by Gillett et al., no definition of incontinence was given in the series [36]. A large series by Bahn et al. reported data on 590 patients with a median follow-up of 5.4 years [37]. Unlike the studies mentioned above, this study utilized second-generation ($n = 350$) and third-generation ($n = 240$) machines. Their definition of PSA recurrence was a PSA rise above 0.5 ng/ml and 1.0 ng/ml. The PSA-recurrences based on these definitions were 62% and 76%, respectively.

Third-generation systems are currently being utilized and have shown decreased complication rates [38]. A report by De La Taille et al. with a follow-up of 9 months reported a PSA-recurrence rate of 30% [32]. Their patient population included

Table 1 Primary prostate cryoablation series ($n > 20$)

Year	Author	*N*	Mean follow-up (months)	Biochemical recurrence-free survival (%)
2002	Donnelly et al. [35], 2nd generation	76	50	59
2002	Aus et al. [34], 2nd generation	54	58.5	39
2002	Bahn et al. [37], 2nd generation	350	64	62
2002	Bahn et al. [37], 3rd generation	240	64	76
2000	De La Taille et al. [32], 3rd generation	35	9	70
2003	Han et al. [39], 3rd generation	122	12	75
2008	Cohen et al. [40], 3rd generation	370	145.8	56
2008	Jones et al. [41], 3rd generation	1,198	24.4	77

35 patients, 19 radiation failures, and 16 patients with newly diagnosed localized prostate cancer. Han et al. revealed results of a multi-institutional trial with a median 1 year follow-up of patients treated for localized disease utilizing a third-generation argon-based system [39]. The PSA-recurrence free survival was reported to be 75% at 1 year.

Recent long-term data by Cohen et al. reported biochemical disease-free survival rates of 80.6%, 74.2%, and 45.5% for low, moderate, and high-risk groups, respectively, at 10 years following primary cryoablation of the prostate (median follow-up 12.6 years) [40]. They defined biochemical recurrence using the Phoenix definition (nadir PSA + 2 ng/dl). The 10-year biopsy negative rate was 77.0%. Jones et al. reported the largest data set to date using the COLD (cryo on-line data) registry on patients undergoing whole gland prostate cryoablation. A total of 1,198 patients were found to have 5-year biochemical free survival rates of 77.1% and 72.9% based on the American Society for Therapeutic Radiology and Oncology (defined as three consecutive increases in PSA) definition and the Phoenix definition respectively [41]. A nadir PSA of 0.6 ng/ml or greater following prostate cryoablation has been shown to correlate with a 29.5% biochemical failure rate at 24 months, thus these patients require close follow-up [42]. Currently, short-term PSA results for cryotherapy appear promising but careful evaluation of long-term results will be needed as it becomes available. Studies designed to prospectively evaluate cryotherapy in comparison to standard treatment modalities for localized prostate cancer will also need to be explored in the future.

8 Complications

Short-term complications following cryoablation of the prostate include urinary retention and penile/scrotal swelling. Urinary retention usually persists for one to two weeks following the procedure and may be dependent on the amount of gland ablated. It is generally managed with a foley catheter or a suprapubic tube and anti-inflammatory agents. Penile and scrotal swelling is generally self-limiting and resolves after the first two weeks of the procedure [28].

Long-term complications include rectourethral fistula, urinary incontinence, erectile dysfunction and urethral sloughing. Fistula formation was the most significant complication that was seen in the early cryosurgery series due to inadequate monitoring during cryoablation and the absence of a urethral warming device. Though the incidence of fistula formation has decreased with advances in technology, patients treated with salvage cryotherapy after radiation therapy are at a higher risk for this complication (0–0.5% in patients undergoing primary cryotherapy versus 0–3.0% in patients undergoing salvage cryotherapy) [28].

During complete gland ablation, there is still a possibility of damage to the external sphincter despite some protection from the urethral warming device. The incidence of urinary incontinence (defined as wearing a pad) ranges from less than 1% to 8%. The use of thermocouple probes placed near the neurovascular bundles

allows monitoring of the temperature as the ice ball extends outside the prostate capsule. The incidence of erectile dysfunction reported in the literature ranges from 49% to 93% at 1 year [28,34,36]. The use of a urethral warming catheter has shown to decrease the risk of urethral sloughing. However, when there is not adequate coaptation of the urethral mucosa with the warming catheter, which can occur near in the sulcus near the verumontanum, urethral sloughing may occur. The reported rates of urethral sloughing in the literature with the use of a urethral warming device range from 0% to 15% [28]. The higher complications noted in older cryoablation series have been attributed to the use of the second-generation (liquid nitrogen based) systems, older ultrasound techniques, and the lack of usage of a urethral warming catheter. Cohen compared the complications between second-generation (liquid nitrogen based) and third-generation (argon based) cryoablation systems and showed a decrease in urinary incontinence and rectourethral fistulas with the newer systems [38].

9 Summary

The role of primary and salvage cryoablation for prostate cancer is becoming better defined. The technological advances with the third-generation systems, the use of a urethral warming devices, and real-time ultrasonographic and thermal monitoring have all contributed to improving our ability to perform cryoablation while minimizing morbidity. We expect further advances in technology and imaging to allow us to refine our surgical technique. The evaluation of long-term clinical results with regard to biochemical recurrence, post-treatment biopsy results, and comparison to conventional treatment modalities will further impact the role that cryoablation plays in the treatment of prostate cancer.

References

1. Chosy SG, Nakada SY, Lee FT et al (1998) Monitoring kidney cryosurgery: predictors of tissue necrosis in swine. J Urol 159:1370–1374
2. Baust JG, Gage AA, Robilotto AT, Baust JM (2009) The pathophysiology of thermoablation: optimizing cryoablation. Curr Opin Urol 19:127–132
3. Klossner PD, Baust JM, VanBuskirk RG, Gage AA, Baust JG (2008) Cryoablative response of prostate cancer cells is influenced by androgen receptor expression. BJU Int 101:1310–1316
4. Gage AA, Baust JG (1998) Mechanisms of tissue injury in cryosurgery. Cryobiology 37:171–186
5. Arnott J (1850) Practical illustrations of the remedial efficacy of a very low or anesthetic temperature I: in cancer. Lancet 2:257–259
6. Gage AA (1992) Cryosurgery in the treatment of cancer. Surg Gynecol Obstet 174:73–92
7. Cooper IS, Lee A (1961) Cryostatic congelation: a system for producing a limited controlled region of cooling or freezing of biologic tissues. J Nerv Ment Dis 133:259–263
8. Gonder MJ, Soanes WA, Shulman S (1966) Cryosurgical treatment of the prostate. Invest Urol 3:372–378

9. Flocks RH, Nelson CM, Boatman DL (1972) Perineal cryosurgery for prostatic carcinoma. J Urol 108:933–935
10. Megalli MR, Gursel EO, Veenema RJ (1974) Closed perineal cryosurgery in prostatic cancer. New probe and technique. Urology 4:220–222
11. Reuter HJ (1972) Endoscopic cryosurgery of prostate and bladder tumors. J Urol 107:389–393
12. Cox RL, Crawford ED (1995) Complications of cryosurgical ablation of the prostate to treat localized adenocarcinoma of the prostate. Urology 45:932–935
13. Porter MP, Ahaghotu CA, Loening SA et al (1997) Disease-free and overall survival after cryosurgical monotherapy for clinical stages B and C carcinoma of the prostate: a 20-year follow-up. J Urol 158:1466–1469
14. Pisters LL, Dinney CP, Pettaway CA et al : (1999) A feasibility study of cryotherapy followed by radical prostatectomy for locally advanced prostate cancer. J Urol 161:509–514
15. Shinohara K, Connolly JA, Presti JC et al (1996) Cryosurgical treatment of localized prostate cancer (stages T1 to T4): preliminary results. J Urol 156:115–120
16. Ghafar MA, Johnson CW, De La Taille A et al (2001) Salvage cryotherapy using an argon based system for locally recurrent prostate cancer after radiation therapy: the Columbia experience. J Urol 166:1333–1337
17. Zisman A, Pantuck AJ, Cohen JK et al (2001) Prostate cryoablation using direct transperineal placement of ultra thin probes through a 17-gauge brachytherapy template-technique and preliminary results. Urology 58:988–993
18. Onik G, Cobb C, Cohen J, Zabkar J, Porterfield B (1988) US characteristics of frozen prostate. Radiology 168:629–631
19. Saliken JC, Donnelly BJ, Rewcastle JC (2002) The evolution and state of modern technology for prostate cryosurgery. Urology 60(suppl 2A):26–33
20. Onik G (2007) Percutaneous image-guided prostate cancer treatment: cryoablation as a successful example. Tech Vasc Interv Radiol 10:149–158
21. Chalasani V, Gardi L, Martinez CH, Downey DB, Fenster A, Chin JL (2009) Contemporary technique of intraoperative 3-dimensional ultrasonography-guided transperineal prostate cryotherapy. Can Urol Assoc J 3:136–141
22. Shen F, Shinohara K, Kumar D, Khemka A, Simoneau AR, Werahera PN, Li L, Guo Y, Narayanan R, Wei L, Barqawi A, Crawford ED, Davatzikos C, Suri JS (2008) Three-dimensional sonography with needle tracking. J Ultrasound Med 27:895–905
23. Onik G, Barzell W (2008) Transperineal 3D mapping biopsy of the prostate: an essential tool in selecting patients for focal prostate cancer therapy. Urol Oncol 26:506–510
24. Mitri FG, Davis BJ, Alizad A, Greenleaf JF, Wilson TM, Mynderse LA, Fatemi M (2008) Prostate cryotherapy monitoring using vibroacoustography: preliminary results of an ex vivo study and technical feasibility. IEEE Trans Biomed Eng 55:2584–2592
25. Futterer JJ (2007) MR imaging in local staging of prosate cancer. Eur J Radiol 63:328–334
26. van den Bosch MA, Josan S, Bouley DM, Chen J, Gill H, Rieke V, Butts-Pauly K, Daniel BL (2008) MR imaging-guided percutaneous cryoablation of the prostate in an animal model: in vivo imaging of cryoablation-induced tissue necrosis with immediate histopathologic correlation. J Vasc Interv Radiol 20:252–258
27. Xu S, Kruecker J, Turkbey B, Glossop N, Singh AK, Choyke P, Pinto P, Wood BJ (2008) Real-time MRI-TRUS fusion for guidance of targeted prostate biopsy. Comput aided Surg 13:255–264
28. Babaian RJ, Donnelly B, Bahn D, Baust JG, Dineen M, Ellis D, Katz A, Pisters L, Rukstalis D, Shinohara K, Thrasher JB (2008) Best practice statement on cryosurgery for the treatment of localized prostate cancer. J Urol 180:1993–2004
29. Cohen JK, Miller RJ, Shuman BA et al (1995) Cryosurgical ablation of the prostate: patterns of failure and 2 year post treatment data as compared to external beam radiation therapy (abstract). J Urol 153(suppl):503A
30. Miller RJ Jr, Cohen JK, Shuman BA et al (1996) Percutaneous transperineal cryosurgery of the prostate as salvage therapy for post radiation recurrence of adenocarcinoma. Cancer 77:1510–1514

31. Pisters LL, Rewcastle JC, Donnelly BJ, Lugnani FM, Katz AE, Jones JS (2008) Salvage prostate cryoablation: initial results from the cryo on-line data registry. J Urol 180:559–564
32. De La Taille A, Benson MC, Bagiella E et al (2000) Cryoablation for clinically localized prostate cancer using an argon-based system: complication rates and biochemical recurrence. BJU Int 85:281–286
33. Theodorescu D (2004) Cancer cryotherapy: evolution and biology. Rev Urol 6(suppl 4): S9–S19
34. Aus G, Pileblad E, Hugosson J (2002) Cryosurgical ablation of the prostate: 5-year follow-up of a prospective study. Eur Urol 42:133–138
35. Donnelly BJ, Saliken JC, Ernst DS et al (2002) Prospective trial of cryosurgical ablation of the prostate: five-year results. Urology 60:645–649
36. Gillett MD, Gettman MT, Zincke H et al (2004) Tissue ablation technologies for localized prostate cancer. Mayo Clin Proc 79(12):1547–1555
37. Bahn DK, Lee F, Badalament R, Kumar A, Greski J, Chemick M (2002) Targeted cryoablation of the prostate: 7-year outcomes in the primary treatment of prostate cancer. Urology 60(suppl 1):3–11
38. Cohen JK (2004) Cryosurgery of the prostate: techniques and indications. Rev Urol 6:S20
39. Han KR, Cohen JK, Miller RJ et al (2003) Treatment of organ confined prostate cancer with third generation cryosurgery: preliminary multi-center experience. J Urol 170(4, pt 1): 1126–1130
40. Cohen JK, Miller RJ, Ahmed S, Lotz MJ, Baust J (2008) Ten-year biochemical disease control for patients with prostate cancer treated with cryosurgery as primary therapy. Urology 71:515–518
41. Jones SJ, Rewcastle JC, Donnelly BJ, Lugnani FM, Pisters LL, Katz AE (2008) Whole gland primary prostate cryoablation: initial results from the cryo on-line data registry. J Urol 180:554–558
42. Levy DA, Pisters LL, Jones JS (2009) Primary cryoablation nadir prostate specific antigen and biochemical failure. J Urol 182:931–937

Applications of Multiscale Overcomplete Wavelet-Based Representations in Intravascular Ultrasound (IVUS) Images

Amin Katouzian, Elsa Angelini, Bernhard Sturm, Elisa Konofagou, Stephane G. Carlier, and Andrew F. Laine

The importance of atherosclerotic disease in coronary artery has been a subject of study for many researchers in the past decade. In brief, the aim is to understand progression of such a disease, detect plaques at risks (vulnerable plaques), and treat them selectively to prevent mortality and immobility. Consequently, several imaging modalities have been developed and among them intravascular ultrasound (IVUS) has been of particular interest since it provides useful information about tissues microstructures and images with sufficient penetration as well as resolution.

A. Katouzian (✉)
Heffner Biomedical Imaging Lab, Biomedical Engineering Department, Columbia University, 1210 Amsterdam Ave., 373 Eng. Terrace, New York, NY 10027
e-mail: amin.katouzian@cs.tum.edu

E. Angelini
Associate Professor of Computer Science: Image & Signal Processing, Telecom ParisTech, 46 rue Barrault, 75013 Paris, France
e-mail: elsa.angelini@telecomparistech.fr

B. Sturm
Manager, Signal and Image Processing, Volcano Corporation, 2870 Kilgore Road, Rancho Cordova
e-mail: bsturm@volcanocorp.com

E. Konofagou
Associate Professor of Biomedical Engineering and Radiology, 351 Engineering Terrace, 1210 Amsterdam Avenue, 8904 New York, NY 10027
e-mail: ek2191@columbia.edu

S.G. Carlier
UZ Brussel, Department of Cardiology, Brussels, Belgium
e-mail: sgcarlier@hotmail.com

A.F. Laine
Vice-Chair, Professor of Biomedical Engineering and Radiology (Physics), 351 Engineering Terrace MC-8904, Biomedical Engineering Department, 1210 Amsterdam Avenue, Columbia University, MC-8904 New York, NY 10027
e-mail: laine@columbia.edu

J.M. Sanches et al. (eds.), *Ultrasound Imaging: Advances and Applications*,
DOI 10.1007/978-1-4614-1180-2_14,

In general, the ultimate goal is to provide interventional cardiologists with reliable clinical tools so they can identify vulnerable plaques, make decisions confidently, choose the most appropriate drugs or implant devices (i.e., stent), and stabilize them during catheterization procedures with minimal risk.

We describe applications of multiscale analysis in IVUS imaging and present two techniques based on two- (2D) and three-dimensional (3D) orthonormal wavelet basis functions that translate ultrasonic information of tissue microstructures as well as blood speckle into visual textures that can be used as features for classification. In this chapter, the main focus is to (1) differentiate between blood and non-blood signals/textures, which can ultimately lead to detection of the lumen border automatically and (2) characterize coronary artery atherosclerotic plaques using IVUS backscattered radiofrequency (RF) signals and/or grayscale images. The ultimate goal of such an effort is to provide interventional cardiologists with reliable clinical tools so they can detect vulnerable plaques, make decisions confidently, and choose the most appropriate drugs or implant devices (i.e., stent) during catheterization procedures with minimal risk. Next, we briefly review IVUS acquisition specifications as well as in vitro and in vivo data collection methodologies. In vivo data are used for detection of luminal borders and in vitro data are employed for automatic characterization of atherosclerotic plaques.

1 IVUS Data Acquisition, Image Formation, and Display

The IVUS RF signals or grayscale images are acquired in vivo during human or animal catheterization procedures by advancing an IVUS catheter on top of the guide wire from the femoral artery toward the site of coronary arterial occlusion (i.e., right coronary artery (RCA), left anterior descending (LAD), left circumflex (LCX)) via aorta. During image acquisition, the catheter is pulled back from the distal to proximal locations. In vitro IVUS data collection and histology preparation methodologies have been comprehensively studied and reported in [1].

Figure 1 displays schematic of an artery, its anatomical structures, catheter, and four distinct IVUS frames acquired with transducers with different center frequencies. During acquisition, IVUS backscattered RF signals that are continuous-time real-valued and band-limited signals, $x(t)$, are digitized $x(nT_s) = x[n] = x_n$ at periodic time intervals of $T_s = 1/f_s$ and stored in hard disk of a computer. The f_s is the sampling rate of digitizing board that may vary from one system to another. For example, in Boston Scientific (Fremont, CA) *Galaxy*™ or *iLab*® imaging systems, the acquisition boards sample IVUS signals at the rate of $f_s = 400\,\text{MHz}$ whereas the sampling rate for Volcano s5™ imaging system is $f_s = 200\,\text{MHz}$. Once the IVUS backscattered signals are digitized, a number of steps need to be taken in order to convert digitized signals into typical eyeball IVUS grayscale images. First, the envelope of signal in each acquisition line is computed by the corresponding analytical signal followed by decimation and interpolation in axial and lateral directions, respectively. The log compression is also used to enhance the image quality followed by quantization (e.g., eight-bit).

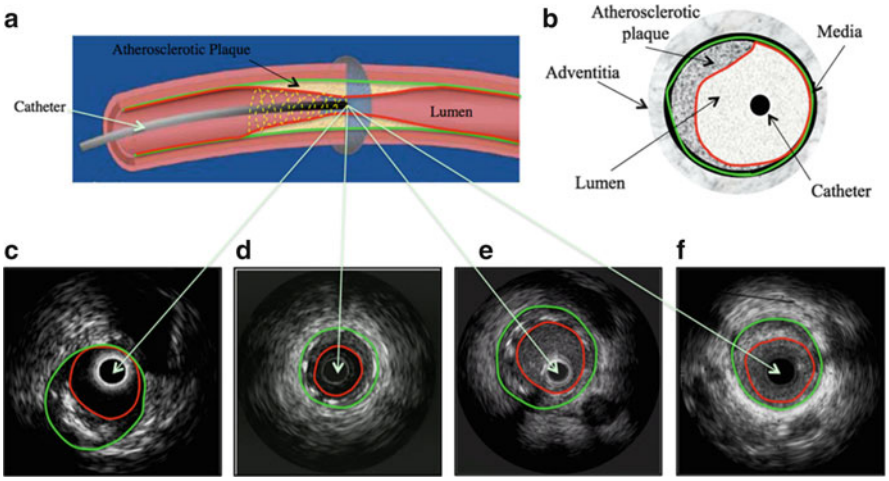

Fig. 1 Schematic of an artery, catheter, atherosclerotic plaque, and IVUS image cross-section (**a**) (reference: http://www.bmj.com), cross-sectional anatomy of arterial wall (**b**). Four distinct IVUS frames acquired with 20 MHz (**c**), 30 MHz (**d**), 40 MHz (**e**), and 45 MHz (**f**) transducers. *Red and green borders* represent vessel wall and lumen borders, respectively. The *yellow dashed line* depicts trajectory of transducer scan lines

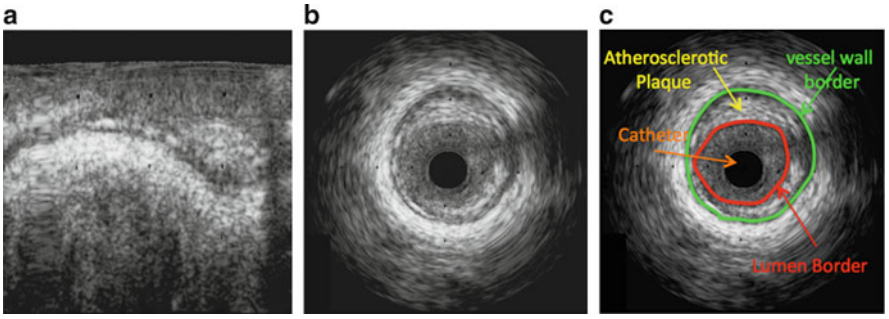

Fig. 2 Grayscale IVUS image in polar (**a**) and Cartesian (**b**) representations along with depicted catheter marker, plaque, vessel wall, and lumen borders (**c**)

As it is depicted in Fig. 1a, the transducer has a spiral trajectory (yellow dashed line) while taking cross-sectional grayscale images with rate of 30 frames per second. This is due to the fact that the transducer rotates and at the same time is pulled back with a speed of 0.5 mm/s that provides IVUS frames of 16.7 μm thickness. Therefore, the original domain of acquisition is polar (r, θ) and the resulting grayscale image should be transformed to (x, y) Cartesian coordinates to construct a typical IVUS frame. Figure 2 illustrates an IVUS grayscale image in polar and Cartesian representations along with depicted catheter marker, plaque, vessel wall, and lumen borders.

2 Automatic Detection of Lumen Borders

IVUS image segmentation has been a subject of interest for researchers due to the rapidly growing use of this imaging modality in catheterization procedures for the following two main reasons. First, one important parameter during angioplasty or stent implantation procedure is the ratio of lumen to artery cross-sectional area in stenotic regions. For instance, the interventional cardiologist uses these measurements to select the most appropriate type, length, and diameter of a stent. Secondly, vessel walls and lumen contours are required to be traced prior to tissue characterization and plaque RF signals extraction. Pullback IVUS data files contain thousands of cross-sectional images, hence, automatic extraction of vessel wall and lumen borders has been the topic of research efforts [2–14] and remains a challenging image processing problem.

Clinical application of automated segmentation methods has seen limited success due to the presence of guide wire, the presence of arc of calcified plaques, the motion of the catheter as well as heart, and appearance of sub-branches. Comparing IVUS ultrasound probes, Fig. 1, the lumen border is better depicted in images acquired with a 64-element phased-array 20 MHz transducer in comparison with those acquired with a single element mechanically rotating 45 MHz transducer. At higher center frequency, spatial resolution is improved, at the cost of more scattering from red blood cells inside the lumen that makes lumen border detection more challenging. In the rest of this section, we present an algorithm for automatic detection of lumen borders through expansion of IVUS sub-volumes onto directional sensitive wavelet like basis functions, called brushlet.

2.1 Motivations

The IVUS provides rich temporal as well as spatial resolution of plaque and arterial wall structures. Due to sufficient temporal resolution (16.7 μm), plaque structures appear to be relatively persistent within limited number of frames (e.g., eight frames) that is defined as *sub-volume*. The strong spatial coherence in the appearance of plaque, arterial wall, and surrounding fats within an IVUS sub-volume is better expressed and visualized in polar representations (the original domain of acquisition) of the image data. Hence, we design our framework upon multiscale analysis of textural features, which is the most compatible analysis to human and mammalian vision processing systems due to its conservation of energy in both spatial and frequency domains [15,16]. We will take advantage of the spatial-frequency-localized expansions such as brushlet analysis and their generalization to 3D to discern the textural patterns on constructed images from backscattered IVUS signals. One of the major advantages of expansion of IVUS sub-volumes onto orthogonal brushlet basis functions is that it is invariant to intensity so that the extracted brushlet coefficients do not depend on intensity but spatial frequency

content of IVUS signals. In addition, the brushlet is a well-localized complex-valued function in time and frequency domains that is suitable for analyzing the local frequency content of IVUS signals and offers an orthogonal transform of the Fourier coefficients, which are Hermitian-symmetric so the phase information might also be used in IVUS image filtering [17] and eventually detection of lumen border.

2.2 Methodology

We design our framework based on what typically interventional cardiologists do to visually delineate the lumen border. They usually go back and forth among consecutive frames to be able to visually locate the lumen contour on a single frame. By doing so, blood speckle and plaque embody visually incoherent and coherent spatial patterns, respectively, suggesting a 3D processing approach. A 3D brushlet analysis has been successfully employed to segregate static and dynamic textured structures within volumes of images in different applications [17–19].

2.2.1 Brushlet Analysis

We are particularly interested in orthogonal localized exponential basis functions since they enable us to characterize valuable information about the direction of textures at different scales, frequencies, and locations. Brushlet basis was first introduced in [20], as a family of steerable functions, that provide projected coefficients associated with particular brushstrokes (of specific sizes and orientations), analogous to a wavelet scaling function, yielding the characterization of textural features with distinct directions corresponding to specific brushlet functions. The functions divide the real axis into subintervals $[a_n, a_{n+1}]$ of length l_n, and define a brushlet analysis function, as follows:

$$u_{j,n}(x) = b_n(x - l_n/2)\mathrm{e}_{j,n}(x) + v(x-a_n)\mathrm{e}_{j,n}(2a_n - x) - v(x - a_{n+1})\mathrm{e}_{j,n}(2a_{n+1} - x). \tag{1}$$

The $b_n(x)$ and $v(x)$ are two localized window functions, providing the orthogonality property. The complex orthonormal basis function, $u_{j,n}(x)$, can be constructed using these two functions along with the complex exponential function $\mathrm{e}_{j,n}(x)$ that is defined as:

$$\mathrm{e}_{j,n}(x) = 1/\sqrt{l_n}\mathrm{e}^{-2i\pi j\frac{(x-a_n)}{l_n}}. \tag{2}$$

Figure 3 illustrates the windowing functions as well as the imaginary and real parts of $u_{j,n}(x)$. Given any one-dimensional signal f in $L^2(R)$, its Fourier transform $\hat{f}$ can be projected onto the brushlet basis as:

$$\hat{f} = \sum\sum \lambda_{j,n} u_{j,n}, \tag{3}$$

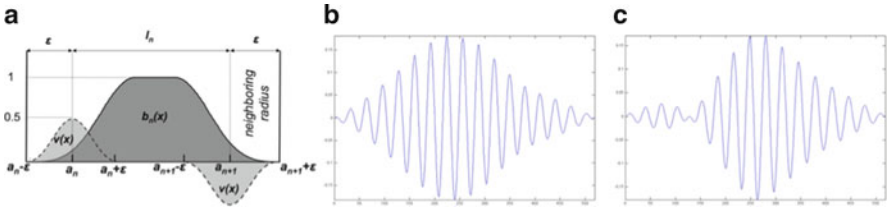

Fig. 3 Windowing functions $b(x)$ and $v(x)$ (**a**). The ε parameter controls the localization degree of brushlet function in time and frequency domains. Real part (**b**) and imaginary part (**c**) of analysis $u_{j,n}$ brushlet function with $l_n = 32$, $\varepsilon = 16$, and $j = 8$

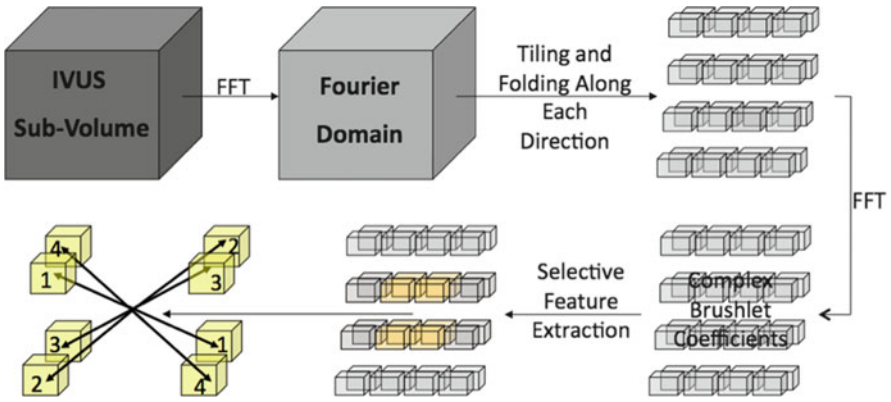

Fig. 4 Schematic expansion of IVUS sub-volumes onto brushlet basis, tiling of frequency domain ($4 \times 4 \times 2$), and selective feature extraction along eight directions corresponding to low-frequency components

where $\lambda_{j,n}$ are the brushlet coefficients. It has been shown that the projection of $\hat{f}$ onto the brushlet basis can be implemented in an efficient fashion using a folding technique and fast Fourier transform (FFT) [22]. The major advantage of brushlet basis over wavelet packets is the unique well-localized frequency response of each extracted coefficient and also arbitrary tiling of the time–frequency plane. The analysis can also be extended to n-D via separable tensor products. Although the primary application of brushlet analysis, presented in [20], was for image compression authors in [23] introduced an overcomplete representation of brushlet analysis and successfully developed a denoising/enhancing scheme to automatically extract left ventricular (LV) endocardial borders in real-time 3D (RT3D) (4D) echocardiograms. Figure 4 demonstrates the schematic of feature extraction procedure (computing brushlet coefficients) and selection of features along arbitrary numbers of directions.

By applying the inverse Fourier transform, we can then compute the decomposition of signal f onto the orthonormal synthesis function $w_{j,n}(x)$ defined as:

$$w_{j,n}(x) = \sqrt{l_n}\mathrm{e}^{(2i\pi a_n - l_n/2)} \times \left[(-1)^j \hat{b}_\sigma(l_n x - j) - 2i\sin(\pi l_n x)\hat{v}_\sigma(l_n x + j)\right] \quad (4)$$

with a scaling factor l_n, translation factor j, and steepness factor $\sigma = \varepsilon/l_n$ The parameter ε controls the degree of localization of brushlet analysis and synthesis functions in time and frequency domains, respectively.

As we can observe, the more cubes for tiling of frequency domain is used, the more orientations (angular resolution) are obtained. Perhaps, there is a tradeoff between spatial and frequency resolutions and the smaller cubes are employed, the better frequency resolution is achieved at the cost of less resolution in spatial domain. As we pointed previously, authors in [21] introduced the brushlet analysis for compression of richly textured images. They further presented an adaptive tiling approach to obtain the most concise and precise representation of an image in terms of oriented textures with all possible directions, frequencies, and locations. Contrary to image compression where the least numbers of coefficients are desirable to be transmitted, we try to preserve as much textural information (coefficients) as possible due to stringent behavior of blood and plaque signals. Thus, overcompleteness of the decomposition is advantageous in IVUS lumen border detection and segmentation. Such redundant representation of the original data in multiscale analysis makes the brushlet analysis shift invariant, which is a suitable for segmentation task.

2.2.2 Frequency Tiling and Overcomplete Representation

We partitioned the IVUS pullback data into temporal sub-volume of analysis without overlap and project them onto 3D brushlet basis. The decomposition of IVUS sub-volumes onto the brushlet orthonormal basis provides selectable textural features with different orientations in the Fourier (brushlet) domain, Fig. 4. Since, we deal with volumetric datasets, this can be reliably performed by tilling the Fourier domain into quadrants (cubes), each representing a specific size and orientation of a brushstroke, which is analogous to a wavelet scaling function. We used an overcomplete multiscale representation of the brushlet coefficients for two reasons. First, we avoided aliasing effect, and secondly, we intended to preserve as much textural information as possible in the transform domain due to the stringent behavior of blood and plaque signals that makes the lumen border detection very challenging. Next, we project 3D IVUS sub-volumes in polar coordinates with brushlet overcomplete expansion. Our hypothesis is that complex brushlet coefficients in transformed domain provide information regarding plaque and blood regions at different orientations.

2.2.3 IVUS Signal Modeling In Fourier Domain and Assumptions

Consider the measurements of an IVUS transducer during pullback. In this case, each acquisition line, f, contains information regarding tissues and flowing blood. We can distinguish the differences in the temporal patterns associated with each tissue and blood by differentiation between their distinct responses to IVUS signal. Hence, we take in the relative magnitudes and phases into the definition of the sources (i.e., blood and non-blood) and represent them in the transformed domain as:

$$\hat{f}_{j,n} = \sum_j \sum_n \alpha_{j,n} \mathrm{e}^{-i\omega\phi_{j,n}} \hat{S}, \tag{5}$$

where $\varphi_{j,n}$ and $\alpha_{j,n}$ are the resulting phase and amplitude of tissue response s to ultrasound signal. Using (5), we rewrite (3) and obtain:

$$\sum_j \sum_n \alpha_{j,n} \mathrm{e}^{-i\omega\phi_{j,n}} \hat{S} = \sum_j \sum_n \lambda_{j,n} u_{j,n}. \tag{6}$$

We call two functions s_1 and s_2 disjoint orthogonal if the frequency supports of their Fourier transforms, $\hat{s}_1$ and $\hat{s}_2$, are disjoint. In other words, the pointwise product: $\hat{s}_p \cdot \hat{s}_q = 0, \forall p \neq q, \text{and} \forall N$. This is a legitimate assumption in our IVUS application because each frequency bin is a function of only and only one tissue's response, which in our case would be blood or non-blood. Since brushlet basis are orthonormal, we can reorganize (6) in the following form:

$$\lambda_{j,n} = \sum_j \sum_n \left\langle \alpha_{j,n} \mathrm{e}^{-i\omega\phi_{j,n}} \hat{S}_{j,n}, u_{j,n} \right\rangle. \tag{7}$$

Looking at (7), we realize that the phase of brushlet functions results in orientation selectivity in transformed space when separable tensor product is used while image phases and amplitudes associated with tissue responses are proportionally preserved in brushlet coefficients. We further hypothesize that the magnitude and phase of brushlet coefficients provide informative features for coherent (non-blood) and incoherent (blood) patterns so we can estimate the lumen border in transformed domain via selection of specific clusters of phases–magnitudes combinations avoiding any thresholding and reconstruction. In the rest of this section, we present a classification framework to associate frequency-based clusters of brushlet coefficients with each tissue type (blood or non-blood).

2.2.4 Construction of 2.5-D Magnitude–Phase Histogram in Complex Brushlet Space

Once the IVUS sub-volumes of size (X, Y, and Z) are projected onto brushlet basis, we end up with sub-volumes of brushlet coefficients in the transformed domain. Corresponding to lower frequencies, we showed that the coefficients in the innermost cubes contain the most informative features regarding blood and

non-blood textures. They can be summed up to span 360° of spatially oriented information and construct the complete arterial wall and plaque in transformed domain [4, 17]. We follow the same procedure and each IVUS frame in brushlet space,$\hat{F}$, contains all spatial coefficients. Taking the union of summed coefficients $\hat{F} = \bigcup_{k=1}^{X\times Y} \alpha_k e^{-i\phi_k}$, we can write:

$$\hat{F}(r,\theta) = \alpha(r,\theta)e^{-i\phi(r,\theta)}, \quad r = 1,\ldots,X, \quad \theta = 1,\ldots,Y. \tag{8}$$

The magnitude and phase associated with each coefficient can be written as:

$$(\alpha(r,\theta),\phi(r,\theta)) = \left(\left|\hat{F}(r,\theta)\right|, \mathrm{R}\hat{F}(r,\theta)\right). \tag{9}$$

A 2.5-D histogram can be constructed for every pair of $(\alpha(r,\theta), \varphi(r,\theta))$ in (α, φ) domain as follows. First, we define a mask for (α, φ):

$$M_{\alpha,\phi,D_\alpha,D_\phi} = \begin{cases} 1: \begin{cases} |\ln\alpha(r,\theta) - n\alpha| < \frac{\Delta_\alpha}{2} \\ |\phi(r,\theta) - \phi| < \frac{\Delta_\phi}{2} \end{cases} \\ 0: o.w. \end{cases}. \tag{10}$$

We are taking the difference between computed magnitude and phase of brushlet coefficients, $\alpha(r,\theta)$ and $\varphi(r,\theta)$ within $\Delta_\alpha/2$ of α and $\Delta_\phi/2$ of φ in the histogram, respectively, where Δ_α and Δ_φ are the magnitude and phase resolution widths of the histogram. Then, the histogram can be defined as follows [21]:

$$h(\alpha,\phi) = \sum_{r,\theta} \left| M_{\alpha,\phi,\Delta_\alpha,\Delta_\phi}(r,\theta)\hat{F}(r,\theta) \right|. \tag{11}$$

Our main interest is the locations of the histogram peaks and the surrounding region, as these shall be used to generate binary masks to label blood and non-blood regions.

2.2.5 Construction of 2.5-D Magnitude–Phase Histogram in Complex Brushlet Space

In order to localize the histogram peaks, we used a K-mean classifier to cluster the data in (11) $(\alpha_{\text{peak}}, \varphi_{\text{peak}})$. The partitioning algorithm minimizes the sum of point-to-centroid distances, summed over all clusters. We assigned each point to the nearest cluster centroid and updated all centroids iteratively. Once the magnitudes and phases corresponding to the Q principal peaks were found, we computed, Q^*, masks based on the following L^2 norm in the histogram space,

$$\forall\left\{(\alpha^l_{\text{peak}}, \phi^l_{\text{peak}}), \quad l = 1,\ldots,K\right\}$$

$$Q_{\alpha^{l^*}_{\text{peak}},\phi^{l^*}_{\text{peak}}}(r,\theta) = \begin{cases} 1: \min\limits_{l} \left(\alpha(r,\theta) - \alpha^l_{\text{peak}}\right)^2 + \left(\phi(r,\theta) - \phi^l_{\text{peak}}\right)^2 \\ 0: o.w \end{cases}, \tag{12}$$

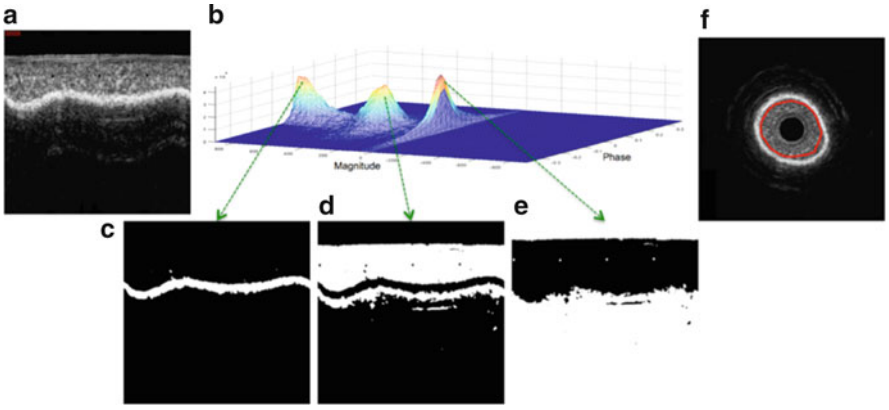

Fig. 5 IVUS grayscale image acquired from phantom cylinder of shrink-wrap material with circulating blood mimicking fluid in polar domain (**a**), constructed 2.5D magnitude–phase histogram (**b**), generated binary masks corresponding to each peak (**c–e**), detected cylinder border (*red*) imposed on the IVUS grayscale image corresponding to (**a**) in Cartesian domain (**f**)

where (12) is minimum over all l and K is the number of tissues (classes). Note that the number of classes defined for the K-means classifier may not be necessarily the same as the number of peaks that we observe in the histogram. We expected that the magnitudes and phases of brushlet coefficients would provide some information about tissue types. Hence, $(a_{\text{peak}}, \varphi_{\text{peak}})$ corresponds to an approximate magnitude–phase for a tissue (class). In (12), we tried to identify specific $(\alpha_{\text{peak}}, \varphi_{\text{peak}})$ among all magnitudes and phases derived from the brushlet coefficients, (α, φ), and estimated the corresponding regions by masking the coefficients that exhibited the closest magnitude and phase to the approximated one. Once the desirable binary mask corresponding to blood regions was found (i.e., the one that contains zeros around the surface of the transducer, as illustrated in Fig. 5c). In the next section, we describe how to estimate the lumen border in constructed binary masks.

2.2.6 Detection of Lumen Border via Surface Function Actives

Although researchers have introduced novel border detection algorithms in IVUS images, challenges associated with this particular problem have not been considered cautiously. The performance of any method, regardless of its implementation technique, could be degraded due to the presence of guide wire, appearance of side branch, reflection from surface of the transducer because of impedance mismatch, and the presence of arc of calcified plaques. Therefore, regularization plays a crucial role in getting the most accurate and reliable borders. One of the main advantages of our proposed technique is that we end up with binary images, which are easier to manipulate for spatial regularization. For example, we can get rid of the guide wire by removing small objects and look for objects with 180° or 0° orientation close to the transducer's surface in order to eliminate any possible reflection.

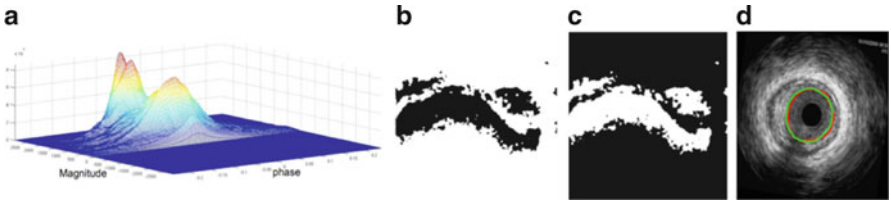

Fig. 6 Constructed magnitude–phase histogram (**a**), generated binary masks (**b and c**), automated (*red*) and manual (*green*) traced borders imposed on original IVUS grayscale image (**d**)

In fact, the major challenges are appearance of side branch, shadows behind guide wire, and the presence of eccentric arc of calcified plaques. These are particularly problematic when a deformable model is deployed, leading to leakage or underestimation of the lumen border. Hence, we employ 1D evolving curve through surface function actives (SFAs) with analytical solution or function basis [24]. SFA not only has great advantages in terms of efficiency and dimensionality reduction but also provides closed form solution, which is a requirement for lumen border, and deals with abovementioned problems. We may choose a 1D surface function with arbitrary bases functions to represent the luminal border in 2D polar domain. The proper choice of bases can be incorporated with some prior knowledge such as smoothness of lumen border and its periodicity along lateral direction. Hence, we opt sine and cosine bases and represent the lumen border as follows:

$$g(a_k, b_k, \theta) = a_0/2 + \sum_{k=1}^{M-1} \left(a_k \cos\left(\frac{2k\pi\theta}{N_\theta}\right) + b_k \sin\left(\frac{2k\pi\theta}{N_\theta}\right)\right), \qquad (13)$$

where N_θ is the number of angles that span 360° in Cartesian space or the width of the image in polar domain. We find the optimal coefficients in an iterative process. Similar approach was also taken by authors in [25].

2.2.7 Experimental Results

In the first experiment, we studied the feasibility of our proposed technique by acquiring IVUS frames from a phantom cylinder using circulating flowing human blood. Figure 5 shows a selected constructed magnitude–phase histogram, binary masks for the two classes, and finally the automated detected phantom wall border. Secondly, we evaluated the algorithm performance on 1,158 IVUS frames acquired from five patients using 45 MHz transducers during catheterization procedure. Figure 6 illustrates a constructed magnitude–phase histogram for a single IVUS frame and automated detected luminal border along with manual traced contour by an expert. Although the peaks are not as well separated as in the case of the phantom data, they still provide good estimate of the relative magnitudes and phases for blood and non-blood regions and hence the detection of the lumen border in

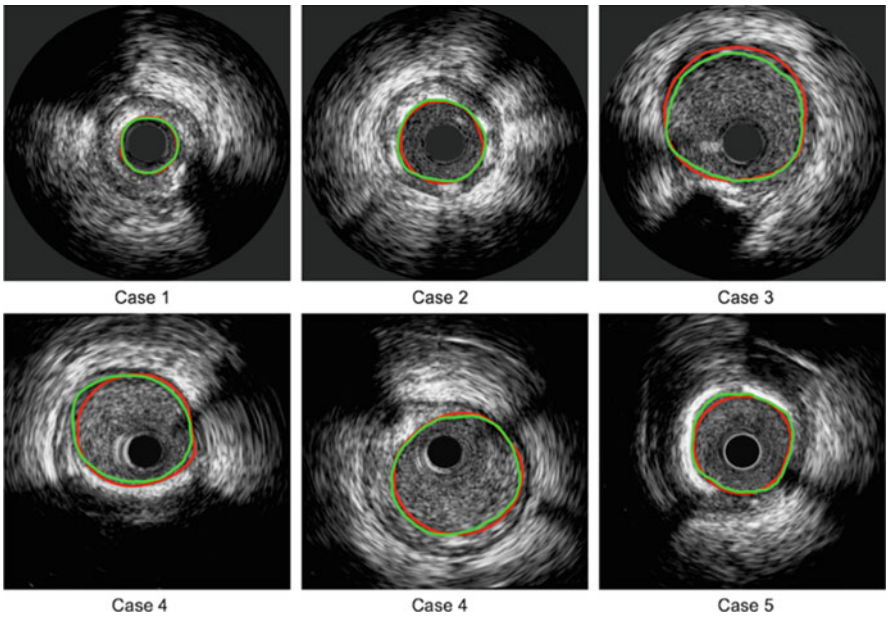

Fig. 7 Resulting automated lumen detected border (*red*) along with manual traced contour (*green*) imposed on six distinct IVUS frames

Table 1 Quantification of automated detected lumen borders compared with corresponding expert manual tracings

Case #	TP	FP	RMSE (mm)
1	96.7 ± 0.05	3.9 ± 0.01	0.01 ± 0.025
2	95.4 ± 0.03	7.8 ± 0.04	0.005 ± 0.004
3	96.5 ± 0.02	7.4 ± 0.06	0.03 ± 0.080
4	91.1 ± 1.00	5.0 ± 0.20	0.03 ± 0.129
5	89.5 ± 0.03	4.7 ± 0.10	0.04 ± 0.195
6	96.5 ± 0.01	5.0 ± 0.01	0.01 ± 0.021

vivo. We quantified the results comparing the automated detected borders with manually traced contours by an expert. Figure 7 also shows resulting automated lumen border detected contours (red) along with manual traced ones (green) for six frames collected from arteries with distinctive pathological and morphological structures. The statistics, true positive (TP), false positive (FP), and root mean square error (RMSE) rates are reported in Table 1.

2.2.8 Summary and Conclusion

We presented a 3D segmentation framework for automatic detection of luminal borders through classification of incoherent (blood) and coherent (non-blood)

patterns in IVUS grayscale images by constructing the joint magnitude–phase histogram of complex brushlet coefficients. This was possible since brushlet offered orthogonal transformation of Fourier domain so we could sum up the brushlet coefficients derived from Hermitian Fourier coefficients. We studied the feasibility of our proposed framework using both phantom and in vivo IVUS data. The main contribution of this work is classification of brushlet coefficients corresponding to blood and non-blood regions through estimation of peaks of relative magnitudes and phases in constructed 2.5-D magnitude–phase histograms. Once the magnitudes and phases were approximated, we generated binary masks corresponding to blood and non-blood regions in transformed domain and employed the same masks to estimate the lumen borders.

Our results showed that the proposed framework performed reliably, detecting the lumen border in images acquired with both 40 and 45 MHz transducers. One of the main advantages of our technique was that the generated binary masks made regularization simpler and therefore detection of lumen border in the presence of guide wire and its shadow, side branch, and arc of calcified plaque became easier and more accurate. We obtained encouraging results by performing our algorithm on 1,158 IVUS frames acquired with single-element 45 MHz transducers, containing distinctive arteries with variety of pathological and morphological structures, collected from five patients.

3 Automatic Characterization of Atherosclerotic Plaques

For chronic disease such as atherosclerosis, which may reoccur after balloon angioplasty, atherectomy, stent deployment, and even bypass surgery, the accurate diagnosis of vulnerable plaques is significantly imperative. In brief, *what make atherosclerosis one of the deadliest diseases is not stenosis alone but failure in detection and proper treatment of vulnerable plaques*. The problem becomes more complicated when we observe that there is no consensus on interpretation of vulnerable plaques from imaging perspectives as well as pathological point of view and it is rather performed in a subjective manner. *Today, more than ever, there is a need for reliable, reproducible, clinically approved atherosclerotic plaque characterization algorithms so interventional cardiologists can make confident decisions and choose appropriate devices/drugs during catheterization procedures*. Furthermore, they can be used to study the efficacy of different agents coated on drug-eluting stents (DESs) and regression of plaques. Undoubtedly, current developments in intravascular coronary imaging systems and atherosclerotic tissue characterization techniques will be a basis for future consistent management and dependable treatment of atherosclerosis. Consequently, more lives will be saved and overwhelming medical expenses burdened on the government and individuals can be considerably reduced.

IVUS findings have shown that sonographic differences yielded visual discrimination among plaque constituents [26, 27]. In other words, variations of intensities

are attributed to repetitive tissue microstructure patterns. These have motivated researchers to develop texture-based algorithms on IVUS images to differentiate tissue types [28–31]. However, none of these studies validated their results with histology images in vitro, an indispensable validation step that is required before deploying any algorithm for in vivo classification. In this section, we present an effective texture-derived atherosclerotic tissue characterization algorithm using discrete wavelet packet frame (DWPF) and a 2D envelope detection technique introduced by Laine and Fan [32] that relies on the Hilbert transform of multiscale overcomplete representations. The extracted textural features of such expansions are perfectly suited for classification and capture characteristics of the plaque with the highest correlation to histology. This resolves one of the main limitations of the IVUS, which is discrimination between fibrous and fatty tissues [33, 34]. A primary work of the proposed technique was reported in [35].

3.1 IVUS-Histology Matching Procedure

In [1], we described a method for systematic marking of regions of interest (ROIs) for histology preparation. The main advantage of presented methodology was that the orientation of the artery was not changed throughout the entire procedure. Therefore, more reliable IVUS-histology pairs could be obtained and the number of cross-section of interest (CSI) per vessel was significantly increased (average of 25 regions) compared to the traditional methods (3–5 regions) [36, 37]. This also made the matching procedure more reliable and the CSIs were obtained more confidently. Generally, experts use histology images, as gold standard, to validate constructed tissue color maps.

3.2 Multi-Channel Wavelet Analysis

We will take advantage of spatial-frequency-localized expansions and their generalization to 2D to discern textural patterns on constructed images from backscattered IVUS signals while geometrically oriented decompositions are provided at this dimension. Unlike the classical discrete wavelet (DWT) [38–40] and discrete wavelet packet transforms (DWPTs) [41], we compute decompositions that are translation invariant in a discrete wavelet frame (DWF) [42] or discrete wavelet packet frame (DWPF), where no decimation (down sampling) occurs between expansion levels (Fig. 8). Although the DWPF seems redundant and insufficient, it has two advantages that benefit texture analysis and multiscale representations: (1) less restriction on filter selection and (2) the variations of the modulus in the transform domain are not corrupted by aliasing.

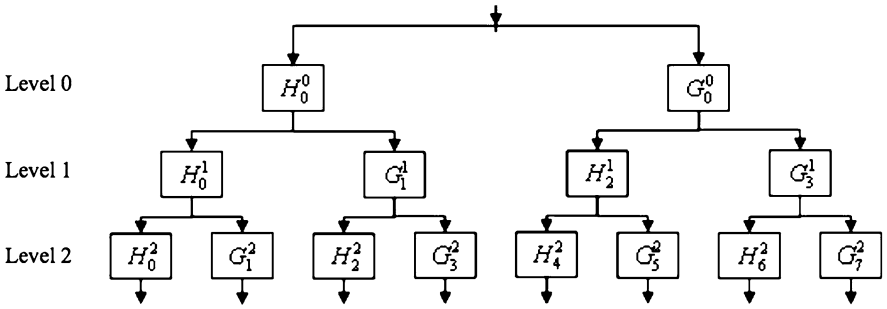

Fig. 8 Tree structure for a discrete wavelet packet frame expansion (DWPF) and its associated multiscale indexes

Wavelet packets are orthonormal in the space of summable-integrable function $L^2(R)$ [43] and described by a collection of functions $\{\xi_j(x)|j \in Z^+, \quad \langle \xi_p, \xi_q \rangle = 0, p \neq q\}$ obtained from:

$$2^{l/2}\xi_{2k}\left(2^l x - n\right) = \sum_{m\in Z} h^l_{m-2n} 2^{l+1/2}\xi_k\left(2^{l+1}x - m\right), \tag{14}$$

$$2^{l/2}\xi_{2k+1}\left(2^l x - n\right) = \sum_{m\in Z} g^l_{m-2n} 2^{l+1/2}\xi_k\left(2^{l+1}x - m\right), \tag{15}$$

where l, n, k, $\xi_0(x) = \phi(x)$, and $\xi_1(x) = \psi(x)$ are the scale index, translation index, channel index, scaling function, and basic wavelet, respectively [39]. We will describe our method and rationale for selection of discrete filters h_n and g_n in more details in the next section. The wavelet packets at different scales can also be found by the inverse relationship as follows:

$$2^{l+1/2}\xi_k\left(2^{l+1}x - m\right) = \sum_n h^l_{m-2n} 2^{l/2}\xi_{2k}\left(2^l x - n\right) + \sum_n g^l_{m-2n} 2^{l/2}\xi_{2k+1}\left(2^l x - n\right). \tag{16}$$

Any function $f(x) \in L^2(R)$ can be decomposed onto a wavelet packet basis by computing the inner product $\langle f(x), \xi_k(2^l x - n)\rangle$. Using (16), we can write:

$$\begin{aligned} 2^{l+1/2}\int_{-\infty}^{\infty} f(x)\xi_k\left(2^{l+1}x - m\right)\mathrm{d}x &= \int_{-\infty}^{\infty} f(x)\left(\sum_n h^l_{m-2n} 2^{l/2}\xi_{2k}\left(2^l x - n\right)\right. \\ &\quad \left. + \sum_n g^l_{m-2n} 2^{l/2}\xi_{2k+1}\left(2^l x - n\right)\right)\mathrm{d}x \\ &= \sum_n h^l_{m-2n} 2^{l/2}\int_{-\infty}^{\infty} f(x)\xi_{2k}\left(2^l x - n\right)\mathrm{d}x \\ &\quad + \sum_n g^l_{m-2n} 2^{l/2}\int_{-\infty}^{\infty} f(x)\xi_{2k+1}\left(2^l x - n\right)\mathrm{d}x. \end{aligned} \tag{17}$$

Defining the decomposition coefficients as:

$$\rho_{k,n}^{l} = 2^{l/2} \int_{-\infty}^{\infty} f(x)\xi_k \left(2^l x - n\right) \mathrm{d}x. \tag{18}$$

Equation (17) can be rewritten as:

$$\rho_{k,\,m}^{l+1} = \sum_n h_{m-2n}^{l} \rho_{2k,\,n}^{l} + \sum_n g_{m-2n}^{l} \rho_{2k+1,\,n}^{l}. \tag{19}$$

Using (14) and (15), the coefficients are calculated by:

$$\rho_{2k,n}^{l} = \sum_m h_{m-2n}^{l} \rho_{k,m}^{l+1}, \tag{20}$$

$$\rho_{2k+1,n}^{l} = \sum_m g_{m-2n}^{l} \rho_{k,m}^{l+1}. \tag{21}$$

In the standard wavelet transform, the index k is restricted to $k = 0$ and only two wavelet packets ξ_0 and ξ_1 are used. Consequently, only the leftmost nodes (ρ_o^l) are decomposed into high and low frequency sub-bands. However, in wavelet packets, the decompositions are performed on both low and high frequency components. Therefore, a tree-structure multiband extension of the standard wavelet transform is constructed (Fig. 8). This can be seen as sub-band filtering and implemented using iterated constructed highpass and lowpass filters in frequency domain. Taking the Fourier transform of both sides of (20) and (21) yields:

$$\Upsilon_{2k}^{l+1}(\omega) = G^l(\omega)\,\Upsilon_k^l(\omega), \tag{22}$$

$$\Upsilon_{2k+1}^{l+1}(\omega) = H^l(\omega)\,\Upsilon_k^l(\omega), \tag{23}$$

where $\Upsilon_k^l(\omega)$ is the Fourier transform of the frame coefficients at channel k and level l. Since the IVUS signals are sampled at the rate of f_s, the original discrete signal is considered as the set of frame coefficients at the first scale ($l = 0$) for the rest of this chapter.

3.3 Filter Selection and Specification

The highpass $G^l(\omega)$ and the lowpass $H^l(\omega)$ filters at each level l can be realized as presented in [40] by: $G^l(\omega) = G^0(2^l\omega)$ and $H^l(\omega) = H^0(2^l\omega)$. Consequently, the multi-channel wavelet schematic in Fig. 8 behaves like a filter bank with channel filters $\{F_k^l(\omega)|0 \le k \le 2^l - 1\}$, where $F_k^l(\omega)$ can be derived recursively as follows:

$$F_k^l(\omega) = G^0(\omega), \quad F_1^0(\omega) = H^0(\omega), \tag{24}$$

$$F_{2k}^{l+1}(\omega) = G^{l+1}(\omega)\,F_k^l(\omega) = G^0\left(2^{l+1}\omega\right)F_k^l(\omega), \tag{25}$$

$$F_{2k+1}^{l+1}(\omega) = H^{l+1}(\omega)\,F_k^l(\omega) = H^0\left(2^{l+1}\omega\right)F_k^l(\omega). \tag{26}$$

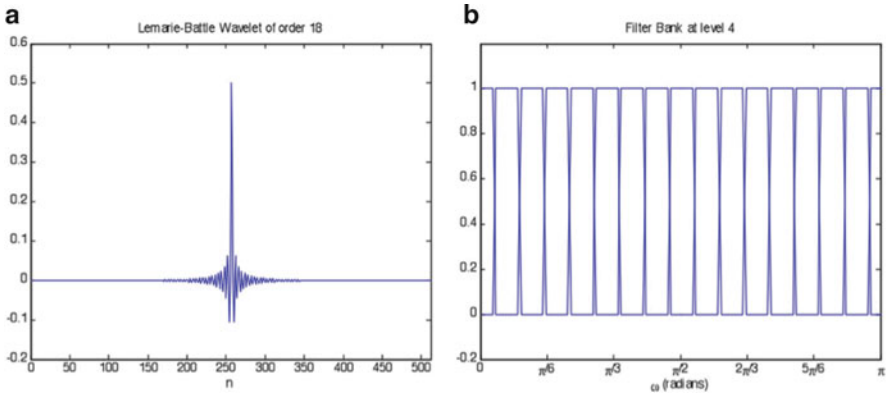

Fig. 9 Lemarie-Battle filter of order 18 (**a**), constructed filter bank at level 4 (**b**)

It has been shown that the selection of the filters $G^0(\omega)$ and $H^0(\omega)$ can have significant impact on texture classification performance [32, 41]. The filter candidates must satisfy necessary criteria such as symmetry as well as boundary accuracy and have optimal frequency response. Hence, we selected Lemarie-Battle [39] wavelets that are symmetric (have linear phase response) and satisfy quadrature mirror filter (QMF) criteria. The former property alleviates boundary effects through simple methods of mirror extension. The discrete HIGHPASS filter g_n^0 is obtained by $g_n^0 = (-1)^n h_n^0$ or $G^0(\omega) = H^0(\omega + \pi)$ in the frequency domain. Figure 9 illustrates the constructed filter bank at level 4 generated by Lemarie-Battle wavelet of order 18. The wavelets using QMF as well as constructed filter bank $\{F_k^l(\omega)\}$ cover exactly the frequency domain and satisfy the property:

$$\left|G^0(\omega)\right|^2 + \left|H^0(\omega)\right|^2 = \left|G^0(\omega)\right| + \left|H^0(\omega)\right| = 1, \tag{27}$$

$$\sum_{k=0}^{2l-1} \left|F_k^l(\omega)\right|^2 = \sum_{k=0}^{2l-1} \left|F_k^l(\omega)\right| = 1. \tag{28}$$

Thus this expansion is pointwise/pixelwise 1:1 (a bi-jection across levels of analysis) and allows for perfect representation (and reconstruction).

3.4 Feature Extraction

We processed the IVUS signals from each raw data frame, represented in the (r, θ) domain, which is the original domain of acquisition, containing 256 lines that span over 360° with 2,048 samples per line. In order to have an optimal frame size with respect to its computational complexity and textural resolution, we decimated and interpolated (via a spline) the signals in axial and lateral directions, respectively, to generate square $M = 512$ pixels frame. Figure 10 demonstrates B-mode images of an IVUS frame in both (r, θ) and (x, y) Cartesian domains.

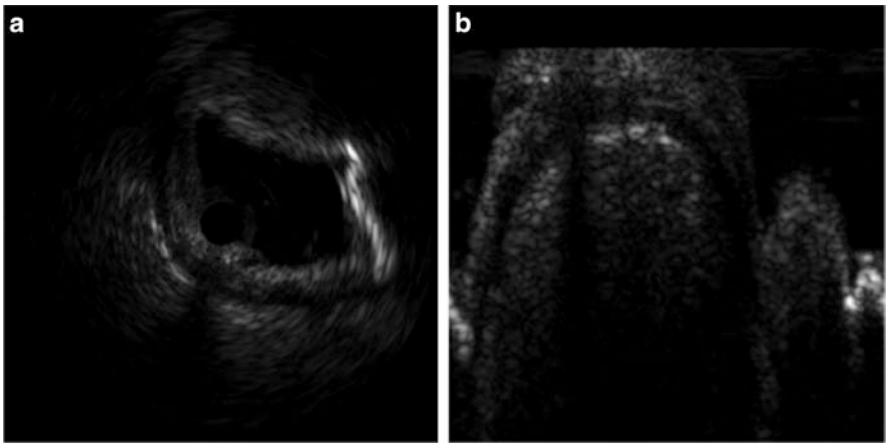

Fig. 10 Sample IVUS image shown in the (r, θ) (**a**) and (x, y) Cartesian (**b**) domains

For each frame, a separable tensor product was used, in which channel filters were denoted by $F^l_{i\times j}(\omega_r, \omega_\theta) = F^l_i(\omega_r)F^l_j(\omega_\theta)$. Consequently, such an extension will lead to orientation selectivity in the decomposition tree. Four possible orientations can be considered excluding the root node, which is omnidirectional.

1. The node last filtered by $G^l(\omega_r)H^l(\omega_\theta)$ corresponds to coefficients having a vertical orientation. The highpass filter G^l and the lowpass filter H^l are applied in the axial and lateral directions, respectively.
2. The node last filtered by $H^l(\omega_r)G^l(\omega_\theta)$ corresponds to horizontal orientation. The lowpass filter H^l and the highpass filter G^l are applied in the axial and lateral directions, respectively.
3. The node last filtered by $G^l(\omega_r)G^l(\omega_\theta)$ is responsive to coefficients in the diagonal orientation. The highpass filter G^l and the highpass filter H^l are applied in the axial and lateral directions, respectively.
4. The node last filtered by $H^l(\omega_r)H^l(\omega_\theta)$ has the same orientation as its parent. The lowpass filter H^l and the lowpass filter H^l are applied in the axial and lateral directions, respectively.

Due to narrowband characteristic of IVUS signals, the envelope of output signals from channel filters was computed using the corresponding 2D analytical signals. Finally, the feature matrices were constructed as follows:

$$\vec{V}^{l,\,k}_{i,\,j} = \left\{ \mathrm{e}^{l,\,k}_{i,\,j} \,\middle|\, 0 \le k \le (2^l - 1), \quad i,\ j = 1, \ldots, M \right\}, \tag{29}$$

where $\mathrm{e}^{l,\,k}_{i,\,j}$ represents the envelope value of pixel (i, j)f or the kth channel at level l.

3.5 Classification

The overall justification of in vivo real-time plaque characterization is performed by the interventional cardiologists through the use of classified tissues. For this reason, we chose ISODATA clustering algorithm in order to classify the tissues and generate the tissue color maps, called prognosis histology (PH) images. We utilized the unsupervised classifier to quantify the reliability of the extracted signatures. Our hypothesis is that if the classification results (PH images) driven by the unsupervised signatures preserve their high correlation with ground truth histology images, then the features could be used reliably in the training data set for supervised classification. We have categorized plaque components into four $N_c = 4$ classes including lipidic, fibrotic, calcified, and background (no tissue).

For every representation matrix, $X_{M\times M}$, a label was assigned to each pixel by modulo N_c. We computed the center of clusters $\{\vec{C}_\kappa | 0 \leq \kappa \leq N_c - 1\}$ by calculating the mean vector for each class. The pixel $\{x_{i,\,j} | i,\ j = 1, \ldots, M\}$ was assigned to the class κ if the Euclidean distance between the corresponding pixel and the class center $\vec{C}_\kappa$ was the closest. The centers of the clusters were updated in an iterative fashion by recomputing the relative mean vectors. The procedure was terminated once no change in labeling occurred.

3.6 Experimental Results

About 83 cross-section of CSIs collected from 32 cadaver hearts, including 19 left anterior descending (LAD), 16 right coronary artery (RCA), and 16 left circumflex (LCX) segments that had more than 30% stenosis, were examined. As we mentioned in the preceding section, we decimated the signals and used spline interpolation to generate 512-by-512 scan converted (Cartesian domain) B-mode images. For each frame, an expert manually segmented the plaque by tracing the vessel wall and lumen borders. The corresponding plaque signals were read and saved in a matrix with the same size of the IVUS image in the $(r,\ \theta)$ domain. We performed our algorithm on 512-by-512 matrices and selected Lemarie-Battle filters of order 18, decomposition level $L = 2$, and number of classes $N_c = 4$. Finally, the resulting classified images were mapped onto Cartesian plane. Figure 11 demonstrates an IVUS grayscale CSI, corresponding Movat Pentachrome histology image, and constructed PH image. The blue, yellow, and pink colors exhibit calcified, fibrotic, and lipidic plaque components, respectively.

3.7 Quantification

For quantification, histology is the best available version of ground truth for in vitro tissue characterization. However, the interpretation of histology images can often

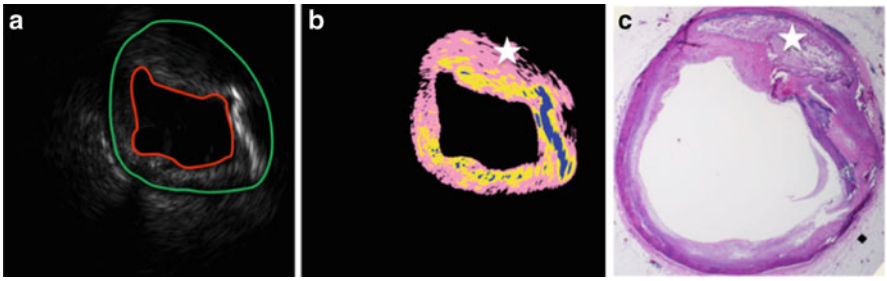

Fig. 11 Manually traced vessel wall (*green*) and lumen border (*red*) on IVUS B-mode image (**a**), resulting PH image generated by the algorithm (*blue*, *yellow*, and *pink* colors represent calcified, fibrotic, and fibro-lipidic components) (**b**), corresponding H&E histology image of cross-section of interest (**c**). The *white star* points to lipid rich pool region that could be the sign of vulnerable plaque if thin fibrotic layer existed on top of it

vary among experts yielding a subjective process. As a result, plaque constitutes can be separated into fibrotic, lipidic, necrotic core, and calcified while another may differentiate between the levels of the presence of fatty materials and add fibro-lipidic to compromise between fibrotic and lipidic. Generally, in supervised classification techniques, the most homogeneous regions, for each tissue type, are selected on histology images and mapped to the corresponding IVUS images manually (Fig. 12c). Subsequently, the features are extracted in order to build the training and testing dataset. Figure 12 demonstrates a CSI, corresponding histology image with manually segmented ROIs by a histopathologist, image containing manually traced labels for each tissue type and constructed PH image. Traditionally, in order to build the training dataset, experts trace the most homogeneous regions for each tissue type and extracted corresponding features, although the homogeneity assumption may not be completely valid.

As we can observe in histology image and corresponding IVUS as well as PH image, the atherosclerotic plaque consists of heterogeneous tissues that makes manual labeling tedious and possibly infeasible. Figure 12a, b, d clearly demonstrates that the manually segmented ROI (Fig. 12c), which presumably should only contain fibrotic tissue, is heterogeneous and contains mixture of fibrotic and lipidic tissues. This may lead to incorrect classification results if used for training of any supervised classifier. For this reason, we designed our tissue characterization framework based on unsupervised classification to substantiate extracted features. In this way, we confidently used the classification results (PH images) as labeled images for building a training set in any supervised classification algorithm.

Due to the nature of the unsupervised classification approach taken, we evaluated the algorithm performance employing an independent histopathologist, by contrasting the histology images corresponding to PH images. We deployed a scoring approach to quantify the results and asked the histopathologist to score each PH image by eye-balling. For higher accuracy, each histology image was divided into distinguishable regions (Fig. 12a). The corresponding PH images were oriented

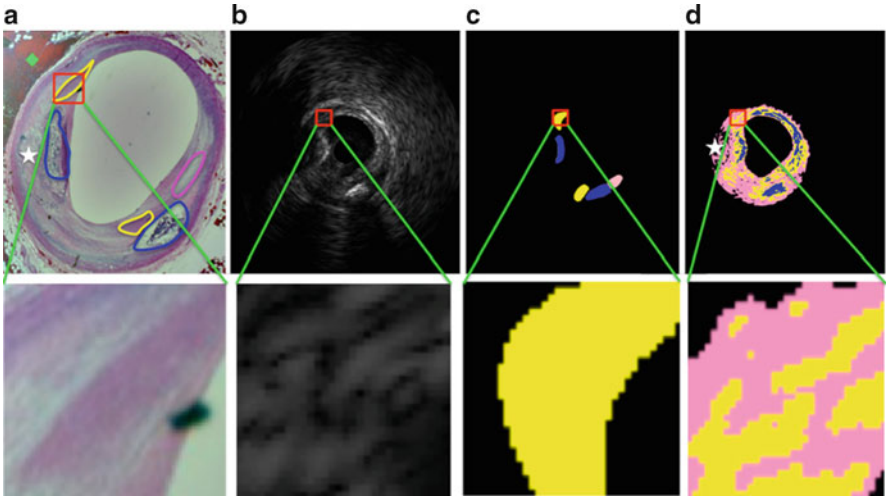

Fig. 12 H&E histology image of CSI with manually segmented ROIs (**a**), corresponding IVUS grayscale image (**b**), manually selected regions corresponding to presumably homogenous regions for each tissue type (**c**), and corresponding PH image (**d**). The bottom row illustrates the magnified version of selected ROI (*red square*) for fibrotic tissue. The inhomogeneity of atherosclerotic tissues are well reflected in (**a, b, and d**). The *white star* points to lipid rich pool region that could be a sign of vulnerable plaque if a thin fibrotic layer existed on top of it

Table 2 Percentage of correct classification as well as misclassification for each tissue type

	Calcified	Fibrotic	Fibro-lipidic	No tissue
Calcified	99.70	0.32	0.07	0.00
Fibrotic	7.17	87.75	5.05	0.00
Fibro-lipidic	1.89	6.50	90.87	0.74

and scaled as the histology image and same divisions were mapped visually. The accuracy of characterization was evaluated for each region separately and averaged for composite rating for each tissue type. Table 2 demonstrates the average values for correct and misclassified tissues in 83 CSIs. For example, the first row shows that 99.70% of calcified tissues in histology images were correctly classified as calcified while 0.32% and 0.07% of them were misclassified as lipidic and fibro-lipidic, respectively. The overall classification performance has been evaluated to be 90.87%, 87.75%, and 99.70% for calcified, fibrotic, and fibro-lipidic tissues, respectively.

3.8 Summary and Conclusion

W presented a reliable texture-derived atherosclerotic plaque characterization algorithm as an alternative to spectrum-based approaches like IVUS-virtual histology

(IVUS-VH) [44] and IVUS-integrated backscatter (IVUS-IB) [45]. We deployed a 2D multi-channel technique and extracted textural features that relied upon over-complete wavelet packet frame representations along with unsupervised ISODATA classifier to generate PH images. The accuracy of the algorithm was evaluated by an independent histopathologist and reported to be 99.70%, 87.75%, and 90.87% for calcified, fibrotic, and fibro-lipidic tissues, respectively, in 83 CSIs collected from 32 hearts ex vivo.

The most important and practical advantage of this algorithm is that it can be performed on both IVUS RF signals as well as grayscale images and reliably classify tissues independently of the transducer center frequency while inconsistency among the spectral-derived features within the functional range of bandwidth still remains a major challenge. Our results showed a fine differentiation between fibrotic and fibro-lipidic components, which had been a major challenge in the field. Above all, we showed that constructed PH images through our unsupervised approach could be reliably used for building training sets in any supervised classification approach without any manual labeling in the typically highly heterogeneous media of atherosclerotic plaques.

References

1. Katouzian A, Sathyanarayana S, Baseri B, Konofagou EE, Carlier SG (2008) Challenges in atherosclerotic plaque characterization with intravascular ultrasound (IVUS): from data collection to classification. IEEE Trans Inf Technol Biomed 12(3):315–327
2. Sonka M, Zhang X, Siebes M, Bissing MS, DeJong SC, Collins SM, McKay CR (1995) Segmentation of intravascular ultrasound images: a knowledge-based approach. IEEE Trans Med Imaging 14(4):719–732
3. Shekhar R, Cothren RM, Vince DG, Chandra S, Thomas JD, Cornhill JF (1999) Three-dimensional segmentation of luminal and adventitial borders is serial intravascular ultrasound images. Comput Med Imaging Graph 23:299–309
4. Plissiti M, Fotidadis D, Michalis L, Bozios G (2000) An automated methos for lumen and media–adventitia border detection in a sequence of IVUS frames. IEEE Trans Inf Technol Biomed 19(10):996–1011
5. Cardinal MR, Meunier J, Soulez G, Maurice RL, Therasse E, Cloutier G (2006) Intravascular ultrasound image segmentation: a three-dimensional fast-marching method based on gray level distribution. IEEE Trans Med Imaging 25(5):590–601
6. Unal G, Bucher S, Carlier S, Slabaugh G, Fang T, Tanaka K (2008) Shape-driven segmentation of the arterial wall in intravascular ultrasound images. IEEE Trans Inf Technol Biomed 12(3):335–347
7. Gil D, Radeva P, Saludes J (2000) Segmentation of artery wall in coronary IVUS images: a probabilistic approach. In: 15th International Conference on Pattern Recognition, Barcelona
8. Gil D, Hernandez A, Carol A, Rodríguez O, Radeva P (2005) A deterministic-static adventitia detection in IVUS images. LNCS-3504, FIMH, pp 65–74
9. Taki A, Najafi Z, Roodaki A, Setarehdan SK, Zoroofi RA, Konig A, Navab N (2008) Automatic segmentation of calcified plaques and vessel borders in IVUS images. Int J CARS 3:347–354
10. Hibi K, Takagi A, Zhang X, Teo TT, Boneau HN, Yock PG, Fitzgerald PJ (2000) Feasibility of a novel blood reduction algorithm to enhance reproducibility of ultra-high-frequency intravascular ultrasound images. Circulation 102(14):1657–1663

11. Balocco S, Basset O, Cachard C, Delachartre P (2003) Spatial aniosotropic diffusion and local time correlation applied to segmentation of vessels in ultrasound image sequences. IEEE Symp Ultrasonics 2:1549–1552
12. Katouzian A, Angelini E, Lorsakul A, Sturm B, Laine A (2009) Lumen border detection of intravascular ultrasound via denoising of directional wavelet representations. In: Functional Imaging and Modeling of Heart
13. Rotger D, Radeva P, Nofrerias EF, Mauri J (2007) Blood detection in IVUS images for 3D volume of lumen changes measurement due to different drugs administration. In: CAIP LNCS 4673
14. Katouzian A, Selver MA, Angelini E, Sturm B, Laine A (2009) Classification of blood regions in IVUS images using three dimensional brushlet-derived features. In: EMBC
15. De Valois R, De Valois K (1988) Spatial vision. Oxford University Press, New York
16. Beck J, Sutter A, Ivry R (1987) Spatial frequency channels Vnd perceptual grouping in texture segregation. Comput vision Graph Image Process 37:299–325
17. Katouzian A, Angelini E, Lorsakul A, Sturm B, Laine A (2009) Lumen border detection of intravascular ultrasound via denoising of directional wavelet representations. In: Functional Imaging and Modeling of Heart, Nice, 2009
18. Katouzian A, Selver MA, Angelini E, Sturm B, Laine A (2009) Classification of blood regions in IVUS images using three dimensional brushlet-derived features. In: European Molecular Biology Conference
19. Angelini E, Laine A, Takuma S, Holmes J Homma S (2001) LV volume quantification via spatio-temporal analysis of real-time 3D echocardiography. IEEE Trans Med Imaging 20(6):57–469
20. Meyer F, Coifman RR (1997) Brushlets: a tool for directional image analysis and image compression. Appl Comput Harmon Anal 4:147–187
21. Yilmaz O, Rickard S (2004) Blind separation of speech mixtures via time-frequency masking, IEEE Trans Signal Process 52(7):1830–1847
22. Ausher P, Weiss G, Wickerhauser MV (1992) Local sine and cosine bases of Coifman and Meyer and the construction of smooth wavelets. In: Chui CK (ed) Wavelets – a tutorial in theory and application, vol 2. Academic, San Diego, pp 237–256
23. Angelini E, Laine A, Takuma S, Holmes J, Homma S (2001) LV volume quantification via spatio-temporal analysis of real-time 3D echocardiography. IEEE Trans Med Imaging 20(6):457–469
24. Duan Q, Angelini ED, Laine AF (2009) Surface function actives. J Vis Commun Image R 20:478–490
25. Ruiz GM, Rivera M, Kakadiaris IA (2008) A probabilistic segmentation method for the identification of luminal borders in intravascular ultrasound images. IEEE Conf Comput Vis Pattern Recognit
26. Tobis JM, Mallery J, Mahon D, Lehmann K, Zalesky P, Griffith J, Gessert J, Moriuchi M, McRae M, Dwyer ML (1991) Intravascular ultrasound imaging of human coronary arteries in vivo. Analysis of tissue characterization with comparison to in vitro histological specimens. Circulation 83:913–926
27. Gad K, Leon MB (1991) Characterization of atherosclerotic lesions by intravascular ultrasound: possible role in unstable coronary syndromes and in interventional therapeutics procedure. Am J Cardiol 68:85B–91B
28. Zhang X, McKay CR, Sonka M (1998) Tissue characterization in intravascular ultrasound images. IEEE Trans Med Imaging 17:(6)889–899
29. Caballero KL, Pujol O, Barajas J, Mauri J, Radeva P (2006) Assessing in-vivo IVUS tissue classification accuracy between normalized image reconstruction and RF analysis. Med Image Comput Comput Assist Interv 82–89
30. Escalera S, Pujol O, Mauri J, Radeva P (2009) Intravascular ultrasound tissue characterization with sub-class error-correcting output codes. J Signal Process Syst 55(1–3):35–47

31. Taki A, Roodaki A, Pauly O, Setarehdan S, Unal G, Navab N (2009) A new method for characterization of coronary plaque composition via IVUS images, IEEE Int Symp Biomed Imaging: from nano to macro (ISBI 2009)
32. Laine AF, Fan J (1996) Frame representation for texture segmentation. IEEE Trans Image Process 5(5):771–780
33. Hiro T, Leung CY, De Guzman S, Caiozzo VJ, Fervid AR, Karimi H, Helfant RH, Tobis JM (1997) Are soft echoes really soft? Intravascular ultrasound assessment of mechanical properties in human atherosclerotic tissue. Am Heart J 133:1–7
34. Jeremias A, Kolz ML, Ikonen TS, Gummert JF, Oshima A, Hayase M, Honda Y, Komiyama N, Berry GJ, Morris RE, Yock PG, Fitzgerald PJ (1999) Feasibility of in vivo intravascular ultrasound tissue characterization in the detection of early vascular transplant rejection. Circulation 100:2127–2130
35. Katouzian A, Baseri B, Konofagou E, Laine AF (2008) Texture-driven coronary artery plaque characterization using wavelet packet signatures proceeding of 5th IEEE International Symposium on Biomedical Imaging (ISBI): from nano to macro
36. Nair A, Kuban BD, Tuzcu M, Schoenhagen P, Nissen SE, Vince DG (2002) Coronary plaque classification with intravascular ultrasound radiofrequency data analysis. Circulation 106(17):2200–2206
37. Katouzian A, Sathyanarayana S, Li W, Thomas T, Carlier SG Challenges in Tissue Characterization from Backscattered Intravascular Ultrasound Signals. In: IEEE Proceedings of SPIE, San Diego, Feb 2007
38. Rioul O (1993) A discrete-time multiresolution theory. IEEE Trans Signal Process 41(8): 2591–2606
39. Mallat SG (1989) A theory of multiresolution signal decomposition: the wavelet representation. IEEE Trans Pattern Anal Mach Intell 11(7):674–693
40. Daubechies I (1992) Ten lectures on wavelets. Society for industrial and applied mathematics, Philadelphia
41. Unser M (1995) Texture classification and segmentation using wavelet frames. IEEE Trans Image Process 4(11):1549–1560
42. Coifman RR, Wickerhauser MV (1992) Entropy-based algorithms for best basis selection. IEEE Trans Inf Theory 38(2):713–718
43. Coifman RR, Meyer Y (1989) Orthonormal wave packet bases. Yale Univiversity
44. Nair A, Kuban BD, Obuchowski N, Vince DG (2001) Assessing spectral algorithms to predict atherosclerotic plaque composition with normalized and raw intravascular ultrasound data. Ultrasound Med Biol 27(10):1319–1331
45. Kawasaki M, Takatsu H, Noda T et al (2002) Noninvasive quantitative tissue characterization and two-dimensional color-coded map of human atherosclerotic lesions using ultrasound integrated backscatter: comparison between histology and integrated backscatter images. J Am Coll Cardiol 38(2):486–492

ERRATUM TO

Chapter 11
Real-Time 4D Cardiac Segmentation by Active Geometric Functions

Qi Duan, Andrew F. Laine, and Jasjit S. Suri

J.M. Sanches et al. (eds.), *Ultrasound Imaging: Advances and Applications*,
DOI 10.1007/978-1-4614-1180-2_11, © Springer Science+Business Media, LLC 2012

DOI 10.1007/978-1-4614-1180-2_15

The publisher regrets that Elsa Angelini, a contributor to Chapter 11, was unfortunately not credited as a contributor to this chapter or listed in the List of Contributors to this book. Dr. Angelini's affiliation is:

Elsa Angelini, PhD
Telecom ParisTech
Département Traitement du Signal et des Images (TSI)
(Department of Signal and Image Processing)
75013 Paris France

The online version of the original chapter can be found at
http://dx.doi.org/10.1007/978-1-4614-1180-2_11

Author Index

J.M. Sanches et al. (eds.), *Ultrasound Imaging: Advances and Applications*,
DOI 10.1007/978-1-4614-1180-2, © Springer Science+Business Media, LLC 2012

Subject Index

J.M. Sanches et al. (eds.), *Ultrasound Imaging: Advances and Applications*,
DOI 10.1007/978-1-4614-1180-2, © Springer Science+Business Media, LLC 2012

Biographies of the Editors

Biography of João Miguel Sanches

João Miguel Sanches received the E.E., M.Sc. and Ph.D. degrees from the Instituto Superior Técnico (IST) in the Technical University of Lisbon, Portugal, in 1991, 1996 and 2003, respectively. He is Assistant Professor at the recently created Department of Bioengineering at the Instituto Superior Técnico, Technical University of Lisbon. Before, he was at the Department of Electrical and Computer Engineering (DEEC) where he has taught in the area of signal processing, systems and control. He has been actively involved in the course of Biomedical Engineering advising master thesis of the Biomedical Engineering course and PhD students of the doctoral program in Biomedical Engineering. He has proposed a PhD course of Medical Image Reconstruction that he has been taught in the last years.

He is researcher at the Institute for Systems and Robotics (ISR) and in the last years his work has been focused on Biomedical Engineering, namely, in Biomedical Image Processing, Physiological-based Modeling of Biological Systems in the perspective of the Systems and Control theory and statistical signal processing

J.M. Sanches et al. (eds.), *Ultrasound Imaging: Advances and Applications*,
DOI 10.1007/978-1-4614-1180-2,

of physiological data. His research activity is focused on the morphological and tissue characterization of tissues from Ultrasound (US) images for the diagnosis of the atherosclerotic disease of the carotids and diffuse diseases of the liver. He is also working in functional Magnetic Resonance Imaging (fMRI) and Fluorescence Confocal Microscope (FCM) imaging in collaboration with the Institute of Molecular Medicine at the Medical School of the University of Lisbon. He is also involved in the development of signal processing algorithms and biomedical applications for mobile phones for the diagnosis of sleep disorders in collaboration with the Electroencephalography and Clinical Neurophysiology Center (Centro de Electroencefalografia Neurofisiologia Clínica – CENC), also with the Medical School of the University of Lisbon.

He is member of the IEEE Engineering in Medicine and Biology Society and Associate Member of the Bio Imaging and Signal Processing Technical Committee (BISP-TC) of the IEEE Signal Processing Society. He is also president of the Portuguese Association of Pattern Recognition (APRP).

Biography of Andrew Laine

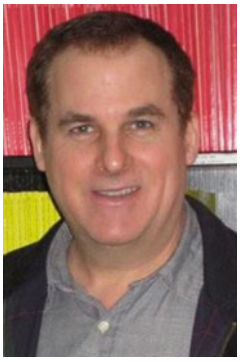

Andrew F. Laine, D.Sc., is Professor of Biomedical Engineering and Radiology (Physics), and the Director of the Heffner Biomedical Imaging Laboratory in the Department of Biomedical Engineering. Since 2001 he has served as Vice Chair of the Department of Biomedical Engineering at Columbia. Professor Laine pioneered the application of multiresolution representations for feature analysis of digital mammography and ultrasound. He served as Associate Editor of *IEEE Transactions on Image Processing* and edited the book, "Wavelet Theory and Applications", Kluwer, 1995. He has jointly chaired the SPIE conference on "Mathematical Imaging: Wavelet Application in Signal and Image Processing", during the years 1993–2003, and co-authored several book chapters including "Wavelet Applications in Medicine and Biology", CRC Press, 1995, and "Time-Frequency and Wavelets

Transforms in Biomedical Engineering," IEEE Press, 1998. He is a member of the Editorial Board of the book series *Emerging Technologies in Biomedical Engineering*, sponsored by the IEEE-EMBS Society and on the Editorial Board of the *Journal of Visual Communication and Image Representation* (Elsevier). He also served on the program committee for the IEEE-EMBS Workshop on Wavelet Applications in Medicine in 1994, 1998, 1999 and 2004. Dr. Laine was recently elected to ADCOM of the IEEE Engineering in Medicine and Biology Society, and is Chair of Technical Committee (TC) on Medical Imaging for the EMBS, and a member of the TC of IEEE Signal Processing Society, BISP (Biomedical Imaging and Signal Processing). He was the Program Chair for the IEEE EMBS conference in 2006, held in New York City and is the Program Co-Chair for IEEE International Symposium on Biomedical Imaging (ISBI) in 2008. He is Vice President elect of Publications for the IEEE EMBS, starting in January 2008. He is a Senior Member of IEEE (Institute of Electrical and Electronics Engineering) and a Fellow of AIMBE (American Institute for Medical and Biological Engineering). His research interests include methods of multi-resolution analysis applied to problems in medical imaging, image analysis and signal processing, computational biology, computed aided diagnosis, pattern recognition in biology, biometrics and applied mathematics.

Biography of Jasjit Suri

Jasjit S. Suri, MS, PhD, MBA, Fellow AIMBE, is an innovator, visionary, scientist, and an internationally known world leader, has spent over 25 years in the field of biomedical engineering/sciences, software and hardware engineering and its management. During his career in biomedical industry/imaging, he has had an upstream growth and responsibilities from scientific Engineer, Scientist, Manager, Director R&D, Sr. Director, Vice President to Chief Technology Officer (CTO) level positions in industries like *Siemens Medical Systems, Philips Medical*

Systems, Fisher Imaging Corporation and Eigen Inc. & Biomedical Technologies, respectively and managed up to 100 people.

He has developed products and worked extensively in the areas of breast, mammography, orthopedics (spine), neurology (brain), angiography (blood vessels), atherosclerosis (plaque), ophthalmology (eye), urology (prostate), image guided surgery and several kinds of biomedical devices from inception phase to commercialization phase, including 510(K)/FDA clearances. Under his leadership, he has obtained over five FDA clearances in Urology, Angiography and Image Guided Surgery Product Lines ranging from 1000 pages to 5000 pages submissions. He has conducted in vivo and ex vivo validations on biomedical devices and surgery systems. Dr. Suri has developed several collaboration programs between University–Industry partnerships. He has managed funds ranging up to ten million dollars. He has very successfully built IP portfolios during his career bringing attraction for larger OEMs spin-offs. *Dr. Suri has over 60 US/European Patents, over 25 books and over 300 peer-reviewed articles*. He is a well-known speaker and has spoken over 50 times at national and international levels. Dr. Suri has won over 50 scientific and extracurricular awards during his career.

He received his Masters from University of Illinois, Chicago, Doctorate from University of Washington, Seattle, and Executive Management from Weatherhead School of Management, Case Western Reserve University (CWRU), Cleveland. Dr. Suri was crowned with President's Gold medal in 1980 and the *Fellow of American Institute of Medical and Biological Engineering (AIMBE)* for his outstanding contributions at Washington, DC. He believes in "getting a job done" using his strengths of innovation, strategic partnerships and strong team collaborations by bringing cross-functional and multi-disciplinary teams together both in-house and outsourcing relationships.